Synthesis of a novel adsorbent-photocatalytic material using a low energy route and its application to the remediation of water from contamination of 17-α ethinyl estradiol

A Thesis Submitted for the Degree of Doctor of Philosophy

By

Angeli Grace Todd

Department of Chemical Engineering, Brunel University London

2026

Table of Contents

Acknowledgements

I would like to extend a heartfelt thank you to my inspiring supervisor, Dr Lorna Anguilano for her wisdom, support, advice and encouragement throughout the duration of my PhD. I would like to thank my secondary supervisor, Prof. Paul Sermon for his knowledge, support and wisdom, all of the staff at the Experimental Techniques Centre, Brunel for their time and expertise, particularly Dr Uche Onwukwe for her brilliance and patience. I would like to thank the staff from environmental sciences at Brunel for their time and their expertise, and the researchers at Kingston University, particularly Dr Heba Ghazal and Bhumi Rajendrakumar. Most importantly, I owe a debt of gratitude to my wonderful loving husband whose faith in me never wavered, and without his unyielding belief in me I could not have finished. This has been a long road fraught with many failures and successes, and I owe the completion of this PhD to the many people who have worked with me and helped me realise my vision.

List of Acronyms and Abbreviations

Abbreviation	Meaning
AC	activated carbon
AFM	Atomic force microscopy
AOP	Advanced Oxidation Processes
ASP	Activated Sludge Process
$Ca(OH)_2$	calcium hydroxide
CaHGMs	calcium carbonate coated hollow glass microspheres
CEC	contaminant of emerging concern
E2	17β-estradiol
EDA	ethylene diamine
EDC	endocrine disrupting compound
EDX	energy Dispersive X-Ray Spectroscopy
EE2	17-α-ethinyl estradiol
EG	ethylene glycol
FT-IR	Fourier Transform Infrared Radiation
GAC	Granular activated carbon
HAP	hydroxyapatite
HAP-HGMs	hydroxyapatite coated HGMs
HGMs	hollow glass microspheres
HPLC	High Performance Liquid Chromatography
HRT	hydraulic retention
KOH	potassium hydroxide
LC-MS	Liquid Chromatography Mass Spectrometry
LoD	Limit of Detection
LoQ	Limit of Quantification
MBR	membrane bioreactor
MeOH	methanol
MLSS	mixed liquor suspended solids
NaOH	sodium hydroxide
PNEC	Predicted no effect concentration
POP	persistent organic pollutant
ROS	Reactive Oxygen Species
ScSh-HAP-anatase	Hydroxyapatite derived from scallop shell doped with anatase
SEM	Scanning electron microscopy
SRT	sludge retention time
SSA	specific surface area
TEOS	tetraethyl orthosilicate
TOC	Total organic carbon
TGA	Thermogravimetric analysis
TNW	Series of reactions using sol gel synthesis
TOC	Total organic carbon
TPA	tetra propyl ammonium hydroxide
UF	ultrafiltration
UV	ultraviolet

Abbreviation	Meaning
UV/Vis	Ultraviolet Visible light
XRD	X-Ray Diffraction

Abstract

Endocrine-disrupting compounds such as 17α-ethinylestradiol (EE2) pose significant risks to aquatic ecosystems and human health, necessitating the development of advanced water purification materials. This thesis presents the synthesis and characterization of a novel composite coating of hydroxyapatite (HAP) and titanium dioxide (TiO_2) applied to hollow glass microspheres (HGMs) for the efficient removal of EE2 from aqueous systems. The composite was fabricated via a sol-gel assisted deposition method, leveraging the high surface area of HGMs and the complementary adsorption–photocatalytic properties of HAP and TiO_2.

Comprehensive material characterization was performed using scanning electron microscopy (SEM), energy-dispersive X-ray spectroscopy (EDX), X-ray diffraction (XRD), Fourier-transform infrared spectroscopy (FT-IR), and atomic force microscopy (AFM) to confirm morphological, structural, and functional properties of the composite. Surface area and porosity were evaluated through BET N_2 adsorption isotherms. EE2 degradation and residual concentrations were quantified through high-performance liquid chromatography (HPLC) and liquid chromatography–mass spectrometry (LC-MS). The composite coatings demonstrated superior adsorption–photocatalytic performance compared to individual HAP and TiO_2 coatings, attributed to synergistic interactions that enhanced EE2 binding and photodegradation efficiency.

Kinetic analysis revealed rapid removal rates, while repeated use confirmed the composite's structural stability and reusability. Notably, the composite materials outperformed the current industry standard – activated carbon – in both removal efficiency and overall cost-effectiveness under comparable experimental conditions. These findings underscore the potential of hydroxyapatite–TiO_2 composites as next-generation materials for sustainable water purification, offering a promising strategy to mitigate emerging contaminants in aquatic environments.

1. Introduction and Research Aim

1.1 Water Contamination

Monitoring the quality of the water supply reveals the presence of contaminants, in particular, a class of compounds referred to as “Contaminants of Emerging Concern” or CECs. CECs refer to chemicals and biological agents – both naturally occurring and of synthetic origins – that are not subject to regulation or are poorly controlled and so are released into the environment without restriction. The list of compounds that are classed as emerging contaminants is extensive and is constantly changing as more emerging contaminants are identified. Persistent Organic Compounds (POPs) fall into this category.

The list of CECs includes but is not limited to pharmaceutical compounds such as antibiotics, anti-inflammatory drugs, antidepressants, anti-diabetics, analgesics, hormones, illegal drugs, cosmetics, sunscreen, insect repellents, surfactants, detergents, disinfectants, nanomaterials, microplastics, pesticides, solvents, fertilisers, drugs, pharmaceutical drugs, recreational drugs, pesticides, hormones, dyes, solvents, raw sewage, heavy metals, endocrine disruptors and pathogens (Rocha R., 2022), (Morin-Crini, et al., 2022).

The compounds mentioned above are intrinsic to the modern lifestyle and their advantages are clear, e.g. fertilisers increase food production and pharmaceutical drugs increase lifespan and improve quality of life. The usefulness of these compounds and their widespread use mean many are continuously released into the environment. The constant discharge of these compounds into the environment can have serious effects on the biosphere, which can include the growth of antibiotic-resistant bacteria, the accumulation of compounds such as microplastics in organisms, and the disruption of the endocrine systems in organisms.

The focus of this work is on the EDC is on 17α-ethinyl estradiol (EE2), which is an EDC that is a synthetic female hormone and its presence in waterways means it has the potential to

seriously disrupt the endocrine systems of living organisms. EE2 is under-researched compared to the natural hormone E2, which has been the subject of more investigations with the aim of removing E2 from water. Processes to removed EDCs from wastewater and potable water are inefficient (Jung, 2013) meaning new technologies must be developed to improve removal rates of EDCs.

The highest EE2 level in water samples was measured in Brazil with 48 mg/L, which exceeds the mass of EE2 contained the combined pill Femodene (Bayer AG, 2023). This exceeds the predicted concentration at which EE2 is thought to have no detectable effect (i.e. its predicted no effect concentration or PNEC; 0.035 ng/L (35ppt or 0.000035 ppm) of EE2 (Klaic, 2022), but there is concern about the limits of detection of EE2 analytically which are often much higher than the PNEC. The methods of control or abatement of EE2 in water systems may be adsorption (Rovani, 2014), chemical (e.g. photocatalysis (de Liz, 2018) or biological, but they should not lead to even more toxic biproducts. The metabolites of EE2 include 2-OH EE2, 3-OG EE2 and 3-OS EE2 (Klaic, 2022), which are displayed in Figure 1. Major human metabolic pathways of EE2.

Figure 1. Major human metabolic pathways of EE2

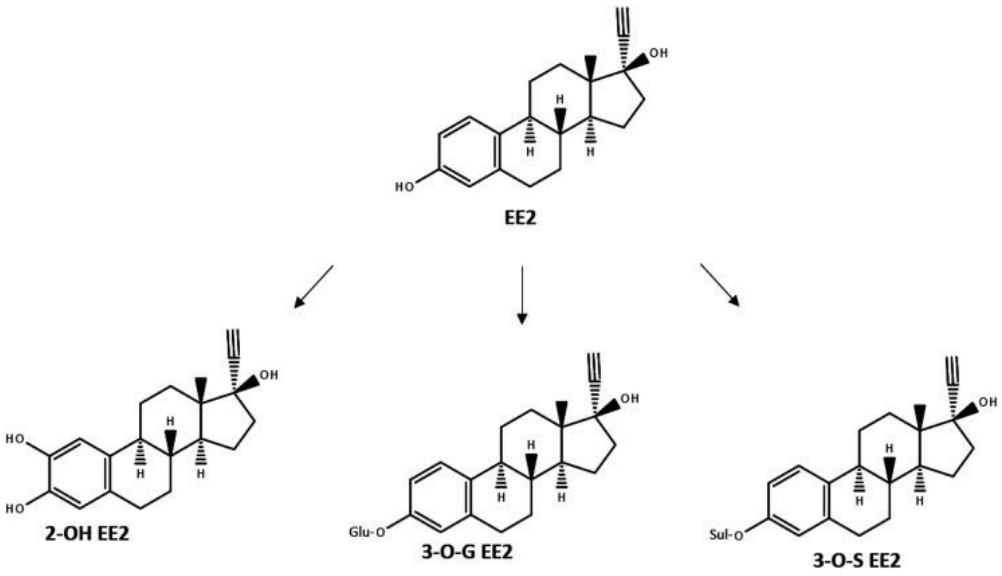

1.2 Extent of EE2 Contamination

The Pirajibu and Sorocaba rivers in Brazil contain more EE2 per litre than the combined hormonal contraceptive pill (de França, 2020). These rivers are the source of potable water for nearby communities and cities, and this excess of estrogen has numerous effects on the people and animals that rely on these rivers for water and their habitats. The Piracicaba River is displayed in Figure 2.

Figure 2. Piracicaba River, Brazil - one of the places with the highest measured EE2 contamination

North America, South America, Europe and Asia also contain lakes, streams, estuaries, groundwater, and seawater where the levels of synthetic estrogen exceed the predicted no effect concentration of 0.035 ng/L (Vella, 2018) – in some cases by several orders of magnitude. Across 282 municipal wastewater treatment plants in 29 countries, the average effluent concentration of EE2 was over 61 times greater than the lowest observed effect concentration (Tang, 2021). The concentrations of E1, E2 and EE2 as measured in the influent and effluent

of wastewater treatment plants are displayed in Figure 3.

Figure 3. Concentrations of E1, E2 and EE2 found in the influent and effluent of wastewater treatment plants globally.

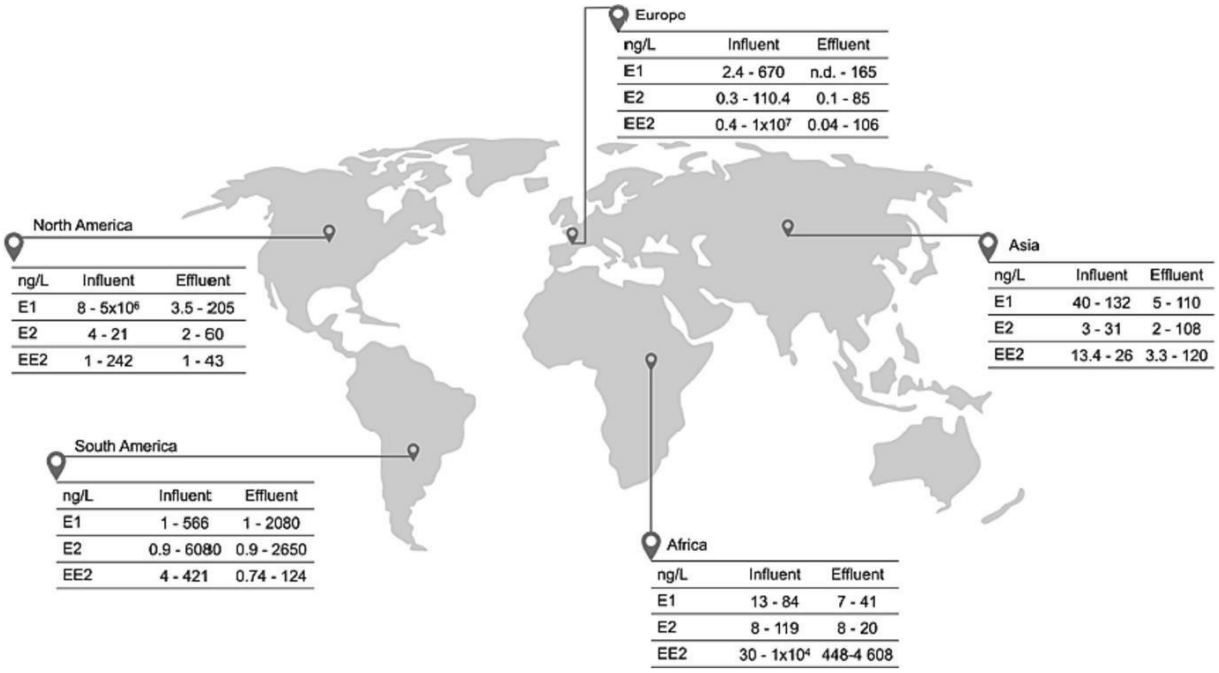

Approximately 720 kg year $^{-1}$ of EE2 is released into water sources (Combalbert, 2010). The major sources of EE2 contamination are through human urine, livestock wastewater, runoffs of manure and sewage sludge used agriculturally (Aris, 2014) and municipal wastewater (Johnson, 2000) as EE2 is discharged into the water due to processes that are capable of only incomplete removal of EE2 (Zhang, 2010). EE2 at low concentrations in the influents of sewage treatment plants is also a major source of EDCs, including EE2 as current methods of water purification are not fully capable of removing EE2 (Zhou, 2012). The concentrations of EE2 found in a selection of specific countries are presented in Table 1. Concentrations of EE2 found in water sources from various locations around the world.

Table 1. Concentrations of EE2 found in water sources from various locations around the world

Location	EE2 Concentration	Ref
Brazil (Sorocaba and Pirajibu Rivers)	4.5-48.2 μg L^{-1}	(de França, 2020)
Brazil (Alto Iguaçu basin)	5.83 μg L^{-1}	(Machado, 2014)
Brazil (Piracicaba River)	194 ng L^{-1}	(Torres, 2015)
Luxembourg (Alzette River)	76 ng L^{-1}	(Pailler, n.d.)
China (Guangzhou Municipal Treatment Station) Raw Sewage	94 ng L^{-1}	(Xu, 2014)
China (Guangzhou Municipal Treatment Station) Treated Sewage	5.6 ng L^{-1}	(Xu, 2014)
Hungary (Danube, Budapest)	0.124 ng L^{-1}	(Klaic, 2022)
Argentina (river water, Potrero de los Funes, San Luis)	8.84 ± 0.21 ng L^{-1}	(Scala-Benuzzi, 2018)
Argentina (Trapiche, San Luis)	7.57 ± 0.33 ng L^{-1}	(Scala-Benuzzi, 2018)
Argentina (Tap water Potrero de los Funes, San Luis)	2.51 ± 0.09 ng L^{-1}	(Scala-Benuzzi, 2018)
Argentina (Tap water San Luis)	1.75 ± 0.05 ng L^{-1}	(Scala-Benuzzi, 2018)
Argentina (Bottled water San Luis)	1.13 ± 0.04 ng L^{-1}	(Scala-Benuzzi, 2018)
Australia (Hawkesbury River)	n.d. – 29 ng L^{-1}	(Klaic, 2022)

1.3 Effect of EE2 on Organisms

As a synthetic hormone, EE2 interacts with organisms and affects the endocrine systems of living organisms. EE2 is therefore classed as an "endocrine disrupting compound" (EDC). The effect of EE2 on wildlife has been examined using species chosen for their relatively fast rates of growth and reproductive cycles. These species include: carp, fathead minnows, zebrafish, and rats. Male rainbow trout exposed to 2 ng/L showed disruption in testicular growth, while *Danio rerio* exhibited sex change ratios from exposure to 6 ng/L of EE2 which were sufficient to produce 100% female population (Clouzot, 2008).

The effects of EE2 on wildlife include premature oestrus, accelerated vaginal openings, low sperm counts, the production of egg cells in the testes, behavioural abnormalities, physical and sexual abnormalities, significantly increased instances of intersex organisms (carp, 3% expected, vs 30% identified). EDCs in general are also a potential cause of prostate and testicular cancer and reduced sperm production in humans, and decreased immune function and fertility in organisms (Rovani, 2014). The Lowest Observed Effect Concentration (LOEC), Predicted No Effect Concentration (PNEC) and maximum permissible concentration of EE2 are outlined in Table 2. Concentrations of EE2 related to safe EE2 levels.

Table 2. Concentrations of EE2 related to safe EE2 levels.

EE2 Measurement Index	Concentration	Ref
Lowest observed effect concentration	1 ng/L	(Leal, 2020)
Predicted No Effect Concentration	0.1 ng/L	(Leal, 2020)
Maximum permissible concentration	0.036 ng/L	(Dias, n.d.)

The impact of the presence of synthetic estrogen above its lowest effective dose are described in more detail in chapter 2, where the most significant effects include the impaired sperm motility, reduced fertilization, reduced embryo and larval survival (Bhandari, 2020), low sperm counts in males, and atypical oestrus cycles in females. Furthermore, at concentrations as low as a few ng/L EE2 is reported to "delay sexual maturity, alter sex determination and decrease the secondary sexual characteristics of exposed organisms" (Aris, 2014). Developing effective strategies, materials and methods for the removal of EE2 from wastewater treatment plant effluent is therefore urgent, timely, and the focus of this body of research.

1.4 Titanium Dioxide as a Photocatalyst for EE2 Destruction

A primary advantage of employing TiO_2 in photocatalytic applications is its robust oxidative capability coupled with chemical stability under UV irradiation. This allows for the efficient breakdown of a wide array of EDCs, including but not limited to pharmaceuticals, personal care products, and various industrial chemicals that exhibit resistance to traditional treatment methodologies.

The electron-hole pairs generated upon UV irradiation participate in redox reactions with water and molecular oxygen generating reactive oxygen species (ROS). The holes oxidize water to produce hydroxyl radicals ($\cdot OH$), while the electrons reduce oxygen to form superoxide anions ($O_2^{\cdot -}$). These ROS are highly reactive and capable of non-selectively oxidizing organic contaminants, including EE2, into CO_2, water, and less harmful byproducts. The benefits of TiO_2 as a photocatalyst are outlined in greater detail in Chapter 3, up to 100% of EE2 has been reported to be removed by TiO_2 photocatalysis (Coleman, n.d.). A potential route for the degradation of EE2 by TiO_2 is displayed in Figure 4. Degradation of pathway of EE2 using TiO2 (25).

Figure 4. Degradation of pathway of EE2 using TiO_2 (25)

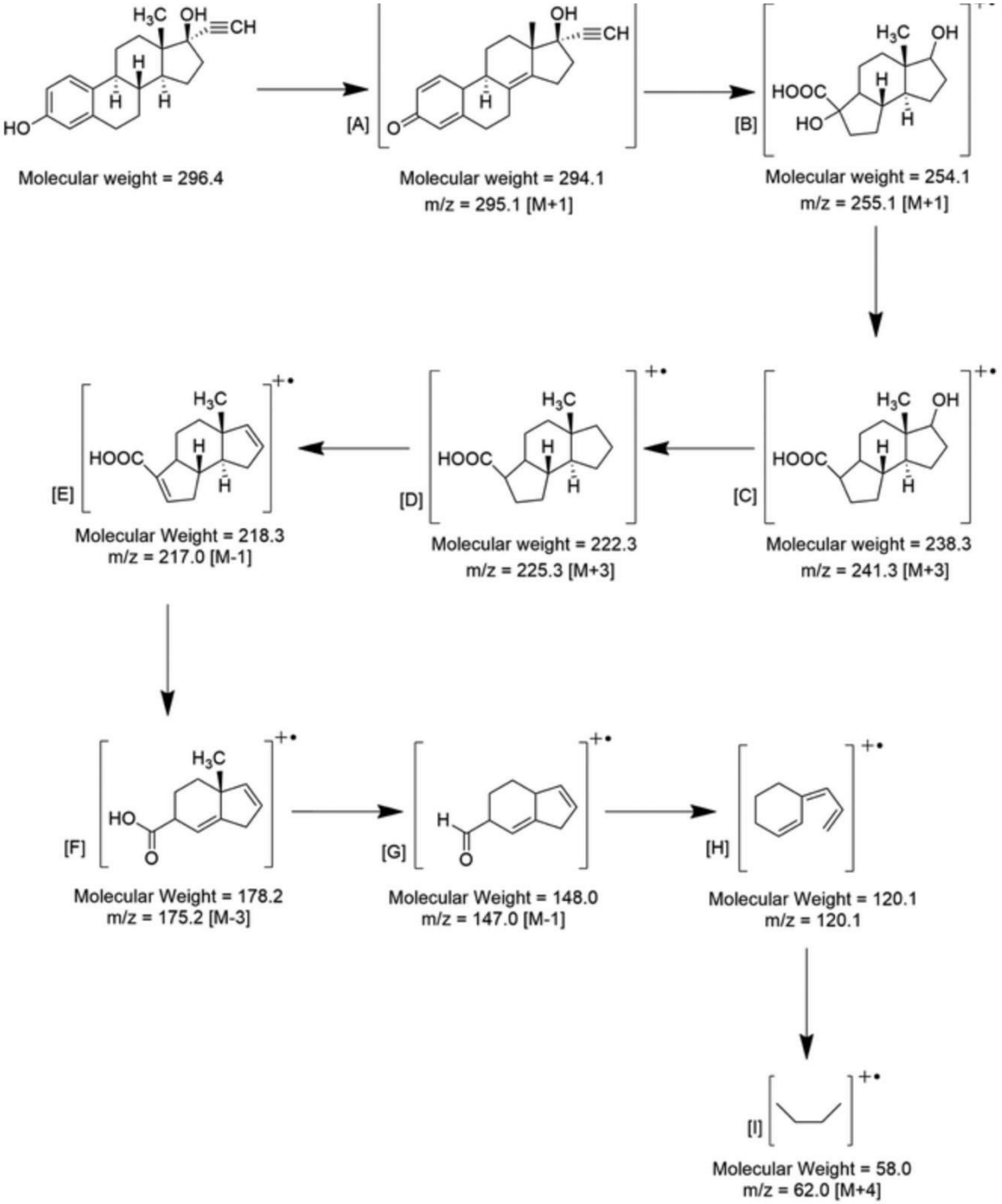

1.5 Hydroxyapatite Use in Water Purification

Hydroxyapatite (HAP) has emerged as a promising material in water purification due to its inherent physicochemical properties, which enable efficient removal of various contaminants from water sources. HAP possesses a high specific surface area and abundant surface functional groups, making it adept at adsorbing diverse contaminants from water. These contaminants include heavy metals, organic pollutants, dyes, and phosphates. The surface of HAP chemistry allows for interactions such as ion exchange, complexation, and surface adsorption, leading to the removal of pollutants from aqueous solutions. The applications of HAP in water purification have been included in Table 3. Applications of hydroxyapatite for water purification.

Table 3. Applications of hydroxyapatite for water purification

Applications of Hydroxyapatite for Water Purification		
Application	Description	Ref
Heavy Metal Removal	HAP demonstrates a particular affinity for heavy metal ions due to its ion-exchange capacity and specific binding sites. The honeycomb structure of HAP also contributes to it ion-exchange properties. The surface phosphate groups in HAP can complex with metal ions, facilitating their removal from water through adsorption or ion exchange processes. This property makes HAP effective in reducing heavy metal concentrations in water, mitigating their harmful effects. Examples include Pb^{2+}, Zn^{2+}, V, Co^{2+}, Sr^{2+}, U, Cr^{3+}	(Xiao. Q., 2024) (Jayaweera, 2018) (Shanika Fernando, 2021)
Fluoride Removal	The high affinity of HAP for fluoride ions in water is attributed to its structural similarity to the mineral component of bones and teeth. HAP has been utilized to adsorb fluoride ions through mechanisms such as ion exchange and surface complexation, aiding in the removal of excessive fluoride concentrations in drinking water, which could otherwise cause health issues like dental or skeletal fluorosis.	(Shanika Fernando, 2021)
Arsenic Mitigation	HAP has shown potential in adsorbing arsenic species from water. Its surface properties allow for interactions with arsenic species, reducing their concentration in water and thereby addressing the health hazards associated with arsenic contamination in drinking water sources.	(Shanika Fernando, 2021)

Microbial Contaminant Control	While primarily recognized for its adsorption capabilities, HAP's bioactive nature and biocompatibility also render it useful for controlling microbial contaminants. HAP-based coatings or materials have been explored for their ability to inhibit bacterial growth and biofilm formation, contributing to water disinfection and hygiene. Examples include Escherichia coli and Staphylococcus aureus	(Jayaweera, 2018)
Removal of Organic Compounds	HAP's adsorption capacity extends to various organic pollutants present in water, including dyes such as blue 19 dye, red 198 dye, methylene blue dye. 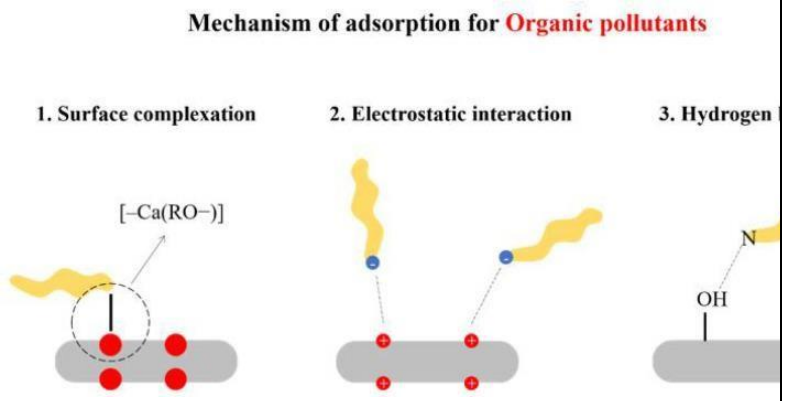	(Balasooriya, 2022)

From the applications given in the table, hydroxyapatite demonstrates multifaceted potential in water purification due to its adsorptive capacity, ion-exchange properties, surface chemistry, and structural characteristics. Its versatility in adsorbing diverse contaminants positions HAP as a promising material for addressing water quality challenges across various applications in environmental remediation and water treatment technologies. One of the questions that this thesis aims to answer, is could HAP be used to adsorb EE2?

1.6 The Solution to EE2 Contamination

This PhD thesis focuses on addressing the challenge of removing EE2 from water by leveraging a novel approach that combines the adsorption abilities of hydroxyapatite with the photocatalytic properties of titanium dioxide. Hydroxyapatite presents a potential opportunity for adsorptive removal of EE2 from aqueous solutions, as it is well known for its high surface area and affinity for various contaminants, which include metal ions, bacteria, and organic pollutants such as dyes. Hydroxyapatite has also been investigated as a drug delivery scaffold, demonstrating its affinity for pharmaceutical compounds. This property is predicted to be applicable to EE2, and HAP has therefore been used in this work to act as an adsorbent for EE2. The use of hydroxyapatite as an adsorbent for EE2 removal is novel as there is currently no existing literature describing the removal of EE2 from aqueous solution using HAP as the adsorbent. However, HAP as an adsorbent for 17β-estradiol has been reported in the literature (Li, 2020), which indicates that HAP is likely to be an effective adsorbent for EE2. This will be tested and reported in the results and discussion section of this thesis.

The adsorbent properties of hydroxyapatite will be complemented by the photocatalytic properties of titanium dioxide. The purpose of hydroxyapatite is to adsorb the EE2 and related compounds, and the purpose of TiO_2 is to destroy the EE2 molecules. The integration of

titanium dioxide as the photocatalyst harnesses the proven ability of titanium dioxide to generate reactive oxygen species upon exposure to UV light, which would then enable the mineralisation of EE2 into carbon dioxide and water. Titanium dioxide is a photocatalyst with a proven ability to cause photocatalytic degradation of EE2, is non-toxic, cheaper than photocatalysts of comparable effectiveness, can be doped with a range of material to tune tis band gap, and can be incorporated into materials either through co-precipitation of TiO_2 powder or layered on substrates using the sol-gel process, where the morphology of the final TiO_2 product can be optimised by altering reaction conditions. This means that titanium dioxide with nanoparticle morphology can be secured to a substrate providing the benefits of nanoparticles – an increase in surface area available for reactions, while avoiding the disadvantages of nanoparticles – difficulty recovering the nanoparticles and also a tendency to aggregate in solution, i.e. loss to the environment and loss of nanoparticle morphology.

The combination of HAP and TiO_2 is expected to yield a robust and efficient EE2 removal system by exploiting the useful properties of the HAP as an adsorbent and TiO_2 as a photocatalyst. This thesis aims to achieve the growth of high surface area hydroxyapatite on the surface of glass microspheres, to explore and elucidate the mechanisms governing the adsorption of EE2 on to the surface of hydroxyapatite, to optimise the process of immobilising titanium dioxide on to the surface of the HAP-coated glass microspheres, and to determine and understand the mechanisms governing the adsorption of EE2 on to the surface of the combined HAP – TiO_2 material – therefore defining whether the presence of TiO_2 hinders the adsorption of EE2 on to the surface of HAP. Furthermore, sustainable resource management and production of green materials have also been considered in this body of work. It is of critical importance to use develop methods that sustainably produce the materials that will be used for the removal of EE2. Hence, a focus of this work has been to used low temperature methods to produce the materials, avoiding high calcination and reaction temperatures, and using chemical

methods at ambient temperatures wherever possible.

The research conducted entails a multi-faceted approach encompassing material synthesis, characterisation, and kinetic studies with the overall aim of generating a new method for EE2 removal from water. By using an innovative approach towards growing hydroxyapatite, optimising the sol-gel method for titanium dioxide synthesis, and integrating fundamental insights from the kinetic studies of adsorption, this study endeavours to provide a deeper understanding of the removal mechanisms and establish a novel, sustainable and efficient methodology for addressing EE2 contamination of water resources.

Research previously conducted on methods to remove EE2 has focused on optimising activated carbon, using biological methods such as the activated sludge process (ASP), using adsorption processes, and using advanced oxidation processes (AOPs). For the purposes of this thesis, the techniques that will be focused on are adsorption processes and AOPs. These techniques will be combined and the efficacy of hydroxyapatite as an adsorbent and subsequently a combined hydroxyapatite-TiO_2 dual system that exploits the adsorptive properties with the photocatalytic properties of titanium dioxide.

Current methods of removing EE2 from water focusing on either physical separation of EE2 from water using membrane processes or adsorbents, which create a secondary waste stream containing EE2, or using advanced oxidation processes to destroy the EE2, which are effective but are either expensive – in the case of ozonation – or are capable of producing transformation products that remain in the water which may be more problematic for the environment than EE2 alone.

1.7 Green Methods for Water Purification

Green water purification methods adhere to the principles of green chemistry and sustainable engineering, while effectively removing contaminants from water. Green methods aim to minimise environmental impact, reduce energy and resource consumption and support long term ecological and human health and safety. In this work five key characteristics have been used to define a method as green: minimal use of hazardous substances during material synthesis and method deployment; energy efficiency and renewable inputs; reusability and facile regeneration of materials; use of abundant, non-toxic and materials with benign products of degradation if released into the environment; and low environmental/carbon footprint and end-of-life impact.

Green water purification avoids or drastically reduces the use of toxic reagents or solvents. For instance, photocatalytic degradation using benign semiconductors (e.g., TiO_2 under solar light) eliminates the need for hazardous oxidants (Fujishima, 2008). Green methods strive for low energy consumption or utilize renewable energy sources. Solar-driven processes like visible-light photocatalysis or passive adsorption mechanisms meet this criterion (Ong, 2016). A feature of green purification is the reusability of adsorbents or catalysts. Materials that maintain performance over multiple cycles without significant degradation reduce waste and resource use (Mohan, 2014). Green methods utilise earth-abundant or naturally-derived materials, which includes clays, agricultural waste-derived adsorbents, or carbon-based materials such as graphene and biochar (Crini, 2019). Green technologies ensure low life-cycle impacts, meaning they create little waste, use fewer synthetic reagents, and cause minimal secondary pollution. They are evaluated based on life cycle assessment (LCA) and eco-efficiency metrics (Corominas, 2013).

1.8 Research Aim

The aim of this thesis is to synthesize a novel hybrid adsorbent-photocatalyst composite material capable of removing EE2 from water, report the characterisation data of the intermediate materials leading to the composite and of the composite itself, while using a green and sustainable, synthetic route. This research aim will be achieved with the following objectives:

1. Create a multilayer composite using hollow glass microspheres as the substrate on to which hydroxyapatite is grown, followed by coating with titanium dioxide. The process developed must be reliable and repeatable, and green, sustainable and low energy.
2. Produce the hydroxyapatite layer from biological (food waste) sources and also chemical reagents to act as the adsorbent material. The process to achieve this must be a low energy process, avoiding the use of high calcination temperatures typical of hydroxyapatite synthesis. The hydroxyapatite produced must have a high surface area typical of hydroxyapatite produced using chemical precipitation, in order to ensure the hydroxyapatite produced has the maximum adsorption potential possible.
3. Grow titanium dioxide on the surface of the hydroxyapatite-hollow glass microsphere composites using an optimised process, where the role of titanium dioxide is to provide photocatalytic capacity to the material. The process used to obtain titanium dioxide must be capable of producing a coating that retains the high surface area of the hydroxyapatite component, meaning the titanium dioxide layer should have defined and consistent microstructures. The synthesis process must avoid the use of high temperatures and minimise the use of chemical reagents in order to be a green and sustainable synthetic route, and the parameters used in the production method must be investigated to optimise the production of the titanium dioxide microstructures.
4. The titanium dioxide microstructures and hydroxyapatite must be grown on a substrate of hollow glass microspheres, where the role of the hollow glass microspheres is to lend

compressive strength and size uniformity to the composite material while also decreasing the density of the composite. It is essential that the HGMs are treated to accommodate a hydroxyapatite layer that is chemically bonded to the entire surface of the hollow glass microspheres, producing a composite material. This is to ensure the novel composite material can be re-used many times, with little risk of the hydroxyapatite becoming dislodged by mechanical action.

5. Characterise the novel composite material using SEM to investigate surface structures and morphology, EDX to investigate the chemical composition of surfaces and boundaries between layers of a cross section of the composite, XRD to determine crystalline phases and their percent compositions, FT-IR to confirm the presence of functional groups in order to characterise the material, and also to track the progress of reactions, BET to elucidate surface area and porosity, AFM to measure surface roughness of the microspheres before and after hydroxyapatite growth, and Raman to characterise the titanium dioxide phases.
6. Finally, this thesis aims to investigate the ability of this novel composite to remove EE2 from aqueous solution at a concentration of 10 mg/L – an environmentally relevant concentration – by measuring the changes in EE2 concentration during and after exposure to the novel composite under UV radiation and using HPLC-UV to determine and quantify EE2 removal. The kinetics of EE2 removal will be investigated and compared with kinetic models in order to assess the model that best describes the kinetics of EE2 removal.

The successful production of purified water is the overall aim of this study, and given the current droughts and wildfires experienced by much of the globe during summer (as a direct result of climate change), scientific research that focuses on green, low energy and sustainable methods of purifying water are critically important, timely and relevant to contemporary issues

of the 21st century. Although every effort has been made to address the relevant issues within this study, this scheme of work has limitations, which include:

1. The concentration of EE2 in ultrapure water was selected to model more realistic environmental concentrations of EE2 found in water systems. However, this study does not include minerals likely to be found in water systems such as Na^{+}, Ca^{2+}, or Mg^{2+}, or natural organic matter (NOM) that could be modelled using humic acid, as it was decided that the addition of these species would impact the adsorption data. Future work would benefit from repeating these adsorption experiments using water spiked with minerals and NOM, however the aim of this body of work is to determine whether hydroxyapatite and calcium carbonate have the ability to adsorb EE2.
2. This work does not attempt to measure the concentration of conjugates of EE2, which can also have estrogenic effects. Future work would be well served by establishing the concentrations of these conjugates and by characterising and determining their chemical structures, which would then allow researchers to use the chemistry of the conjugates to design new and effective removal strategies.
3. This study has not sought to optimise the photocatalyst, but only intends to determine whether the presence of the photocatalyst TiO_2 impedes the adsorption of EE2 by hydroxyapatite in a way that materially decreases the effectiveness of the adsorption of EE2. The band gap of TiO_2 is high and requires ultraviolet light to excite electrons enough to cross the band gap. Doping the TiO_2 with elements that reduce the size of the band gap to allow visible light to be enough to cause excited electrons to cross the band gap would allow the material to be usable in the presence of sunlight, making this material a truly green and sustainable way of purifying water.

1.9 Thesis Structure

This thesis follows the traditional structure of introduction, literature review, methods, results, discussion, conclusion and future work. The content of the thesis is outlined below.

1. Chapter 1 – Introduction: this chapter introduces the problem that is estrogen contamination of water sources, and explains the proposed solution to the problem that will be explored and investigated in this body of work, namely, a combined system using hydroxyapatite as an adsorbent and titanium dioxide as a photocatalyst. The research aims and objectives of this body of work, and a description of subsequent chapters.
2. Chapter 2 – Estrogen Contamination of Water: this chapter describes the problem of water contamination with contaminants of emerging concern (CECs), the extent of estrogen contamination globally, the chemical properties of natural and synthetic estrogenic molecules, sources of estrogen release into the environment, the amounts of estrogen found in water sources, the effects of elevated levels of estrogen on wildlife, current conventional methods for estrogen removal from water, an assessment of the effectiveness of existing estrogen removal methods, and reports recent advances in estrogen removal with a focus on adsorbents used for estrogen removal and photocatalysts used for estrogen removal.
3. Chapter 3 – Titanium dioxide: chapter 3 is dedicated to the properties of titanium dioxide, description of polymorphs, morphologies generated by various synthetic routes, mechanism of photocatalysis and outcomes of using TiO_2 as photocatalyst to degrade estrogenic molecules as reported in the literature. Methods to synthesise composites of titanium dioxide and hydroxyapatite are included in this section. The procedures to scale up from lab-scale, to bench-pilot scale, to pilot-scale, to field deployment are outlined here.

4. Chapter 4 – Hydroxyapatite (HAP): this section of the thesis describes the properties of hydroxyapatite and common production methods. Also included in this section are the outcomes of hydroxyapatite made from biological sources and comparison of morphologies and properties where available in the literature. When possible the porosity achieved by each method is reported. The use of HAP as an adsorbent for contaminants of emerging concern is discussed – in particular pharmaceutical drugs and organic compounds similar to estrogen. At the end of this chapter recent literature on composites of TiO_2 and HAP are described and reported, including information pertaining to synthesis methods, morphologies generated and applications.
5. Chapter 5 – Hollow Glass Microspheres (HGMs): contained in this chapter is a description of the properties of HGMs and their typical uses. Also discussed in this chapter is literature where HGMs have been used as substrates for floating photocatalysts and the outcomes of these experiments. The characterisation data obtained for hollow glass microspheres is contained in this section.
6. Chapter 6 – Methods chapter: the methods chapter lists all of the characterisation techniques used including brief description of how the process works with diagrams, instrument detection limits and advantages, disadvantages and limitations of the techniques. This chapter goes on to describe the synthesis routes developed for growing hydroxyapatite on the HGM substrates and depositing TiO_2 microstructures onto these Hydroxyapatite-HGMs. Also included in the methods chapter is the process used to measure the changing EE2 concentration using UV/Vis spectroscopy.
7. Chapter 7 - Results of HGM selection and surface preparation: this chapter contains a report on the results of characterisation of the hollow glass microspheres, on methods of surface preparation attempted and the results of the different methods used to prepare the hollow glass microspheres for coating.

8. Chapter 8 – Results of Hydroxyapatite growth on HGMs: this chapter is dedicated to the characterisation data on the HAP-HGM composite produced, and contains an assessment of the most effective way to ensure complete conversion of calcium carbonate into hydroxyapatite. This section contains a comparison of hydroxyapatite produced from food waste and hydroxyapatite produced from chemical reagents. Both methods are evaluated and the method most appropriate for producing hydroxyapatite for EE2 removal are explained with reasons given.
9. Chapter 9 – Results of TiO_2 Method Optimisation and Deposition on HAP-HGMs: here the results of the experiments designed to optimise the synthesis of the titanium dioxide microstructures are reported, and the characterisation data on the full composite of TiO_2-HAP-HGM is included here.
10. Chapter 10 – Characterisation of the final material: this chapter contains the characterisation data for the final material, a hierarchical structure consisting of hollow glass microspheres coated in hydroxyapatite, which is coated with titanium dioxide.
11. Results of EE2 Removal from Aqueous Solution: contained in this chapter are the results of EE2 removal from water using the composite, HAP-HGMs, calcium-carbonate coated HGMs, anatase, and a composite of HAP-HGMs and anatase, measured using HPLC with a fluorescence detector. Also included here is a comparison of kinetic adsorption models where the adsorption model that best fits the data for EE2 removal is determined.
12. Chapter 12 – Discussion: this chapter discusses the results reported in chapter 7, 8, 9 and 10, comparing the characterisation data for the hydroxyapatite and titanium dioxide produced with data reported in the literature for hydroxyapatite and titanium dioxide. The characterisation data for the novel composite is compared to data for its constituent species, and an explanation for the differences between the two is attempted. Finally, a comparison is made between the removal efficiencies obtained by the novel TiO_2-HAP-

HGM composite and water purification methods previously described in Chapter 2 in the literature review section.

13. Chapter 13 – Conclusions: this final chapter refers back to the aims of the project, recalls the objectives of this work and gives a short summary of the outcomes that were achieved, an assessment of the extent to which these objectives were achieved, an explanation regarding which outcomes were not achieved and why, and reiterates the originality of this project and its timeliness with respect to contemporary challenges. Finally, this chapter briefly discusses the natural progression of this work, predicting how this hybrid adsorbent-photocatalytic composite will impact the field of water purification in the years to come.
14. Chapter 14 – References: the papers and literature cited throughout this body of work are listed in this chapter.

2. Chapter 2 – EE2 Contamination of Water

2.1 Introduction

The prevalence of endocrine-disrupting compounds (EDCs) in water sources has become a paramount concern in recent years due to their adverse effects on aquatic ecosystems and potential risks to human health. Among these compounds, 17α-ethinylestradiol (EE2), a synthetic estrogen commonly used in oral contraceptives, has gained significant attention for its persistence in aquatic environments and detrimental impact on aquatic life. EE2, even at trace concentrations, poses a substantial threat as it can interfere with the endocrine systems of aquatic organisms, leading to reproductive and developmental abnormalities.

The widespread occurrence of EE2 in water bodies is primarily attributed to its chemical stability, prolonged presence in wastewater effluents, and the inefficiency of conventional water treatment processes in completely eliminating this compound. Conventional methods, including coagulation, sedimentation, activated carbon adsorption, and biological treatments, although effective to some extent in removing certain pollutants, often fall short in efficiently targeting and eliminating EE2 due to its low concentrations and resistance to degradation.

Coagulation and sedimentation processes, commonly employed in water treatment, often lack specificity in selectively removing EE2, resulting in limited efficiency. While activated carbon adsorption exhibits promising adsorptive capabilities, it encounters challenges with EE2's low aqueous solubility and competition with other dissolved organic compounds, reducing its efficacy. Biological treatments, though environmentally friendly, are often inadequate in completely degrading EE2 to non-toxic byproducts.

The limitations of these conventional methods necessitate innovative and advanced treatment strategies to mitigate the EE2 contamination crisis in water sources. The urgency to develop

efficient, sustainable, and cost-effective techniques for EE2 removal from water has prompted extensive research into alternative approaches that can complement or surpass the limitations of existing treatment methodologies.

This chapter aims to provide a comprehensive overview of the challenges posed by EE2 contamination in water and critically evaluates the strengths and limitations of conventional water treatment methods in addressing EE2 removal. By examining the shortcomings of these techniques, this chapter lays the groundwork for the subsequent discussion on novel approaches, including adsorption, photocatalysis, and hybrid systems, exploring their potential in overcoming the limitations and achieving enhanced EE2 removal efficiencies in water treatment processes. Additionally, this exploration will consider factors such as cost, scalability, and environmental impact, providing insights into the holistic landscape of EE2 removal technologies and paving the way for innovative solutions in water remediation strategies.

2.2 17 α-ethinyl estradiol (EE2)- the Contaminant of Interest

This section describes the physical and chemical properties of 17α ethinyl estradiol (EE2), before using these properties to describe why EE2 is comparatively more resistant to degradation than its natural analogue, E2, and why EE2 presents such a problem to the aquasphere. Included in this section are the chemical structures, physical and chemical properties such as molecular masses, solubility in water, pK_a, limits of quantification and detection, and lowest effective dose. The molecule displayed below in Figure 5 is EE2 with carbons numbered according to the IUPAC system.

Figure 5. The chemical structure of EE2, note the alkyne group bonded to C-17.

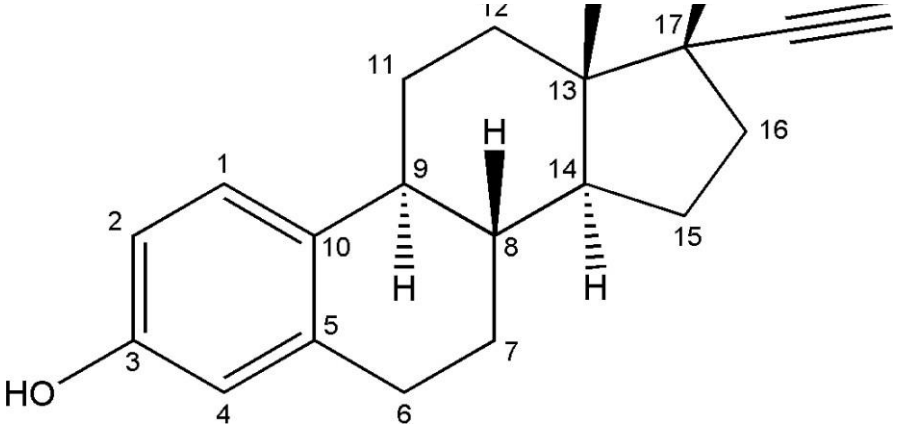

The three natural estrogens estrone (E1), 17β estradiol (E2), and estriol (E3), in addition to 17α ethinyl estradiol (EE2). The structures of the estrogens are very similar, with the main differences being the functional groups bonded to C_{17} and C_{16}. A ketone group is bonded to C_{17} in E1, while E2 contains a hydroxyl group. The chemical structures of the three natural and one synthetic estrogen are displayed below in Table 4. The names, abbreviations and chemical structures of the natural estrogens E1, E2 and E3 and the synthetic estrogen.

Table 4. The names, abbreviations and chemical structures of the natural estrogens E1, E2 and E3 and the synthetic estrogen EE2.

Estrone – E1	17β estradiol – E2
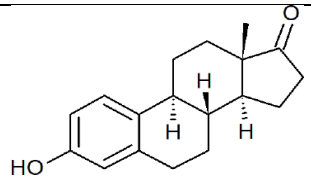	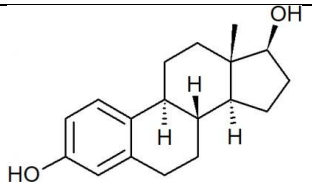
Estriol – E3	17α ethinyl estradiol – EE2
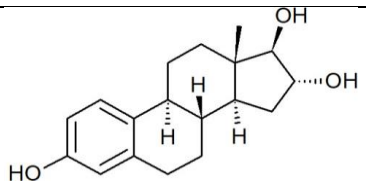	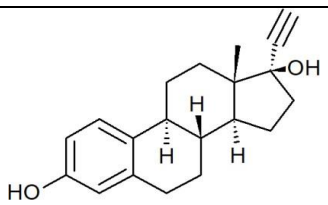

The octanol/water partition coefficient – K_{ow} – is a chemical property of EE2 that is key to understanding the extent of the lipophilic and hydrophobic properties of EE2. $LogK_{ow}$ quantifies the tendency of EE2 to partition between aqueous (water) and organic (octanol) phases, where octanol is used to simulate a lipid rich system, and water is used as the aqueous phase. The equation used to obtain K_{ow} is formed by dividing the equilibrium concentration of EE2 in octanol by the equilibrium concentration of EE2 in water:

$$K_{ow} = \frac{[EE2]_{octanol}}{[EE2]_{water}} \quad \text{Eqn. 1}$$

A high value for K_{ow} indicates that a given molecule exists in higher concentrations in the organic phase, which suggests a hydrophobic and/or a lipophilic nature. A strong lipophilic nature would mean the target molecule has the potential to bioaccumulate in fatty tissues. Conversely, lower values of K_{ow} indicate the target molecule prefers the aqueous phase, and a hydrophilic and/or lipophobic nature, meaning the potential for bioaccumulation in fatty tissues is more limited than for a higher K_{ow}. The lipophilic nature of EE2 means it can also be sequestered in organic matter/sediments/biofilms limiting the interaction of EE2 with cells, in comparison with E2 which is more hydrophilic than EE2 so is less readily sequestered than EE2.

The values of $logK_{ow}$ for the natural estrogens E1, E2, and E3 and the synthetic estrogen EE2 are given in Table 2, where the $logK_{ow}$ for EE2 is 4.14, and the value of $logK_{ow}$ is 2.94. This means that EE2 has a concentration in the octanol phase that is more than a factor of 10 greater than the concentration of E2 in the octanol phase. This significantly higher affinity for the organic phase indicates that EE2 is much more hydrophobic and/or lipophilic than E2, which itself may indicate that EE2 has a higher potential for bioaccumulation in comparison to E2.

In addition to the higher potential for bioaccumulation indicated by the greater $logK_{ow}$ of EE2

compared to E2, EE2 is more resistant to degradation than E2. It is thought that the alkyne group enhances the chemical stability of EE2 in contrast to E2, due to steric hindrance within EE2 caused by alkyne bond attached to the C_{17}, which may be where degradation of E2 begins. Furthermore, it is possible that alkyne groups impede enzymatic action, preventing the enzyme from binding to EE2 or preventing EE2 from interacting effectively with the active site of the enzyme, therefore prevent enzymatic degradation. Another possible mechanism which may disrupt EE2 degradation by enzymes is that EE2 interaction with established enzymatic pathways such as cytochrome p450, monooxygenases and β-glucuronidases may cause irreversible binding of EE2 to active sites, furthermore EE2 also forms stable metabolites with estrogenic activity, from hydroxylation (Combalbert, 2010) via CYP enzymes, intestinal sulfation, and hepatic oxidation, glucuronidation, and sulfation (Klaic, 2022), which are depicted in Figure 1**Error! Reference source not found.**. These EE2 metabolites may still express estrogenic activity.

To summarize, EE2 is more resistant to degradation than E2 due to a number of factors, which include: steric hindrance relating to the presence of the alkyne group in EE2; that is absent in E2; the formation of stable metabolites of EE2 which exhibit estrogen potency, the inhibition of enzymes by EE2 that readily catalyse the breakdown of E2; and the greater affinity of EE2 for organic phases resulting in a higher instance of sequestration of EE2 relative to E2, that then limits the ability of microbes to access EE2 to initiate degradation. A comparison of the molecular weights, solubility in water at 25 °C, pK_a, estrogenic potency, and Relative Binding Affinity (RBA) and $LogK_{ow}$ are contained in Table 5. The names, physical and chemical properties of the natural estrogens and the synthetic estrogen (33).

Table 5. The names, physical and chemical properties of the natural estrogens and the synthetic estrogen (33).

Compound	Symbol	Mol wt. g/mol	Solubility in water mg/L at 25 °C	pKa	Estrogenic Potency	RBA	LogKow	Ref
Estrone (Least abundant female hormone)	E1	270.37	30	10.40	0.38	0.44	3.43	(Zhang, n.d.)
17β-estradiol (Primary female sex hormone)	E2	272.38	3.9	10.71	1	1	3.94	(Zhang, n.d.)
17α-ethinylestradiol (Synthetic hormone used in birth control pill)	EE2	296.41	11.3	10.33	1.19 – 1.34	1.4	4.15	(Zhang, n.d.)

2.3 Factors Influencing EE2 Removal Efficiencies from Water

The removal efficiency of 17α-ethinylestradiol (EE2) from water is influenced by various factors that impact the performance of treatment methods. Understanding these factors is crucial for optimizing and enhancing the efficacy of EE2 removal processes. Some key factors influencing EE2 removal efficiencies include the pH of the solution, the temperature, the initial EE2 concentration, the nature of the water matrix and the species contained within, the presences of ionic chemical species in the water matrix, the contact time flow rate of the EE2 containing water with the treatment material, and the chosen mechanism of removal. These factors are described in more detail in Table 6. Factors influencing EE2 removal from water. Consideration and control of these factors are essential in designing, optimizing, and implementing effective EE2 removal strategies to ensure the successful remediation of water contaminated with this endocrine-disrupting compound.

Table 6. Factors influencing EE2 removal from water.

Factor	**Effect**
pH of the Solution:	Changes in pH alter the surface charge of both the adsorbent materials and the EE2 molecules, affecting their interactions. A neutral pH was selected for this work in order to model a realistic water treatment plant. However, lower pH may cause protonation of adsorbing materials, which may interfere with EE2 adsorption.
Temperature	Higher temperatures might enhance adsorption kinetics or catalytic activity, affecting the efficiency of removal methods such as adsorption or photocatalysis. However, variations in temperature can also affect the stability of the treatment materials and impact their performance. For this work ambient temperatures are preferred to model a realistic water treatment environment, while also maintaining the dev elopement of a low energy process.
Nature of Water Matrix	The presence of other organic and inorganic compounds in water can impact EE2 removal. Coexisting substances may compete for adsorption sites, hinder photocatalytic reactions, or interfere with the efficacy of treatment methods, affecting overall removal efficiency. In research this effect is often modelled by using humic acid (HA) to represent natural water matrices which contain natural organic matter (NOM). Researchers using molecularly imprinted polymers (MIPs) and non-template imprinted polymers (NIPs) adsorb EE2 reasoned that HA could play a number of

	roles – justifying its use to represent NOM in the water matrix, which include: i) Entering and occupying selective binding sites in MIPs and NIPs. ii) Entering into the larger pores of MIPs and NIPs and blocking the path of EE2 to the binding site. iii) HAP may interact with EE2 through hydrogen bonding, which means EE2 may not be able to enter the selective binding cavities of the adsorbent (Zhang, n.d.).
Presence of Coexisting Ions	Certain ions present in water, such as chloride, sulphate, or carbonate, can influence EE2 removal. These ions may form complexes or affect the surface charge of the treatment materials, altering their affinity towards EE2 and thus impacting removal efficiency. The lipophilic EE2 molecule is also expected to be less soluble when ions are present in water. NaCl was found to enhance the adsorption capacity of EE2 on molecularly imprinted polymers (Li, 2020).
Adsorbent or Catalytic Material Characteristics	The properties of the adsorbent or catalytic materials used play a crucial role. Surface area, pore size distribution, functional groups, and surface charge of adsorbents significantly impact adsorption capacity. Similarly, the crystal structure, surface area, and photoactivity of catalysts affect photocatalytic degradation efficiency.
Contact Time and Flow Rate:	The duration of contact between the treatment material and EE2 in water (contact time) and the flow rate through the treatment system can influence removal efficiency (Lopez-Velasquez, 2021) (Han, 2013).

2.4 Adsorption for EE2 Removal

2.4.1 Activated carbon

Activated carbon is a commonly used adsorbent that is highly effective for removing organic compounds from water. The adsorption of EE2 onto activated carbon is a result of complex interactions between the EE2 molecule and the porous surface of the activated carbon. The adsorption mechanism is primarily governed by physical and chemical forces, including van der Waals interactions, hydrophobic interactions, hydrogen bonding (Han, 2013) and π-π electron donor- acceptor interactions (Pan, 2008). Activated carbon is also characterised by a high surface area ranging from hundreds of metres to a few thousand metres – this high surface area ensures there are numerous sites available for EE2 to interact with and adsorb to.

EE2 has hydrophobic properties and consequently exhibits a high affinity for the hydrophobic sites within the activated carbon structure, allowing it to readily partition into the micropores and mesopores of the carbon material. The π electrons of the aromatic rings in EE2 can engage in π-π interactions with the aromatic surfaces of the activated carbon, further facilitating the adsorption process. In addition, the presence of functional groups such as hydroxyl (-OH) and carboxyl (-COOH) groups, on the activated carbon surface can contribute to hydrogen bonding with the functional groups in EE2, which contributes to the overall adsorption capacity.

The efficiency of the removal of EE2 by activated carbon is affected by a range of factors, including properties of the activated carbon such as: surface area, surface chemistry (i.e. presence or absence of functional groups such as hydroxyl and carboxyl), pore size distribution, and relative abundance of micro-pores temperature. The chemistry of the activated carbon is important for EE2 removal. The EE2 removal efficiency can be affected by factors such as concentration of EE2, temperature, pH, contact time, agitation rate, and the composition of the water matrix, which may include dissolved organic matter (DOM), or salts (Gao, 2023).

2.4.2. Activated sludge

The activated sludge process (ASP) is a biological wastewater treatment method that involves the use of microbial communities to degrade organic contaminants, such as EE2, in order to remove the organic contaminants from wastewater. The ASP typically proceeds through several key stages, including:

i. Aeration
ii. Activated sludge treatment
iii. Sedimentation
iv. Sludge recycling

During the initial aeration phase, a microbial culture is added to the water intended for treatment in an aerated tank, which supplies oxygen for the growth and metabolic activities of microorganisms. The activated sludge microorganisms, including bacteria and protozoa, metabolize organic matter present in the wastewater as an energy source, leading to the breakdown and biodegradation of contaminants such as EE2. The biodegradation of EE2 occurs through enzymatic reactions and metabolic pathways within the microbial community, resulting in the transformation of EE2 into various products.

The efficient removal of EE2 through the activated sludge process is influenced by various factors, including the composition and concentration of EE2 in the wastewater, the microbial community dynamics, the operational conditions, and the hydraulic and organic loading rates. The concentration of EE2 in the wastewater directly affects the rate of removal, with higher initial concentrations potentially requiring extended treatment times and optimized process parameters to ensure effective degradation. Moreover, the biodegradability of EE2 by the activated sludge microorganisms is contingent on the specific microbial community composition and the presence of specialized microbial populations capable of metabolizing and degrading EE2.

The composition of the microbial community in the activated sludge system plays a critical role in the biodegradation of EE2 and the overall treatment efficiency. Microorganisms capable of co-metabolizing EE2, either aerobically or anaerobically, can facilitate the complete degradation of EE2 into simpler, non-estrogenic compounds. The presence of specific microbial populations, such as nitrifying bacteria, denitrifying bacteria, and heterotrophic bacteria, contributes to the transformation and mineralization of EE2, leading to the removal of estrogenic activity from the wastewater. The microbial diversity and the acclimation of the activated sludge to the presence of EE2 are essential for maintaining a stable and resilient microbial community capable of efficiently degrading the target contaminant.

The operational conditions and process parameters employed during the activated sludge treatment significantly influence the removal efficiency of EE2. Factors such as the aeration rate, the mixed liquor suspended solids (MLSS) concentration, the hydraulic retention time (HRT), and the sludge retention time (SRT) are critical in maintaining optimal conditions for microbial growth and activity. The aeration rate affects the oxygen transfer efficiency and the metabolic activity of the microorganisms, thereby influencing the biodegradation kinetics of EE2. The MLSS concentration, representing the concentration of suspended solids in the mixed liquor, reflects the biomass concentration and the microbial activity within the system. Adequate MLSS levels are crucial for ensuring sufficient microbial biomass and enzymatic activity for the effective degradation of EE2.

The HRT and SRT are essential parameters that dictate the duration of wastewater treatment and the retention of biomass within the system. Longer HRTs allow for extended contact time between the wastewater and the activated sludge, promoting the degradation of EE2 and other organic pollutants. Similarly, appropriate SRTs are necessary for maintaining a stable microbial population and preventing washout of essential microorganisms responsible for EE2 degradation. Process modifications, such as the introduction of anoxic and anaerobic zones within the treatment system, can create favourable conditions for the co-metabolic degradation of EE2 and the removal of estrogenic activity from the wastewater.

Furthermore, advancements in process optimization and technological innovations have been implemented to enhance the treatment efficiency of EE2 using the activated sludge process. The integration of advanced oxidation processes (AOPs), such as ozonation, ultraviolet (UV) irradiation, and advanced oxidation with hydrogen peroxide (H2O2), in conjunction with the activated sludge process has shown promising results in the degradation of recalcitrant organic compounds, including EE2. AOPs can facilitate the transformation of EE2 into less estrogenic

intermediates or mineralize it into simpler, non-toxic end products, complementing the biodegradation capabilities of the activated sludge microorganisms.

Moreover, the incorporation of membrane bioreactor (MBR) technology into the activated sludge process enables the efficient removal of suspended solids and the retention of microbial biomass, thereby enhancing the treatment efficiency for EE2 and other persistent contaminants. MBR systems offer superior effluent quality and provide a physical barrier for the retention of microorganisms, allowing for extended sludge retention times and improved degradation kinetics. The combination of MBR technology with biological treatment processes can lead to the development of sustainable and energy-efficient wastewater treatment solutions for the removal of EE2 and other emerging contaminants. Removal efficiencies obtained using the activated sludge process range from 41% to 98%, as shown in Table 7.

Table 7. EE2 removal efficiency for biological processes, Tang et al. (2021) (10) n.d. means not detectable.

Removal Efficiency using Activated Sludge Process	**Ref**
71.5%	(Tang, 2021)
41% - mainly due to sorption on sludge	(Zhou, 2012)
34-45%	(Cargou et, 2004)
77-98%	(Ivanets, 2019)
81%	(Svenso n, 2003)

Several disadvantages are associated with employing the activated sludge process for EDC removal, thereby warranting critical consideration in wastewater treatment strategies. EDCs often exhibit resistance to microbial degradation due to their stability and persistence, leading to incomplete removal and potential persistence in treated effluents, leading to a variable removal efficiency. Furthermore, the ASP risks the generation of transformation by-products:

Intermediary metabolites or transformation by-products may form which possess altered toxicological profiles compared to their parent compounds. The potential accumulation of these by-products in treated effluents underscores the necessity for comprehensive monitoring and mitigation strategies to safeguard environmental and human health.

Despite undergoing partial degradation, certain EDCs or their metabolites may persist within the activated sludge biomass, leading to bioaccumulation and subsequent biomagnification in along the aquatic food chain. This phenomenon highlights the ecological risk posed by EDCs, particularly within receiving water bodies, and underscores the necessity of wastewater management approaches that fully remove EDCs from water to effectively mitigate adverse impacts on ecosystem health. The operation and maintenance of activated sludge treatment facilities also require substantial energy inputs and resource allocation, particularly in terms of aeration, sludge management, and process optimization, potentially exacerbating economic burdens for wastewater treatment utilities.

To summarize, although the activated sludge process can be an effective method for the removal of EDCs from wastewater, removal efficiencies are variable, there is a material risk of producing toxic by-products, and the ASP is best supplemented by a complementary EE2 removal method, as is the case with membrane bioreactors.

2.4.3. Ozone

Ozone gas is primarily used to disinfect water through the destruction of micro-organisms including protozoa, bacteria and viruses. However, ozone gas can destroy organic contaminants through the mechanism of oxidation. Free radicals are produced which can attack and degrade organic molecules, with the potential to completely mineralise these contaminants. Such processes are referred to as “advanced oxidation processes” and constitute an important avenue for removal of organic contaminants from water.

The advantages of using ozone include the strong oxidative power of ozone, which makes it highly effective in degrading a wide range of organic compounds, including EE2. Through direct oxidation or the generation of reactive oxygen species (ROS), ozone can theoretically mineralise EE2 completely into CO_2 and H_2O. In addition, the almost indiscriminate reactivity of ozone enables the oxidation of diverse pollutants, meaning it is effective not only against EE2 but also against various organic contaminants, pesticides, pharmaceuticals, and pathogens present in water. Furthermore, ozone has rapid reaction kinetics, which allows for efficient treatment processes with shorter contact times, contributing to enhanced operational efficiency, relative to slower water treatment methods. An additional benefit of ozone is the fact that no residual byproducts from ozone itself are formed: as ozone decomposes into diatomic oxygen without leaving harmful or persistent residues in the treated water. Its ability to break down EE2 into non-toxic compounds or mineralize it into carbon dioxide and water reduces concerns regarding secondary pollution or residual toxicity.

The disadvantages of using ozone to employ the AOP method include high operational costs as the production of ozone typically requires specialized equipment and consumes significant energy, which is costly. In addition, implementing ozone-based water treatment systems requires careful design and engineering to ensure efficient ozone delivery and proper mixing within the water. The complexity of system design increases capital investment and operational complexity. Furthermore, ozone is inherently unstable and can decompose rapidly, especially in the presence of organic matter or certain dissolved compounds. This decomposition limits its persistence and necessitates on-site generation to ensure adequate concentrations for effective treatment, which is a limiting factor as it is generally accepted that ozone cannot be transported. The formation of byproducts is another disadvantage of using ozone – while ozone itself does not leave harmful residues, its reactions with certain organic compounds may form disinfection byproducts (DBPs), potentially contributing to water quality concerns. Monitoring

and managing the formation of DBPs are essential considerations. Finally, ozone has a limited effectiveness in high organic load situations: ozone's effectiveness for EE2 removal may diminish in water sources with high organic content or turbidity due to increased competition for ozone or potential reactions with other organic compounds, necessitating pre-treatment or additional processes.

To summarize, while ozone exhibits strong oxidizing capabilities and broad-spectrum activity against many contaminants in water, challenges related to high operational costs, complex system design, potential byproduct formation, and limitations in highly organic water matrices require thorough evaluation and optimization for its successful application in water treatment (Sun, 2019), (Margot, 2013). These advantages are summarised in Table 8. Advantages and disadvantages of ozone for removal of EE2 from water.

Table 8. Advantages and disadvantages of ozone for removal of EE2 from water.

Advantages	**Disadvantages**
O_3 is strongly oxidising	High operational costs
Indiscriminate reactivity	Complex system
Broad spectrum application	Ozone decomposition occurs rapidly
Complete mineralisation of organics	Formation of disinfection by products
Fast reaction kinetics	Limited in cases of high organic load
No byproducts from ozone formation/ decomposition	

2.4.4. Ultrafiltration

Ultrafiltration is a membrane-based separation technique utilized for the removal of 17α-ethinyl estradiol (EE2) from water due to its distinct advantages. However, it is accompanied by certain limitations that warrant consideration in its application. The advantages of

ultrafiltration (UF) includes the possession of fine pores by the membrane (typically in the range of 1-100 nm), which allows for the effective removal of EE2 molecules and other contaminants based on size exclusion. This method offers high removal efficiency, particularly for larger molecules like EE2, while allowing smaller molecules and ions to pass through. The pore size distribution of ultrafiltration membranes enables selective separation, targeting specific molecular sizes, including EE2, without significantly affecting the essential properties or constituents of water.

This selectivity contributes to efficient EE2 removal while preserving water quality. Ultrafiltration systems can operate continuously, ensuring a consistent and uninterrupted process for EE2 removal. This characteristic is advantageous for large-scale applications in water treatment facilities, providing a steady output of purified water. Compared to some conventional treatment methods, ultrafiltration often requires fewer or no chemical additives for EE2 removal. The reliance on physical sieving mechanisms minimizes the need for additional chemicals, thereby reducing operational costs and environmental impact. Ultrafiltration systems typically have a smaller physical footprint compared to conventional treatment processes, allowing for ease of installation in various settings. This advantage is particularly valuable in situations where space is limited or where modular systems are required.

The disadvantages of UF include: membrane fouling: one of the primary challenges associated with ultrafiltration.. EE2, along with other organic matter and particles, can accumulate on the membrane surface or within the pores, hindering water flow and reducing filtration efficiency. Periodic cleaning or maintenance is necessary to mitigate fouling, adding to operational costs. Furthermore, the initial investment and operational costs of ultrafiltration systems can be relatively high, especially for high-quality membranes capable of effectively removing EE2. Additionally, expenses related to membrane replacement, maintenance, and energy

consumption contribute to overall costs. Another factor that is also a disadvantage for UF is the limited removal of low molecular weight compounds: while ultrafiltration efficiently removes larger molecules like EE2, it may be less effective for smaller organic contaminants and dissolved ions. This limitation necessitates complementary treatment methods for comprehensive water purification. The sensitivity to feed water quality also presents a disadvantage for UF: variations in feed water quality, such as fluctuations in particle concentration, organic content, or pH, can impact the performance and efficiency of ultrafiltration. Adjustments or pre-treatment processes might be required to optimize EE2 removal under varying conditions. The advantages and disadvantages of ultrafiltration are outlined in Table 9. The advantages and disadvantages of ultrafiltration for contaminant removal from water.

Table 9. The advantages and disadvantages of ultrafiltration for contaminant removal from water.

Advantages	**Disadvantages**
High removal efficiency	Membrane fouling
Selective separation	High costs
Continuous operation	Limited removal of low molecular weight compounds
Reduced chemical usage	Sensitivity to feed water quality
Minimal footprint	

In summary, while ultrafiltration offers notable advantages in terms of high removal efficiency and selective separation of EE2 from water, challenges related to membrane fouling, costs, limitations in removing smaller molecules, and sensitivity to feed water quality necessitate careful consideration and integrated approaches for effective EE2 removal in water treatment applications (Heo, 2012).

2.5 State of the Art Laboratory Scale EE2 Removal

In this section the experimental outcomes for EE2 removal via adsorption and separately photocatalysis are reported. These findings represent recent advances reported in the literature for the removal of EE2, and are valuable for the new information and avenues of investigation they provide. However, it must be noted that poor performances are unlikely to be reported in the literature, meaning the information contained in this section will only be representative of the best available EE2 removal techniques. Currently state of the art research in adsorbing materials can be roughly classed into the following categories:

i. Commercial activated carbon
ii. Biochar based materials
iii. Carbon nanotube materials
iv. Graphene based materials
v. Polymer based materials
vi. Molecularly imprinted polymers
vii. Silica based mesoporous materials

Adsorbent	Adsorption Capacity	Conditions/Notes	Ref
Peanut Shells (Arachis hypogaea)	Close to 90% removal efficiency	500 rpm stirring, 2 g of adsorbent mass, pH 6, 24 hours contact time	(da Silva Procópio, 2023)
Fe–Mn Binary Oxide (FMBO)	97% removal efficiency at equilibrium	0.2 g/L of FMBO, initial EE2 concentration of 10 mg/L, pH 6.0, room temperature, equilibrium reached in about 30 min	(Jiang L., 2017)
Magnetic MXene Composite Fe3O4@Ti3C2	95.34% removal efficiency	Optimized conditions of 6.7 h adsorption time, pH 6.4, initial concentration 0.98 mg/L, adsorbent dose 88.9 mg/L	(Xu, 2021)
Polyamides (PA612 and PA12)	Higher adsorption capacities than PA6	Specific data on capacities not provided but noted as significantly higher compared to PA6 for EE2 removal in water	(Larcher, 2012)

Granular Activated Carbon	99.8% removal efficiency	Varying initial concentration 5-20 µg/L	(da Silva Procópio, 2023)

2.6 Adsorption Mechanisms for EE2 Removal

The main adsorption mechanisms that contribute to estrogen removal – which can be extrapolated to EE2 removal, are hydrophobic interactions, π-π interactions, hydrogen-bonding interactions or a combination of their effects. Kovalova et l. (Kovalova, 2013) describes EE2 as apolar, and indicates that activated carbon is used to remove apolar contaminants, with adsorption occurring via non-specific interactions and dispersive forces. The authors assumed that hydrogen bonding is most likely to occur between the site and water. This is consistent with Pan et al. (Pan, 2008) where it is reported that that π-π bonding interactions contributed to estrogen removal.

However, Sun et al. (Sun, 2011) report that EE2 has H-bonding capability and state that an additional mechanism is needed to describe EE2 adsorption, in addition to the pore-filling mechanism established by their research. The conclusion that H-bonding is responsible for EE2 binding is supported by density functional theory calculations which showed that the mechanism of binding of EE2 to the photocatalyst $Bi_2MoO_6\{010\}$ is chemisorption through the binding of hydroxyl groups (Shi, 2023).

Adsorption experiments for EE2 removal that employ activated carbon often highlight the surface area of the activated carbon used. There is a noticeable preference for high surface area materials, which is a rational choice as a material with a high surface area would be expected to have more sites available for adsorption However, Han et al. (Han, 2013) found that EE2 adsorbed to polyamide with a surface area of 20.1 m^2/g significantly faster than high surface area activated carbons, Darco and Norit, whose surface areas were 637.4 m^2/g and 989.2 m^2/g.

The kinetics of EE2 adsorption to the polyamide was also found to be pseudo second order, indicating dual mechanisms causing the adsorption. The authors state: “adsorption of EE2 on PA612 is predominantly driven by Lewis acid-base interactions between EE2 and PA612 amide functionalities and facilitated by the hydrophobic partitioning of EE2 solutes in water”. This is

supported by an earlier finding by Han in 2012, which found that hydrophobic partitioning is not the dominant mechanism for EE2 adsorption, and instead adsorption is driven by Lewis acid – Lewis base interactions, which are most likely hydrogen bonds forming between the amide groups of PA612 and proton-donating moieties of EE2 (Han, 2012).

Table 7. Properties of adsorbing carbon-based materials.

Properties	**Adsorbent**		
Product name	Darco	Norit	Orgasol
Material	Activated carbon	Activated carbon	Polyamide 612
Surface area (m^2 g^{-1})	637.4	989.2	20.1
Particle size (µm)	900 – 1300	600 – 700	10 (average)
Adsorption capacity	27.6 mg g^{-1}	10.4 mg g^{-1}	25.2 mg g^{-1}
Adsorption (mg) per m^2	0.01 – 0.04	0.01 – 0.04	1.26
EE2 removed in 30 min	44.8%	16.5%	72.5%

Han et al. provided an image containing a simulation of the regions of electron density of EE2. This diagram shows there are regions of strong electron density in EE2 centred on the oxygen atoms, and further regions of electron density centred around the alkyne bond and π- system of the benzene ring. Quantum mechanical calculations were used to investigate the possible hydrogen bonds that could form between EE2 and the polyamide molecule. The results showed that the strongest hydrogen bonds formed between the carbonyl amide groups from polyamide 612 and the hydroxyl groups attached to the phenol ring and the cyclopentane ring in EE2. This finding provides further evidence that the mechanism of adsorption of EE2 to polyamide 612 is due to hydrogen bonding, and factors such as porosity of the adsorbent and surface area are not the dominating factors (Han, 2013).

Figure 6. Electron density map of EE2, Han et al (2013) (Han, 2013).

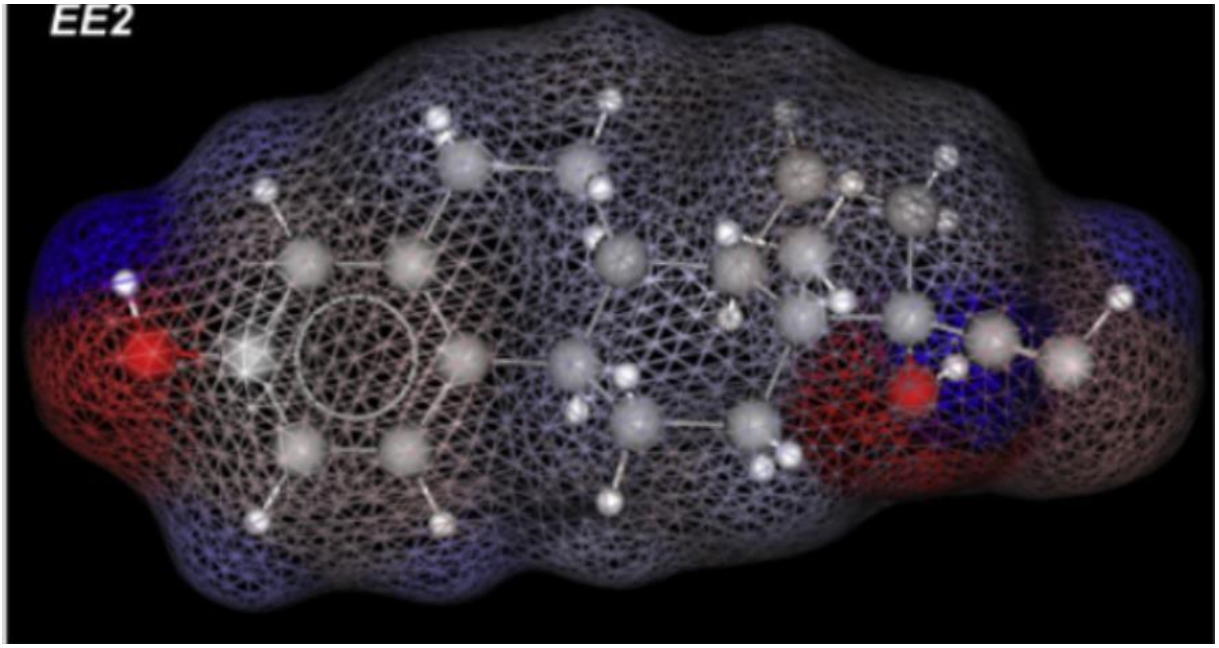

Surface area was also shown to be a less decisive factor than chemistry by Prokic et al. (Prokić, 2020), where it was found that adsorption efficiency could be enhanced by up to 30% by increasing acidic oxygens on the surface of chemically modified activated carbon cloths. The mean sorption energy indicated that physisorption was the dominant mechanism for E1, E2 and EE2 removal, which further indicates that hydrogen bonding is likely the dominant mechanism that causes adsorption.

In contrast, Zhang and Hu used MIPs and NIPs as adsorbents and found that the mechanism of binding of EE2 was not hydrogen bonding, and that there was no significant effect on the adsorption capacity of MIPs and NIPs when the ionic strength of the solution was altered, nor was there a significant effect of pH on the adsorption capacity when the pH was varied from 3.1 to 9. These combined facts means that hydrophobic interactions were the driving force behind EE2 adsorption, however it must be noted that MIPs and NIPs were strongly hydrophobic (characterized by contact angle >100 °) (Zhang, n.d.) which means that the adsorbents may not have had the ability to hydrogen bond due to their chemical properties,

and that the EE2 molecule could not hydrogen bond to the adsorbent, meaning there are multiple routes and mechanisms possible for EE2 binding.

The mean sorption energy calculated by Prokic et al. (Prokić, 2020) contained in Table 10. Mean sorption energy for three estrogens to chemically modified activated carbon cloths also indicates that the process of adsorption is occurring by physisorption, which is most likely to be due to hydrogen bonding occurring between the adsorbent and EE2. However, the mean sorption energies are given to a very degree of accuracy that is not realistic

Table 10. Mean sorption energy for three estrogens to chemically modified activated carbon cloths

Hormone	Mean Sorption Energy kJ/mol	Ref
E1	1.45	(Prokić, 2020)
E2	1.34	(Prokić, 2020)
EE2	1.05	(Prokić, 2020)

Overall, these findings indicate that although EE2 is an organic molecule with a benzene ring, there are more interactions occurring than van der Waals forces between EE2 and the adsorbent. EE2 has hydroxyl groups that have the ability to engage in hydrogen bonding, and when the adsorbent material contains moieties capable of hydrogen bonding, the adsorbent outperforms materials that do not hydrogen bond, as is the case for the research conducted by Han et al. (Han, 2012), where an adsorbent capable of hydrogen bonding with a surface area of 20 m^2/g outperformed commercially available activated carbons with surface areas of 637.4 m2/g and 989.2 m^2/g (Han, 2013).

2.7 Kinetics of EE2 Removal

The dynamics of the adsorption process can be investigated by comparing experimental adsorption data with the following kinetics models, calculating the kinetic constant of adsorption, then producing a linear regression correlation coefficient (R^2) where the closer the R^2 value is to 1 the better the fit of the model to the adsorption data. The specific kinetics models that will be used to elucidate the likely dynamics of the adsorption process are:

i) Pseudo-first-order kinetic model (indicates rate limiting step may be physical process (Lu, 2021).

ii) Pseudo-second-order kinetic model (assumes the rate-limiting step is chemisorption).

iii) Elovich kinetic model (second order kinetics assuming the surface is energetically heterogenous).

iv) Weber and Morris kinetic model (intraparticle mass transfer diffusion).

The kinetics of EE2 removal have been determined using various adsorbents with varying results. The kinetics are obtained by a blank experiment containing no adsorbent is conducted to account for glassware adsorption, and the equilibrium adsorption of EE2 is obtained by calculating the difference between the residual EE2 and the EE2 in the controlled flask (Feng, 2010).

These results have indicated conflicting kinetics, with some adsorbents producing removal graphs that are best matched to first order, pseudo first order, second order and pseudo second order (Feng, 2010). This means that the kinetics of EE2 removal via adsorption depends on the adsorbent and the interaction between the adsorbent and EE2, which includes chemical and physical interaction. The kinetics of EE2 removal are most often found to be pseudo-second order, although other kinetics models such as diffusion controlled have been found to fit the

adsorption data best.

Also of note, is that EE2 concentration measurements can initially produce fluctuating concentrations (Feng, 2010), which is not consistent with steady and irreversible removal of EE2 from solution. Instead in the chart below, the kinetic model found to be the best fit for the EE2 adsorption data was pseudo-second order. The pseudo-second order kinetic model assumes that “the rate limiting step is chemisorption” (Tapas Ranjan Sahoo, 2020).

Figure 7. Initially fluctuating concentration of EE2 Reference (Feng, 2010).

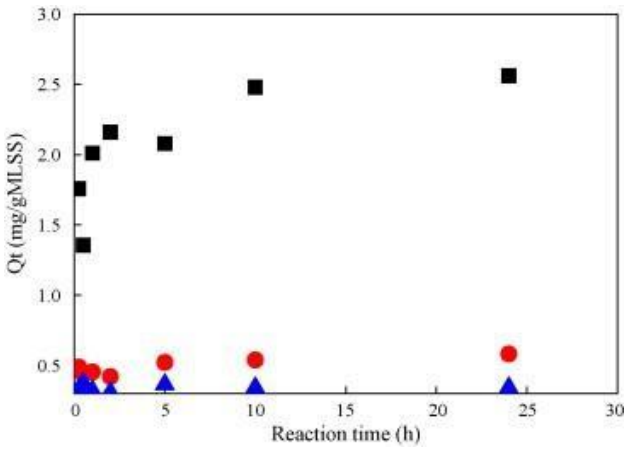

The kinetics models that best fit the adsorption data for various kinetic models are in included in Table 11. Kinetic models applied to EE2 adsorption on various materials, where it can be seen that the pseudo-second order kinetic model is the dominant model. This means that the most common mechanism for EE2 adsorption is most likely to be chemisorption, and hence the most likely mechanism for chemisorption is hydrogen bonding, due to the presence of the hydroxyl groups at C_3 and C_{17}.

Table 11. Kinetic models applied to EE2 adsorption on various materials.

Adsorbent	Kinetics model	Ref
Inactivated Sewage Sludge	Pseudo-second order	(Feng, 2010)
Peanut Shells, 66 °C	Pseudo-first order* *Adsorption does not occur by a single mechanism	(da Silva Procópio, 2023)
Polyamide 612	Pseudo-second order	(Han, 2013)
Electrospun polymeric nanofiber membranes	Pseudo-second order	(Yasir, 2022)
Recycled waste cigarette electrospun fibers	Pseudo-second order	(Yasir, 2022)
Magnetic MXene composite Fe_3O_4@Ti_3C_2	Pseudo-second order	(Xu, 2021)
Aerobic granular sludge	Pseudo-second order	(Zheng, 2021)
Carbon nanomaterials	Improved pseudo-second order	(Pan, 2010)
Activated carbon	Diffusion controlled (Weber Morris)	(Pan, 2010)
Polyvinyl chloride	Pseudo second order	(Lu, 2021)
Biochar from fungiculture	Pseudo second order	(Leite Vieira, 2022)

2.8 Method for measuring adsorbent capacity

Methods for measuring estrogen concentration in water reported in the literature are generally chromatographic methods, either using HPLC-MS, HPLC-UV, or LC-MS. Bioassays (e.g. yeast estrogen screen) have been used to determine the estrogenicity of a given sample (Czerwonka G., 2012) (Huang B., 2015) (Sanseverino, 2005), however a bioassay is not preferred as these measure estrogenicity as an E2-equivalent concentration, so can be activated by estrogenic species (not just EE2) meaning this is not the best method for quantifying EE2, although this is useful for assessing the estrogenicity of a given sample, and for assessing

whether the sample could have an effect on wildlife.

2.9 Removal Efficiencies Obtained by Adsorption

The removal efficiencies obtained by state-of-the-art adsorption techniques are included in the following table.

EE2 Removal Efficiency Using Adsorption			
Adsorbent	**Conditions**	**Removal Efficiencies**	**Ref**
Granular Activated Carbon (GAC)	750 mL of GAC in a 2 L upflow bioreactor, 5000 – 20 000 ng/L EE2, hydraulic retention time 1.2 h, vessel wrapped in foil to prevent photodegradation	>99.8%	(Johnson, 2000)
Iron hydroxide modified activated carbon fibres	1.3 – 1.8 mg EE2/g Fe-ACF, 500 µg/L EE2, stored in HDPE bottles and filtered through 0.45 µm acetate membrane – analysed using HPLC with fluorescence detector (ref 233, Yoon et al)	99%	(Al-Hajji, 2021)
Polyamide 612 Polyamide 12	Agitated batch: Polyamide (PA) particles (0.1 or 0.2 g/L) were added to 200 mL of 300 µg/L EE2 solution. Filtered with cellulose syringe filters. Repeated with EE2 150 – 6000 µg/L Fixed bed adsorption column, compared with amberlite XAD4 as benchmark. Rapid column: 1.0 g PA and 30 – 3000 µg/L EE2 Analysed with HPLC-UV	>99% (EE2 reduced to non-detectable levels)	(Han, 2012)
Polyamide 612	200 µg/L EE2 solution with 72.5% achieved after 30 min. Adsorbent was 0.2 g/L.	72.5%	(Han, 2013)
Modified Bentonite	Bentonite clays modified with sodium, $FeCl_2.4H_2O$, and L-tryptophan		(Gallouze, 2021)
Biochar from fungiculture		89%	(Leite Vieira, 2022)

2.10 Summary of Adsorption for EE2 Removal

Adsorption as a mechanism for EE2 removal from water has its advantages and disadvantages. The advantages include high removal efficiencies, relatively inexpensive adsorbents, a wide range of potential adsorbents to choose from, and the potential to select adsorbents produced from green processes. The most significant and relevant disadvantage of using adsorption to remove contaminants from water, is that that a secondary waste stream containing the contaminants is created.

2.11 Photocatalysis for EE2 Removal

Photocatalysis is an advanced oxidation technique that has the potential to completely mineralise (and hence destroy) EE2 in water. Many efforts to use photocatalysis to remove EE2 have been successful, with up to 100% EE2 removal efficiencies being obtained. Although Photocatalysis is an established method for removing organic pollutants from water, this method for water purification has advantages and disadvantages.

The advantages include the potential to completely degrade and mineralise organic pollutants into water and carbon dioxide. This is an advantage over adsorption processes because adsorption is effective at removing EE2, however adsorption does not destroy the EE2 molecule, meaning the secondary waste stream must be treated to remove EE2. In contrast, photocatalysis can remove EE2 by destroying the EE2 molecule. Other advantages include the speed at which photocatalysis can be performed

The mechanism of EE2 destruction via photocatalysis proceeds via several possible routes, the most common mechanism is initiated by a hydroxyl radical attacking the EE2 molecule.

2.12 Removal Efficiencies Obtained by Photocatalysis

The EE2 removal efficiencies obtained by established and modified photocatalysts is included in the table below to demonstrate typical EE2 removal efficiencies obtained by photocatalysis. Although the removal efficiency is important in selecting the most appropriate photocatalyst, other critical factors include cost, light wavelength that activates the photocatalysis process (with visible light being the ideal), recyclability, recoverability, synthesis method and ability to improve the photocatalytic by adjusting the morphology of the photocatalyst or doping the photocatalyst with other species. The photocatalyst selected in this scheme of work is titanium dioxide and it is discussed and explained in Chapter 3. A list of photocatalyst that have been used to degrade EE2 successfully is contained in Table 12. Photocatalysts used to degrade EE2, where it can be seen that TiO_2 is capable of removing 100% of the EE2 in solution.

Table 12. Photocatalysts used to degrade EE2.

Photocatalyst	**EE2 Removal Efficiency %**	**Ref**
TiO_2	100%	(Colemman, n.d.)
Au/TiO_2	100%	(Al-Hajji, 2021)
ZnO	80%	(Liu, 2014)
Graphitic Carbon Nitride	82 – 100%	(Kumar, 2020)
WO_3 immobilised on Amorphous-SiO_2	98%	(Soares Filho, 2018)

2.13 Combined Methods for EE2 Removal

Previously it was highlighted that although adsorption is highly effective for EE2 removal from water, adsorption only moves the EE2 from one medium to another, creating a secondary waste stream and the EE2 still requires disposal. In contrast, photocatalysis has the ability to destroy EE2, however the reaction pathways that result in the mineralisation of EE2 proceeds through multiple steps, generating transformation products which may have a higher toxicity than the original EE2 molecule, as there is a risk that the free radical attack on EE2 does not go to

completion.

An innovative strategy to overcome the failures of single mechanism removal methods is to combine two different methods of EE2 removal. The aim of this strategy is to produce an EE2 removal method that utilises the advantages of different methods, while minimising the effects of the disadvantages.

2.14 Membrane Bioreactors

Membrane Bioreactors (MBR) combine a reaction chamber containing a biocatalyst which may be an enzyme, microorganism or a plant or animal cells (Luis, 2018) or antibodies (Lima, 2014), with a membrane system for separation of EE2. Membrane bioreactors demonstrate that EE2 can be separated and metabolized (and therefore destroyed) very effectively in a system that combines a standard separation technique (membrane filtration) with biological oxidation. This implies that EE2 removal techniques that combine a separation technique with a destructive technique is an effective strategy for implementing EE2 removal. The disadvantage of combing membrane filtration with biological oxidation is that the micro-organisms that cause the degradation of EE2 require specific conditions in order to function optimally, and furthermore the degradation times can be slow, in the region of 3 – 7 days. This means that although the act of combining membrane separation with biological oxidation is an effective and reliable method of purifying EE2 contaminated water, the slow processing time is a significant disadvantage for membrane bioreactors.

2.15 Adsorption and Oxidation

An Fe-Mn binary oxide (FMBO) formed *in situ* achieved a removal efficiency of 96% in 30 min in an EE2 solution with the pH maintained at 6.0. uses adsorption followed by oxidation to remove and destroy EE2 (Jiang L., 2017).

2.16 Adsorption and Photocatalysis

Systems that are optimised to have both photocatalytic and adsorptive properties show improved abilities to remove EE2 from solution (Shi, 2023) (Chen, 2022) (Song, 2023). The

figures contained in the table below demonstrate that combining adsorption and photocatalysis have excellent results for the removal of EE2 from water. The reactions are relatively fast, the removal efficiencies are high, and the products of photocatalysis could be adsorbed, increasing removal of EE2 from water. Some combined methods are included in Table 13. Combined methods for EE2 removal.

Table 13. Combined methods for EE2 removal.

EE2 Removal Efficiencies Using Combined Methods		
Combined Methods Description	**Removal Efficiencies**	**Ref**
The coagulants aluminium sulfate (AS) and polyaluminium chloride (PACl) were used in conjunction with powdered activated carbon (PAC). When PAC (2.5 mg/L) was added as a pre-treatment before the coagulants and contact time was 120 min, highest RE (99.9%) was observed	30 – 99.9%	(Yamamoto H., 2004)
An Fe-Mn binary Oxide (FMBO) formed *in situ*, achieved a removal efficiency of 96% in 30 min at pH 6.0	96%	(Jiang L., 2017)
ZnO/Bi_2MoO_6 {0 1 0} composite photocatalyst was modified to have improved adsorption properties by decreasing the surface hydrophilicity	90%	(Shi, 2023)
Ag_2MoO_4/$BiVO_4${0 1 0} modified with hexamethyldisilane – a photocatalyst modified to have improved adsorption propertied by decreasing the surface hydrophilicity	100%	(Shi, 2023)
Bi_2SiO_5/$Bi_4Si_3O_{12}$ heterostructure catalyst removed EE2 using a synergistic adsorption/photocatalysis reaction. $Bi_4Si_3O_{12}$ was hollow and spherical and Bi_2SiO_5 had nanosheet morphology	99.4%	(Chen, 2022)
Activated carbon/TiO_2 composites, where the introduction of activated carbon increased the EE2 removal rate to >90% from 30%, and was attributed to the adsorption capacity of AC preferentially transferring hydrophobic EE2 on to adsorption sites of TiO_2/AC composites in the presence of humic acid and natural organic matter. SiO_2 and $CaCO_3$ were used as template the reaction	>90%	(Song, 2023)

2.17 Future of EE2 Removal

Combining methods for EE2 removal presents an effective strategy for ensuring maximum EE2 removal, and the combination of adsorption and advanced oxidation processes presents a strategy that allows the EE2 molecules to be captured via adsorption and then destroyed via oxidation. A combined system utilising adsorption and photocatalysis for EE2 removal has not

yet been explored, meaning there is an opportunity to fill this knowledge gap with this thesis.

2.18 Conclusions

EE2 is a synthetic estrogen that has been demonstrated to have serious negative effects on organisms exposed to levels of EE2 in excess of 0.36 ng/L**,** including when the exposure was acute and not a prolonged event. The effects on organisms include behavioural abnormalities, physical abnormalities, sexual abnormalities, low sperm counts in males, the production of vitellogenin in males, the development of egg cells in testes, a significantly increased occurrence of intersex individuals, premature oestrus, and accelerated development of female sexual organs. The impact on wildlife populations of these physical and reproductive abnormalities is deleterious and in model populations results in a complete population crash, with the resulting gap in the food chain or hole in the biodiversity web having a domino effect on the populations that rely on consuming the EE2-affected organisms for sustenance.

EE2 is resistant to established methods capable of degrading its natural analogue – E2, and biological methods that are effective at degrading E2 may not work as effectively for EE2, due to reasons that may include steric hindrance from the alkyne group at C_{17} in EE2, a limited ability of EE2 to form the enzyme-substrate complex that is possible for E2 due to differences in the molecular structure, or due to EE2's much lower affinity for aqueous solutions relative to E2, resulting in EE2 becoming adsorbed to soil, NOM, or bioaccumulating.

EE2 has been the subject of limited research in comparison to E2, meaning that focusing efforts on understanding how EE2 removal will produce novel work. and there exists an opportunity to develop and implement a combine adsorption – photocatalysis system in order to achieve fast purification of EE2 contaminated water.

Chapter 3 – Titanium Dioxide as the Photocatalyst

3.1 Introduction

Titanium dioxide is a well-established photocatalyst with a proven effectiveness for the destruction of toxic organic compounds and pollutants in water, meaning titanium dioxide should also degrade EE2 in water effectively. TiO_2 presents a cost-effective choice as it is cheaper than photocatalysts with comparable photocatalytic efficiencies, meaning that its inclusion in a water purifying material would be more accessible to lower income regions, increasing the number of potential regions over which the water purifying material could be used. Furthermore, titanium dioxide can also be applied to surfaces using the low temperature method of the sol gel process, meaning that the application titanium dioxide to a surface – lending photocatalytic properties to the surface can be achieved in a green, sustainable and potentially eco-friendly manner, while simultaneously achieving immobilising of the TiO_2 particles, preventing or at least significantly hindering their release and loss to the environment, further improving the sustainability of the water purifying material. For these reasons titanium dioxide was selected to add the photocatalytic component to the materials designed to have photocatalytic and adsorbent features for the purpose of water purification by removing EE2.

3.2 Properties of Titanium Dioxide

The main polymorphs of titanium dioxide are anatase and rutile, although other much rarer polymorphs of titanium dioxide such as brookite and panguite also exist. This chapter focuses on the properties of anatase and rutile because these polymorphs are the dominant polymorphs produced by titanium dioxide synthesis methods. The three crystal lattices are shown in Figure 8. Structures of the main forms of TiO2 (74).

3.2.1 Anatase

Anatase is the polymorph of TiO_2 that is favoured for photocatalytic applications and is based on a cubic close packed arrangement of O^{2-} ions. Anatase is metastable and will transform to rutile at temperatures between 450 – 850 °C (Zhang, 2020). This wide temperature range can be

attributed to the effect that impurities within the anatase TiO_2 and the general conditions experienced by the mineral during the transformation process.

3.2.2 Rutile

Rutile has a hexagonal close packed arrangement of O^{2-}, with Ti(IV) situated in half of the octahedral holes. Rutile is the preferred polymorph for use in pigments due to its brilliant white colour and chemical stability.

3.2.3 Brookite

Brookite's structure is based on a cubic close packed arrangement of O^{2-} ions. Brookite is a much rarer polymorph of TiO_2 and will not feature heavily in this body of work, but its properties are included in Table 14. Band gap, crystal system and space group of three polymorphs of TiO2.

Figure 8. Structures of the main forms of TiO_2 (74).

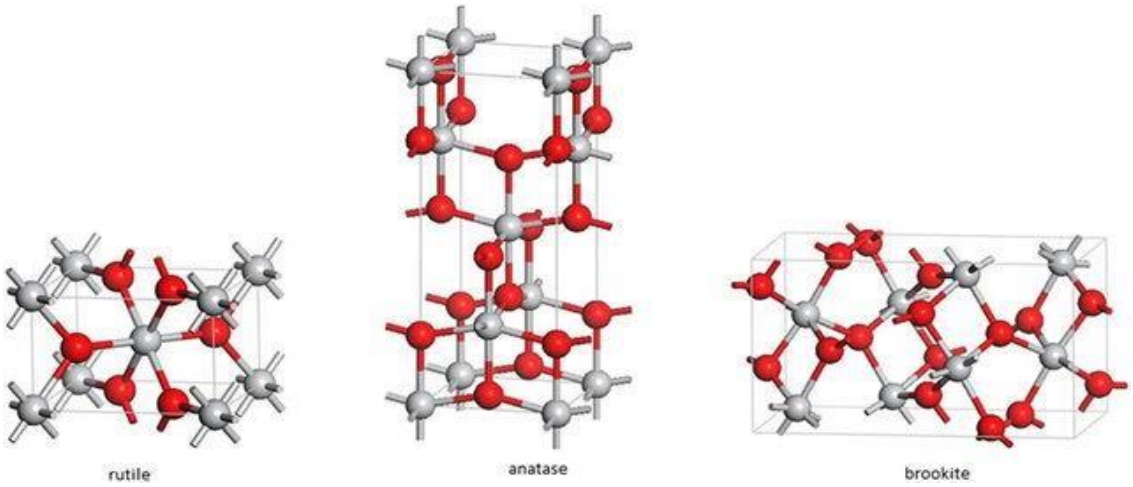

Table 14. Band gap, crystal system and space group of three polymorphs of TiO_2.

	Mineral			
Property	**Anatase**	**Brookite**	**Rutile**	**Ref**
Band Gap	3.2 eV	3.2 eV	3.0 eV	(Zhang, 2019)
Crystal System	Tetragonal	Orthorhombic	Tetragonal	(Gennari, 1998)
Space Group	$I4_1/amd$	Pcab	$P4_2$ mnm	(Gennari, 1998)

3.3 State of the Art Synthesis Routes for Titanium Dioxide

The following methods are state of the art synthetic routes towards achieving titanium dioxide reported in the literature.

3.3.1 Sol – gel Process

The sol-gel method is a wet chemical technique that involves the transformation of a colloidal solution (sol) into a gel and then into a solid material (gelation). The sol-gel method begins with titanium-containing precursors, often titanium alkoxides such as titanium isopropoxide, being dissolved in a solvent, typically alcohol or water, to form a clear solution. The following stages are hydrolysis and condensation, where the precursor solution undergoes hydrolysis as water molecules react with the titanium precursor to form titanium oxide compounds. This is followed by condensation reactions, leading to the formation of a three-dimensional network. The sol undergoes gelation, transforming into a three-dimensional gel network. The gel can be dried to obtain a porous, amorphous structure known as xerogel. Finally, the wet gel or xerogel is dried to remove the solvent. Subsequent calcination at elevated temperatures results in the formation of crystalline TiO_2. An optional stage is milling where the calcined TiO_2 powder may be milled to achieve a desired particle size and improve homogeneity.

The sol-gel process can have relatively long processing times due to the need for drying and calcination steps. The duration depends on factors such as the specific precursor used, the desired characteristics of the final product, and the chosen drying and calcination conditions. The sol-gel method is generally cost-effective. Titanium alkoxides can be used as precursors, and the solvents are commonly affordable. However, the cost may vary based on the purity of reagents and the energy costs associated with the drying and calcination processes. Titanium alkoxides, typically titanium isopropoxide, are common precursors. Solvents like alcohol or water are used for the preparation of the precursor solution. Acid or base catalysts may also be employed during hydrolysis. The sol-gel method is considered relatively straightforward, making it suitable for both laboratory and industrial applications. However, control over

reaction conditions, such as pH during hydrolysis and the drying process, is essential to achieving the desired properties of the TiO_2 product.

The sol-gel method allows for the synthesis of TiO_2 with a variety of morphologies. The precursor, solvent, and processing conditions influence the particle size, shape, and crystallinity of the final product. The resulting TiO_2 can exhibit different morphologies, including nanoparticles, nanotubes, or thin films. The porous nature of the gel structure can also be useful for certain applications, such as catalyst support or sensor materials.

The sol-gel process is particularly useful for producing titanium dioxide as the conditions can be moderated and adapted to generate different morphologies and structures, and can be used to apply a coating of titanium dioxide, while using simple and readily available equipment. Furthermore, the sol gel method allows the optimization of energy costs, in contrast to other methods of titanium dioxide synthesis (Mironyuk, 2020).

Titanium dioxide synthesis techniques that are appropriate for applying coatings of TiO_2 are limited to the sol gel process and chemical vapour deposition. The latter requires specialist equipment, training and technology, whereas the sol gel process can be accomplished using ambient temperatures and is a facile process to execute. For this reason, the sol gel process was selected as the most suitable method for applying the TiO_2 coating on to the hydroxyapatite – hollow glass microsphere beads.

The sol gel process was used to apply a coating of TiO_2 and ZnO to clay beads for the purpose of immobilising the photocatalysts while exploiting the advantages of nanoparticles. The degradation rate remained high at 87%, which is lower than the 95 – 99% degradation rates possible for TiO_2, however, 87% degradation is still high and the fact that nanoparticle agglomeration was prevented by immobilisation on to the clay particles, in addition to the fact that nanoparticle loss to the environment was minimised means this method for applying TiO_2

coatings to a surface for the purpose of photocatalysis has demonstrated that the sol gel process is appropriate for achieving TiO_2 coatings that are functional and fit for purpose as a photocatalyst (Krishnan, n.d.). Two applications of TiO_2 in photocatalysis have been reported in Table 15. TiO2 produced by sol gel reaction for photocatalytic applications.

Table 15. TiO_2 produced by sol gel reaction for photocatalytic applications.

Application	**Reagents/Conditions**	**Outcome**	**Product morphology**	**ref**
Photocatalytic Reactor	Titanium isopropoxide, 2-propanol, acetic acid, triethanolamine, ZnO powder	Dip coating method produced clay beads coated in immobilised nanoparticles and agglomerates of TiO_2/ZnO with highest photocatalytic efficiency of 87% reduction in methylene blue.	Small agglomerates and nanoparticles	(Krishnan, n.d.)
Photocatalysis	$Ti(OBUt)_3$, butyl alcohol, nitric or hydrochloric acid	Sol-gel method resulted in modified hydroxyapatite for photocatalysis, efficiency was 92% of P25 TiO_2	Fluffy HAP aggregated becomes coarser with TiO_2 sol, to 50 75 μm	(Khamova, 2018)

3.3.2 Hydrothermal

The hydrothermal process involves the reaction of titanium-containing precursors in an aqueous solution at elevated temperatures and pressures. Titanium-containing precursors, such as titanium sulphate or titanium chloride, are dissolved in water to form a solution. Additional reagents, such as a hydroxide source (e.g., sodium hydroxide), are added to the solution to initiate the hydrolysis and precipitation of titanium compounds. The main hydrothermal reaction occurs when the reaction vessel is sealed, and the solution is heated under high pressure (typically above 100°C) for an extended period (hours to days). This hydrothermal environment promotes the formation and growth of TiO_2 particles. The resulting product is washed to remove impurities and unreacted precursors. The washed material is then dried to obtain the final TiO_2 product.

The hydrothermal process typically requires long reaction times, ranging from several hours to days, depending on the desired particle size and crystallinity. This prolonged reaction time can contribute to the overall processing time. The cost of the hydrothermal synthesis process can be influenced by factors such as the purity of reagents, energy consumption during the hydrothermal reaction, and post-synthesis purification steps. Titanium-containing precursors can be relatively expensive, contributing to the overall cost. Common reagents include titanium salts (sulphate, chloride) and a hydroxide source (e.g., sodium hydroxide). The choice of reagents affects the reaction kinetics, product purity, and ultimately, the cost of the process. The hydrothermal synthesis of TiO_2 is generally considered a moderate-level synthesis technique. Control over reaction conditions, such as temperature, pressure, and reagent concentrations, is crucial to achieving desired particle characteristics.

The hydrothermal process can yield TiO_2 nanoparticles with controlled morphology. Factors like reaction temperature, pressure, and precursor concentrations influence the particle size, shape, and crystalline structure. Typically, hydrothermal synthesis produces nanoscale TiO_2

particles, and the resulting morphology may include various shapes such as nanorods, nanowires, or nanospheres, depending on the specific reaction conditions employed. The controlled morphology is advantageous for applications like photocatalysis, where surface area and reactivity are crucial (Mamaghani, 2019).

3.3.3 Solvothermal

Titanium-containing precursors, often titanium alkoxides or titanium chloride, are dissolved in a suitable solvent such as ethanol, isopropyl alcohol or ethylene glycol. Additional reagents, such as a hydroxide source or water, may be added to the solution to control the pH and promote the hydrolysis and condensation reactions of titanium precursors. As with the hydrothermal method the reaction mixture is sealed in a high-pressure reaction vessel and heated to an elevated temperature, typically ranging from 150°C to 300°C. The solvothermal process generally requires shorter reaction times compared to some other synthesis methods. Reaction times can vary from a few hours to up to three days, depending on the specific reaction conditions and desired particle characteristics.

The cost of the solvothermal synthesis process can be influenced by the choice of titanium precursors, solvents, and additional reagents. Titanium alkoxides, which are commonly used as precursors, can be relatively expensive. The overall cost may also depend on the energy consumption during the synthesis and post-synthesis purification steps. The reagents used as precursors in the solvothermal process are often titanium alkoxides (e.g., titanium tetraisopropoxide) Solvents such as alcohols and additional reagents like hydroxides or water may be used to control reaction conditions and promote the formation of TiO_2. Again, as with the hydrothermal method the solvothermal synthesis is generally considered a moderate-level synthesis technique. It requires careful control of temperature, pressure, and reagent concentrations.

The solvothermal process can yield TiO_2 nanoparticles with controlled morphology. The

specific conditions of temperature, pressure, and precursor concentrations influence the particle size, shape, and crystalline structure. The resulting TiO_2 nanoparticles may exhibit various morphologies, such as nanospheres, nanorods, or nanowires, depending on the synthesis parameters chosen. The ability to control morphology is valuable for tailoring TiO_2 properties for specific applications, such as photovoltaics or catalysis (Mamaghani, 2019).

3.3.4 Micro-wave Template

The microwave template method uses microwave irradiation to generate a template or scaffold for the controlled growth of TiO_2 nanoparticles. The template material serves as a structure-directing agent for the formation of TiO_2 nanoparticles. Titanium-containing precursors (e.g. titanium alkoxides) are impregnated into the template material. The impregnated template is subjected to microwave irradiation which accelerates the chemical reactions, resulting in the decomposition of the titanium precursor and TiO_2 nanoparticles. The resulting TiO_2 product is washed to remove any residual template or by-products, then dried to obtain the final TiO_2 product. The overall synthesis time is often shorter compared to conventional methods. The cost of the microwave template method can vary depending on the choice of template material and titanium precursor. Titanium alkoxides may be used as precursors, and certain templates could be more expensive than others. However, the shorter reaction times can contribute to energy savings, potentially offsetting costs. Proper control of microwave irradiation, precursor concentrations, and template removal steps is important for obtaining the desired TiO_2 morphology. However, the method is known for its efficiency and relatively straightforward procedure compared to some other synthesis techniques.

The microwave template method allows for the controlled growth of TiO_2 nanoparticles with a tailored morphology. The choice of template material influences the final structure, and common morphologies include nanospheres, nanorods, or other shapes guided by the template. The advantage of this method lies in its ability to produce well-defined and uniform TiO_2 nanoparticles with enhanced properties for applications such as catalysis and sensing

(Mironyuk, 2020) (Bao, n.d.).

3.3.5 Chemical Vapour Deposition

Chemical Vapour Deposition is a technique where a thin film or coating of a material is deposited onto a substrate by introducing volatile precursors into a reaction chamber. TiO_2 can be synthesized using CVD in a number of steps which begin with precursor vapourisation: where volatile titanium-containing precursors, such as titanium tetrachloride ($TiCl_4$) or titanium tetraisopropoxide (TTIP), are vapourised. The vaporized precursors are then carried into a reaction chamber by an inert carrier gas, such as nitrogen or argon. The precursor vapours come into contact with a heated substrate, which is when the reaction occurs. The thermal energy causes the precursors to decompose, leading to the formation of TiO_2 on the substrate. The final stage which is optional is the annealing stage, where post-deposition, the substrate may be annealed to enhance the crystallinity and optimize the properties of the TiO_2 film.

CVD processes are generally considered to be relatively fast, with deposition occurring in a matter of minutes to hours. However, the overall time can depend on factors such as the desired film thickness and the complexity of the equipment. The set-up cost of CVD can be moderate to high due to the specialized equipment required. The cost of precursors, such as $TiCl_4$ or TTIP, can also contribute to the overall cost. However, the technique is efficient, and large-scale production may provide economies of scale. The choice of precursor is crucial in CVD. Common titanium precursors include $TiCl_4$, TTIP, or titanium tetrabutoxide. Carrier gases and other reactants may also be used to control deposition conditions. CVD processes are considered moderately complex. Precise control over temperature, pressure, and precursor concentrations is essential to achieve uniform and high-quality TiO_2 films. Maintenance of the specialized CVD equipment adds an additional layer of complexity.

The morphology of TiO_2 deposited using CVD depends on the specific conditions of the deposition process. CVD allows for the production of thin films with controlled thickness and

excellent uniformity. The resulting TiO_2 films can have various morphologies, including smooth films, nanostructured films, or even patterned structures, depending on the deposition conditions and the substrate used. CVD offers versatility in tailoring film properties for applications such as thin-film solar cells, sensors, and optical coatings (Zhang, 2020) (Mironyuk, 2020) (Zhang, 2020).

3.3.6 Green Methods

Green synthesis methods aim to minimize the environmental impact of the synthesis process, reduce energy consumption, and often use eco-friendly or sustainable reagents. Several approaches can be considered for green synthesis of TiO_2, which include using natural sources or waste materials as titanium precursors. For example, titanium-containing agricultural residues or waste from industrial processes can be used as the starting material. Another green method is bio-inspired synthesis, where biological entities such as plant extracts (Manikandan, 2022) including green tea extract are used as reducing or stabilizing agents. These biological agents can facilitate the conversion of titanium precursors into TiO_2 nanoparticles under mild conditions. In addition, using solar photocatalysis as an energy source for the synthesis process can improve the green aspect of a method by reducing reliance on energy from fossil fuels or non- sustainable sources. In this method, titanium-containing precursors can be subjected to photocatalysis using solar radiation, promoting the green and sustainable production of TiO_2. Conventional solvents can be replaced with environmentally friendly alternatives, such as water or bio-based solvents, to reduce the environmental impact of the synthesis process.

Green synthesis methods may exhibit varying processing times depending on the specific approach. Bio-inspired methods might take longer, while solar photocatalysis can be achieved more quickly. The overall time required could be influenced by factors like precursor type, reaction conditions, and the desired characteristics of TiO_2. Green synthesis methods often aim for cost-effectiveness by utilizing renewable resources or waste materials. However, costs can

still vary depending on the chosen green reagents and the scale of production. Generally, green methods strive to reduce costs associated with energy consumption and hazardous materials. The reagents in green synthesis are chosen to be environmentally friendly. Natural precursors, biological agents, and green solvents are commonly used to minimize the use of toxic or harmful substances. The emphasis is on sustainability and reducing the environmental footprint. Green synthesis methods can range in complexity. Bio-inspired methods might require careful control of biological parameters, while solar photocatalysis might be more straightforward. The overall difficulty depends on the specific green synthesis approach chosen.

The morphology of TiO_2 synthesized using green methods can vary depending on the chosen approach. Green synthesis approaches often result in nanoparticles with diverse shapes and sizes. For instance, bio-inspired methods may lead to TiO_2 nanoparticles with unique morphologies influenced by the biological entities involved. Additionally, the use of green solvents and mild conditions may contribute to the formation of well-dispersed and environmentally friendly TiO_2 nanomaterials. The porous and nanoscale characteristics of the final product could make it suitable for various applications such as catalysis, sensing, or environmentally friendly coatings (Yamamoto H., 2004).

3.4 Health Hazards of Titanium Dioxide

3.4.1 Legal Classification

On 6th May 2021 TiO_2 was reclassified by the European Food Safety Authority when it concluded that TiO_2 "can no longer be considered safe [as] a food additive". Prior to 2021 TiO_2 had been used in paints, pigments, foods and medicines under the name E171. The reason for this change in classification from "safe for consumption" to "no longer considered safe" is that evidence linking TiO_2 to genotoxicity was reconsidered and the potential for TiO_2 to be genotoxic was considered serious enough to remove TiO_2 from food products.

3.4.2 Routes of Exposure

There are a number of potential routes of exposure which could lead to the accumulation of TiO_2 in the body, including inhalation, ingestion, injection and dermal penetration. The route of exposure influences the destination of the TiO_2 nanoparticles in the body, and accordingly the consequences are different. However, once TiO_2 nanoparticles enter the cardiovascular system they are borne by the bloodstream to all parts of the body.

Rodent studies conducted by Mühlfeld et Al. found that translocation of TiO_2 nanoparticles occurred from the pulmonary airways to other pulmonary compartments and the destination was time dependent, i.e. 1 hr after exposure the NPs were found in the connective tissue and 24 hr after exposure NPs were located in the capillary lumen. Aerosolized TiO_2 NPs exposure triggered progressive epithelial and fibroproliferative changes in the rodent's lungs and lymph nodes and the rate of removal of TiO_2 NPs from the lungs of the test subjects was reduced (Muhlfeld C, 2007), (Shi, 2013). Sadrieh (2010) and Newman (2009) found that the livers and lymph nodes of test subjects treated with three types of TiO_2 particles (uncoated submicron size, uncoated nano sized and coated nano sized) showed no increase in titanium relative to the control subjects, although their epidermises showed elevated levels of titanium. Despite the presence of titanium in the epidermis, the lack of a pattern of titanium distribution led the authors to conclude that the few isolated particles of TiO_2 found were likely to be from

contamination and that overall, intact uninjured epidermis does not permit signification penetration of TiO_2 nanoparticles (Sadrieh, 2010). The routes of exposure and accumulation sites of TiO_2 are outlined in Figure 9Figure 9. Toxicokinetics and accumulation sites for TiO2 nanoparticles - dotted lines represent unconfirmed but speculated routes. (Shakeel, 2015)

Figure 9. Toxicokinetics and accumulation sites for TiO_2 nanoparticles - dotted lines represent unconfirmed but speculated routes.

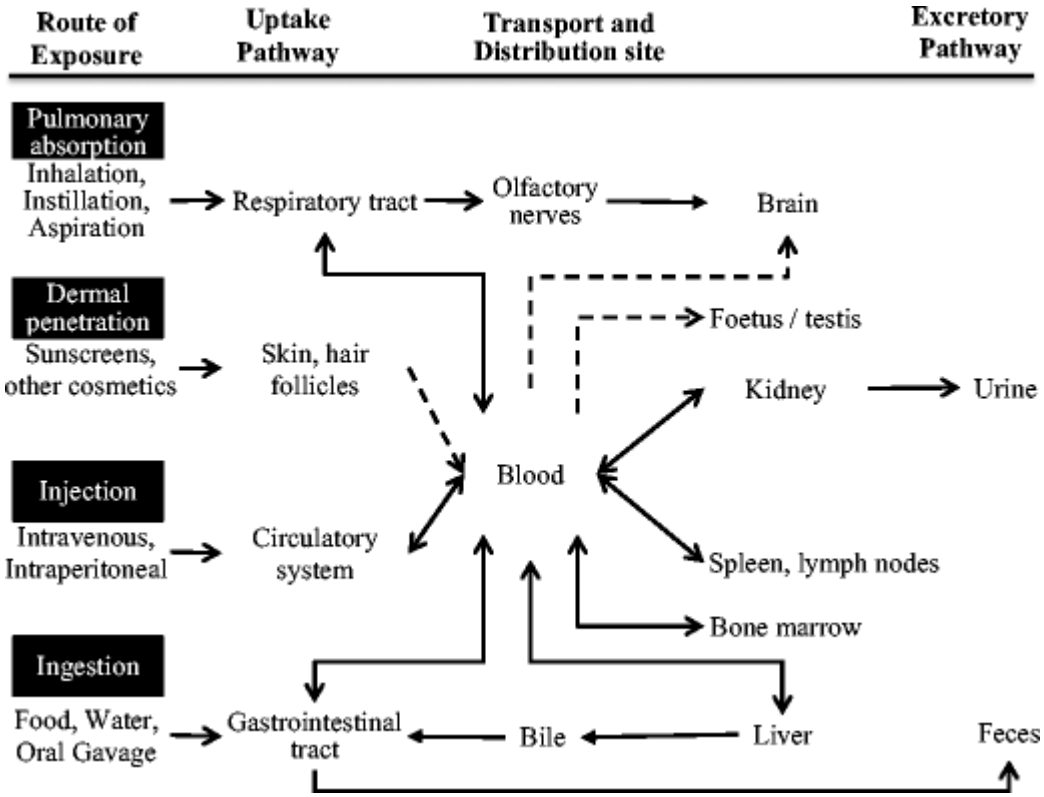

The potential for titanium dioxide nanoparticles to accumulate in soft tissues means that the release of TiO_2 nanoparticles into the environment should be avoided. Immobilising the TiO_2 nanoparticles on to a substrate allows the reactivity and high surface area of the nanoparticles to be exploited while avoiding NP release into the environment and preventing accumulation in soft tissues. This is why it has been chosen to immobilise the TiO_2 component of the adsorbent/photocatalytic material.

3.5 Characterisation Methods for Titanium Dioxide

Characterisation of TiO_2 in its solid state is mainly performed using XRD to confirm the crystal lattice, along with Raman spectroscopy also being used to characterise anatase and rutile. The XRD *hkl* peaks for anatase and rutile along with their 2theta locations and intensities are contained in Table 16. XRD Pattern of Anatase and Table 17. XRD Pattern of Rutile .

Table 16. XRD Pattern of Anatase (Horn, n.d.)

2Theta	**Intensity**	***hkl***
25.23	100.00	101
36.86	6.27	103
37.72	20.20	004
38.46	7.12	112
47.89	28.21	200
53.77	17.94	105
54.89	17.65	211
62.51	13.73	204
74.83	10.28	215

Table 17. XRD Pattern of Rutile (Swope, 1995)

2Theta	**Intensity**	***hkl***
27.39	100.00	110
35.97	45.00	101
39.09	6.47	200
41.11	18.38	111
43.92	6.43	210
54.12	52.79	211
56.44	15.73	220
62.46	7.29	002
63.82	7.29	310
68.73	17.89	301
69.46	8.72	112

Titanium dioxide produced via sol-gel process at temperatures below 200 °C produce XRD patterns with wide and broad peaks, however calcination at increasingly higher temperatures increases particle size, crystallite size, and crystallinity of the TiO_2 produced, which in turns results in sharper more define peaks in the XRD pattern. This can be seen in Figure 10. XRD pattern of TiO2 particles after calcination at temperatures ranging from 300 °C to 800 °C (Phromma, 2020).

Figure 10. XRD pattern of TiO_2 particles after calcination at temperatures ranging from 300 °C to 800 °C (Phromma, 2020).

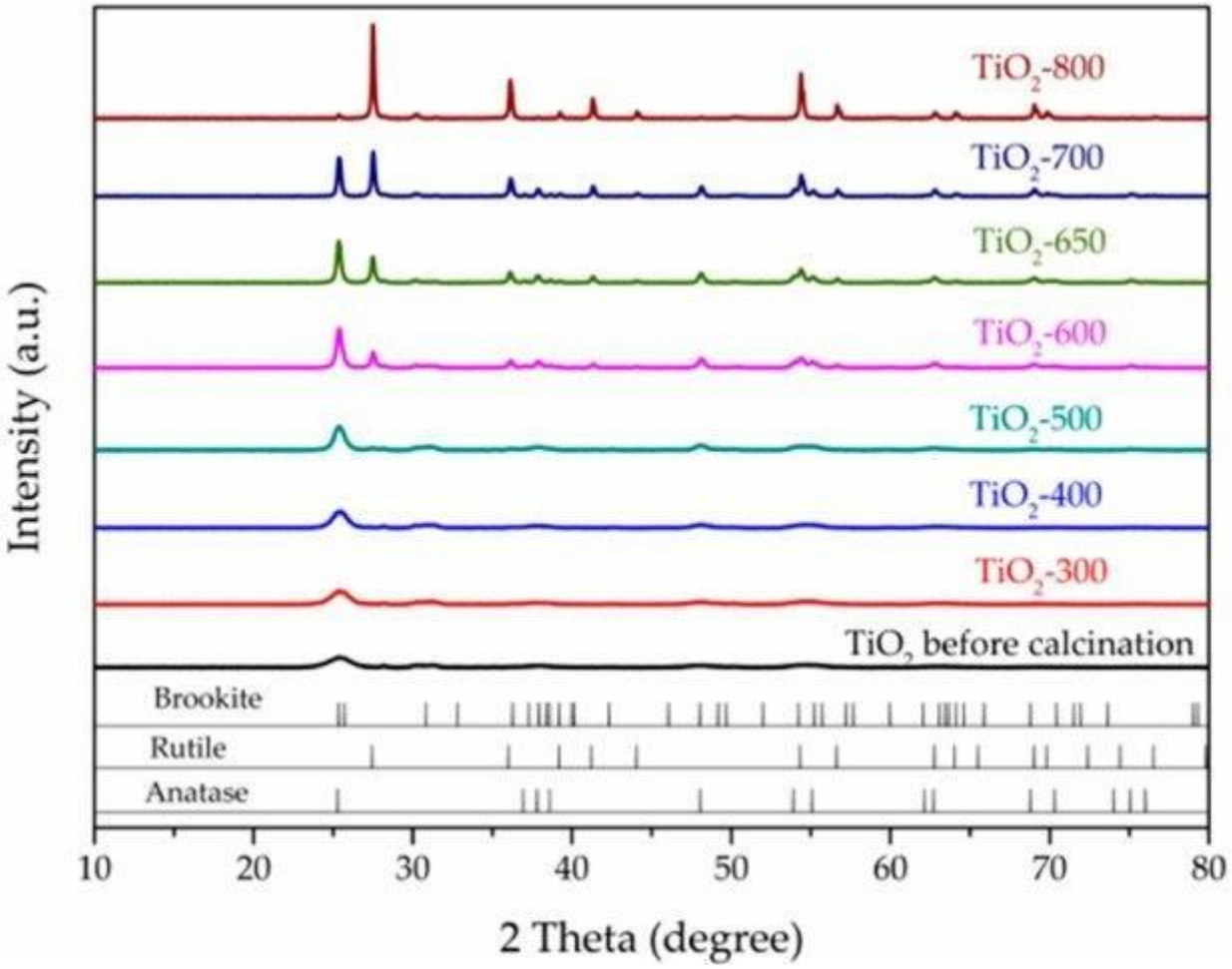

The Raman bands characteristic of anatase and rutile are depicted in Figure 11. Raman shift of anatase (a) and rutile (b) (89), while the frequencies and band assignments are contained in

Figure 11. Raman shift of anatase (a) and rutile (b) (89).

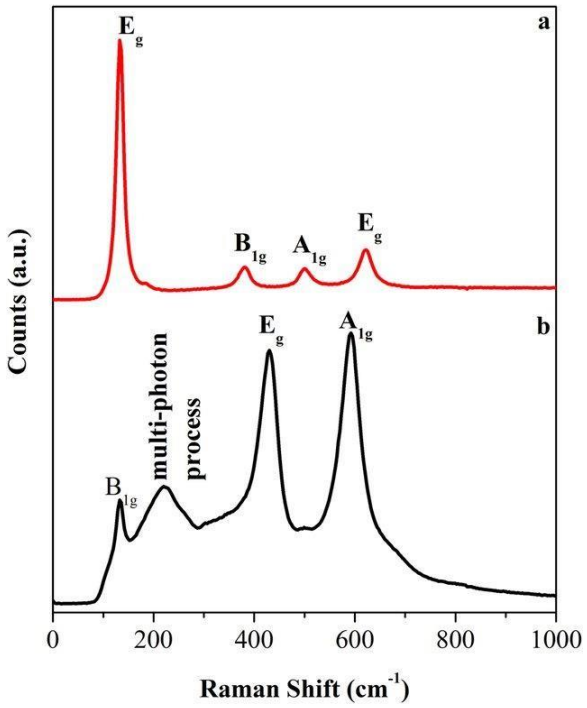

Table 18. Raman spectrum anatase and Table 19. Raman spectrum rutile .

Table 18. Raman spectrum anatase (Challagulla, 2017).

Raman Shift cm $^{-1}$ – Anatase	**Band**
144	E_g
198	E_g
394	B_{1g}
514	A_{1g}, B_{1g}
634	E_g

Table 19. Raman spectrum rutile (Challagulla, 2017)

Raman Shift cm^{-1} – Rutile	**Band**
140	B_{1g}
230	Multi photon scattering process
430	E_g
610	A_{1g}

3.6 Morphologies Generated

3.6.1 Nanoparticles

A curing step at 90 °C was employed by researchers who then calcined the titania bearing material at temperatures between 700 °C and 900 °C, achieving amorphously shaped nanoparticles that nevertheless had very consistent sizes, approximately 50 nm diameters, when calcined at 700 °C. The crystals grew larger and more irregular in shape as the calcining temperature was increased to 900 °C (Bachina, 2021).

3.6.2 Nanotubes

The nanotubes presented by Hussein et al. were prepared via electrochemical anodization of Ti foils in an electrolyte solution consisting of ethylene glycol (99.5%) and ammonium fluoride (0.5%) (Hussain, 2016). A similar result was achieved more recently, again through anodization of Ti foils in ammonium fluoride (Pio, 2018). Ethylene glycol together with ammonium fluoride has also been used in the synthesis of titanium dioxide nanotubes from anodic oxidation of titanium foil (Farrugia, 2021). Electrochemical anodization of titanium metal or a titanium foil appears to be the most common method of producing titanium dioxide nanotubes reported in the literature. This may be because when the nanotubes are grown on a flat surface, such as foil or metal substrate, the tubes grow along one axis and are possible to identify as tubes. If produced in solution, the nanotubes would be oriented randomly and it would not be as obvious that the nanotubes are hollow, instead appearing as rods or cylinders in shape from inspection of SEM images. An example of TiO_2 nanorods produced from anodizing titanium foil are depicted in Figure 4 (Hussain, 2016).

Figure 12. TiO_2 nanotubes produced by Hussein et al. (Hussain, 2016).

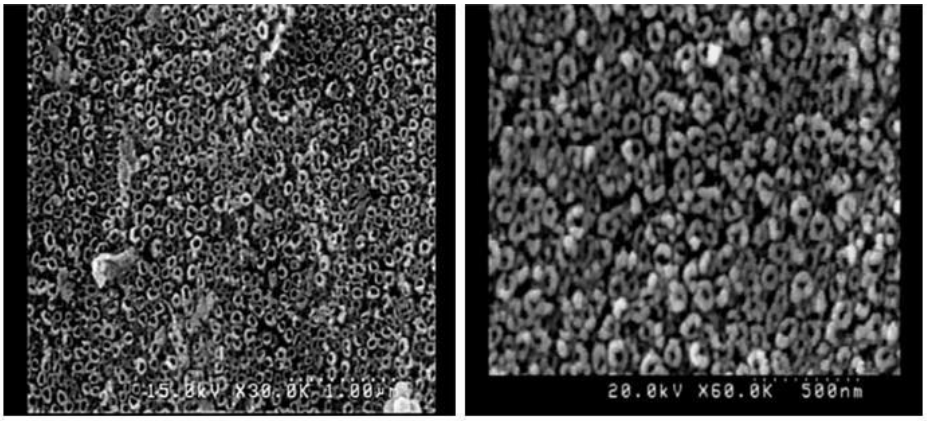

3.6.3 Nanorods

Acidic reaction control was employed to obtain TiO_2 needle type structures using sucrose esters to assist the reaction. The products were found to be excellent for the degradation of methylene blue (Anwar, 2010). Autoclaves have been used to achieve a carpet of titanium dioxide nanorods attached to fluorine tin oxide glass using acidic control of the reaction and using titanium tetrabutoxide as the titanium bearing reagent. This reaction process results in titanium dioxide rod-like structures aligned along the same plane. These researchers also found that by increasing the temperature in 10 °C increments from 150 °C to 170 °C resulted in the diameter of the nanorods also increasing, an image of these nanorods are shown in Figure 13. TiO2 nanorods produced by Qasim et al. (Qasim, 2017).

Figure 13. TiO_2 nanorods produced by Qasim et al. (Qasim, 2017).

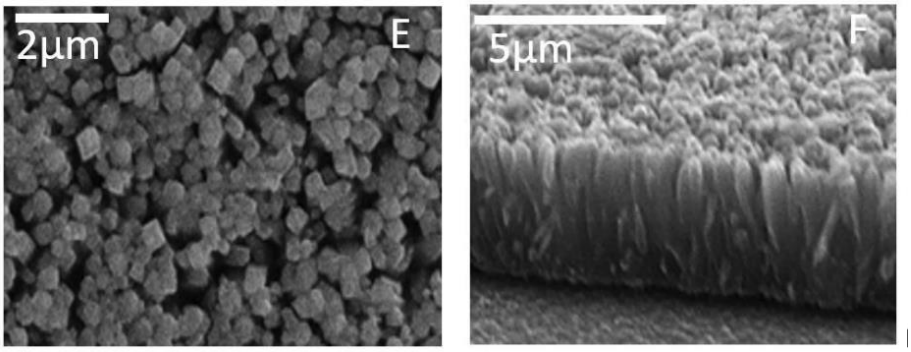

Nanorods were produced where the nanorods produced were free with no distinct arrangement of nanorods. The reaction used titanium tetraisopropoxide and ethylene glycol in a preparation termed a polyol mediate solvothermal process. The nanorods produced had high photocatalytic activity, achieving 98.1% destruction of methylene blue dye after 120 min under UV radiation. Anatase was the main form of TiO_2 produced after calcination at 450 °C, and it is likely that the high photocatalytic activity was due to anatase being the form of titanium dioxide produced, which is more photocatalytically active than rutile or amorphous titanium dioxide. The nanorods produced by Alosfur et Al. are shown in Figure 14. Different magnifications of TiO2 produced by Alosfur et al. (Alosfur, 2019).

Figure 14. Different magnifications of TiO_2 produced by Alosfur et al.

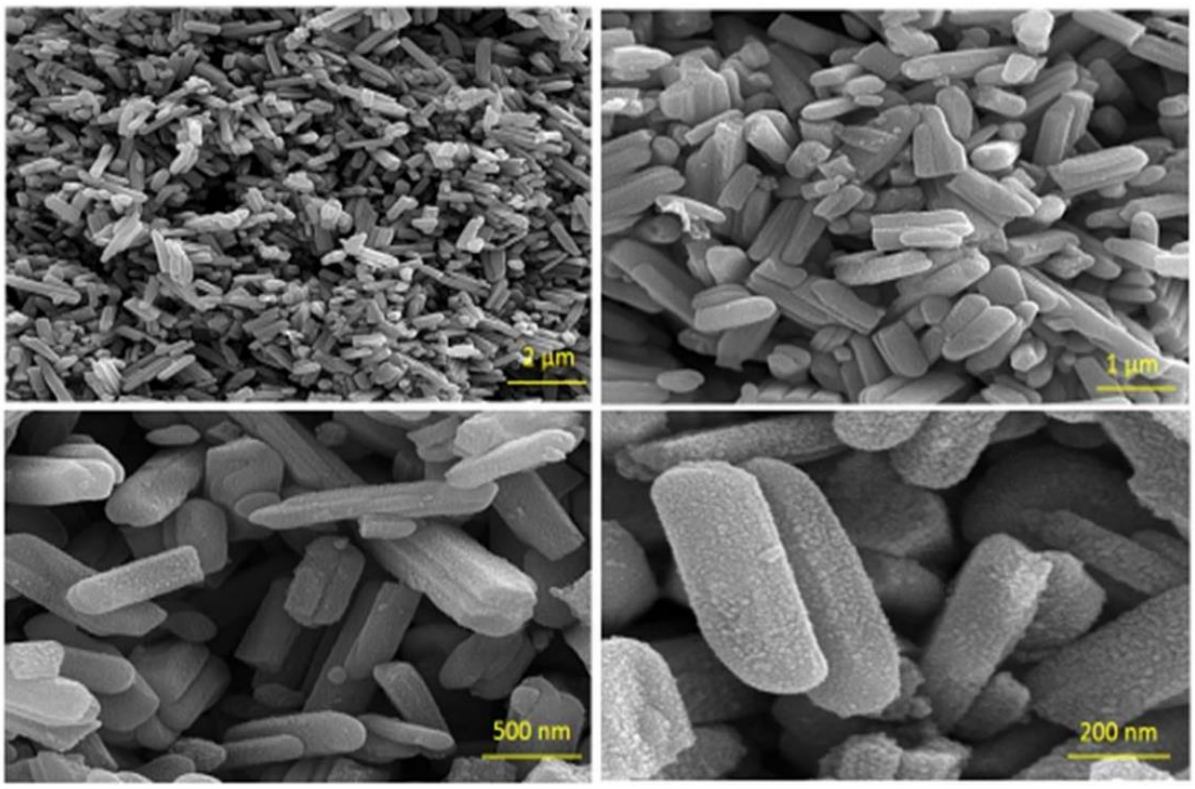

3.6.4 Exotic Structures

Sea urchin-like particles were produced using tetrabutyl titanate in the presence of organic acid (oleinic acid) and HCl, followed by heating in an autoclave for four hours. Here, acidic control has been employed to guide crystal growth – a common theme in TiO_2 NP synthesis. The products of this reaction are pictured in Figure 7 (Tang, 2021).

Figure 15. The "blooming nanoflowers" of TiO_2 produced by Tang (2021) (Tang, 2021).

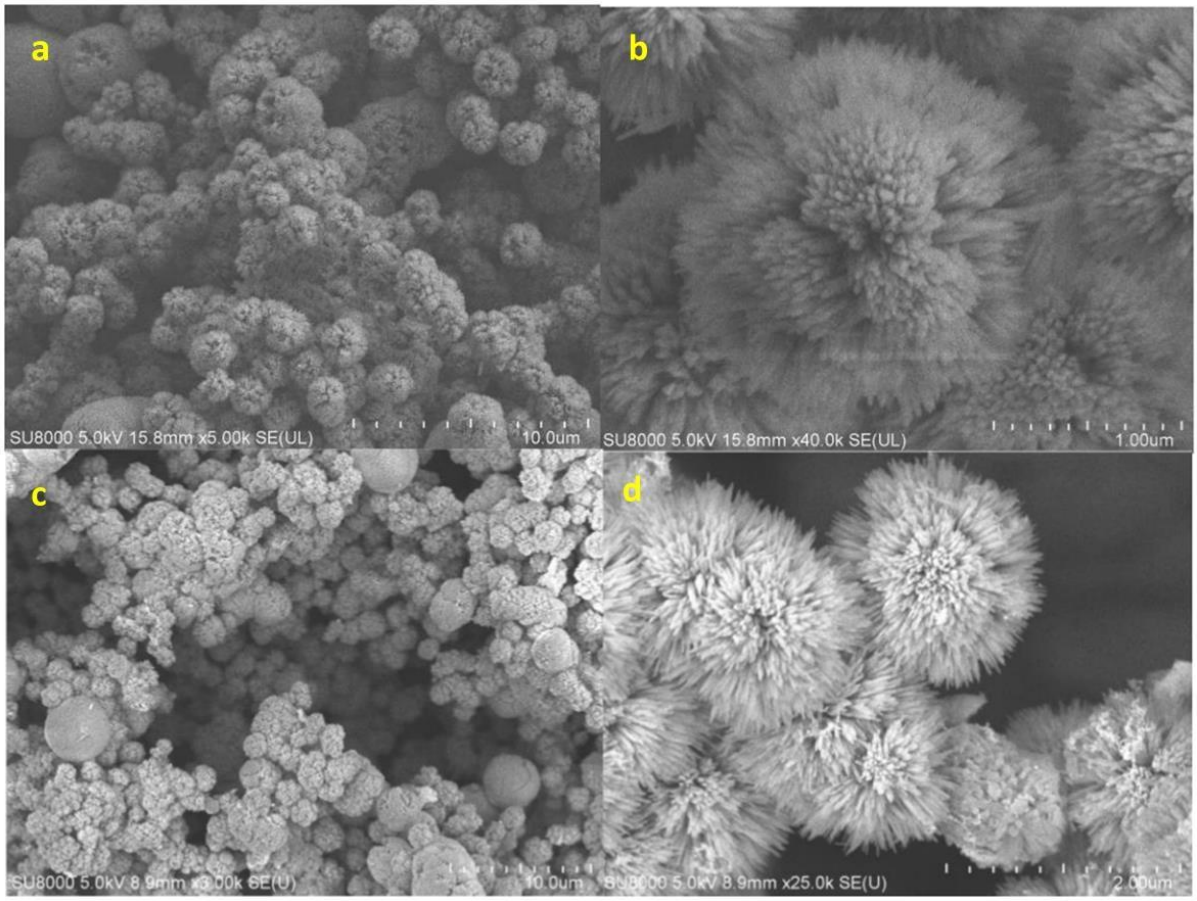

3.6.5 Nanowhiskers

TiO_2 nanowhiskers loaded with porphyrin (tetra sulphonatophenyl porphyrin) were found to be helpful in reducing autoimmune reactions associated with rheumatoid arthritis (Rehman, 2016). The same porphyrin-TiO_2 nanocomposite was demonstrated to reduce the blood sugar level of Type II diabetic mice with effects lasting over 24 hours (Rehman, 2016). The mechanism by which the porphyrin- TiO_2 nanocomposite works is by acting as the photosensitizer in photodynamic therapy – irradiating this nanocomposite after its injection into the target tissue produces reactive oxygen species which are thought to cause cell necrosis by interacting with cell signalling pathways, or by oxidising DNA bases.

3.7 EE2 Degradation and Removal Efficiencies by TiO_2

TiO_2 has been reported to remove 70-100% of EE2 from water when used as a photocatalyst. The removal of EE2 by TiO_2 is reported in Table 20. Removal of EE2 obtained by TiO2 using photocatalysis, where it is evident that significant amounts of EE2 can be removed in short timescales. Here DES refers to diethylstilbestrol, another synthetic estrogen.

Table 20. Removal of EE2 obtained by TiO_2 using photocatalysis.

E	E Conc.	pH	UV lamp	Removal	Vol.	TiO_2 Catalyst	Time	ref
DES **E1** **E2** **E3**	10 ppm & 5 ppm	7.5 +/- 0.5	500 W Xe-arc lamp	97.2% - 100%	500 mL E	1.0 g/L	75 min	(Rocha, 2022)
EE2	-	-	-	100%	-	-	-	(Wei, 2018)
E1 **E2** **EE2**	26 18 140	8	-	>70%	24 L/min	50 ppm TiO_2	-	(Bentotti, 2009)
EE2	100 µg/L	8	sunlight	84.5% - 89.9%	300 mL	250-1500 mg/L, 750 mg/L best	90 min	(Wahab, 2019)
E2 **EE2**	200 ug/L in EtOH	4.5	2 x 10 W	-	-	TiO_2 coated Raschig rings	-	(Colina-Márquez, 2015)
E1 **E2**	10 mg/L	7.6 pH tested 2 - 10	150 W 238-579 nm 15 W 253 nm	97% 98%	0.4 L 0.7L	1 g/L or 2 g/L	4h 1h	(Moreira, 2016)
EE2	20 ug/L	-	-	100%	-	-	-	(Kiat Ng, 2017)
E2	1 ng/L 1 ug/L	6	400 W 254 nm	>85%	14 L	100 mg/L	60 min	(Orozco-Hernánde

								z, 2019)
E1 **EE2**	10 mg/L	4 and 6	50 W or 80 W 405 nm	93% 90%	40 mL	Ti- 0.5 wt.%W alloy, formed with HF	40-50 min 20 °C	(Oliveira, 2020)
EE2	10 mg/L (34 μmol/L)	6.9	400 W solar simulator	10-3.6 mg/L	-	TiO_2 TiO_2/WO_3	4 h	(Oliveira, 2015)

3.8 Critical Assessment of Doping Strategies to Enhance TiO_2 Photocatalysis for Water Purification

Titanium dioxide remains one of the most widely researched and deployed photocatalysts for water purification due to its high oxidative potential, non-toxicity, low cost, and strong chemical stability. Its ability to degrade a wide range of organic pollutants, pathogens, and pharmaceutical residues has made it central to AOPs in water treatment. However, a fundamental limitation of TiO_2-based photocatalysis is its wide bandgap – 3.2 eV for anatase, which restricts photoactivation to the ultraviolet UV spectrum – comprising less than 5% of terrestrial solar irradiance. This significantly hampers its solar-driven efficiency and large-scale deployment in outdoor or energy-scarce settings. To overcome this, strategies have been investigated to:

- sensitize TiO_2 to the visible spectrum, increasing the range of electromagnetic frequencies that can be exploited by the TiO_2-containing material, thus expanding its utility in solar-assisted water purification systems; and
- reduce electron-hole recombination, often using heterojunctions, to promote spatial separation between charge-carrier pairs, increasing the likelihood of interfacial redox chemistry per absorbed photon.

The ultimate aims of doping strategies are to increase the proportion of photons received from the sun that are capable of exciting electrons within the TiO_2-containing material lattice and hence increasing the amount of energy produced per m^2 of material, resulting in a clear financial benefit for the energy producer and consumer.

While TiO_2 doping strategies have and continue to demonstrate promise, their application in real-world aqueous environments presents distinct challenges. An alternative to investigating and researching doping strategies is to develop new wide-spectrum semi-conductor materials, which reduces the need for band-structure manipulation, which is required to allow TiO_2-

containing materials to exploit a greater proportion of terrestrial solar irradiance. Salient examples of alternatives to TiO_2 are polymeric carbon nitride (g-C_3N_4) (Feng, 2010), (Kumar, 2020), which has the benefits of being a stable, metal-free photocatalyst with a demonstrated ability to use visible light to for H_2 production. Similarly, environmental photocatalysis has also been successfully demonstrated using WO_3 (Oliveira, 2015), (Soares Filho, 2018). The advantages of seeking new wider spectrum materials for environmental photocatalysis is that materials can be selected for their existing responsiveness to visible light, rather than continuously altering and fine-tuning TiO_2. However, while the band gap of a material such as g-C_3N_4 may be smaller and hence more responsive to visible light, there are other disadvantages that must be recognised, namely:

- issues with stability and durability in real-world scenarios, e.g. surface deactivation, oxidation and in certain conditions potentially bio-fouling, particularly in complex water matrices, which raises complications regarding maintenance during the service lifetime of the material, even when initial activity is deemed high;
- band-edge limitations, wherein some visible light-absorbing materials require co-catalysts, hence a wider spectrum material may not necessarily correspond to an overall net improvement in performance;
- manufacturability and integration risks, as scientific research may fall into the "valley of death" where complex manufacturing requirements, lack of necessary infrastructure to integrate or complicated reactor designs result in an inability to progress the material through higher technology readiness levels (TRLs) through to full scale deployment.

In contrast, choosing to engage in doping strategies to optimise TiO_2 for visible light-responsiveness may be assumed to be more likely to result in a product that be escalated quickly through TRLs into full-scale deployment once a suitable material has been confirmed. It is for this reason that TiO_2 was selected as the preferred photocatalytic material for the purpose of water remediation, as TiO_2 has the potential to be further optimised while still displaying useful

and reliable photocatalytic properties and resilience in a complex water matrix. The following section evaluates the advantages and drawbacks of doping TiO_2 with respect to its performance, stability, and viability for sustainable water purification technologies.

3.8.1 Advantages of Doping TiO_2 for Water Purification

3.8.1.1 Solar-Driven Photocatalytic Activation

Doping introduces impurity levels or mid-gap states that lower the excitation energy required to activate TiO_2, enabling photocatalysis under visible light (>400 nm). This enhances its suitability for passive, solar-driven water purification systems, reducing reliance on artificial UV light sources and associated energy costs (Chen, 2008) (Khan, 2002). As such, doped TiO_2 is particularly advantageous for use in remote or developing regions where electricity supply is intermittent or absent.

3.8.1.2 Degradation of Recalcitrant Organic Pollutants

Several classes of emerging contaminants—including endocrine-disrupting compounds (e.g., EE2), pharmaceuticals, pesticides, and industrial dyes—are resistant to conventional biological treatment. Doped TiO_2 has been shown to degrade these under visible light with comparable or superior efficiency to UV-activated TiO_2 (Li, n.d.). Doping can also enhance surface hydroxylation and adsorption affinity, facilitating faster and more selective oxidation of target compounds.

3.8.1.3 Antimicrobial Activity in Low-Light Conditions

Photocatalysis not only degrades chemical pollutants but also generates reactive oxygen species ROS that exhibit strong antimicrobial properties. Doping enhances the ability of TiO_2 to produce ROS under ambient or indoor light, thereby expanding its potential for pathogen inactivation in drinking water or greywater reuse systems (Zhang, 2021).

3.8.1.4 Tailored Material Properties for Specific Contaminants

Non-metal and transition-metal dopants can be used to fine-tune the electronic structure and surface charge of TiO_2 making it more selective for specific classes of pollutants. For example, nitrogen-doped TiO_2 shows enhanced affinity for aromatic compounds due to π–π interactions, while iron-doping can improve redox cycling and Fenton-like activity for H_2O_2-assisted degradation (Asahi, 2001).

3.8.2 Limitations and Challenges of Doping TiO_2 in Aqueous Environments

3.8.2.1 Stability and Leaching of Dopants in Water

Many doped TiO_2 materials, particularly those doped with non-metals (e.g., N, C, S), are prone to instability in aqueous environments. Under prolonged light exposure or fluctuating pH, dopants may leach or oxidise, leading to reduced activity and possible contamination of treated water. This is a significant concern for drinking water treatment systems requiring high regulatory compliance (Liu, 2013).

3.8.2.2 Formation of Secondary Pollutants and Byproducts

Incomplete photocatalytic degradation, especially under sub-optimal visible-light activation, can result in the formation of toxic byproducts such as aldehydes, chlorinated intermediates, or quinones. Dopants that interfere with oxidative pathways or reduce hydroxyl radical formation may exacerbate this issue (Di Valentin, 2007). Thorough toxicological assessment of effluent is essential when using doped catalysts.

3.8.2.3 Trade-Off Between Visible-Light Absorption and Charge Carrier Dynamics

Although doping narrows the bandgap, it may introduce mid-gap states that act as recombination centres, thereby reducing the lifetime and mobility of photogenerated carriers.

In aqueous photocatalysis, this limits ROS generation and lowers degradation efficiency, especially in turbid or complex matrices with high organic load (Scanlon, 2013).

3.8.2.4 Synthesis Scalability and Environmental Cost

Doping processes often require precise thermal treatment, chemical precursors, or vacuum deposition techniques that are not easily scalable. Moreover, dopants such as chromium or vanadium can pose environmental hazards if not fully incorporated into the lattice or if the catalyst degrades. This undermines the sustainability and circularity goals of green water purification technologies (ang, 1994). Furthermore, doping introduces additional material costs and may increase the number of steps taken to produce the photocatalyst, which could decrease the economic viability of the project.

3.8.2.5 Heterogeneous Performance in Natural Waters

Natural waters contain a variety of inorganic ions (e.g., Cl^-, SO_4^{2-}, HCO_3^-), dissolved organic matter, and microbial communities that can interact with both dopants and the active surface of TiO_2. These constituents may scavenge radicals, block active sites, or facilitate dopant leaching, leading to inconsistent performance across different water sources (Li, n.d.).

3.8.3 Conclusion

Doping TiO_2 represents a compelling strategy to overcome the spectral limitations of pristine TiO_2 and realise solar-assisted photocatalytic water purification. Enhancements in visible-light absorption and pollutant degradation have been well-documented in controlled laboratory conditions. However, the deployment of doped TiO_2 in real-world water matrices reveals several unresolved issues – namely, stability under irradiation, dopant leaching, and unpredictable performance due to environmental interferences. To maximise the benefits of doped TiO_2, future research must prioritise the development of synthesis routes that anchor

dopants securely within the TiO_2 lattice, while maintaining structural integrity and charge transport. Furthermore, long-term pilot studies in real water systems are essential to establish the viability, safety, and environmental impact of these materials. This would ensure that doped TiO_2 transition from a promising material in laboratory research to a reliable technology in global water purification systems.

3.9 Photocatalysis: Scale-up Operation Introduction & Key Challenges

Transitioning a bench-scale photocatalyst – typically TiO_2 or advanced doped nanomaterials – from beaker tests to full-scale deployment demands attention to material engineering, reactor design, light management, mass transport, and sustainability (Alalm, 2021). Critical hurdles include:

- Catalyst recovery: Ensuring stable immobilization to avoid nanoparticle release.
- Light distribution: Maximizing oxidative photon flux across the reactor volume.
- Mass transfer limitations: Achieving adequate contact between pollutants, light, and active sites in turbid water.
- Durability under real-world conditions: Chemical fouling, catalyst deactivation, and harsh water matrices (Plakas, 2017).

3.9.1 Catalyst Immobilization Techniques

3.9.1.1 Flat Immobilized Layers

In bench- to pilot-scale systems, forming planar films of photocatalyst on substrates such as glass, ceramic tiles, or mesh grids is a common method to improve catalyst recovery. These layers are typically applied via dip-coating or sol–gel techniques, followed by thermal treatment to enhance adhesion and crystallinity. For example, TiO_2–SiO_2 mixtures have been successfully immobilized onto glass beads using dip-coating, yielding a composite film with increased mechanical stability while retaining photocatalytic efficiency in degrading phenol under UV irradiation. The planar geometry also facilitates uniform fluid flow and optical exposure but demands compromise between surface area and ease of light penetration (Oliveira, 2022).

Advantages: straightforward fabrication, catalyst reuse, reduced nanoparticle release. **Limitations**: lower active surface area per volume, potential deactivation due to fouling or micro-cracking, barriers related to their fixation in the system.

3.9.1.2 Submerged Photocatalytic Membrane Reactors

Hollow-fibre and flat-sheet membrane reactors embed photocatalysts within the membrane matrix—for instance, Cu_2O nanoparticles entrapped in polyvinylidene fluoride (PVDF) hollow fibres. The result is a dual-functional system: simultaneous photocatalytic degradation of contaminants and membrane filtration to retain catalyst particles. This design substantially mitigates catalyst leaching, enhances mass transfer, and allows operation under constant flow. Scaling these from laboratory prototypes (100–500 mL) to pilot volumes (~10–100 L) requires addressing uniform catalyst loading, shear stress resilience, and fouling behaviour in complex feeds (Noor, 2022).

3.9.1.3 Photocatalytic Nanofiltration Reactors (PNFR)

PNFRs combine nanofiltration membranes and immobilized TiO_2-coated monoliths within module assemblies. A notable pilot-scale implementation processed approximately 1.2 m^3/day of agrichemical wastewater, achieving 95 % water recovery and effective degradation of pesticide residues like thiabendazole and acetamiprid. This design emphasizes modularity: each PNFR unit can operate in parallel, simplifying maintenance and scaling. Performance evaluations under real wastewater streams revealed retention of photocatalytic activity over weeks, although fouling control and UV light penetration were identified as critical operational parameters (Theodorakopoulos, 2023).

3.9.2 Reactor Configuration & Light Design

3.9.2.1 Annular Batch and Continuous Reactors

The annular reactor contains a central UV lamp enclosed within a quartz sleeve and surrounded by photocatalyst-laden fluid, which permits uniform irradiation. Initially applied at bench scale (~750 mL), this geometry was scaled to pilot sizes (10–50 L) by increasing lamp number or altering sleeve configurations. Optical modelling guides lamp spacing, fluid circulation, and reflector design to ensure minimal photon loss. However, in continuous flow setups, challenges such as hydraulic dead zones and increased residence-time distribution complexity arise, necessitating computational fluid dynamics (CFD) studies and residence-time validation to guarantee replicable treatment efficiencies (Rabahi, n.d.).

3.9.2.2 Compound Parabolic Concentrators (CPCs)

CPCs concentrate diffuse sunlight onto reactor tubes where the catalyst is suspended in slurry or immobilized. Examples from literature demonstrate CPC arrays treating up to hundreds of litres nightly, with inlet sedimentation filters and downstream drying units enabling feed conditioning and zero-liquid discharge. Such systems harness solar UV-A while minimizing

dependence on grid power, making them ideal for remote or rural installations. Scale-up challenges include tracking optimal tilt and orientation, climatic adaptations, and establishing protocols for catalyst replenishment under variable solar irradiance (Jiang, 2020).

3.9.2.3 LED-Driven Photocatalytic Systems

LEDs offer tuneable, targeted illumination (e.g., 365–385 nm). Recent pilot units deploying high-output UV-C LEDs (e.g., 52 W arrays) achieved diclofenac degradation in hospital effluent at ~1.2 m^3/day. The modularity of LED panels allows fine control over irradiance but introduces heat management, electrical efficiency, and capital-cost considerations. Unlike legacy UV lamps, LEDs enable instantaneous switching, dimming, and spectral tuning to activate novel visible-light–responsive catalysts (e.g., doped TiO_2, WO_3, g-C_3N_4). Thermal management systems (e.g., heat sinks, liquid cooling) become necessary at scale to uphold LED efficacy and lifetime in continuous operation (Kubiak, n.d.).

3.9.3 Performance in Real Water Matrices

3.9.3.1 Matrix Complexity and Photonic Efficiency

Realistic water matrices (agricultural runoff, urban stormwater, industrial effluent) contain natural organic matter (NOM), and inorganic scavengers (Cl^-, CO_3^{2-}, HCO_3^-). These species absorb and scatter photons, reducing light penetration and creating competitive quenching with reactive oxygen species (ROS). Field-scale systems typically require catalyst duction rates two- to threefold higher or retention times 1.5-2× longer than lab-based clear-water tests. Pilot studies have standardized matrix-adjusted performance metrics – such as UV-transmittance ($UV_{t(240)} < 20$ %) and total organic carbon (TOC) > 5 mg L^{-1} – so that degradation rates reflect more realistic operational conditions (Alalm, 2021).

3.9.3.2 Pilot-Scale Validation Outcomes

In multiple pilot evaluations:

- PNFR modules demonstrated ~80–90 % degradation of pesticides at ~1 m^3/h volumetric flow, enabling sustainable water reuse for agricultural irrigation (Theodorakopoulos, 2023).
- LED-driven units maintained >70 % removal of pharmaceutical micropollutants (e.g., diclofenac, carbamazepine) over sustained periods (> 30 days) with limited catalyst loss (Kubiak, n.d.).
- CPC-powered systems achieved 3-log reduction value for E. coli and 5-log reduction value for E. faecalis in synthetic urban wastewater. In the presence of the photocatalyst and solar irradiation the combined thermal and UVA effects accelerated the bacterial degradation process resulting in 6-log reduction in E. coli and E. faecalis observed after solar exposure periods of 20 min (solar dose), using 0.5 and 0.7 mM of persulfate in isotonic water (Ferreira, 2020).

3.9.4 Scale-Up Strategies & Lifecycle Evaluation

3.9.4.1 Modular vs. Monolithic Architectures

Modular systems – such as stacked hollow-fibre cartridges or replaceable monolith arrays – enable phased capacity increases and facilitate regular maintenance (e.g., cartridge-swapping, backwashing). In contrast, monolithic systems are often engineered as integrated panels or CPC tubes, which simplify construction in centralized facilities and maximise throughput. Selecting the architecture depends on factors such as treatment capacity, infrastructure, and maintenance strategy. Economic modelling suggests modular systems are preferable for distributed, small-scale use, while monolithic installations are better suited for municipal plants with predictable inflows.

3.9.4.2 Solar Integration & Off-Grid Adaptation

Solar-CPC systems illustrate how sunlight can offset energy costs; however, geographic irradiance distribution and climatic variability must be accounted for. In regions with seasonal cloud cover, hybridization with grid-powered LED arrays ensures consistent treatment. Life cycle assessments (LCAs) comparing photovoltaic-powered LEDs vs. fossil-fuel–derived energy sources show that LED arrays paired with renewables can reduce the carbon footprint by up to 60 % relative to conventional halogen lamp systems.

3.9.4.3 Combined Advanced Oxidation Processes (AOPs)

Coupling photocatalysis with Fenton or ozonation increases oxidant flux and broadens pollutant degradation profiles. For example, injecting low doses of H_2O_2 in photocatalytic flow reactors accelerates HO• generation while minimizing UV-power requirements. Continuous Fenton–photo modules equipped with EC dosing loops have been piloted to treat refractory industrial effluents with promising reductions in energy per log-removal metrics (~30 % lower than photocatalysis alone) (Noor, 2022).

3.9.4.4 Environmental & Economic Assessment

A rigorous economic and environmental assessment is central to scaling decision-making. Capital costs (reactor, electronics, catalyst), operating expenditures (electricity, replacement parts), and environmental costs (embodied energy, nanoparticle release) must be mapped across all potential scales. Sensitivity analyses highlight that optimizing catalyst lifetime (e.g., >1 y), minimizing fouling intervals, and energy sourcing greatly influence project viability. Life Cycle Impact Assessment (LCIA) metrics – expressed as CO_2-eq per m^3 treated – remain under 0.15 kg CO_2-eq/m^3 for optimized LED-diesel hybrid systems, with room for further improvement through renewables (Alalm, 2021).

3.9.4.5 Scaling Blueprint: Stage-by-Stage Pathway

The stages between a lab-scale investigative study of a potential material for water purification and full-scale field deployment of an effective method are outlined in Table 21. Stages of water treatment from bench scale research to full field deployment.

Table 21. Stages of water treatment from bench scale research to full field deployment.

Stage	Objectives	Key Considerations
Lab-scale (mL)	Synthesize novel catalyst, assess bandgap, evaluate ROS generation, screen pollutant degradation in model water	Determine material optical properties, quantum yields, adsorption isotherms
Bench-pilot (L)	Investigate mass transfer, catalyst stability, reactor configurations (e.g., slurry vs. immobilized)	Optimize catalyst loading (e.g., g-C_3N_4/TiO_2 heterojunctions), prevent settling, refine lamp placement
Pilot (10 L–100 L / 0.5–5 m^3/day)	Investigate mass transfer, catalyst stability, reactor configurations (e.g., slurry vs. immobilized)	Use scaled reactors (annular, CPC, LEDs); build instrumentation for flow, irradiance, catalyst wear
Field deployment (100 m^3/day and above)	Ensure long-term reliability, adapt to solar cycles, integrate with pre-/post-treatment systems, conduct socio-economic feasibility	Monitor year-round performance, maintenance cycles, cost-recovery models, regulatory compliance

3.9.5 Conclusion & Future Recommendations

To transition a novel photocatalyst from bench discovery to operational deployment, the following critical actions are recommended:

1. Design robust immobilization strategies – preferably employing modular, scalable substrates (e.g., hollow fibres, monoliths).
2. Engineer advanced photoreactor systems – select between solar CPC arrays and electrically powered LEDs based on site resources.
3. Account for real matrix effects early – lab tests should simulate turbidity, NOM, ionic strength, and target analytes.

4. Optimize hybrid process integration – combine photocatalysis with complementary AOPs for energy-efficient and robust contaminant removal.
5. Undertake comprehensive lifecycle assessments – covering environmental impact, economic cost breakdown, and regulatory footprint.
6. Pilot with modular design – to enable phased scaling, easy maintenance, and distributed deployment.
7. Establish standard metrics – report quantum efficiencies, energy per log removal, monetary unit removal cost, and catalyst stability duration.

   Finally, future research directions include: enhancing visible-light response via bandgap engineering; harnessing artificial intelligence for real-time process control and predictive catalyst lifespan; and exploring natural sunlight usage in tropical and subtropical regions to reduce energy inputs sustainably.

3.10 Chapter 3 Summary

In Chapter 2 the strategies for EE2 removal from water using titanium dioxide were reported, with efficiencies ranging from 85 – 99%. Titanium dioxide was selected as the photocatalytic material due to the established photocatalytic properties of TiO_2, cheaper cost relative to photocatalysts with similar efficiencies, and for the ability to apply coatings of TiO_2 using methods that do not require harsh conditions such as high temperatures via the sol gel method. Furthermore, the morphology of TiO_2 can be controlled with the synthesis route, allowing the production of TiO_2 crystals with tuned morphologies. This chapter reviews literature focusing on the sol-gel methods for TiO_2 synthesis, the properties of the TiO_2 generated using this process, gives information on the physical and chemical properties of TiO_2, before discussing the health hazards associated with titanium dioxide nanoparticles. The common synthesis routes and state of the art synthesis routes towards achieving titanium dioxide are briefly discussed, including the typical morphologies generated from these routes.

4. Hydroxyapatite

4.1 Background

In this work hydroxyapatite (HAP) was investigated for its potential application as the adsorbing component in the hierarchical adsorbent-photocatalytic material designed for EE2 removal from water. The features that make HAP suitable for water purification are proposed to also be applicable to the removal of EE2, which has not yet been explored in the literature. This chapter describes the rationale for exploring HAP for its water purification abilities, where it is explained why the application of HAP as a drug delivery scaffold indicates that HAP could have excellent potential as an adsorbent for pharmaceuticals and in particular for EE2, the application of HAP in water purification, before describing various forms of HAP, the sources and synthesis methods used to obtain HAP, and finally more detailed discussion of the state-of-the-art methods used to synthesise HAP using the chemical precipitation method and also to obtain HAP from food wastes, a green and sustainable resource. In summary, the applications, composition, and synthesis routes of hydroxyapatite will be described in this chapter.

4.2 Introduction

This chapter reports the properties, characterisation data, synthesis routes, and applications of hydroxyapatite, before explaining how hydroxyapatite is proposed to be an effective adsorbent for the endocrine disrupting compound, EE2. HAP has been researched as a material used for water purification and also as a drug delivery scaffold, however, there is currently no research published on the use of hydroxyapatite for the removal of EE2 from water.

This chapter focuses on hydroxyapatite produced by ambient temperature chemical precipitation, as this method is low cost, sustainable, and green. Finding low cost and low energy routes towards materials are extremely important aspects of material design and synthesis in the context of research in the 2020s, with the effects of climate change and energy

shortages being felt keenly around the world. The properties of hydroxyapatite produced by low energy and low-cost chemical precipitation methods are reported here and where appropriate compared to hydroxyapatite produced by more conventional means.

The characterization data for HAP produced by this method is reported, emphasising the X-Ray Diffraction pattern with assignment of *hkl* peaks, FT-IR spectra with assigned peaks, SEM images and where available, EDX quantification of elemental composition and the BET N_2 specific surface area. Following this chemical precipitation methods that produce hydroxyapatite as a coating on a substrate as opposed to the production of powders of hydroxyapatite are highlighted, and other common synthesis routes are also briefly explained. The effects of the reaction conditions of pH and sintering temperature are discussed, with explanations offered for the outcomes of optimising these parameters.

The applications of hydroxyapatite as a material for water purification and as a drug delivery scaffold are then discussed, where applications that use hydroxyapatite as a material for the removal of pharmaceuticals from water are evaluated for their efficacy.

4.3 Properties of Hydroxyapatite

The empirical formula of HAP is $Ca_5(PO_4)_3(OH)$ although the structure is more appropriately described as $Ca_{10}(PO_4)_6(OH)_2$ denoting the presence of two-unit cells within its structure. HAP is the mineral component of bones and teeth, can be harvested from biological sources or mineral sources, and has been used previously for water purification and as a drug delivery scaffold due to its ion-exchange properties, porous structure, high surface area, biocompatibility, and chemical affinity for pharmaceuticals The ratio of calcium to phosphorus can vary, although stoichiometric HAP has a Ca/P ratio of 1.667.

Hydroxyapatite can form in two structures: monoclinic and hexagonal. Stoichiometric HAP has a monoclinic structure, whereas hexagonal structured HAP is derived from biological and

mineralogical sources. HAP produced from synthetic methods is also known as stoichiometric HAP due to the control over the chemical composition afforded by artificial manufacture, while HAP harvested from natural sources is referred to as non-stoichiometric HAP due to the presence of impurities such as Mg, Fe, Cr, CO_3^{2-} within the HAP lattice (In, 2020). The two main crystal structures of HAP are displayed in Figure 16. Exposed ions on different faces of HAP crystal lattice. The lattice parameters of both types of HAP crystal are outlined in Table 22. Properties of stoichiometric and non-stoichiometric HAP.

Figure 16. Exposed ions on different faces of HAP crystal lattice. (In, 2020).

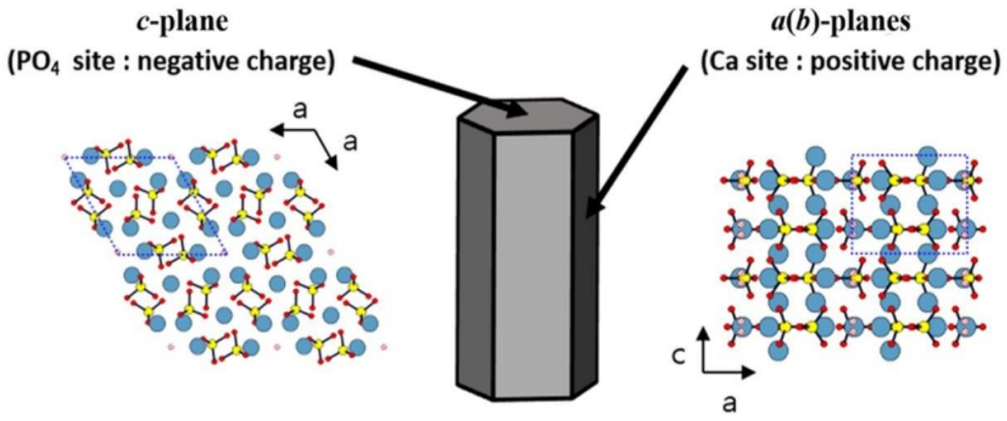

Table 22. Properties of stoichiometric and non-stoichiometric HAP. (Teoh, 2023).

Parameter	Stoichiometric	Non-stoichiometric
Origin	Synthetic	Mineral and Biological
Space Group	-	$P6_3/m$
Crystal system	Monoclinic	Hexagonal
a Å	9.4215	9.41
b Å	2a	-
c Å	6.8815	6.88
Unit cell volume Å^3	-	527.59
Ca/P ratio	1.67	Variable

4.4 Characterisation Data

The *hkl* peaks associated with HAP at their characteristic 2Theta values are essential for identifying the presence of HAP phases within a sample, and are used in Chapter 8 and Chapter 10 to identify HAP. The Miller indices and their 2Theta values for HAP are included in Table 23. hkl peaks of HAP.

Table 23. hkl peaks of HAP. (Fleet, 2004).

2Theta	***hkl***
25.94	(002)
32.19	(112)
34.00	(202)
39.81	(310)
46.69	(222)
49.45	(213)
53.23	(004)

The FT-IR spectrum of HAP is characterised by peaks representing the vibrational modes of the phosphate group in HAP, with a small peak possible in the OH region, and carbonyl region if carbonate is present in the lattice. Typical frequencies for vibrational modes associated with HAP are presented in Table 24. FT-IR peaks associated with HAP. An FT-IR spectrum characteristic of HAP is displayed in Figure 17. FT-IR spectra of HAP. The charasteric phosphate region is enlarged in Figure 18. FT-IR spectra of HAP, close up of phosphate region.

Table 24. FT-IR peaks associated with HAP. (Xiao. Q., 2024).

Wavenumber cm^{-1}	**Assignment**
472	$\nu 2$ vibration mode of PO_4^{3-}
564/603	$\nu 4$ vibration mode of PO_4^{3-}
876	C=O asymmetric stretch of CO_3^{2-}
962	$\nu 1$ vibration mode of PO_4^{3-}
1034/1096	$\nu 3$ vibration mode of PO_4^{3-}
1410-1450	C=O asymmetric stretch of CO_3^{2-}
1634	Stretching mode H_2O
3447	Bending mode H_2O

Figure 17. FT-IR spectra of HAP. (Teoh, 2023).

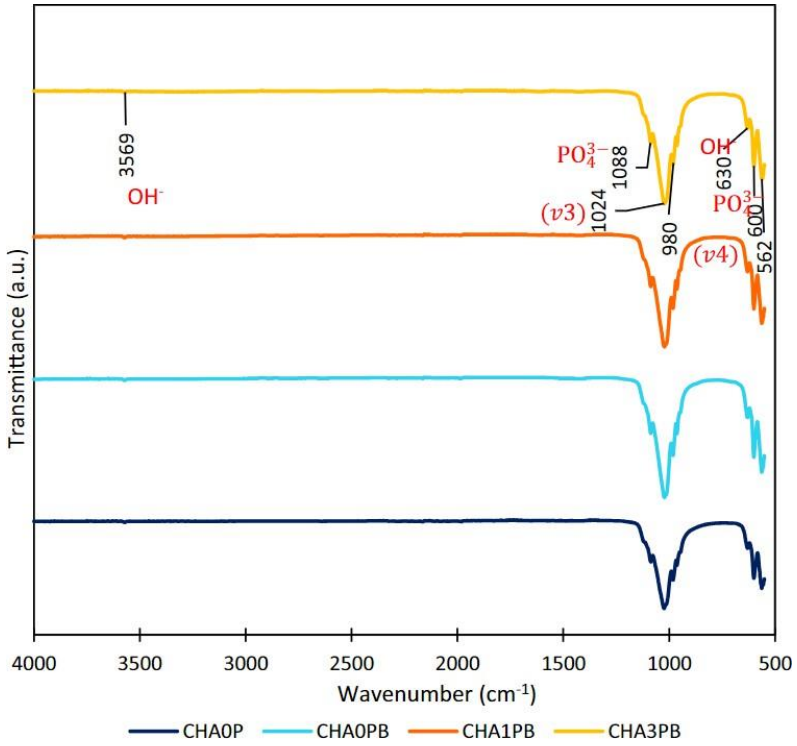

Figure 18. FT-IR spectra of HAP, close up of phosphate region. (In, 2020).

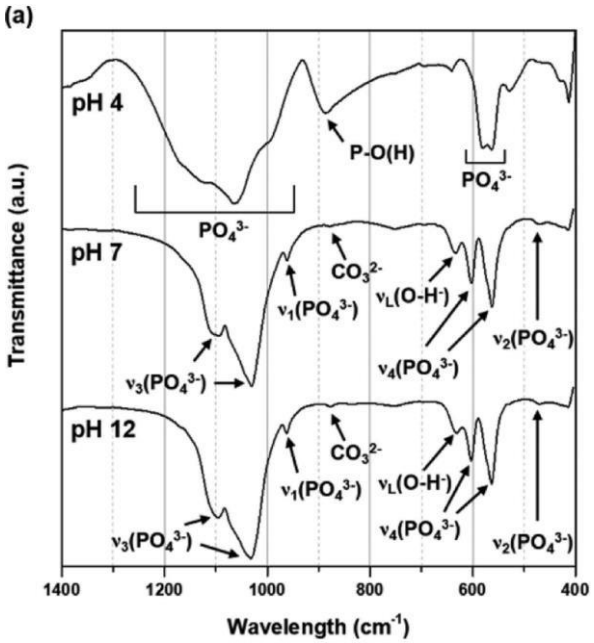

4.5 Sources and Synthesis Routes of Stoichiometric of Natural Hydroxyapatite

Non-stoichiometric or natural HAP can be obtained from mineral sources and biological sources, while stoichiometric or synthetic HAP is produced by artificial means. Non- stoichiometric HAP can be harvested from the bones of mammals or fish, or the shells of molluscs and shellfish. Sources of non-stoichiometric include: red snapper fish scales (Ulfyana, 2018), Asiatic Hard Clam, Blood Cockle (Murugiah, 2021), Asian moon shell scallop, clam shells, mussel shells, oyster shells, mammalian bones, domesticated jungle fowl eggshells, (Adeogun, 2018), ark clam shell (Khiri, 2016), eggshells (Goh, 2022) and land snail shells (Salma-Ancane, 2016). Plants have also been used as precursors for hydroxyapatite synthesis: calendula flowers and papaya and khat, basil, mint, green tea and trifolium and red algae (Shaltout, 2100), have all been used successfully in the production of hydroxyapatite. This diverse range of feedstocks for non-stoichiometric HAP can be reliably sourced from around the globe, with the added benefit that its production can be used as a strategy to reduce food waste. Furthermore, the fact that these sources of calcium can be easily obtained in developing countries means that composites that incorporate hydroxyapatite are not restricted to wealthier regions, but can be employed globally. This is relevant because conventional methods of purifying water that can remove organic pollutants and destroy micro-organisms are restricted to expensive technologies such as ozonation and other advanced oxidation processes.

4.6 Stoichiometric or Synthetic Hydroxyapatite

Hydrothermal Synthesis of Hydroxyapatite

The hydrothermal method of HAP synthesis uses high temperature and pressure to increase the reactivity of the starting materials, and the HAP produced is highly crystalline with good control over Ca/P ratio afforded by this method (Moreno-Santos, 2023) (Zhou, 2017) (Yu, 2017). Hydrothermal synthesis allows control over the size, porosity and morphology of HAP; however, very high temperatures are required for calcination which presents an energy cost and the need for specialised equipment and trained staff. This method for HAP synthesis is therefore only suitable for applications where the high cost is worth the outcome, e.g. to produce HAP that will be used in medical applications, where high control over the features of HAP is necessary and the high cost can be offset by the improvement in quality of life offered by a bone implant. This method is not appropriate for producing HAP on a large scale for applications such as water purification, where large amounts of HAP would need to be produced on a large scale, and some level of phase impurity or less strict control over the size and morphology of the HAP produced has minimal consequences as long as the HAP produced retains its ability to adsorbed contaminants.

Chemical Precipitation for Hydroxyapatite Synthesis

This section reports and evaluates chemical precipitation methods used to produce coatings of the hydroxyapatite on solid surfaces. Many methods reported in the literature for synthesis of a hydroxyapatite coating are specifically for the purpose of growing a layer of hydroxyapatite on bone replacement implants, where the role of the hydroxyapatite is to provide a biocompatible surface to improve osseointegration. This means that a large number of papers that report methods for growing a coating of hydroxyapatite focus on growing the hydroxyapatite on titanium alloy joint replacements, with few papers describing the growth of

HAP on other surfaces. Methods reported for HAP synthesis by chemical precipitation focus on the synthesis of HAP powders, not HAP coatings (Ulfyana, 2018) (Goh, 2022) (Gomez-Vazquez, 2021).

One of the gaps in the literature identified in this work is HAP grown via chemical precipitation as a coating on a non-titanium alloy substrate for the purpose of water purification. The use of hydroxyapatite as a biomaterial destined for implants within the human body also means that much attention is paid to methods that produce HAP safe for use within the human body, meaning that strict control on the calcium phosphate phases produced are necessary. HAP destined for use in water purification requires less strict control, and the high temperature calcination step that is used to ensure that only the HAP phase is present is unnecessary for water purification. Furthermore, templating reagents that produce distinct morphologies are also unnecessary, as the objective for producing HAP for water purification is high surface area hydroxyapatite grown on a supporting scaffold, and templating agents guide the growth of crystals. Therefore, for this scheme of work the most important factors for producing hydroxyapatite in a green and sustainable way are: minimal reagents, ambient conditions, neutral or alkaline pH, and avoidance of a calcination step. Synthesis routes that conform to these specifications are reported below, with the surface area and morphology of the products reported where these have been included in the literature. The synthesis method that best fits these criteria is chemical precipitation.

4.7 Reaction Conditions for Assorted HAP Synthesis Methods

A comparison of various HAP synthetic techniques is displayed in Table 25. Comparing HAP synthesis methods.

Table 25. Comparing HAP synthesis methods. (Munir, 2022).

Method	Reaction time	Temp (°C)	Size (µm)	Distribution	Shape	Crystallinity	Phase purity	Cost	Ref
Hydrothermal	<24 hr	150 - 400	>0.05	Wide	Needle	High	High	High	(Madhumathi, 2009)
Sol-gel		37 - 85	>0.001	Narrow	Diverse	Variable	Variable	Variable	(Cai, 2007)
Chemical precipitation	>24 hr	RT	>0.1	Variable	Diverse	Low	Variable	Low	(Lak, 2008)
Core-shell	>24 hr	60 - 120	>0.01	Narrow	Diverse	Variable	Variable	Variable	(Della Bella, 2018)
Electrospinning	>24 hr	-	10 x 30 nm	Variable	Fibres	High	Variable	Variable	(Fadeev, 2003)
Electro-spraying		-	75 x 40 nm	Wide	Diverse	Variable	Variable	Low	(Wu, 2018)
Microemulsion	>24 hr	RT	>1	Narrow	Needle	Low	Variable	High	(Wu, 2018)
Microwave irradiation	<24 hr	-	100 x 25 nm	Narrow	Diverse	High	High	Variable	(Zhang, 2008)

4.8 Effect of Reaction Conditions on Morphology of Hydroxyapatite

Different methods of producing HAP produce different morphologies, and factors such as sintering temperature, pH, starting materials, and direction of growth of the HAP crystal affect the properties of the HAP product.

Sintering temperature

Sintering temperature affects the hardness and crystallinity of the HAP product formed. Sintering temperature affects the composition of the HAP formed: when sintering is performed in the 1000 – 1350 °C range the only detectable phase using XRD analysis is HAP, with the optimum sintering temperature being 1250 °C (Muralithran, 2000), although a temperature of 1150 °C was found to be adequate to trigger a growth in grain size and a decrease in pores. However, the application of this HAP was for bone tissue engineering, which requires strict controls on morphology (Teoh, 2023). Above 1400 °C XRD analysis reveals two phases in the sample: HAP and α- tricalcium phosphate. At 1450 °C significant changes in the crystal structure of HAP begin to occur, as evidenced by the presence of α-tricalcium phosphate, β-tricalcium phosphate, tetracalcium phosphate and calcium oxide phases detected using XRD (Muralithran, 2000). HAP sintered at different temperatures is displayed in Figure 19. HAP sintered at (a) 1050, (b) 1150, (c) 1250 °C at 2500× magnification.

Figure 19. HAP sintered at (a) 1050, (b) 1150, (c) 1250 °C at 2500× magnification. (Teoh, 2023).

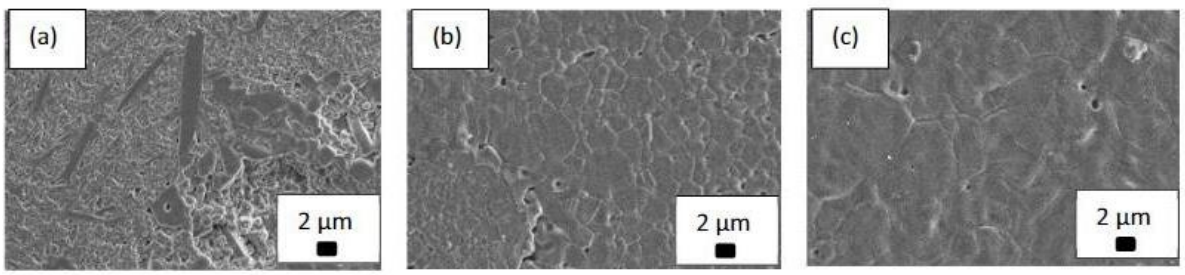

Increasing sintering temperatures decreases peak width in the XRD pattern of HAP, which can be seen in Figure 20. Effect of sintering temperature on XRD pattern of HAP (Aarthy, 2019). Broad and overlapped peaks in the XRD pattern of hydroxyapatite are indicative of the formation of nano-HAP with low crystallinity (Xiao. Q., 2024). Peaks located at 27.96° and 31.26° are associated with β-tricalcium phosphate (Teoh, 2023).

Figure 20. Effect of sintering temperature on XRD pattern of HAP (Aarthy, 2019).

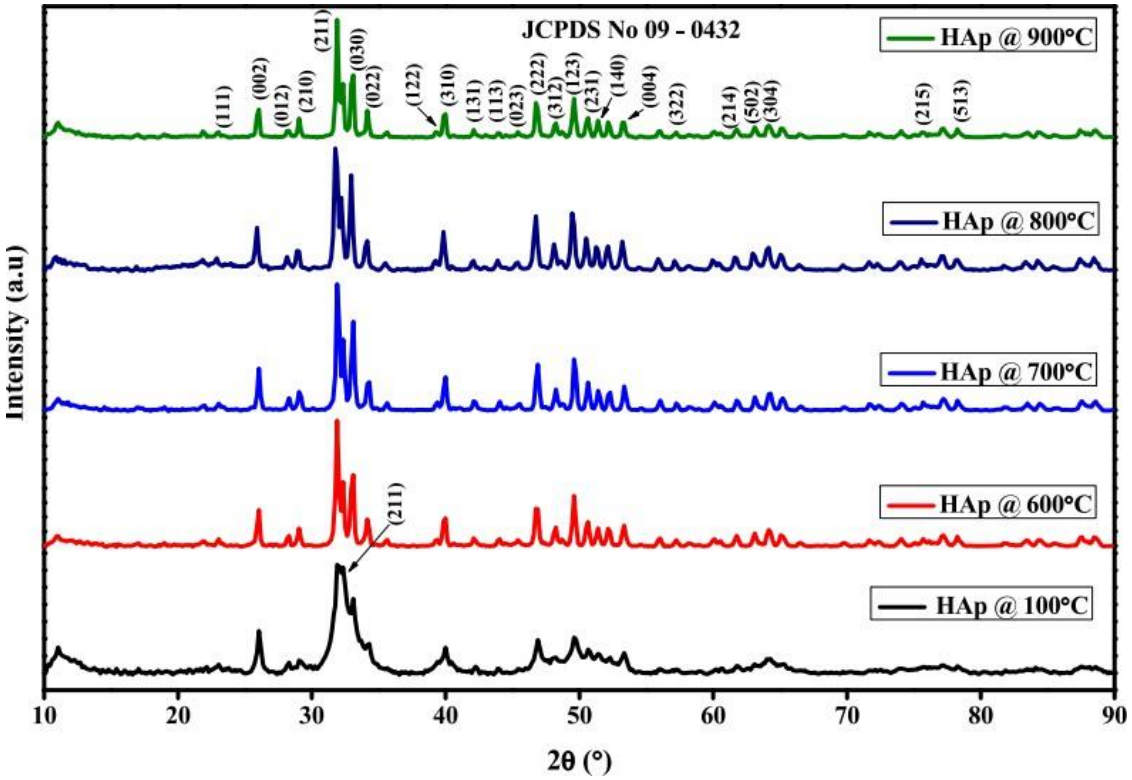

Effect of pH on Morphology

Reaction conditions affect the morphology of the hydroxyapatite produced - in particular the pH of the reaction mixture can change the morphology of the final HAP product significantly. It was found that as pH increases, crystal size decreases (In, 2020). The differences in morphology based on pH could be due to the availability of OH ions at higher pHs, which could mean that because more OH ions are available at high pH, more unit cells of HAP could form, meaning smaller particles. In contrast, the large well-defined rods formed at lower pHs could be due to the fact that OH ions are less common, and may be formed and taken into the structure

through the dissociation of water. As cations such as Ca^{2+} have fewer OH groups in their coordination spheres, it is more likely that the cations will coordinate with phosphate groups, as opposed to OH groups, which would allow the crystals to grow much longer than in high pHs. The figure below shows the effect of pH on morphology (Javadinejad, 2021). The morphologies obtained for synthetic routes using a pH range from 7 – 12 have resulted in morphologies ideal for water purification: high surface area due to the webbing effect of the HAP on roughly spherical particles. See Figure 21 for SEM images of HAP produced at different pHs which show high pH resulting in HAP with high surface area, while low pH synthesis results in dicalcium phosphate phases with much lower surface areas.

Figure 21. Dicalcium phosphate is produced at low pH, while HAP is produced at higher pH (In, 2020).

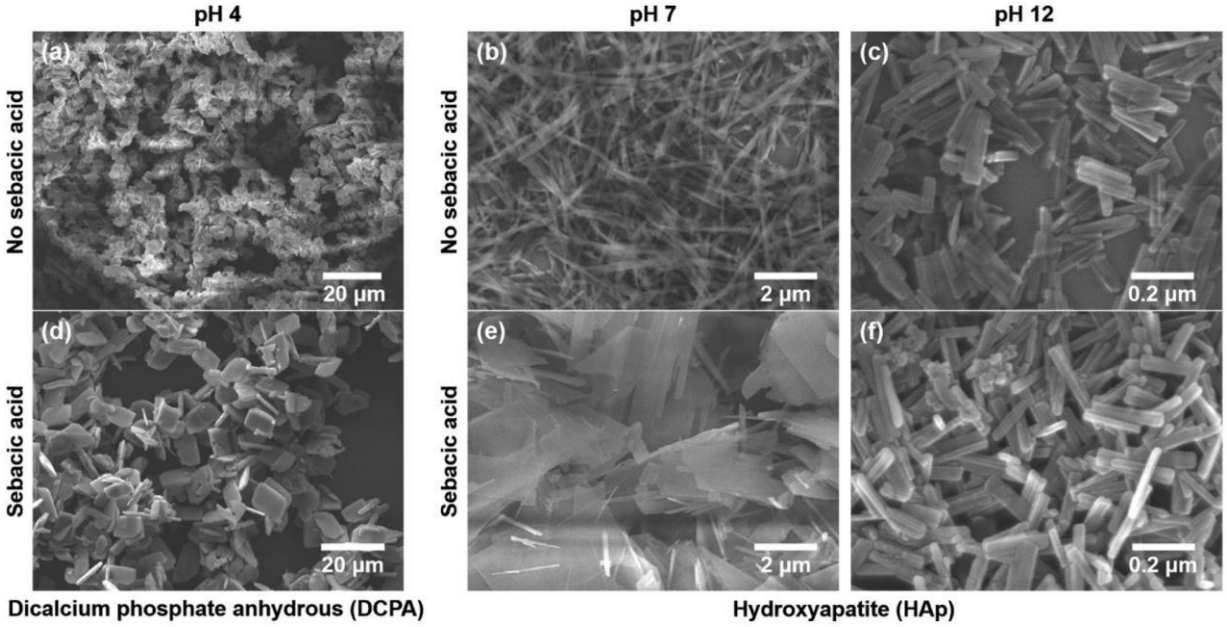

In the pH 10 experiment the particle on the right-hand side in the middle of Figure 22 below is hollow, which would indicate a high surface area, ideal for water purification applications (Javadinejad, 2021).

Figure 22. Images of the HAP products after calcium carbonate was soaked in 1mol dm^{-3} K_2HPO_4 solution at varying pH. (Javadinejad, 2021).

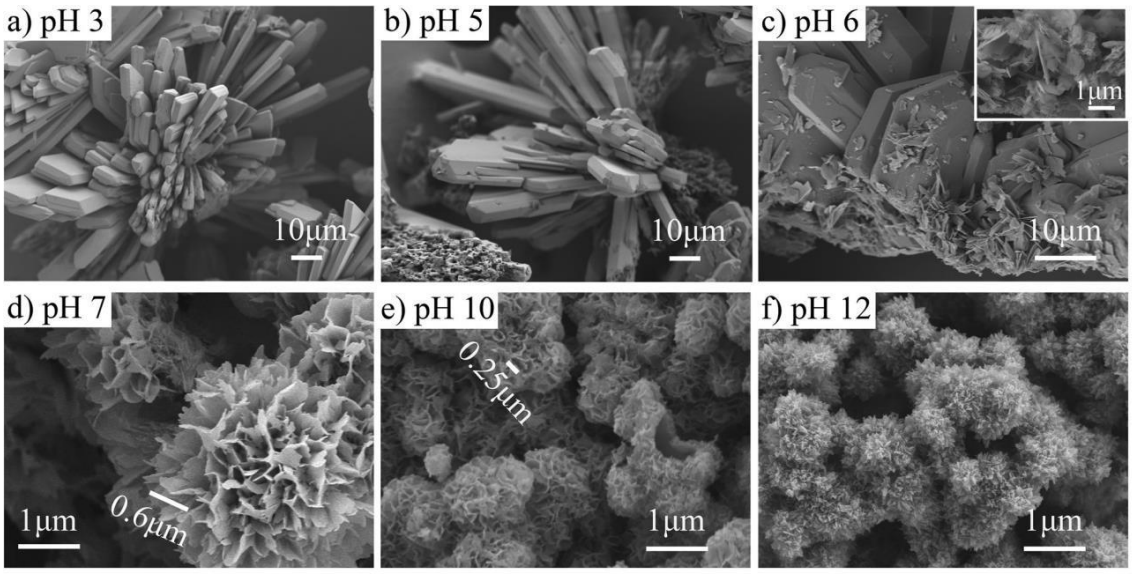

Effect of Calcination Temperature on Phase and Grain Size

HAP powders prepared via solid state reaction at 25 °C before calcination at 450 °C, 500 °C, 600 °C, 650 °C, 750 °C, 850 °C and 950 °C revealed that particles of HAP became more crystalline with increasing calcination temperature, with calcination at 600 °C and above producing XRD patterns with sharply defined peaks indicating a single crystalline phase, allowing the authors to conclude that "increasing [calcination] temperature was in favour of the crystallization of HAP" (Guo, 2013). The SEM images (see Figure 23. HAP sintered at varying temperatures, note increase in grain size with increase in temperature) produced in this study show crystals with varying size and shape at lower temperatures, while at higher temperatures there is no obvious trend in how calcination temperature affects particle size, although with increasing temperature the particle morphology becomes more consistent and clearly defined:

Figure 23. HAP sintered at varying temperatures, note increase in grain size with increase in temperature (Guo, 2013).

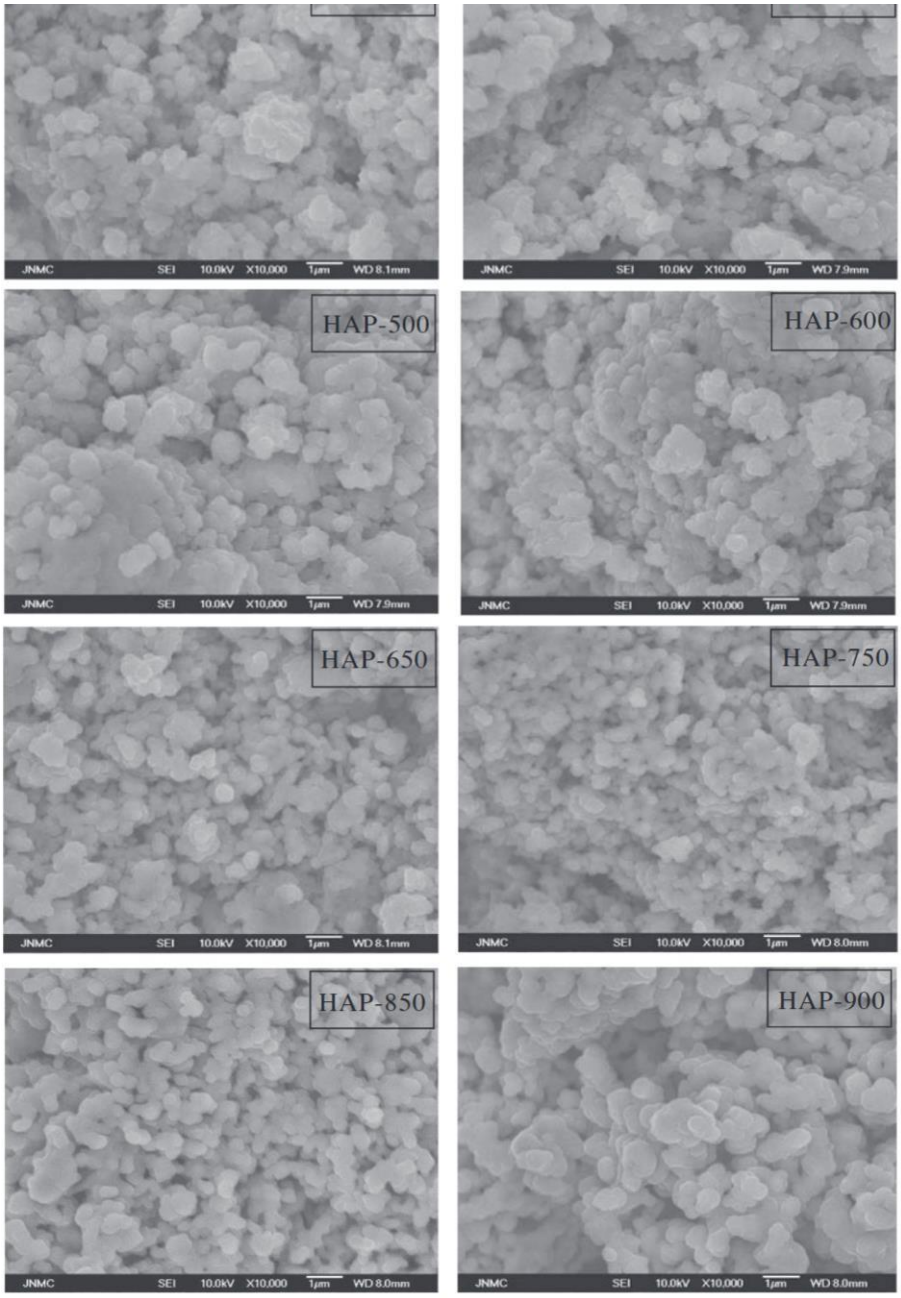

4.9 Hydroxyapatite Use in Water Purification

Hydroxyapatite (HA) has emerged as a promising material in water purification due to its inherent physicochemical properties, which enable efficient removal of various contaminants from water sources. Table 26. Applications of HAP produced by chemical synthesis contains examples of hydroxyapatite used for water purification that was produced via chemical precipitation.

Table 26. Applications of HAP produced by chemical synthesis.

HAP produced by chemical precipitation for water treatment	Ref
Optimized synthesis of cysteine-functionalized nanocrystalline hydroxyapatite for synchronous decontamination of Cd(II) and Pb(II)	(Xiao. Q., 2024)
Synthesis of multifunctional activated carbon nanocomposite comprising biocompatible flake nano hydroxyapatite and natural turmeric extract for the removal of bacteria and lead ions from aqueous solution	(Jayawe era, 2018)
Biopolymer-Based Nanohydroxyapatite Composites for the Removal of Fluoride, Lead, Cadmium, and Arsenic from Water	(Shanika Fernand o, 2021)
New heterogeneous synthesis of mixed Ti-Ca-Mg phosphates as efficient sorbents of 137Cs, 90Sr and 60Co radionuclides	(Ivanets, 2019)
High efficient multifunctional Ag_3PO_4 loaded multifunctional nanowires for water treatment	(Li, 2015)
In situ fabrication of ternary TiO2 doped grafted chitosan/hydroxyapatite nanocomposite with improved catalytic performance for the removal of organic dyes: Experimental and systemic studies	(Vignes hwaran, 2021)
HAP synthesised from $Ca(OH)_2$ and H_3PO_3 used to removed oxytetracycline (antibiotic) from aqueous solution	(Harja, 2018)

A calcination step was avoided entirely and their method resulted in a product that was highly capable of removing organic dyes, bacteria and Pb(II) ions HAP produced in this method was multifunctional and demonstrated that loaded HAP with photocatalytic materials is a highly effective technique for water purification from a range of contaminants. However, the authors acknowledge that the Ag_3PO_4 component used to provide photocatalytic properties to their composite is slightly soluble in water, releasing Ag^+ ions. This may mean that the material has a limited lifespan, as once a sufficient amount of silver dissolves in the surrounding water the

material would no longer have sufficient photocatalytic properties. The Ag_3PO_4 component was also poorly dispersed across the surface of the HAP nanowires, which may limit the efficacy of the composite. Nevertheless, this Ag_3PO_4 – hydroxyapatite composite demonstrates the potential of a combined photocatalytic/adsorbent system based on HAP as the adsorbent in the field of water purification, where the composite was able to significantly decrease the concentration of organic dyes, bacteria, and Pb(II) ions (Li, 2015). Some methods of HAP synthesis for water remediation are included in Table 27. Comparison of methods for HAP synthesis for water remediation.

Table 27. Comparison of methods for HAP synthesis for water remediation.

Method of HAP synthesis	Target Species	Removal Capacity	Removal efficiency	Ref
HAP composites with biopolymers were prepared via in situ chemical precipitation. $(NH_4)_2HPO_4$ and $Ca(NO_3)_2{\cdot}4H_2O$ were mixed to give a Ca/P ratio of 1.67. pH was kept at 10, the mixture was stirred then aged for 3 h then 24 hr.	Fluoride, Lead, Cadmium, Arsenic	3000, 3000, 2600, and 2000 mL/g for Pb(II), Cd(II), As(V), and F-	-	(Ivanets, 2019)
$Ca(NO_3)_2.4H_2O$, NaH_2PO_4, urea and gelatin were sealed in an autoclave at 160 °C for 12 h. $AgNO_3$ solution was poured over a layer of the HAP six times	Methyl orange, Rhodamine Blue, Methyl Blue, E. Coli, S. Aureus, Pb(II)	250 mg/g Pb (II) E. Coli and S. Aureus destroyed	-	(Li, 2015)
Hydrolysis of titanium tetrisopropoxide to produce TiO_2, then chemical precipitation of $((NH_4)H_2PO_4)$ with $CaCl_2$ in the presence of NaOH, then the HAP powder and TiO_2-chitosan powder were mixed in methanol then filtered and dried	Methyl Blue Rhodamine Blue	-	98.6% 97.6%	(Vigneshwaran, 2021)

4.10 Composites of TiO_2 and Hydroxyapatite

Combining multiple water treatment techniques enhances water purification (Rocha, 2025) (Kato, n.d.) (Oana, 2015) (Nonami, 2004) (Athanasiou, 2016). The enhanced photocatalytic degradation effect of HAP and TiO_2 relative to unsupported TiO_2 (Carvalho, 2017) (Luo, 2019) (Linsebigler, 1995) is the focus of this work as this composite is effective at degrading organic pollutants (Wang, 2009) and removing dyes and antibiotics (Nayak, 2021). In this work, a composite material of TiO_2 and HAP has been developed using green methods where the role of the HAP is to adsorb the EE2 and the TiO_2 decomposes the EE2. The synergistic effect of TiO_2 and HAP has been exploited for the removal of: bacteria, organic compounds and dyes (Rajesh, 2012) (Ramesh, 2018), *Escherichia coli*, acetaldehyde and nitrogen oxides (Pan, 2014). Destruction of Legionella, coliform and heterotrophic bacteria (Xu, 2021) through enhanced photocatalytic action. The enhancement mechanism is yet to be fully determined (Carvalho, 2017), although it is likely the TiO_2/HAP composite mitigates charge carrier recombination (Linsebigler, 1995) and the HAP acts as a support for the TiO_2, adsorbing organic contaminants, resulting in a higher concentration of organic pollutants around TiO_2, resulting in a higher overall photoreaction rate (Carvalho, 2017).

Table 28. TiO_2-HAP composites and their applications for degradation of a range of pharmaceutical, biological and gaseous species.

Materials	Contaminant	Removal	Ref.
TiO_2-HAP incorporated into polysulfone membrane	Chloramphenicol (antibiotic)	degradation of 61.59% was observed for the polysulfone membrane with 4 wt.% TiO_2-HAP nanocomposites incorporated into the membrane	(Singh, 2021)
Two-stage process – HAP used to adsorb the bulk of the contaminant and TiO_2 used in a subsequent step to mineralise remaining low concentration ciprofloxacin	Ciprofloxacin (antibiotic)	Maximum degradation efficiency achieved was 98.5 – 100%. Removal percentage of 82% achieved within 90 minutes.	(Cheikh, 2023)
HAP-coated anatase	Dimethyl sulfoxide, methylene blue	Preliminary study – >80% removal of both methylene blue and dimethyl sulfoxide achieved in 3 h.	(Sugita, 2013)
TiO_2-HAP composite powder	Sulfamethoxazole	99.98% removal achieved in 3 h using an 18 W UV-lamp	(Chun, 2014)
TiO_2-HAP composite, composition 70:30 TiO_2:HAP	S. aureus, E. coli (bacteria)	Zone of inhibition around bacteria increased by approximately 25% relative to either TiO_2 or HAP in presence of TiO_2-HAP composite	(Noviyanti, 2022)
TiO_2@Er-HAP	Ciprofloxacin, methylene blue	Ciprofloxacin – 71.16% removed; methylene blue – 100% removed. Solution after treatment was found to be non-toxic, with OH radicals as the main species	(Rocha, 2025)

Materials	Contaminant	Removal	Ref.
		produced in photocatalysis process	
TiO_2-Ag-HAP	L. pneumophila (Legionella bacterial)	No bacterial activity was observed after 5 h with treatment of 1g/100 mL of material, or 9 h with 0.5 g/100 mL of material.	(Oana, 2015)
TiO_2-HAP@PVDF composite ultrafiltration membranes	Bovine Serum Albumin	The composite membranes had a higher pure water flux (350 L/(m^2/h)) than the pristine membrane indicating an increase of 59%	(Li, 2023)
TiO_2-HAP	Methyl Orange	Initial concentration of composite ranged from 10 mg/L to 200 mg/L and removal ranged from 96.2% to 99.8%	(Sheng, 2011)
TiO_2-HAP	Oxides of Nitrogen	Aim of research was to use TiO_2-HAP for sensing of NOx – successful development of sensor demonstrates TiO_2-HAP ability to adsorb HNO_3 and NO_2	(Komazaki, 1999)

4.11 State-of-the-art Methods for Growing TiO_2 on Hydroxyapatite

Many examples in the literature of composites of titanium dioxide and hydroxyapatite are applications where the HAP was grown on the TiO_2, with the TiO_2 serving as an intermediate layer to connect the HAP to a titanium metal substrate. The target architecture of this work is a material where TiO_2 has been grown on HAP, the opposite outcome to the aims of the available literature. The most relevant examples in the literature of hydroxyapatite coated with TiO_2 would be hydroxyapatite doped with TiO_2. For example, hydroxyapatite was grown on marble to form a protective layer for preventative conservation, and a 2 wt% titanium dioxide suspension was introduced to the process, after the addition of diammonium phosphate (DAP) solution and before the addition of limewater. The DAP and limewater solutions react together to form hydroxyapatite at low temperature and were cured at room temperature for 48 hours. The hydroxyapatite forms via chemical reaction encapsulating the TiO_2 nanoparticles within the HAP matrix (Sassoni, 2018). The chart below contains Raman spectra of the untreated marble, marble coated with HAP, TiO_2, HAP then TiO_2, and hap with TiO_2. An important distinction is that the sample named: HAP then TiO_2 means the already formed HAP layer had a solution of 2 wt.% TiO_2 nanoparticles dispersed in a mixture of 80-20 wt.% water – isopropanol applied to the HAP surface using a single brush stroke. The starred (*) peaks are calcite peaks Figure 24. XRD pattern of HAP and TiO2 combined .

Figure 24. XRD pattern of HAP and TiO_2 combined (Sassoni, 2018).

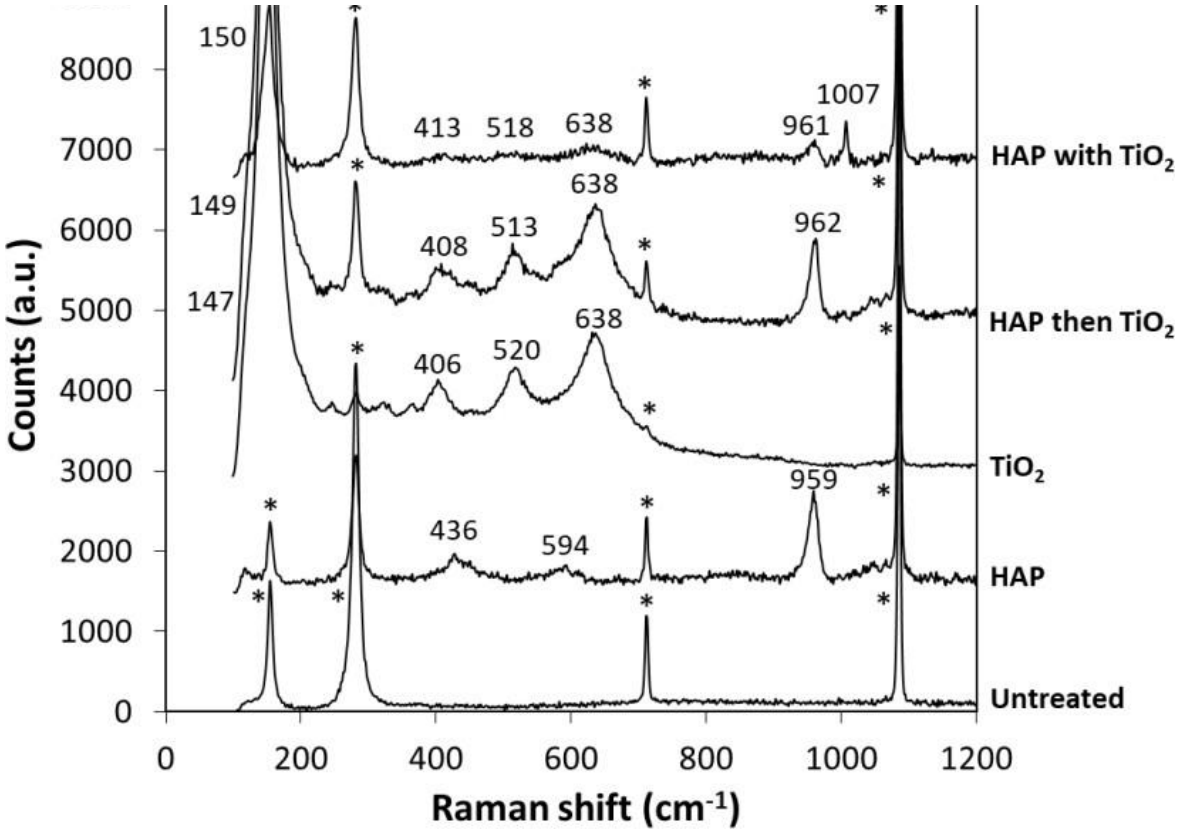

Although the Raman spectra produced by these researchers is useful for confirming the presence of titanium dioxide, this research would benefit from the inclusion of XRD patterns for the composite materials, as HAP when produced at low temperatures has very broad peaks, and it would be helpful for other researchers to understand the difference in XRD patterns between calcined HAP (sharp distinct peaks) and uncalcined HAP (broad peaks).

It is likely that this method of HAP growth on marble works well because marble is composed of a high proportion of lime (CaO: 38 – 42%) (Wahab, 2019) meaning there are adequate CaO bonds present that the DAP can react with to form the HAP layer that anchors the HAP to the marble. What is also relevant is that marble contains 20 – 25% silica (SiO_2) meaning this finding potentially indicates that HAP growth on silica can be obtained via the reaction of DAP and limewater in the presence of silica. However, an intermediate layer to anchor the HAP to the silica may still be necessary, and it is preferred if this layer contains a high proportion of CaO.

Co-precipitation was used as a method to support TiO_2 on hydroxyapatite derived from bovine bones for the purpose of photo-reforming of glycerol to produce hydrogen gas, as shown in Figure 25. Mechanism of photo-reforming of glycerol to produce H2 – a successful use of a HAP-TiO2

Figure 25. Mechanism of photo-reforming of glycerol to produce H_2 – a successful use of a HAP-TiO_2 (Adam, 2023).

This method used TiO_2 powder which simplified the reaction, although the hydroxyapatite was produced from bovine bones which were then calcined at 900 °C and the mixed TiO_2/HAP powder was calcined again at 450 °C. This method benefits from the recycling of bovine of bones by using a sustainable feedstock for the HAP, however the high calcination temperatures mean this route is energy intensive and cannot be described a green route towards TiO_2/HAP composites. Nevertheless, the TiO_2 powder/HAP composite showed an increased rate of glycerol reforming and hence H_2 production, and an added benefit is that TiO_2 powder can easily be doped with other metal oxides by adding the metal oxide powder to the TiO_2 to improve the photocatalytic ability of the material. This route therefore offers the option to significantly increase the photocatalytic ability of the material via doping – a benefit which may overcome the disadvantage of the high temperatures required for the material synthesis. The FT-IR spectra produced for various composites of HAP-TiO_2 are displayed in Figure 26. FT-IR spectra of HAP-TiO2 composite.

Figure 26. FT-IR spectra of HAP-TiO_2 composite. (Adam, 2023).

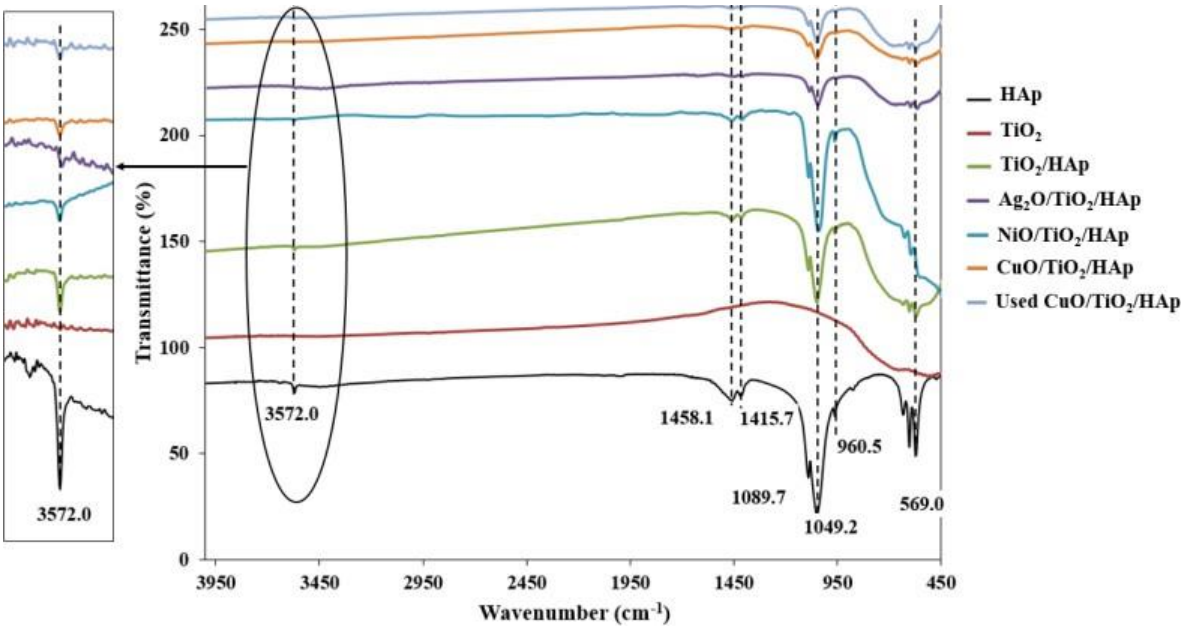

A core-shell composite of hydroxyapatite with anatase was produced by synthesising HAP using the reverse precipitation method, then modifying the HAP with anatase via the sol-gel process. The surface area of the unmodified hydroxyapatite was 41 m^2/g, while the anatase modified HAP had a surface area of 53 m^2/g. These researchers found that the composite had a photocatalytic activity 92% that of the commercial photocatalyst P25. The XRD pattern of this anatase-HAP composite is depicted in Figure 27. XRD pattern of composite of HAP and anatase. .

Figure 27. XRD pattern of composite of HAP and anatase. (Khamova, 2018).

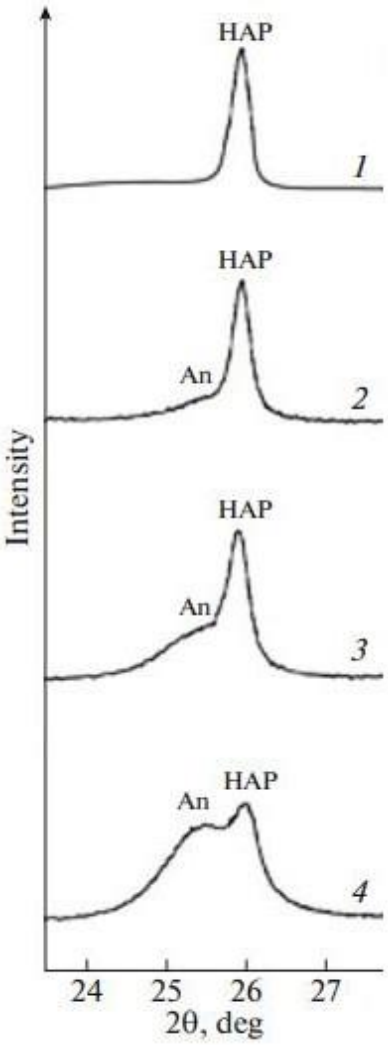

TiO_2 was loaded on to hydroxyapatite powder by immersing HAP in the Ti-sol before the gelation stage. This material was produced to degrade organic pollutants in water with an organic dye used as the target material. The HAP was chosen for its biocompatibility with organic substances and was found to be highly effective at destroying Acid Red B dye. Images of these composites are shown in Figure 28. The SEM of TiO2/skeleton (a), TiO2/dens (b), TiO2/HAP (c) with 30 wt% TiO2 under 500 degrees C and 50 min heat-treatment .

Figure 28. The SEM of TiO_2/skeleton (a), TiO_2/dens (b), TiO_2/HAP (c) with 30 wt% TiO_2 under 500 degrees C and 50 min heat-treatment (Wang, 2010).

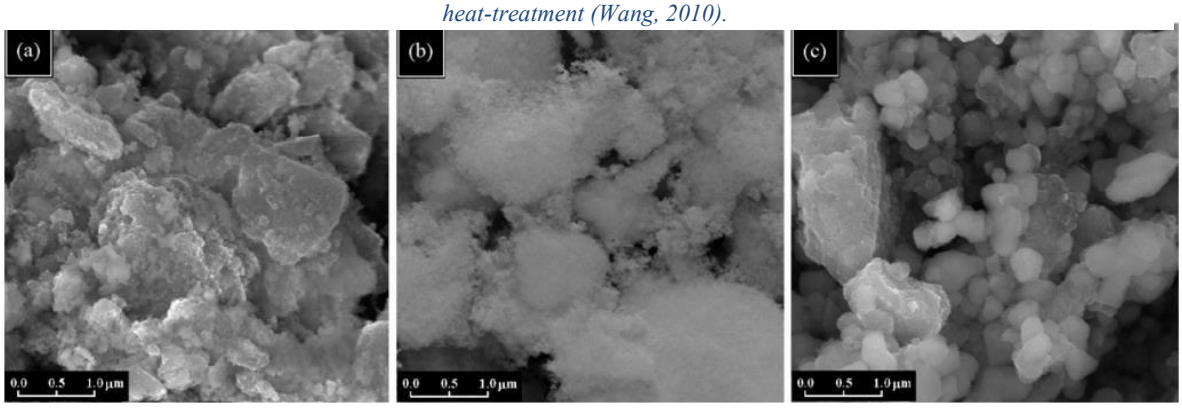

In conclusion, using hydroxyapatite as a scaffold for titanium dioxide for the purpose of destroying organic contaminants has been tested in a small number of cases with promising results. The hydroxyapatite supports the titanium dioxide well and when applied to photocatalysis, the composite of titanium dioxide and hydroxyapatite generally has efficiency within 90% of commercially available P25. The small loss in efficiency is compensated by the ease of recovery of the titanium dioxide particles due to immobilisation on the HAP scaffold. However, due to the method of preparation the titanium dioxide may be encased within the hydroxyapatite matrix, preventing the substrate molecules from reaching the titanium dioxide. This means that although the TiO_2-hydroxyapatite composite may have favourable results for the removal of the EE2 contaminant from water, this must be investigated experimentally in order to determine whether the TiO_2-hydroxyapatite material is more effective or if there are other contributing factors.

4.12 - Summary

In summary, hydroxyapatite demonstrates multifaceted potential in water purification due to its adsorptive capacity, ion-exchange properties, surface chemistry, and structural characteristics. Its versatility in adsorbing diverse contaminants positions HAP as a promising material for addressing water quality challenges across various applications in environmental remediation and water treatment technologies. In addition, when paired with TiO_2 to form the TiO_2/HAP composite this material has been shown to be highly effective at removing, destroying and adsorbing a variety of contaminants, ranging from dyes, antibiotics, bacteria, EDCs and pharmaceutical drugs. It is therefore predicted that the TiO_2/HAP composite will also be effective at removing the synthetic estrogen, EE2, from water and this remains the justification for this research.

5. Chapter 5 – Hollow Glass Microspheres as The Support Structure

5.1 Introduction

The purpose of hollow glass microspheres (HGMs) in this work is to act as the support structure where the components that provide the useful chemistry are applied as a coating. The HGMs provide size uniformity, a chemically stable scaffold, buoyancy – which can increase the change of light absorption as the HGMs float at the surface of effluent. The HGMs are also transparent to visible light, have high compressive strength, can contribute to a reduction in density when included in the matrix of a structure, and are non-toxic. Furthermore, by growing or grafting nano-sized particles on to the surfaces of the HGMs it is possible to benefit from the dramatically increased surface area and reactivity provided by nanoparticles, while minimizing the risk of losing the nanoparticles to the environment. The loss of nanoparticles to the environment can result in bioaccumulation in living organisms, and cause cell toxicity or result in carcinogenic effects. Catalytic materials secured to the surfaces of HGMs are also easier to separate from the reaction system may therefore be more reusable than the unsecured catalytic powder, and also increase the adsorption capacity relative to an unsecured catalytic material (Zhang, 2016) (An, 2019) (An, 2020).

The use of HGMs as support materials for floating photocatalysts is still a relatively undeveloped field, with the search engine webofknowledge returning just seven research papers for the search term hollow glass microspheres, and within this search term floating photocatalysts, Chart 1Chart 1. Number of papers on HGMs per year since 2015 shows the number of hits returned for this search per year since 2015.

Chart 1. Number of papers on HGMs per year since 2015.

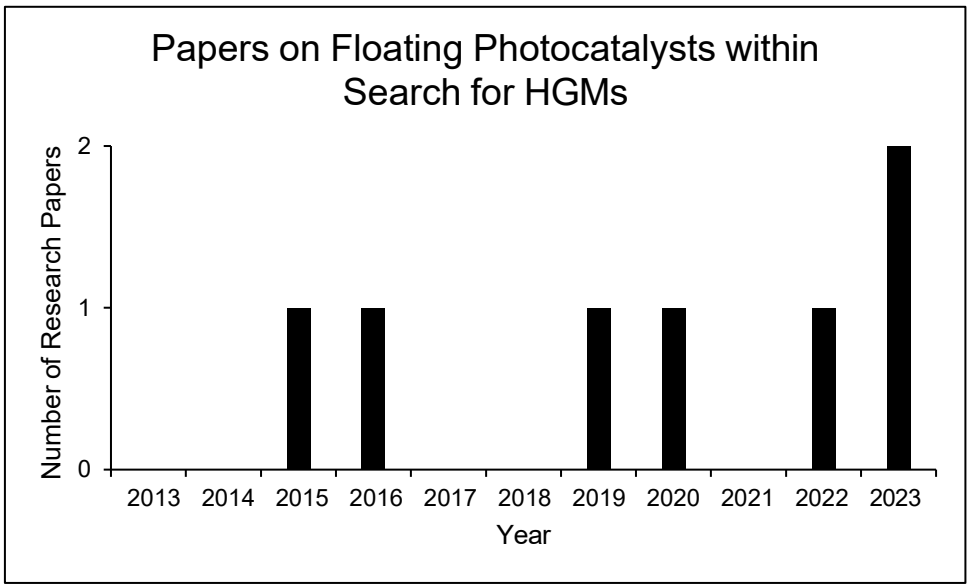

Hollow glass microspheres (HGMs) have been used extensively in construction to add strength and reduce density of concrete mixtures, and more recently HGMs have been applied to a range of purposes where they decrease the density of the bulk material while adding compressive strength. These HGMs can be functionalised through chemical reactions and given new and complex properties. The application of HGMs outside of construction involve being subjected to coating processes in order to apply these functional groups, and give the HGMs their application specific chemistry.

5.2 Physical Properties of HGMs

The physical properties of HGMs vary, but the key properties are their mean particle size, average density and collapse pressure. These values for a typical particle produced by Trelleborg have been reproduced in Table 29 (Trelleborg, 2024).

Table 29. Physical properties of a type of HGM produced by Trelleborg (Trelleborg, 2024).

Trelleborg Eccospheres SID-230Z	**Typical Property**
Mean Particle size (diameter)	45 µm
Average Density	0.35 ± 0.02 (g/cc)
Collapse pressure	6510 psi
Theoretical Thermal Conductivity	0.12 K/mK

5.3 Methods to Apply Coatings to Hollow Glass Microspheres

Applying coatings to HGMs that adhere strongly to the surfaces of the HGMs can be difficult to achieve. SiO_2 is not strongly reactive, meaning that prior to the coating process efforts must be made to prepare the surfaces of the HGMs to receive the intended coating. There are several methods reported in the literature to prepare HGMs for coating, which include washing with acid, washing with base, and treatment with silane coupling agent. These methods are summarised in Table 30.

Washing HGMs with acid achieves surface modification by removing material from the surfaces of the HGMs, as HCl was used by Hoyle et al. (Hoyle, 2020) and HF was used by Zhang et al. (Zhang, 2005) and Zogheib et al. to prepare HGM surfaces for coating. The effect of HF on the flexural strength of the HGMs was to decrease the flexural strength by 24.7% after just three minutes of etching (Zogheib, 2011). The changes in morphology reported by Zhang and the significant decrease in flexural strength reported by Zogheib indicate that this established method of introducing texture to glass surfaces may not be appropriate for introducing surface texture to glass microspheres with walls 500 nm to 2 µm thick. Furthermore, working with HF is extremely hazardous and is not typically a first choice when other alternatives are available.

Although the acid washing method does introduce surface texture, the mechanism by which

this is achieved is by removing material from the surfaces of the microspheres, and as the microspheres are so small, removing enough material to result in a change in surface texture appears to remove enough material to substantially change the mechanical properties of the microspheres. An SEM image of the HGMs after treatment with HF is displayed below. Many of the HGMs in the following image have multiple holes and show signs of extensive damage. Several of the HGMs have become welded together, likely due to the process of silica dissolution in HF. Some of the HGMs are still recognisable as spheres, however many are not. This effect can be seen in Figure 29. HGMs after treatment with HF to induce surface roughness and introduce texture.

Figure 29. HGMs after treatment with HF to induce surface roughness and introduce texture (Zogheib, 2011).

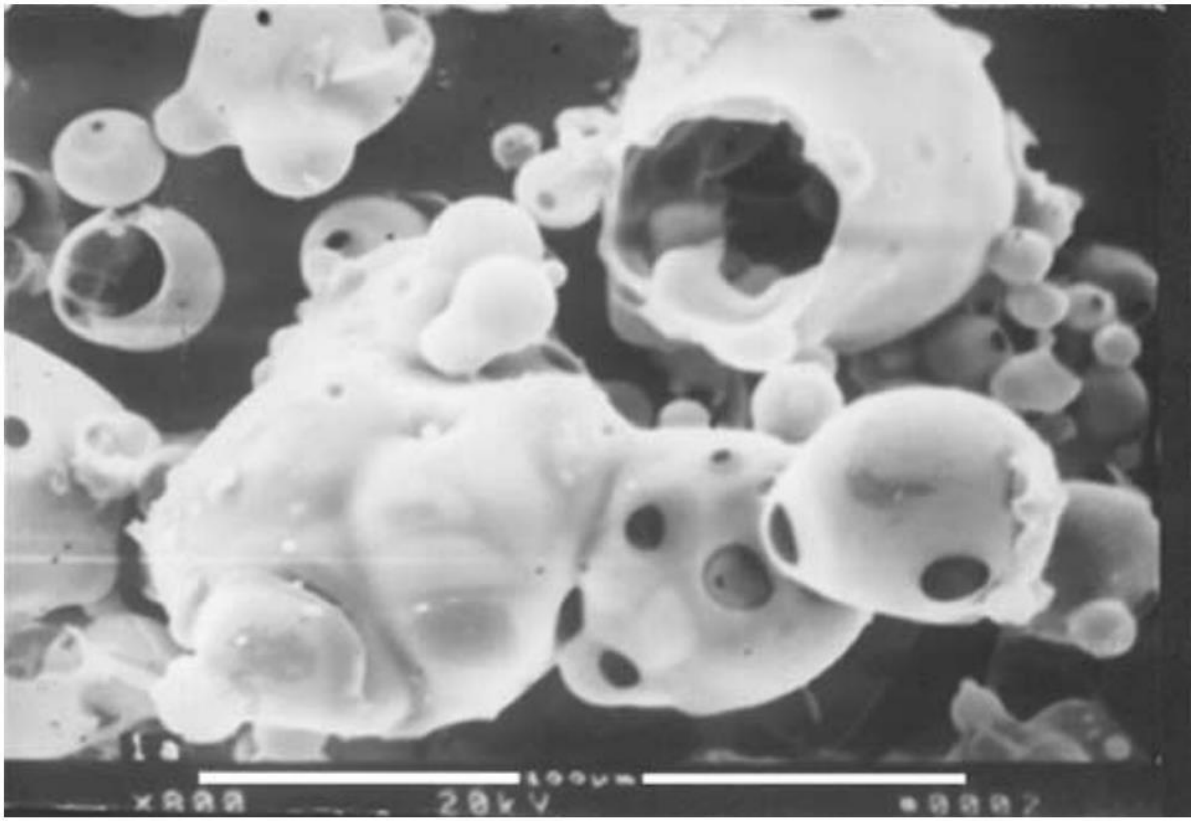

Treatment of HGMs with sodium hydroxide increased the roughness ratio (defined as percentile ratio of average roughness to particle radius) resulted in a roughness ratio increase from 0.42% for untreated HGMs, to 1.4% to HCl treated HGMs, and to 4.44% to NaOH treated HGMs (Hoyle, 2020). Figure 30. HGMs - a) untreated, b) treated with HCl, and c) treated with NaOH shows the outcomes of acid washing vs alkali washing. This means that sodium ions reacted with the surfaces of the microspheres to form sodium silicate and it is through this mechanism of sodium silicate crystal growth that surface texture and roughness was increased. This work would have been improved if the researchers had provided XRD patterns and analysis to support their assertion that sodium silicate formed. In the absence of XRD patterns or elemental analysis, the researchers are only able to assume the identities of the crystals on the microsphere in Figure 30.

Furthermore, the work of Hoyle et al. would have benefited from attempts to establish any potential changes to the mechanical properties of the HGMs, i.e. if a similar decrease in flexural strength occurred as had happened during the HF etching process. However, inspection of the SEM image in Figure 30 shows crystals growing on the surfaces of the HGMs, with no obvious cracks, damage or changes to the morphology of the HGMs themselves – the spherical shape of the HGMs have been preserved and are still obvious despite the patchy coverage of the sodium silicate crystals. Judging from the SEM image alone, the increase in surface roughness is due to the growth of sodium silicate crystals on the surfaces of the HGMs. Alkali washing appears to be a more appropriate method of increasing the surface texture of HGMs without causing significant particle damage.

Figure 30. HGMs - a) untreated, b) treated with HCl, and c) treated with NaOH (Hoyle, 2020).

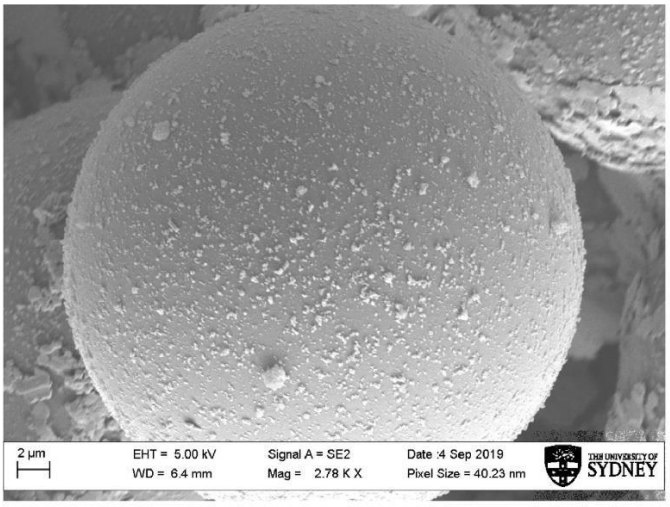

(a)

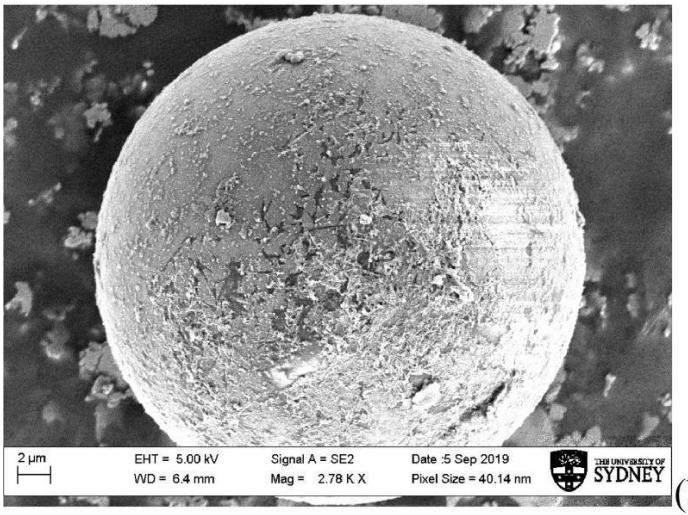

(b)

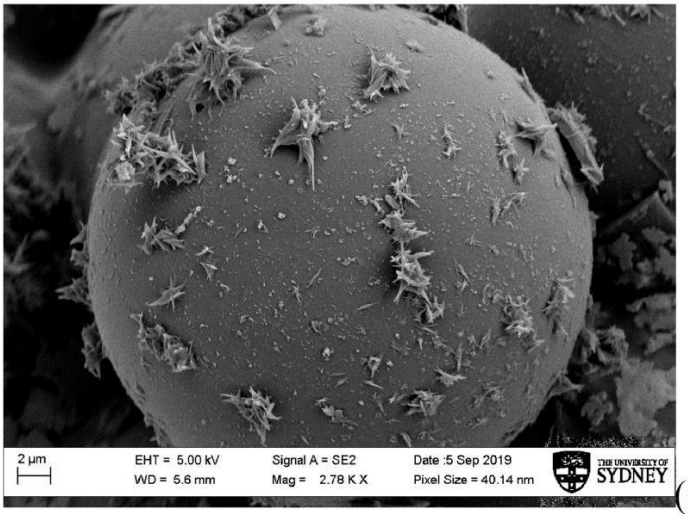

(c)

Silane coupling agents present an alternative method for preparing HGMs, where the purpose of silane coupling agents is to add functional groups to facilitate other reactions. If a method to add the coating directly to the HGMs can be created, the use of silane coupling agents can be omitted, which improves the atom economy of the overall process.

Table 30. Methods to prepare HGMs for coating.

Coating Method	Outcomes/Significance	Ref
Silane coupling agent	Increases population of OH groups on the surfaces of the HGMs. Various silane coupling agents can be used. Other functional groups can be supplied using silane coupling agents.	(Zhang, 2016) (An, 2019) (An, 2020)
Immersion in alkali solution	Increases population of OH groups on surfaces of the HGMs. Can result in the growth of sodium silicate crystals on the surfaces of the HGMs.	(Hoyle, 2020)
Washing in acid	Acid washing is method aimed at cleaning the surfaces of the HGMs and increasing surface texture/roughness.	(Hoyle, 2020) (Zhang, 2005) (Wang, 2015)

5.4 Applications as Floating Photocatalysts

Examples of successfully produced floating photocatalysts where HGMs are functionalised

with application-specific chemical moieties in order to provide photocatalytic properties are included in this section. The HGMs provide a substrate with compressive strength, silica chemistry, consistent size, and reduce the overall density of the bulk material.

In a paper titled "Cr/S/TiO_2-Loaded hollow glass microspheres as an efficient and recyclable catalyst for the photocatalytic degradation of indigo carmine under visible light" Cr/S/TiO_2-HGMs were found to have a slightly greater photocatalytic efficiency than Cr/S/TiO_2 powder and were deemed to be a more reusable catalyst than the powder. While absorbing more strongly than the powder over all wavelengths in the UV spectra. The surface area of the Cr/S/TiO_2-HGM was 176 m^2/g after multiple rounds of loading the HGMs with Cr/S/TiO_2, while TiO_2 was 47 m^2/g, Cr/S/TiO_2 was m^2/g, and the HGMs were 132 m^2/g. The increase in photocatalytic activity was attributed to the increase in surface area due to the HGMs. The researchers concluded that loading this catalyst on to HGMs was an effective and promising method for improving catalyst recycling and recovery, with the potential for applications in the field of water treatment (Zhang, 2016).

The preparation and visible-light photocatalytic properties of the floating hollow glass microspheres - TiO_2/Ag_3PO_4 composites were reported with a schematic shown in Figure 3. The silane coupling agent in this paper was used to graft amine groups on to the surfaces of the HGMs in order to provide the useful chemistry necessary for the final product. Use of a silane coupling agent (3-aminopropyl triethyoxysilane), followed by hydrolysis of titanium butoxide resulted in polymerisation of titanium (IV) hydroxide, forming a network which collapses on to the HGMs. Ti and N have a strong affinity for each other as N is similar in size to oxygen, and N-doping or interstitial N sites within the TiO_2 lattice lowers the band gap, improving the optical absorption capability (An, 2019). The process of coating HGMs with the TiO_2/Ag_3PO_4 composites is shown in Figure 31. Coating HGMs using a silane coupling agent . .

Figure 31. Coating HGMs using a silane coupling agent (An, 2019).

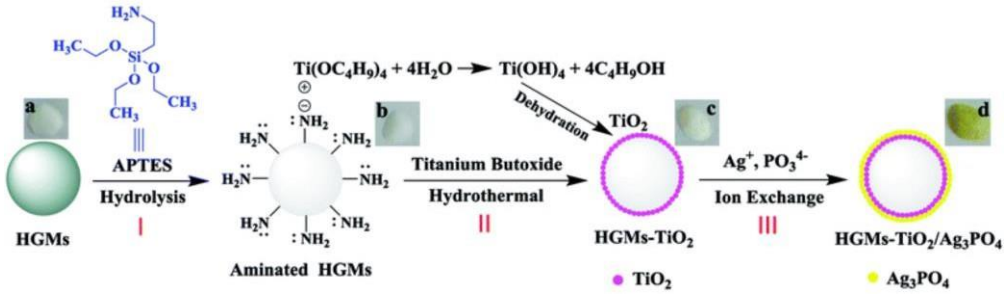

A silane coupling agent was also used to add amine groups to the surface of HGMs, which was followed by an ion-exchange process to add Ag^{+}, and finally addition of Na_2HPO_4 provide the PO_4^{3-} ions. In this process, the silane coupling agents acts a bridge between the HGMs and the Ag^{+} ions. The amine groups introduced by the silane coupling agents act as electron pair donors to Ag^{+}, indicating that the if used, the silane coupling agent should be carefully chosen for its ability to add functional groups that assist in later stages of the reaction. Therefore, silane coupling agents may not be appropriate for all methods of coating HGMs, especially if other alternatives are available. However, in this case, the silane coupling agent increased the catalyst loading by 52% (An, 2020). The steps of this reaction are displayed in Figure 32. Schematic of synthesis using silane coupling agent.

Figure 32. Schematic of synthesis using silane coupling agent (An, 2020).

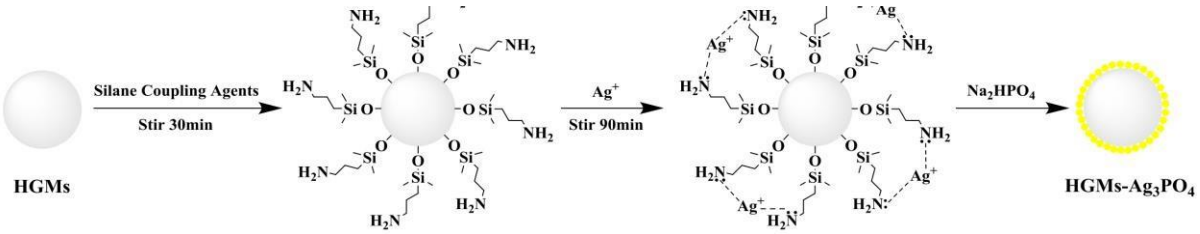

The preparation of hollow TiO_2 supported on HGMs also used a silane coupling agent, however this method used HF in the process to prepare the surfaces of the HGMs. The severe hazards associated with HF mean this reaction is difficult to replicate and undesirable on a larger scale. The purpose of HF was to introduce moderate corrosion to increase particle roughness (which was not quantified). The silane coupling agent improved the adhesion of the polystyrene template, which was then loaded with TiO_2 through the use of titanium tert-butoxide. Hollow TiO_2 on the surface of the HGMs increased the degradation of rhodamine blue and phenol from 16% and 22% respectively, to 68% and 73% - however, the use of HF in this process is

problematic due to the hazards, and alternative method omitting HF should be sought. The schematic for this process is shown in Figure 33. Process to coat HGMs with TiO2 spheres (Wang, 2015).

Figure 33. Process to coat HGMs with TiO_2 spheres (Wang, 2015).

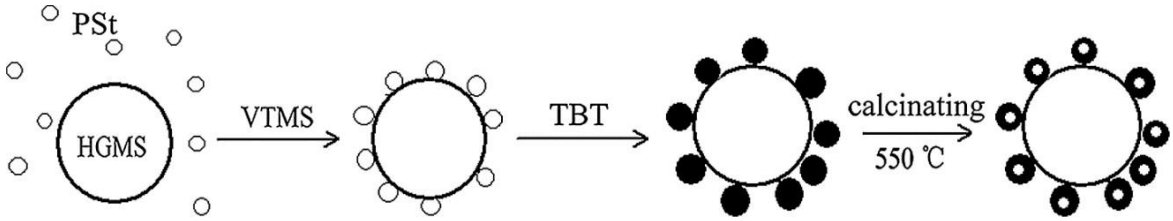

HGMs were loaded with a silica zeolite and TiO_2 to produce a floating photocatalyst/adsorbent material. In this synthetic process tetrapropyl ammonium hydroxide (TPA) and tetraethyl orthosilicate (TEOS) were used as the structure directing agent and additional silica source to prepare the zeolite component on the HGMs. Some silica dissolved from the HGMs for the formation of the silica zeolite, and additional silica was supplied from the TEOS. The TEOS was necessary for the formation of the zeolite, however these findings imply that in cases where the coating is not silica based, TEOS is not necessary. The TPA also formed a layer at the surface of the HGMs, which indicates that a hydroxide containing species can be used to add chemical species to the surfaces of the HGMs. The schematic for this is in Figure 34. Adsorbent/photocatalytic material added to the surfaces of the HGMs .

Figure 34. Adsorbent/photocatalytic material added to the surfaces of the HGMs (Nijpanich, 2022).

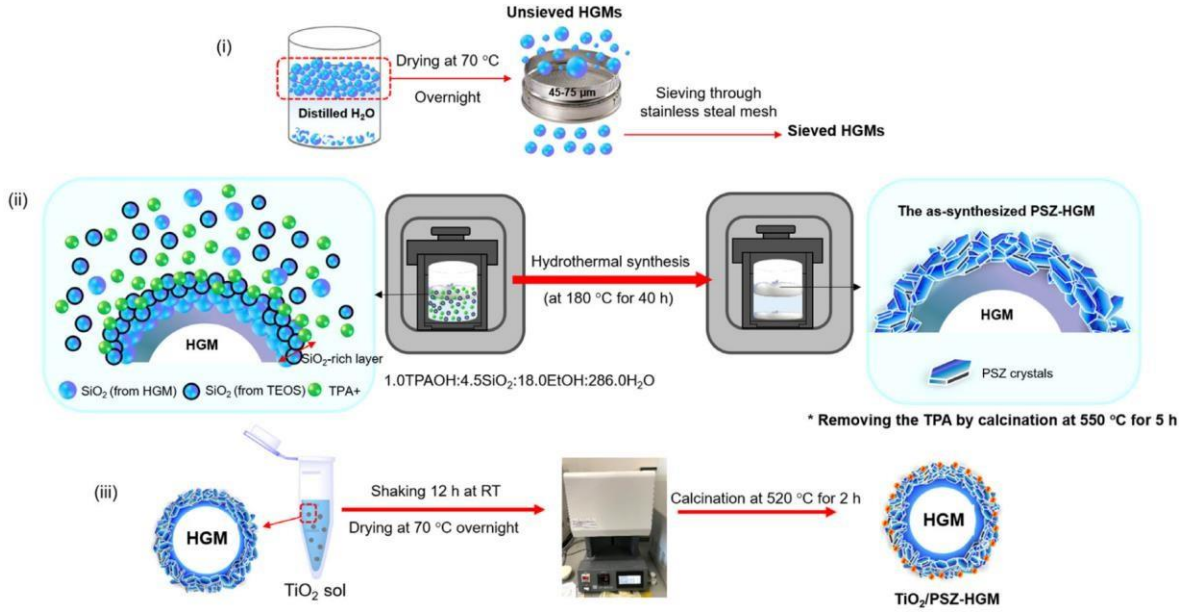

5.5 Methods to Characterise HGMs

HGMs can be analysed using SEM, EDS, XRD, FT-IR, and other standard solid characterisation techniques. Scanning Electron Microscopy (SEM) is a common technique used to produce images of HGMs given their average size is between 1 – 100 µm and is appropriate for generating images showing the dispersion of HGMs within a matrix or for showing the extent of the coating applied to HGMs, e.g., whether the coating has been applied in an even consistent layer or whether the coating has aggregated into larger crystals leaving bare patches on the HGMs. SEM imaging is particularly useful for examining the effect the coating processes had on the HGMs, for example if the coating conditions were excessively severe resulting in mass HGM weakening and/or particle fracturing. SEM can also be used to obtain images of cross sections of the HGMs, which shows the thickness and consistency of the coating applied. The cross sections can be obtained by capturing a sample of the coated HGMs in an epoxy resin, and polishing the HGM-epoxy resin solid with increasingly fine grit polishing paper until sufficient material has been removed exposing cross sections of the coated

HGMs embedded in the epoxy resin. The advantages of this method are that the images captured can be examined closely to determine the average thickness obtained by a given coating process. Furthermore, samples prepared for SEM imaging can also be used for EDX analysis.

SEM

SEM analysis reveals that a method to produce HGMs coated with Cr/S/TiO_2 (Zhang, 2016) produced a coat of consistent thickness on the first coating, however successive coatings resulted in a cracked and peeling coating. Hence, multiple rounds of coating to add more of the functional coating may actually be a waste of material.

SEM can also be used examining the morphology of the material deposited on the HGMs by coating processes, where highly magnified images of the HGMs can be used to confirm the presence of crystalline materials, and the extent to which these materials have coated the HGMs, the coverage of the HGM surface is incomplete, however the particles on the HGM surface are less evenly distributed (An, 2019) and more evenly distributed (An, 2020). Damage to HGMs can also be visualised using SEM (Wang, 2015). Finally, SEM can be used to show where a coating method has overloaded some of the HGMs in the sample, while also leaving many HGMs uncoated, indicating that the coating process requires further optimisation (Linley, 2023). HGMs that have been overloaded can be seen in Figure 35. Coatings of HGMs are cracked and peeling, indicating poor coating and Figure 36. Incomplete coverage of HGMs.

.

Figure 35. Coatings of HGMs are cracked and peeling, indicating poor coating (Zhang, 2016).

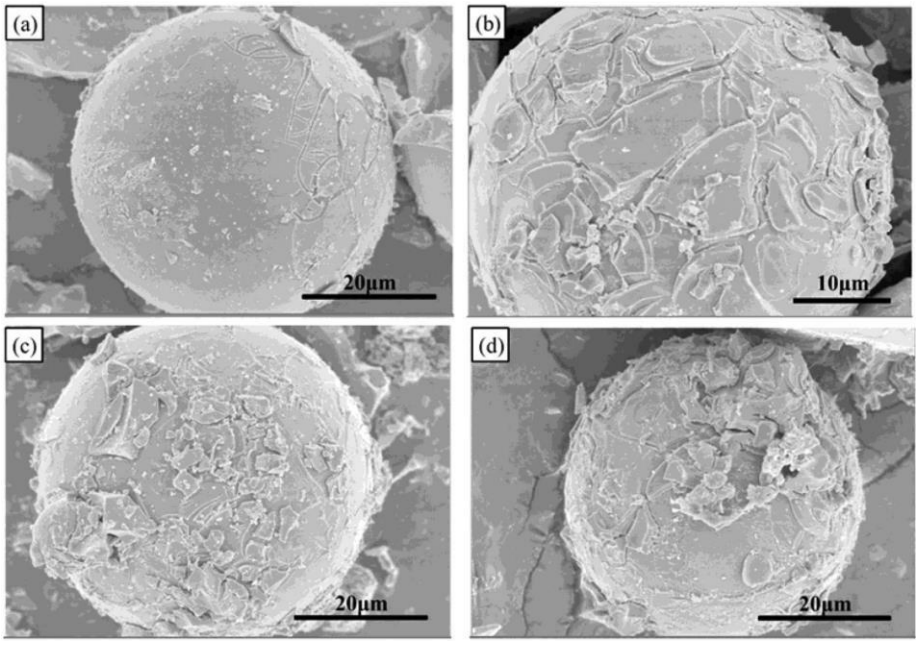

Figure 36. Incomplete coverage of HGMs. (An, 2019).

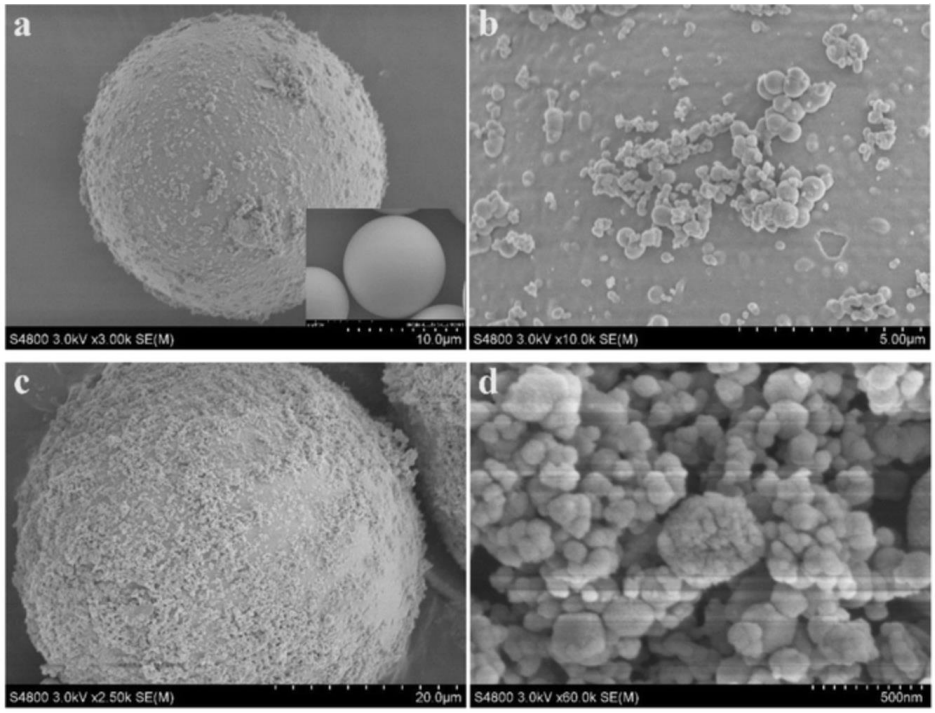

In the case where no pretreatment of the HGMs was performed prior to addition of the silane coupling agent, the coverage of the HGM achieved is often incomplete, as in Figure 37. Incomplete coverage of HGMs Figure 37. Incomplete coverage of HGMs (An, 2020).

Figure 37. Incomplete coverage of HGMs (An, 2020).

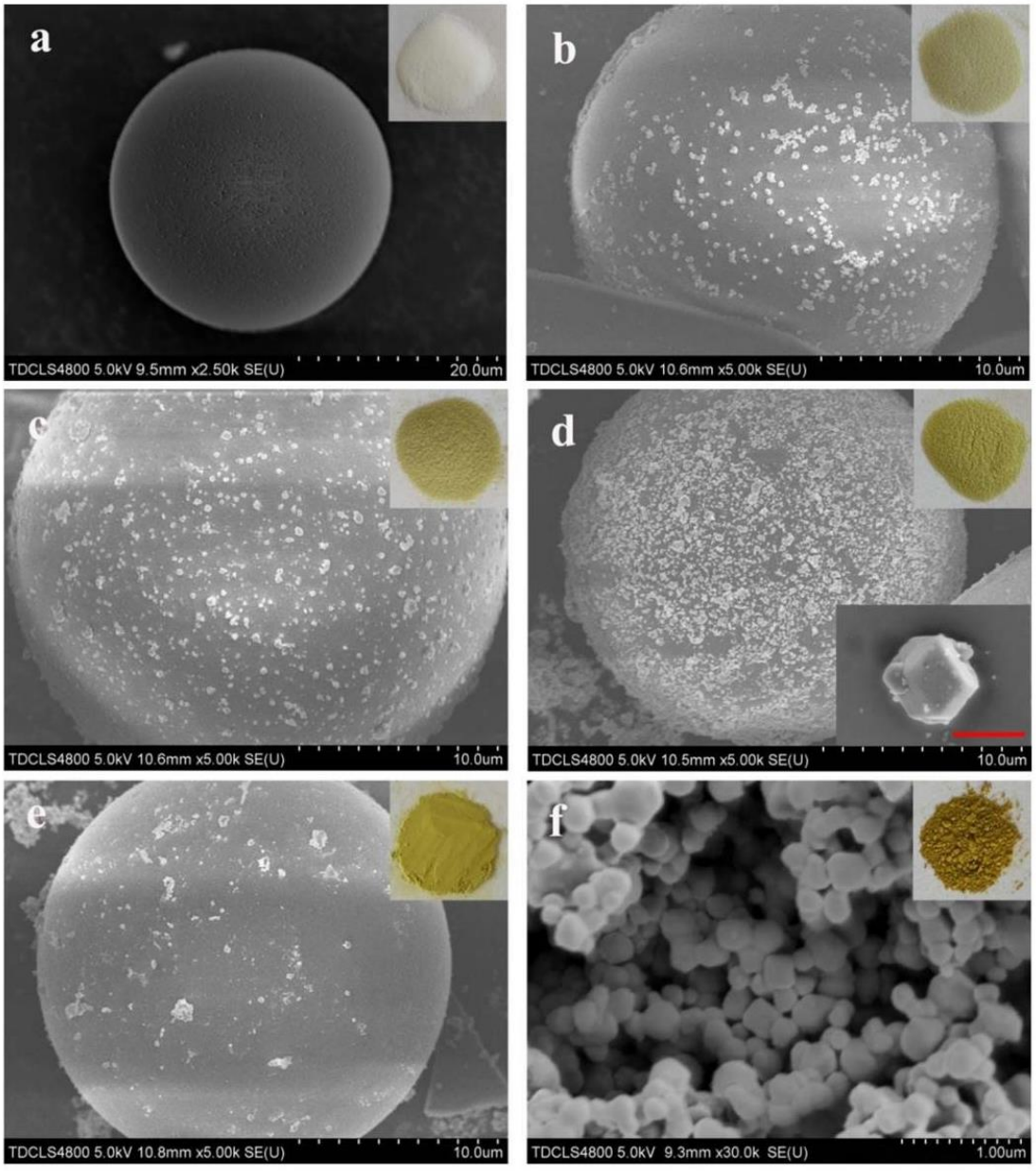

Attention should be paid to the inconsistency of the coating, where some HGMs are overloaded and sealed to other HGMs. The coating has also not adhered strongly to the HGMs, evidenced by the presence of “caps”: objects that are fractions of a sphere that show where the coating has been dislodged from the surfaces of the HGMs. Clumps of HGMs and caps from dislodged coatings can we seen in Figure 38 (Nijpanich, 2022).

Figure 38. Poor coating method that has caused the HGMs to clump together (Nijpanich, 2022).

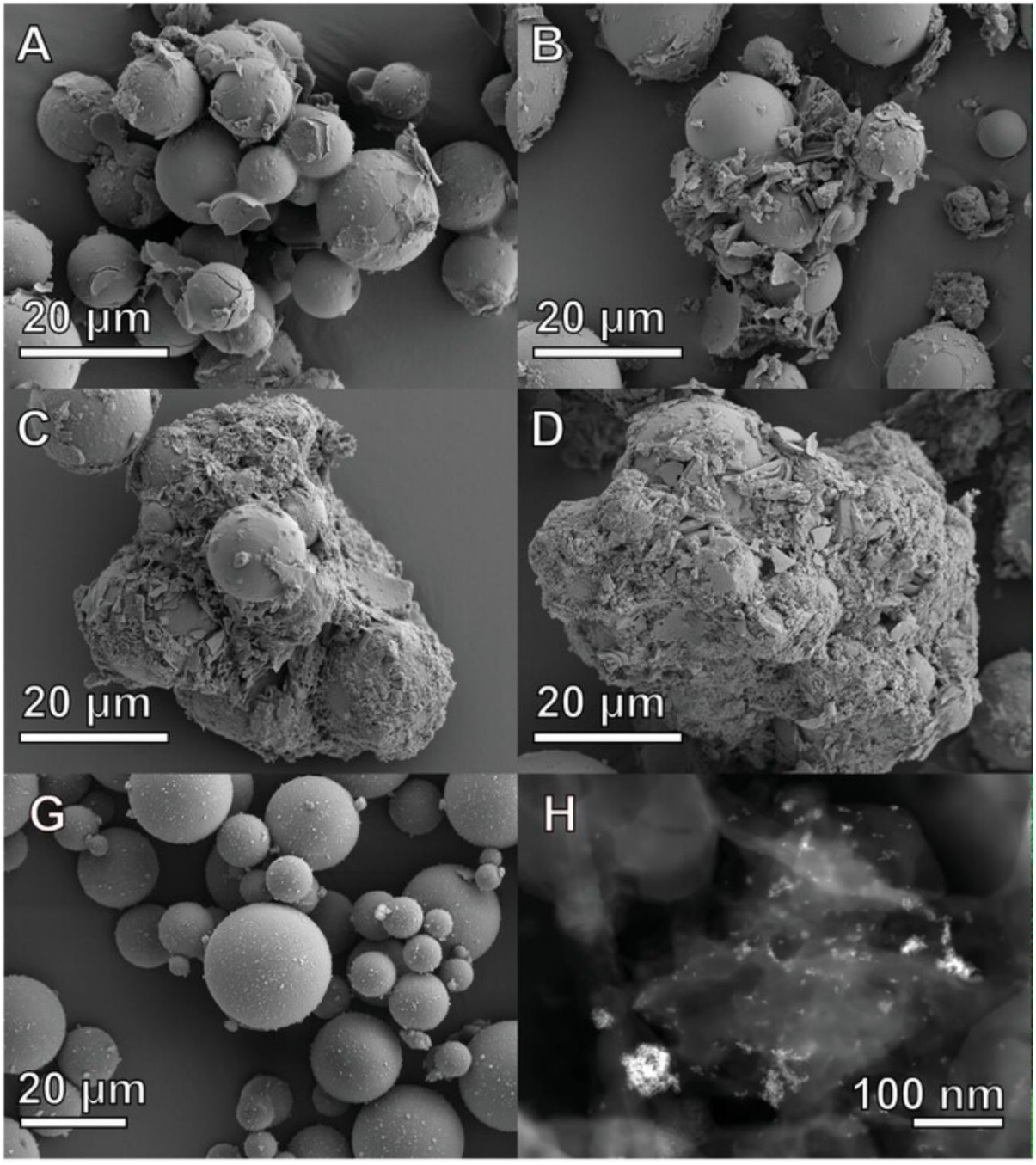

A much more even and consistent coating was achieved by treating the HGMs with TPA and TEOS, where total coverage of the HGMs was achieved with a highly crystalline material, which can be seen in Figure 39 (Nijpanich, 2022).

Figure 39. Improved coating method using silane coupling agent (Nijpanich, 2022).

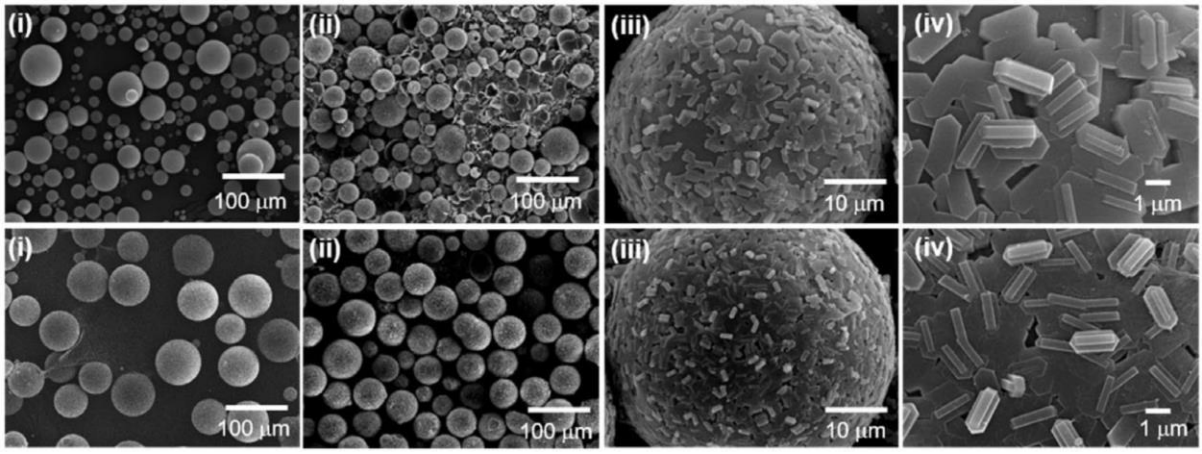

EDX

Elemental maps produced using EDX can show the extent and consistency of coatings, i.e., whether the coating has formed one layer of uniform thickness or whether the reagent has aggregated into large grains leaving patches of bare silica on the HGMs. In this way EDX is also useful for giving information regarding whether the particles supported on the HGMs are evenly or unevenly distributed on the HGM surface. EDX spectra has been used to confirm the presence of the coating on the surfaces of the HGMs by comparing EDX spectra before the coating in Figure 40 and after the coating process in Figure 41 (Zhang, 2016).

Figure 40. HGM prior to treatment to add Cr/S/TiO2 coating (Zhang, 2016).

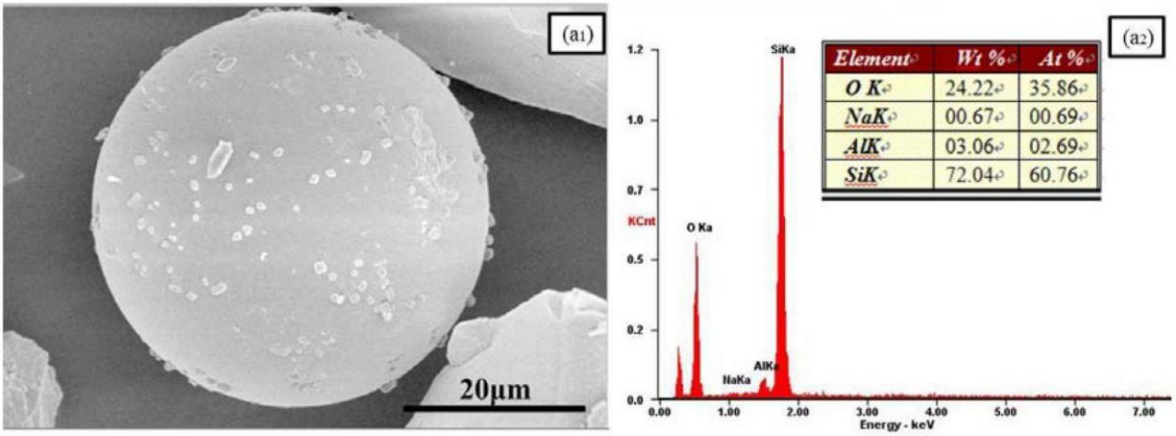

Figure 41. HGM after treatment to apply a coating of Cr/S/TiO2. Y-axis scale is Kilo-Counts. (Zhang, 2016).

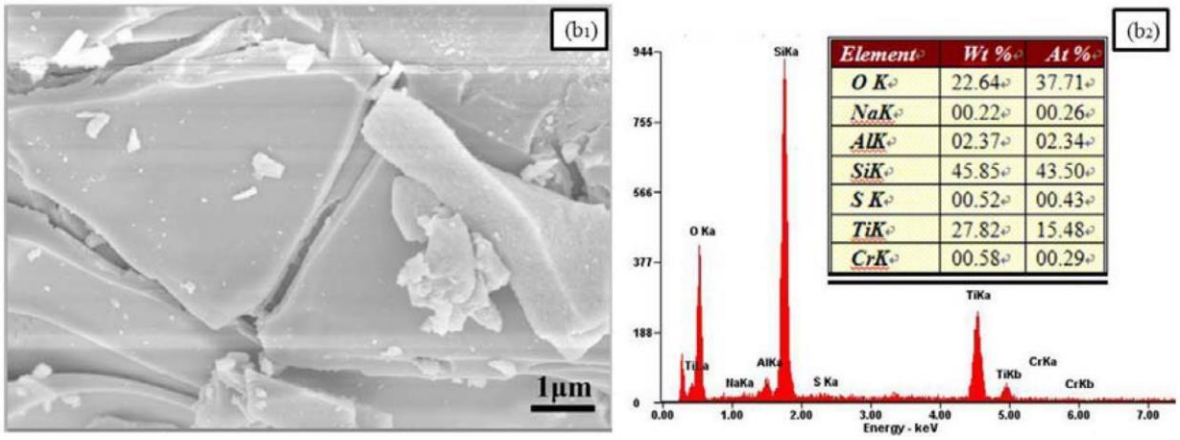

EDX elemental mapping can also be used to infer the distribution of the coatings applied to HGMs, where an even distribution of the TiO_2 coating can be seen on the HGMs in Figure 42. EDX map showing an even distribution of the coating on the HGMs. Y-axis on EDX spectrum is counts meanwhile an uneven distribution of platinum on the HGMs can be seen in Figure 43. EDX map showing an uneven distribution of the Pt coating on the HGMs (Linley, 2023).

Figure 42. EDX map showing an even distribution of the coating on the HGMs. Y-axis on EDX spectrum is counts (Linley, 2023).

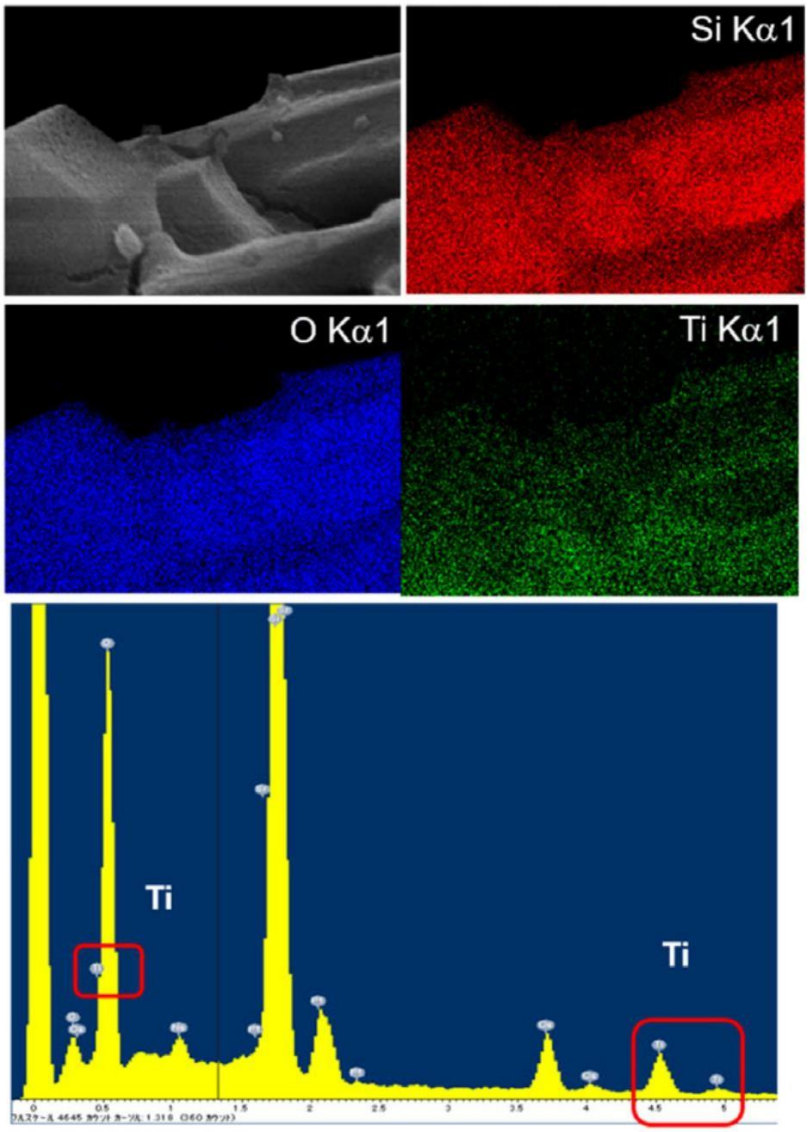

Figure 43. EDX map showing an uneven distribution of the Pt coating on the HGMs.

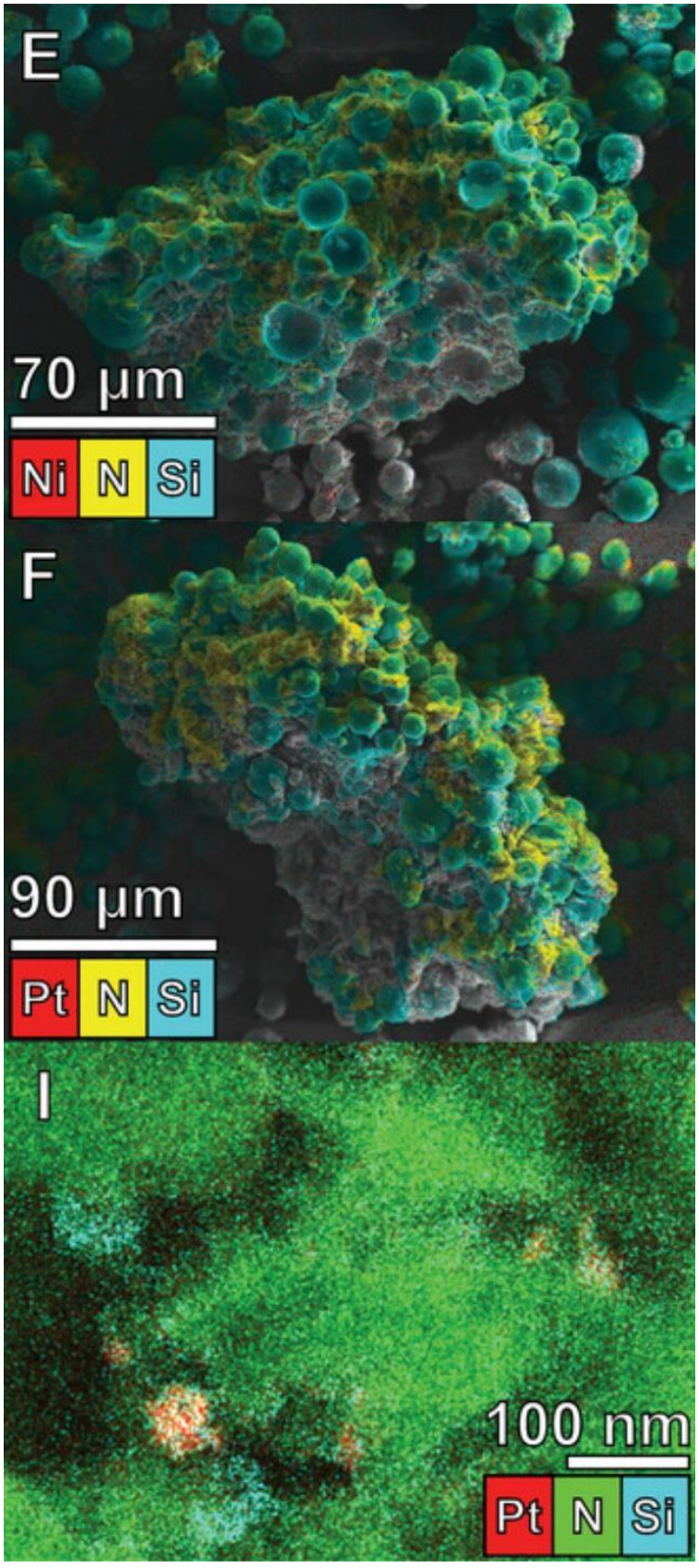

XRD

X-Ray Diffraction (XRD) is used to confirm the presence of particles deposited on to the surfaces of HGMs. HGMs produce an XRD pattern comparable to amorphous silica with a single large broad peak with a maximum around 2theta = 23° (Zhang, 2016). The addition of silver, copper, aluminium, calcium or phosphates or other combinations of inorganic elements with XRD patterns recorded in crystallographic databases can be seen as peaks in the typical range for the crystal often overlaid on the typical curve of amorphous silica, with the stipulation that the analytes must be at least 1% of the sample by volume.

Although the XRD patterns of inorganic coatings on the HGMs are generally recognisable, there may be small shifts in the XRD pattern if the height of the sample varies to the HGMs. Table 4 shows XRD patterns obtained from samples coated HGMs, where the influence of the HGM on the shape of the patterns can be perceived by the shape of the baseline between 2Theta = 22-24 °, where the baseline of the peaks is pushed upwards in the same area that the peak maxima occur for the untreated HGMs. However, there is the risk that the influence of the HGMs is barely perceptible on the baseline between 2Theta = 22-24 °, which indicates that although the presence of HGMs in an XRD pattern is likely to be seen, it is also possible that the presence of HGMs may not be perceptible. Hence, complementary characterisation techniques should be used to support the XRD analysis. These XRD patterns are displayed in Figure 44. XRD patterns of HGMs, coated HGMs, and materials used to coat HGMs (Zhang, 2016), Figure 45. XRD patterns of the HGMs, the materials used for coatings, and the HGMs coated with silver Figure 46. XRD pattern of coated and uncoated HGMs. Anatase peaks are visible on the peak maxima for the HGMs.

Figure 44. XRD patterns of HGMs, coated HGMs, and materials used to coat HGMs (Zhang, 2016)

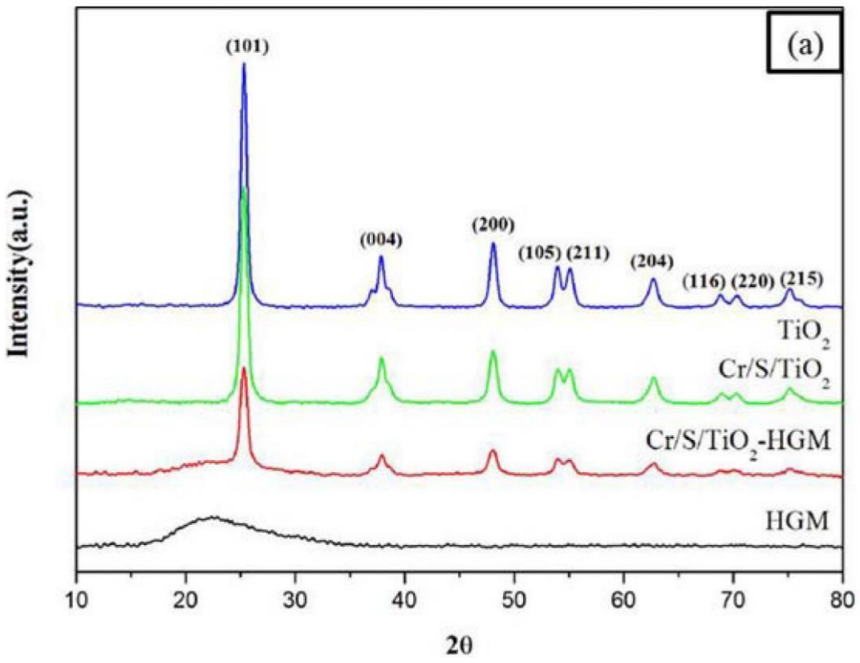

Figure 45. XRD patterns of the HGMs, the materials used for coatings, and the HGMs coated with silver (An, 2020).

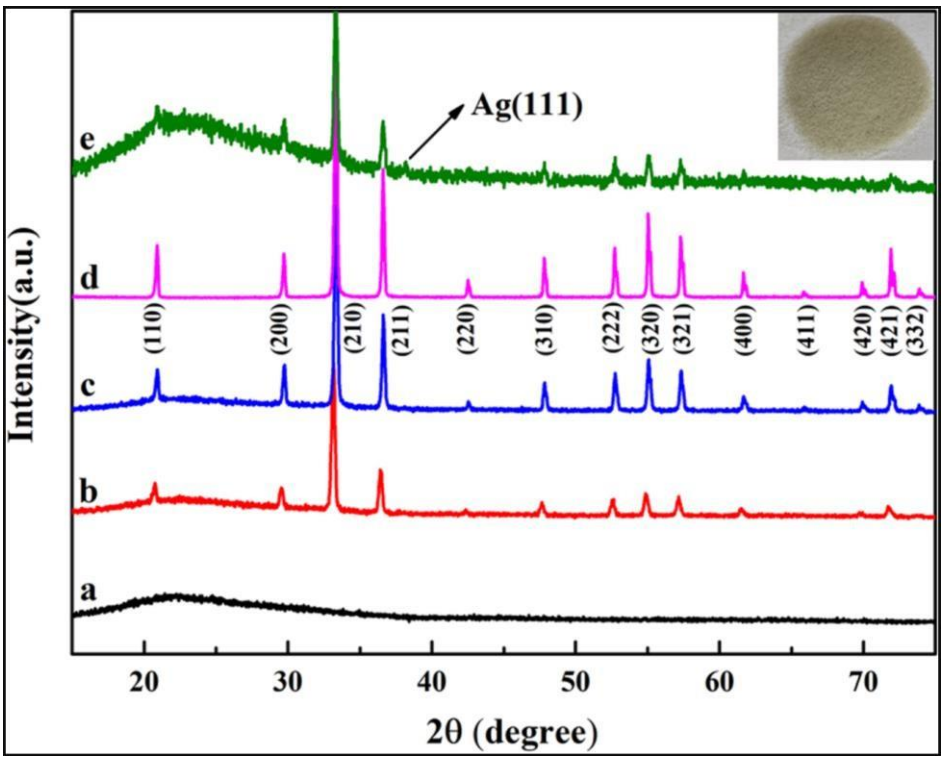

Figure 46. XRD pattern of coated and uncoated HGMs. Anatase peaks are visible on the peak maxima for the HGMs. (Wang, 2015)

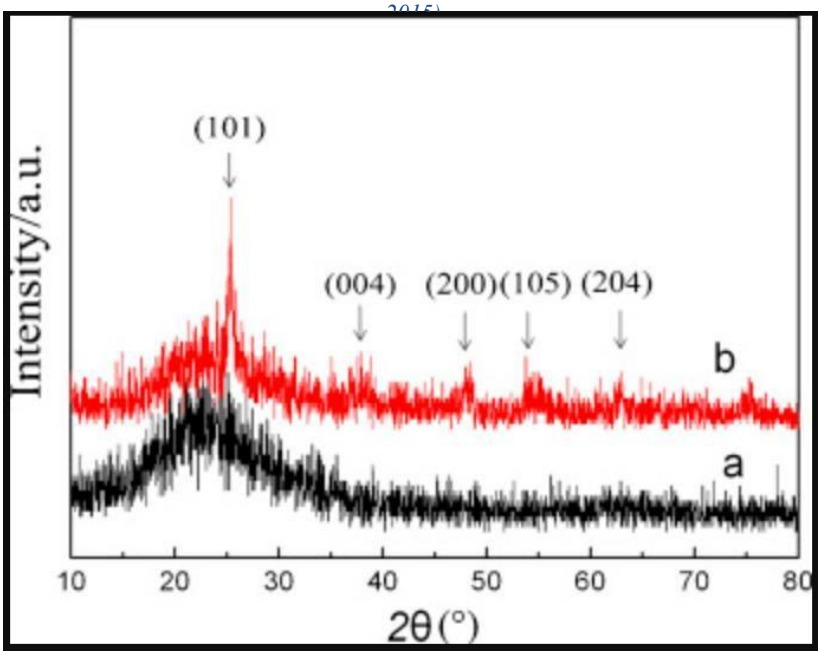

5.6 Chapter Summary

Methods to coat HGMs reported in the literature often use a silane coupling agent in order to facilitate the addition of further coatings. However, pre-treatment of the HGMs in order to prepare their surfaces for the addition of functional groups supplied by the silane coupling agents may be required in order to ensure total coverage of the HGMs. Pre-treatment has been performed using HF, however this is undesirable due to the hazards of working with HF. Pretreatment of the HGMs can also be accomplished using acid or alkali solutions, and alkali solutions may dissolve small amounts of silica from the surfaces of the HGM that then reforms, introducing surface texture. Washing with NaOH was reported to introduce more surface texture than washing with HCl. Coated HGMs can be characterised using XRD pattens as the pattern is dominated by the peaks of the coating, with the baseline lifting between 2Theta = 22 ° and 24 °, in the range that is characteristic of the HGMs. SEM images can be used to asses to extent to which the coating has been applied, and EDX can be used to examine the distribution of elements in the coating.

6. Chapter 6 – Materials, Analytical Methods and Synthesis Routes

6.1 Materials

i. Hollow Glass Microspheres (HGMs) - obtained from Trelleborg and were washed and fragments of broken microspheres removed before use.

ii. Calcium hydroxide - obtained from Sigma Aldrich

iii. Sodium hydroxide - obtained from Sigma Aldrich

iv. Potassium hydroxide - obtained from Sigma Aldrich

v. Scallop shell - *Pectinidae maximus*, were recovered from food waste and calcined and/or boiled in sodium hydroxide solution to remove organic matter.

vi. Dipotassium phosphate trihydrate - obtained from Sigma Aldrich

vii. Anatase – obtained from Sigma Aldrich

viii. Titanium tetraisopropoxide - obtained from Sigma Aldrich

ix. Ethylene Glycol - obtained from Sigma Aldrich

x. Ethylene Diamine - obtained from Sigma Aldrich

xi. Granular Activated Carbon (GAC) removed from a water filter obtained from Aqua House, produced code AH-GAC10

xii. MilliQ de-ionised water – prepared on site

xiii. Ethanol – obtained from Merck

6.2 X-Ray Powder Diffraction

X-Ray diffraction is used to study the structure of crystalline materials and through identification of the crystalline phases present can be used to extract information about the sample's chemical composition. The limitations of this technique are that XRD cannot reliably identify amorphous materials, often producing one large broad peak.

All XRD patterns were obtained on a Bruker D8 Advance X-Ray Diffractometer in the Experimental Techniques Centre at Brunel University, and analysed using EVA software or TOPAS.

Crystallite sizes were calculated using the Scherrer equation, Eqn. 2:

$$D_{hkl} = \frac{K\lambda}{\beta cos\theta} \qquad \text{Eqn. 2}$$

Where K = shape factor (0.9)

λ = X-Ray wavelength 0.154 Å

β = full width at height maximum of the peak

θ = diffraction angle

6.3 Scanning Electron Microscopy (SEM)

Scanning electron microscopy (SEM) is a microscopy technique that gives information about the topology of the sample. The SEM instrument used in this work was the Zeiss Supra 35VP scanning electron microscope in the Experimental Techniques Centre at Brunel University. Samples were prepared for SEM analysis by coating with conductive graphite using an Agar turbo carbon coater.

A significant limitation of SEM is that the sample must be prepared in a particular way to increase its electrical conductivity – if it is not already conductive – and this process of mounting on conductive tape and coating with gold or platinum or graphite under vacuum risks producing artefacts in the same that could be misidentified as a feature of the sample. In addition, there is a risk of missing important features because one aspect or area of the sample was over-analysed, as this technique is based around focusing on and imaging one area of the sample, and does not analyse the whole sample.

The ionising radiation used in SEM is destructive for biological or polymer type samples, although metals and inorganic compounds are more resistant to damage from the electron beam. Charging of the sample is common in SEM imaging and this can lead to scanning faults and poor image quality. Finally, the interaction volume is limited as SEM images are restricted to surface/near surface analysis only.

6.4 Energy-Dispersive X-Ray Spectroscopy (EDX)

Energy-dispersive x-ray spectroscopy (EDX) is used to analyse the surface of a sample in order to determine its elemental composition. EDX were used to produce elemental maps of a surface, where different phases can be identified.

The instrument used was an EDAX Trident (EDS-EBSD-WDS) in the Experimental Techniques Centre in Brunel.

6.5 Preparing sample cross sections for EDX

EDX analysis was performed on the cross sections of samples in order to obtain information about the chemical compositions of the walls of the microspheres before and after hydroxyapatite was grown on the HGMs. The process involves embedding a small mount (20 – 100 mg) of the microspheres in epoxy resin (4:1 ratio of epoxy resin to epoxy cure), allowing the resin to cure for 24 hr to ensure the resin had set before polishing with increasingly fine grit paper, starting at 250 grit, then 1200, then 2500 grit. The resin- embedded samples were wiped clean from debris with isopropyl alcohol, before undergoing coating with conductive graphite for 50 seconds under vacuum for EDX analysis.

6.6 Fourier Transform Infrared Spectroscopy (FT-IR)

Fourier transform infrared spectroscopy (FT-IR) uses infrared (IR) radiation to interact with solids, liquids or gases and the absorption, emission or reflection spectrum of the IR radiation is recorded. An IR spectrum is unique to a molecule and the wavelength at which at atomic bonds vibrate is specific, giving information about the type of vibration, e.g., bending, symmetric stretching, asymmetric stretching and scissoring. This technique is particularly useful for detecting specific functional groups with absorption bands in the range of 4000 – 600 cm^{-1}. FT-IR spectra were obtained on a Perkin Elmer Spectrum One Fourier Transform Infrared (FT-IR) spectrometer in the Experimental Techniques Centre in Brunel was used.

6.7 Atomic Force Microscopy

Atomic force microscopy (AFM) uses a sharp probe tip to scan across the surface of the sample, and the forces between the surface of the sample and the tip of the probes are measured, and this data is used to build up a topographic map of the surface of the sample. The probe is attached to a cantilever (horizontal beam extending into space), and the interatomic forces that arise when the probe is brought into close proximity to the sample deflect the cantilever. The distance between the tip and the sample surface is proportional to the signal produced by piezoelectric and optical sensors, which monitor this deflection. The sample's surface features are mapped by maintaining a constant force between the tip and the sample surface.

The AFM instrument used was a Nanoscope II (Digital Instruments *Inc.,* Santa Barbara. CA*, USA*) in the Experimental Techniques Centre in Brunel and measurements were conducted in air.

6.8 Raman Spectroscopy

Raman spectroscopy is a non-destructive type of vibrational spectroscopy, where light is used to measure the frequency of scattered light emitted by a molecule after it has been excited with light from a laser source. Incident light from a high intensity laser is scattered elastically (Rayleigh scattering) and inelastically (Raman scattering). Rayleigh scattered light is the same wavelength as the incident light so does not yield descriptive information, but Raman scattered light is characteristic of the analyte and can therefore give information on the chemical structure of the analysed molecule. In this work, a Renishaw inVia Micro Raman system fitted with a 514 nm laser was used to obtain Raman spectra in the Experimental Techniques Centre in Brunel was used.

6.9 Ultra-violet Visible Light Spectroscopy (UV/Vis)

Ultra-violet visible light spectroscopy (UV/Vis) measures the difference in the amount of light that has passed through a sample compared to light that has been shone through a blank sample. This technique typically uses light in the wavelength range 200 nm – 1000 nm, and records the absorbance or reflectance spectra of the analytes. The Beer-Lambert law, Eqn. 3:

UV/Vis can be used to determine the concentration of the analyte in solution if the absorbance, path length and molar absorption coefficient are known, or conversely, can be used to calculate the molar absorption coefficient if the absorbance, path length and concentration are known.

$$A = \varepsilon c l \qquad \text{Eqn. 3}$$

In this work, a UV/Vis Perkin Elmer UV/Vis/NIR spectrometer Lambda 1050+ at the Experimental Techniques Centre in Brunel was used.

6.10 Thermo-gravimetric Analysis

Thermo-gravimetric analysis (TGA) heats the analyte at a steady rate in a controlled gas environment while recording the mass change of the sample. If the analyte contains that decompose within the temperature range used during TGA, the step change in the mass at this temperature can be indicative of the percent of the overall mass that is comprised of this particular substance. However, if the decomposition temperatures of the components of the analyte overlap significantly or exceed the temperature range of the TGA instrument, this method cannot quantify the percent mass of the component within the sample.

In this work, TGA was performed on a TA Instruments SDT-600 instrument. All measurements were conducted in air.

6.11 BET (Brunauer Emmett Teller) Surface Area

The specific surface area of the various materials was calculated using the BET technique from N2 adsorption isotherms at 77 0.5 K using the Belsorp machine (BEL JAPAN, INT). The materials were evacuated (105 mm Hg) at 100°C for 90 minutes before the adsorption experiments. BET was used to analyse the alk-TiO_2-HAP-HGMs, the anatase-HAP-HGMs, and the HAP-HGM. The samples were placed in the machine for 12 hours.

These measurements were obtained by researchers at Kingston University, who have given their permission for these results to be included in this thesis.

6.12 Hollow Glass Microspheres (HGMs)

This section contains all the experiments performed in order to produce the final composite material.

Hollow Glass Microsphere Selection

A range of microspheres from Trelleborg were examined using SEM and ImageJ in order to determine the average thicknesses of the HGM shell and the particle size (diameter) distribution of the HGMs.

The way in which this was achieved was by acquiring SEM images of the HGMs and ImageJ software used to measure the particles sizes and calculate the particle size distribution. The software was instructed to assume the HGMs were spherical, and particles over 60 μm and under 1 μm in diameter were excluded as microspheres >60 μm or <1 μm were indistinguishable from fragments of microsphere or aggregates of multiple microspheres. The SEM images used were acquired at a magnification ranging between 200x and 500x, and the scale in ImageJ was set using the scale bar recorded in the SEM image.

Hollow Glass Microsphere Characterisation

The HGMs were characterised thoroughly before attempts were made to add the coatings. Characterization was performed using SEM, EDX, XRD, FT-IR, TGA and DSC.

Removing Hollow Glass Microsphere fragments

HGMs (2.5 g) were immersed in deionised water in a separation funnel and allowed to stand. Broken fragments settled in the lower part of the vessel while intact spheres remained buoyant and stayed floating at the top of the container.by opening the tap and allowing most of the mixture to escape, reserving the upper 50% of the mixture which contained intact spheres.

This process was monitored using SEM and it was determined that the process of washing had been successful when <1 mL retrieved from the surface of the mixture obtained after allowing the HGM fragments to settle was dried on to an SEM stub, and the images obtained showed no particle fragments. Particles that had cracked were tolerated, although more than two cracked particles visible at a magnification of x200 were determined to be excessive, and the washing process was repeated until no more than two cracked particles were found in the image. During this process metal spatulas were replaced and wooden spatulas used instead in order to avoid causing particle damage.

Hollow Glass Microsphere Surface treatment with Alkali

The HGMs were immersed in NaOH, KOH, or $Ca(OH)_2$, at concentrations of either 0.02 mol dm^{-3} or 0.005 mol dm^{-3} for either 1 hr or 24 hr. The white products that floated to the top of the mixture were removed via pipette and dropped into 200 mL of DI and stirred briefly. The white precipitate that floated to the surface of the mixture was again removed via pipette and added to ethanol or water, in a ratio of 2 mL white precipitate mixture to 3 mL ethanol or water. To determine if the particles grown on the Ca-HGMs could be dislodged 1 mL of the Ca-HGM mixture (containing Ca-HGMs and the calcium hydroxide mixture) were added to 5mL water or ethanol and ultrasonicated for 1 hr using a 48 W ultrasonicator, before drying for 2 hr at 100 °C. Masses of salts and HGMs used are included in Table 31. Masses of salts and HGMs used in this work.

Table 31. Masses of salts and HGMs used in this work.

Solution	Mass salt	Vol H_2O	Mass HGMs
KOH	1.12 g	100 mL	0.2 g
NaOH	0.8 g	100 mL	0.2 g
$Ca(OH)_2$	1.48 g	100 mL	0.2 g

6.13 Hydroxyapatite

This section contains the experiments performed in order to produce hydroxyapatite coated microspheres, where the hydroxyapatite is chemically bonded to the microsphere and is not applied as a coating that can be dislodged. This section begins with an attempt to produce hollow calcium carbonate microspheres, which could then be reacted to produce hydroxyapatite. However, the microspheres produced were fragile, and it was decided that growing calcium carbonate on HGMs before conversion into hydroxyapatite would give strength and uniformity to the hydroxyapatite produced. This section also includes attempts to produce hydroxyapatite from biological sources, which was successful, although full conversion of the calcium carbonate into hydroxyapatite was not observed. However, adding the calcium carbonate derived from biological sources could be introduced to the calcium carbonate coated microspheres in order to increase the surface area of the hydroxyapatite-HGMs.

Hydroxyapatite Synthesis with Chemical Reagents- Soaking Calcium Carbonate derived from scallop shell in Dipotassium Hydrogen Phosphate solution

This route was replicated using scallop shells calcined for 2 hr at 200 °C to remove organic material, before the shells were washed with ethanol. The calcined shells were then manually broken using a pestle and mortar, before ball-milling at a frequency of 15 Hz for 2 min in loads of approximately 8 g each. Then the $CaCO_3$ powder was dispersed in solutions of either 1.0 mol dm^{-3} or 0.1 mol dm^{-3} of K_2HPO_4 solution, with a solid ($CaCO_3$) to liquid (K_2HPO_4 solution) ratio of 1:4. The mixtures were allowed to rest for 7 days in screw top plastic sample containers, and every day the samples were manually agitated for 1 min. After 7 days, the white precipitates were filtered from the solution using filter paper and washed with de- ionised water (50 mL), before being dried in an oven at 40 °C for hr.

Growing Hydroxyapatite on Hollow Glass Microspheres

The calcium treated HGMs (Ca-HGMs) were the substrate used for hydroxyapatite growth. The presence of calcium on the surfaces of the Ca-HGMs were hypothesised to promote the growth of a HAP layer when the Ca-HGMs were immersed in a stoichiometric amount of phosphate ions to produce a Ca/P ratio of 1:1.67.

The Ca-HGMs were dispersed in solutions of either 1.0 mol dm^{-3} or 0.1 mol dm^{-3} of K_2HPO_4 solution, with a solid ($CaCO_3$) to liquid (K_2HPO_4 solution) ratio of 1:4. The mixtures were allowed to rest for 7 days in screw top plastic sample containers, and every day the samples were manually agitated for 1 min. After 7 days, the white precipitates were filtered from the solution using filter paper and washed with de-ionised water (50 mL), before being dried in an oven at 40 °C for 2 hr.

6.14 Titanium Dioxide

The parameters used in method 4 were then explored and optimised, and a full characterisation of the products used SEM, EDX, XRD, FTIR, TGA, and Raman.

Route for Obtaining Titanium Dioxide

Sodium chloride (80 mg) was dissolved in ethylene diamine (4 mL), before ethylene glycol (16 mL) was added in 4 mL portions, all with stirring. After 15 min stirring titanium tetra-isopropoxide (0.4 mL) was added dropwise, then H_2O (0.5 mL) was also added dropwise. The conical flask containing the reaction mixture was placed in an oven at 90 °C for 18 hr, then removed from the oven and the orange mixture was swirled, before being replaced in the oven at 200 °C for a further 18 hr.

Titanium dioxide Synthesis Using Sol-Gel Method with Alkoxide Reagent

NaCl (75 mg) was dissolved in ethylene glycol (16 mL) before ethylene diamine (4 mL) was added with stirring. To the pale-yellow solution titanium isopropoxide (TTIP, 0.4 mL) was manually added dropwise at a rate of 0.5 mL/hour. The mixture was then stirred for 15 min, before H_2O (0.5 mL) was added and the mixture immediately placed in a sealed oven at 90 °C for 18 hours. The mixture was allowed to cool and the vessel swirled before being heated to 200 °C for 18 hours where the solvents were vaporised and collected through distillation. The black solids were washed with EtOH, HCl, and H_2O until the colour of the solids changed from black to dark metallic grey.

Optimisation of Titanium Dioxide Synthesis

The reagents used in the synthetic route to produce the TiO_2 component of the material were altered to in order to understand and investigate their effects on the products, and hence to better understand the role of the reagents in the reactions.

Table 32. Amounts of reagents used in iterations of TiO_2 synthesis.

Sample	Titanium Tetra-isopropoxide mol	Ethylene Glycol mol	Ethylene diamine mol	H_2O mol
TNW1	1.35×10^{-3}	0.286	0.06	0.027
TNW2	1.35×10^{-3}	0.286	0.06	0.027
TNW3 (autoclave)	1.35×10^{-3}	0.286	0.06	0.027
TNW4	1.35×10^{-3}	0.286	0.03	0.027
TNW5	1.35×10^{-3}	0.286	0.12	0.027
TNW6	1.35×10^{-3}	0.286	0.24	0.027
TNW7	1.35×10^{-3}	0.286	0.06	0.0135
TNW8	1.35×10^{-3}	0.286	0.06	0.0054
TNW9	1.35×10^{-3}	0.286	0.06	0.0405
TNW10	1.35×10^{-3}	0.286	0.06	0.027
TNW11	1.35×10^{-3}	0.286	0.00	0.027
TNW12	0	0.286	0.06	0.027

Synthesis of the Novel TiO_2-Hydroxyapatite-HGM Composite

This section involves combining all the previous steps to grow a layer of hydroxyapatite on the surfaces of the HGMs, followed by an optimised method for adding titanium dioxide to the surfaces of the HAP-HGMs.

Table 33. Reagents used to synthesise hydroxyapatite.

	$CaCO_3$		**K_2HPO_4**		**TiO_2**	
Mixture	**Source**	**Mass (g)**	**Conc (mol dm^{-3})**	**Vol (mL)**	**Type**	**Mass (g)**
10	Scallop shell	0.25	1.0	10 mL	Anatase NP	0.75 g
11	Scallop shell	0.25	0.1	10 mL	Anatase NP	0.75 g
12	Scallop shell	0.25	1.0	10 mL	Anatase NP	0.028 g
13	Scallop shell	0.25	0.1	10 mL	Anatase NP	0.028 g
14	Ca-HGM	0.25	1.0	10 mL	Anatase NP	0.75 g
15	Ca-HGM	0.25	0.1	10 mL	Anatase NP	0.75 g
16	Ca-HGM	0.25	1.0	10 mL	Anatase NP	0.028 g
17	Ca-HGM	0.25	0.1	10 mL	Anatase NP	0.028 g

Synthesis of Hydroxyapatite-Hollow Glass Microsphere Composite Doped with Anatase

Anatase was dispersed ultrasonically in water, before being added to a mixture containing dipotassium hydrogen phosphate (1.0 mol/dm^3, 10 mL) and CaHGMs (0.125 g). The mixtures were agitated in an ultrasonic bath for 30 min, before aging for 7 days with an additional 1 min of agitation per day. After 7 days, the mixtures were filtered and washed with water (50 mL) before being allowed to dry for 24 hr in ambient conditions.

Synthesis of the Novel Composite: Titanium Dioxide – Hydroxyapatite – Hollow Glass Microsphere (alk-TiO_2-HAP-HGMs)

NaCl (75 mg) was dissolved in ethylene glycol (16 mL) before ethylene diamine (4 mL) was added with stirring. Then, 0.1 g HAP-HGMs were added and stirred for 15 min. To the pale-yellow solution titanium isopropoxide (TTIP, 0.4 mL) was manually added dropwise at a rate of 0.5 mL/hour. The mixture was then stirred for 15 min, before H_2O (0.5 mL) was added and the mixture immediately placed in a sealed oven at 90 °C for 18 hours. The mixture was allowed to cool and the products filtered and washed with water (50 mL), before being allowed to dry for 24 hr in ambient conditions.

6.15 Estrogen Removal Measured Using UV/Vis Spectroscopy

A stock solution of EE2 (0.0051 g) in acetonitrile (100 mL) was prepared and diluted down to a concentration of 50 µg/L in order to obtain the EE2 solution used for the UV/Vis measurements. Then 0.5 g/L of catalyst were dispersed in 50 mL of EE2 stock solution (50 µg/L) and allowed to equilibrate for 5 min under a telstar PV 30/70 fume hood installed with a 660 W UV light. Every 2 minutes a 5 mL aliquot was withdrawn and analysed in a Perkin Elmer UV/Vis spectrophotometer from 400 nm to 183 nm with 1.00 nm intervals.

6.16 Estrogen Removal Measured Using HPLC-Fl

EE2 removal was assessed using a Varian 920-LC chromatograph equipped with an autosampler, quaternary gradient pump, and Agilent 1260 fluorescence detector (FLD, λ_{ex} = 282 nm and λ_{em} = 306 nm) in conjunction with high-performance liquid chromatography (HPLC). An injection volume of 20 µL was employed, and a flow rate of 1 mL/min was maintained, with each sample being subjected to a seven-minute run. The method was isocratic and the mobile phase consisted of acetonitrile: water (50:50) (v/v). The column was conditioned by passing the mobile phase through the machine for 30 minutes before any samples were added. The experiments were performed in triplicate.

The materials were prepared at Brunel University, and researchers at Kingston University performed this HPLC analysis. The researchers Kingston have given their permission for the results to be included in this thesis.

6.17 Estrogen Removal Measured Using HPLC-UV

HPLC-UV was the analytical method chosen to quantify the changing concentration of EE2 over time after the addition of the adsorbing materials. The column used was an Agilent Xorbax XDB-C18 column, 3.5 µm, 4.6 x 150 mm. The make and model of the HPLC instrument was

an Agilent 1260 Infinity II equipped with a quaternary pump, auto sampler and UV detector, measuring EE2 concentration at 220 nm (primary wavelength – best results) and 280 nm (secondary wavelength – second best results). The method was isocratic with the pressure maintained at 220 – 230 bar and the mobile phase was MeOH:H_2O 75:25 with a flow rate of 1 mL/min. The mobile phase was pre-mixed and drawn from one reservoir. The retention time of each sample was set at ten minutes, to allow the column to be flushed through with the mobile phase to remove any contaminants.

A calibration curve was prepared using EE2 concentrations of 0 ppm (blank), 0.25 ppm, 0.5 ppm, 1 ppm, 2 ppm, 3 ppm, 4 ppm, and 5 ppm, prepared from a stock solution of EE2 25mg in 10 mL MeOH, which was then diluted with 990 mL ultrapure milliQ water. The flocculent mixture was ultrasonicated with a 48 W ultrasonicator for 5 hr in a water bath with an initial temperature of 14 – 15 °C that increased to 31 – 32 °C with ultrasonication. Once all of the floc has dispersed and the mixture exhibited a colour change from transparent with white flocs to an opaque milky with no discernible flocs, the stock solution was used to prepare the calibration standards. The standards were adjusted to contain 1% MeOH.

Figure 48. Calibration graph used to determine concentration of EE2.

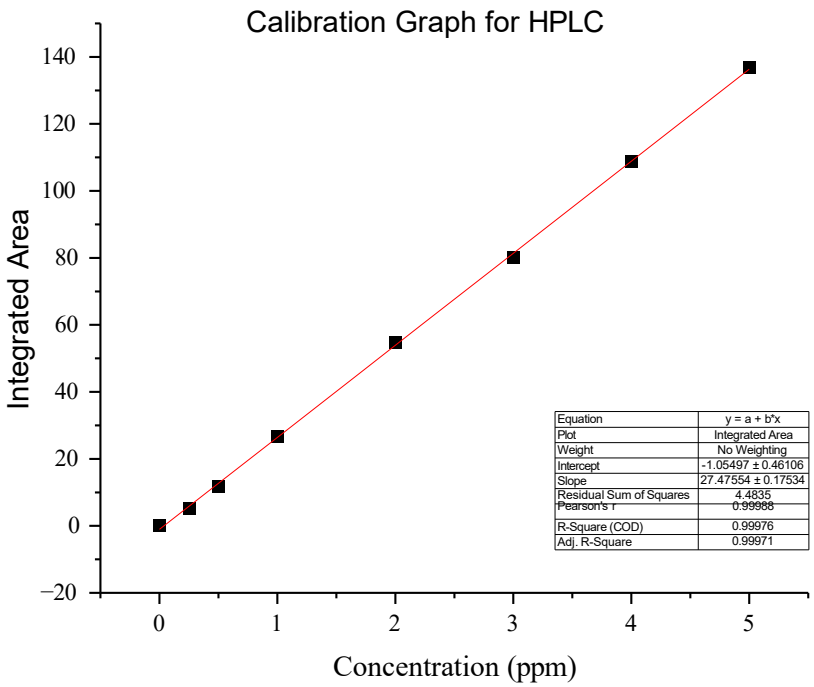

Limit of Detection (LOD) and Limit of Quantification (LOQ)

The limit of detection (LoD) was calculated using Eqn. 4:

$$LoD = 3.3 \times \frac{\sigma}{S} \qquad \text{Eqn. 4}$$

The limit of quantification (LoQ) was calculated using the Eqn. 5:

$$LoQ = 10 \times \frac{\sigma}{S} \qquad \text{Eqn. 5}$$

Table 34. LoD and LoQ calculated for HPLC experiment

Parameter	Value (ppm)
LoD	0.06
LoQ	0.17

Where σ = standard deviation of the intercept and S = slope of the calibration cure.

6.18 Kinetic Models

Pseudo-First Order Model

Non-linear form used in this work to produce a plot of q_t vs t is shown in Eqn. 6:

$$Q_t = Q_e\,(1 - e^{-kt}) \qquad \text{Eqn. 6}$$

Pseudo-Second Order Model

The non-linear form is the preferred approach as the original equation describing pseudo second order kinetic models is in the non-linear. Hence it has been used in this work and the non-linear form used to produce a plot of Q_t vs t is shown in Eqn. 7:

$$Q_t = \frac{k_2 Q_e^2 t}{1 + k_2 Q_e t} \qquad \text{Eqn. 7}$$

Elovich Model

The non-linear form is preferred and hence used in this work. The equation used is shown in Eqn. 8:

$$Q_t = \frac{1}{\beta}\, ln(\alpha\beta + 1) \qquad \text{Eqn. 8}$$

Where:

α = Initial adsorption rate

β = Desorption constant during each experiment

q_t = Amount adsorbed at time t

Intraparticle Diffusion Kinetic Model

The equation used to describe the intraparticle diffusion kinetic model is shown in Eqn. 9:

$$Q_t = K_{diff} t^{\frac{1}{2}} + c \qquad \text{Eqn. 9}$$

Where:

Q_t = amount adsorbed at time t

K_{diff} = rate constant

$t^{1/2}$ = square root of contact time

c = intercept.

6.19 Liquid Chromatography – Mass spectrometry

The Agilent triple quad 6410 mass spectrometer was used to separate and identify intermediates generated during the photocatalytic degradation of EE2 in aqueous medium mediated by alk-TiO_2-HAP-HGMs. Several intermediates were produced during photocatalytic EE2 degradation, but only a handful were recognized and validated by Photocatalysis for EE2 removal Using Hydroxyapatite Doped with TiO_2. First, a 2 ppm EE2 solution was prepared as a standard sample for LC-MS. Following this, the EE2 solution that had been exposed to the Alk-TiO_2-HAP-HGMs was analysed.

These results were obtained by researchers at Kingston University who have given their permission for these results to be included in this thesis.

6.20 Regeneration of the materials after EE2 Removal

Material was recovered from the batch settling experiment and stirred in ethanol (100 mL) for 2hr. the solids were filtered, rinsed with water and dried overnight at 80 °C.

7. Chapter 7 – Selection Process, Characterisation and Surface Preparation of the Hollow Glass Microspheres

7.1 Introduction

This chapter contains the results of the selection process, characterization and surface preparation protocol for the hollow glass microsphere (HGMs). The aims of the selection process, and how these aims were achieved and the outcomes of the process are described here, followed by the methods used to prepare the HGMs for coating. The HGMs received from the manufacturer were analysed to determine:

1. The size distribution (in micrometres) of the microspheres
2. Thickness of HGM shells
3. The extent of microsphere breakage
4. Chemical composition
5. Crystallinity

7.2 Determining the size distribution of the microspheres

A selection of hollow glass microspheres (HGMs) was investigated to determine their particle size distribution. This was achieved by capturing an SEM image of the HGMs loaded on carbon tape, and using ImageJ software to assess the average outer radius of the microspheres. The HGMs with the most consistent sizes and smallest standard deviation relative to the particle radius were selected, as it was determined that having a HGM substrate of regular and consistent size would be preferred for the creation of the final composite material. Histograms of the particle sizes for the four different HGM samples are depicted in Charts 1 – 4, and Table 1 contains the mean particle diameter, standard deviation of particle diameter from the mean, and error. The images used to calculate this data contained a range of sizes, and the software was instructed to select exclusively spherical particles, in order to avoid miscounting

aggregates of particles as a single very large particle. The method is described in Chapter 6.

The particle radius distribution of the sample referred to as HGM4 is displayed in Chart 4. Of the various types of HGM analysed HGM4 was found to have the most consistent radius with the least deviation from the mean. The average particle size was found to be 20 µm ± 0.4 µm with a standard deviation of 6 µm. This data is recorded in Table 35. Average outer radii of the four HGMs samples, plus the standard deviations and errors.

Table 35. Average outer radii of the four HGMs samples, plus the standard deviations and errors.

Radius (µm)	Average (µm)	Standard dev (µm)	Error (µm)
HGM1	7.17	3.92	0.44
HGM2	29.91	10.47	1.18
HGM3	22.02	8.98	1.01
HGM4	20.14	6.13	0.69

The image used for particle size analysis of HGM1 is shown in Figure 47. HGM1 - SEM image used for particle size distribution analysis, while a histogram representing the particle size distribution is shown in Chart 2. Particle size distribution of sample HGM1.

Figure 47. HGM1 - SEM image used for particle size distribution analysis.

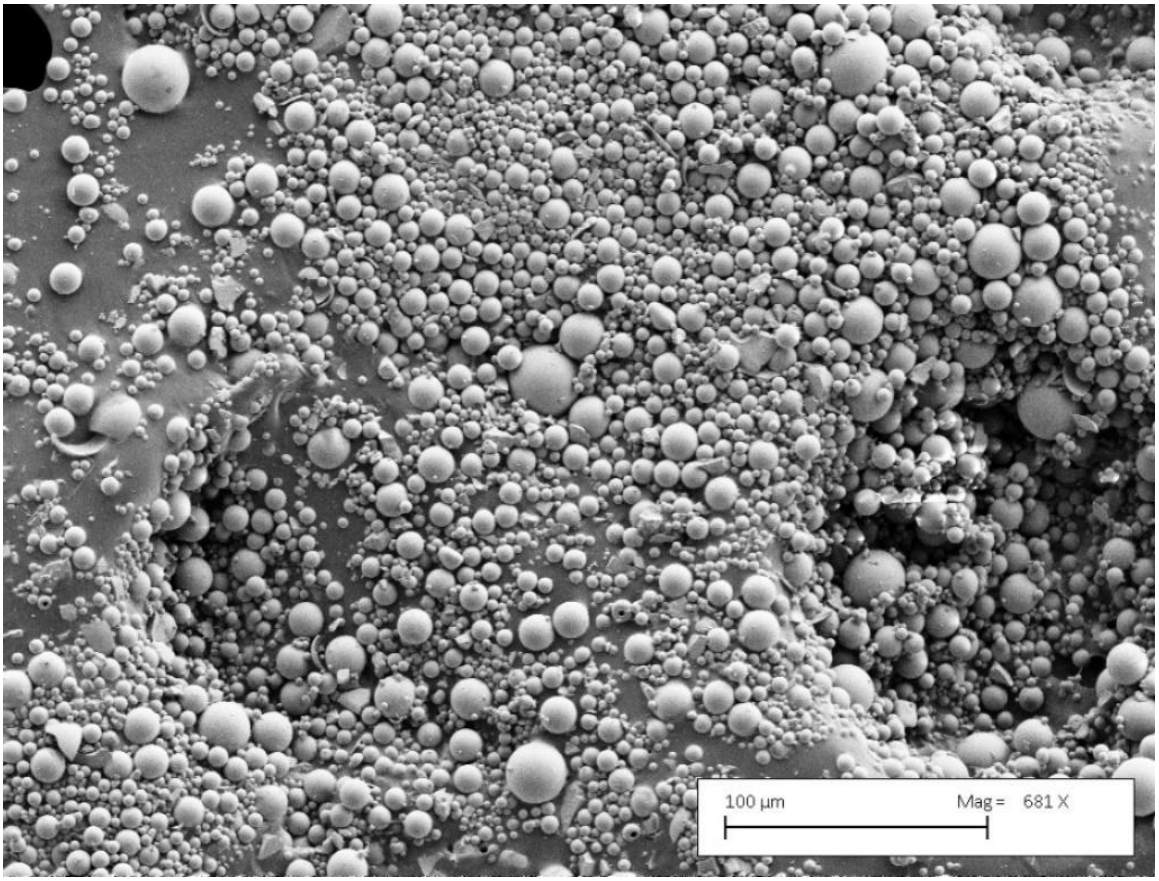

Chart 2. Particle size distribution of sample HGM1.

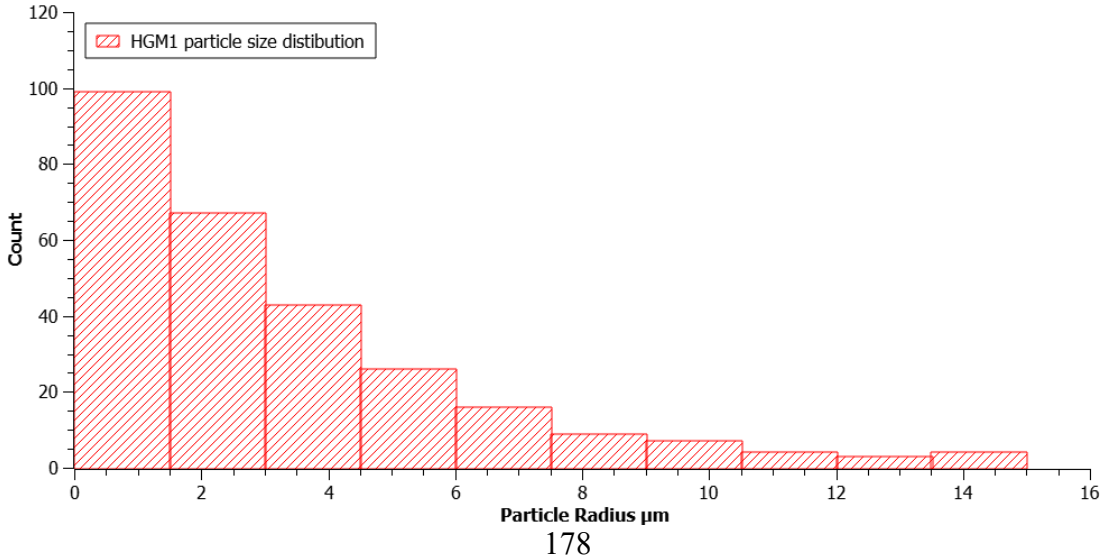

The image used for particle size analysis of HGM1 is shown in Figure 48. HGM2 - SEM image used for particle size distribution analysis while a histogram representing the particle size distribution is shown in Chart 3. Particle size distribution of sample HGM2.Chart 2. Particle size distribution of sample HGM1

Figure 48. HGM2 - SEM image used for particle size distribution analysis.

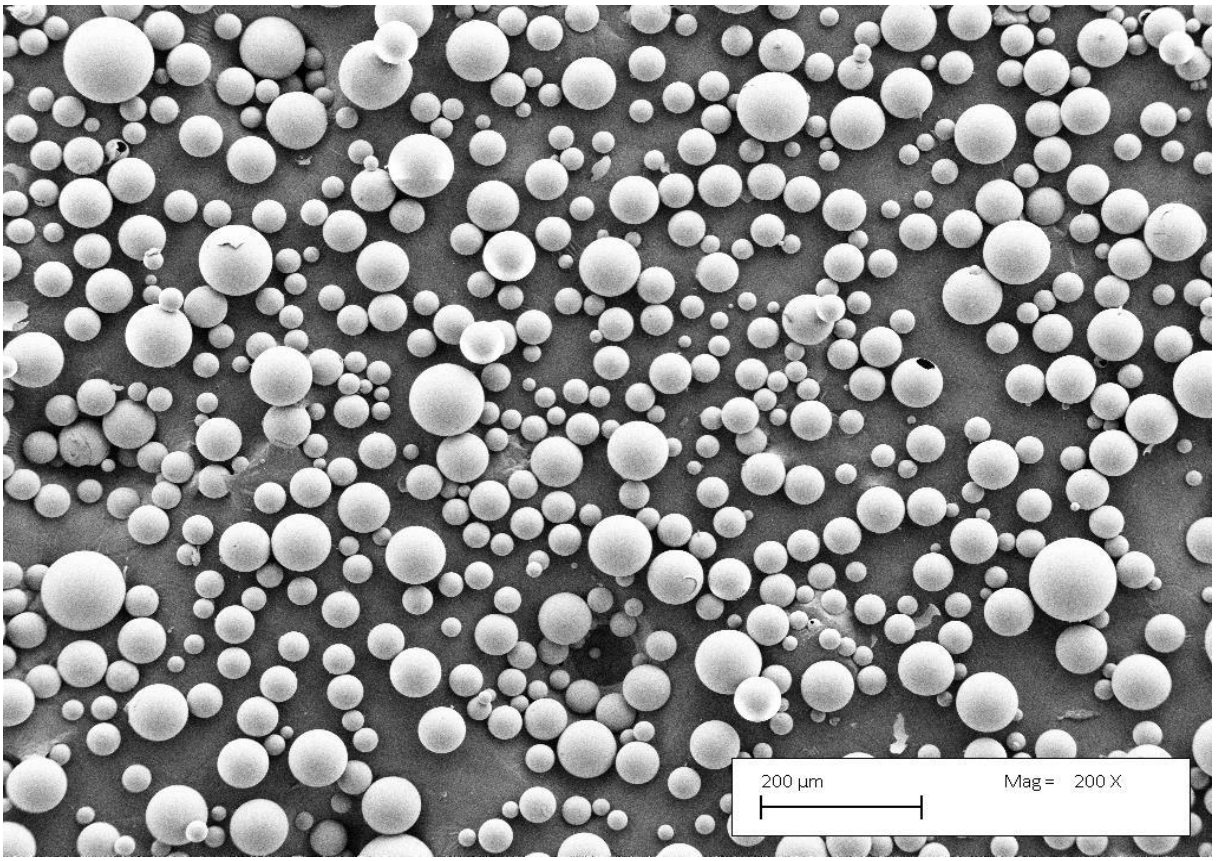

Chart 3. Particle size distribution of sample HGM2.

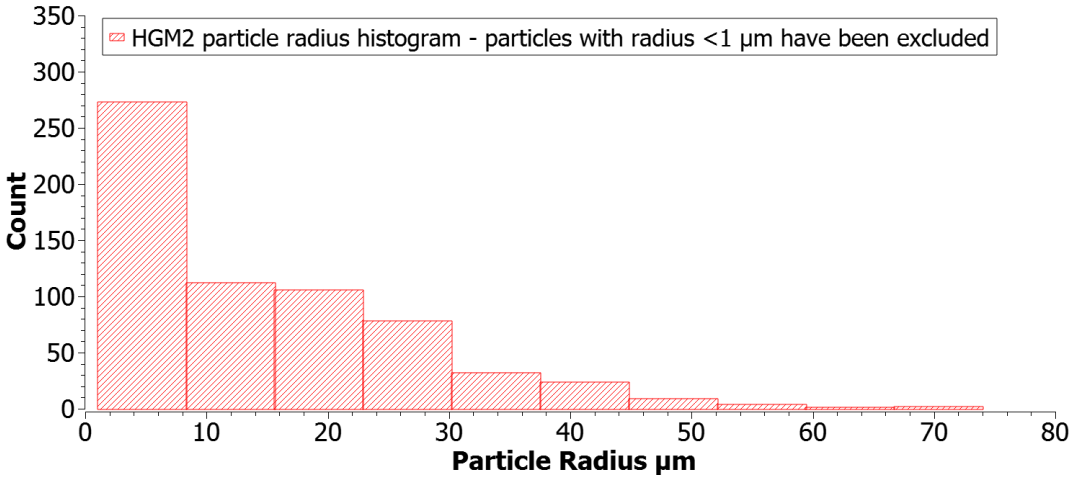

The image used for particle size analysis of HGM1 is shown in Figure 49. HGM3 - SEM image for particle size distribution analysis, while a histogram representing the particle size distribution is shown in Chart 4. Particle size distribution of sample HGM3.

Figure 49. HGM3 - SEM image for particle size distribution analysis.

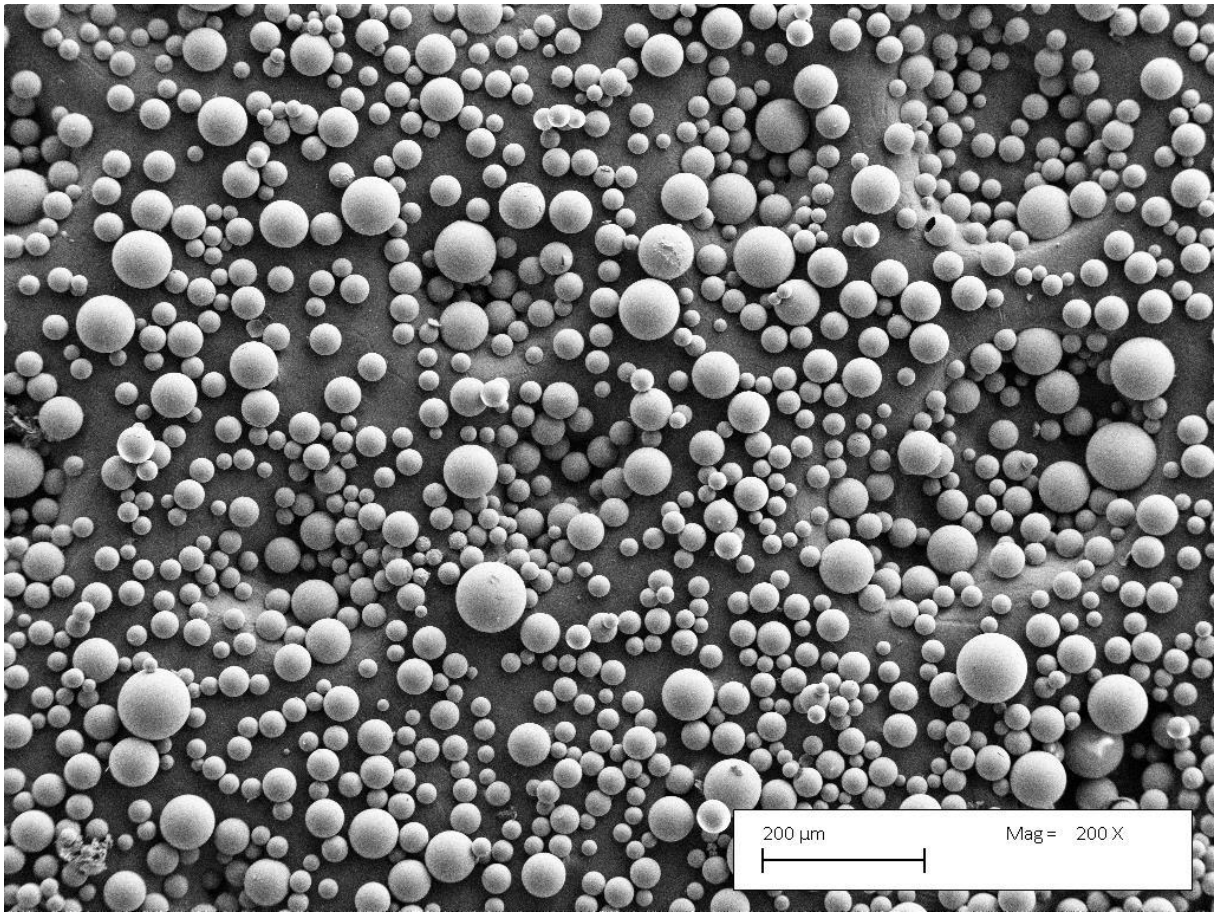

Chart 4. Particle size distribution of sample HGM3.

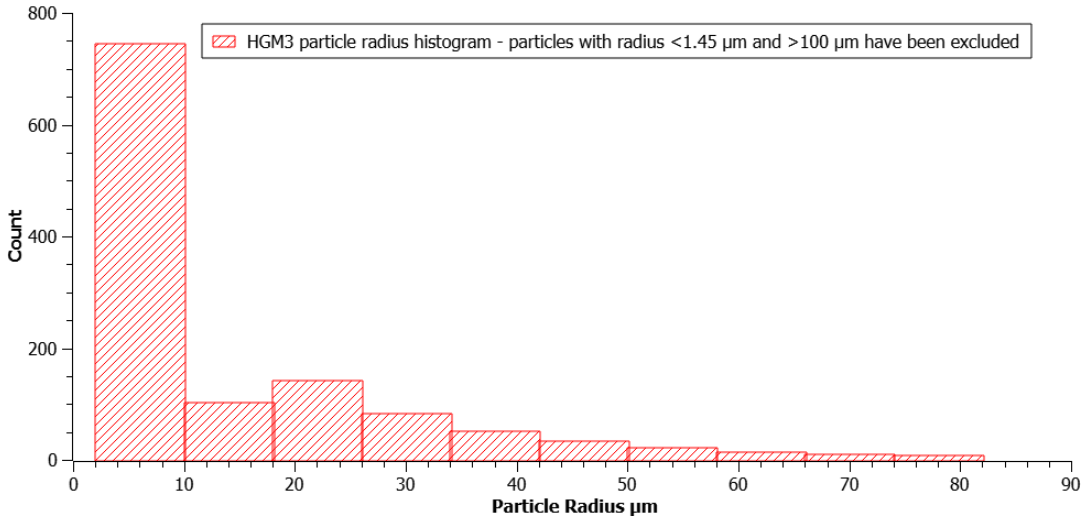

The image used for particle size analysis of HGM1 is shown in Figure 50. HGM4 - SEM image used for particle size distribution analysis, while a histogram representing the particle size distribution is shown in Chart 5. Particle size distribution of sample HGM4Chart 4. Particle size distribution of sample HGM3.

Figure 50. HGM4 - SEM image used for particle size distribution analysis.

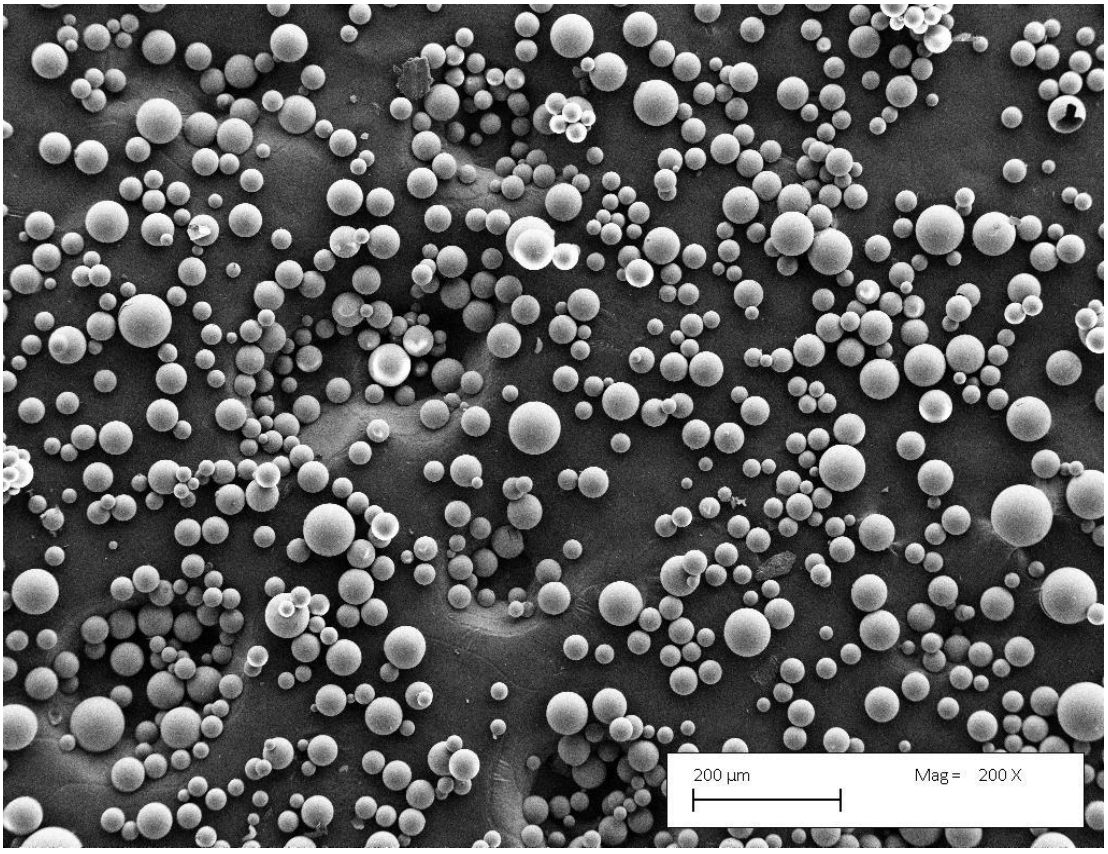

Chart 5. Particle size distribution of sample HGM4

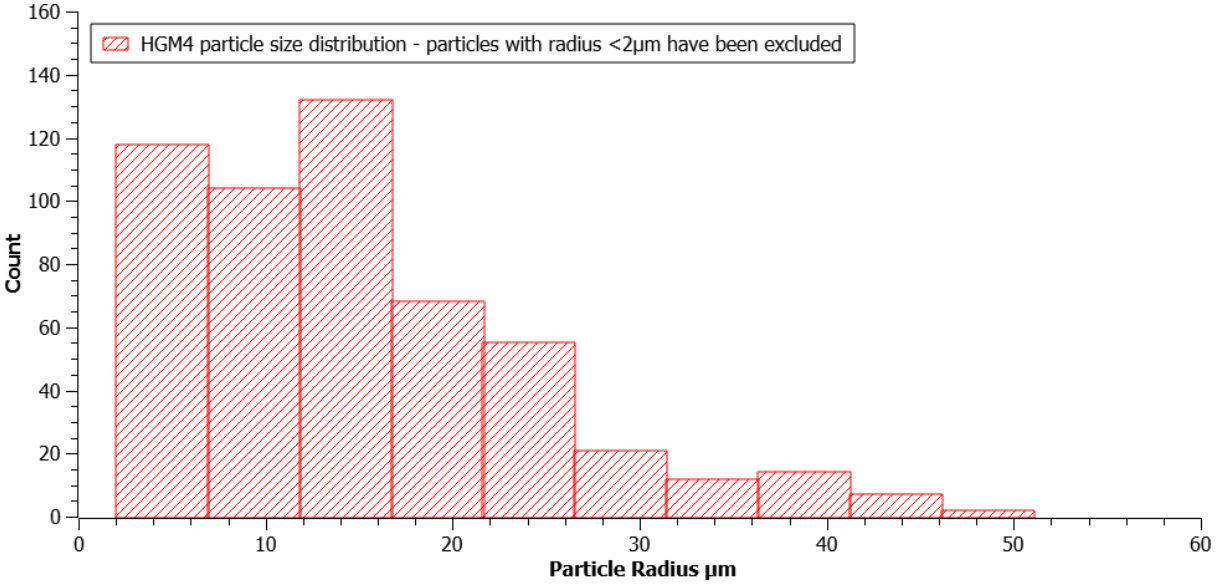

7.3 Determining HGM shell thickness

Analysis of shell thickness concluded with choosing sample HGM4 as the substrate for the composite. Shell thickness was assessed by cracking the HGMs using mechanical force and using SEM imaging to measure the width of the shell of the HGMs. The minimum number of shell fragments measured was 100 for each sample, however shell fragments originating from the same HGM could have been measured, as there was no feasible way to avoid this. The criteria for HGM selection at this stage were HGMs with the thickest shells relative to their size with the aim of choosing the most robust microspheres, as a high ratio of inner radius to outer radius indicates a thinner shell and hence is likely to be more fragile than other samples. Although HGM1 had the lowest inner/outer radius ratio, the small size of the HGMs in this sample was decided to be too small, and presented a possible health risk in the context of water purification. The larger particles of HGM4 with shells of medium thickness relative to the other samples was therefore chosen as the most appropriate substrate. The calculated values are contained in Table 36. Average inner and outer radii of the four HGM samples, plus standard deviations and errors. Typical particles are shown in Figure 51.

Table 36. Average inner and outer radii of the four HGM samples, plus standard deviations and errors.

Radius(µm)	Average	Standard dev.	Error	Radius-inner/Radius-outer
HGM1-Inner radius	6.80	3.87	0.44	0.95
HGM1 Outer Radius	7.17	3.92	0.44	-
HGM2-inner Radius	29.56	10.37	1.17	0.99
HGM2 Outer Radius	29.91	10.47	1.18	-
HGM3-Inner radius	21.45	8.87	1.00	0.97
HGM3 outer radius	22.02	8.98	1.01	-
HGM4 inner radius	20.14	6.13	0.69	0.97
HGM4 outer Radius	19.46	6.03	0.68	-

Figure 51. SEM image of untreated HGM4 magnified by a factor of 6880, showing the cavity of a large HGM into which smaller HGMs have become lodged. Scale bar is 10 um.

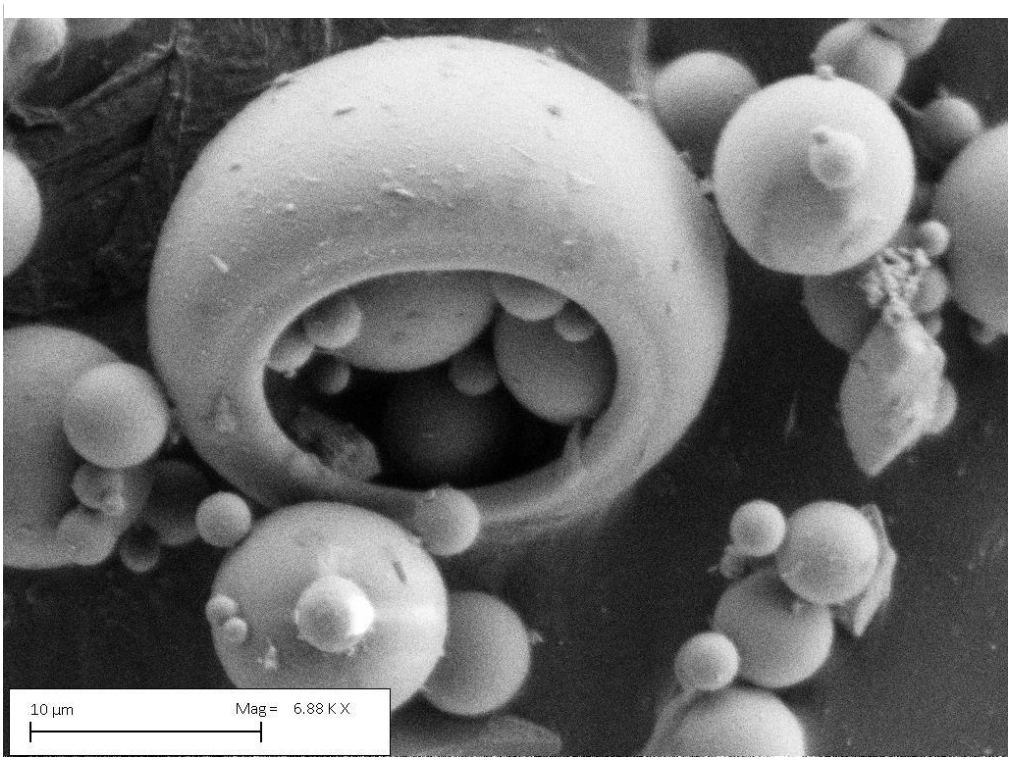

7.4 Energy Dispersive X-ray Spectroscopy (EDX)

EDX was used to assess the relative proportions of elements located on the surfaces of the HGMs, and to provide a comparison between the untreated, the etched, the coated, and the etched & coated HGMs. Due to the relatively low number of electrons in carbon's valence shells relative to calcium or silicon or similarly heavier elements, EDX is not the best way to quantify the amount of carbon present in a given sample. A typical HGM is shown in Figure 52 which has been magnified by a factor of 50 000. The EDX spectrum of the unwashed and untreated HGMs are displayed in

Table 37. Elements quantified from EDX analysis for surface of HGM4, where the spectrum is dominated by silicon and oxygen, with smaller amounts of carbon and aluminium.

Figure 52. The region of an HGM used in EDX analysis. Notice the fragments on the surface of the unwashed HGM. Magnified by 50 000x

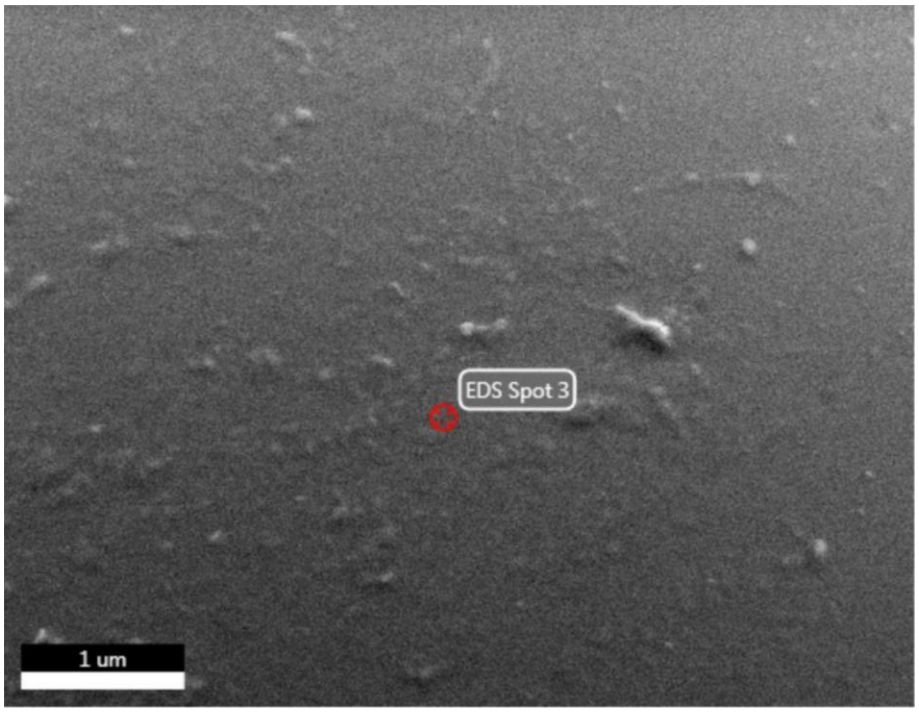

Table 37. Elements quantified from EDX analysis for surface of HGM4

Element	Weight %	Atom %
Carbon	7.5	11.8
Oxygen	51.4	60.6
Aluminium	0.7	0.5
Silicon	40.30	27.1

Chart 6. EDX spectrum of surface of HGM4, x-axis is X-Ray Energy, y-axis is Counts

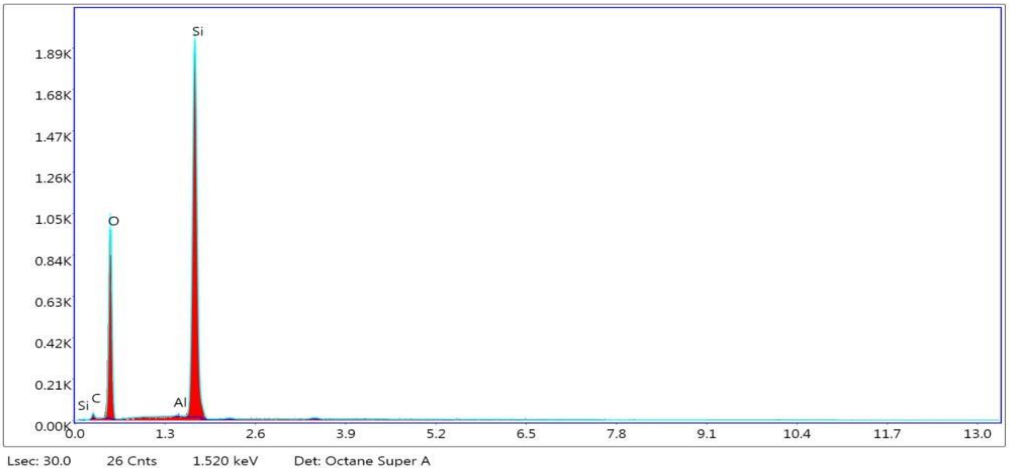

Fragments of HGM dust measuring in the nanometres were found on the surfaces of HGMs prior to washing, as shown in. The carbon may come from impurities on the surfaces of the HGMs or possibly from the carbon tape used to immobilise the HGMs, while the aluminium could be intrinsic within the HGMs, or possibly due to the aluminium stub onto which the HGMs were mounted – this should be resolved by repeating the EDX analysis on a non-aluminium containing stub. The EDX data for these fragments is contained in Figure 53, Table 38 and Chart 7. EDX analysis for particle on surface of HGM4.

Figure 53. One of the particles on surface of HGM used for EDX analysis, magnified by 50 000x

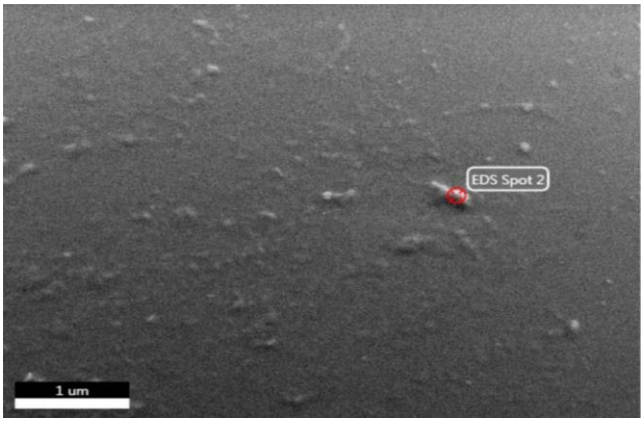

Table 38. Elements quantified from EDX analysis for particle on surface of HGM4

Element	Weight %	Atom %
Carbon	6.6	10.5
Oxygen	51.4	61.0
Aluminium	0.7	0.5
Silicon	41.30	27.9

Chart 7. EDX analysis for particle on surface of HGM4, x-axis is X-Ray Energy, y-axis is Counts

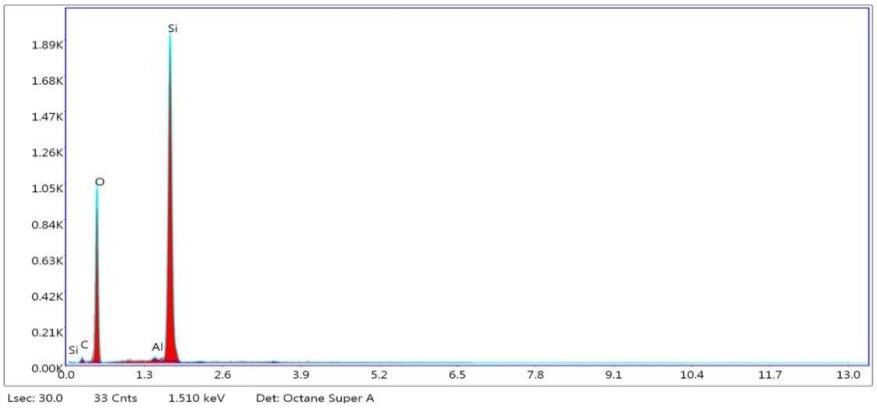

7.5 Fourier Transform Infrared Spectroscopy (FT-IR)

FT-IR was used to determine the functional groups present in a sample, and to provide information on the progress of reactions by comparing spectra from before and after a reaction to understand whether any new peaks had appeared after treatment. The spectrum displayed in Figure 10 is the spectrum for untreated and unwashed HGMs, where the peaks associated with Si-O-Si, Si-OH bonds are visible in the region from 1110-1080 cm^{-1}, which a characteristic broad shoulder at ca. 1220 cm^{-1}. There is no significant evidence of physisorbed water as there are no peaks between 3600-3200 cm^{-1}, however, the small peak around 3000-2900 cm^{-1} is characteristic of C-H bonds and may be indicative of organic impurities, indicating a need for a washing process for the HGMs. There is no evidence for the presence of Si-H bonds which would be found in the region of 2150-2000 cm^{-1}. This is shown in Chart 8. FT-IR Spectrum of an untreated and unwashed HGM.

Chart 8. FT-IR Spectrum of an untreated and unwashed HGM. Y-axis is percent transmittance; X-axis scale starts at 500 cm^{-1} on the left-hand side and increases in increments of 100 $cm^{-1}$to reach 400 cm^{-1}on the right-hand side

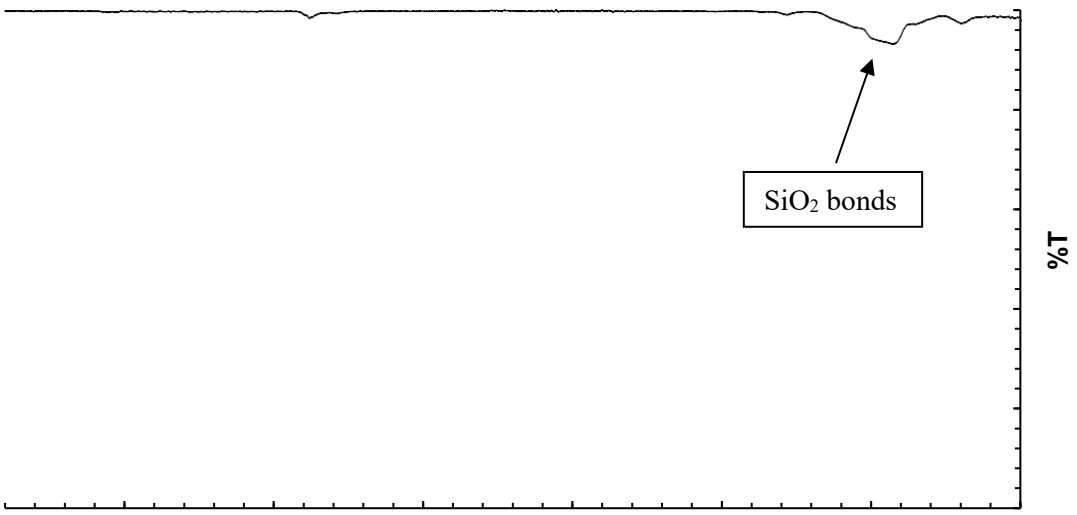

7.6 Atomic Force Microscopy (AFM)

Atomic force microscopy was used to investigate and image the surface texture of the HGMs. The texture of unwashed and untreated HGMs is reasonably smooth, with an average roughness of 20.9 nm. Small structures are present at random on an otherwise smooth surface, which can be seen in Figure 54, Figure 55 and Figure 56. However, despite the information obtained from using this microscopy technique, AFM was found to not be appropriate for further particle analysis due to a number of technical issues that arose due to the morphology of the microspheres, which included the spherical morphology of the HGM causing the tips of the probe to slip, as AFM is more suitable for analysing 3D features on flat surfaces. Instrumental noise was generated whenever the probe slipped, which interrupted image formation and necessitated a complete restart of the process.

AFM analysis was performed at two different scales, 5 µm and 10 µm. AFM on more particle was attempted, however data collection was significantly hindered by events such as the probe slipping and launching the HGM that was the subject of analysis away from the probe, vibrations from nearby footfall causing noise in the data collected, and HGMs becoming stuck to the AFM probe. In addition, because the 10 µm scale was large enough the curvature of the HGM was perceptible, the Z range attained at this scale is not deemed reliable, as this could be due to the difference in height caused by the curvature of the HGM. However, the 5 µm was zoomed in enough that the curvature was less perceptible, and this value of 188 nm be considered in the context of the difference in surface texture between the HGMs, and the sample obtained later of HGMs treated with calcium hydroxide. This data is contained in Table 39. AFM data defining the roughness of HGMs measure at scales of 5 µm and 10 µm, and Figure 54. AFM of untreated and unwashed HGM, scale is 10 µm, Figure 55. AFM of untreated and unwashed HGM from different angle, scale is 10 µm, Figure 56. AFM of untreated and unwashed HGM from third angle. Scale is 10 µm, show 3D images of the particle surface.

Figure 54. AFM of untreated and unwashed HGM, scale is 10 µm

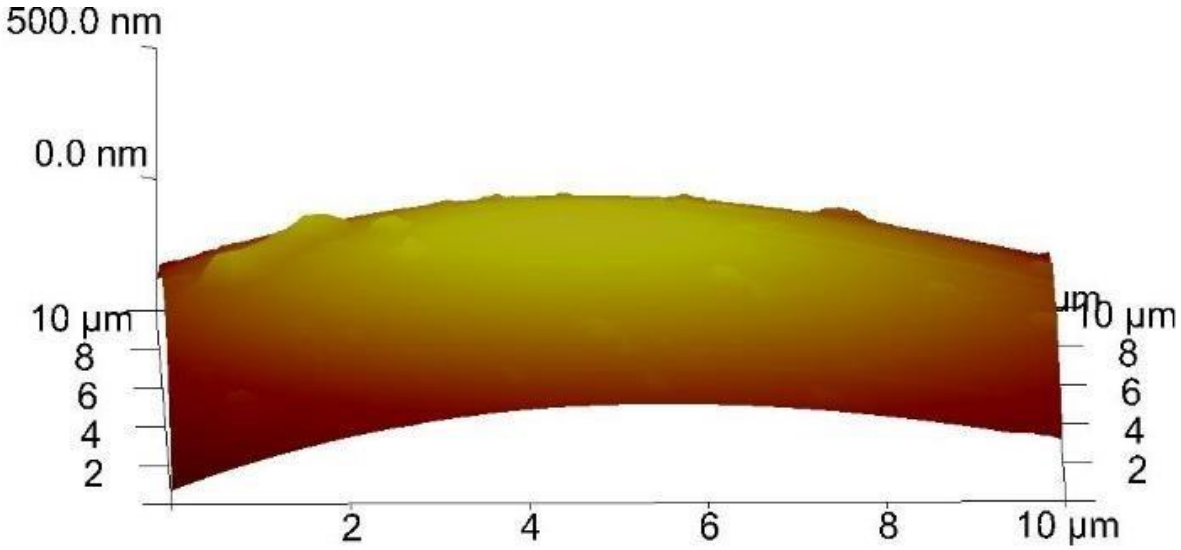

Figure 55. AFM of untreated and unwashed HGM from different angle, scale is 10 µm

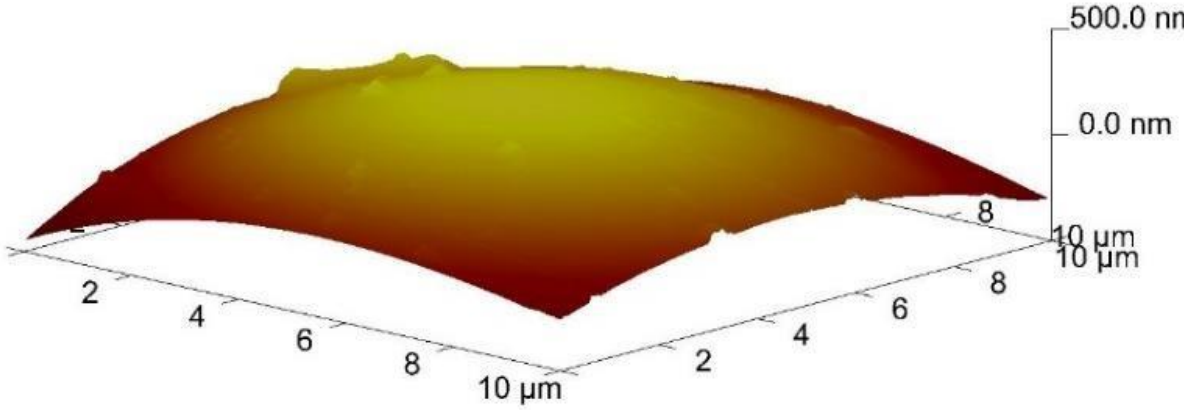

Figure 56. AFM of untreated and unwashed HGM from third angle. Scale is 10 µm

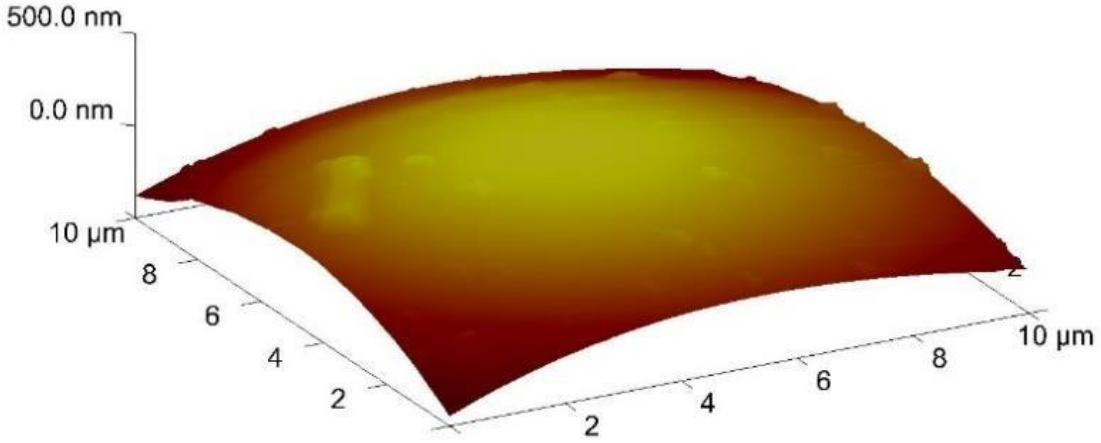

Table 39. AFM data defining the roughness of HGMs measure at scales of 5 µm and 10 µm

Parameter	Sample A	Sample B
Scale (µm)	5	10
Image surface area (μm^2)	25.0	100.0
Image R_a (nm)	20.9	99.7
Image Z range (nm)	188	665
Surface area difference	0.83%	0.89%

7.7 Thermogravimetric Analysis (TGA)

The TGA of untreated and unwashed HGM4 shows a steady rate of mass loss from 30 °C to 150 °C in Chart 9 TGA of unwashed and untreated HGM from 40 - 800 degrees Celsius., at which point 1.75% of the total mass has been lost. This step is assumed to be the dehydration step and is consistent with Belkiri (2022) who found a similar mass loss at this temperature and also assumed the temperature at which H_2O had largely been completed was 150 °C. However, although the rate of mass loss slows significantly at 175 °C, mass loss continues at a slower rate until a temperature of 200 °C is reached, which is in accordance with Zhuravlev, who found that dehydration of silica occurs up to 200 °C. Therefore, it can be concluded that dehydration is largely complete by 150 °C, although continues at a reduced rate until fully dehydrated at around 200 °C, which is shown in Table 40. Events occurring in various temperature ranges when HGMs undergo TGA analysis.

Chart 9 TGA of unwashed and untreated HGM from 40 - 800 degrees Celsius.

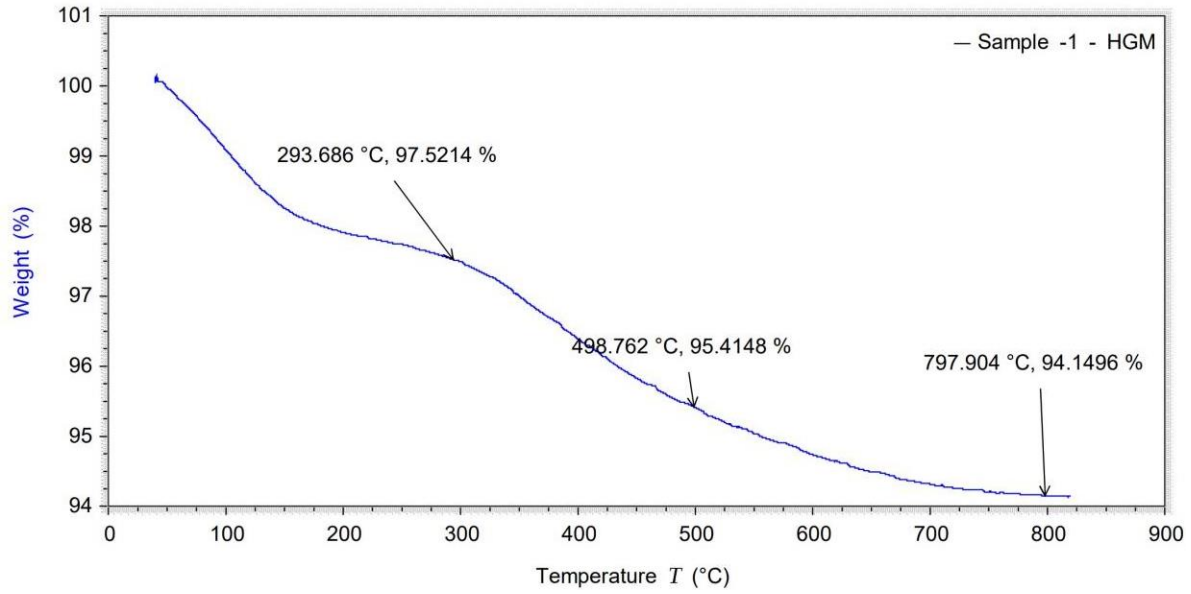

Table 40. Events occurring in various temperature ranges when HGMs undergo TGA analysis

Temperature Range (°C)	Event
30 - 200	Dehydration
200-300	Dehydroxylation
550.59 – 818.75	Melting of HGMs

7.8 X-Ray Diffraction

The x-ray diffraction pattern of the HGMs is characteristic of HGM reported in the literature, a single very wide and broad peak occurring with a maximum ranging between 2Theta = 21 ° – 23 °. This XRD pattern is consistent with the XRD pattern of HGMs reported in the literature, with the same characteristic peak centred around 23 ° (in the literature). The height maxima of the peaks occur in slightly different places – 21 ° vs 23 °, w2hich may be due to a difference in sample height between this sample and HGMs reported in the literature. The diffraction pattern for untreated and unwashed HGMs is displayed in Chart 10. An XRD pattern of the HGMs.

Chart 10. An XRD pattern of the HGMs.

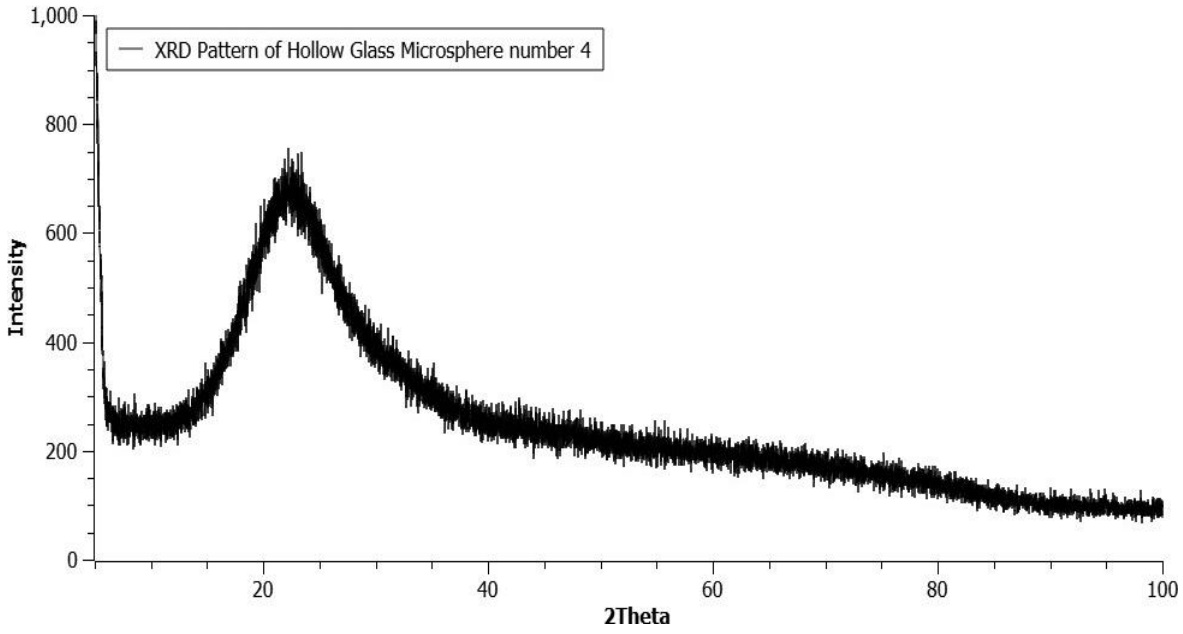

7.9 Removing Fractured Particles

The HGM pictured in Figure 57 has fragmented resulting in sharp edges. These types of HGM should be removed from the bulk as part of the washing process to ensure consistency within the sample. It is assumed that the cracked HGMs do not float and so by washing the bulk HGM powder and skimming the top layers off the solution only intact HGMs were obtained. Fragments of fractured particles can be seen in the SEM image obtained prior to floating in water to remove the broken particles in Figure 57. After the first round of floating the particles in water in a separatory funnel, the HGMs were recovered and pictured in Figure 18, which shows a large decrease in the number of fragments. However, fractured particles were still present, necessitating a second round of particle removing by floating in water. The second round of treatment in this manner was successful, as is evident by the absence of fragments in Figure 58 and Figure 59. It is not assumed that all fragment had been removed, although enough fragments had been removed to conclude that two rounds of floating in water was adequate treatment to remove the fragments of particles, resulting in an 80% recovery ratio by mass.

Figure 57. An HGM as received from the manufacturer.

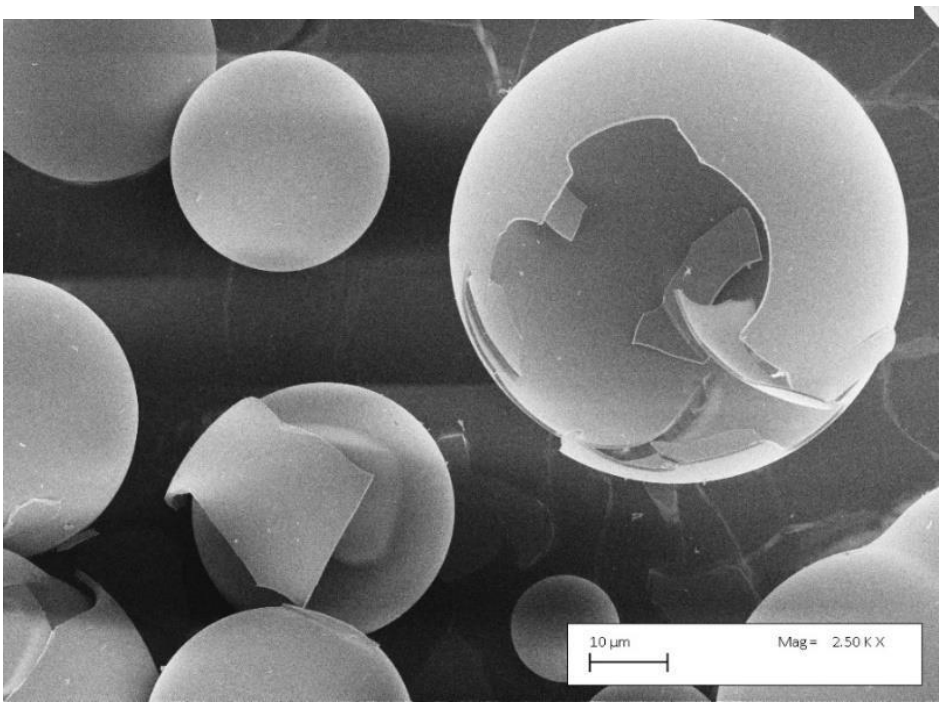

Figure 58. HGMs that have been treated to remove fragmented particles.

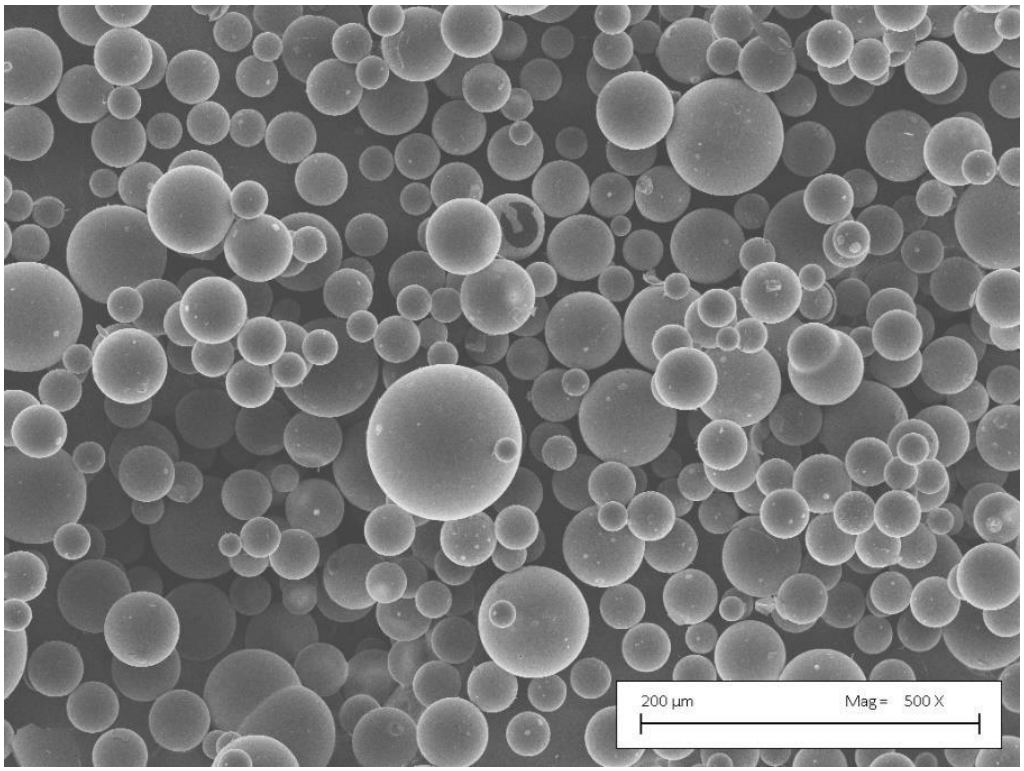

Figure 59. Hollow Glass Microspheres magnified by a factor of. Scale bar is 100 µm.

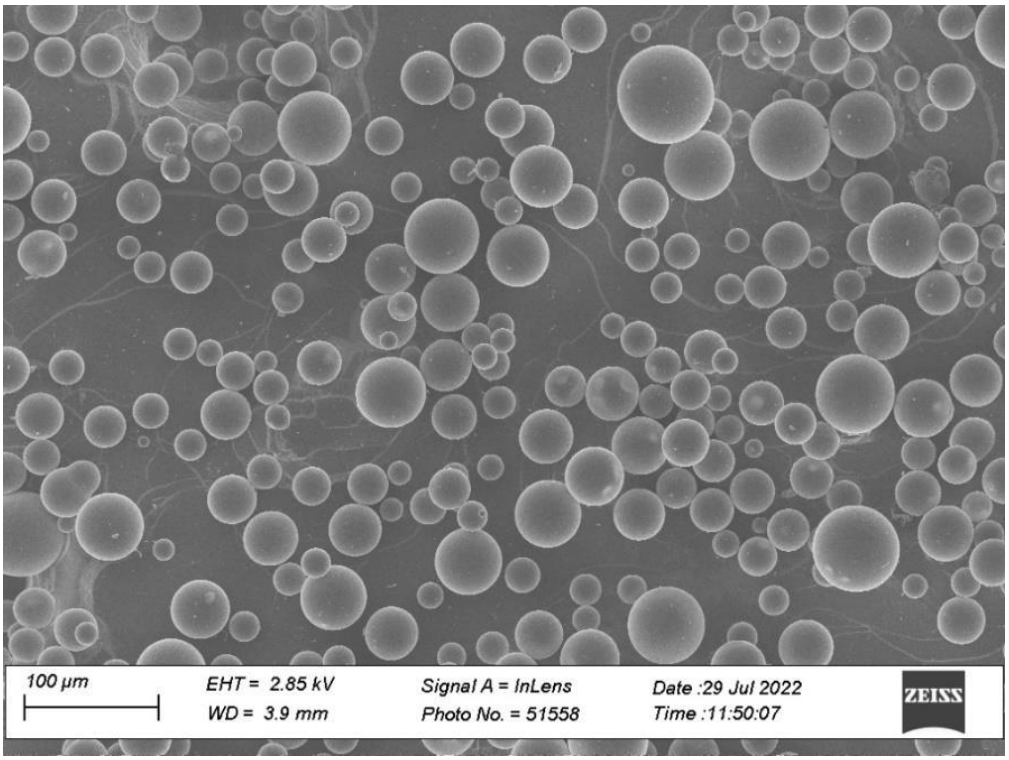

7.10 Preparing the Surfaces of the HGMs for Coating

Recovery Ratio

In order to prepare the HGMs for coating with hydroxyapatite the surfaces of the HGMs required cleaning to remove the organic residues from the synthesis process. The outcomes of treatment with basic solutions were then again floated in water in a separatory funnel and the lower portion removed by opening the tap and draining the water containing the fragments, reserving the upper portion which contained intact spheres.

The recovery ratio was calculated using Eqn. 10:

$$\frac{mass\ of\ HGMs\ recovered\ after\ washing\ process\ (g)}{initial\ mass\ of\ HGMs\ (g)} \times 100\% \qquad \text{Eqn. 10}$$

It must be acknowledged that the accuracy of this method is not high, as it was anticipated that the sample of HGMs treated with sodium hydroxide could result in the formation of sodium silicate on the surfaces of the HGMs, resulting in an increase in overall mass of the sample. If the mass was greater than the 100% then the difference would be assumed to the addition of sodium ions into the silica matrix of the HGMs. The percent by mass of HGMs recovered after each treatment with basic solution is contained in Table 41. The recovery ratios of the various alkali treatments applied to the HGMs.

Table 41. The recovery ratios of the various alkali treatments applied to the HGMs.

	Percent by mass of HGMs recovered after immersion for:	
Treatment	**1 hr**	**24 hr**
KOH 0.02 mol dm^{-3}	**10%**	**0%**
KOH 0.005 mol dm^{-3}	**30%**	**0%**
NaOH 0.02 mol dm^{-3}	**20%**	**10%**
NaOH 0.005 mol dm^{-3}	**20%**	**20%**
$Ca(OH)_2$ 0.02 mol dm^{-3}	**>80%**	**>80%**
$Ca(OH)_2$ 0.005 mol dm^{-3}	**>80%**	**>80%**

Washing the HGMs in sodium hydroxide and potassium hydroxide caused catastrophic to the HGMs, resulting in widespread particle destruction as the particles shattered, or were so severely weakened by the washing process that the structural integrity of the particles was compromised. Varying the concentration of the alkali and the time the HGMs spent soaking in alkali had similar outcomes – the HGMs were no longer usable. The implications of this are that the sodium hydroxide washing process widely used to clean the HGMs risks damaging the microspheres, and if sodium hydroxide solutions are used to clean the surfaces of the HGM, the solutions used should be dilute and the time the HGMs spend in the sodium hydroxide solution should be limited to a timescale of minutes rather than hours. In order to visualise the results of the HGM treatment with sodium hydroxide and potassium hydroxide, SEM images were obtained of the HGMs directly after treatment with basic solution, and the results are displayed in Table 42. A table of SEM images of HGMs immersed in KOH concentrations of 0.02 or 0.005 mol dm-3 for 1 hr or 24 hrsTable 42 Judging from these results, it was therefore concluded that washing the HGMs with sodium hydroxide and potassium hydroxide were not suitable methods for cleaning the surfaces of the HGMs, and instances in the literature where sodium hydroxide was successfully used the clean the HGMs were likely for HGM samples with significantly thicker shells.

Table 42. A table of SEM images of HGMs immersed in KOH concentrations of 0.02 or 0.005 mol dm^{-3} for 1 hr or 24 hrs.

KOH	0.005 mol dm^{-3}	0.02 mol dm^{-3}
1 hr	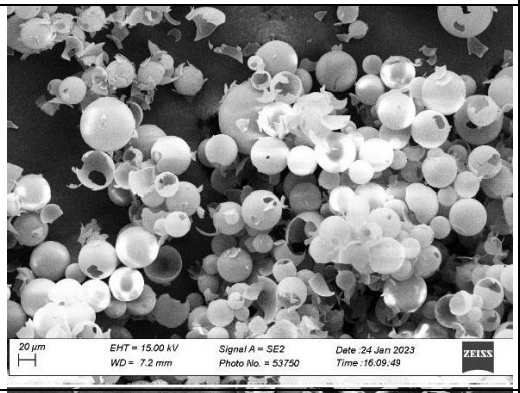	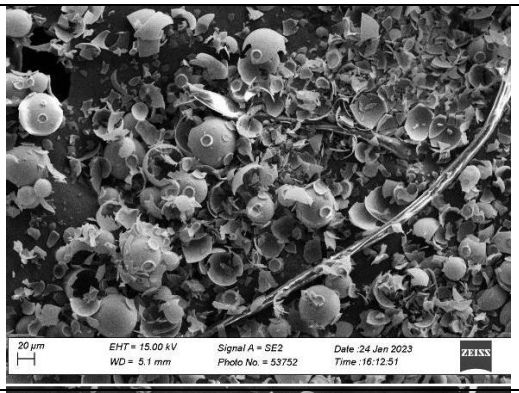
24 hr	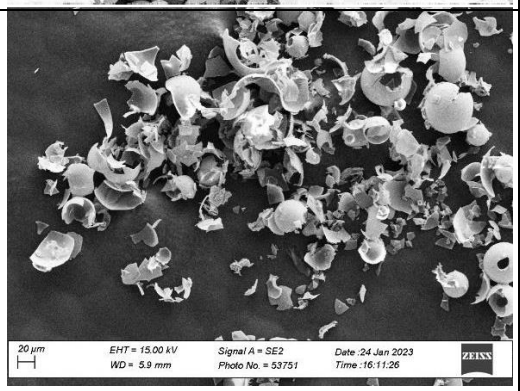	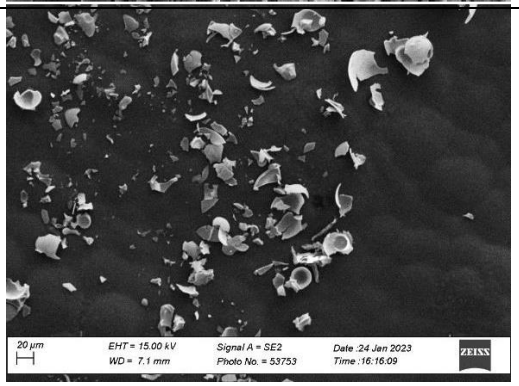
NaOH	0.005 mol dm^{-3}	0.02 mol dm^{-3}
1 hr	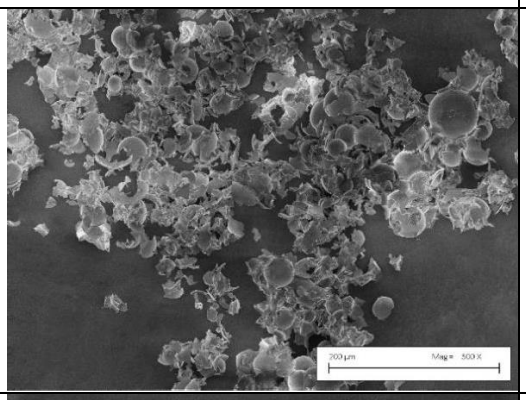	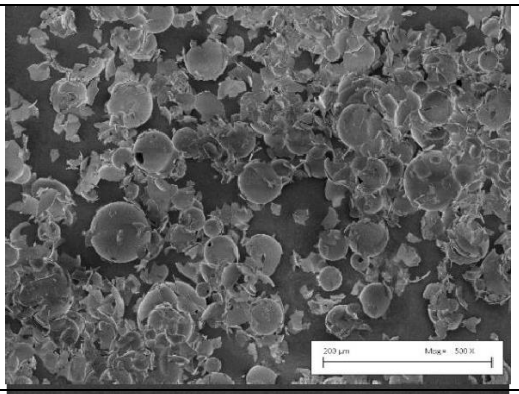
24 hr	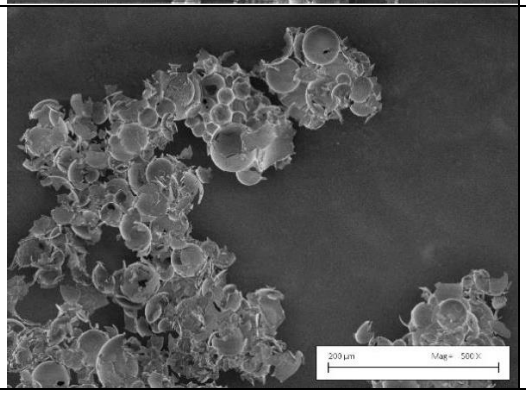	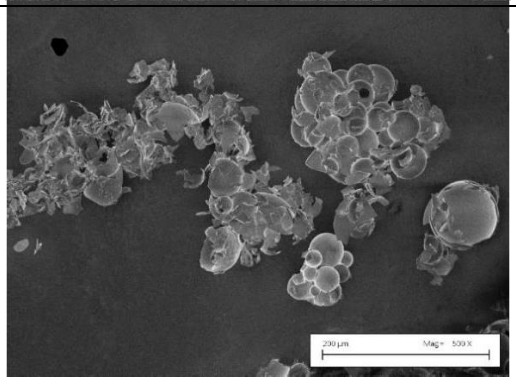

The results of the treatment of the surfaces of the HGMs with calcium hydroxide were significantly different to washes using the sodium hydroxide and potassium hydroxide solutions. No significant amounts of HGM destruction were identified, and after the HGMs were immersed in calcium hydroxide solutions for 1 hr and 24 hr and washed with an excess of water, the HGMs were subject to SEM imaging which reveal the growth of crystals on the surfaces of the HGMs. Large structures with highly crystalline morphology had formed on the HGMs after 1 hr of treatment with calcium hydroxide, as seen in Figure 60. After 24 hr of treatment, the HGM surfaces were covered with crystals and the large crystals had re-dissolved forming crystals of much smaller morphology. The results of treatment with calcium hydroxide can be seen in Table 43. SEM images of HGMs washed in calcium hydroxide, termed “CaHGMs”. This was considered progress in the development of a method to prepare the HGMs for the growth of hydroxyapatite, and the next step was to identify the chemical composition of the crystals. The products of treatment of the HGMs with calcium hydroxide solutions were termed “CaHGMs”.

Figure 60. Magnified view of surface of CaHGM after 24 hr of stirring.

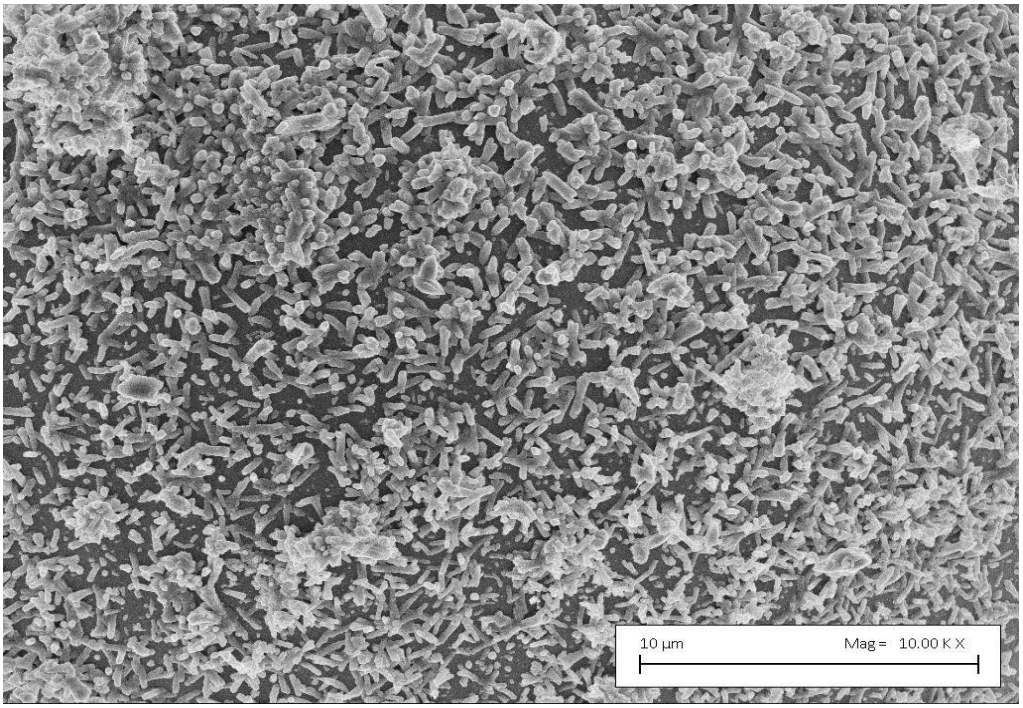

Table 43. SEM images of HGMs washed in calcium hydroxide, termed "CaHGMs".

Immersion in $Ca(OH)_2$ (0.02 mol dm^{-3}) with Stirring resulting in "CaHGMs"
Below: 1 hr immersion time
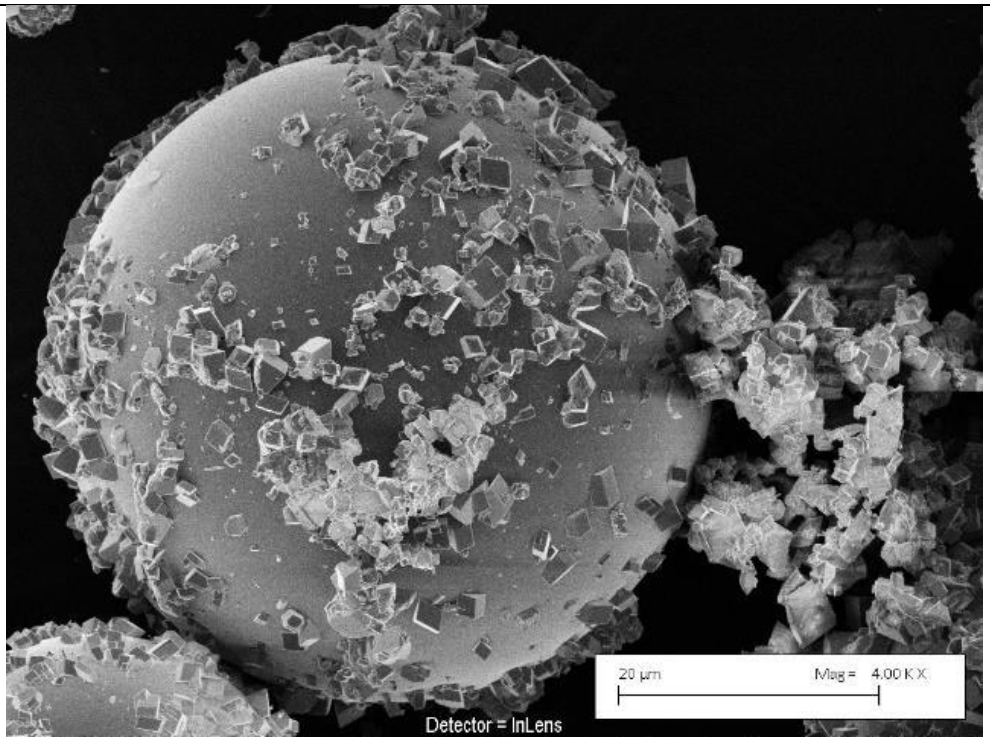
Below: 24 hr immersion time
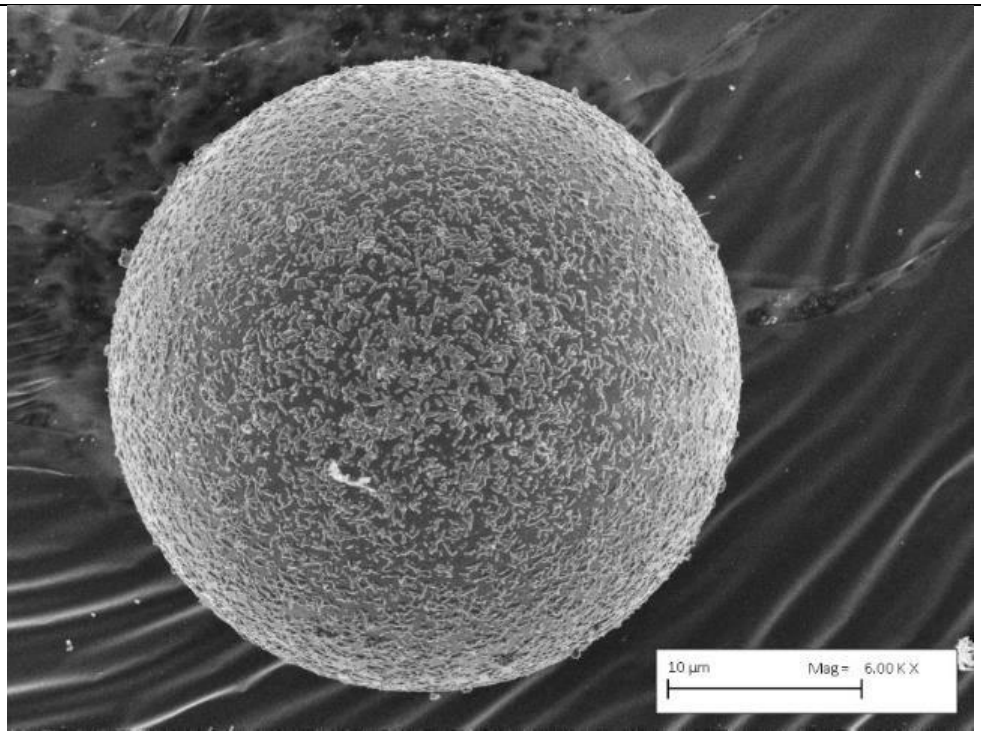

In order to identify the crystals that formed on the surfaces of the HGMs, XRD patterns were obtained of:

i. the product of HGM treatment with calcium hydroxide (0.02 mol dm^{-3}, 24 hr)
ii. the calcium hydroxide powder used to produce the calcium hydroxide solutions
iii. the untreated HGMs

The XRD patterns were overlaid to allow for comparison between the patterns of the HGMs, the calcium hydroxide powder used to produce the calcium hydroxide solution, and the CaHGMs. The CaHGMs contain a mineral component that is not the original calcium hydroxide, and this phase was identified as portlandite, or calcium carbonate. Minute amounts of calcium carbonate can be seen in the XRD pattern of calcium hydroxide, however the large proportion of calcium carbonate in the XRD pattern of the HGMs indicate that the calcium carbonate formed *in situ*. This is depicted in Chart 11. XRD patterns of untreated HGMs, calcium hydroxide as received and the Ca-HGMs

Chart 11. XRD patterns of untreated HGMs, calcium hydroxide as received and the Ca-HGMs.

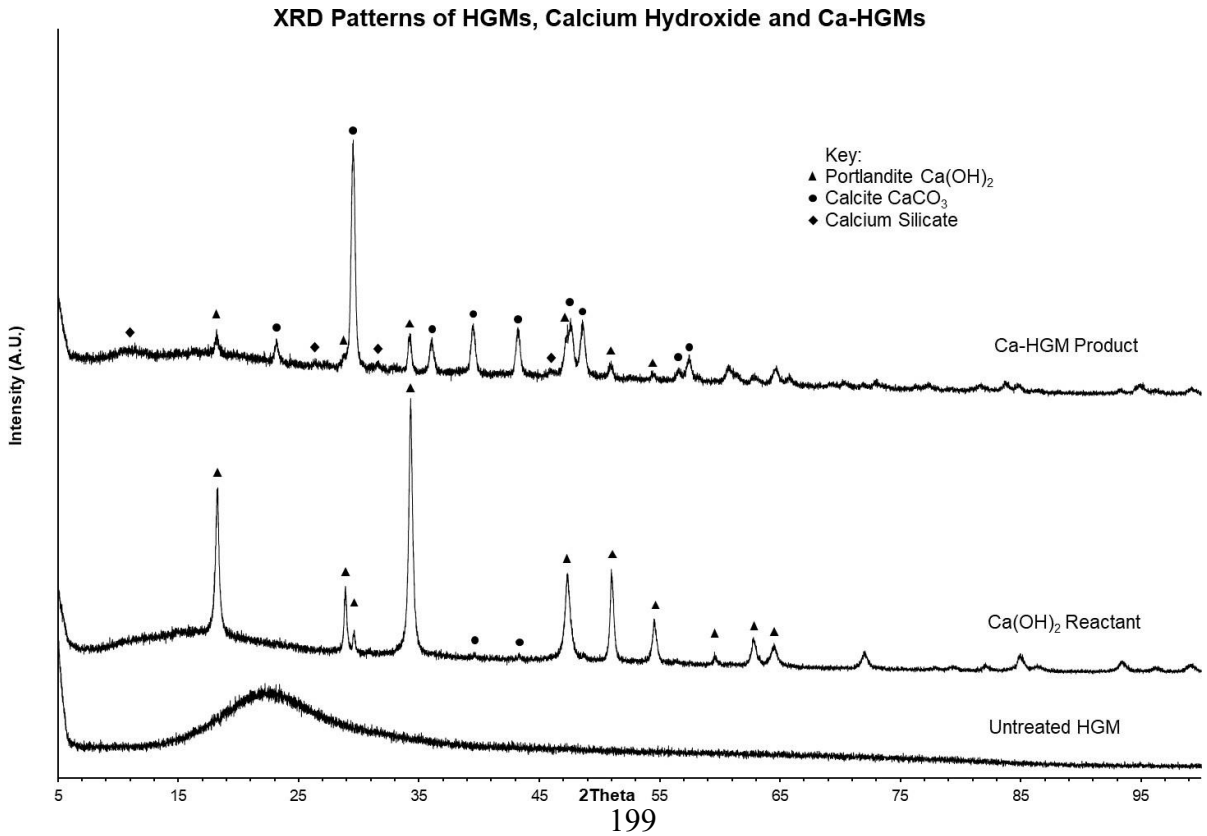

TOPAS analysis of the XRD pattern of the CaHGMs after accounting for the HGMs revealed that the crystals were calcium carbonate (93%), calcium hydroxide (6%) and jaffeite ($Ca_6Si_2O_7(OH)_6$, 1%), as shown in Table 44. Quantification of the crystal phases identified in the XRD pattern of CaHGMs.

Table 44. Quantification of the crystal phases identified in the XRD pattern of CaHGMs.

Species	Crystal phases on CaHGM
$CaCO_3$	93%
$Ca(OH)_2$	6%
CaO_3Si	1%

Further Rietveld refinement in TOPAS of the three species present on the surfaces of the HGMs was conducted and the cell volumes, lattice parameters *a* and *c*, the crystallite sizes (nm) and space groups were identified, and are listed in Table 45. Phase information obtained from the XRD analysis of the chemical species that formed on the HGMs.

Table 45. Phase information obtained from the XRD analysis of the chemical species that formed on the HGMs.

Species	$CaCO_3$	$Ca(OH)_2$	$Ca_6Si_2O_7(OH)_6$
Cell volume (Å^3)	365.2	54.5	654.0
a (Å)	4.99	3.58	10.04
c (Å)	16.92	4.90	7.50
Crystallite size (nm)	22.4	37.7	58.4
Space Group	R_{3c}	P_{3m1}	P_3

The (I/I_0) ratios of the largest peaks in the XRD pattern of show that the preferred orientation of the calcium hydroxide in the CaHGMs is along the (100) plane, which is different to the (101) plane reported in the literature. This information is contained in Table 46. A table of peak intensities with the ratio of all peaks to the peak with the greatest intensity.

Table 46. A table of peak intensities with the ratio of all peaks to the peak with the greatest intensity.

	Integrated					
2Theta	**Ca-HGM**	**Ratio**	***hkl* JCPDS 04-0733**	**$Ca(OH)_2$**	**Ratio**	***hkl* JCPDS 04-0733**
18.27	376	0.29	(001)	706	0.65	(001)
29.54	1283	1.00	(100)	165	0.15	(100)
34.34	350	0.27	(101)	1089	1.00	(101)
50.98	219	0.17	(110)	404	0.37	(110)

7.11 Calcium Carbonate Hollow Glass Microspheres – EDX Spectra

EDX spectra of the CaHGMs were obtained in order to determine the identity of the crystals that had grown on the surfaces of the HGMs after treatment with calcium hydroxide. The proportion of calcium present in Table 47. Elemental composition from EDX spectrum for one CaHGM, the quantification of the elements located at the surface of the HGM is not high, forming just 0.8% of the atoms identified, however in the EDX analysis of the untreated HGM, no calcium was identified. In addition, the calcium is pervasive throughout the surface of the HGM. The EDX spectrum is shown in Chart 12. EDX Spectrum of one CaHGM, while the elemental maps of the CaHGM are contained in Table 48. Elemental maps of the CaHGMs obtained by EDX analysis.

Table 47. Elemental composition from EDX spectrum for one CaHGM.

Element	Weight %	Atomic %	Error %
Carbon	60.1	69.7	7.2
Oxygen	28.7	25.0	9.6
Sodium	0.3	0.2	7.3
Alumini	0.3	0.2	3.9
Silicon	8.3	4.1	2.6
Calcium	2.2	0.8	1.5

Chart 12. EDX Spectrum of one CaHGM, x-axis is X-Ray Energy, y-axis is Counts.

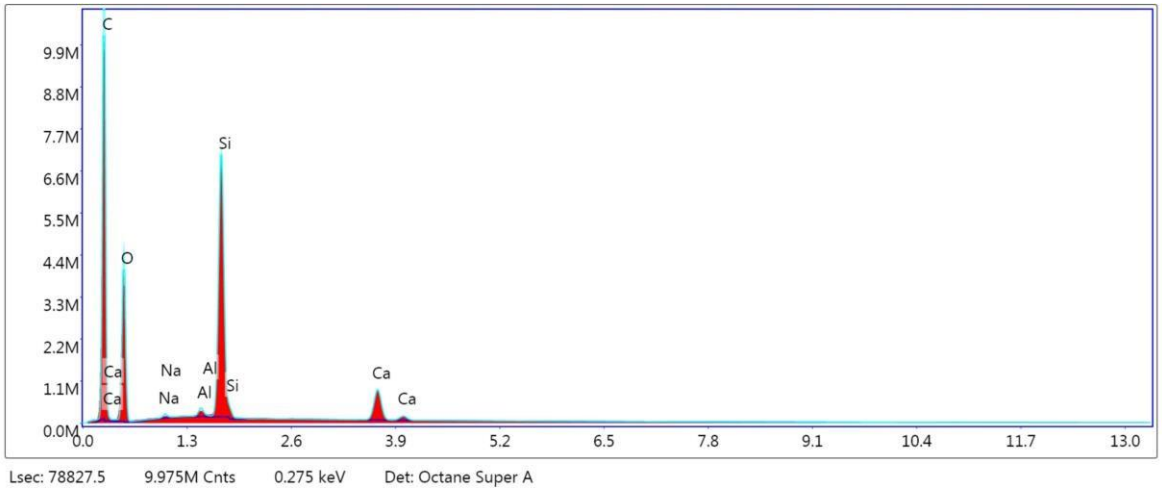

Table 48. Elemental maps of the CaHGMs obtained by EDX analysis.

Below: proportion of each phase present in the CaHGM particle	Below: phase map of the CaHGM
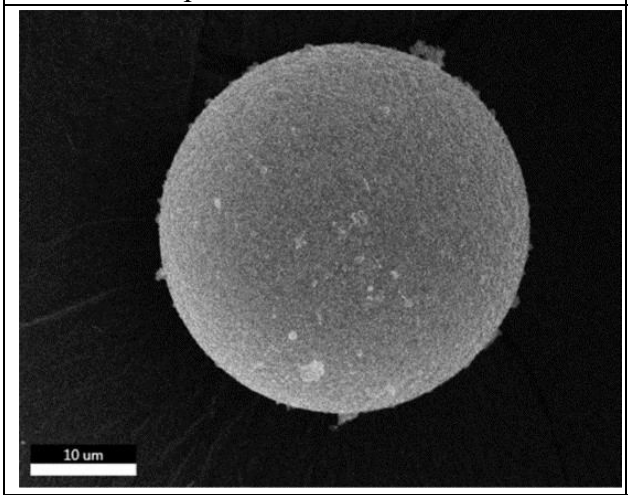	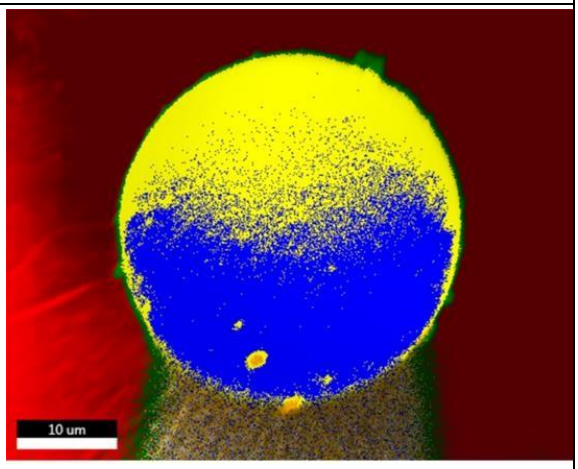
Below: all elements overlaid in a map of the elements	Below: Blue corresponds to calcium
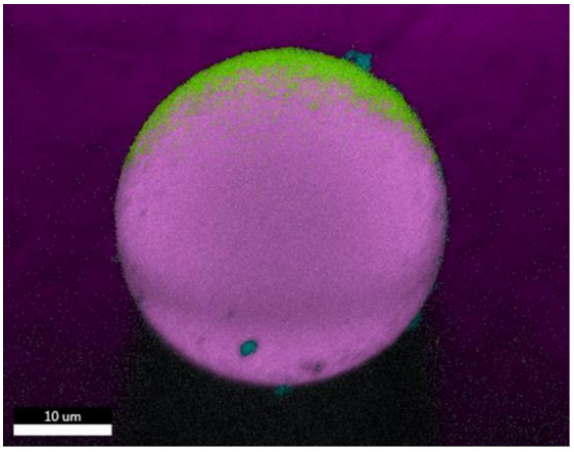	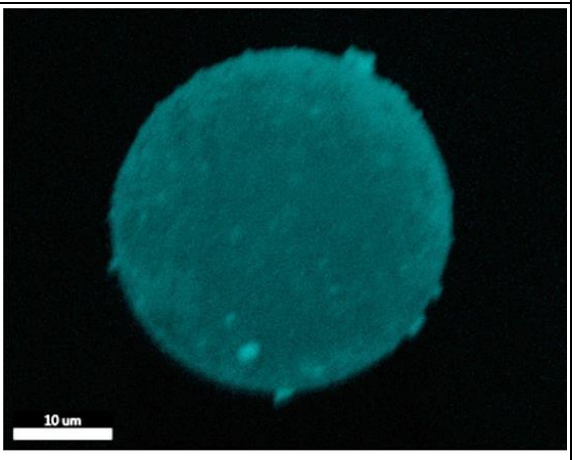
Below: green corresponds to oxygen	Below: pink corresponds to silicon
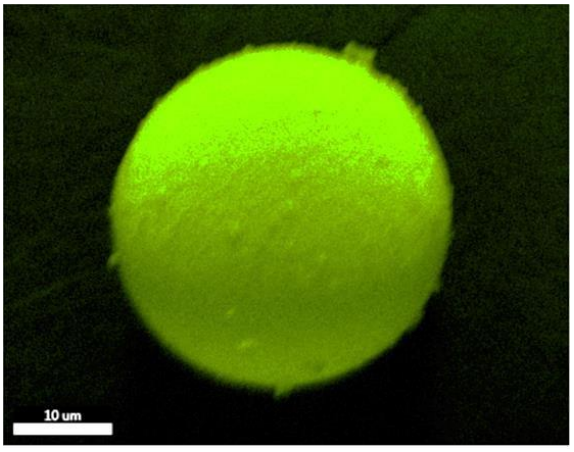	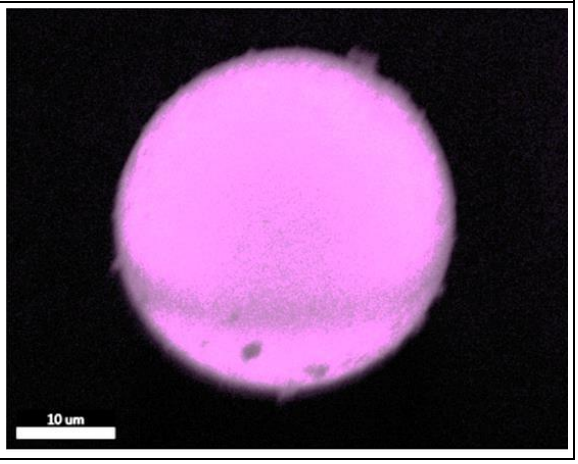

The EDX analysis confirms that the crystals grown on the surfaces of the HGMs contained calcium. The calcium bearing particles were evenly dispersed across the surfaces of the HGMs, although coverage was not 100% which can be seen in Table 49. Quantified elemental percentages for the crystals on the CaHGM surface as there are two phases present, one containing silicon and oxygen pictured in blue (this was anticipated due to the silicon dioxide composition of the HGMs) and a second phase containing calcium, silicon and oxygen (pictured in red). The elements present in the EDX spectrum Chart 13. EDX Spectrum of crystals on CaHGM have been quantified and are listed in Table 49. Quantified elemental percentages for the crystals on the CaHGM surface.

Chart 13. EDX Spectrum of crystals on CaHGM, x-axis is X-Ray Energy, y-axis is Counts.

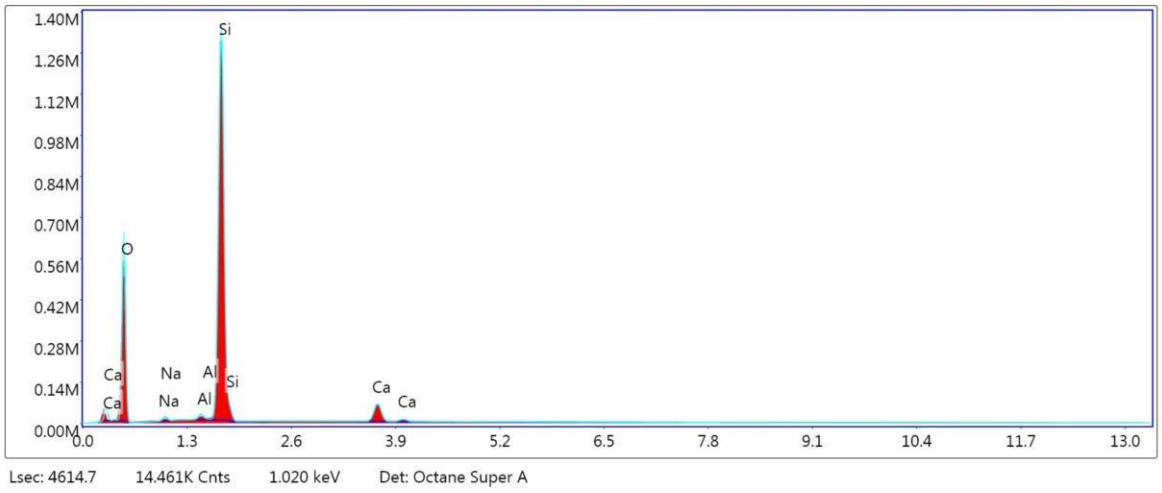

Table 49. Quantified elemental percentages for the crystals on the CaHGM surface.

Element	Weight %	Atomic %	Error %
Oxygen	51.3	65.4	8.1
Sodium	1.0	0.9	8.1
Aluminium	0.6	0.5	4.8
Silicon	42.5	30.9	3.2
Calcium	4.7	2.4	2.2

Table 50. EDX elemental maps of elements present in crystals on surface of CaHGMs.

SEM image of region used for EDX	All elements overlaid
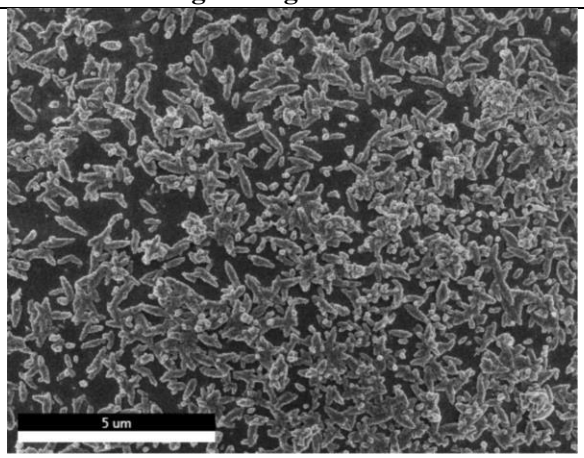	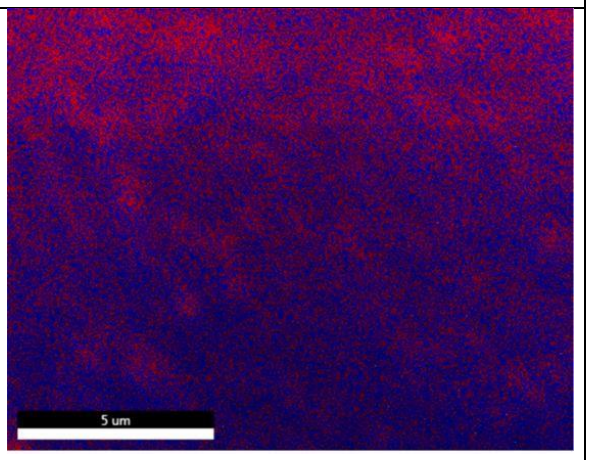
All elements overlaid	**Silicon**
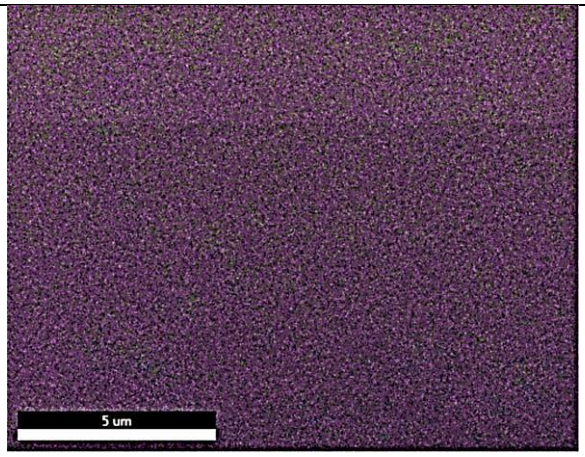	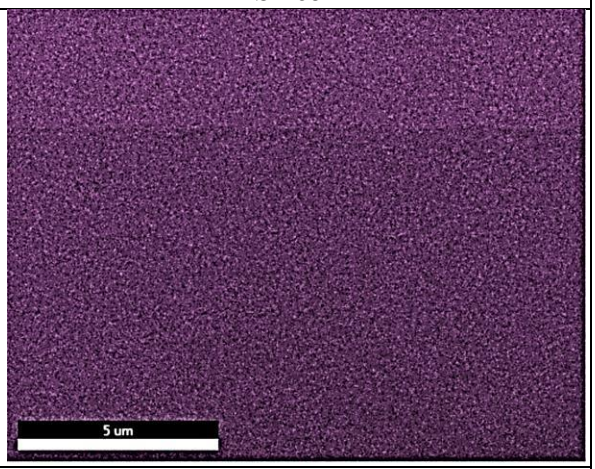
Oxygen	**Calcium**
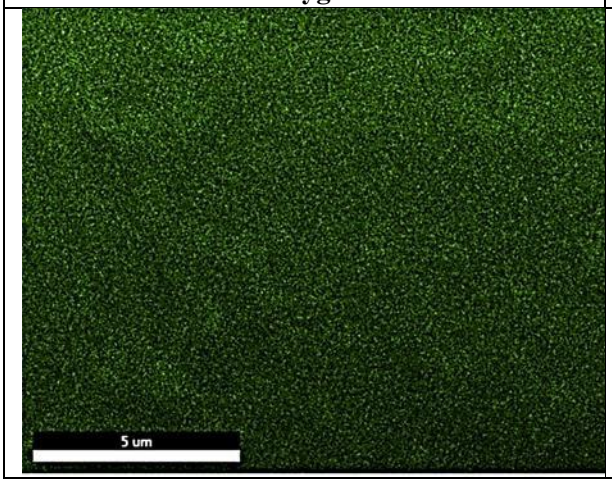	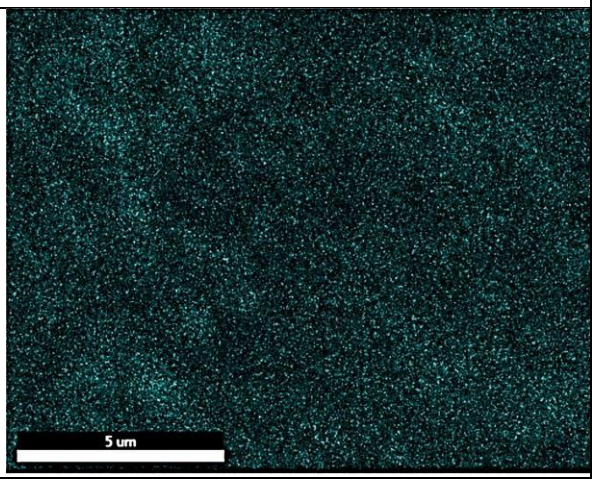

7.12 EDX Surface Analysis

CaHGM immersed in 0.02 mol dm^{-3} calcium hydroxide solution for 24 hr and ultrasonicated with ethanol.

The chemical composition of different crystals on the surfaces of the HGMs were investigate using EDX to determine if the concentration of the calcium hydroxide solution played a major role in crystal formation. The region of interest in Figure 61 used for EDX is highlighted in Figure 62 and it is the large structure formed from an aggregate of smaller white crystals. The high amount of silicon in Table 51. EDX element quantification of CaHGM (0.2 mol dm-3 solution of $Ca(OH)_2$) ultrasonicated in ethanol shows silicon constitutes 21.5 weight % and 16.7 atomic %, and is assumed to be from the HGMs. There is a high proportion of calcium present in the region of interest, constituting 33.4% weight % and 18.1% atomic %, making it the second most abundant element in the region analysed, after oxygen. The EDX spectrum is depicted in Chart 14. EDX Spectrum of CaHGM immersed in $Ca(OH)_2$) for 24 hr and ultrasonicated in ethanol. A second particle found on the surface of the CaHGM is shown in Figure 63. CaHGM immersed in 0.02 M solution of $Ca(OH)_2$) and ultrasonicated in ethanol - region 2, the quantified elements are shown in Table 52. EDX element quantification of CaHGM in 0.2 mol dm-3 solution of $Ca(OH)_2$) and ultrasonicated in ethanol, and the EDX spectrum in shown in Chart 15. EDX Spectrum of CaHGM 0.2 mol dm-3 ultrasonicated in ethanol region 2, which are substantially different.

Figure 61. CaHGM - 0.2 mol dm^{-3} Ca(OH)$_2$) ultrasonicated in ethanol.

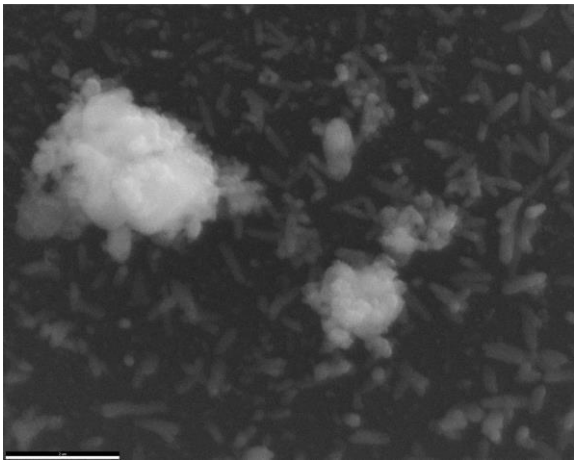

Figure 62. CaHGM 0.2 mol dm^{-3} Ca(OH)$_2$) solution – region of interest.

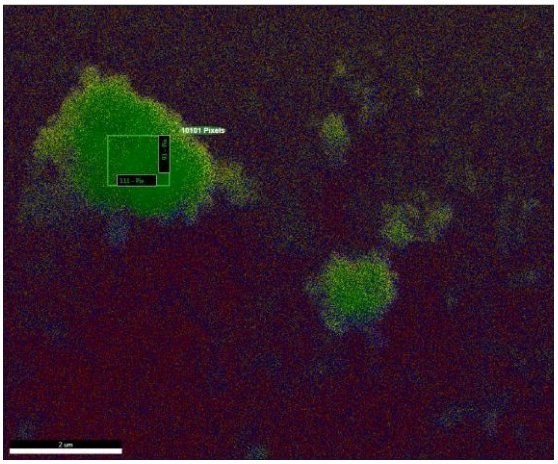

Table 51. EDX element quantification of CaHGM (0.2 mol dm^{-3} solution of Ca(OH)$_2$) ultrasonicated in ethanol.

Element	Weight %	Atomic %	Error %
C	9.6	17.3	5.8
O	34.9	47.4	6.7
Na	0.1	0.1	73.6
Mg	0.2	0.1	17.3
Al	0.3	0.2	10.1
Si	21.5	16.7	1.6
K	0.1	0.1	45.4
Ca	33.4	18.1	1.5

Chart 14. EDX Spectrum of CaHGM immersed in Ca(OH)$_2$) for 24 hr and ultrasonicated in ethanol, x-axis is X-Ray Energy, y-axis is Counts.

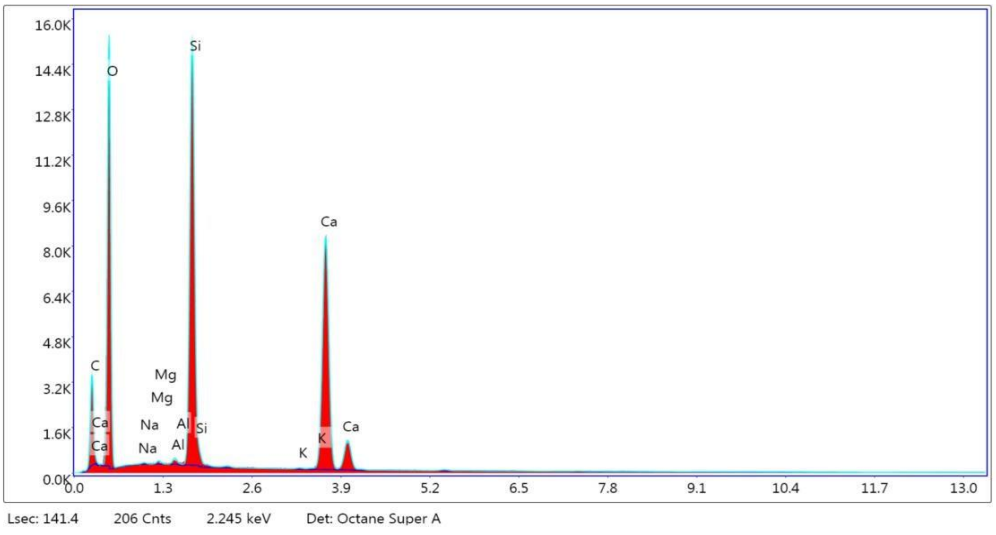

Figure 63. CaHGM immersed in 0.02 M solution of $Ca(OH)_2$) and ultrasonicated in ethanol - region 2.

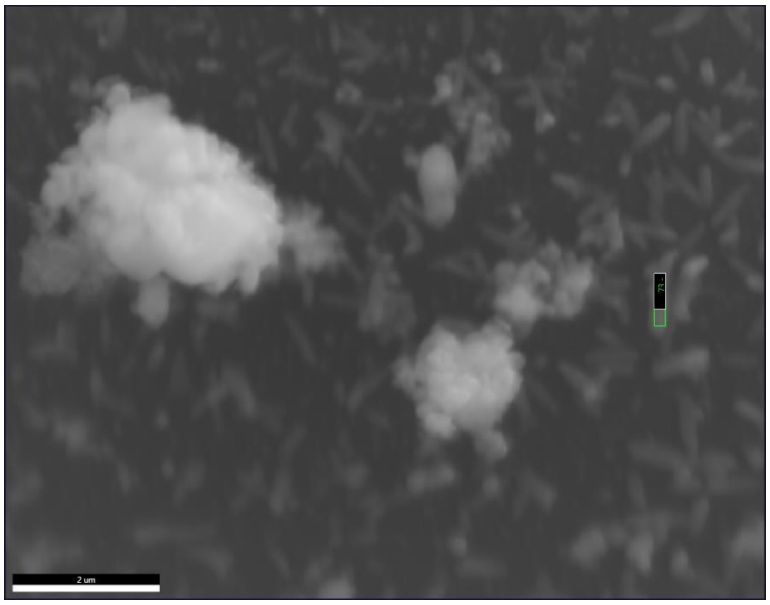

Table 52. EDX element quantification of CaHGM in 0.2 mol dm^{-3} solution of $Ca(OH)_2$) and ultrasonicated in ethanol.

Element	Weight %	Atomic %	Error %
Carbon	15.4	25.8	11.1
Oxygen	29.6	37.3	7.1
Aluminium	0.3	0.2	62.9
Silicon	43.1	30.7	1.9
Potassium	0.3	0.1	91.4
Calcium	11.4	5.7	6.2

Chart 15. EDX Spectrum of CaHGM 0.2 mol dm^{-3} ultrasonicated in ethanol region 2, x-axis is X-Ray Energy, y-axis is Counts.

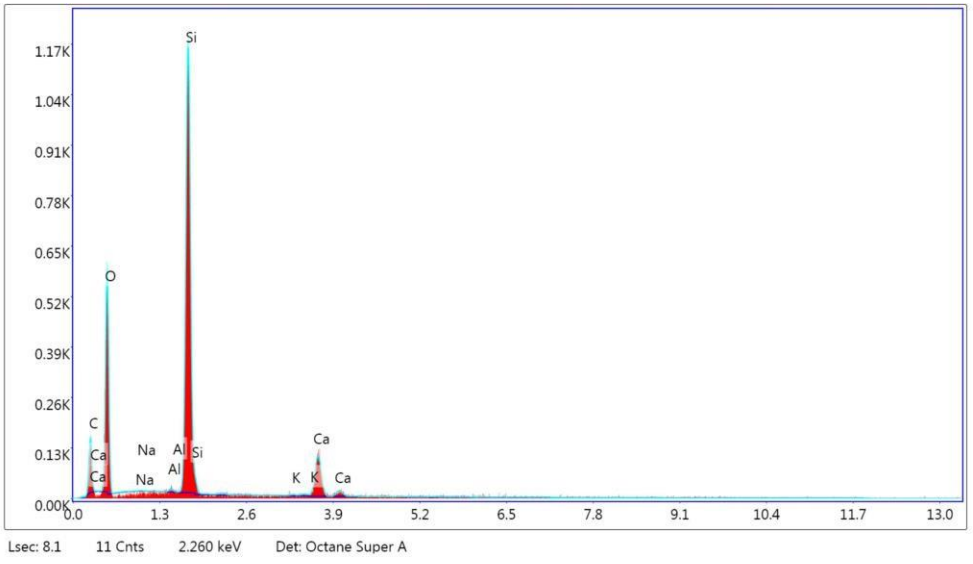

7.13 Atomic Force Microscopy (AFM)- CaHGMS

AFM was used to investigate the surface topology of the CaHGMs, as it had been predicted that etching with base would increase surface roughness that would improve the results of ensuing coating processes. Instead, AFM reveals that the results of treatment of HGMS with calcium hydroxide resulting in the formation of structures on the surfaces of the HGMs. Again, AFM images were difficult to obtain as the curved surfaces of the CaHGMs caused the AFM probe to slip, generating unacceptable noise in the image and requiring the process of data collection to start again. Nevertheless, the 3-dimensional map of the surface of the CaHGMs provide valuable insight into the changes that occurred on to the surface of the HGMs, resulting in the formation of the HGMs, confirm that crystals grew on to the surface of the CaHGMs, resulting in an increase in the roughness of the HGMs and a change in texture of the surface of the HGMs, which was the ultimate goal of the treatment with calcium hydroxide solution. The surface texture parameters obtained for the different concentrations are contained in Table 53. Values obtained with AFM for samples of HGMs treated with 0.02 mol dm-3 and 0.005 mol dm-3 $Ca(OH)^2$ solution, while Figure 64, Figure 65, Figure 66, Figure 67 show the 3D differences in surface texture obtained with the varying concentrations of $Ca(OH)_2$ solution.

Table 53. Values obtained with AFM for samples of HGMs treated with 0.02 mol dm^{-3} and 0.005 mol dm^{-3} $Ca(OH)^2$ solution.

Parameter	**0.02 mol dm^{-3} $Ca(OH)_2$**	**0.005 mol dm^{-3} $Ca(OH)_2$**
Scale (µm)	4	4
Image surface area (μm^2)	16.0	16.0
Image R_a (nm)	115	59.7
Image Z range (nm)	1482	452
Surface area difference	156%	21.0%

Figure 64. AFM topology map of a CaHGM formed using 0.02 mol dm^{-3} $Ca(OH)_2$ solution.

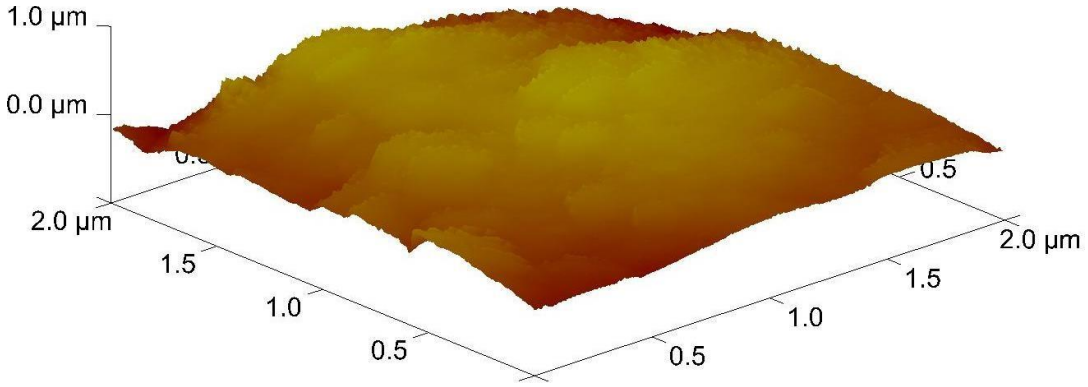

Figure 65. Surface of CaHGM made with 0.02 mol dm^{-3} obtained using AFM.

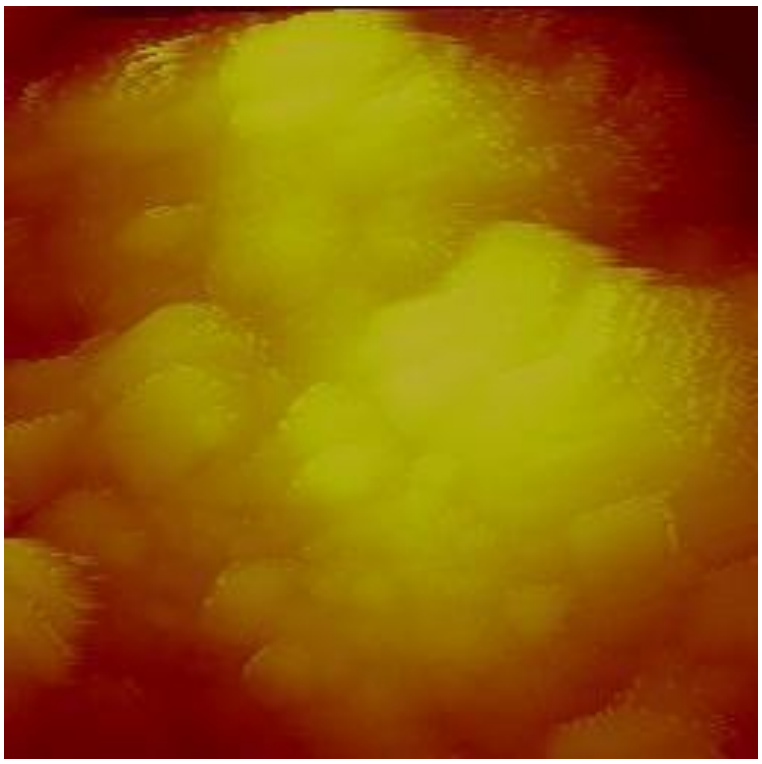

Figure 66. AFM topology map of HGMs treated with 0.005 mol dm^{-3} calcium hydroxide.

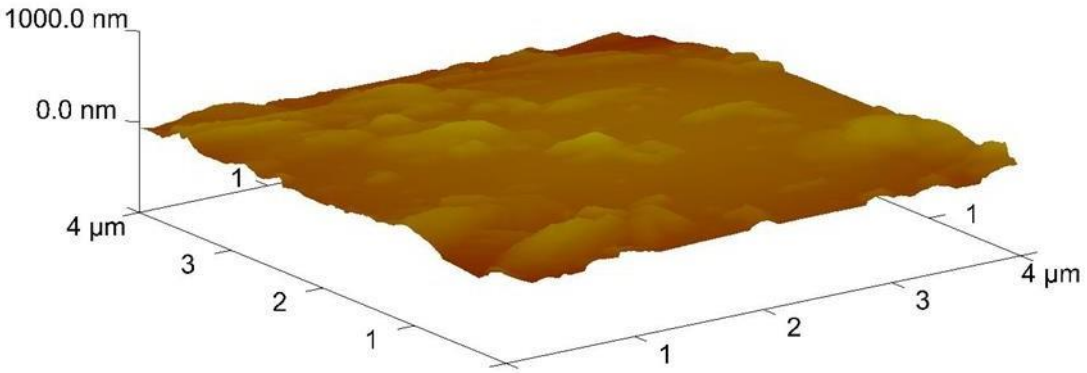

Figure 67. Surface of CaHGM made with 0.005 mol dm^{-3} obtained using AFM.

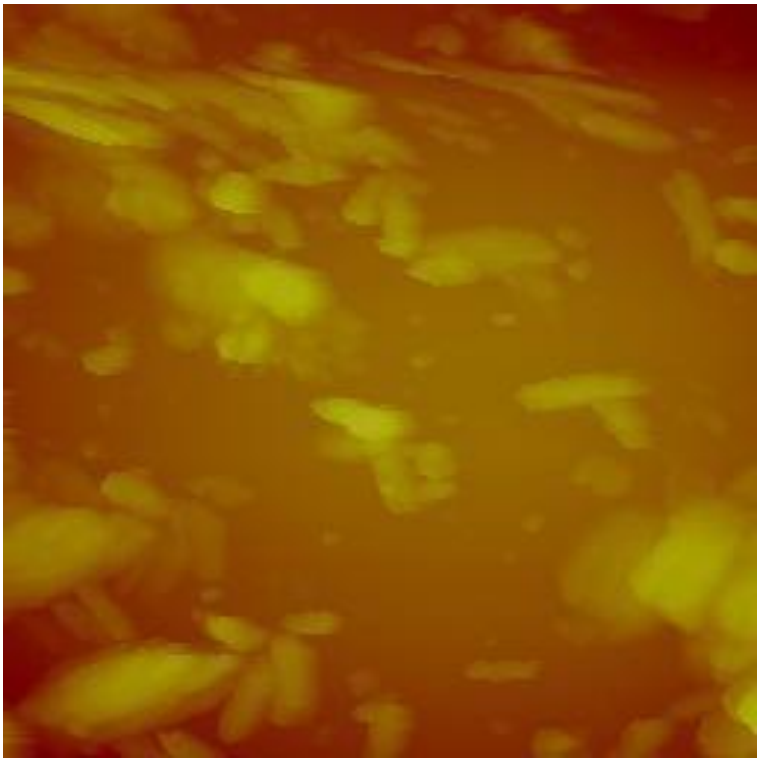

7.14 Thermogravimetric Analysis- CaHGMs

The initial mass loss in the region of 30 – 200 °C is assumed to be from the loss of water, both from atmospheric water adsorbed on the surface of the CaHGMs, and then water of crystallisation that may have become locked into the calcium hydroxide during crystallisation. The thermal decomposition of calcium hydroxide has an onset that occurs in the region of 300 – 400 °C, and is evident in the TGA curve that begins slowly with a small step at 300 °C and is complete before the temperature reaches 425 °C, with the sudden drop in mass beginning at around 390 °C. Calcium carbonate decomposes at 650 °C, and so it is assumed the final step of the TGA curve that begins around 600 °C corresponds to the thermal decomposition of the calcium carbonate component of the CaHGMs. Calcium carbonate decomposes into calcium oxide and carbon dioxide, so the mass loss that occurs in this region is assumed to be due to the formation of carbon dioxide, which constitutes 14.18% of the overall sample. The TGA curve is shown in Chart 16. TGA curve of CaHGMs, while the mass loss events are shown in Table 54. Mass loss events occurring in the TGA curve.

Chart 16. TGA curve of CaHGMs.

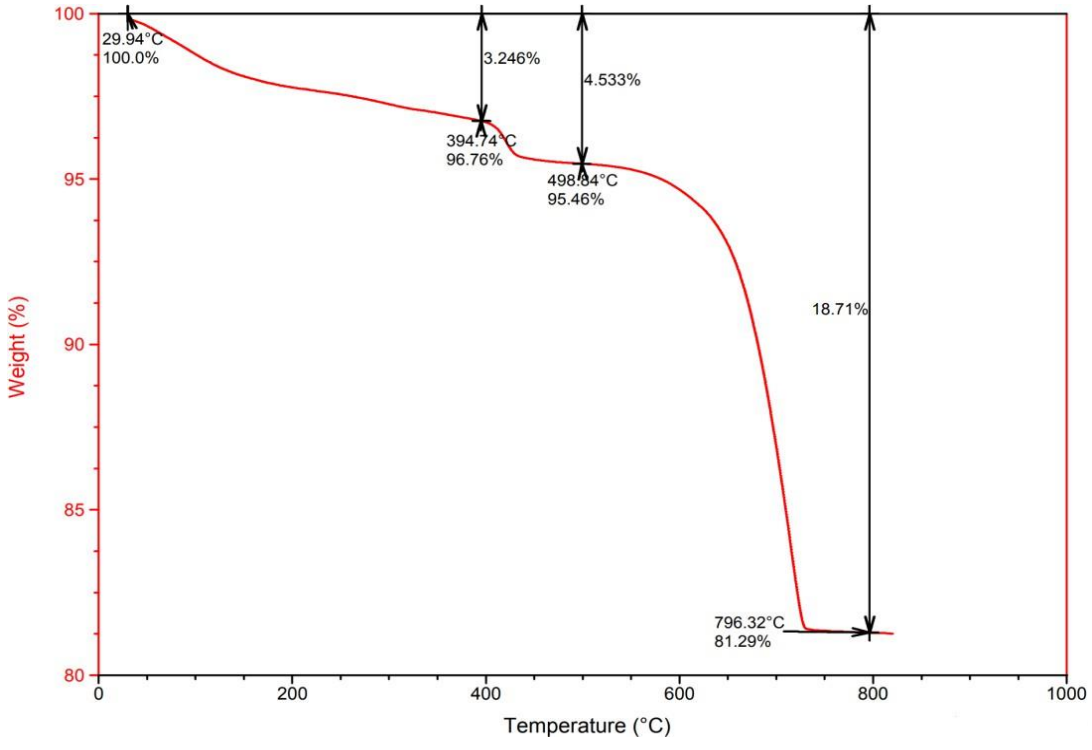

Table 54. Mass loss events occurring in the TGA curve.

Temperature Range °C	Event
30-200	Loss of water
200-400	Decomposition of calcium hydroxide
600-700	Decomposition of calcium carbonate

7.15 Summary of Chapter 7

The HGMs prior to treatment were characterised using SEM, EDX, XRD, AFM and TGA, and were found to be consistent with characterisation data reported in the literature. The HGMs were selected based on a criterion of size uniformity and shell thickness, with uniform sizes and low standard deviations from the average size preferred. A low ratio of inner radius to outer radius was preferred, as this indicates a thicker shell. It was assumed that HGMs with thicker shells would be more robust than HGMs with thinner shells. However, the inner radius of shells was measured from broken HGMs, and it is acknowledged that the thinner shelled HGMs in a sample would be more likely to fracture than the thicker shelled HGMs, skewing the data towards a thinner shell than the true value of shell thickness.

After treatment with NaOH and KOH the HGMs experienced catastrophic particle damage that resulted in the HGMs being unusable. After treatment with calcium hydroxide, crystals grew on the surfaces of the HGMs, and the newly produced CaHGMs were recoverable at a rate of around 80%. However, due to the extra mass on the HGMs caused by the crystals, this rate of recovery is based on the mass of the recovered HGMs, and not the actual number of HGMs.

The untreated HGMs have very small particles on their surfaces, assumed to be fragments of other broken spheres, while the HGMs treated with calcium hydroxide grew resulted in intact HGMs covered with much larger particles that were not from fragments of broken HGMs. The FT-IR of the HGMs shows a very small peak associated with C-H bond in the region from 3000-2850 cm^{-1}, which is assumed to be impurities from the manufacturing process, indicating the necessity of a washing process to clean the surface of the HGMs, and also peaks associate

with Si-O bonds, in the region from 1110-1080 cm^{-1} the XRD pattern shows very wide broad peak with a maximum between 2Theta = 21 ° and 23 °, which is highly characteristic of the XRD patterns recorded in Chapter 5. The XRD pattern of the CaHGMs shows a significant difference to the HGMs, as the presence of calcium carbonate, calcium hydroxide and calcium silicate has been detected, and their relative compositions identified, and found to be 93%, 6% and 1% of the structures that formed on the CaHGMs. This is an advantage for the production of hydroxyapatite, which will be discussed in the next chapter.

EDX analysis shows the surfaces of the HGMs largely consist of 27% silicon and 60-61% oxygen, with a small contribution from carbon, which could be from the conductive graphite used to prepare the samples for SEM and EDX imaging, or from the carbon tape background, and any residue from the carbon tape used to secure the HGMs. In contrast, the CaHGMs contain a significant contribution from carbon, which has increased from 10-11% in the HGMs to 17-25% in the CaHGMs, and calcium which was not present in the HGMs, has increased to 18% in the largest aggregate identified on the surface of the CaHGMs, providing evidence to confirm the identity of the structures on the surface of the CaHGMs as being mostly calcium carbonate.

TGA indicates there is some matter within a sample of untreated HGMs, assumed to be water due to the temperature range of the initial mass loss up to approximately 200 °C, which constitutes approximately 2.5% of the sample. A second step corresponding to a mass loss of <1% occurs in the region from 200 – 300 °C, and is attributed to the process of dihydroxylation, while the final last step begins with an onset of around 300 °C which continues until the end of the curve at 800 °C, with the rate of mass loss slowing at approximately 500 °C. The TGA of the CaHGM sample shows a different curve with two distinct steps that were present in the TGA curve of the HGM, and these have been assigned to the decomposition of calcium hydroxide, and the decomposition of calcium carbonate.

AFM was employed to assess the surface roughness of the HGMs and CaHGMs, and to generate a 3D topological map of the surface of the HGMs and CaHGMs. AFM was found to not be an appropriate characterisation method for the microspheres, as the AFM probe often slipped when moving across the surface of the HGMs and CaHGMs. This resulted in the microspheres being launched across the sample, necessitating a complete restart of the process with another microsphere, or extreme noise being generated in the topological map when the pressure applied to the surface was too high by the AFM probe. In addition, working on the 10 μm scale was found to produce an image Z range of 665 nm that is more likely due to the curvature of the HGM, rather than features on the surface pf the HGM. Working at a scale of 4-5 μm was found to give a more realistic value of Z range and, at this scale the R_a was found to be 21 nm, and the surface Z range was found to be 188 nm for the HGMs, which is consistent with SEM imaging. The R_a and image Z range for the CaHGMs treated with 0.02 mol dm^{-3} calcium hydroxide solution was found to be 115 nm and 1482 nm, and for the CaHGMs treated with 0.005 mol dm^{-3} the image Z range was found to be 452 nm, and the R_a was 60 nm, indicating that treatment of the HGMs with the more concentration solution produced greater surface texture.

8. Chapter 8 – Hydroxyapatite Synthesis & Characterisation

8.1 Introduction

This chapter contains the results of experiments designed to produce hollow glass microspheres (HGMs) coated with hydroxyapatite (HAP) to produce the material termed in this work "HAP-HGMs". The substrate used for the HAP-HGMs is the CaHGMs produced in Chapter 7, as it was established that the crystals on the CaHGMs were 93% calcium carbonate, and treatment of calcium carbonate with a solution containing phosphate ions can be used to produce hydroxyapatite.

This chapter begins with scanning electron microscope (SEM) images showing the progress made towards producing the hydroxyapatite coated HGMs (HAP-HGMs), where the surfaces of the HGMs are shown, followed by the CaHGMs, and finally the HAP-HGMs. SEM images of the microspheres after changing reaction conditions have been included to explore the effects such parameters have on the product are included. These parameters are: immersion time in calcium hydroxide, concentration of calcium hydroxide and ultrasonication solvent.

Energy dispersive x-ray spectroscopy data is included next, where the structures growing from the surfaces of the CaHGMs were investigated to determine if silicon atoms were present within these structures. showing the chemical composition of the surfaces of samples of CaHGMs and HAP HGMs. The boundary between the silica glass component and the hydroxyapatite component are emphasized using an elemental linescan, which shows the relative proportions of identified elements across the HAP-HGM.

FT-IR spectroscopy was used to confirm the presence of functional groups within the CaHGMs, and the HAP-HGMs, and the comparison used to provide further evidence that the transformation of the calcium carbonate portion of the CaHGMs to the calcium phosphate of

the HAP-HGMs was complete. A TGA curve was obtained of the HAP-HGMs in order to determine if the HAP-HGMs contained significant amounts of calcium carbonate.

Characterisation of the HAP-HGMs was continued by obtaining an XRD pattern of the HAP-HGMs, and this pattern was compared to commercially available Bio-Oss, the mineral component of bovine bone. Further analysis of the XRD pattern of the HAP-HGMs was performed in order to produce a table of the lattice parameters of the HAP-HGMs.

8.2 Scanning Electron Microscopy

Scanning electron microscopy was used to investigate surface morphology of the microspheres and to view the progress of the reactions designed to grow hydroxyapatite. The progress of the reaction can be seen with the untreated HGM and a magnified view of itsa surface in Figure, followed by the results of treating the HGMs with calcium hydroxide solution to produce CaHGMs, where a magnified view of the surface of the CaHGMs, followed by a single HAP-HGM, and a magnified view of its surface is displayed in Figure 8.

Optimising the Coating of HGMs with Calcite

Treating the HGMs with calcium hydroxide (0.02 mol dm^{-3}) resulted in the growth of calcite on the surfaces of the HGMs, which can be seen in Figure 68. The effect of changing the concentration of the calcium hydroxide solution was investigated, where it can be seen that treatment with 0.02 mol dm^{-3} solution of calcium hydroxide provides greater coverage of the HGMs than treatment with 0.005 mol dm^{-3} calcium hydroxide solution. Furthermore, the reason that 0.02 mol dm^{-3} calcium hydroxide was initially selected was because this concentration provides adequate Ca^{2+} ions to increase the proportion of calcium in the CaHGM sample to be consistent with the 24% Ca present in bioglass. The comparison between the results of treatment with 0.02 mol dm^{-3} and 0.005 mol dm^{-3} can be seen in Table 55. SEM images of HGMs treated with different concentrations of $Ca(OH)_2$.

Ultrasonication of the CaHGMs was performed in water and ethanol, and ultrasonication in water removed less material (from inspection using SEM) than ultrasonication in ethanol. This may be because the CaHGMs had a greater tendency to aggregate in ethanol than in water, causing friction due to more collisions between CaHGMs, resulting in the calcite crystals becoming dislodged due to mechanical action. This effect can be seen in Table 56. The effect of ultrasonication in ethanol and water.

Figure 68. The calcium coating has begun to grow over the sharp edges of the fragment.

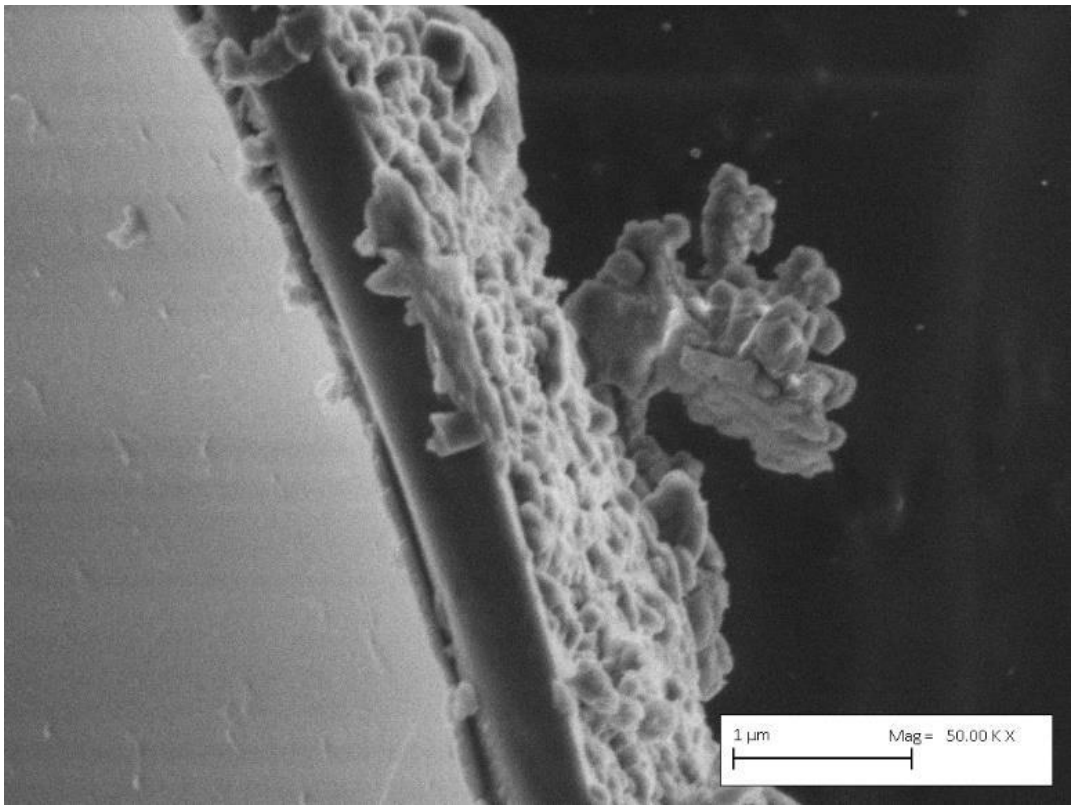

Table 55. SEM images of HGMs treated with different concentrations of $Ca(OH)_2$.

Immersion in $Ca(OH)_2$ (0.005 mol dm^{-3}) with Stirring for 24 hr
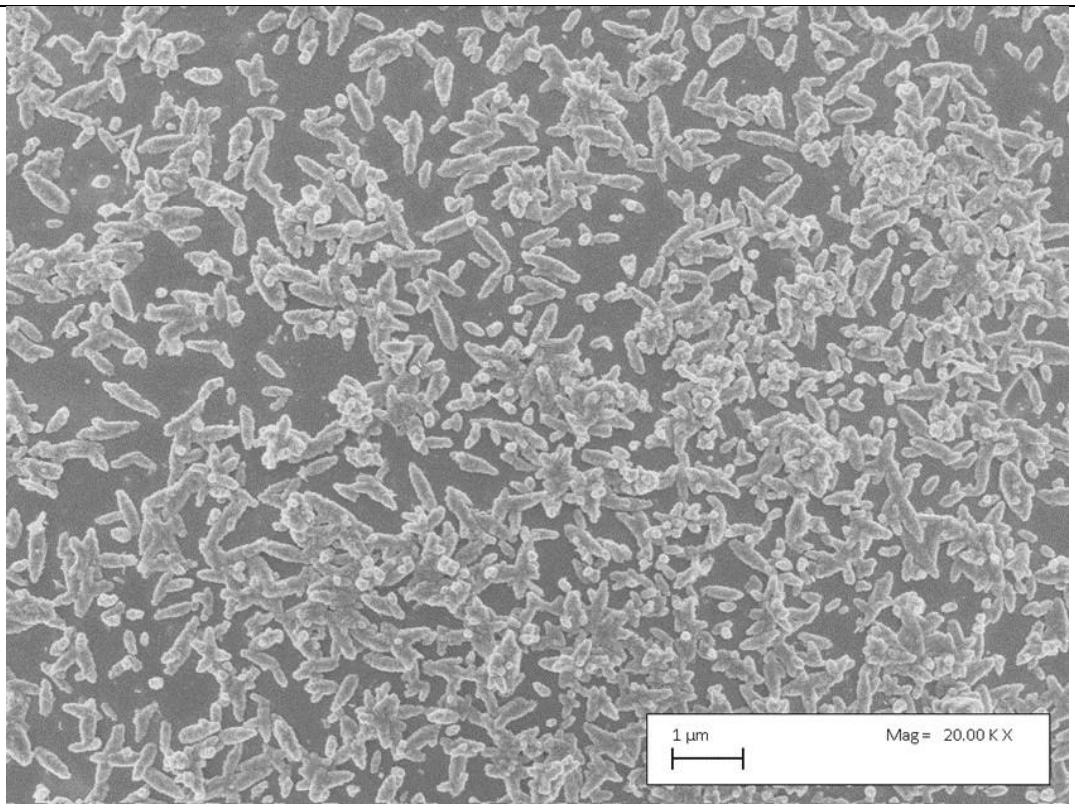
Immersion in $Ca(OH)_2$ (0.02 mol dm^{-3}) with Stirring for 24 hr
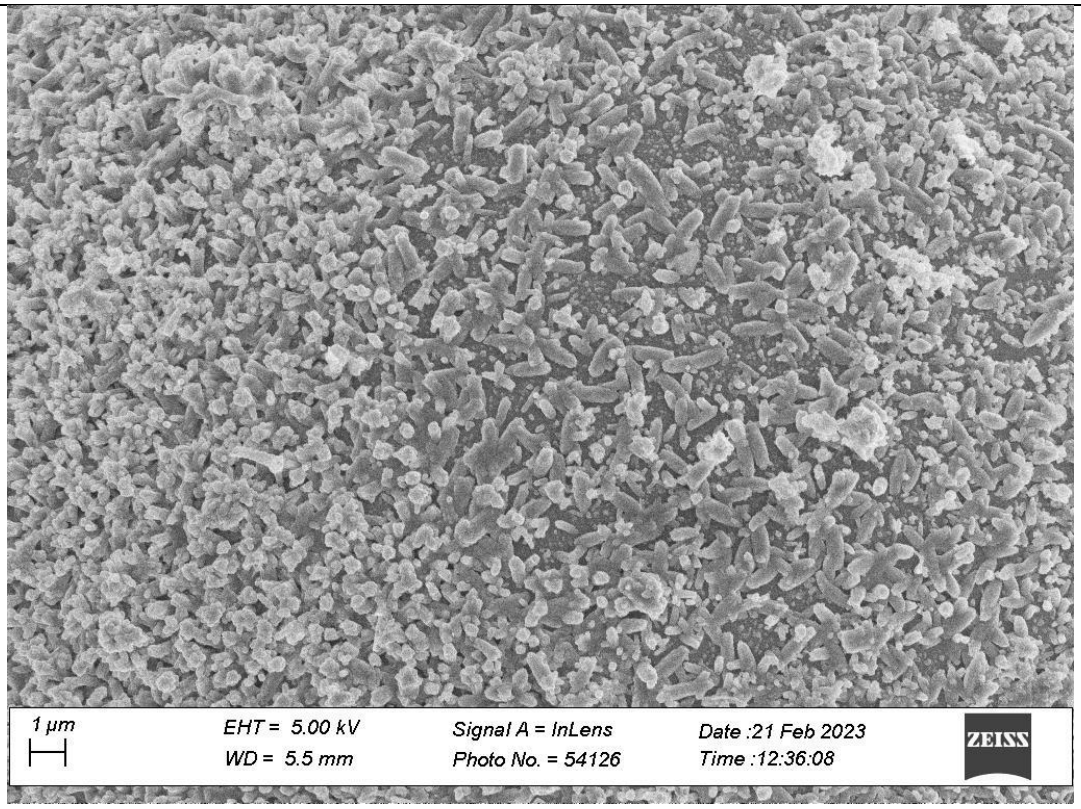

Table 56. The effect of ultrasonication in ethanol and water.

Ultrasonication Solvent
CaHGM ultrasonicated in water
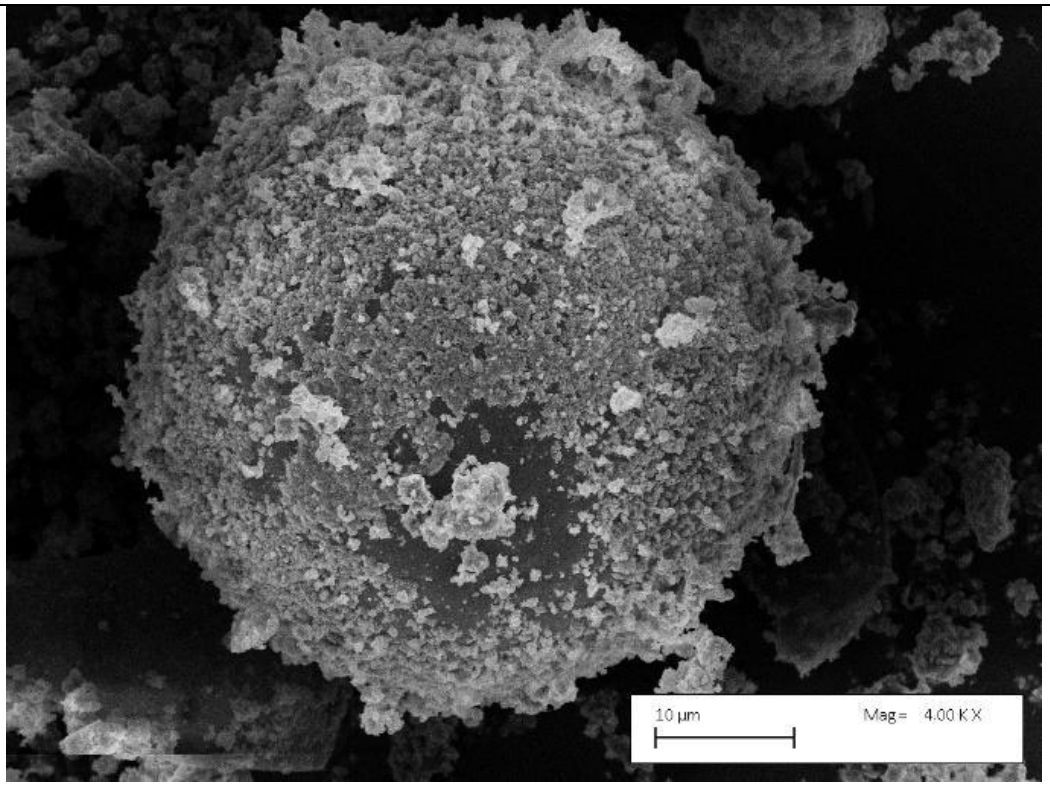
CaHGM ultrasonicated in ethanol
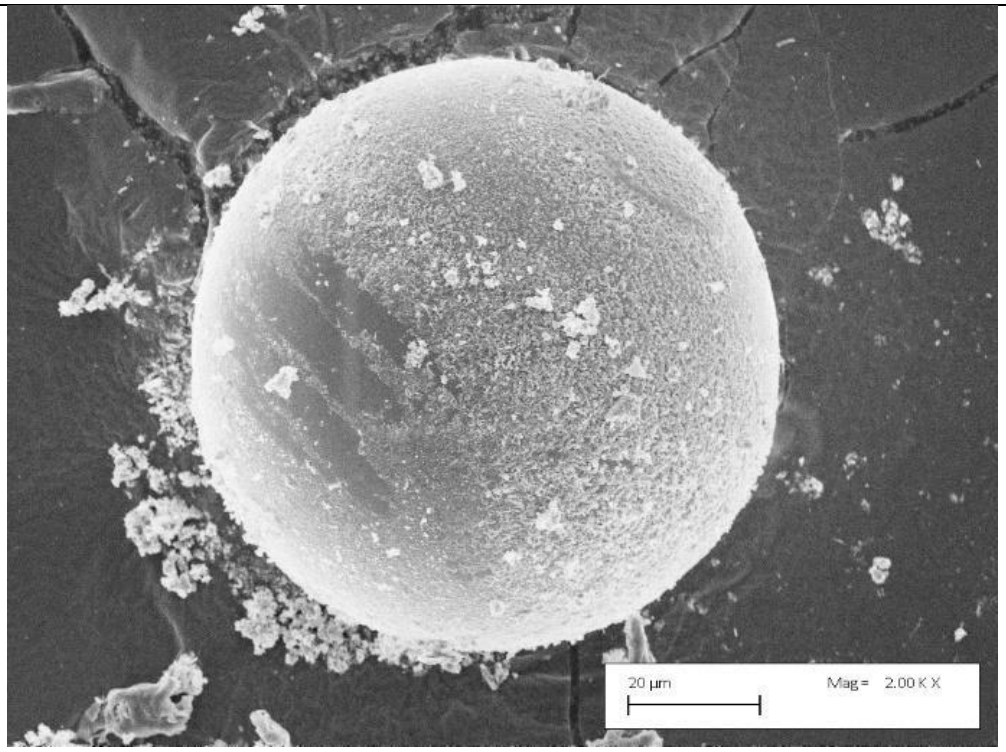

Washing the CaHGMs in water and ethanol resulted in some loss of the particles on the surfaces of the CaHGMs, and hence washing with ethanol was not implemented in the processes of preparing the CaHGMs. This effect can be seen in Table 57.

Table 57. Comparison of the washing process after treatment with different concentrations of $Ca(OH)_2$ solution.

0.02 M 24hr, washed with water & ethanol	0.005 M 24 hr washed with water & ethanol
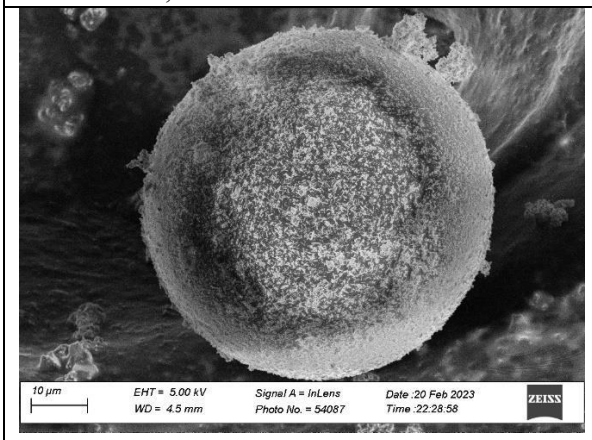	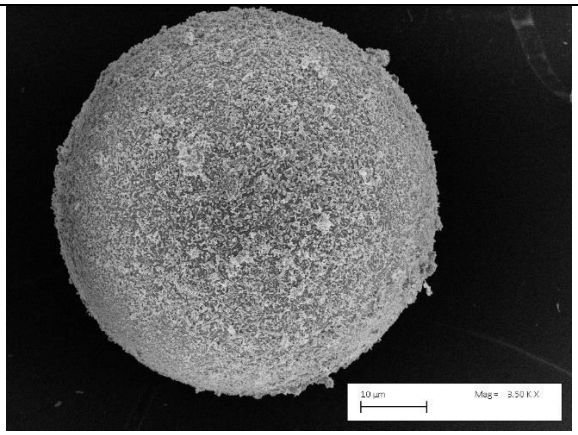
Below: close up of surface of 0.02 M 24hr, washed with water & ethanol	Below: close up of 0.005 M 24hr, washed with minimal & ethanol
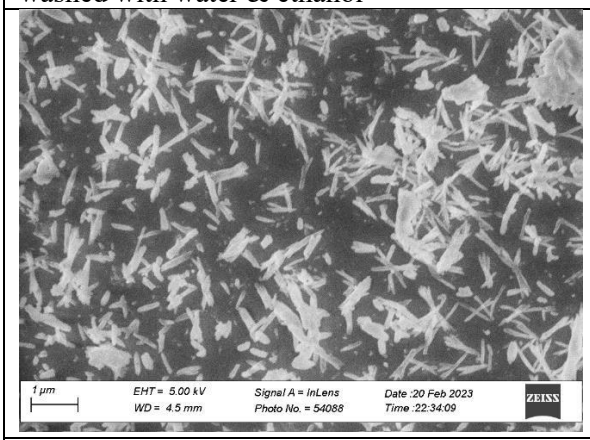	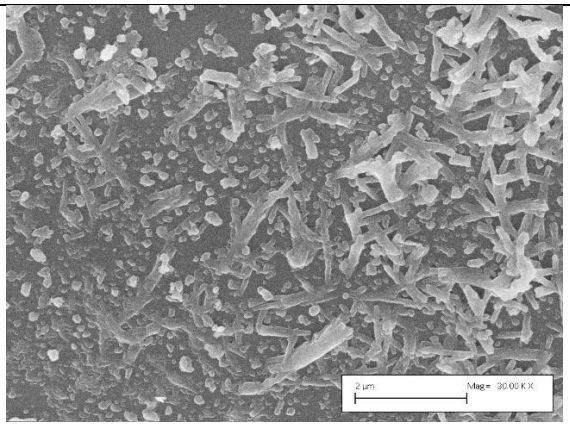
0.02 M after ultrasonication in ethanol	0.005 M after ultrasonication in ethanol*
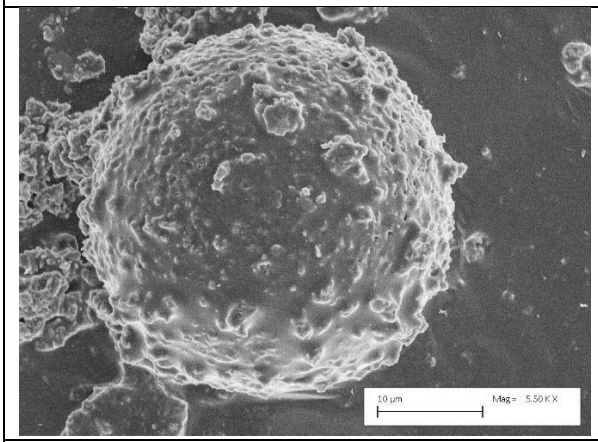	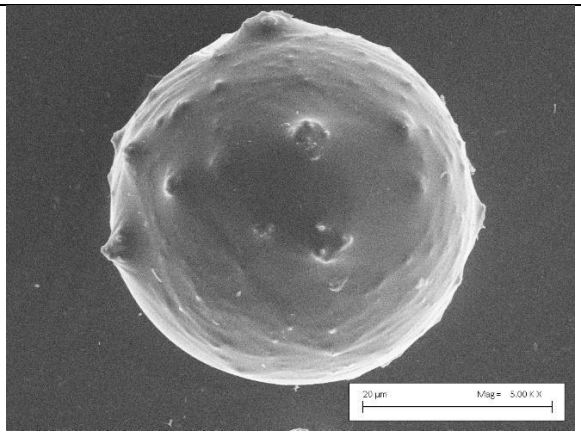
* This is not a typical particle, however this shows a change in surface morphology from smooth to studded with particles to roughened surface	

The progress of the coating processes from untreated HGM to HAP-coated HGM (HAP-HGM) is shown in Table 58, Table 59 and Table 60.

Table 58. Untreated HGMs above; and untreated HGMs surface below.

Below: untreated hollow glass microsphere
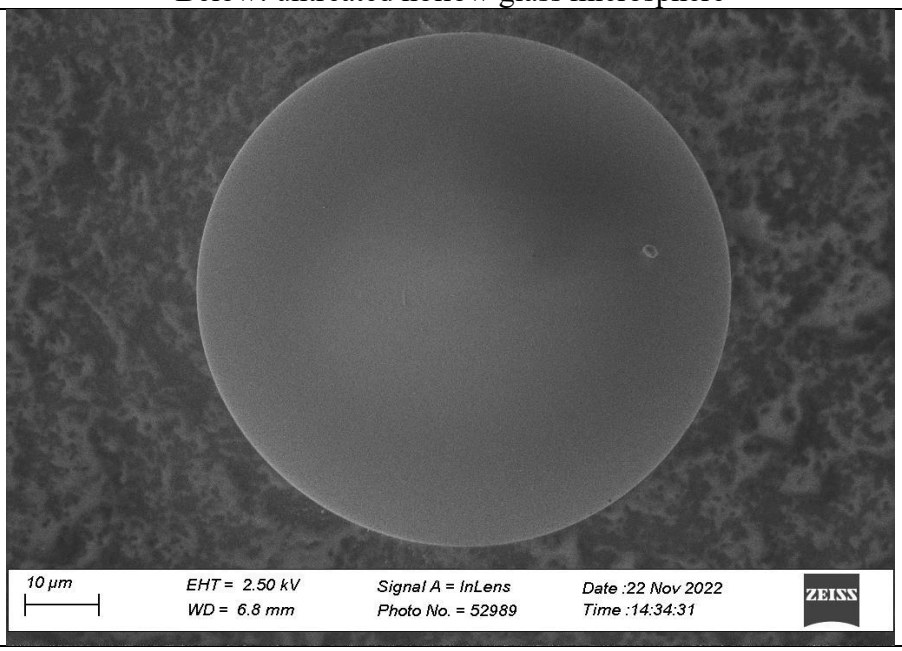
Untreated HGM surface magnified by 50,000
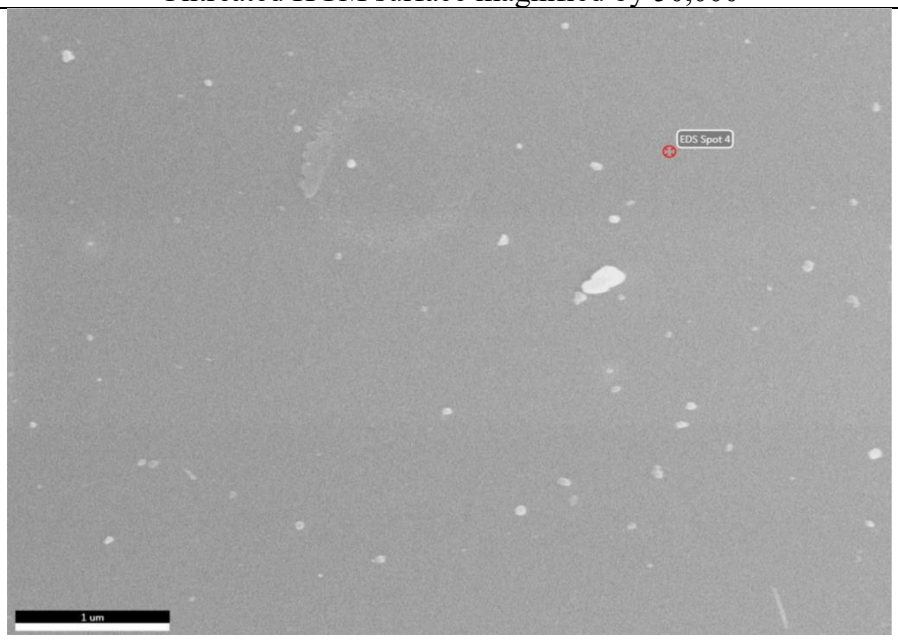

Table 59. Calcium carbonate "CaHGM" (a); and magnified surface of CaHGMs (b).

Below: calcium carbonate hollow glass microsphere produced by immersing the hollow glass microspheres in saturated calcium hydroxide solution for 24 hr with stirring

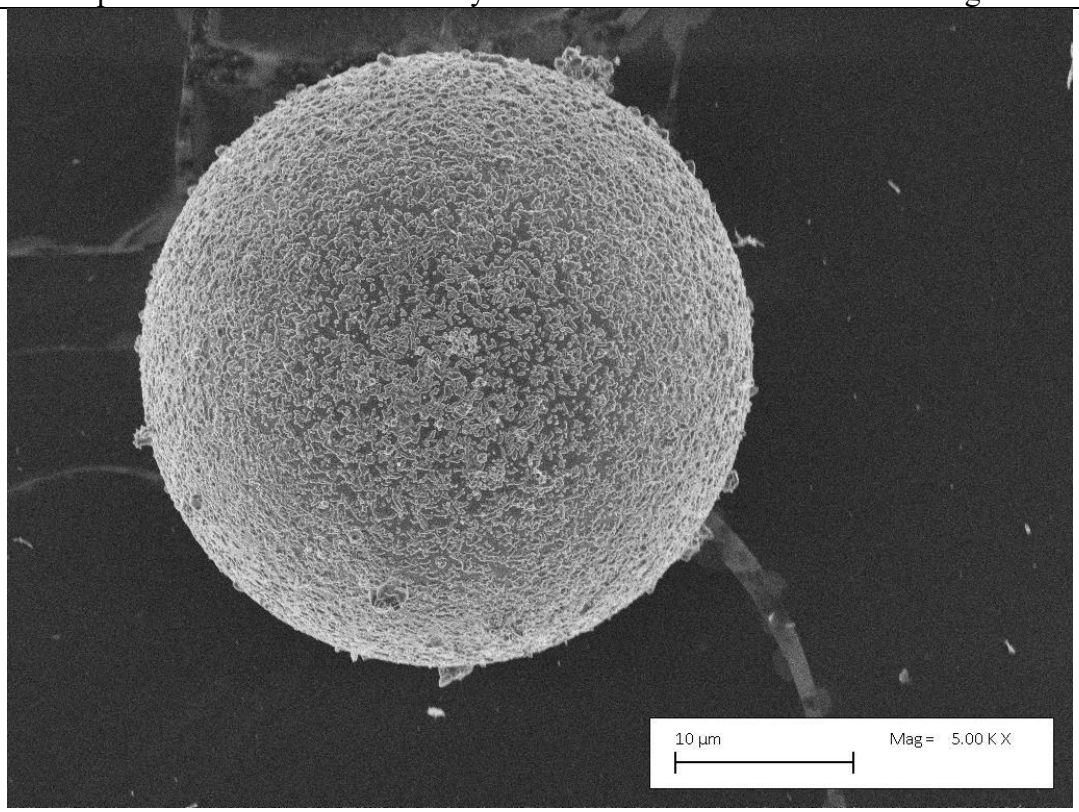

Below: surface of the CaHGMs, magnified with a scale bar of 200 nm

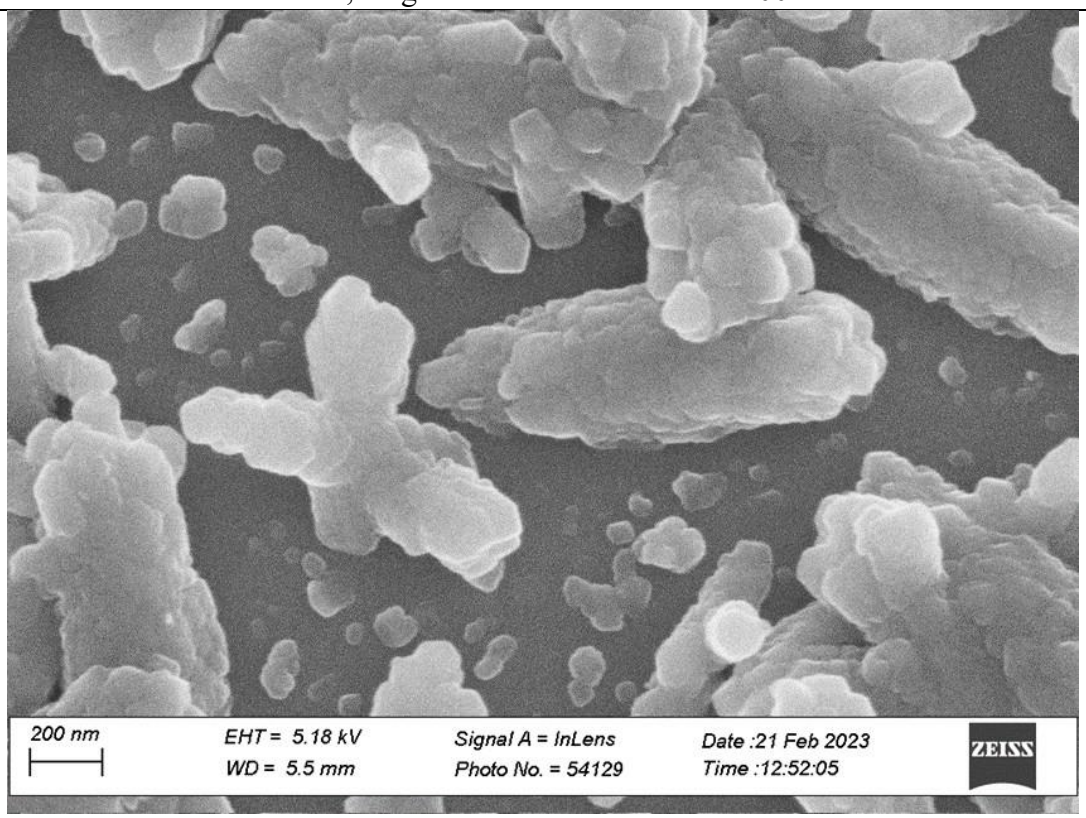

Table 60. SEM images of the hydroxyapatite coated HGMs, or HAP-HGMs.

Below: hydroxyapatite hollow glass microspheres produced by soaking the calcium carbonate hollow glass microspheres in dipotassium hydrogen phosphate solution for 5 days at ambient temperature, producing hydroxyapatite with a high surface area

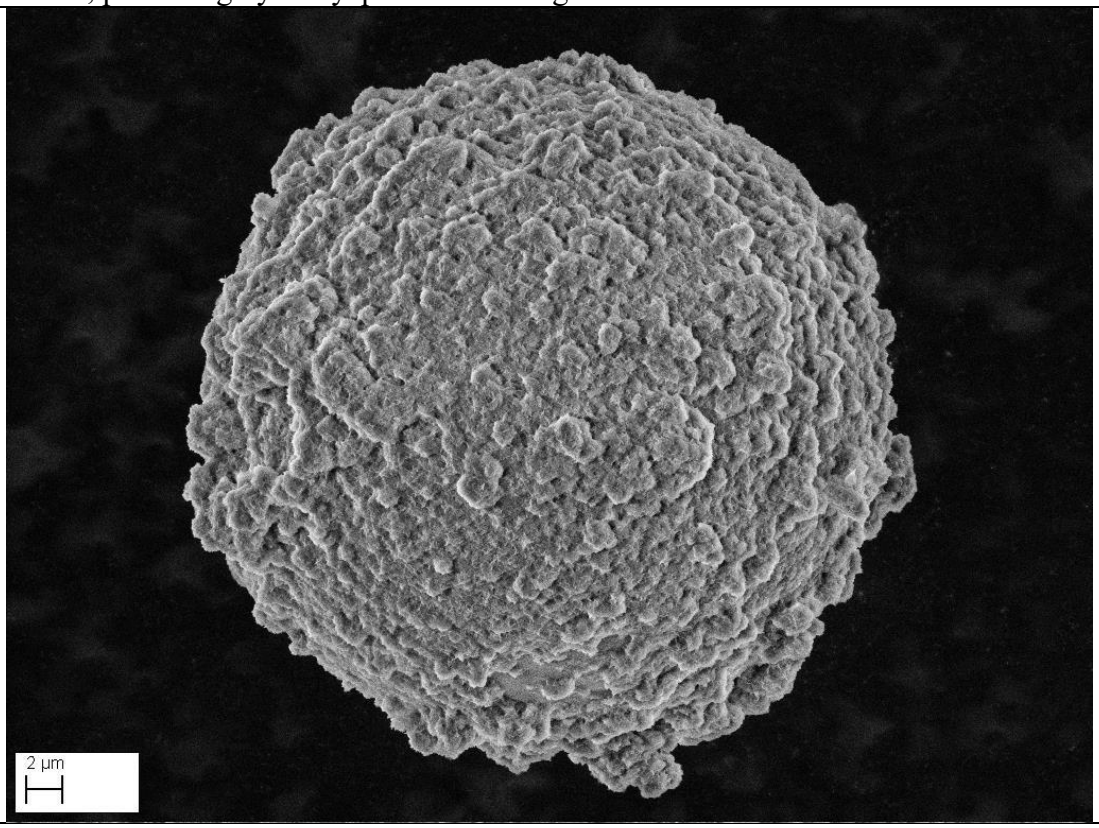

Below: surface of the hydroxyapatite coated HGM showing both sheet and needle morphology

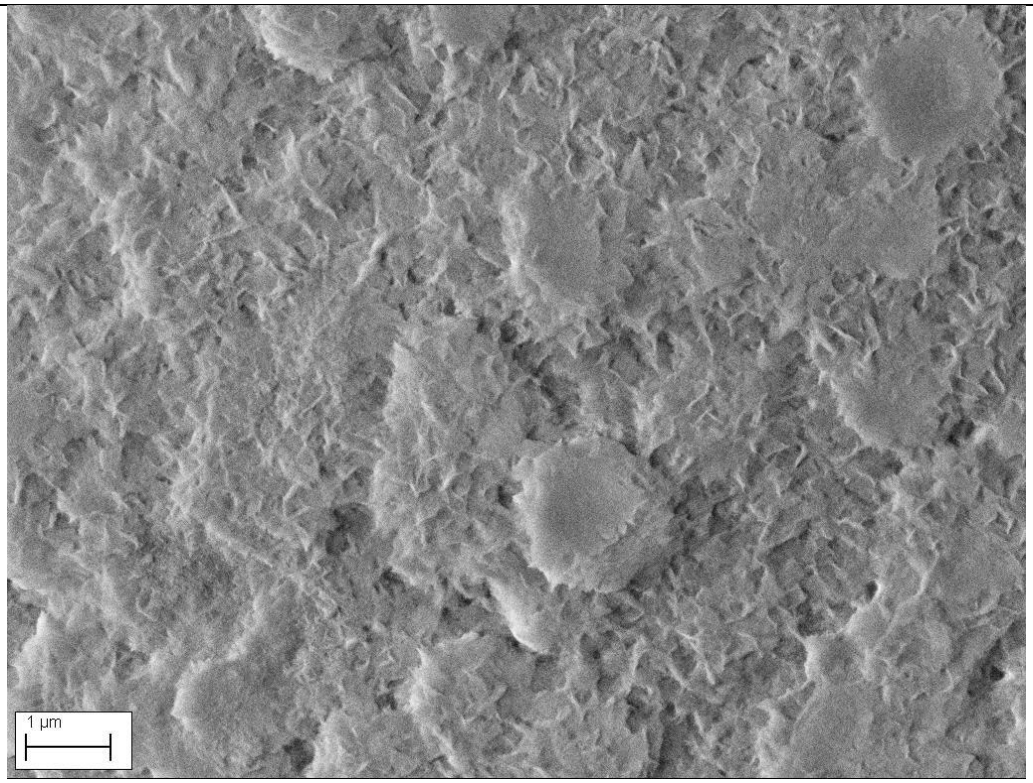

Hydroxyapatite coated HGMs – “HAP-HGMs”

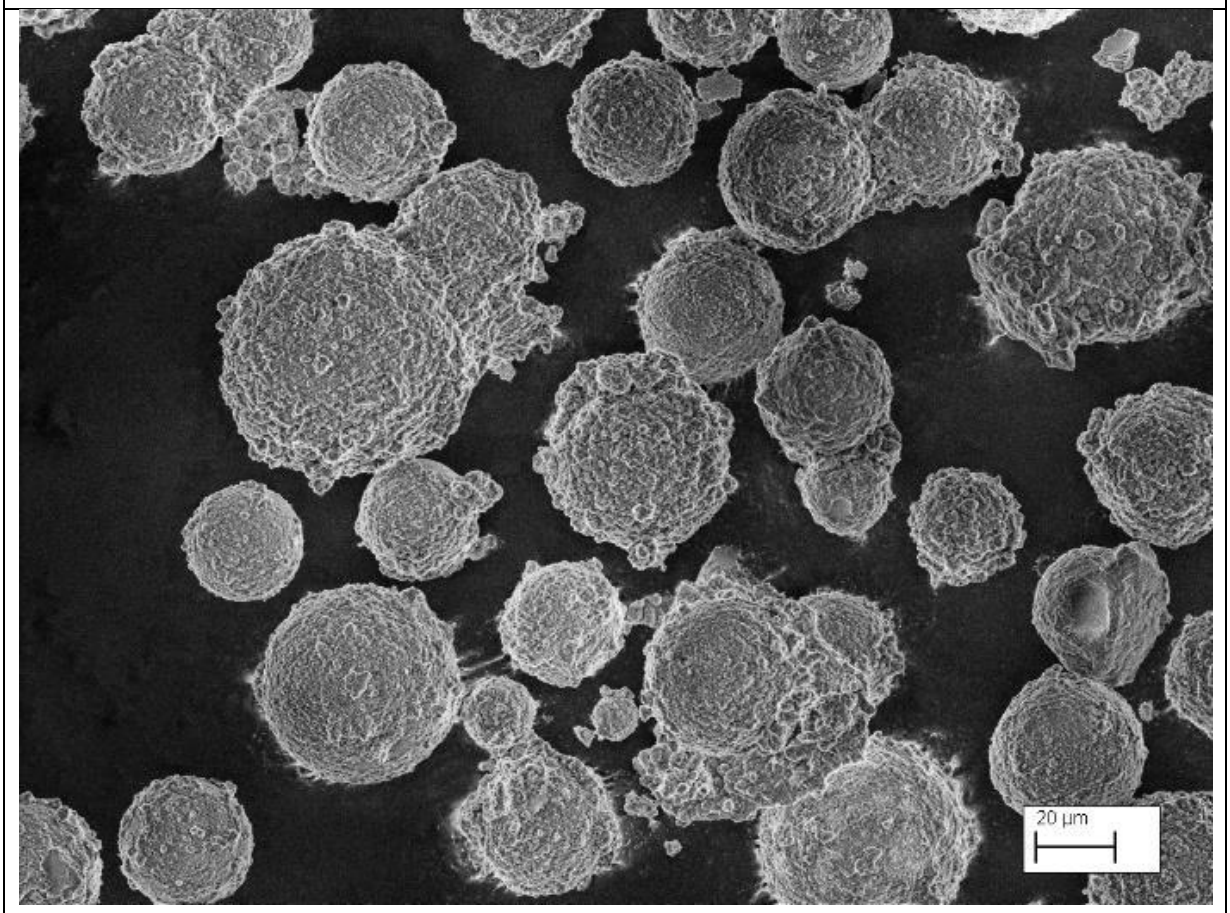

8.3 EDX Spectroscopy – Calcium silicate established in CaHGMs

In Chapter 7, a small amount of calcium silicate was identified in the XRD pattern of the After the particles formed on the surface of the CaHGMs were established as calcium carbonate, and also that these particles were not dislodged by ultrasonication, EDX analysis was conducted with the aim of determining the identities of the elements within the crystals on the surface of the CaHGMs. This was done in order to rule out the possibility that calcium silicate was forming in solution and not on the surfaces of the CaHGMs.

The crystals that grew on the HGMs during immersion in calcium hydroxide were investigate for their chemical composition with the elements quantified in Table 61, and in Table 62. Elemental maps of showing silicon outside the radius of the HGM. The corresponding EDX spectrum is shown in Chart 17. EDX Spectrum of CaHGM (0.02 mol dm-3 $Ca(OH)_2$) close attention is paid to the triangular structure growing from the lower segment of the microsphere, where silicon is found outside the radius of the HGM. The presence of silicon outside of the HGM radius could be due to sample drift which can occur in EDX spectra when elemental mapping is performed at high magnifications over long periods, however the presence of silicon inside the triangular mass growing on the outside of the HGM indicated that calcium silicate is forming on the outside of the HGM.

Table 61. EDX element quantification for CaHGM (0.02 mol $dm^{-3}Ca(OH)_2$.

Element	Weight %	Atomic %	Error %
Carbon	18.3	34.6	3.6
Oxygen	19.1	27.1	7.6
Magnesium	0.1	0	16.2
Aluminium	0.2	0.2	7.8
Silicon	12.1	9.7	1.5
Chlorine	0.4	0.3	4.9
Calcium	49.8	28.2	1.4

Table 62. Elemental maps of showing silicon outside the radius of the HGM.

CaHGM made with 0.02 mol dm^{-3} calcium hydroxide	
Below: all elements overlaid	Below: element quantification
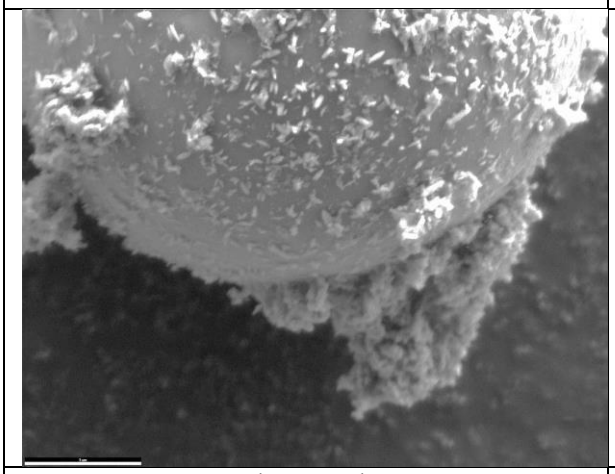	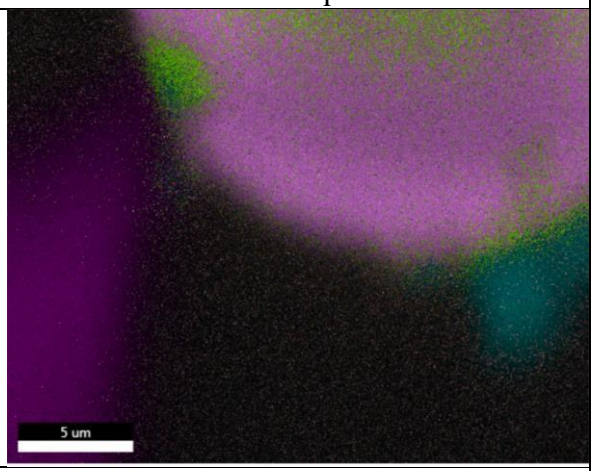
Below: carbon	Below: silicon
	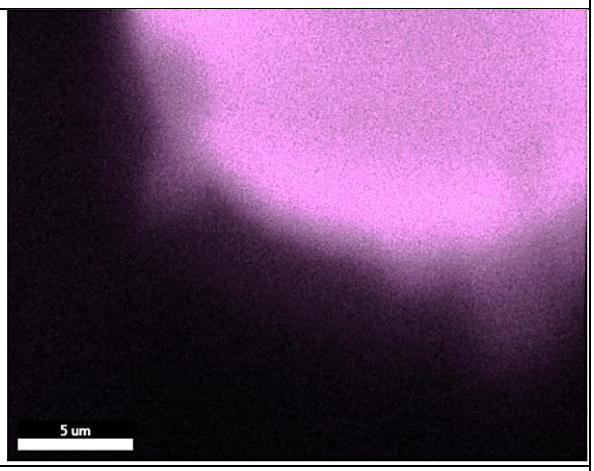
Below: oxygen	Below: calcium
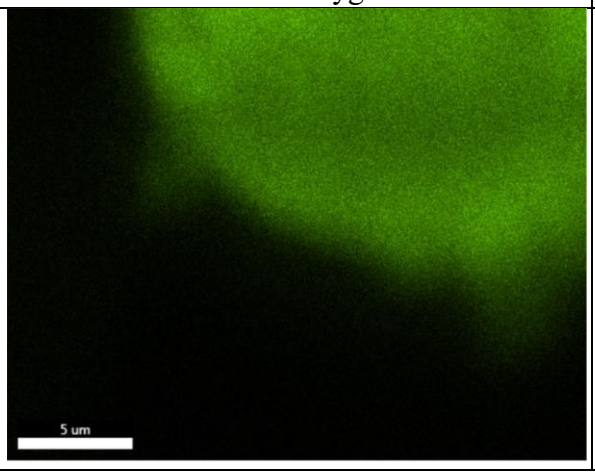	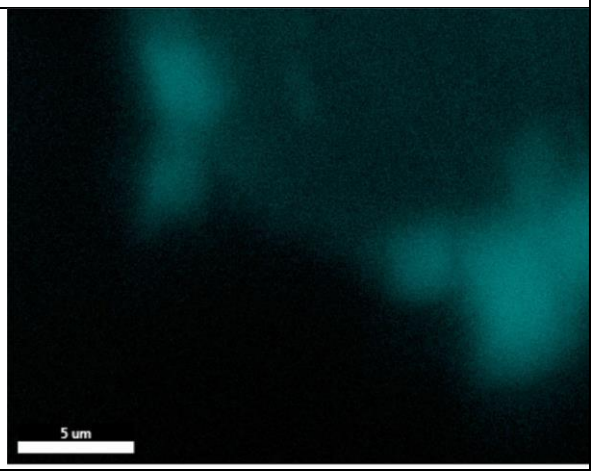

Chart 17. EDX Spectrum of CaHGM (0.02 mol dm^{-3} $Ca(OH)_2$), x-axis is X-Ray Energy, y-axis is Counts.

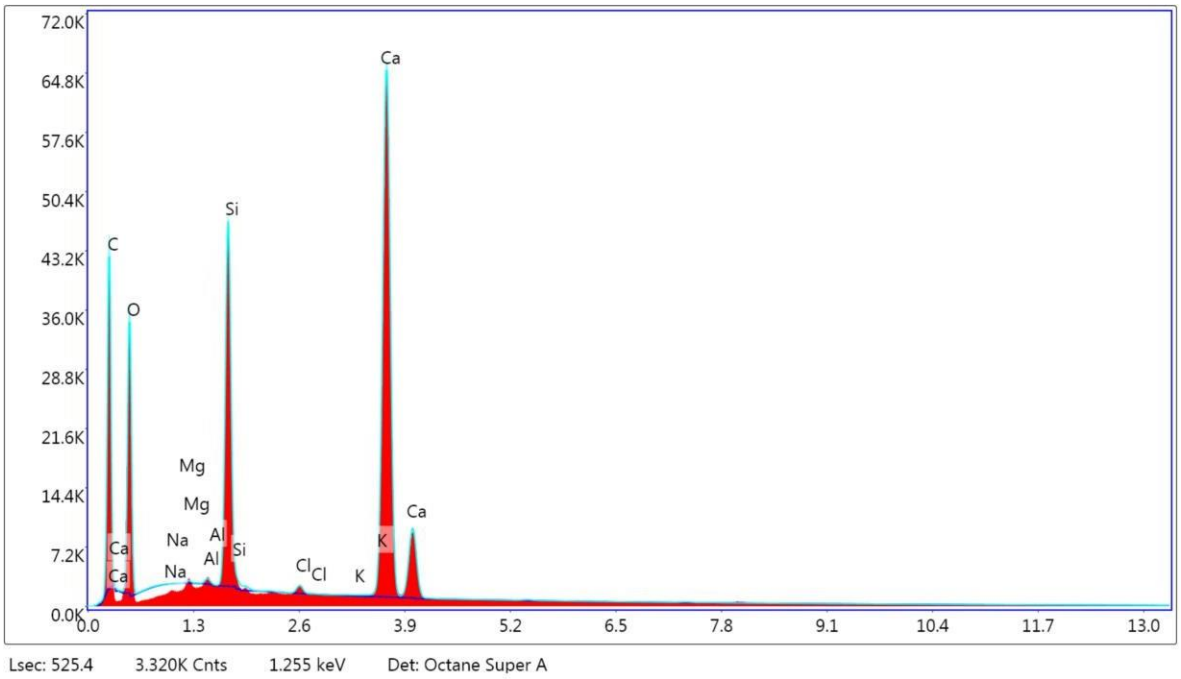

8.4 EDX Spectroscopy – HAP-HGMs

EDX elemental mapping across the edge of a broken HAP-HGM shows the distribution of elements at the interface of the HAP component and edge of the silicon dioxide HGM. The elemental map indicates that the entire HGM is not transformed in HAP, as is the case with bioglass, however a boundary exists between the silicon and calcium components. Silicon and oxygen are found to be pervasive through the sample, which is expected as the HGM is the substrate. Calcium and phosphorus show a dark patch that cuts diagonally across the image, which corresponds to the sharp edge of the HGM. The linescan across the image shows the edge of the HGM to have high the highest amounts of silicon, which is where the amount is calcium and phosphorus decrease. The linescan supports the conclusion that HAP is not penetrating deeply with the surface of the HGM. The linescan is pictured in Table 63. EDX linescan performed across HAP-HGM particle. The EDX spectrum of the HAP-HGM shows the elements that dominate are silicon, oxygen, calcium and phosphorus and is depicted in

Chart 19. EDX Spectrum for Hydroxyapatite coated HGMs - "HAP-HGMs". The quantification of the element shows that the carbon contribution not the overall sample is small, indicating providing evidence towards the transformation of calcium carbonate into HAP. The quantified elements are contained in Chart 19. EDX Spectrum for Hydroxyapatite coated HGMs - "HAP-HGMs".

Table 63. EDX linescan performed across HAP-HGM particle.

Region used for EDX analysis	All elements overlaid
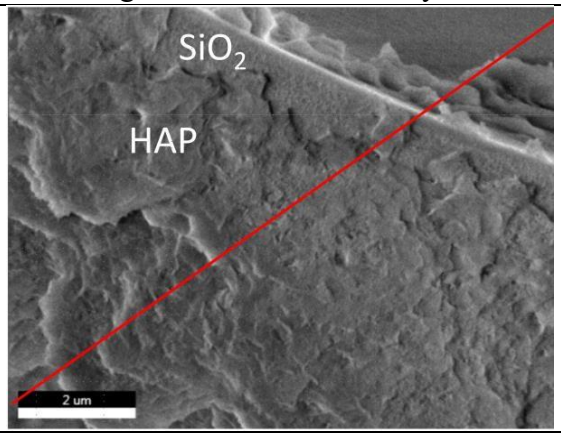	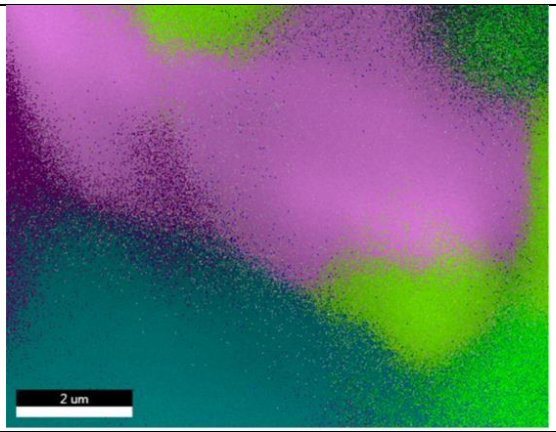
Silicon	Oxygen
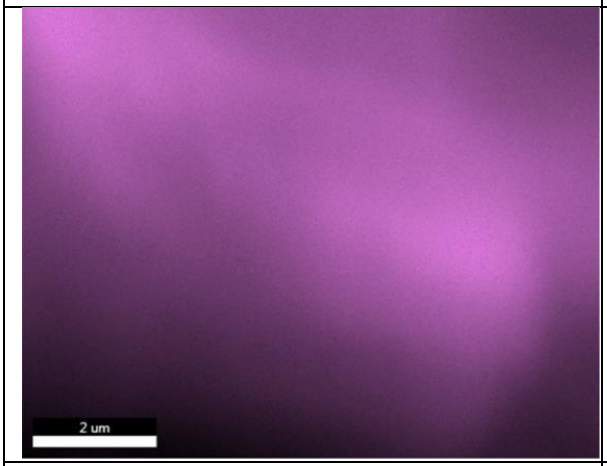	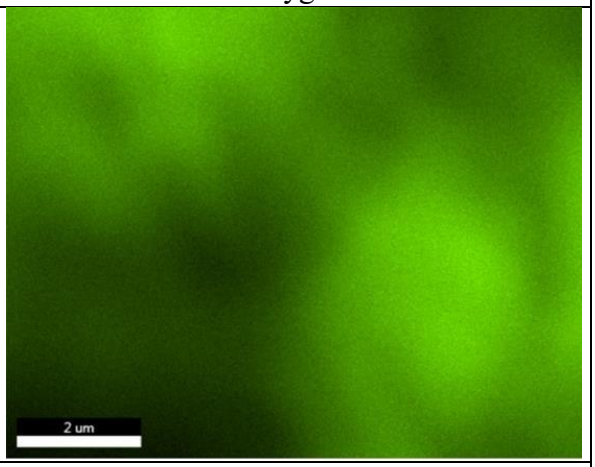
Phosphorus	Calcium
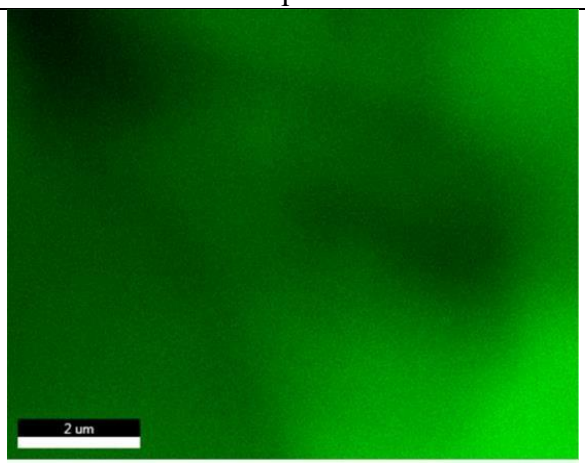	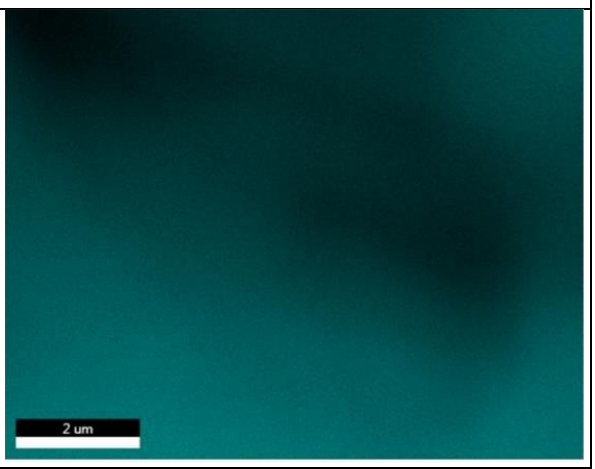

Chart 18. Linescan of HAP-HGM as shown on an x-y graph.

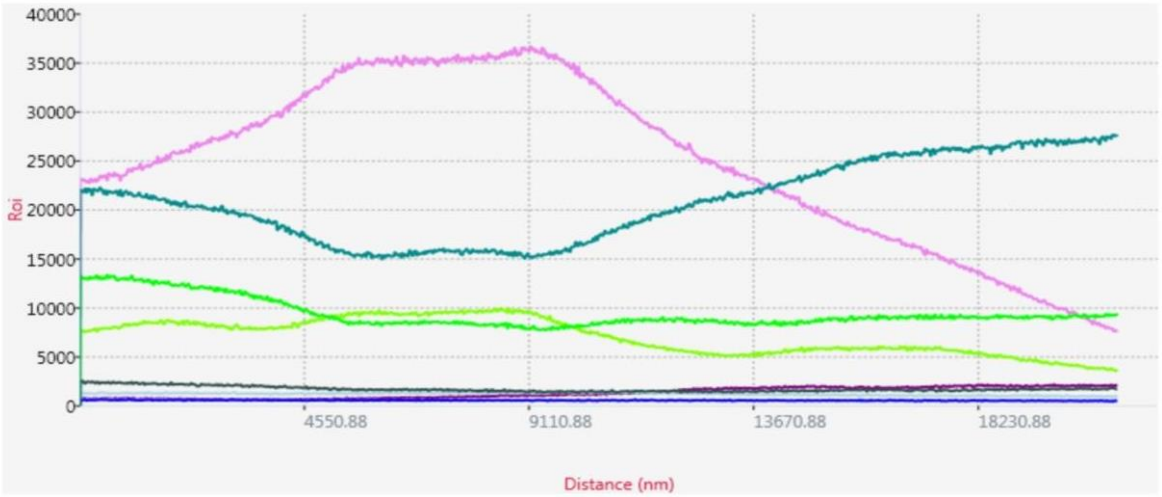

Table 64. Suggested mechanism for growth of hydroxyapatite on HGMs.

Element	Weight %	Atomic %
Carbon	3.8	8.3
Oxygen	20.8	34.0
Aluminium	0.4	0.4
Silicon	23.0	21.4
Phosphorus	11.7	9.8
Chlorine	0.1	0.1
Argon	0.2	0.1
Potassium	2.1	1.4
Calcium	38.0	24.7

Chart 19. EDX Spectrum for Hydroxyapatite coated HGMs - "HAP-HGMs", x-axis is X-Ray Energy, y-axis is Counts.

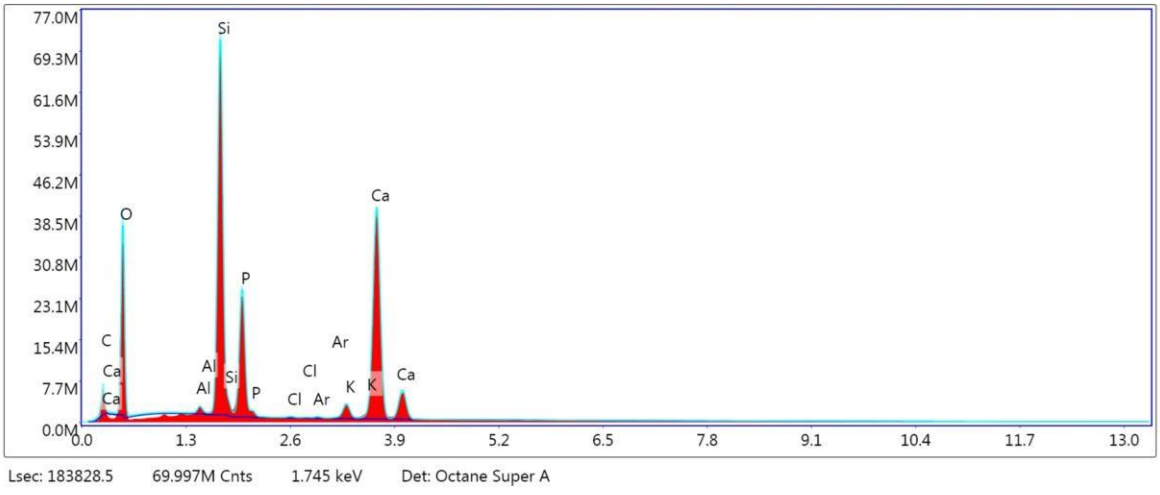

A suggested mechanism for HAP growth on the HGM is shown in Figure 69. Suggested mechanism for growth of hydroxyapatite on HGMs.

Figure 69. Suggested mechanism for growth of hydroxyapatite on HGMs.

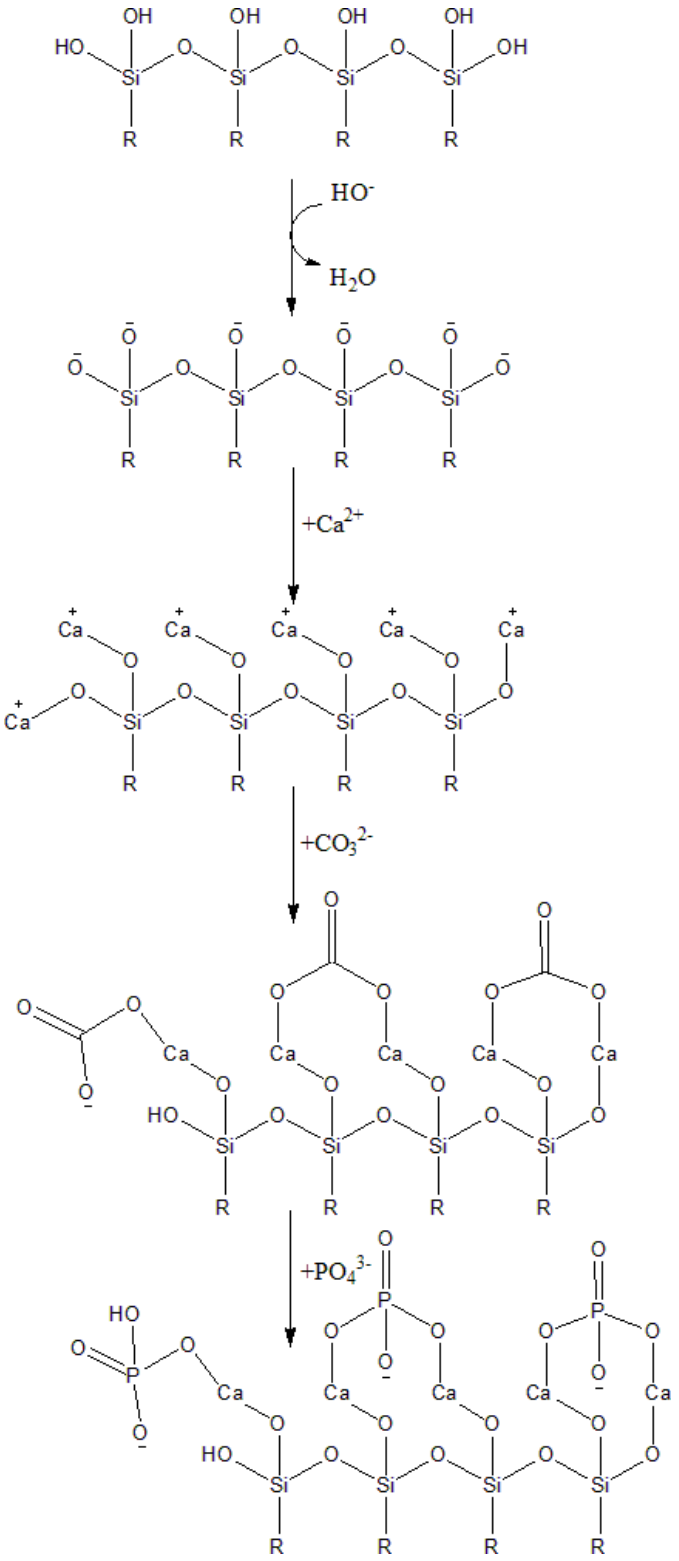

8.5 FT-IR Spectroscopy

The FT-IR spectra of the HGM, the CaHGMs treated with 0.02 mol dm^{-3} and 0.005 mol dm^{-3} calcium hydroxide solution, and the HAP-HGMs were compared, allowing the progress of the reactions to be followed. The HGMs contain few functional groups, which is evident by the two main peaks occurring between 1130 – 1000 cm^{-1} corresponding to the Si-O-Si stretching band, which is broad due to the length of the silicon chain. A much smaller peak occurs at 804 – 710 cm^{-1}, which is associated with the Si-O symmetric stretch. Finally, a barely detectable peak occurs between 3000 – 2950 cm^{-1} which is associated with the C-H stretching vibration. The presence of C-H bonds in the sample of untreated HGMs indicates impurities remaining from the manufacturing process, which necessitates the cleaning of the HGMs.

The CaHGMs treated with calcium hydroxide indicates the presence of calcium carbonate due to the presence of peaks in the region from 1800 – 1600 cm^{-1}, which is associated with C=O bonds. These spectra also show the appearance of a peak that is present in neither the HGMs nor the calcium hydroxide spectra between 990 – 875 cm^{-1} which corresponds to the $CaSiO_3$ group, and also strong peaks in the Si-O-Si range. The IR spectra of the CaHGMs shows some similarities with the spectrum for calcium hydroxide, namely the strong peak at 1417 cm^{-1} which is strongest in the CaHGM samples, but much weaker in the $Ca(OH)_2$ sample. It is assumed that this peak belongs to the carbonate component of the CaHGMs, and impurities of carbonate in $Ca(OH)_2$ formed from carbon dioxide from the air dissolving the $Ca(OH)_2$ solution, which explains why the peak is strong in the CaHGM samples which contain a significant component of carbonate, but is much weaker in the $Ca(OH)_2$, where carbonate is only present as an impurity. These spectra are presented in one graph in Chart 20. FT-IR spectra of HGMs, CaHGMs from two concentrations of $Ca(OH)_2$, and $Ca(OH)_2$ and Chart 21. FT-IR spectrum of HAP-HGMs. The FT-IR spectrum of HAP-HGMs is dominated by a large peak in the region corresponding to the phosphate functional group in the region around 1100

cm^{-1}, with a smaller peak between 1600 – 1500 cm^{-1}, corresponding to a carbonyl C=O functional group, assumed to be from a small amount of calcium carbonate remaining in the sample. The very broad shallow peak between 3400 – 3200 cm^{-1} corresponds to a small amount of water in the sample. The assignment peak frequencies are contained in Table 65. The frequencies associated with various functional groups in the CaHGMs and the HAP-HGMs.

Table 65. The frequencies associated with various functional groups in the CaHGMs and the HAP-HGMs.

Freq cm-1	**Functional Group**
3400 - 3200	O-H Stretching
2967	C-H Stretching
1800 - 1600	C=O stretching vibration
1300 -750	Si-O-Ca broad stretching vibration
1200 - 1100	Phosphate stretching vibration
1130 - 1000	Si-O-Si stretching, band becomes broader as silicon chain gets longer
940 - 990	$CaSiO_3$
875	$CaSiO_3$
804	Si-O symmetric stretch
710	Si-O symmetric stretch
609	Ca-O bond

Chart 20. FT-IR spectra of HGMs, CaHGMs from two concentrations of $Ca(OH)_2$, and $Ca(OH)_2$.

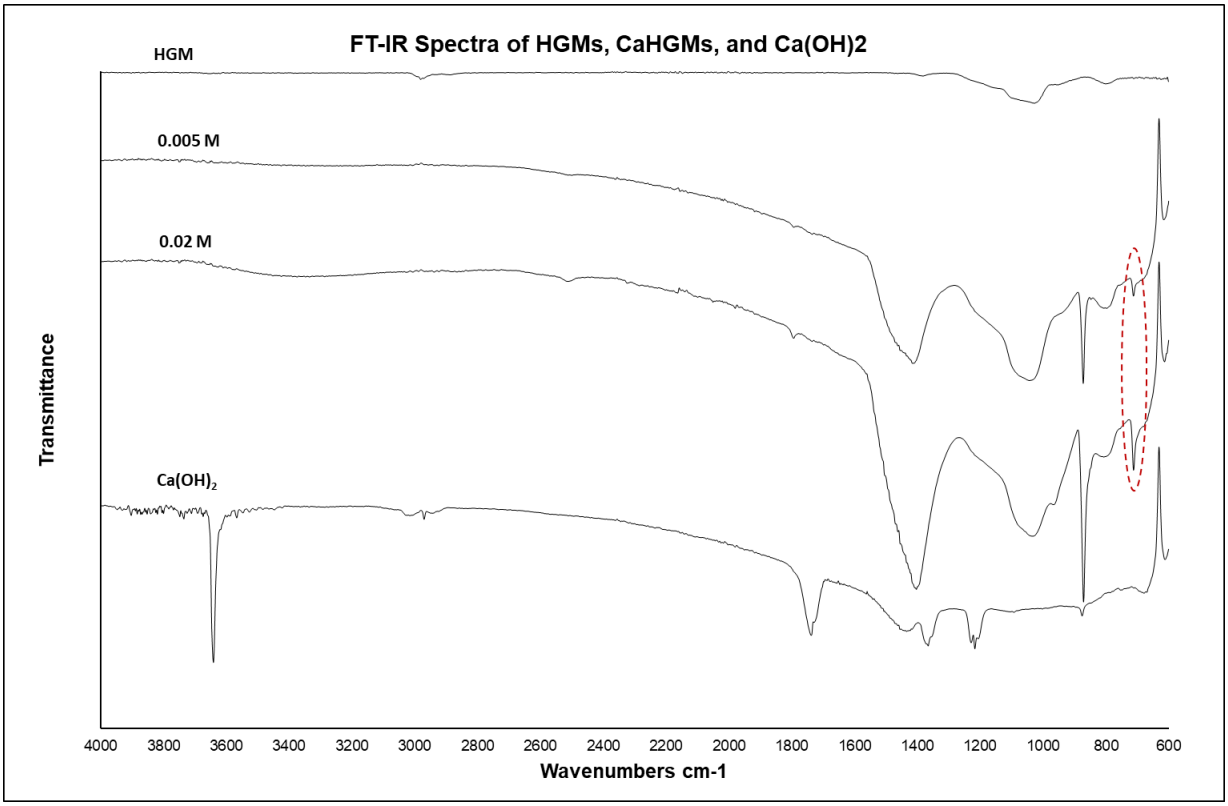

Chart 21. FT-IR spectrum of HAP-HGMs.

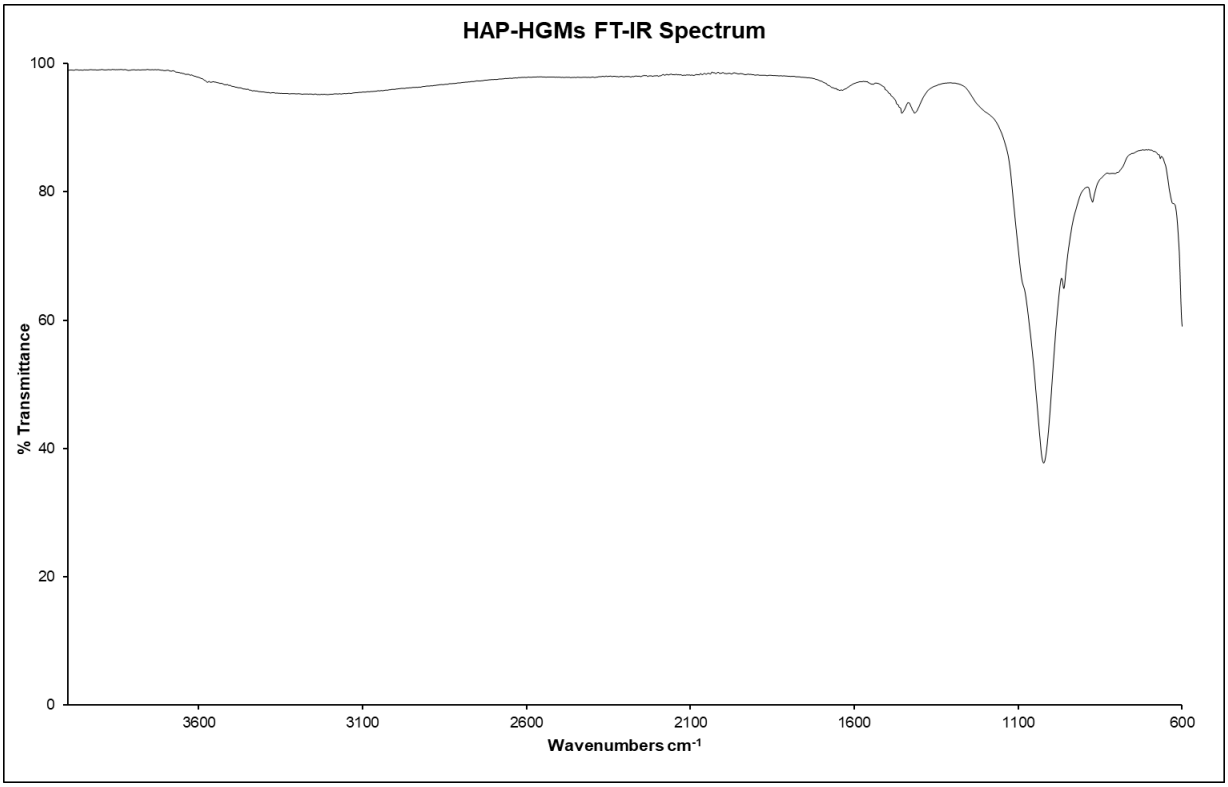

8.6 Thermogravimetric Analysis – HAP-HGMs

The TGA graph of HAP-HGMs shows a steady rate of mass loss until approximately 175 °C, which is generally associated with the loss of water. It is assumed that the water was locked into the lattice of the HAP portion of the HAP-HGM during the formation of the HAP component as HAP was formed at ambient temperature using chemical precipitation with water as the solvent. The loss of water in this step represents a 6.9% mass loss. From 175 °C onwards, the rate of mass loss occurs at a slower rate and is steady until the temperature reaches the range of 500 – 575 ° C, at which point the TGA curve becomes shaky, indicating gas escaping form the sample. The shaky portion of the curve may be due to the changing pressure on the TGA balance plate as gas escapes. The thermal decomposition point of calcium carbonate occurs at around 650 °C, and as there is no sudden mass loss at this point, it can be assumed that there is no significant component of calcium carbonate in the HAP- HGMs. The overall mass loss recorded at 797 °C is 13%. This is shown in Chart 22. TGA curve of HAP-HGMs.

Chart 22. TGA curve of HAP-HGMs.

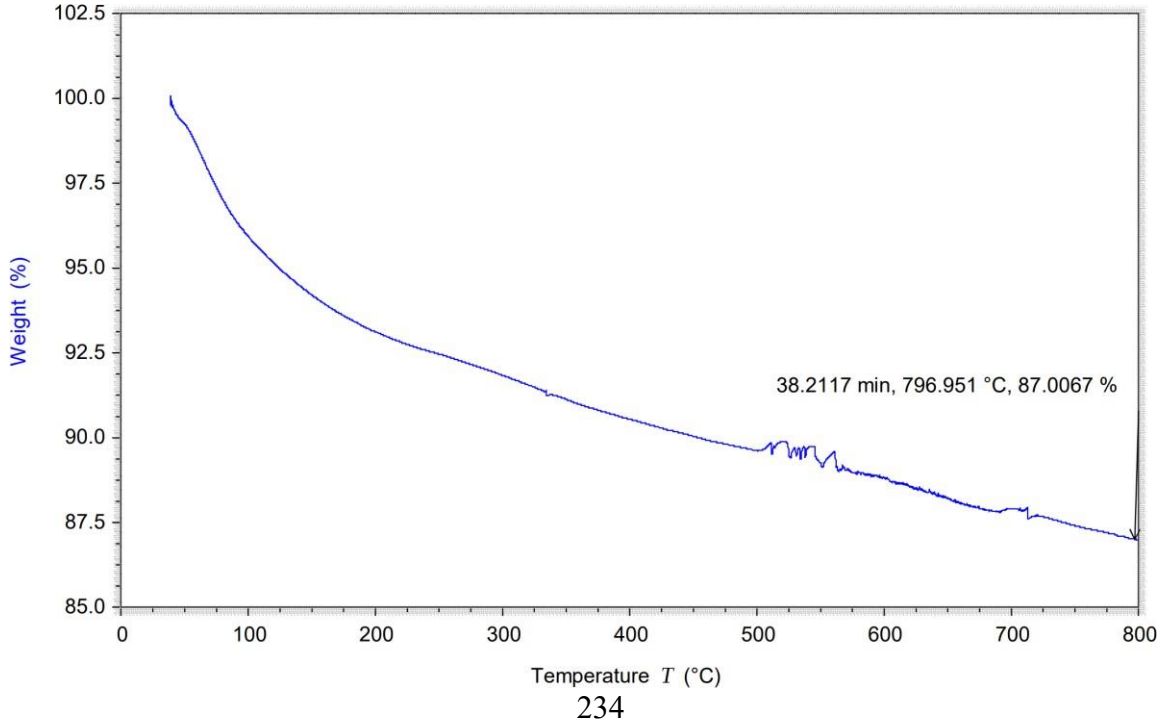

8.7 X-Ray Diffraction Patterns – HAP-HGMs

XRD patterns were obtained of Bio-Oss, a form of hydroxyapatite present in bovine bones, and was used as a benchmark for the comparison of the HAP in HAP-HGMs, as both are formed at ambient temperatures, and therefore show large broad peaks. HAP created using high temperature methods has much sharper narrower peaks, and therefore cannot be used as the benchmark. In Bio-Oss, the dominant peaks are associated with the (121) plane and the (002) plane. Other peaks are identifiable, such as the (310) plane, the (222) plane, and the (123) plane, in both Bio-Oss and the HAP-HGMs.

The main difference between the two XRD patterns in Chart 23. XRD patterns of HAP-HGMs with Bio-Oss for reference is that the peak associated with the (300) plane is present in the pattern of Bio-Oss, but is not distinguishable in the pattern for the HAP-HGMs due to the overlap of the peaks found in this region. Furthermore, the peak associated with the (113) plane is present in the HAP-HGMs XRD pattern, but is not present, or is indistinguishable from the background, in Bio-Oss. Due to the overlap of peaks, it was not possible to determine the average crystallite size from the XRD pattern of either the HAP-HGMs or Bio-Oss. Nevertheless, analysis of the lattice parameters of the HAP component of the HAP-HGMs using TOPAS determined that the lattice parameters were comparable to Bio-Oss, with a = b = 9.42 for the HAP-HGMs, while a = b = 9.39 for Bio-Oss, indicating a slight elongation in the a and b direction. In contrast, the lattice parameter c was the same for the HAP-HGMs and Bio-Oss. The cell volume was also similar for the HAP-HGMs and Bio-Oss, at 529.1 $Å^3$ for the HAP-HGMs, and 525.6 $Å^3$ for Bio-Oss. Overall, the lattice parameters indicate that the HAP component of the HAP-HGMs is comparable to commercially available Bio-Oss, a form of hydroxyapatite derived from bovine bone. The lattice parameters are listed in Table 66. Lattice parameters for the HAP component of the HAP-HGMs and Bio-Oss for comparison.

Chart 23. XRD patterns of HAP-HGMs with Bio-Oss for reference

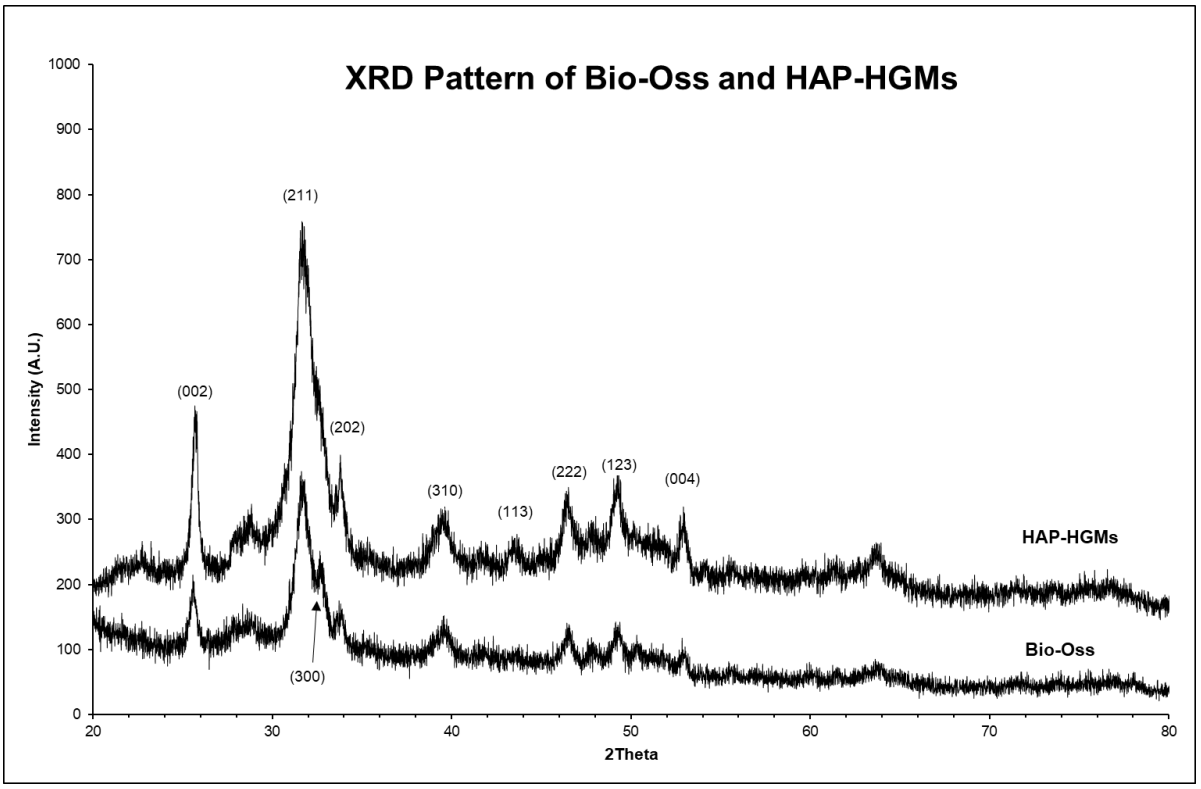

Table 66. Lattice parameters for the HAP component of the HAP-HGMs and Bio-Oss for comparison

Lattice Parameter	**Hydroxyapatite Component of HAP-HGM**	**Bio-Oss** (Xu, 2023)
Cell volume (Å^3)	529.1	525.6
a (Å)	9.42	9.39
b (Å)	9.42	9.39
c (Å)	6.88	6.88
α	90 °	90 °
β	90 °	90 °
γ	120 °	120 °
Space group	$P_{63/m}$	-

The hydroxyapatite derived from treatments of crushed and calcine scallop shells with the dipotassium phosphate solution did not show complete transformation of the calcium carbonate into the calcium phosphate phase of HAP, although peaks associated with the (002), (211), (202) and (004) planes of HAP are present. These peaks are labelled in the XRD Pattern in Chart 24. Hydroxyapatite derived from scallop shell.

Chart 24. Hydroxyapatite derived from scallop shell.

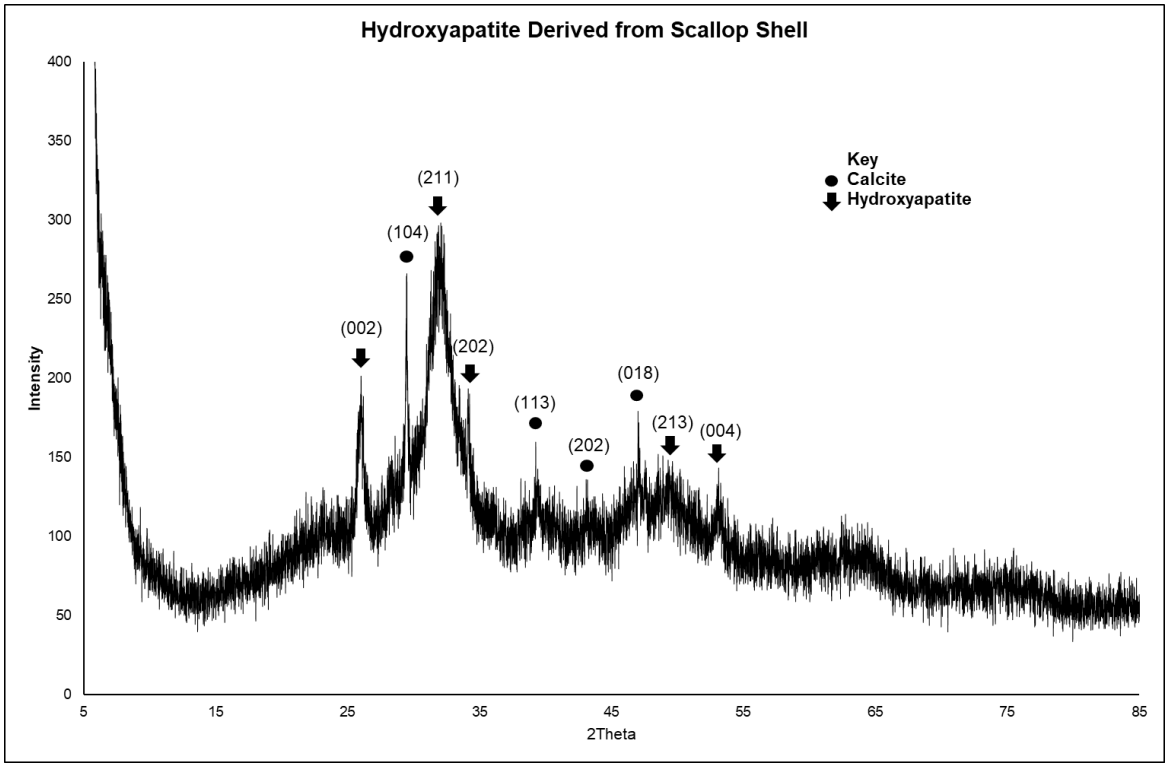

8.7 BET N_2 Adsorption – HAP-HGMs

The specific surface area of the HAP-HGMs was calculated to be 54.7 m^2/g from the BET plot of the HAP-HGMs, which is depicted in Chart 26. BJH plot for HAP-HGMs. The adsorption desorption isotherm in Chart 25. Adsorption desorption isotherm using N2 for the HAP-HGMs, indicating a type III isotherm is characteristic of a type III isotherm, as the uptake of N_2 appears to increase exponentially with increasing pressure indicating that the type of isotherm that best fits this curve is a type III. This indicates weak interaction between the HAP-HGMs and the adsorbed N_2.

There is a type H3 hysteresis loop within the isotherm, shown in Chart 25. Adsorption desorption isotherm using N2 for the HAP-HGMs, indicating a type III isotherm, which can be representative of platelike particles resulting in slit shaped pores. The average pore size can be deduced form the BJH plot, where the majority of the pores are in the range 2 – 11 µm, indicating that the most appropriate classification of pore size is mesopores. These parameters are listed in Table 67. Parameters determined from BET N2 adsorption isotherm for the HAP-HGMs.

Table 67. Parameters determined from BET N_2 adsorption isotherm for the HAP-HGMs.

Parameter	**HAP-HGM**
S_{BET} (m^2/g)	54.7
Mean pore diameter (nm)	22
Total pore volume cm^3/g	0.301

Chart 25. Adsorption desorption isotherm using N2 for the HAP-HGMs, indicating a type III isotherm.

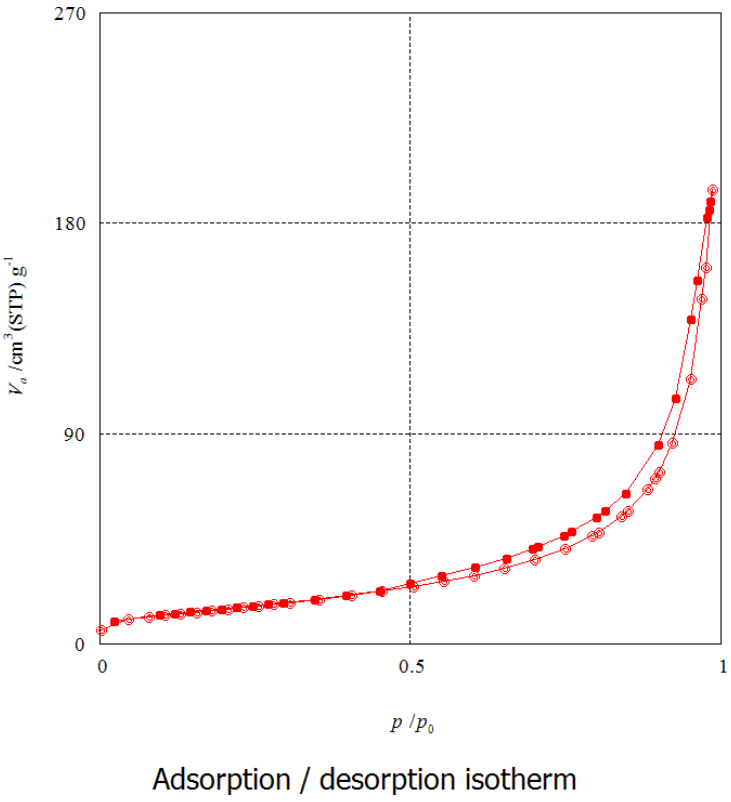

Chart 26. BJH plot for HAP-HGMs.

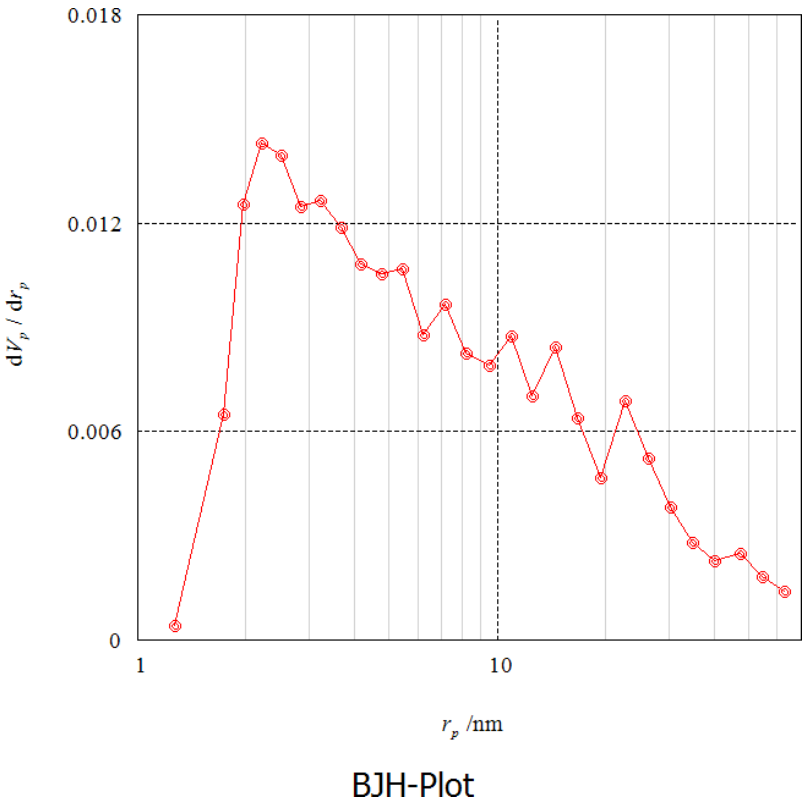

8.8 Chapter Summary

It was discovered that washing the HGMs in calcium hydroxide solution resulted in the growth of calcium carbonate crystals anchored to the surfaces of the HGMs by a small amount of calcium silicate at the boundary of the hollow glass microsphere and the calcium carbonate crystal. In order to form the calcium silicate, the HGMs were treated with a stoichiometric amount of calcium hydroxide designed to add calcium to the HGMs resulting in a composite with a percent composition of calcium that is 24%, and therefore comparable to bioglass. XRD analysis using TOPAS revealed the constitution of the crystals included a small amount of calcium silicate (0.6%), and crystallized calcium hydroxide (3.4%), while calcium carbonate was the major constituent of the crystals, forming 96% of the crystals.

Given that calcium carbonate could be grown on the HGMs directly, and the hollow calcium carbonate microspheres produced were fragile and easily destroyed by mechanical action, it was decided that the most resource efficient route towards growing hydroxyapatite on the HGMs would be to combine the washing of the HGMs with the growth of calcium carbonate on their surfaces by washing the HGMs in calcium hydroxide solution. This method decreases the number of reagents required for the synthesis of hydroxyapatite coated HGMs, while also ensuring that the surface area of the hydroxyapatite produced is high, as chemical precipitation produces hydroxyapatite with the highest surface area.

The calcium carbonate HGMs (CaHGMs) were investigated to assess how the calcium carbonate was attached to the surfaces of the HGMs. EDX analysis of particles formed at the surfaces of the HGMs to confirm the presence of silicon outside of the radius of the smooth HGMs, which would indicate a reaction was occurring at the surface of the HGMs that involves silicon dioxide. Large protruding crystals in particular were analysed using EDX. FT-IR spectra were obtained for HGMs soaked in solutions of calcium hydroxide with

concentrations of 0.02 mol dm^{-3} and 0.005 mol dm^{-3}, in order to search for peaks associated with calcium silicate. Finally, XRD patterns were obtained of the CaHGMs, which were further analysed using TOPAS software in order to confirm if any calcium silicate was present, and the relative proportion of calcium silicate quantified using TOPAS.

This intermediate product – calcium carbonate hollow glass microspheres "CaHGMs" – was then converted into hydroxyapatite by soaking the CaHGMs in dipotassium hydrogen phosphate solution over 5 days at alkaline pH. This results in the calcium carbonate component of the CaHGMs being transformed into hydroxyapatite, and the product is a material composed of silicon dioxide and hydroxyapatite chemically bonded together, named HAP-HGMs in this work. This means that the hydroxyapatite cannot be easily dislodged – which would be possible if the hydroxyapatite was just a coating. Therefore, a composite material consisting of silicon dioxide hollow glass microspheres (HGMs) and hydroxyapatite has been formed.

The XRD pattern of the HAP-HGMs is comparable to the XRD pattern of commercially available HAP derived from bovine bone, called Bio-Oss. The lattice parameters of the HAP-HGMs and Bio-Oss are similar, with a slight elongation along the a and b direction present in the HAP-HGMs relative to Bio-Oss. The cell volume is also very similar, with Bio-Oss being slightly smaller at 525.7 $Å^3$, relative to the cell volume of the HAP in the HAP-HGMs, which is 529.1 $Å^3$.

The specific surface area of the HAP-HGMs was determined from a BET plot and found to be 54.7 m^2/g, which is less than the 79.1 m^2/g SSA of Bio-Oss, however it should be noted that the HAP-HGMs are completely hollow, and SSA of 54.7 m^2/g represents the surface of the 1-2 μm thick crust of HAP formed on the outside of the HAP-HGMs. This means it is not possible to do a gram for gram comparison of the SSA of the HAP-HGMs against the HGMs,

as the HAP-HGMs include far fewer microspheres due to their increased weight. Nevertheless, this measured SSA indicates that the HAP component of the HAP-HGMs has SSA comparable to commercially available Bio-Oss. The adsorption desorption isotherm is characteristic of a type III isotherm which is indicative of a mesoporous material, where the majority of the pores are in the range 2 – 11 μm, and the SSA of the HAP-HGMs was determined using BET and found to be 54.7 m^2/g.

9. Chapter 9 – Synthesis and Characterization of the Titanium Dioxide Component

9.1 Introduction

This chapter contains the results of the experiments used to synthesise and characterize the titanium dioxide component of the combined adsorption/photocatalysis system. The sol gel process was selected to synthesise TiO_2, due to the advantages described in chapter 3, which include ambient reaction temperatures, simple method which exploits wet chemistry, and ability to tune the morphology of the final product, permitting the formation of nanorods. Nanorods were preferred over nanoparticles, as nanorods were predicted to have higher recovery rates, while still offering the benefit of increased surface area and hence increased reactivity relative to standard powder.

The first use of the sol gel method produced titanium dioxide in needle or whisker-type morphology which was interspersed with layers of crystalline carbon. These titanium dioxide whiskers had coalesced around a central point, which contained a single intact sodium chloride crystal. As this method had achieved the desired morphology, this method was repeated with various factors changed in order to better understand the role each reactant or reaction condition played in the synthetic route. These individual experiments were named TNW1 through to TNW10.

The products generated by reactions 1 through to 10 were characterised using optical microscopy, scanning electron microscopy, energy dispersive X-ray spectroscopy, FT-IR, Raman spectroscopy, and X-ray diffraction. Optical microscopy was used to view the products of the sol gel reaction to understand the likely morphology of the products, while SEM was used to obtain high quality images of the titanium dioxide products. EDX was used to confirm the presence of titanium and oxygen and hence define the chemical composition of the titanium

dioxide rods. Due to the low crystallinity of the titanium dioxide, it was initially difficult to confirm the identity of the titanium dioxide component of the products using XRD. For this reason, Raman was also used to characterise the titanium dioxide products, where the peaks of anatase and rutile are distinct and can be used to characterise materials containing anatase and rutile.

9.2 Reaction Conditions for Titanium Dioxide Synthesis

The parameters of the sol gel reaction were adjusted in order to improve understanding of the role each reactant played in the reaction, and how adjusting a given parameter could affect the morphology of the final product. The parameters that were adjusted were: heat source, ratio of ethylene diamine to ethylene glycol, ratio of the titanium alkoxide to water, identity of the chloride salt, and identity of the alkoxide itself. The amounts of the reagents used are included in Table 68. Reaction conditions of various alkoxide hydrolysis reactions used to produce TiO2.

Table 68. Reaction conditions of various alkoxide hydrolysis reactions used to produce TiO_2.

No.	Variable	Salt	Vol Ethylene Diamine	Vol Ethylene Glycol	Vol Alkoxide	Vol H_2O	Curing
1	Heat Source – Oven	NaCl	4	16	Titanium tetra - isopropoxide 0.4 mL	0.5	90 °C for 18 hr, then 200 °C for 18 hr
2	Heat source – reflux	NaCl	4	16	Titanium tetra - isopropoxide 0.4 mL	0.5	90 °C for 18 hr, then 200 °C for 18 hr
3	Heat source – autoclave	NaCl	4	16	Titanium tetra - isopropoxide 0.4 mL	0.5	90 °C for 18 hr, then 200 °C for 18 hr
4	Diamine/ Glycol ratio	NaCl	2	16	Titanium tetra - isopropoxide 0.4 mL	0.5	90 °C for 18 hr, then 200 °C for 18 hr
5	Diamine/ Glycol ratio	NaCl	8	16	Titanium tetra - isopropoxide 0.4 mL	0.5	90 °C for 18 hr, then 200 °C for 18 hr
6	Diamine/ Glycol ratio	NaCl	16	16	Titanium tetra - isopropoxide 0.4 mL	0.5	90 °C for 18 hr, then 200 °C for 18 hr
7	Alkoxide/ H2O ratio	NaCl	4	16	Titanium tetra - isopropoxide 0.4 mL	0.25	90 °C for 18 hr, then 200 °C for 18 hr
8	Alkoxide/ H2O ratio	NaCl	4	16	Titanium tetra - isopropoxide 0.4 mL	0.1	90 °C for 18 hr, then 200 °C for 18 hr
9	Alkoxide/ H2O ratio	NaCl	4	16	Titanium tetra - isopropoxide 0.4 mL	0.75	90 °C for 18 hr, then 200 °C for 18 hr
10	Salt	KCl	4	16	Titanium tetra - isopropoxide 0.4 mL	0.5	90 °C for 18 hr, then 200 °C for 18 hr
11	Reagent	NaCl	4	16	0 mL of alkoxide	0.5	90 °C for 18 hr, then 200 °C for 18 hr

9.3 Optical Microscopy – Images of Titanium Dioxide Products

Optical images were captured of the products of the TNW series where possible, and these images are labelled and displayed in Figure 70, Figure 71, Figure 72, Figure 73 and Figure 74. Reactions TNW1, TNW2, TNW4, TNW5 and TNW10 resulted in the formation of TiO_2 micro-rods which would be suitable for the final composite material of TiO_2-HAP-HGMs. In contrast, reactions TNW6, TNW7, TNW8 and TNW9 resulted in samples that were mostly liquid with an insignificant solid component. This means that an excess of ethylene diamine or water, or insufficient water are not favourable conditions for the production of TiO_2 micro-particles. In order to obtain optical microscopy images glass slides were inserted into the reaction mixture after all the reagents had been added and before the reaction vessel was subjected to the curing stages in the oven. The structures the formed in samples TNW1, TNW4, TNW5 and TNW10 were micro-rods of TiO_2 that had coalesced around a central point to form a larger spherical structure with diameters ranging from 200 μm to 800 μm, an example of which is shown in Figure 70. The morphology of the micro-rods would be desirable for coating to the surfaces of HAP-HGMs, however the micro-rods must be prevented from coalescing around a central point, and instead directed to grow on the surfaces of the HAP-HGMs.

Figure 70. Image obtained of TNW1 dried on to glass slide using optical microscopy.

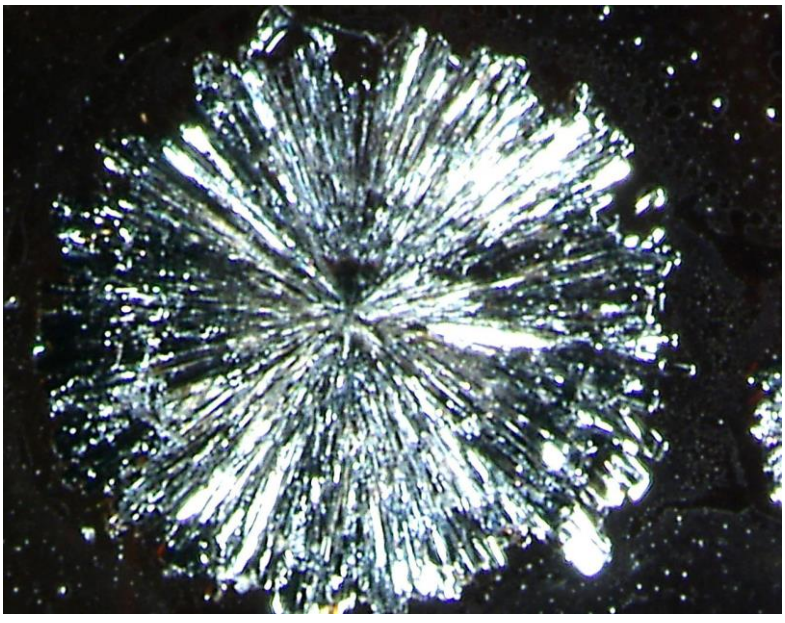

Samples TNW2, TNW6, TNW7 and TNW8 were captured using a digital light microscope as the structures contained within these samples were unable to be clearly resolved using the light microscope. Sample TNW2 produced micro-rods that had coalesced around a central point, but on a much smaller scale than samples TNW1, TNW4, TNW5 and TNW10, indicating the refluxing the reagents together is a more effective way of producing the TiO_2 component of the final material. This can be seen in Figure 71.

Figure 71. Sample TNW2 captured using optical light microscopy.

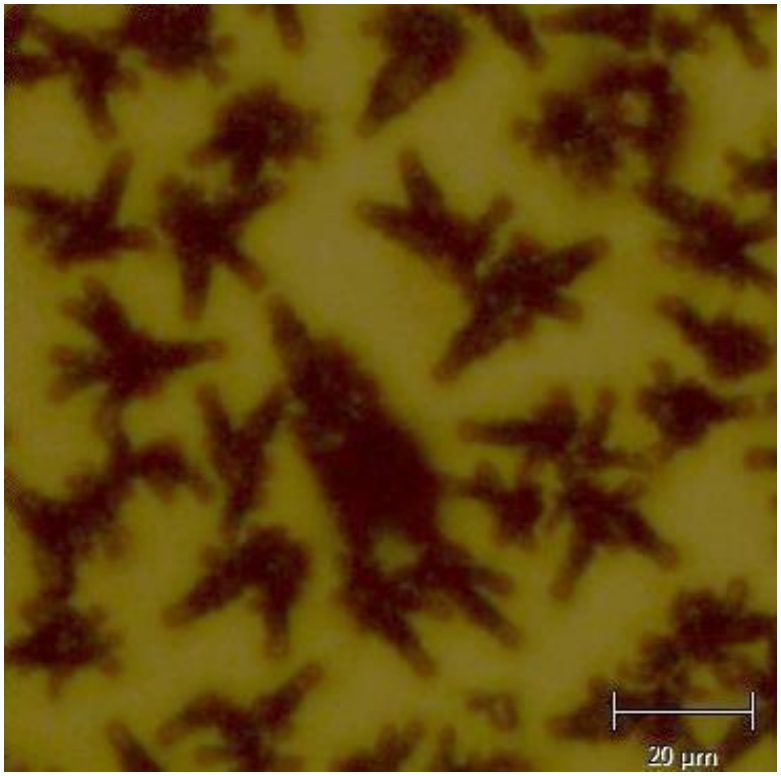

Sample TNW6 formed as a black viscous product with no obvious solid components, however, microscopy revealed the presence of a small number of hexagonal structures approximately 100 μm in diameter, which can be seen in Figure 72. Given the lack of micro-rods of TiO_2, it was included that sample TNW6 was likely not an appropriate synthetic route towards TiO_2, although further analysis was performed using the XRD pattern, Raman shifts and FT-IR spectrum of TNW6 to confirm this.

Figure 72. Sample TNW6, note the hexagonal structure of the crystal.

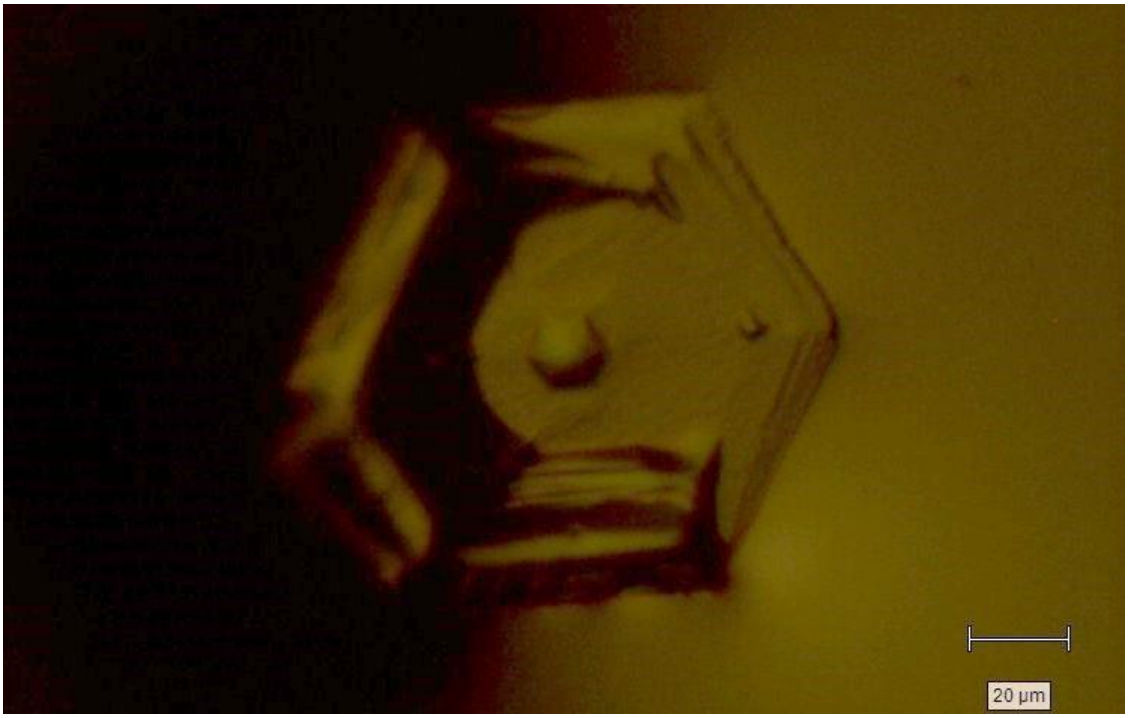

Samples TNW7 and TNW8 used less water than the original TNW1 reaction, and although micro-rods formed, the number of micro-rods was significantly fewer than the micro-rods produced in reactions TNW1, TNW2, TNW4, TNW5 and TNW10. It seems clear than insufficient water was available to fully hydrolyse the titanium tetraisopropoxide, and are therefore not suitable synthetic routes for TiO_2 synthesis. This can be seen in Figure 74 and Figure 73.

Figure 74. Sample TNW7 - the micro-rods formed cross structures.

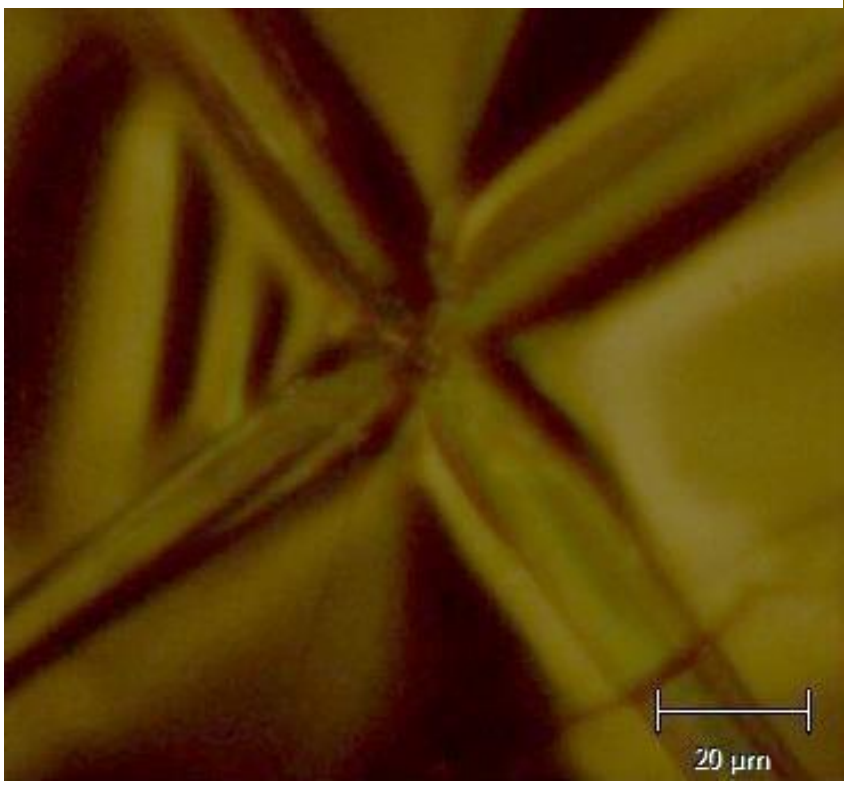

Figure 73. Sample TNW8 - the micro-rods formed much smaller cross structures than TNW7.

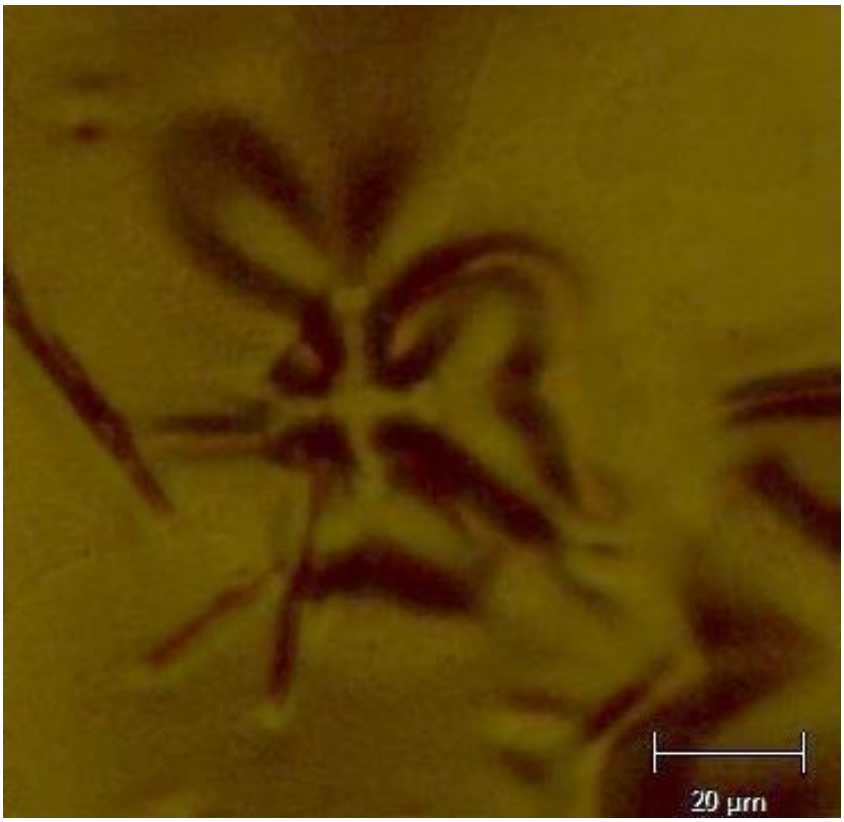

9.4 X-Ray Diffraction Patterns – TNW Series

Sample TNW1

Peaks at 2theta = 19 ° and 23 ° were thought to be due to polymeric polyethylene glycol (Barron, 2003). The peaks associated with halite are particularly well defined due to the high crystallinity of NaCl, which formed large cubic crystals that were the nucleation points for the titanium dioxide whiskers. Halite was present in a highly crystalline form, which is evident from the sharp, tall symmetrical peaks. Halite is missing a peak at 2theta = 56.49 °, which is associated with the *hkl* peak of the (222) plane. The peak at 31.93 °of halite is also displaced from the powder pattern for R070292 which places this peak at 31.73 ° signifying a displacement of 0.2 °. This peak is also elongated significantly along the (200) plane, indicating crystal growth in this direction.

Solid crystalline polyethylene glycol (PEG) is associated with the peaks found at 2theta = 13.61 °, 19.23 °, 23.34°, and an asymmetric peak at 34.65 °. The polyethylene glycol formed a lattice with repeating structure indicating high crystallinity, which is due to the presence of ethylene glycol in high concentrations as the solvent, which polymerised during the curing stages. The peaks associated with anatase in the (101) plane is located at 2theta = 25. 29 ° which is consistent with the literature value of 25.23 °. The rutile peak at 2theta = 27.45 ° is also consistent with the literature, however the peak intensities for anatase and rutile are both low and almost indistinguishable from the background noise. The peaks for anatase and rutile are very small and broad indicating low crystallite size. The dominant TiO_2 peak in this spectrum is the anatase peak at 2Theta = 47.23 °, which corresponds to the (200) plane, indicating elongated growth along this axis. Calculation of crystallite size was performed for this peak, and was found to be 57 nm, however as only one peak was defined enough to perform this calculation, this value of 57 nm is not definitive, but an indication of possible crystallite size and is only useful as a comparison against the crystallite sizes of the other TNW samples. The

XRD pattern of TNW1 is shown in Chart 27.

Chart 27. XRD pattern of TNW1.

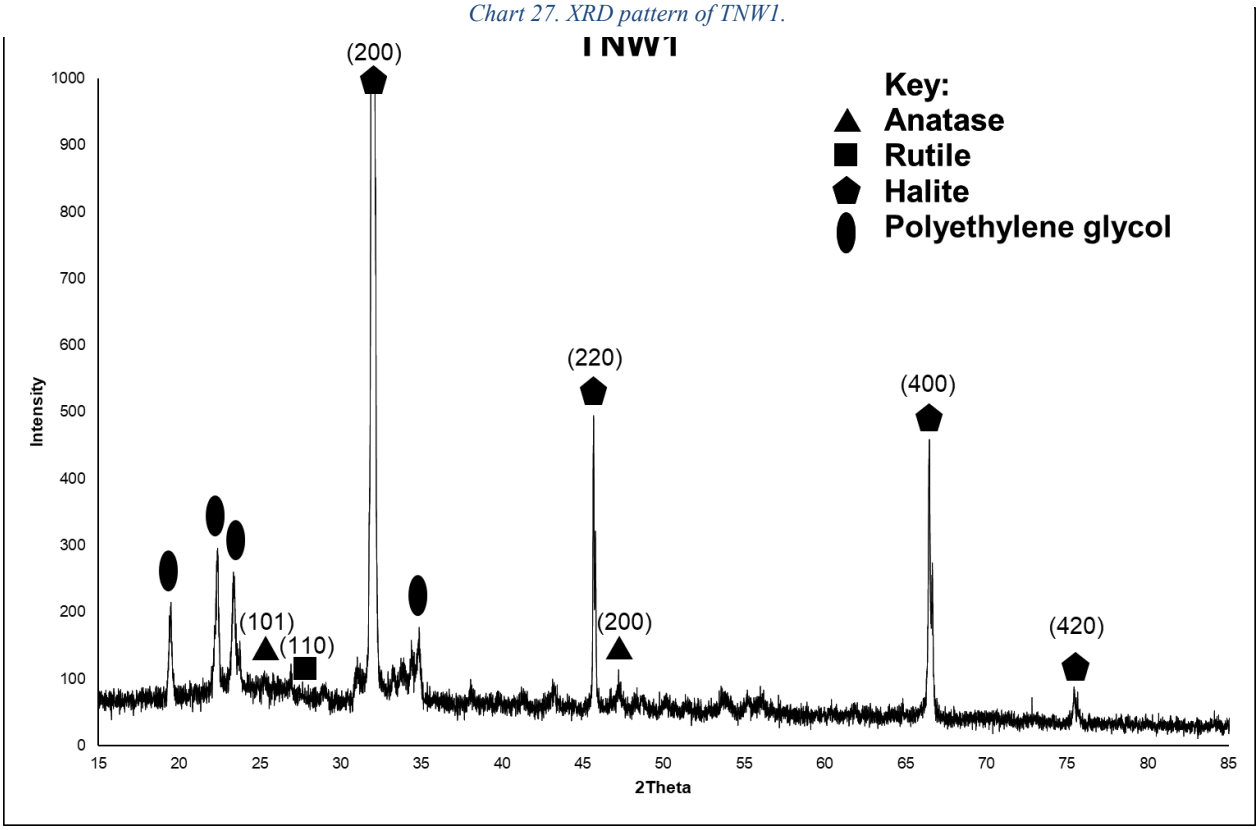

Sample TNW2 (heat source – refluxing the reagents)

Conducting the reaction under reflux resulted in much smaller crystals, and avoided the formation of large amounts of crystalline PEG as peaks associated with PEG in the region 2theta = 19 ° - 24 ° are not large and well defined as in the XRD pattern of TNW1. Instead, a large, broad peak is present in this region, which is associated with amorphous material. This XRD pattern of TNW2 indicates that conducting the reaction under reflux avoids the formation of crystalline carbonaceous by-products, although the large amorphous peak indicates there is still impurities as a result of the ethylene glycol solvent.

Sample TNW2 produced an XRD pattern with a defined rutile peak at 2Theta = 27.5 °, which is close to the literature value of 2Theta = 27.45 ° and is evidence that the hydrolysis of titanium tetraisopropoxide was largely completed resulting in the formation of the rutile polymorph without intervening layers of crystalline carbon or polyethylene glycol. Rutile is the more thermodynamically favourable polymorph of TiO_2. The absence of the asymmetric peak around 2Theta = 34 ° is further evidence that solid polyethylene glycol did not form in the solid product. This means that refluxing the reagents together could potentially be a favourable way forward in the production of TiO_2. The crystallite size of rutile in this XRD pattern was calculated to be 22 nm using the rutile peak at 2Theta = 27 ° and the Scherrer equation. As only one peak associated with rutile was identifiable, this value for crystallite size is not very reliable, and is useful only as a comparison to the other crystallite sizes calculate from other TNW samples. The XRD pattern of TNW2 is shown in Chart 28. XRD pattern of TNW2.

Chart 28. XRD pattern of TNW2.

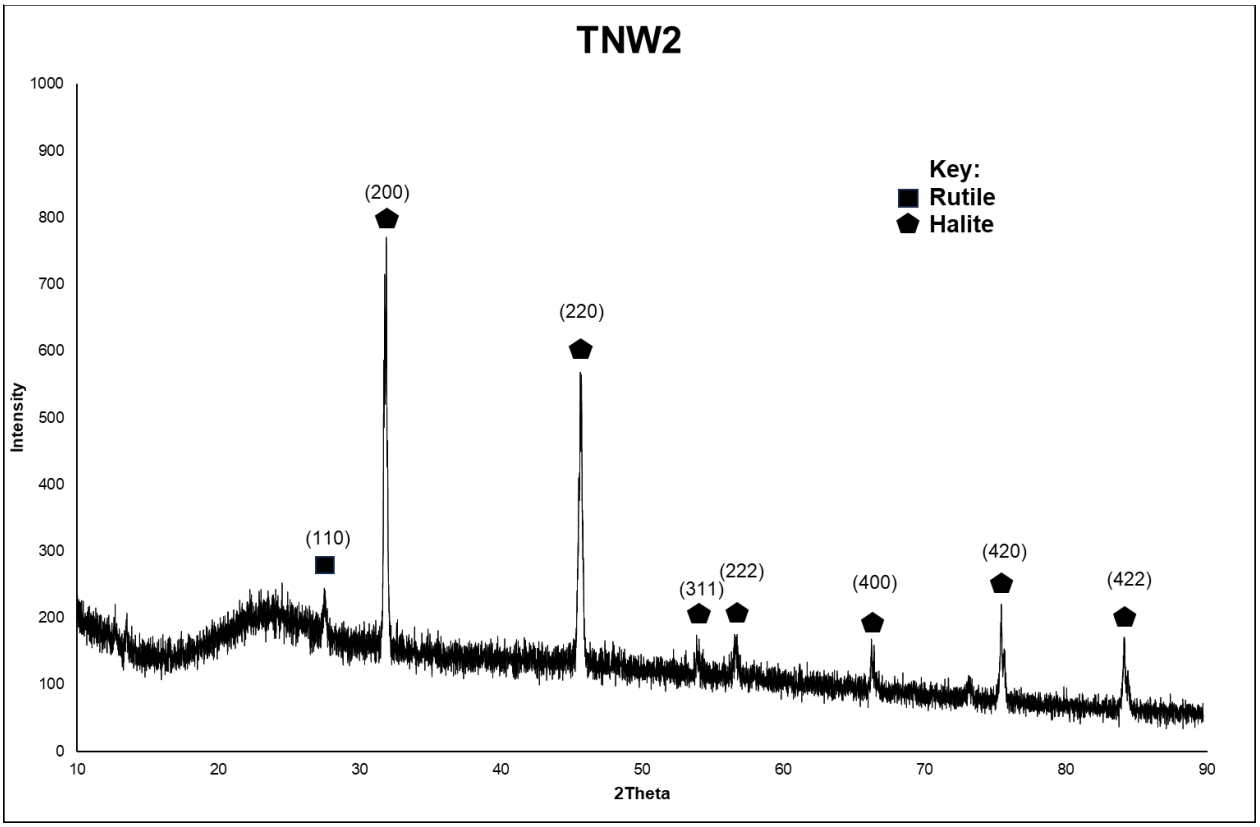

Sample TNW4 (-50% ethylene diamine)

Sample TNW4 was produced using the same reaction conditions as TNW1 with the key difference being that 50% less ethylene diamine was used in the reaction. The peaks characteristic of polyethylene glycol appears in this pattern at 2Theta = 19.3 °, 22.2 °, 23.2 ° and 34.5 °. Halite is present and evident from the peaks at 2Theta = 31.6 ° and 45.4°, although other peaks corresponding to halite are poorly resolved and were not labelled. Peaks associated with anatase are beginning to appear above the baseline but are difficult to distinguish due to noise, nevertheless they can be identified at 2Theta = 25.2 °, 37.9 ° and 47.2 °. Peaks associated with rutile are also beginning to be visible; however, these are also poorly distinguished from the baseline and are not appropriate for further analysis to determine crystallite size. The XRD pattern of TNW4 is shown in Chart 29.

Chart 29. XRD pattern of TNW4.

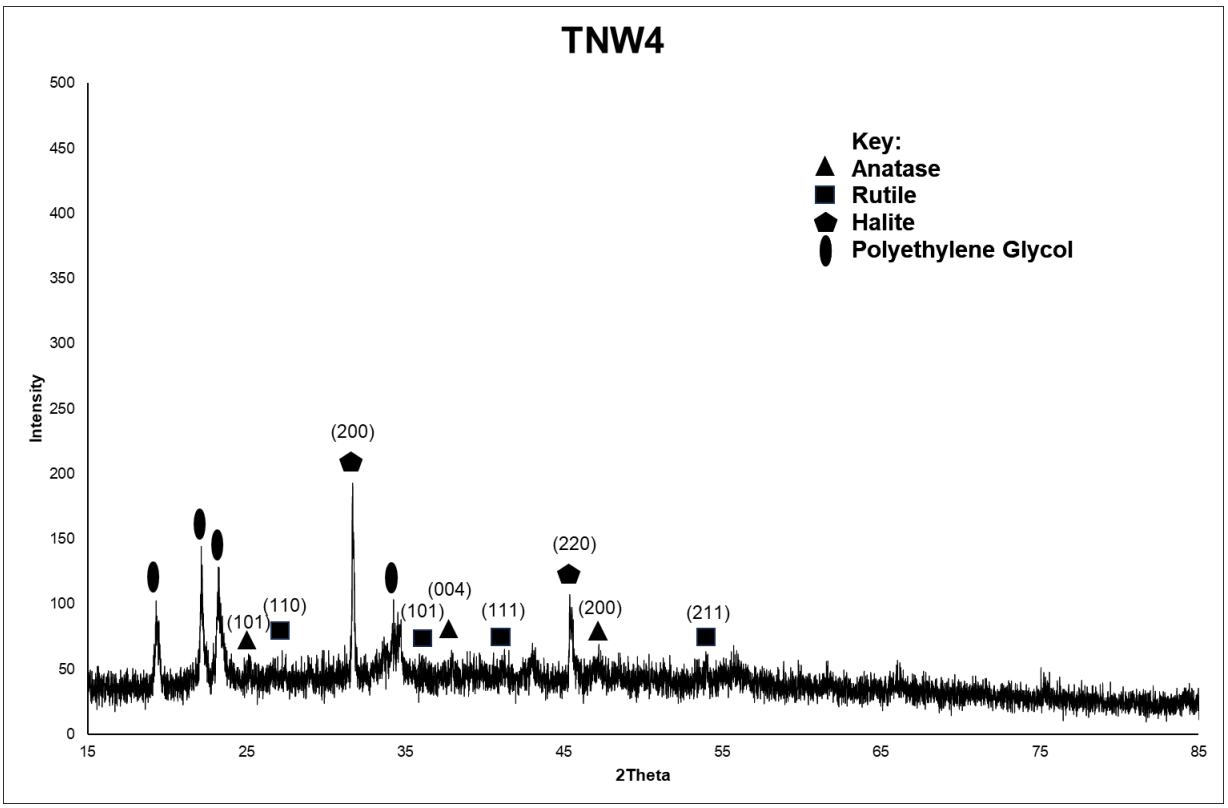

Sample TNW5 (+100% ethylene glycol)

Sample TNW5 was obtained using the same reaction conditions as TNW1, however the volume of ethylene glycol was double that of TNW1. The rutile peak occurs at 2Theta = 27.43 °, which corresponds to the (110) plane and is in close agreement to the literature value of 2Theta = 27.45 °. The average crystallite size of the rutile component was calculated from this peak and the Scherrer equation, and was found to be 33 nm. The smaller crystallite size was assumed to be due to the larger volume of ethylene diamine interacting with the forming TiO_2 structure, where the amine group of the ethylene diamine interacts with the titanium part of the structure and interrupts crystal growth, resulting in a smaller average crystallite size. However, as there was only one rutile peak that was distinct enough from the baseline to perform this calculation for crystallite size, this value of 33 nm is limited in its reliability.

The asymmetric peak associated with polyethylene glycol at 2Theta = 34 ° is not clearly resolved in this sample, however the other peaks associated with polyethylene glycol appear with low intensities at 2Theta = 19.3 °, 22.1 ° and 23.1 °. The peaks associated with halite occur in their characteristic 2Theta values 31.7 °, 45.4 °, 56.5 °, 75.3 °, and 83.9 °. The XRD pattern of TNW5 is shown in Chart 30.

Chart 30. XRD pattern of TNW5.

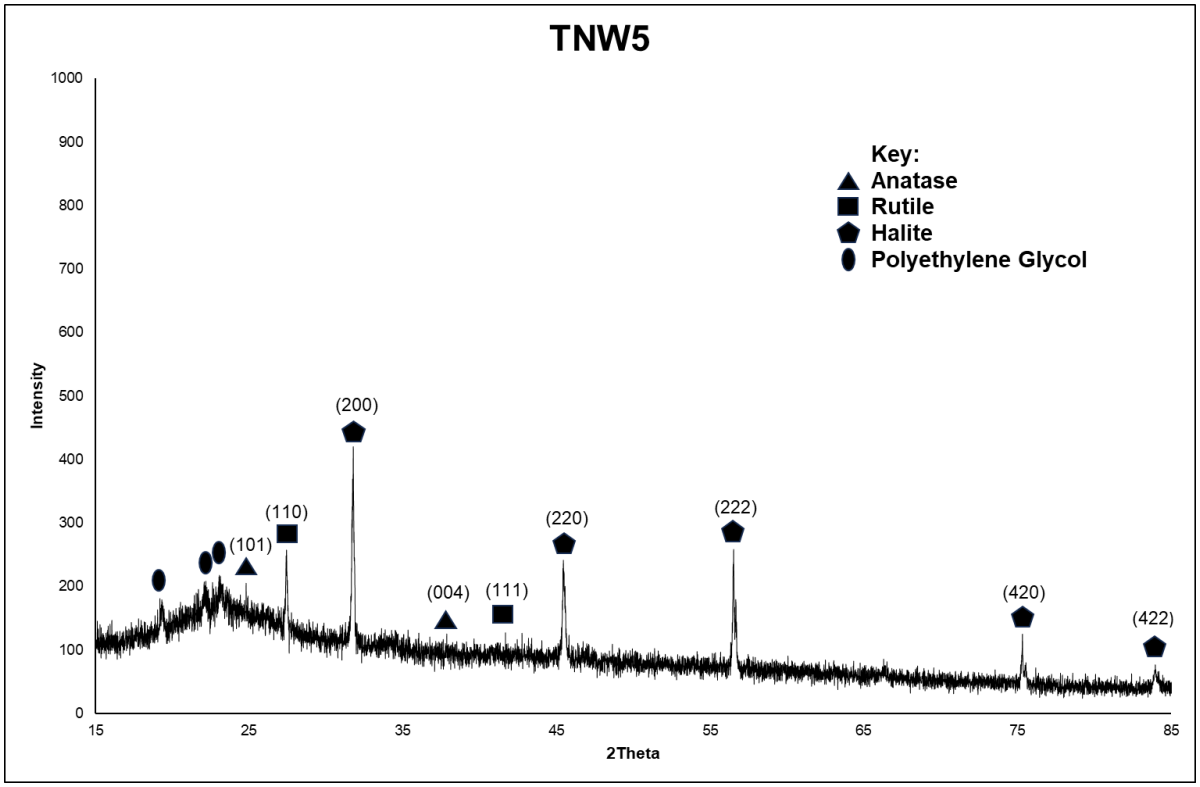

Sample TNW6 (+300% ethylene diamine)

Sample TNW6 was produced using a volume of ethylene diamine of 16 mL in order to understand the effect of ethylene diamine on the reaction. A black sludge had formed after heat treatment, and none of the TiO_2 rod shaped structures that were present in previous samples were visible. Attempts have been made at assigning peaks in Chart 31. XRD pattern of TNW6, however this is to show where peaks that are present in other samples are located, rather than definitively assigning peaks that are difficult to distinguish from background noise. No attempt has been made to calculate crystallite size due to the possibility that assigned peaks are actually background noise. It is likely that the TiO_2 component of this reaction catalysed a polymerisation reaction between ethylene glycol and ethylene diamine to form a polymeric material that became black upon heat treatment. The lack of halite peaks is indicative that there is are no significant crystalline structures within this sample.

Chart 31. XRD pattern of TNW6.

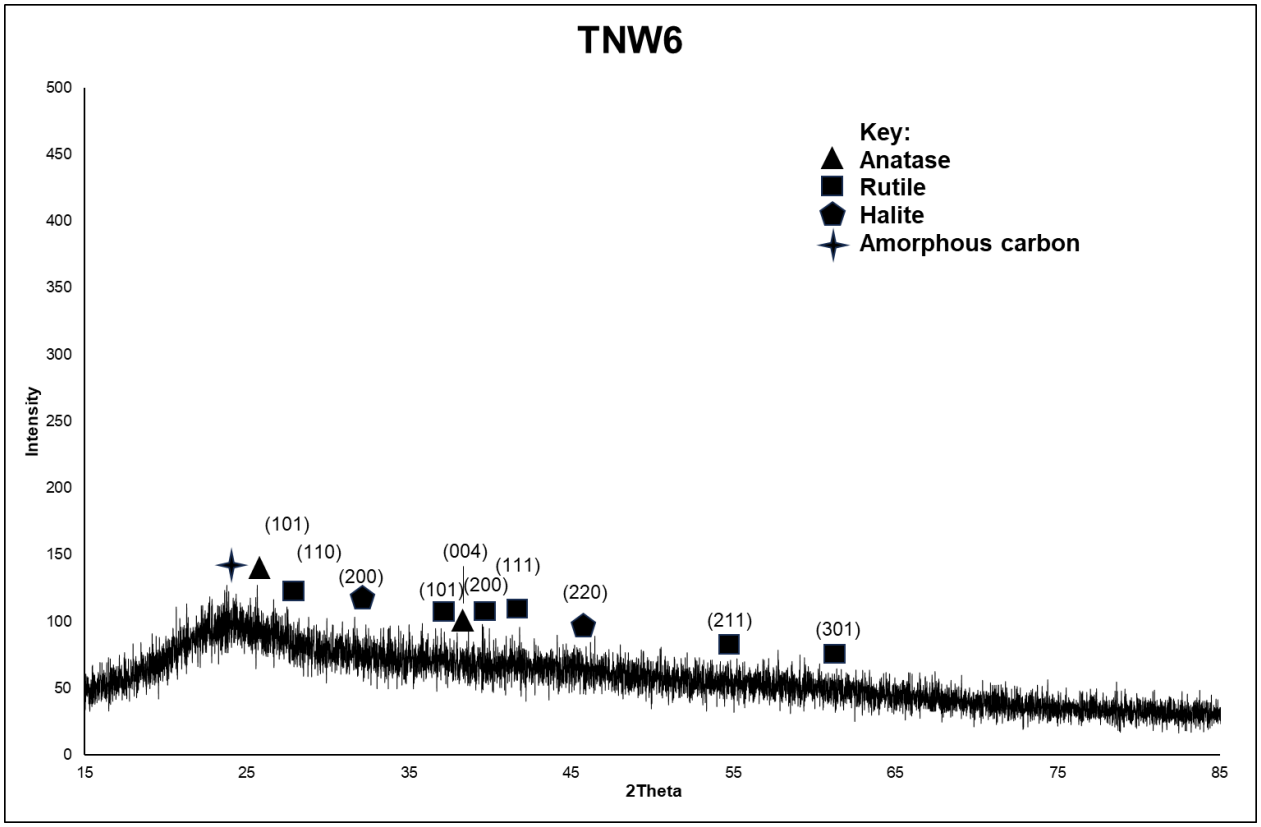

Sample TNW7 (-50% Titanium tetraisopropoxide)

Sample TNW7 contained 50% of the titanium tetraisopropoxide of sample TNW1, and accordingly any peaks associated with titanium dioxide in this XRD pattern are indistinguishable from the background due to noise in the pattern. The peaks associated with polyethylene glycol occur at much lower intensities than sample TNW1, which provide evidence that the presence of titanium dioxide may be catalysing the polymerisation of the ethylene glycol and ethylene diamine solvents into a mass of carbon. Any peaks associated with TiO_2 were not clearly resolved enough to attempt to calculate the average crystallite size. The XRD pattern of TNW7 is displayed in Chart 32. XRD pattern of TNW7.

Chart 32. XRD pattern of TNW7.

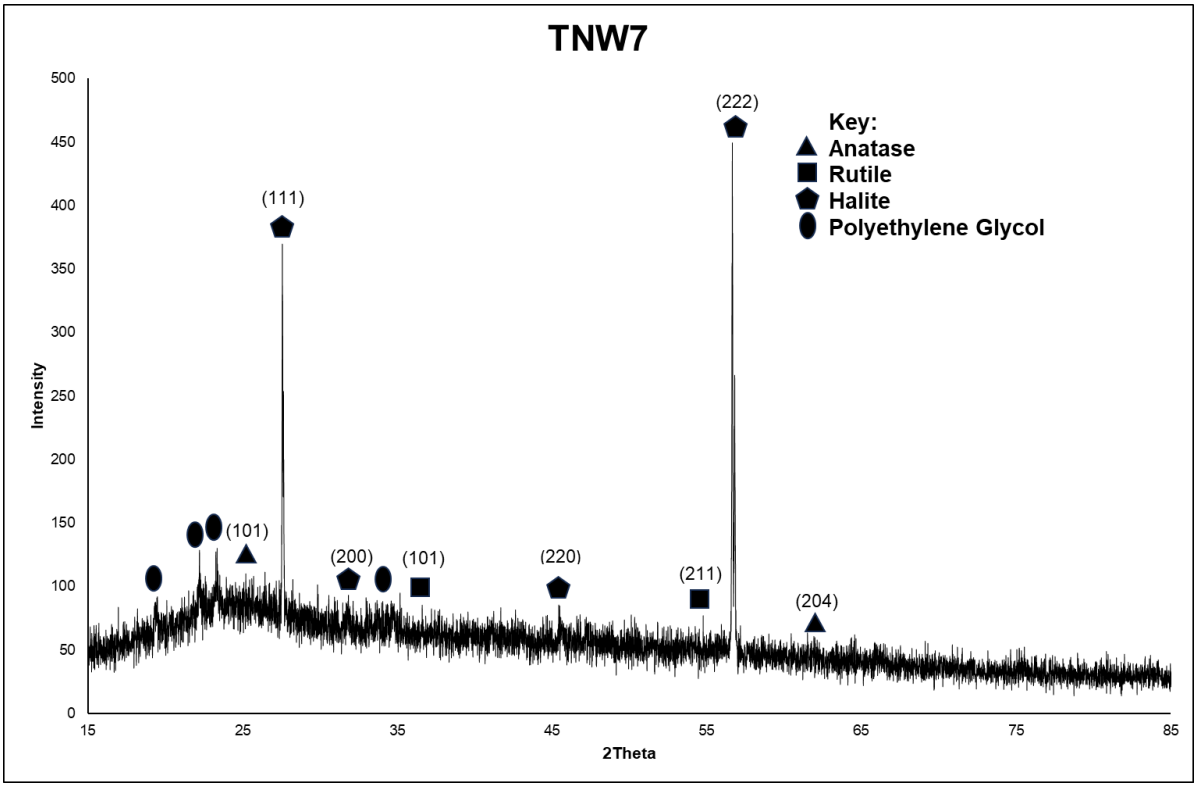

Sample TNW (-80% H_2O)

Sample TNW8 used 80% less water in the reaction, and accordingly there is limited TiO_2 formation. The role of H_2O in the reaction is to hydrolyse titanium tetraisopropoxide, and in the absence of sufficient water the hydrolyse reaction cannot go to completion. Peaks associated with polyethylene glycol were identified at 2Theta = 19. °, 22.1 ° and 23 .1°, indicating the polyethylene glycol may form in the absence of TiO_2, however the intensity of these peaks is low, indicating that TiO_2 may play a role in assisting the formation of polyethylene glycol, as in the absence of $TiO_2$the intensity of the peaks associated with polyethylene glycol is much lower than in patterns where there is a more significant amount of TiO_2. Calculation of average crystallite size was not attempted for this sample, as the peaks associated with TiO_2 are too low and difficult to distinguish from background noise, and hence no reliable value for the FWHM could be obtained. The XRD pattern of TNW8 is displayed in Chart 33.

Chart 33. XRD pattern of TNW8.

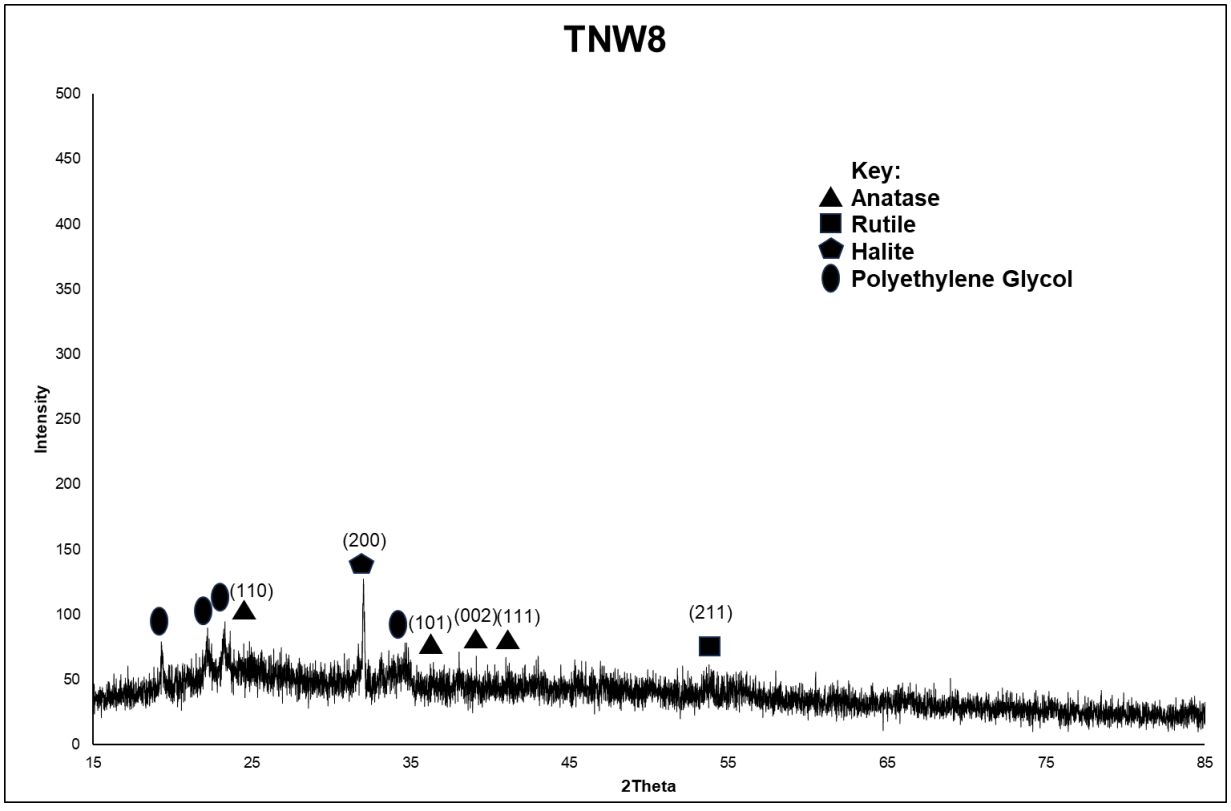

Sample TNW9 (+50% H_2O)

Sample TNW9 used 50% more water than the reaction to produce TNW1, and the rutile peak in this sample is clearly resolved, indicating that the excess water hydrolysed the titanium tetraisopropoxide effectively to form TiO_2 in the rutile form. The effect of additional water in the reaction also appears to have hindered the formation of the polymerised carbon, as there are no identifiable peaks belonging to polyethylene glycol or crystalline carbon in this XRD pattern. The rutile peak occurs at 2Theta = 27.4 °, which is in close agreement to the literature value of 27.39 °, representing the (110) plane. The average crystallite size of rutile in this sample was calculated from the (11) peak at 2Theta = 27.41 ° to be 43 nm using the Scherrer equation. However, as there was only one rutile peak available for this calculation, this is not a definitive calculation, and its value lies in its consistency with the similar crystallite sizes calculated for other TNW samples. This is shown in Chart 34. XRD pattern of TNW9.

Chart 34. XRD pattern of TNW9.

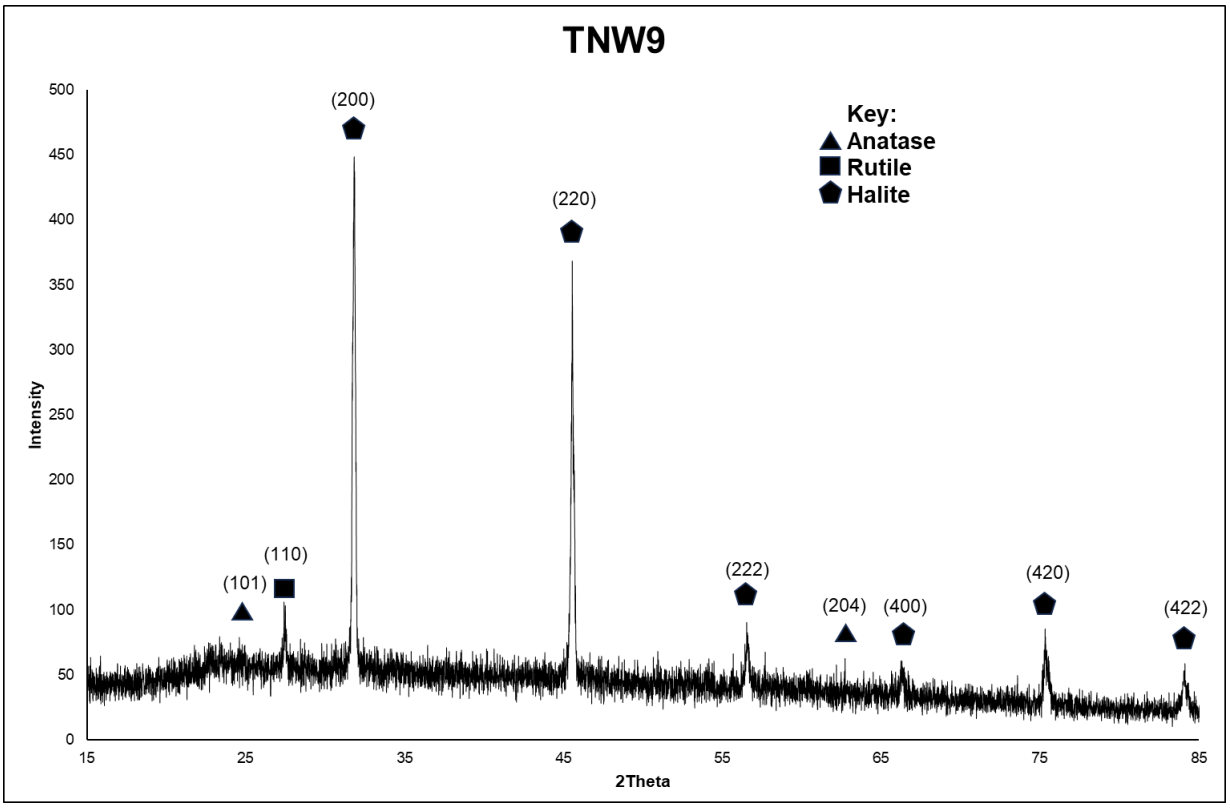

Sample TNW10 (KCl used as the salt)

Sample TNW10 was obtained using the same reaction conditions as TNW1, however the NaCl salt used in TNW1 was replaced with KCl in TNW10. Peaks associated with sylvite (KCl) are sharp with high intensities relative to the other components of the sample. The characteristic peaks of polyethylene glycol are present at 2Theta = 19.3 °, 22.1 °, 23.1 ° and the asymmetric peak occurs around 2Theta = 34 °. There is limited evidence for rutile as the two possible peaks corresponding to rutile are barely distinguishable from the baseline, although the presence of rutile 2Theta = 27.4 ° indicates that rutile is possibly forming. Peaks associating with anatase are visible although small, at 2Theta = 25.3 ° (101), 38.5 ° (112), 47.9 ° (200), 53.8 °, (105), although this last peak is overlapping with another anatase peak at 54.9 ° (211) of the same intensity. The TiO_2 formed is elongated in the (112) plane, as this peak occurs at a much lower intensity in the literature (7% I/I_0) when compared to TNW10 (81%). This effect may be due to the presence of the KCl salt acting as a nucleation point for the growth of the TiO_2 crystals. The role of the salts as nucleation points is discussed in more detail in the EDX section of this chapter. The average crystallite size of the anatase TiO_2 component of TNW10 ranges from 41-43 nm, calculated using the Scherrer equation applied to the (101), (112) and (200) peaks. The XRD pattern of TNW10 is shown in Chart 35.

Chart 35. XRD pattern of TNW10.

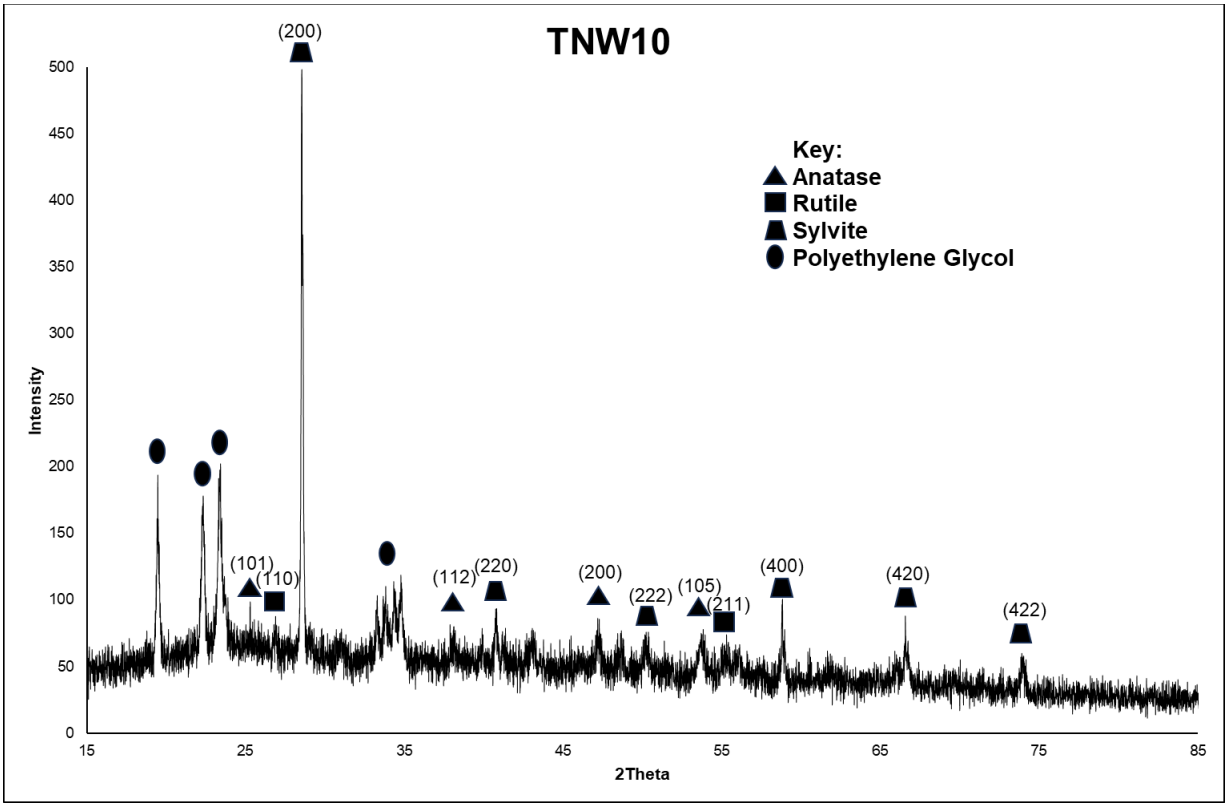

Confirmation of TiO_2 in TNW series

The products of TNW4 were calcined to 1200 °C and an XRD pattern obtained in order to confirm the presence in the TNW samples. In previous samples in Charts 1 – 9 it was not always possible to distinguish peaks associated with TiO_2 – which was expected as the samples had not been annealed in an effort to produce a low energy method for the synthesis of TiO_2. High temperatures are required to reduce the effects of defects in the lattice structure resulting in peak broadening, while also promoting the growth of larger crystallites within the sample.

The XRD pattern of the residue of sample TNW4 after calcination to 1200 °C shows clearly define peaks associated with anatase and rutile, confirming the presence of TiO_2 within the sample. However, as calcination at 1200 °C is an energy intensive process, this was only repeated to demonstrate the existence of TiO_2 in the other TNW samples. These XRD patterns are shown in Chart 36.

Chart 36. XRD patterns showing reagent, TNW4, and TNW4 after heating showing sharp peaks associated with anatase and rutile.

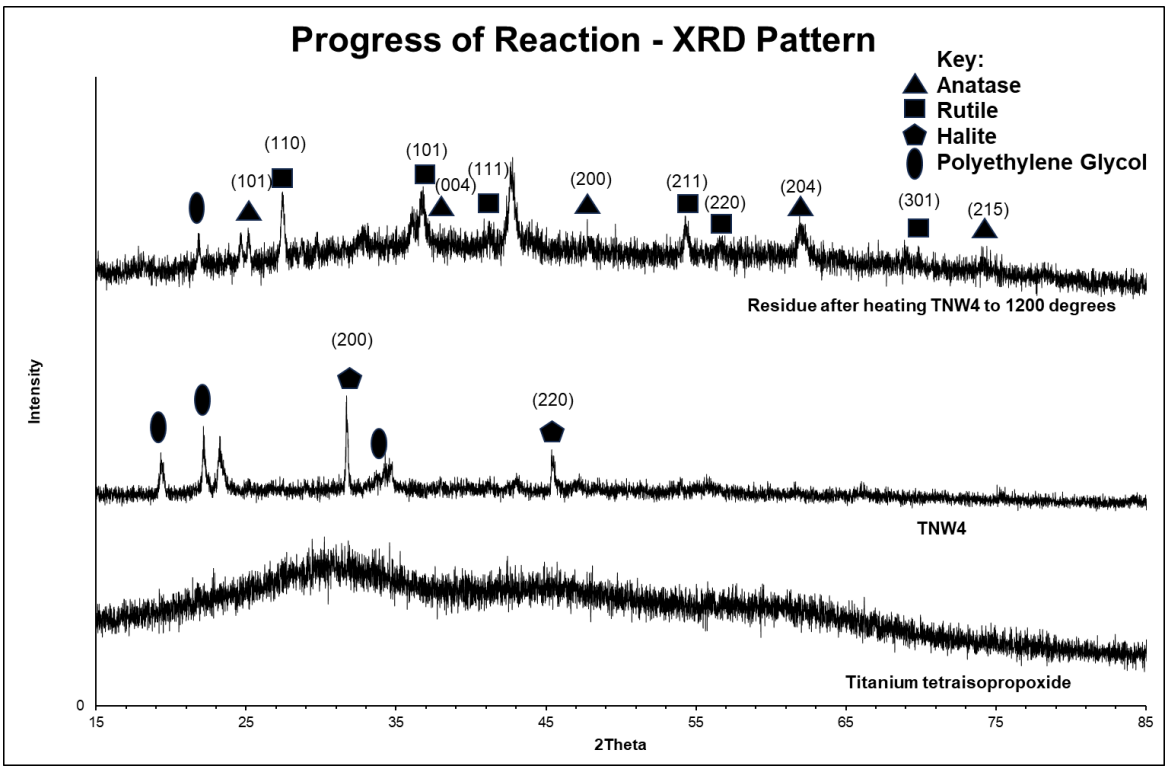

Reaction in Absence of Titanium Tetraisopropoxide

The reaction was repeated in the absence of titanium tetraisopropoxide, and there was no evidence for the formation of polyethylene glycol, although two peaks associated with amorphous carbon formed. This indicates that TiO_2 in the previous TNW series was catalysing the polymerisation of ethylene glycol into polyethylene glycol. In the absence of TiO_2, polyethylene glycol does not form, as there are no peaks at 2Theta = 19.3 °, 22.1 °, 23.1 ° or around 34 ° in Chart 11. The halite peak at 2Theta = 27.4 ° is visible, and occurs at an intensity that is characteristic of halite. This is shown in Chart 37.

Chart 37. XRD pattern of product of reaction without titanium tetra-isopropoxide.

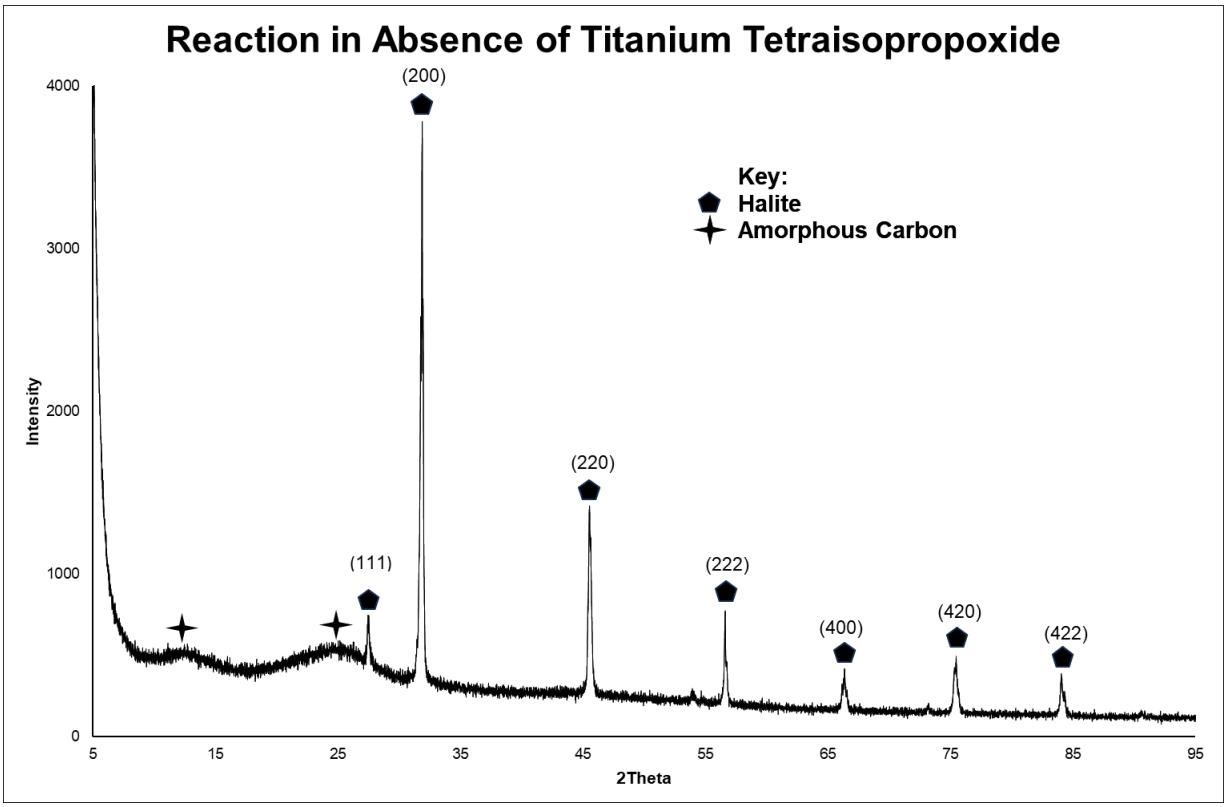

Reaction in Absence of Ethylene Diamine

Performing the reaction in the absence of ethylene diamine produce a material with a highly crystalline polyethylene glycol, with sharp peaks at 2Theta = 19.1 °, 22.1 °, 23.1 ° and the asymmetric peak occurs around 2Theta = 34 °. This indicates that the TiO_2 is catalysing the polymerisation of the ethylene glycol solvent. The TiO_2polymorph that formed produced peaks characteristic of anatase, which is a deviation from the previous TNW series where rutile was the dominant form of TiO_2. Peaks associates with halite do not dominate this pattern, which indicates that halite is not present in significant quantities in its crystalline form. This XRD pattern is shown in Chart 38.

Chart 38. XRD pattern of the product of the reaction obtained in the absence of ethylene diamine.

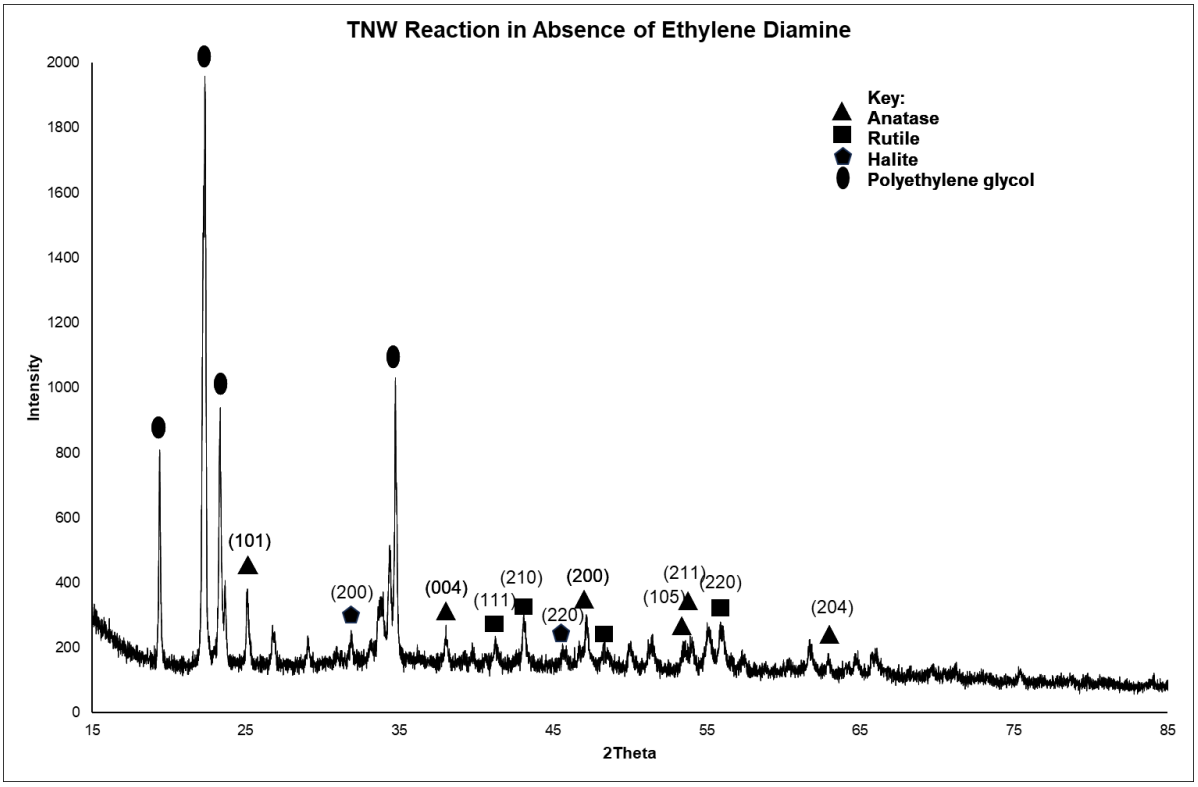

9.5 FT-IR spectroscopic analysis of TNW series

FT-IR analysis of the TNW samples confirmed the presence of significant amounts of carbon-hydrogen bonds, carbon-carbon bonds and carbon-nitrogen bonds – all of which were not desirable for the development of a low energy sol-gel route towards the production of titanium dioxide. This means that the preparations that contain low % transmissions at wavelengths associated with C-H, C-O, and N-H are less suitable for the synthesis of TiO_2, due to the presence of impurities. The band associated with Ti-O bonds is difficult to discern, necessitating Raman analysis to explore the TiO_2 component further. The assignment of the various functional groups found in the FT-IR spectra of the TNW samples is contained in Table 69. Wavenumbers of functional groups found in the TNW samples and the spectra are displayed in Chart 39. FT-IR spectra of the TNW samples.

The impurities are evident in the 3600 – 3200 cm^{-1} region which is associated with O-H bonds and N-H bonds, and although the shape and location of this peak is usually associated with water present in a sample, in this case it has been assigned to impurities from the ethylene glycol and ethylene diamine. The C-H bonds present in the sample are evident from the two medium peaks centred around 2950 cm^{-1} and 2800 cm^{-1} are further evidence that impurities from the ethylene glycol and ethylene diamine are present in significant quantities, and the region from 1600 – 600 cm^{-1} is characteristic of carbon chains containing C-C bonds, C-N bonds, C-H bonds and N-H bonds in in stretching, bending and wagging modes.

TNW8 contained the lowest amount of TiO_2 across all the TNW series, and also has the lowest amounts of carbon-based impurities. This may indicate that the TiO_2 in the sample is catalysing the polymerisation of the solvents ethylene glycol and ethylene diamine, resulting in the larger amounts of carbon containing impurities present in the other TNW samples. In contrast, sample TNW6 which contained the highest volume of solvents produced an FT-IR spectrum that contained the among the highest amounts of carbon-based impurities. TNW2 had among the

lowest amounts of carbon containing impurities, further indicating that the reflux method of heating is the most favourable for the development of a sol-gel synthetic route towards TiO_2. However, the continued presence of carbon impurities means that this route has not yet been fully optimised, and requires further work.

Table 69. Wavenumbers of functional groups found in the TNW samples.

Wavenumber cm^{-1}	**Bond**	**Functional Group**
3500 – 3200 (s,b)	O-H stretch, H-bonded	Alcohols
3000 – 2850 (m)	C-H stretch	Alkanes
680 –1640 (m)	–C=C– stretch	Alkenes
1650 –1580 (m)	N–H bend	primary amines
1630	O-H bend	Water
1470 – 1450 (m)	C-H bend	Alkanes
1370 – 1350 (m)	C-H rock	Alkanes
690	Ti-O stretch	TiO_2

Chart 39. FT-IR spectra of the TNW samples.

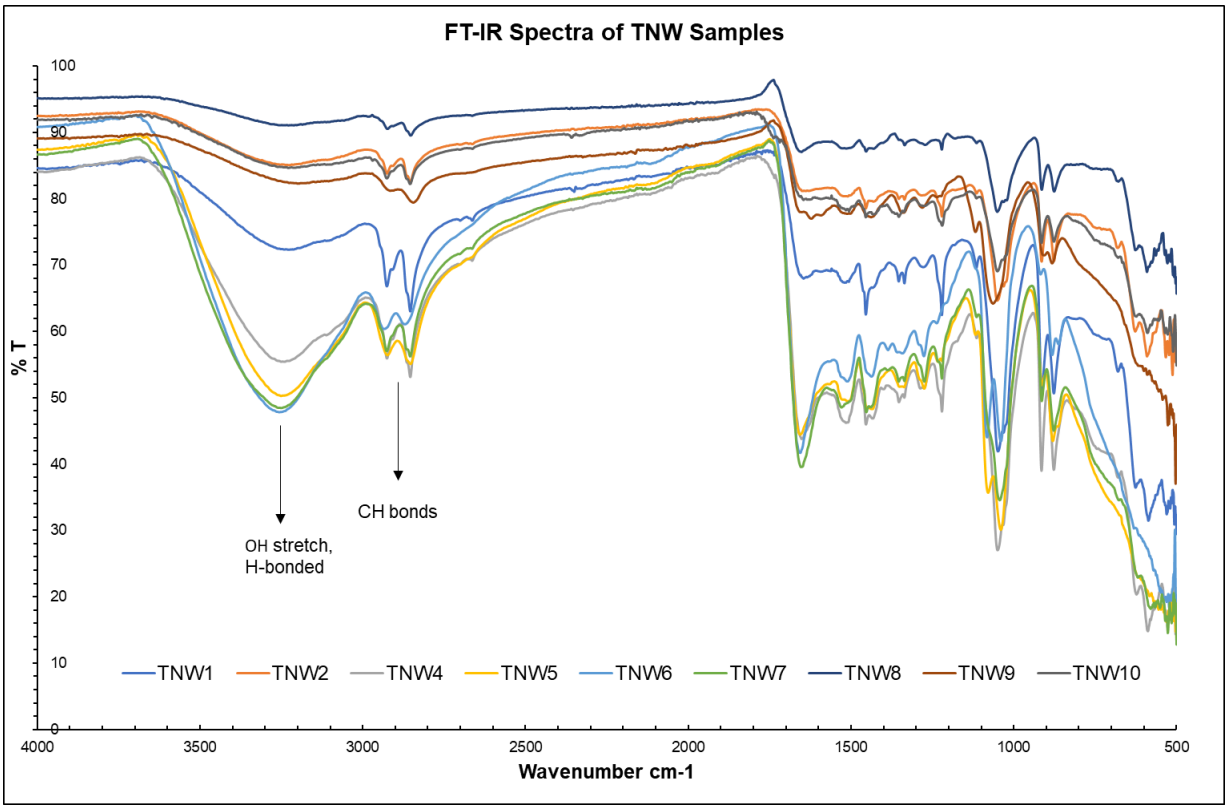

9.6 Raman spectroscopic analysis of TNW series

The shapes of the spectra in Chart 15 are mostly characteristic of rutile, however the values are displaced from the values indicated in Chapter 3 – titanium dioxide, indicating strain on the Ti-O bonds due to the characteristic peaks of anatase and rutile appearing at higher wavenumbers. This is consistent with layers of polyethylene glycol forming in between the titanium dioxide layer, where the crystalline polyethylene glycol encased the titanium dioxide structures, resulting in an interaction between the polyethylene glycol and terminal Ti-O bonds. Some limited evidence for anatase can be seen at 390 cm^{-1}, where a shoulder corresponding to anatase forms on the peak at 430 cm^{-1} which corresponds to rutile. However, the Raman spectrum of anatase is dominated by the E_g peak which occurs at 144 cm^{-1} and is much taller than other peaks, which is not the case for any of the TNW series samples, indicating that anatase is not the dominant TiO_2 polymorph in any of the samples.

The assigned Raman bands for the TNW series correspond to rutile, although the experimentally observed bands occur at slightly higher wavenumbers than those reported in the literature. For example, the B_{1g} band is reported to be at 143 cm^{-1} in the literature, whereas in the TNW samples this value ranges from 150 – 153 cm^{-1}. The Raman bands associated with the multi-photon scattering process occur in a higher range in the TNW samples than in the literature, where the literature value is given at 237 cm^{-1}, whereas the TNW series occurs in the range of 248 – 260 cm^{-1}. Greater agreement is seen for the E_g band where the literature report s value of 430 cm^{-1}, while the TNW series shows band in the same region, from 424 – 434 cm^{-1}. In addition, the A_{1g} for the TNW series also shows greater agreement with the literature, where the range of the report bands in the A_{1g} region ranges from 600 – 610 cm^{-1}, compared to the literature value of 605 cm^{-1}.

These results indicate that rutile is the main form of TiO_2 present in the TNW series, and the slight differences in wavenumbers with the corresponding bands are likely from slight

variations due to the lack of calcination at high temperature (which rutile is generally subjected to before characterisation and analysis. Furthermore, the influence of the layer of carbon that forms from the polymerisation of ethylene glycol may also be causing differences in the interface of TiO_2 and the carbon containing component if the carbon is chemically bonded to the TiO_2. The Raman shifts of the products of the TNW experiments are shown in Chart 40. Raman shifts of all the TNW samples, and the assigned Raman bands are shown in Table 70. Assigned Raman bands found in TNW series Raman Spectra.

Chart 40. Raman shifts of all the TNW samples.

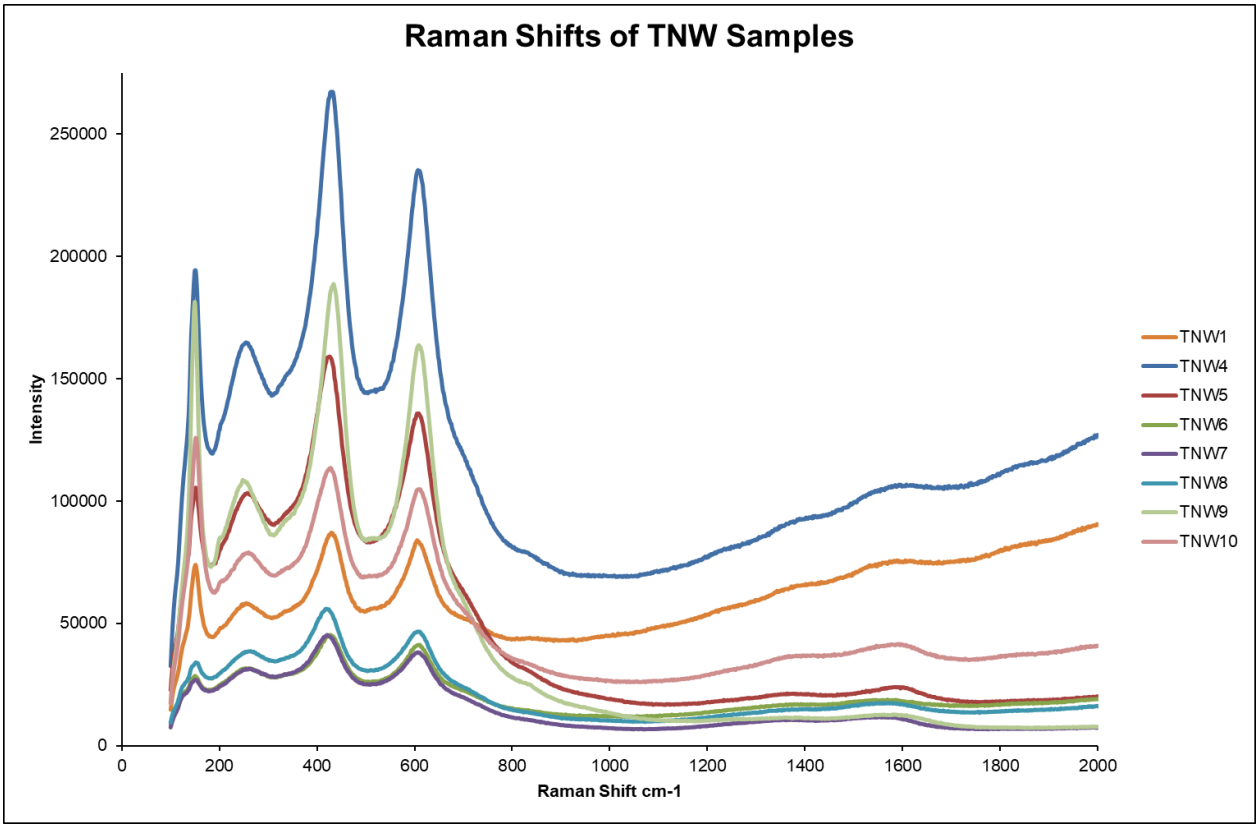

Table 70. Assigned Raman bands found in TNW series Raman Spectra.

	Raman Bands – Rutile cm^{-1}			
	B_{1g}	**Multi photon scattering process**	**E_g**	**A_{1g}**
Literature	143	237	430	605
TNW1	151	255	429	607
TNW2	153	260	424	600
TNW4	151	251	431	608
TNW5	151	253	426	607
TNW6	150	251	427	610
TNW7	150	255	420	607
TNW8	151	260	424	603
TNW9	150	248	434	608
TNW10	151	256	427	605

9.7 Scanning Electron Microscopy of TNW series

Scanning electron microscopy was used to investigate the morphology of the TiO_2 structures formed in the TNW reactions. Samples TNW1 (shown in Figure 75. SEM of the TiO2 rods formed from the TNW1 reaction and Figure 76. End-on view of the ends of the titanium dioxide fibres of TNW1), TNW4, TNW5, and TNW10 were all of micro-rod morphology that coalesced around a central point. Samples TNW6, TNW7, TNW8, and TNW9 had significant quantities of liquid the impeded investigation and were not appropriate for SEM imaging.

Figure 75. SEM of the TiO_2 rods formed from the TNW1 reaction.

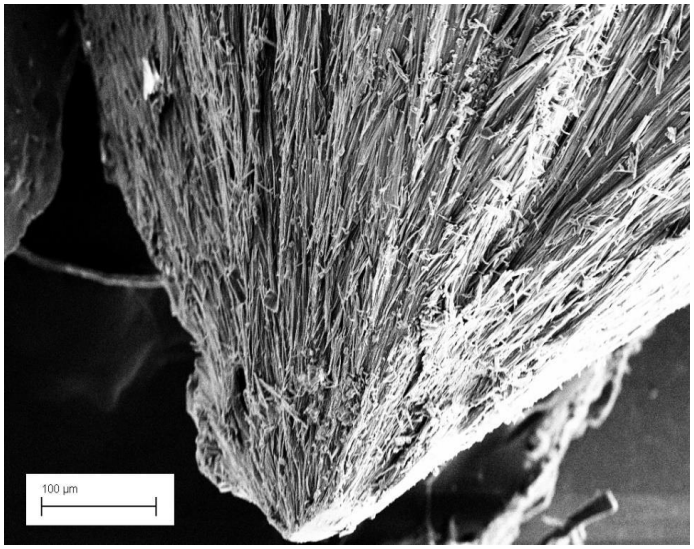

Figure 76. End-on view of the ends of the titanium dioxide fibres of TNW1.

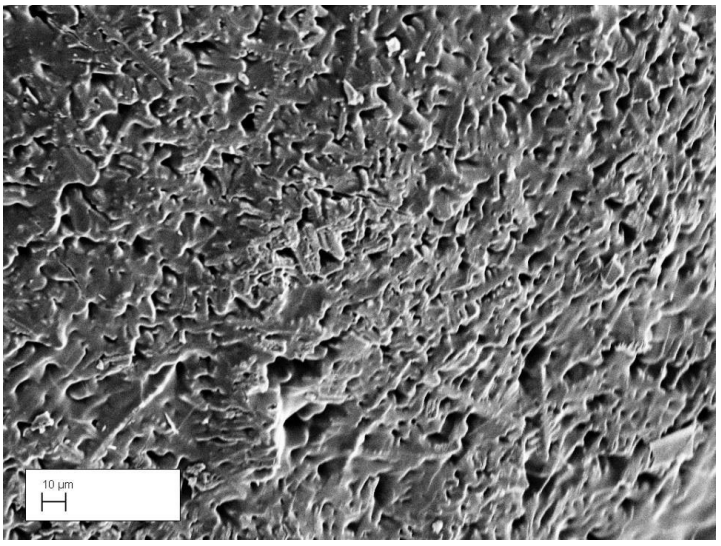

The image in Figure 77. New titanium tetra-isopropoxide with no ethylene diamine is the result of performing the reaction under the same conditions, but this time not using ethylene diamine in the reaction. The products formed have significantly different morphologies, with the crystals formed being much wider and more cuboidal, in contrast to the original synthesis route, which produced crystals that were much longer and thinner, with morphology more similar to whiskers. The cuboidal crystal pictured below is also wrapped in a thin layer of carbon containing material, indicating that the solvent may have still polymerised, resulting in a layer of crystalline carbon encasing the titanium dioxide product. The conclusion that can be made from this image is that ethylene diamine plays a key role in directing the growth of the TiO_2 crystals along a 1-dimensional axis, resulting in much thinner rods of TiO_2.

Figure 77. New titanium tetra-isopropoxide with no ethylene diamine.

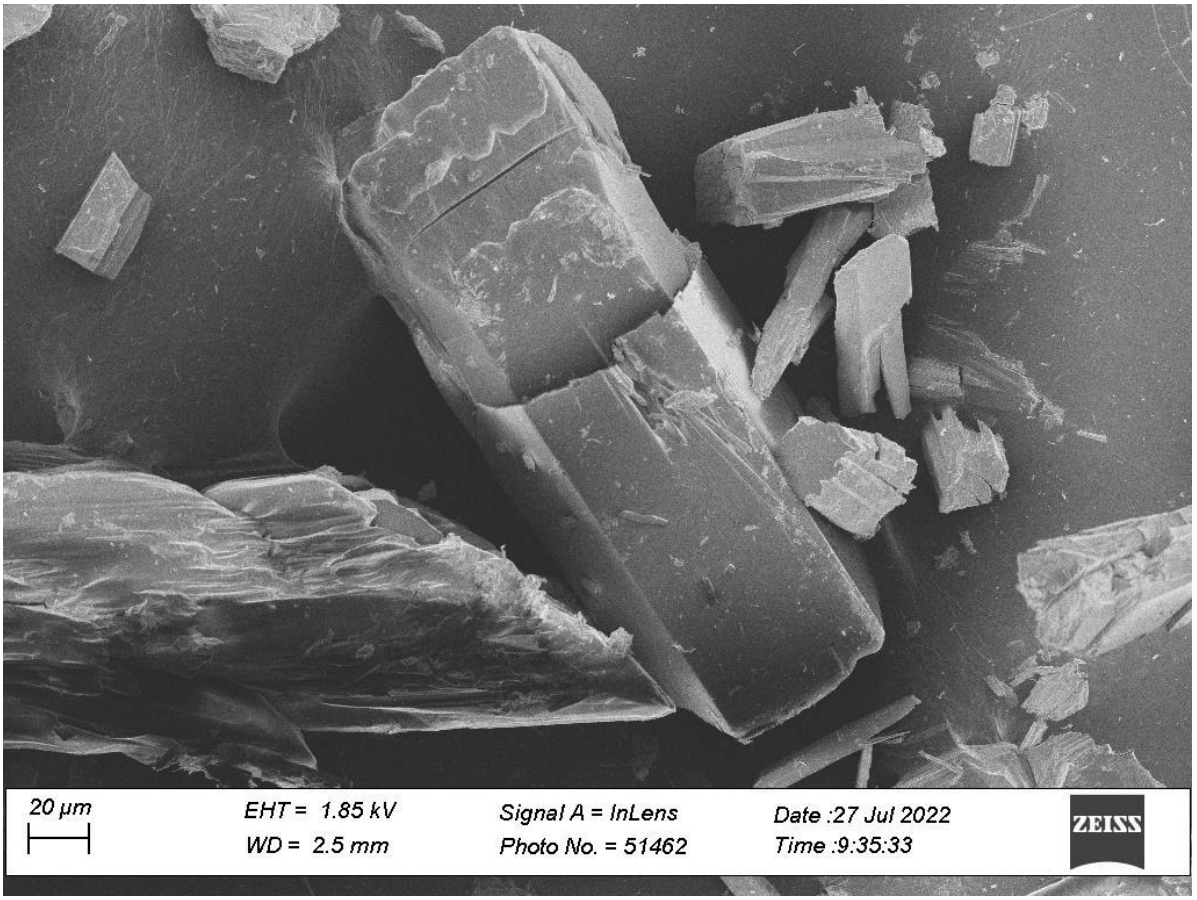

The same wider more cuboidal crystals were evident in sample TNW4, which decreased the volume of EDA used by 50%. This is a strong indication that the presence of EDA is necessary for the formation of the whisker type morphology. The presence of EDA guides the growth of the titanium dioxide crystals along a single 1-dimensional axis, whereas in the absence of EDA the growth of titanium dioxide is able to occur with less restriction in three dimensions, resulting in a morphology that is cuboidal. This is shown in Figure 78. TNW4 (-50% ethylene diamine)

Figure 78. TNW4 (-50% ethylene diamine).

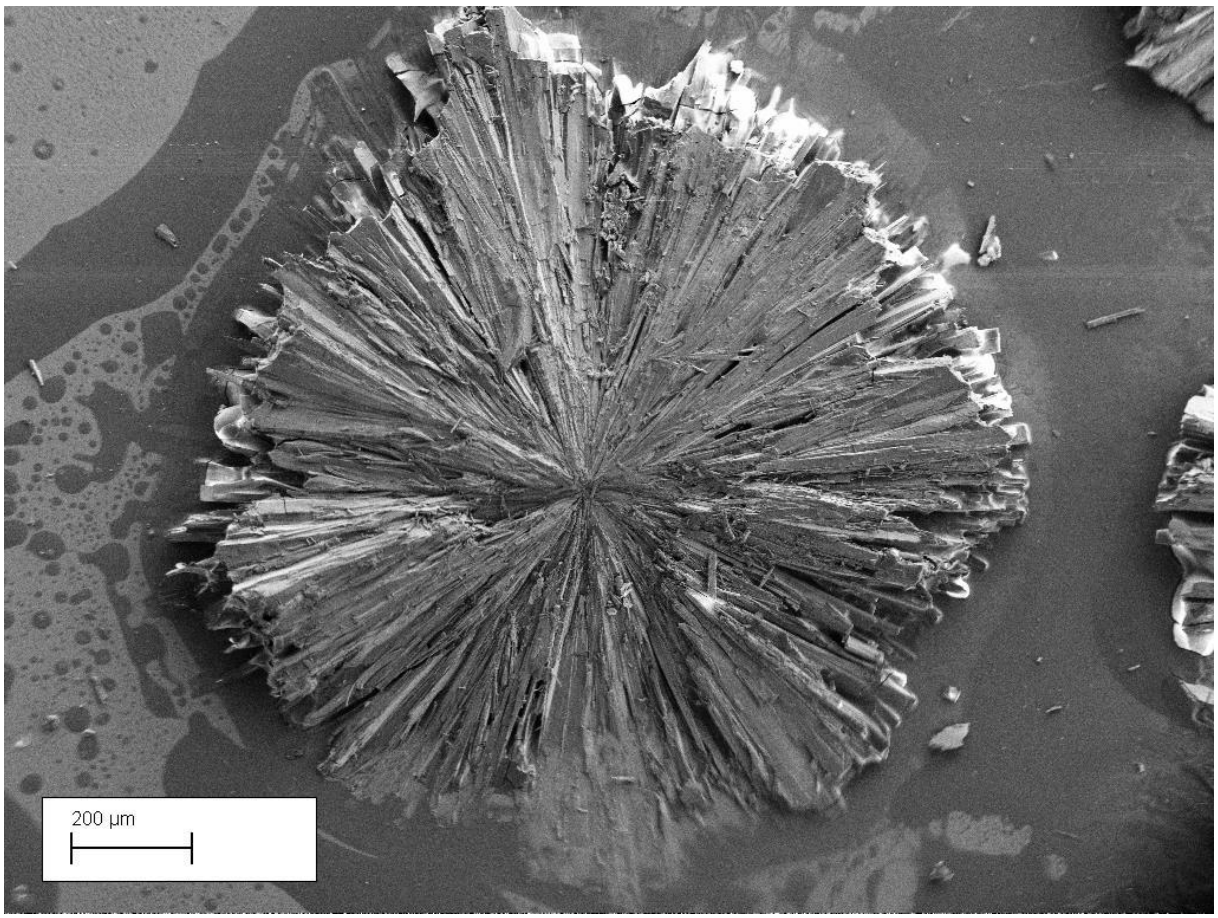

A magnified view of the TNW10 micro-rods in Figure 79. TNW10 micro-rods reveals that the rod-like structures are formed of smaller rod-like structures arranged in layers atop other rod-like structures. The material is clearly formed from multiple layers of rod-like structures. The micro-rods arranged in layers are characteristic of the morphology of the TNW1, TNW4, TNW5 and TNW10 samples.

Figure 79. TNW10 micro-rods.

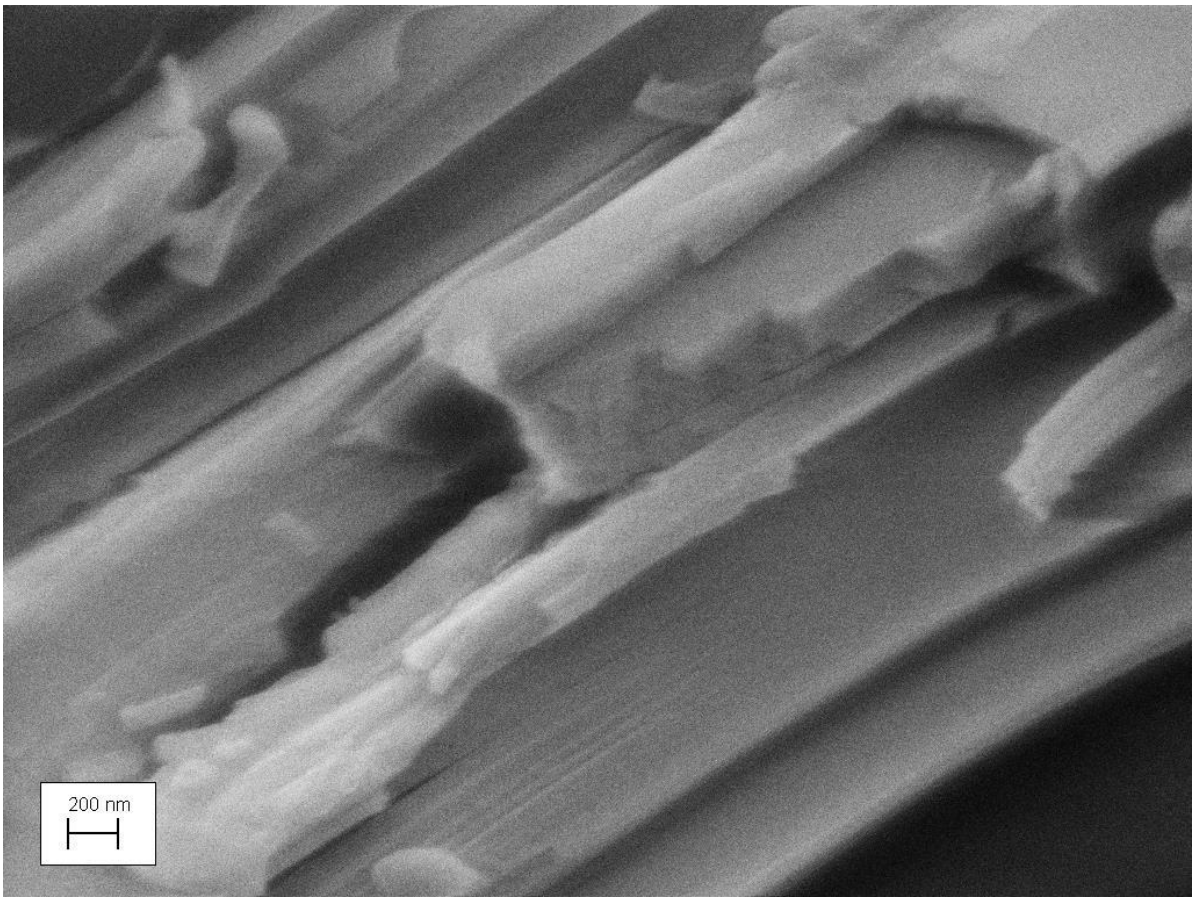

9.8 Energy Dispersive X-ray Spectroscopy of TNW series

Maps of the elements contained within the sample of TNW1 were produced using EDX in order to understand the distribution of elements within the sample. The atomic % of titanium contained within the sample ranged from 19.3% to 25.8%.

TNW Series- TNW1 Elemental Map

EDX elemental analysis was used to investigate the distribution of elements qualitatively, in a sample of TNW1 that had been broken open, exposing a shiny and silvery inner region of micro-rods. For sample TNW1 the region of the sample sued for imaging was dominated by titanium atoms. Analysis of this sample shows very small amounts of carbon, and no contribution from sodium or chloride, indicating that sodium and chloride were not incorporated into the rod-like structures – either as individual ions or as sodium chloride.
This provides evidence that the sodium chloride component featured in the XRD patterns is not likely to be a part the rods, but were the nucleation point around which the rods formed, potentially due to electrostatic interactions occurring during the reaction.

The low percentage of oxygen found in this sample does not indicate that the rods are pure titanium – it is more likely that due to the relatively low atomic number of oxygen, the intensity of X-ray emissions from oxygen is lower, resulting in difficulty visualising the oxygen component of the micro-rods. This is not the case for elements with higher atomic numbers such as sodium and chlorine, which is why the absence of sodium and chlorine in the EDX map is evidence they do not occur within the micro-rods, whereas a low percentage of oxygen in the EDX maps does not indicate an absence of oxygen from the sample. The region used to obtain the EDX map of TNW1 is pictured in Figure 80. Image of sample TNW10 used in spectroscopic analysis, the quantification of elements from EDX analysis is listed in Table 71. EDX elemental quantification for TNW1, although this is only valid for the surface of the

sample, and the elemental maps are contained in Table 72. Elemental maps for sample TNW1

Table 71. EDX elemental quantification for TNW1.

Element	Weight%	Atomic %	Error %
Carbon	0.7	2.7	2.9
Oxygen	2.1	6.2	8.7
Titanium	92.8	90.1	1.3
Gold (coating)	4.4	1.0	8.3

Figure 80. Image of sample TNW10 used in spectroscopic analysis.

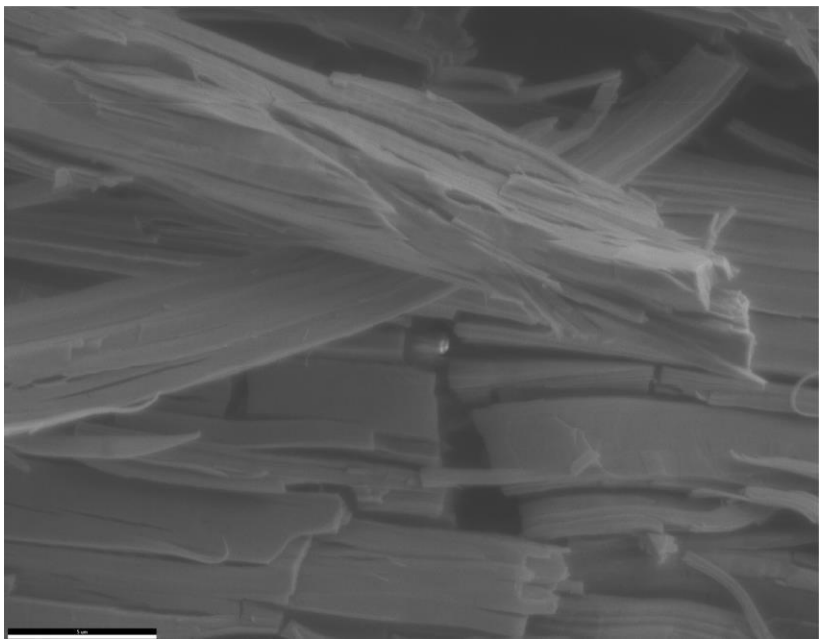

Table 72. Elemental maps for sample TNW1.

All elements overlaid	Carbon
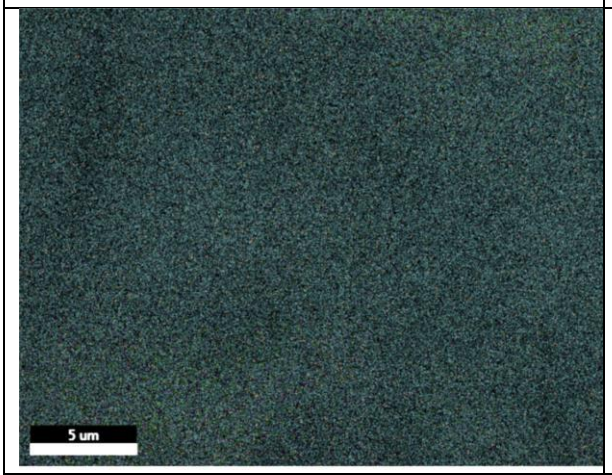	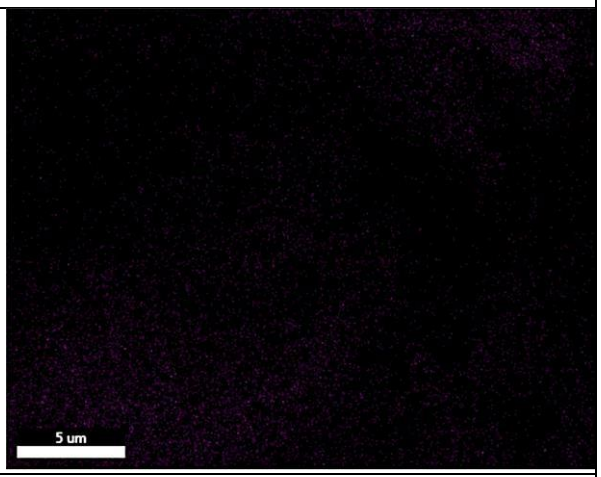
Oxygen	**Titanium**
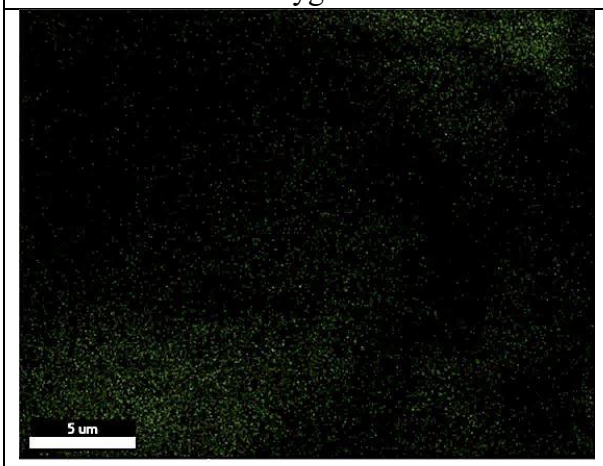	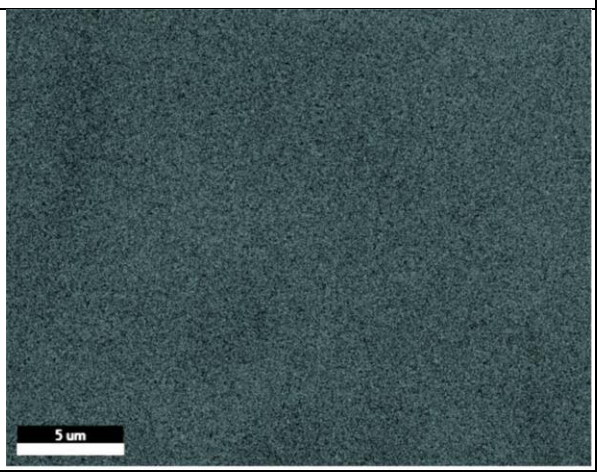

TNW Series – TNW10 Elemental Map

EDX analysis demonstrated that there were no significant concentrations of potassium and chlorine within the micro-rods formed from reaction TNW10. There was, however, a high proportion of carbon found in all samples. This means that potassium chloride is not likely to be forming in significant amounts inside the micro-rods, but a significant carbon component – likely the polyethylene glycol, is present. The EDX area analysis of TNW10 is shown in Figure 81.

Figure 81. TNW10, region encircled in red was analysed using EDX spectroscopy.

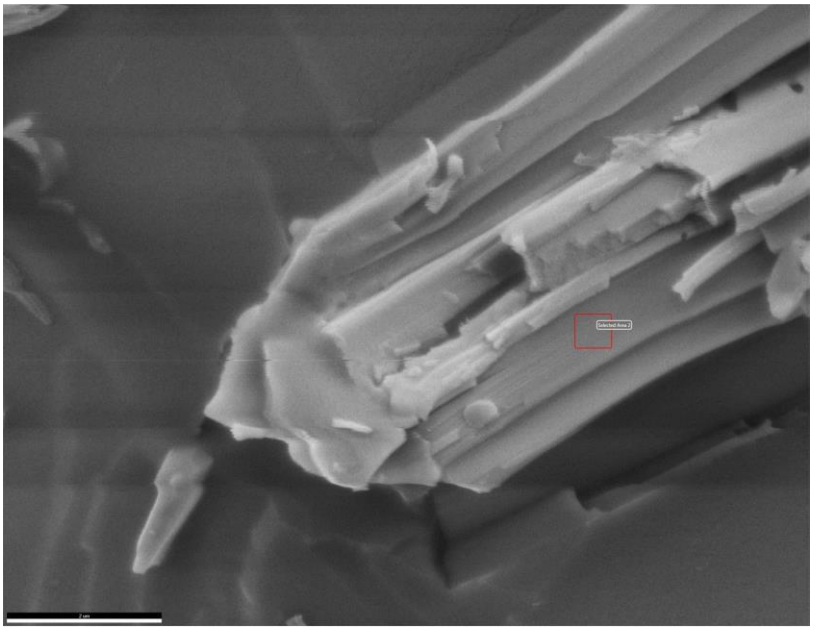

The distribution of carbon atoms in the following elemental maps in Table 73 indicate the carbon component is on the outside of the micro-rods, suggesting a coating and not suggesting that the titanium dioxide is chemically bonded to the carbonaceous material. This was concluded from the carbon elemental map, which shows a dark region in the lower left quarter, where titanium is present is significant amounts. The high atomic % of carbon in Table 74 may be due in part to the coating of the carbonaceous layer that forms on the TiO_2 microrods, but may also be due to the background of carbon on to which the sample TNW10 was loaded.

Table 73. Elemental map of sample TNW10.

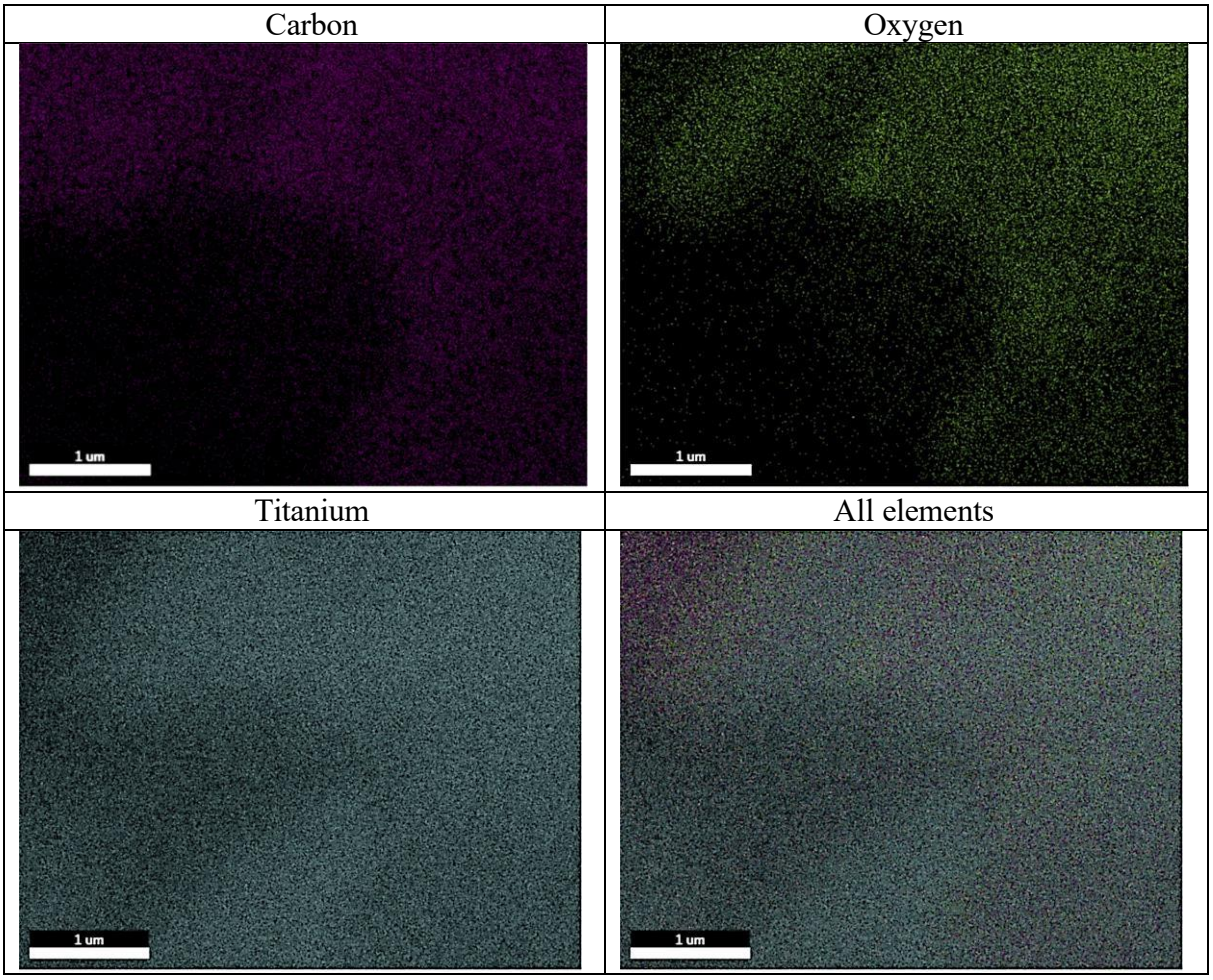

Table 74. Elemental composition of region of TNW10 used in EDX analysis.

Element	Weight %	Atomic %
Carbon	17.7	35.9
Oxygen	23.9	36.4
Chlorine	0.7	0.5
Potassium	1.3	0.8
Titanium	50.6	25.8
Gold	6.0	0.7

TNW Series – TNW4 Elemental Map

The EDX spectra indicate that there is a significant presence of carbon – more than would be expected from coating the sample with graphite to facilitate SEM/EDX analysis. This finding illustrates one of the issues with EDX – that EDX analysis primarily detects X-rays from the surface of a sample and hence identifies elements located at the surface of a sample, which may then result in a high concentration of an element being identified which forms part of a coating, but is not intrinsic to the sample. This provides evidence that the carbon-based solvents are undergoing a reaction resulting in the polymerisation of the ethylene glycol and potentially the ethylene diamine. This means that the reaction must be adapted to allow the removal of the titanium dioxide phases before the possibility of polymerisation of the solvents occurs and hence coating of the TiO_2 microrods with the carbonaceous layer. The area used for EDX analysis of TNW4 is shown in Figure 82, the elemental maps of TNW4 are shown in Table 75, while the quantified elements found are shown in Table 76.

Figure 82. Image of sample TNW4 (-50% ethylenediamine) used for EDX spectroscopic analysis.

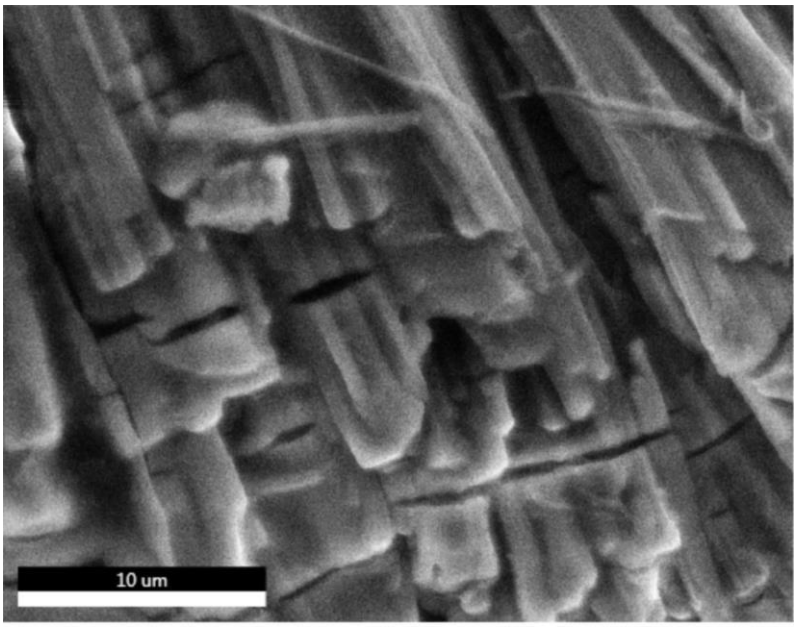

Table 75. Elemental maps of the constituent elements of TNW4.

All elements overlaid	Carbon
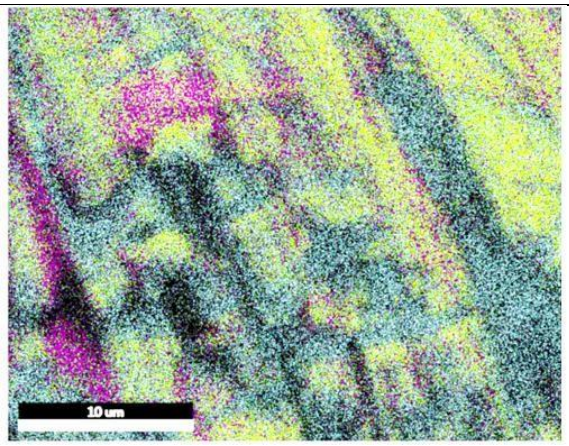	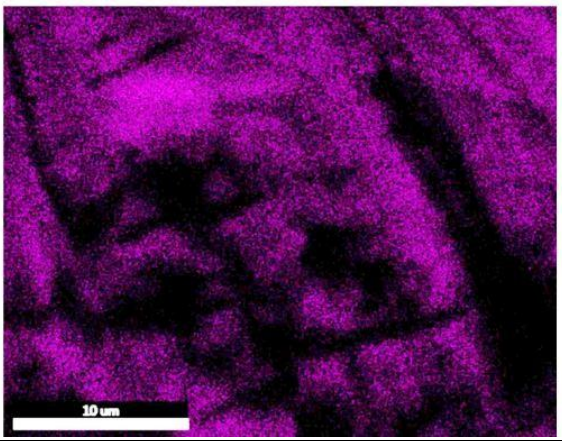
Oxygen	**Titanium**
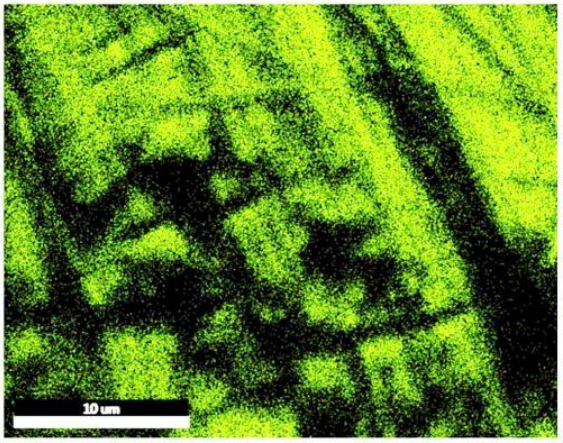	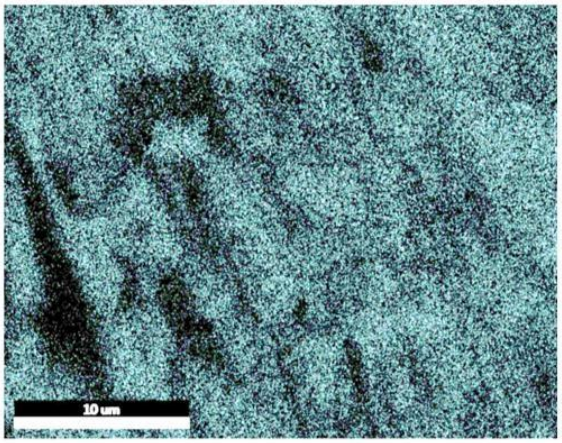

Table 76. Quantified elemental composition of TNW4.

Element	Weight %	Atomic %	Error %
Carbon	16.1	36.9	2.5
Oxygen	12.9	22.2	6.7
Titanium	72.0	40.9	3.6

EDX – Sample TNW4

Sample TNW4 was embedded in epoxy resin and the surface polished away in order to investigate the identity of the chemical species at the centre of the TNW spherical structures, shown in Figure 83. The carbon from the epoxy resin dominated the sample and concealed much of the titanium component. This was due to the polishing process, which would have spread some of the material polished away across the surface of the polished region. The carbon and oxygen form the epoxy resin is prevalent across the surface, which can be seen as a ring of higher concentration of carbon around the exposed surface of the centre of the TNW4 spherulite.

The concentration of titanium is highest in the centre of the image, where the TNW4 structure has been exposed. However, a cubic crystal of NaCl was identified at the centre of the structure, which provides confirmation that NaCl does not form a part of the structure of the micro-rods, but instead acts as a nucleation point around the TiO_2 microrods have grown. This is shown in Table 77. Elemental maps of constituent elements of TNW4 embedded in epoxy resin. The process of producing EDX analysis of a cross section of a TNW4 spherulite would have been improved by slicing across the sample using a laser, instead of manually polishing away the epoxy resin.

Figure 83. TNW4 embedded in epoxy resin.

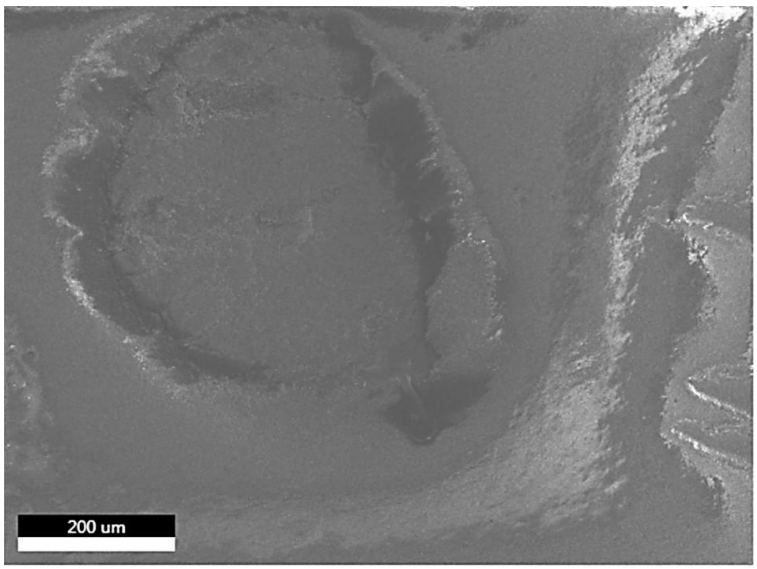

Table 77. Elemental maps of constituent elements of TNW4 embedded in epoxy resin.

All elements overlaid	Carbon
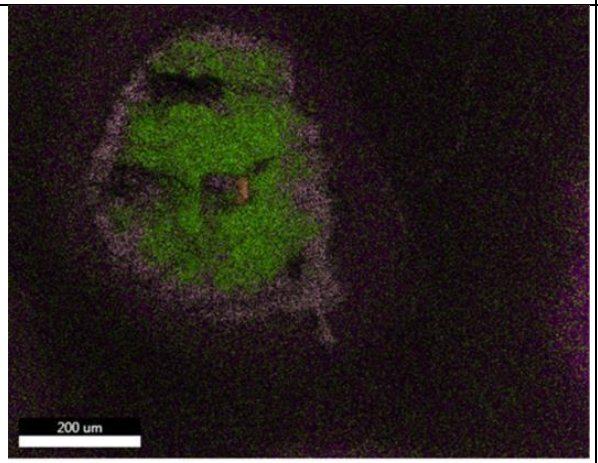	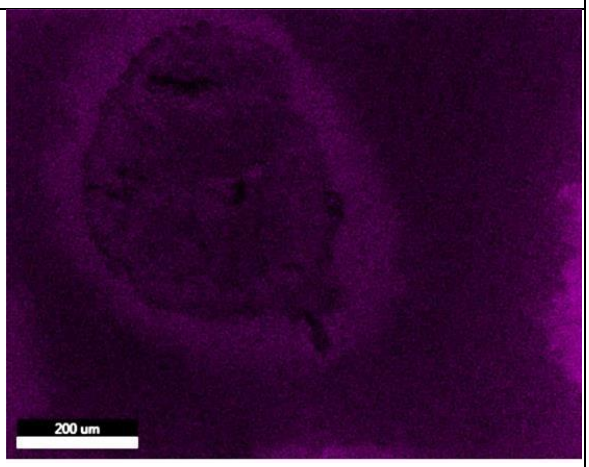
Sodium	**Oxygen**
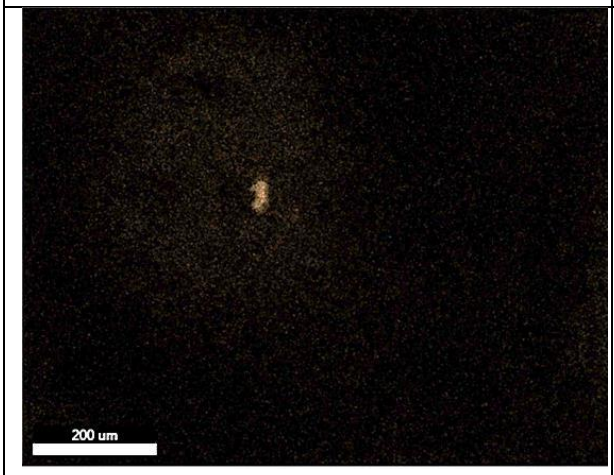	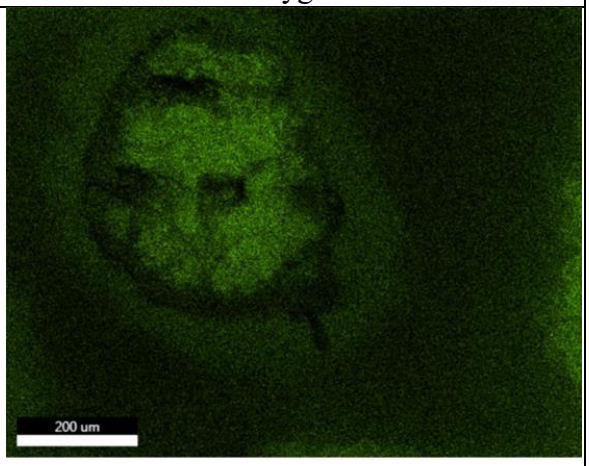
Chlorine	**Titanium**
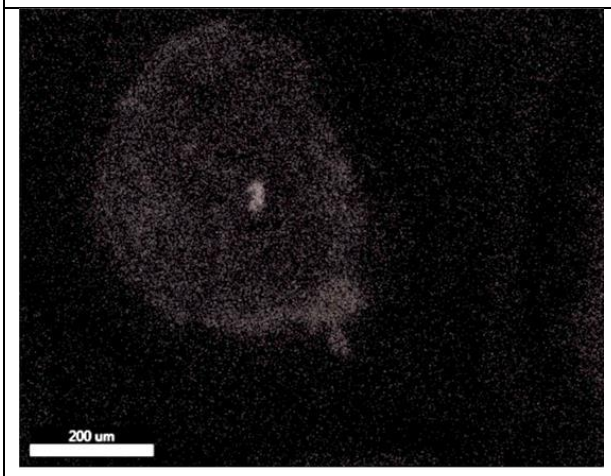	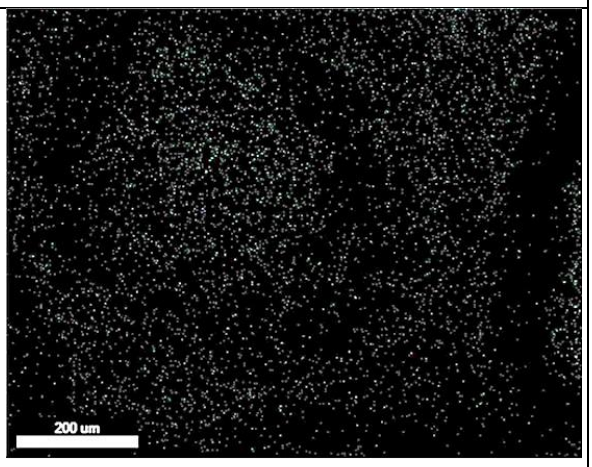

9.9 Summary of Synthesis and Characterisation of Titanium Dioxide

In this phase of development of the TiO_2-HAP-HGM the process for synthesising titanium dioxide from the sol-gel reaction was optimised, and the impact of various reagents on the final morphology of the TiO_2 was investigated by altering the amounts of the reagents, and characterising the products. The sol-gel reaction was chosen because this method has the potential to produce a coating of TiO_2 on a surface, which is the desired outcome for the final material.

The initial experiment produced sample TNW1, which consisted of silvery-grey spherulites coated with a layer of black material. The black material had coated the inside of the reaction vessel, and was determined the be from the solvent polymerising and producing a carbonaceous material that was pervasive throughout the TNW samples. In the XRD pattern of TNW1, the (101) and (110) peaks characteristic of anatase and rutile were barely visible again the background noise. Instead, the most intense peak corresponding to TiO_2 was the anatase peak at (200) and from this peak the crystallite size was calculated to be 57 nm.

The XRD pattern of TNW2 displayed a peak characteristic of rutile at 2Theta = 27.48 °, which is in good agreement with the literature value of the (110) rutile peak which is found at 2Theta = 27.45 °. There was also less contamination from crystalline carbon or polyethylene glycol, evidenced from the lack of the asymmetric peak at 2Theta = 34 °. This finding means that refluxing the reagents together is more likely to produce titanium dioxide without the layers of carbonaceous material, representing a step towards the development of the synthesis method to coat the HAP-HGMs with TiO_2. The crystallite size of rutile in TNW2 was found to be 134 nm. It should be noted that it is possible that this rutile peak at 2Theta = 27.48 ° representing the (110) planes could have been misidentified as belonging to halite as halite also has a peak at 2Theta = 27.38 ° representing the (111) plane. However, in halite this peak has an intensity

that is 8.8% of the (200) plane that occurs at 2Theta = 31.72 °, and the peak at 27.48 ° has a small shoulder at 27.37 °, and it was therefore concluded that this peak belonged to halite, while the larger peak at 27.48 ° belonged to rutile. The crystallite size calculated from the XRD pattern of TNW2 was 22 nm. It is thought that by conducting the experiment under reflux, the average crystallite size was smaller due to the movement of solvent interrupting crystallite growth and lack of a flat surface for the TiO_2 microrod to grow on. In addition, the micro-rods formed in TNW2 did not coalesce together into a larger spherulite, which was characteristic of samples TNW, TNW4, TNW5 and TNW10.

The effect of overlapping peaks of halite at 27.37 ° and rutile at 27.43 ° can also been seen in the XRD pattern of TNW5, where it was again concluded that the larger peak belonged to rutile, based on the shoulder of the larger peak at a smaller angle of 2Theta, and on the relative intensity of the peaks relative to the I_0 peak for halite, where the halite peak would be expected to have a relative intensity of 50 arbitrary units, while the peak at 27.43 ° has a relative intensity of 257 arbitrary units. Hence it was concluded that the larger peak belonged to rutile, and the crystallite size was calculated to be 33 nm using the Scherrer equation. It is thought that the average crystallite size in TNW5 was larger than TNW2 because the larger volume of solvent more physical space for the growth of TiO_2 crystals.

The role of the TNW10 was to produce an XRD pattern from a salt with no peaks in the region of 2Theta = 27.45 °, in order confirm that the peaks found in this region in the other TNW samples were due to rutile, and to exclude the possibility that these peaks belonged to the (111) plane of halite, which occurs with a low intensity in the literature of 8.8%. The peaks associated with the sylvite present in TNW10 are strong and sharp, and differ significantly from the low broad peaks associated with TiO_2. This allows the conclusion that the peak found at 2Theta = 27.23 – 27.5 ° in the TNW series belongs to rutile and not to halite. The average crystallite size of the TiO_2component of the TNW10 sample was 41 – 43 nm.

A reoccurring issue was that the avoidance of a high temperature calcination in an effort to develop a low energy synthetic route towards the final TiO_2-HAP-HGM product meant the XRD patterns (with the exception of TNW2) did not show tall sharp peaks associated with either anatase or rutile, which are the most common polymorphs of TiO_2. This is expected as the curing temperature did not exceed 200 °C, and in order to achieve sharp peaks and high crystallinity a calcination temperature in excess of 450 °C is required. As the XRD pattern does not show clear define peaks indicating the presence of anatase and rutile, it is therefore necessary to employ other methods of characterization in order to confirm or refute the presence of anatase and/or rutile.

Halite crystals were identified at the centre of some spherulites, indicating that NaCl may act as a nucleation point from which TiO_2 grows outwards. This was evident in the EDX chemical maps in Table 10, where a cubic region at the centre of the spherulite is recorded, which is very high in sodium and chlorine.

The FT-IR spectra of the TNW shows show similarities across all samples – there is a large contribution from OH groups in the region of 3400 – 3200 cm^{-1}, which is associated with water within a sample, or H-bonded OH groups. This band is thought to be due to the OH groups from ethylene glycol, as the heating process is expected to have vapourised the water from the sample. All samples contain a much smaller peak in the region from 3000 – 2850 cm^{-1}, which is associated with C-H bonds and is thought to be due to the carbonaceous layer that formed as a coating on the TiO_2 microrods. The region from 1800 – 680 cm^{-1} is associated with C=C stretch, C-H rocking, N-H rocking, and O-H rocking, and all samples show evidence of these functional groups. The Ti-O stretch occurs around 690 cm^{-1}, and all samples show lower transmission in this region than in region from 1800-860 cm^{-1}, indicating that the peaks associated with the C=C bonds, N-H bonds, O-H bonds and C-H bonds are obscuring the peak associated with Ti-O, nevertheless the lower transmission % in this region is indicative of the

presence of Ti-O bonds. Samples TNW8, TNW2 and TNW10 had the least contamination from the carbonaceous layer, however TNW8 did not have sufficient water to cause the complete hydrolysis of the titanium tetra-isopropoxide, which is evident from the lack of distinguishable peaks in the XRD pattern of sample 8. Samples TNW4, TNW5, TNW6 and TNW7 showed large amounts of contamination from the carbonaceous material, as evidenced by the low transmission % in the regions associated with O-H, N-H, C-H and C=C bonds.

The Raman spectra of the TNW samples most closely resembled rutile, with characteristic peaks of rutile being identified, although for the B_{1g} band the literature value is recorded as 143 cm^{-1}, whereas in the Raman spectra of the TNW series the band identified as the B_{1g} bands ranges from 150-153 cm^{-1}. The peak associated with the multi-photon scattering process also occurs at higher wavenumbers than that reported in the literature for rutile, which is reported as 237 cm^{-1}, whereas in the TNW series the corresponding band occurs between 248 – 260 cm^{-1}. In contrast, the E_g and A_{1g} bands are much closer to the literature values, with the E_g being reported at 430 cm^{-1}, while in the TNW series this band occurs within is 420 – 434 cm^{-1}. The A_{1g} band is reported to be 605 cm^{-1} in the literature, while in the TNW series this band occurs between 600 – 610 cm^{-1}.

The EDX analysis of samples TNW1, TNW4 and TNW10 the titanium recorded ranges from 25% - 90%, however this is most likely due to the limitation of EDX being that only X-rays generated from the surface are recorded, so if the region analysed had a layer of the carbonaceous material, the % composition of titanium would be low. However, when the spherulite was broken open, exposing the silver-grey micro-rods, the percentage of titanium identified was much higher. There was no significant sodium chloride component identified from within the micro-rods, indicating that although the XRD pattern shows a large amount of NaCl, this was likely due to the high crystallinity of NaCl, and not because NaCl was intrinsic

to the micro-rods. Instead, NaCl was identified at the centre of the spherulites, and is evident in the centre of a spherulite, where a small cubic region is extremely high in sodium and chloride, relative to the rest of the sample.

In conclusion, the most appropriate TNW product for the synthesis of TiO_2 micro-rods appears to be TNW2, produced by refluxing the reaction mixture. TNW2 shows small micro- rods that have not crystallised around a central point to produce spherulite morphology, but remain relatively free, although form in much smaller clusters with a limited number of micro-rods. This sample shows clear evidence for the formation of rutile, which is not always evident in the other TNW series, with a crystallite size that is the smallest, at just 22 nm.

TNW2 shows among the lowest amount of contamination from the carbonaceous material, and shows bands in the Raman spectrum that is consistent with rutile, with the small deviation from the Raman values reported in the literature likely due to the synthesis process. These would be most appropriate for loading on to the HAP-HGMs, which is the focus of the next chapter.

10. Chapter 10 – Characterization of the Composite Material

10.1 Introduction

This chapter contains the SEM, EDX, XRD, FT-IR, TGA, N_2 adsorption isotherm and BET surface area analysis for a selection of the TiO_2-HAP composite materials. The hierarchical composite of hollow glass microspheres from which hydroxyapatite has been grown, which has then been covered in titanium dioxide using the sol-gel process will be referred to as "alk-TiO_2-HAP-HGM" from this point onwards, denoting the alkoxide hydrolysis reaction used to produce the TiO_2 component developed in Chapter 9. The sample name "anatase-HAP-HGMs" were produced from including anatase nanoparticles in the chemical precipitation reaction to produce the HAP-HGMs. TiO_2-HAP composites developed from scallop shells and anatase use the shortened name scsh-HAP-anatase. The characterization data for alk-TiO_2-HAP--HGMs includes SEM images of the whole composite and a close up of the surface of the composite, EDX elemental mapping and line-scans showing the element count along a one-dimensional line, XRD patterns labelled with the various components of the finished composite, FT-IR spectra showing the functional groups, N_2 BET and BJH plots showing the surface area, pore size and pore volume, and TGA showing information relating to thermal decomposition and phase change properties. Also included are HAP-HGMs where anatase has been added in to the chemical mixture and dried on, and where the titanium dioxide micro-rods have been synthesized separately and dried on to the HAP-HGMs, in order to provide XRD patterns for comparison with the finished composite.

10.2 SEM Imaging of composite materials

The SEM images gathered show that the microspheres were all coated with the titanium dioxide component, with all microspheres showing some form of coating and with appearances that differed from the HAP-HGMs. There seemed to be a small tendency towards aggregation, although most particles were found as separate and distinct objects. The microsphere in Figure 84 is an example of a microsphere with extensive coverage after treatment with titanium dioxide.

Figure 84. The final finished composite Alk-TiO_2-HAP-HGM, a composite of hydroxyapatite-hollow glass microspheres coated with titanium dioxide using the sol-gel process.

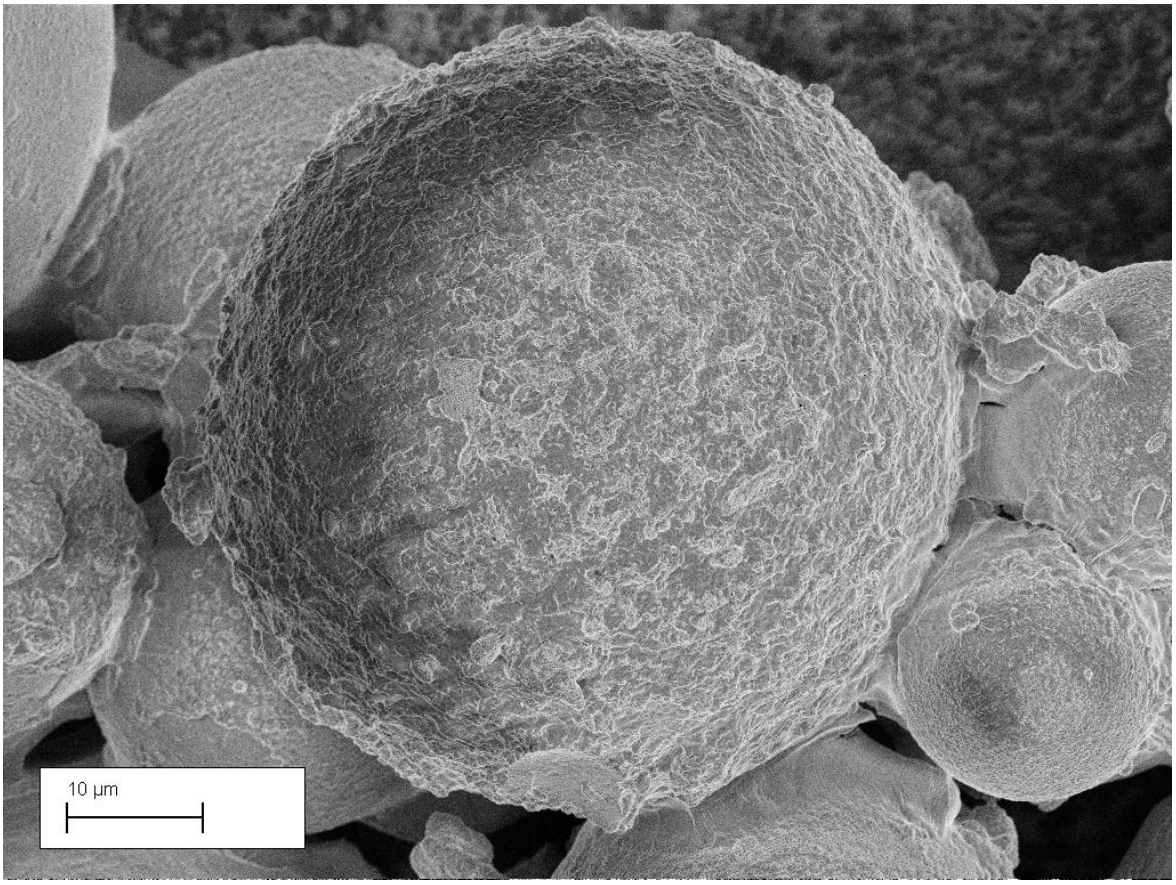

The majority of microspheres did not form an aggregate and grew a consistent layer of titanium dioxide on their surfaces. The microsphere displayed in Figure 85 has an appearance that is more typical of the microspheres produced in the final process. A magnified view of the surface of the microspheres contained in Figure 85 is displayed in Figure 86

Figure 85. The final composite - one particle of alk-TiO_2-HAP-HGM.

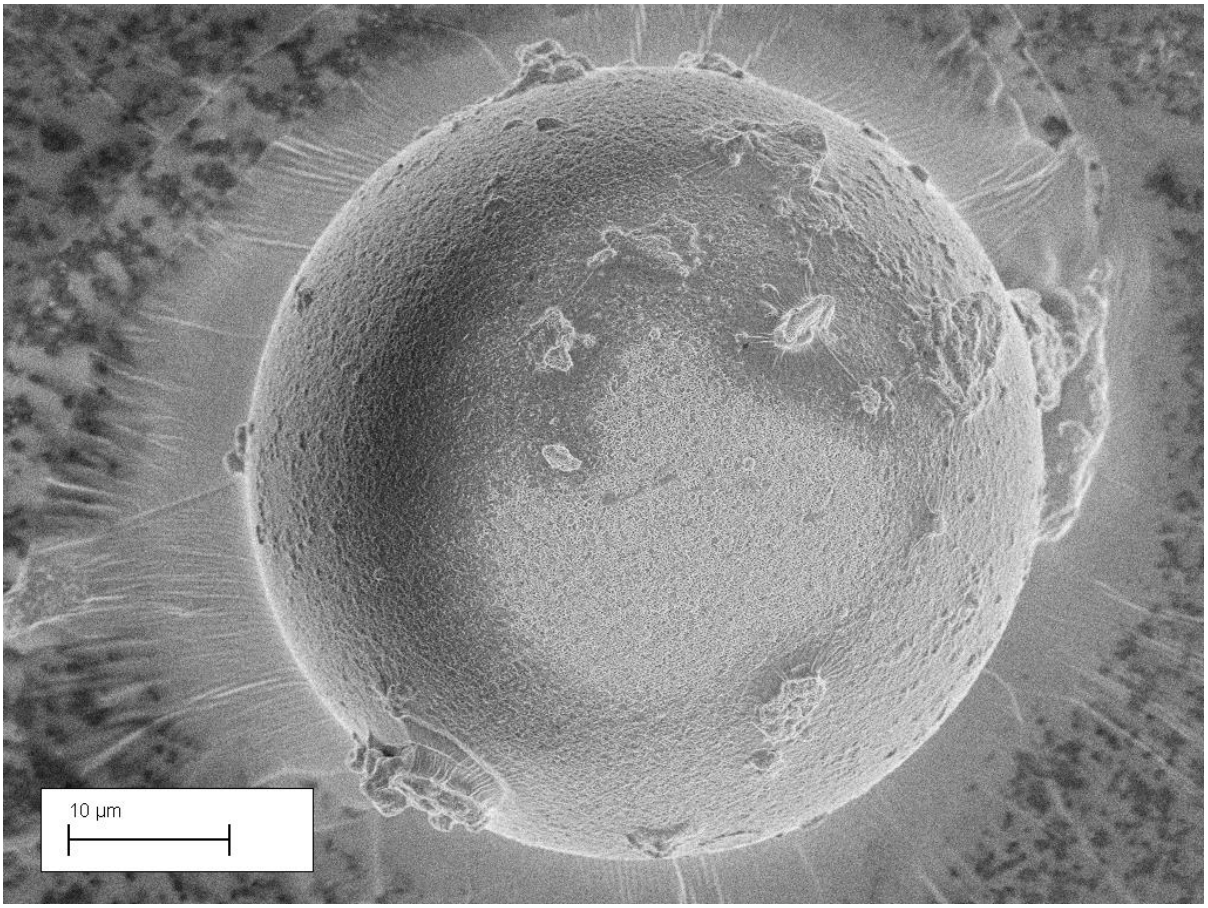

The magnified surfaces of the alk-TiO_2-HAP-HGMs were captured using different detectors. The scanning electron (SE) detector used to capture Figure 86 shows a 3D image of the surface, while the inlens detector was used to capture Figure 87, showing enhanced contrast and therefore more detail than in Figure 86. The TiO_2 micro-rods have been added to the surfaces of the HAP-HGMs to produce the material termed alk-TiO_2-HAP-HGMs.

Figure 86 surface of the bead captured using SE detector, showing 3D surface topology.

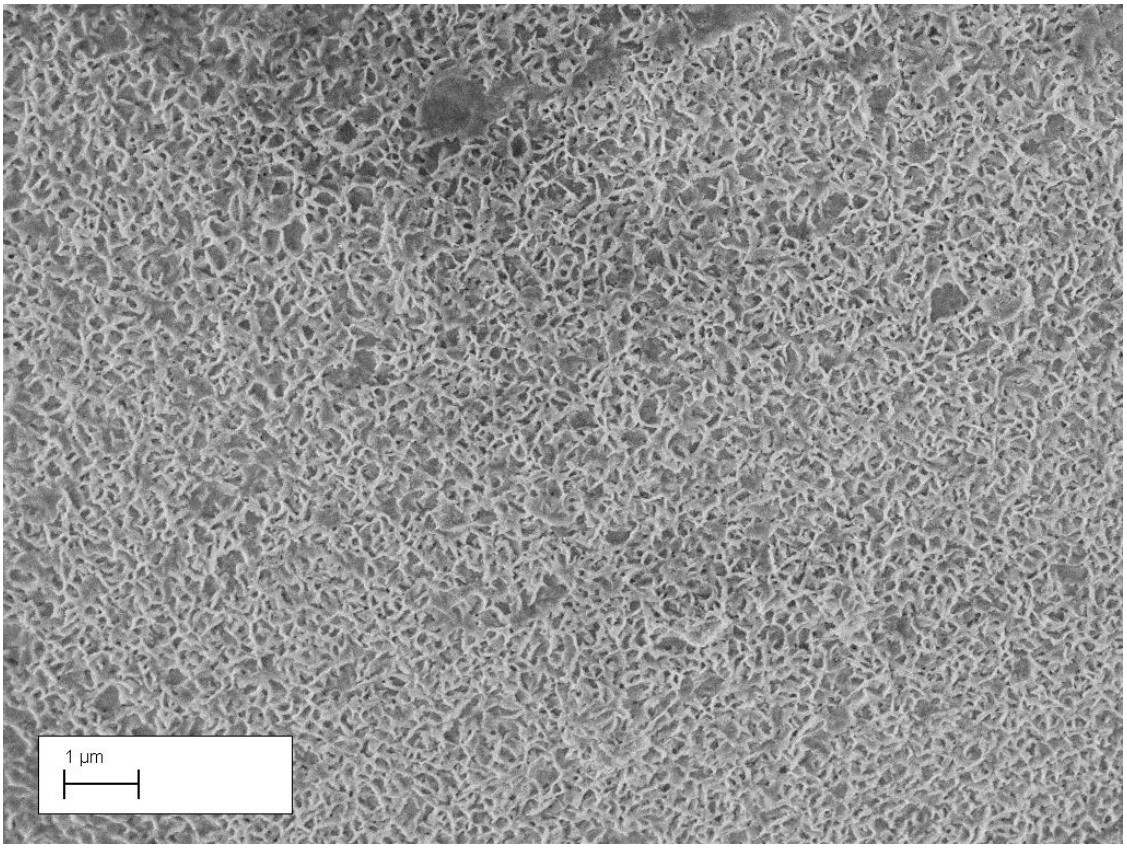

Figure 87 SEM images of the alk-TiO_2-HAP-HGM material with close up of surface.

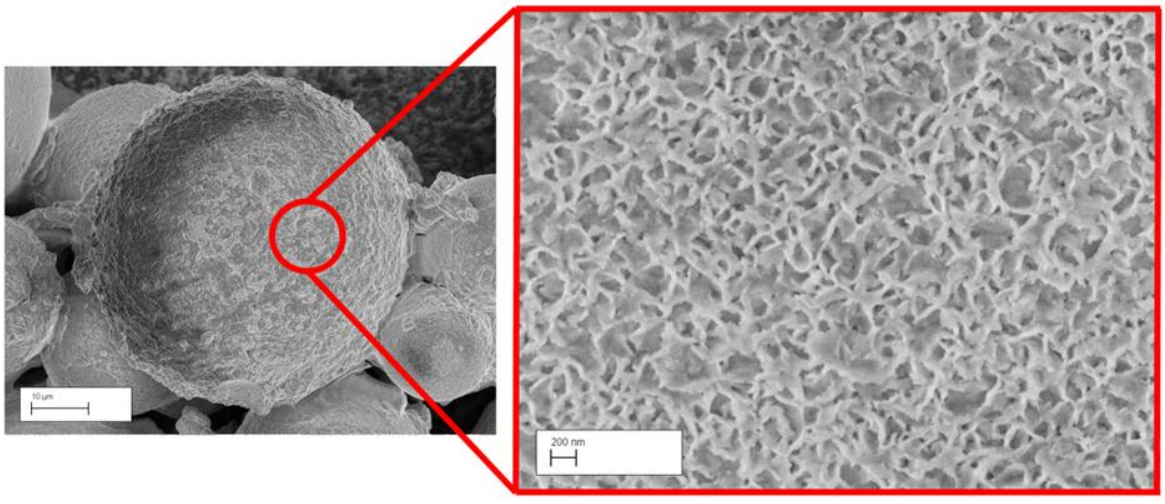

During the optimisation process the TiO_2 micro-rods were formed separately and then dried on to the surfaces of the HAP-HGMs. The products of this method are displayed in Figure 88. The microsphere in Figure 88 shows the TiO_2 layer cracking a peeling off, indicating that drying the TiO_2 component on to the microspheres is not an appropriate method for applying a sturdy and resilient TiO_2 layer.

Figure 88 product TNW1-HAP-HGM where TiO_2 micro-rods were synthesized separately and dried on to the HAP-HGM. The TiO_2 layer is peeling off – hence drying pre-made TiO_2 on to the HAP-HGMs is not appropriate.

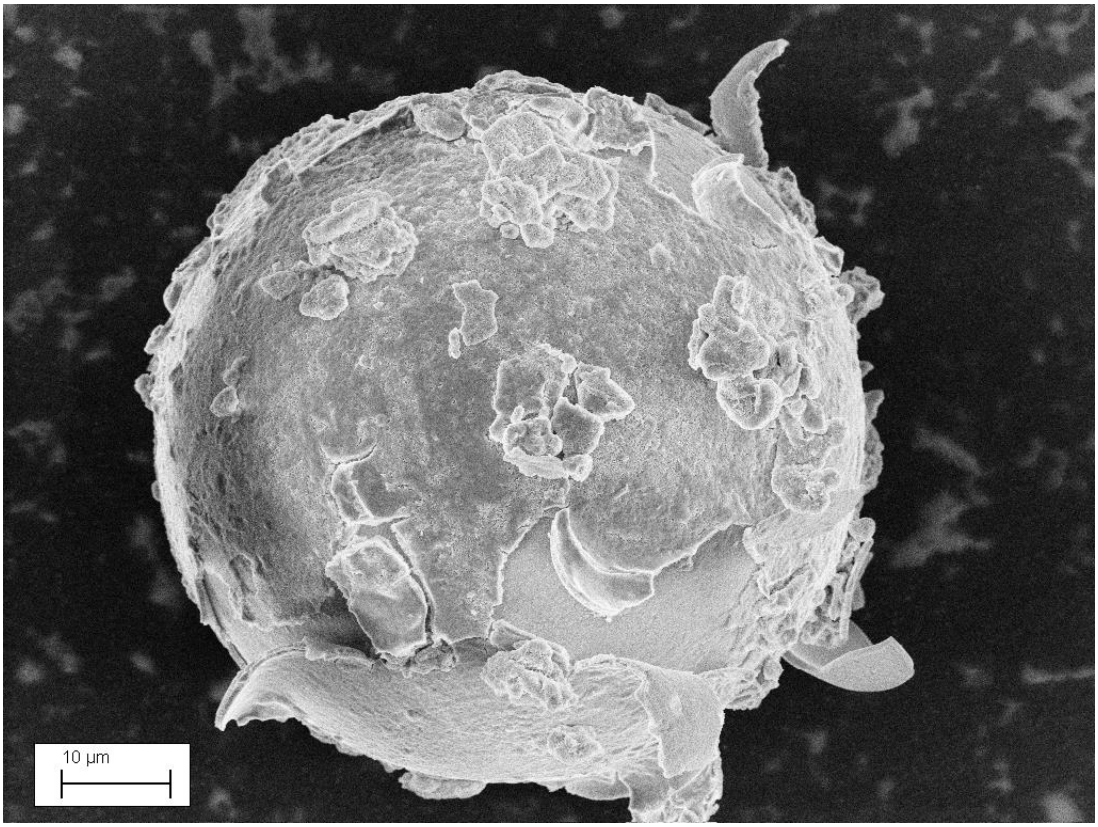

Dispersing anatase nanoparticles into the dipotassium hydrogen phosphate solution before calcium carbonate was added produced the composites termed anatase-HAP-HGMs. Although anatase was incorporated into many of the microspheres, the products were inconsistent in size and morphology, and large aggregates of hydroxyapatite doped with anatase formed independent of the microspheres. The microsphere pictured in Figure 89 was produced using method, and it is clear that this method was not suitable for producing microspheres of consistent sizes with consistent amounts of HAP and anatase.

Figure 89 Anatase-HAP-HGM formed by adding anatase nanoparticles into HAP-HGM reaction mixture.

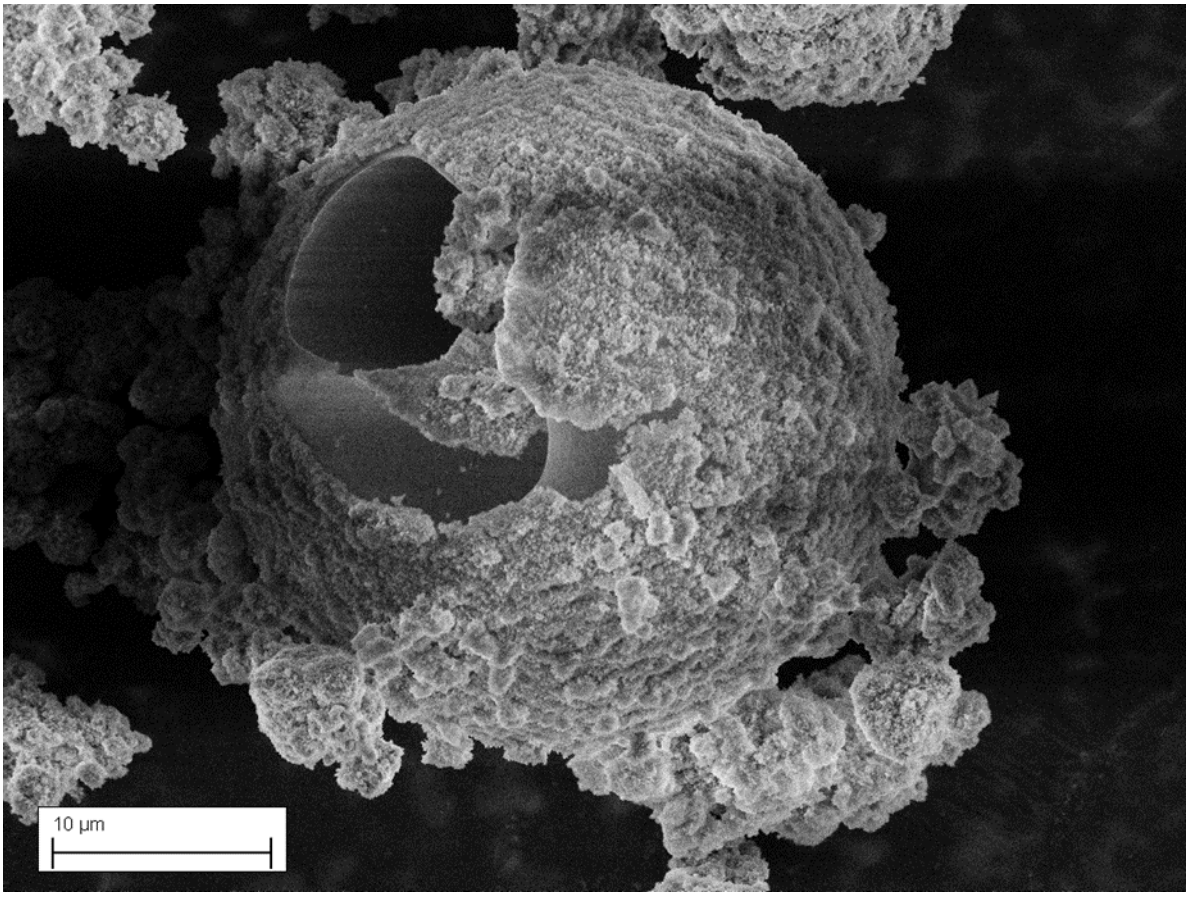

10.3 EDX Elemental Analysis of composite materials

EDX analysis was used to map the locations of the various elements and their distributions across the composite microspheres. In samples where anatase nanoparticles were added into the reaction mixture of calcium carbonate-microspheres and dipotassium hydrogen phosphate the anatase was not well incorporated into the structure of the material. The anatase nanoparticles instead formed aggregates which were unevenly deposited across the spheres. The images contained in Table 78 SEM image of anatase-HAP-HGM (sample 16) with anatase added into reaction mixture are the elemental maps for the anatase doped HAP-HGM. The titanium map shows uneven distribution of titanium over the microspheres, while the calcium and phosphorus maps show large aggregates of calcium phosphate not secured to the HGMs. The EDX spectrum is shown in Chart 41. EDX spectrum of anatase-HAP-HGM.

Table 78 SEM image of anatase-HAP-HGM (sample 16) with anatase added into reaction mixture.

Below: anatase-HAP-HGM	Below: all elements overlaid
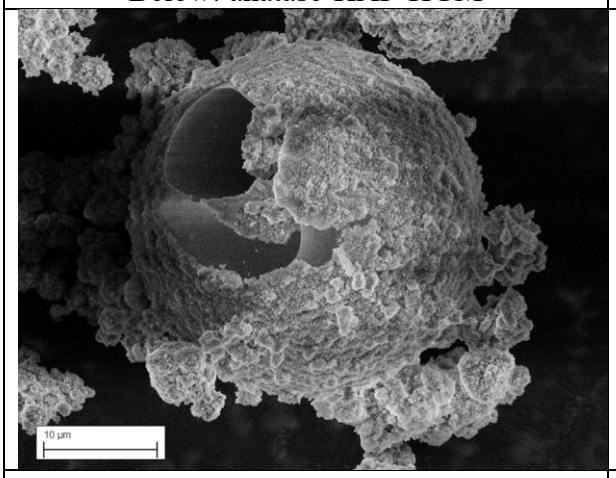	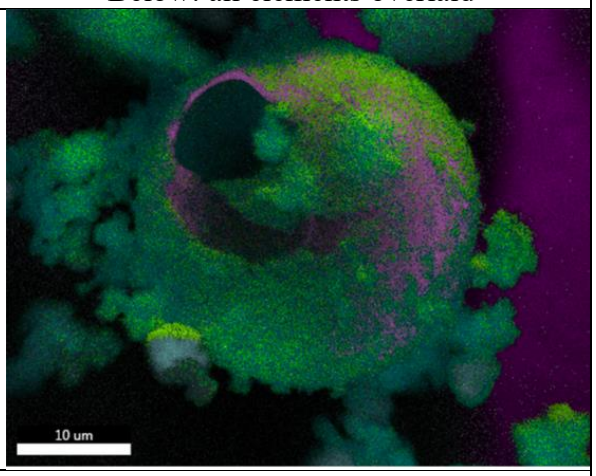
Below: silicon	Below: oxygen
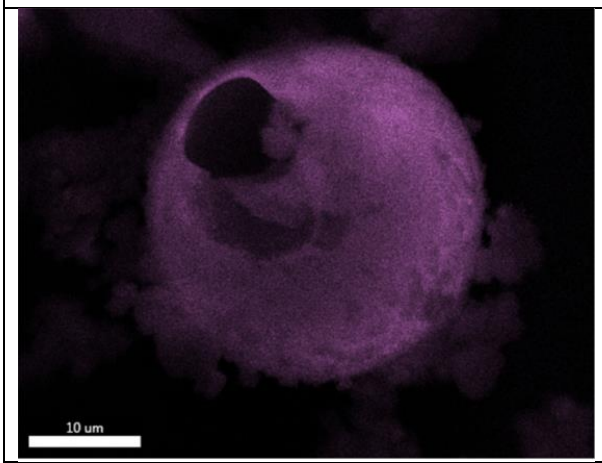	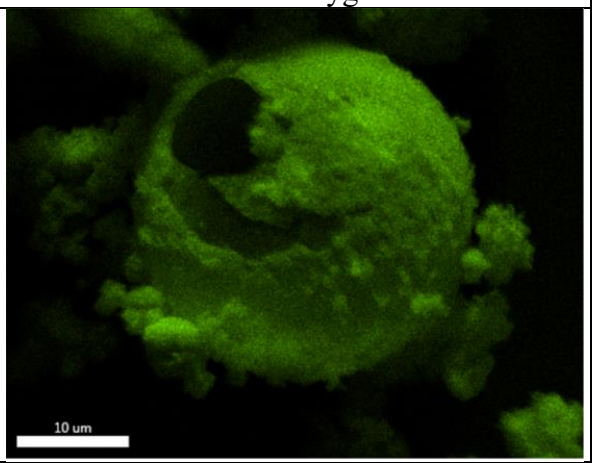

Below: phosphorus	Below: calcium
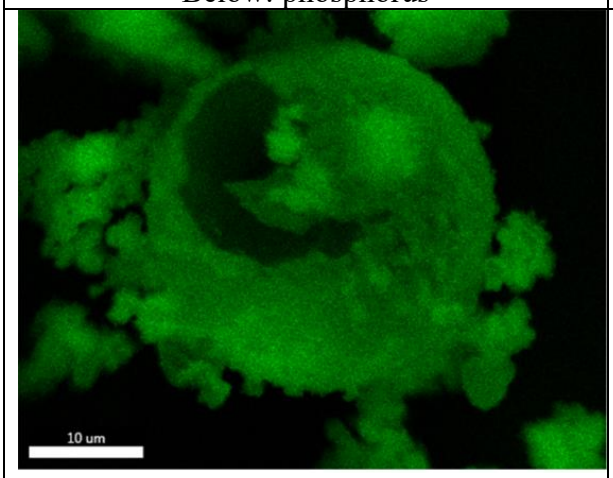	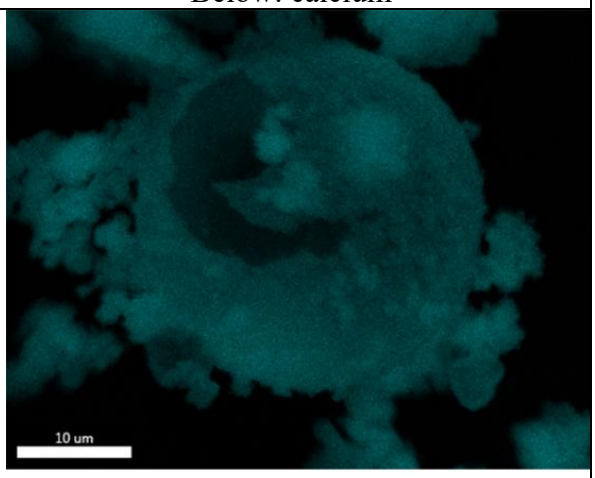
Below: titanium	**Below: carbon (background – not bead)**
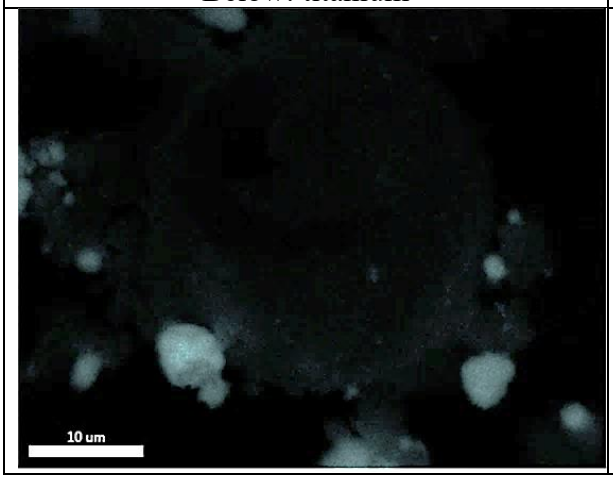	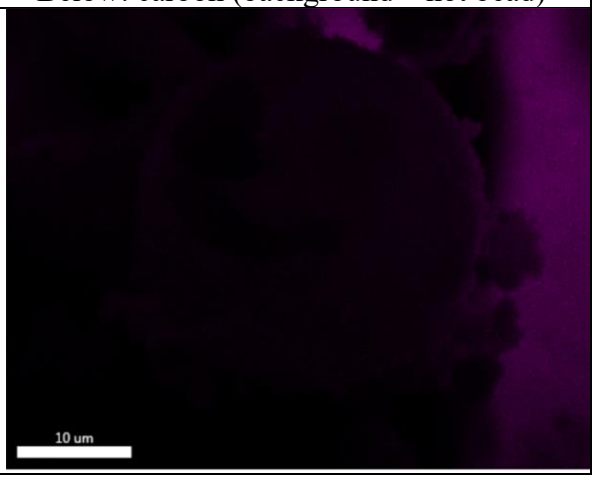

Chart 41. EDX spectrum of anatase-HAP-HGM, x-axis is X-Ray Energy, y-axis is Counts.

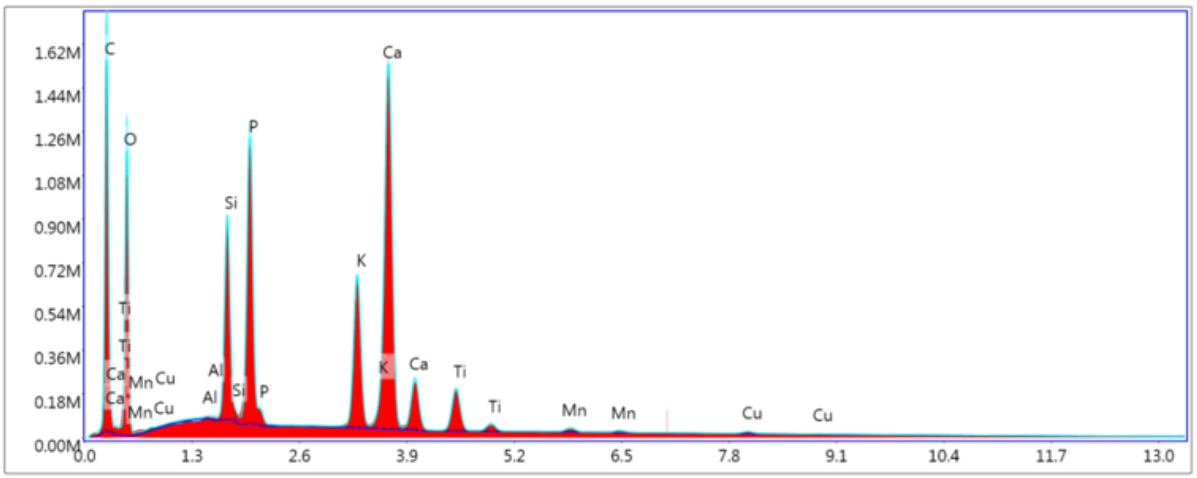

EDX spectroscopy was used to identify the phases present and to produce elemental maps of the elements identified in the sample produced by coating the HAP-HGMs with titanium dioxide using the sol gel process to produce the alk-TiO_2-HAP-HGMs. with the results included in Table 79. Elements quantified from EDX analysis of anatase-HAP-HGM (sample 16).

The anatase-HAP-HGMs are mounted on the SEM stub using conductive carbon tape and EDX analysis for the anatase-HAP-HGMs shows that the carbon component arises from the background of the image, not the anatase-HAP-HGMs. This is consistent with the calcium carbonate of the CaHGMs being successfully converted into hydroxyapatite, resulting in minimal carbon left on the surface of the anatase-HAP-HGMs. The EDX technique analyses the surface of the anatase-HAP-HGMs and is not capable of probing deeply into the surface of the analyte, meaning there may still be some carbonate remaining in the interior of the HAP component, resulting in carbonate substitutions in the hydroxyapatite lattice within the structures close to the silica-hydroxyapatite boundary. In theory, carbonate substitutions within the hydroxyapatite lattice could be detected by distortions in the XRD pattern, as described in Chapter 4.

Table 79. Elements quantified from EDX analysis of anatase-HAP-HGM (sample 16).

Element	Weight %	Atomic %	Error %
Carbon	33.0	48.5	8.0
Oxygen	30.8	34.0	9.7
Silicon	3.8	2.4	2.4
Phosphorus	7.2	4.1	2.7
Potassium	5.4	2.5	1.6
Calcium	16.5	7.3	1.5
Titanium	2.5	0.9	1.9

The alk-TiO_2-HAP-HGM (a hydroxyapatite-hollow glass microsphere coated with TiO_2 using the sol-gel process) was analysed to determine the distribution of elements present within the sample using EDX spectroscopy. The elements that constituted major components of the alk-TiO_2-HAP-HGM were silicon, oxygen, calcium, phosphorus and titanium. The high carbon component is assumed to be from the background, as the element maps show no significant carbon on the alk-TiO_2-HAP-HGM itself. This is shown in Table 80. EDX elemental maps of alk-TiO2-HAP-HGM.

Table 80. EDX elemental maps of alk-TiO_2-HAP-HGM.

Below: image used for EDX analysis	Below: all elements overlaid
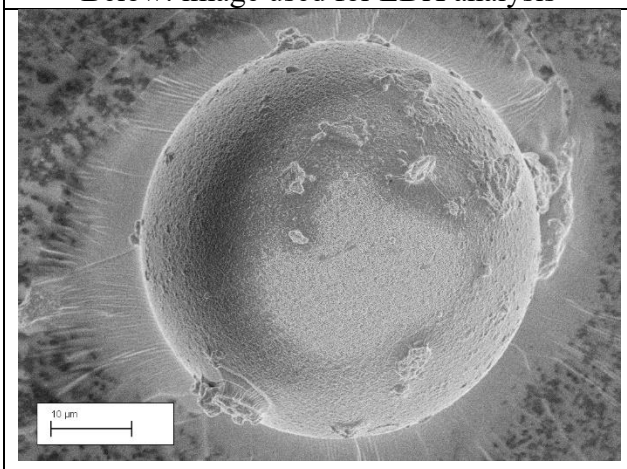	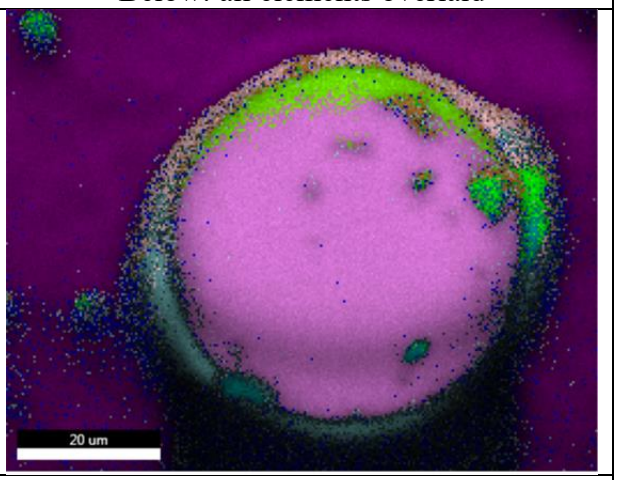
Below: carbon	Below: silicon
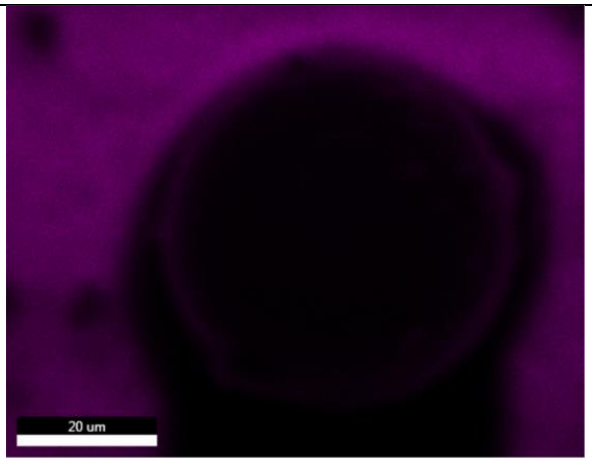	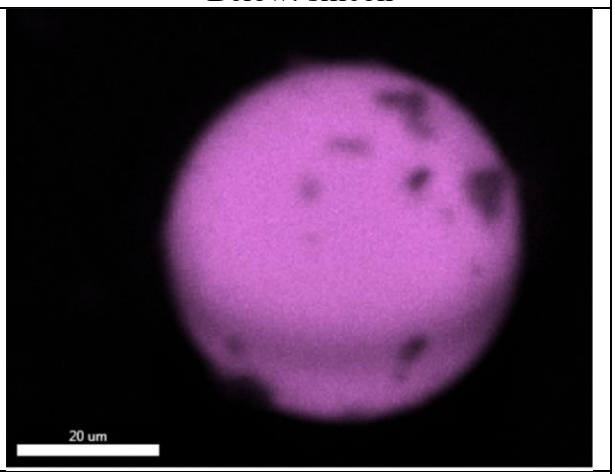
Below: phosphorus	Below: oxygen

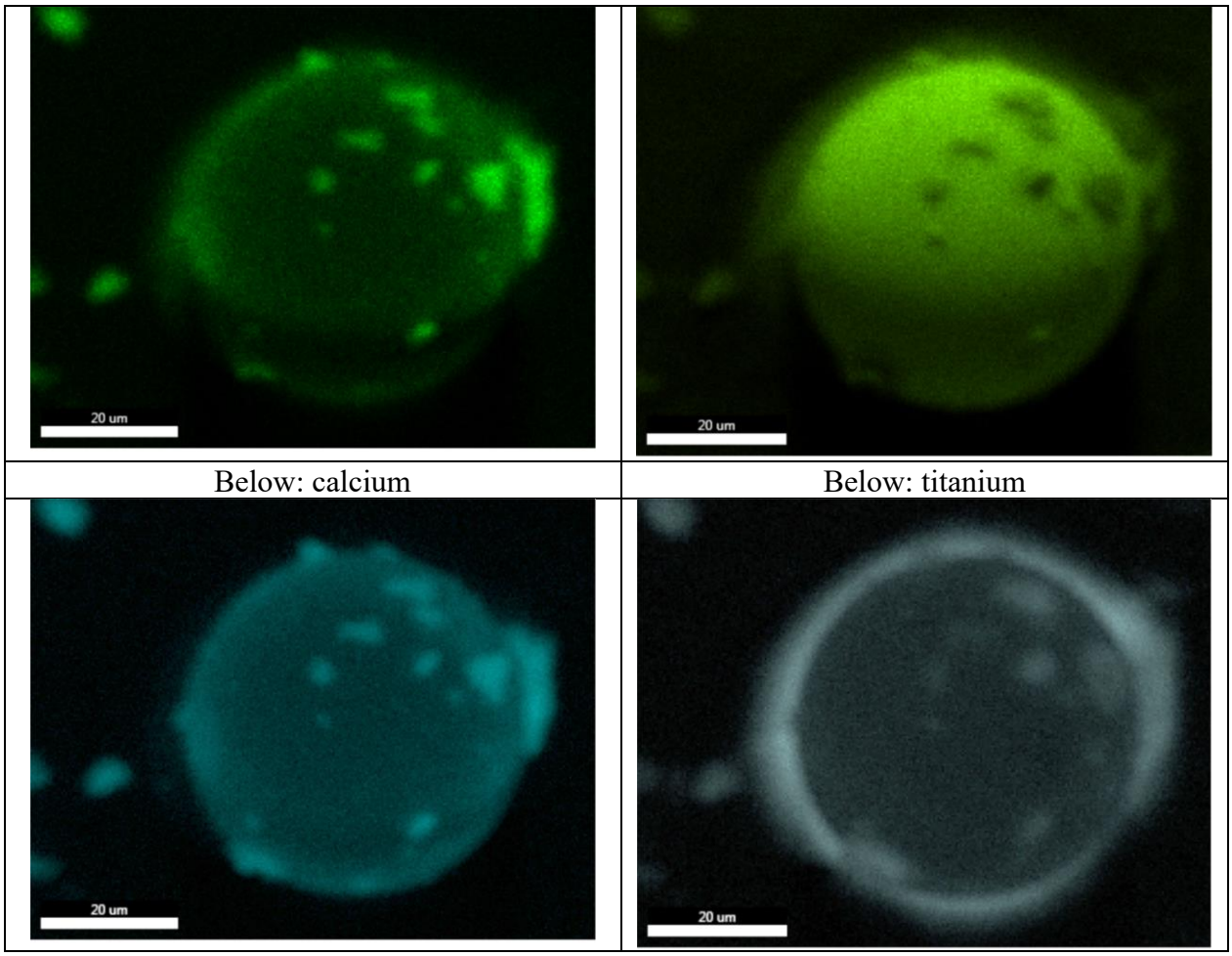

The EDX spectrum in Chart 42. EDX spectrum of alk-TiO2-HAP-HGM (titanium dioxide coated HAP-HGM), x-axis is X-Ray Energy, y-axis is Counts. shows the elements identified and their counts over the course of EDX analysis.

Chart 42. EDX spectrum of alk-TiO_2-HAP-HGM (titanium dioxide coated HAP-HGM), x-axis is X-Ray Energy, y-axis is Counts.

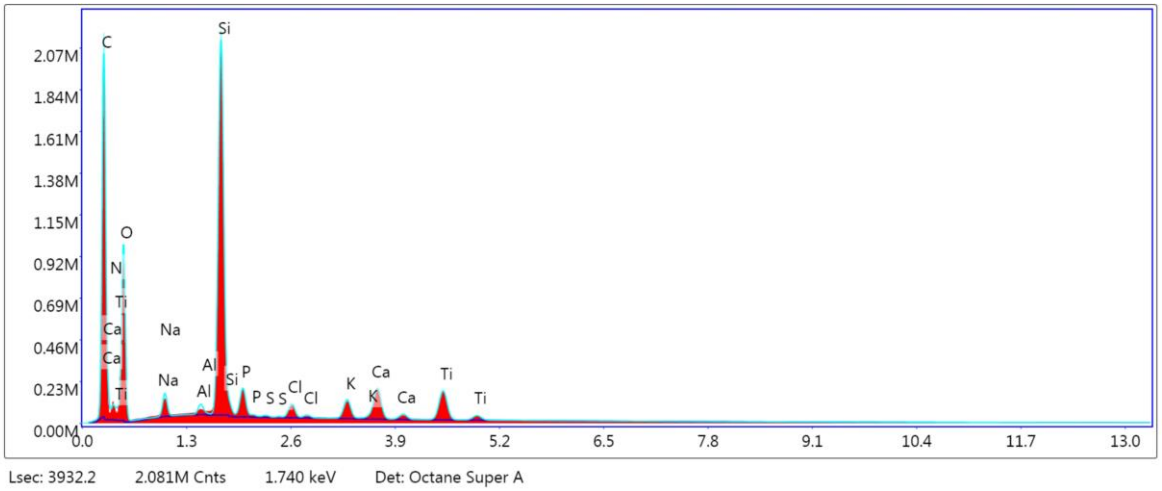

It should be noted that EDX analysis is not effective for quantifying elements deep within the sample as the electron beam cannot penetrate deeply within the sample without causing damage and also resulting in charging effects that impair the quality of the image produced, making EDX spectroscopy more appropriate for surface analysis. Calcium constitutes 1.89% of the sample, and phosphorus constitutes 0.46%, resulting in a Ca/P ratio of 1.5, meaning the surface of hydroxyapatite formed is slightly calcium deficient, falling short of the Ca/P ratio of 1.67 which is characteristic of stoichiometric HAP. This could be due to potassium or sodium from the reaction mixture substituting calcium in the lattice, which would lead to distortions in the lattice, which could potentially be identified in the XRD pattern. The full results for elemental quantification are contained in Table 81. The elements identified and quantified based on weight % and atomic % for the alk-TiO2-HAP-HGM.

Table 81. The elements identified and quantified based on weight % and atomic % for the alk-TiO_2-HAP-HGM.

Element	Weight %	Atomic %	Error %
Carbon	52.3	63.8	7.8
Oxygen	25.5	23.3	9.7
Sodium	1.2	0.8	7.1
Aluminium	0.3	0.2	4.0
Silicon	9.7	5.0	2.7
Phosphorus	1.0	0.5	3.7
Chlorine	0.6	0.2	2.0
Potassium	1.0	0.4	1.6
Calcium	1.9	0.7	1.4
Titanium	2.3	0.7	1.6

EDX spectroscopy also produced a linescan across the surface of the particle, where the elements are quantified at 1000 individual points across a given line. The linescan in Chart 43 corresponds to the alk-TiO_2-HAP-HGM in Table 80. In this linescan the calcium and phosphorus components are found across the surface of the microsphere, as evidenced from the maxima of the calcium and phosphorus lines which lie within the line for silicon. In contrast, the maxima for the titanium line falls outside of the sharp rises in the silicon line, indicating the titanium is found mostly around the outside of the microsphere.

Chart 43. Linescan (EDX) of whole sphere of alk-TiO_2-HAP-HGM.

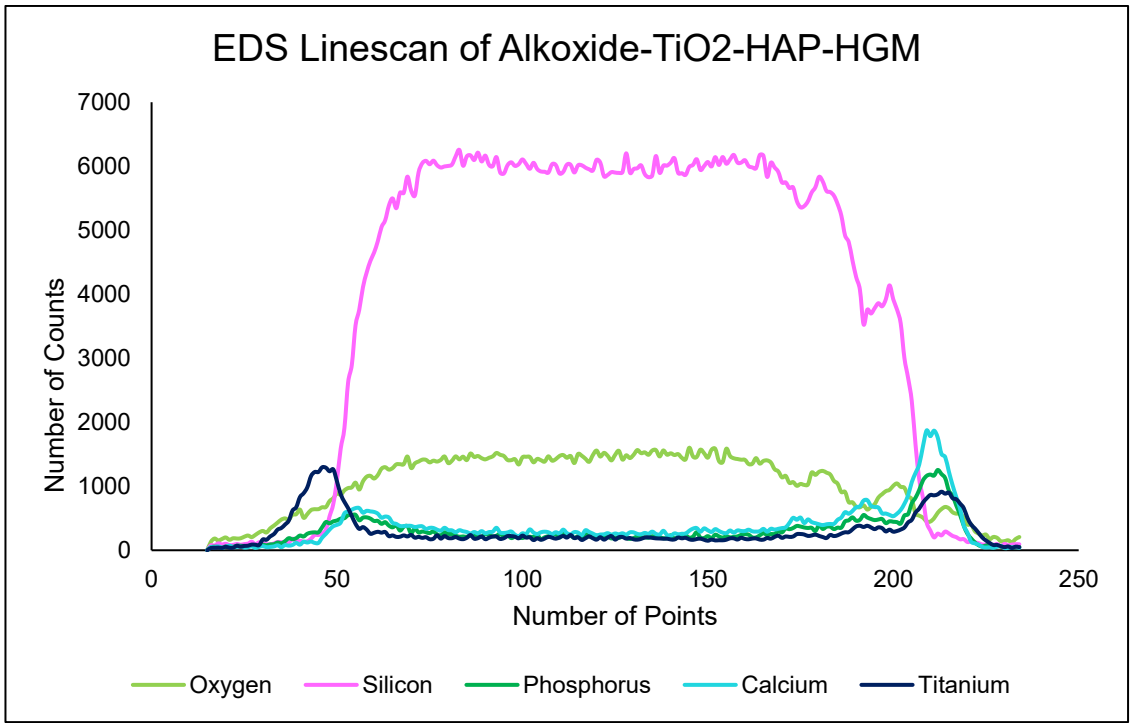

The cross section of the alk-TiO_2-HAP-HGM was also investigated using EDX elemental analysis in order to determine the distribution of elements across the boundaries and internal area of the bead. The beads were embedded in epoxy resin and polished using increasingly fine grit sandpaper, as described in the methods section. The cross section used is shown in Table 82. Also visible is a portion of another sphere cross section at the top of the image.

Table 82. Cross section of alk-TiO_2-HAP-HGM used for the linescan in Chart 3.

Below: original image	Below: all elements overlaid
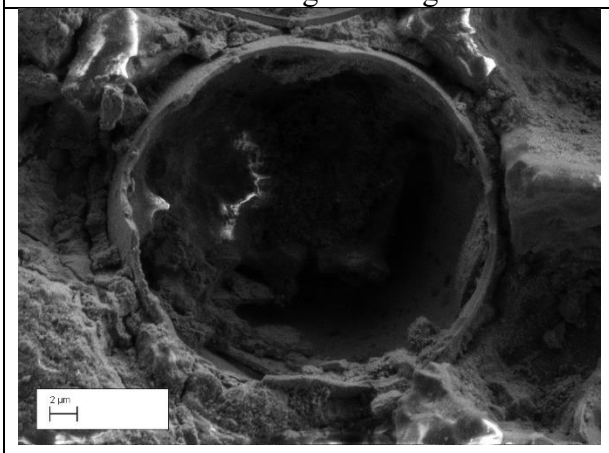	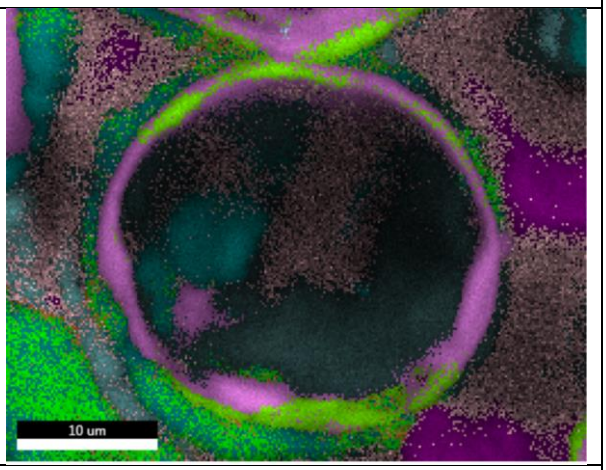
Below: silicon	Below: carbon
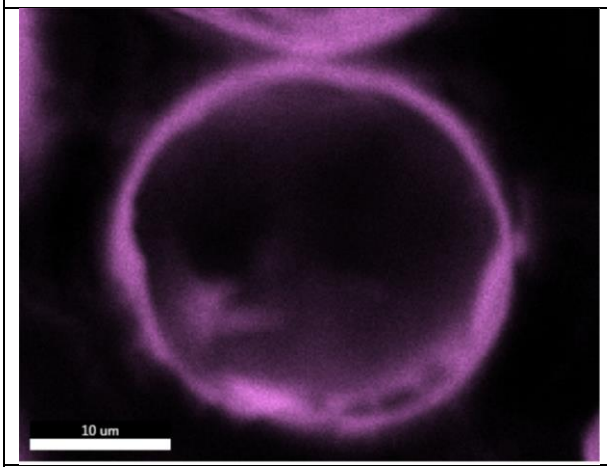	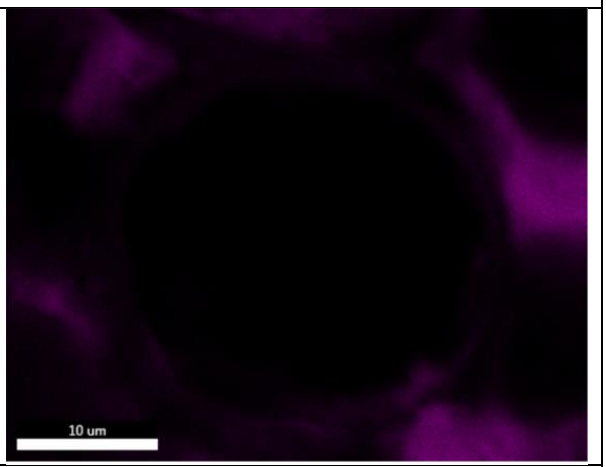
Below: phosphorus	Below: oxygen

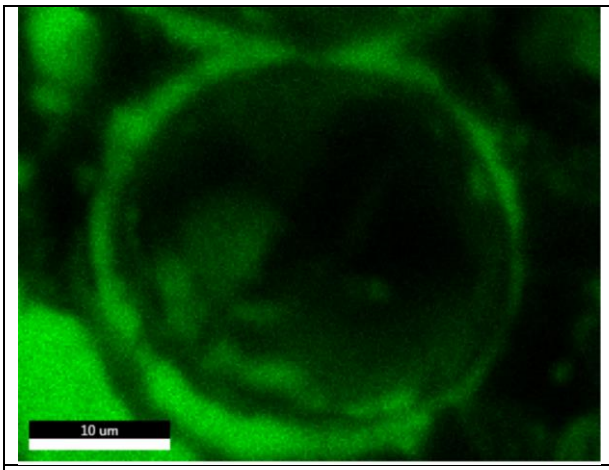	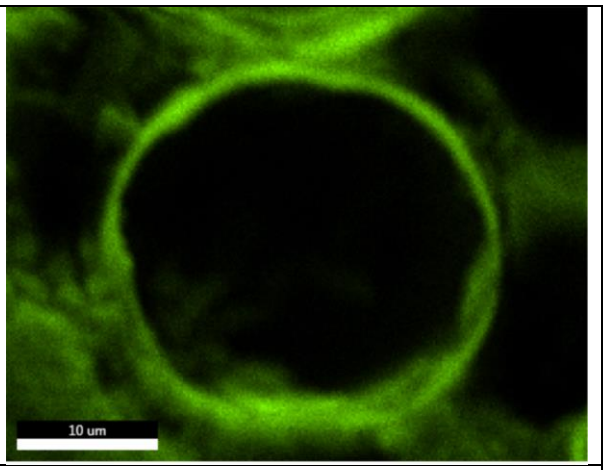
Below: calcium	Below: titanium
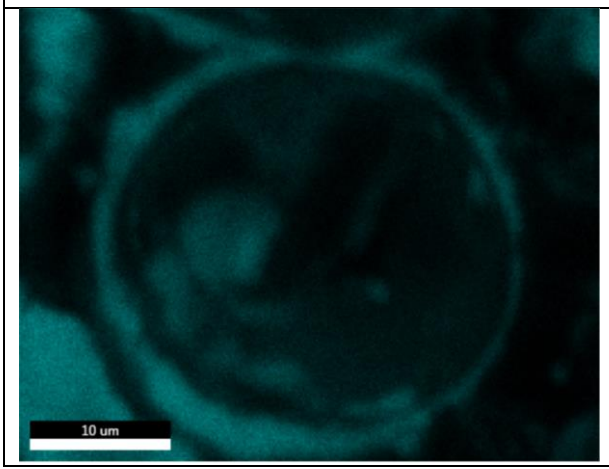	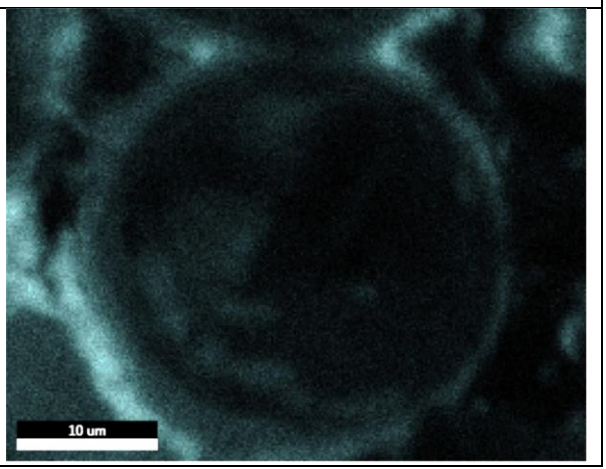

The EDX linescan across the cross section of the alk-TiO_2-HAP-HGM microspheres (shown in Chart 44) was obtained by embedding the microsphere in epoxy resin and polishing away the surrounding area. This technique shows the direction of polishing, which does not totally invalidate the results, but makes the titanium atoms on the outside of the alk-TiO_2-HAP-HGM less clear than in the linescan of an intact particle.

Chart 44. Linescan chart over cross section of alk-TiO_2-HAP-HGM.

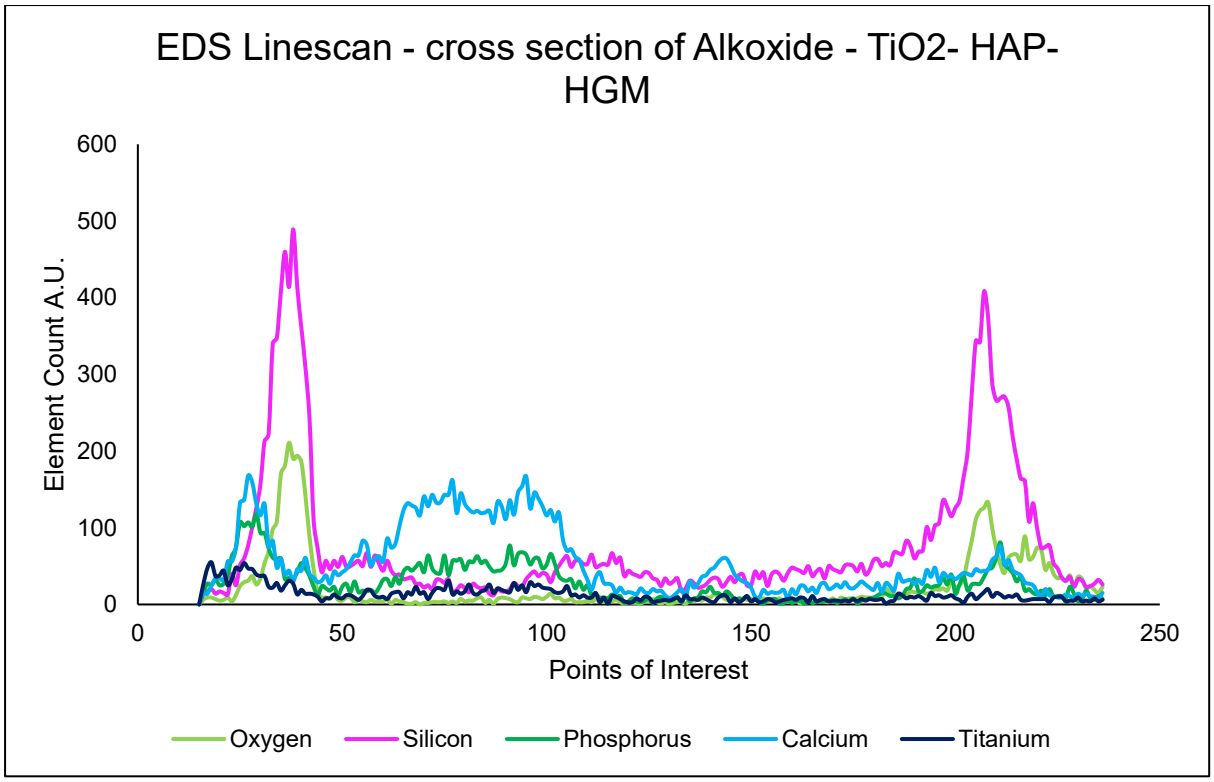

10.4 XRD – Phase Analysis and Quantification of composite materials

The XRD pattern of the alk-TiO_2-HAP-HGM (hydroxyapatite-hollow glass microspheres coated with TiO_2 using the sol-gel process) contains peaks characteristic of hollow glass microspheres (amorphous silicon dioxide), hydroxyapatite formed via chemical precipitation, and amorphous titanium dioxide. The crystal data for peaks that could be identified are included in labelled and displayed in Table 83. Crystal data for identified peaks in alk-TiO2-HAP-HGM, while the XRD pattern is shown in Chart 45. XRD Pattern of the alk-TiO2-HAP-HGM, with the various phases identified labelled. The silicon dioxide component contributes one very broad and shallow peak, with a maximum around 2theta = 23 °.

Due to the issue of overlapping peaks corresponding to HAP, particularly in the region around 2theta = 25 ° where the (201) and (002) peaks overlap, and the regions around 2theta = 32 ° where the (121), (211), (112) and (300) peaks overlap, determination of crystallite size was not attempted. In addition, although peaks belonging to anatase and rutile were identifiable, these appeared too close to the background noise to attempt crystallite size determination. The percentage composition of the alk-TiO_2-HAP-HGMs were instead calculated by mass increases, accounting for particle loss due to washing, and are presented in Table 84. The components of the alk-TiO2-HAP-HGMs given as % composition by mass. The assignment of the possible (although obscured by the HAP component) anatase peaks are listed in Table 85, and the assignment of the HAP peaks are listed in Table 86.

Table 83. Crystal data for identified peaks in alk-TiO_2-HAP-HGM.

Material	**Anatase**	**Rutile**	**Hydroxyapatite**	**Quartz**	**Sodium Chloride**
Pattern number	PDF 01-071-1166	PDF 01-071-0650	PDF 01-074-9765	PDF 01-070-2516	PDF 00-005-0628
Formula	TiO_2	TiO_2	$Ca_{4.914}(H_{0.072}(PO_4)_3(OH)_{0.9}$	SiO_2	NaCl
System	Tetragonal	Tetragonal	Hexagonal	Hexagonal	Cubic
Space Group	I_{41}	$P_{42/mnm}$	$P_{63/m}$	P_{3221}	F_{m-3m}
a	3.784	4.594	9.417	5.02	5.6402
c	3.784	2.959	6.9	5.56	-
Volume Å^3	136.25	62.45	529.91	121.34	179.43
Density	3.889	4.260	3.116	2.467	2.164

Chart 45. XRD Pattern of the alk-TiO_2-HAP-HGM, with the various phases identified labelled.

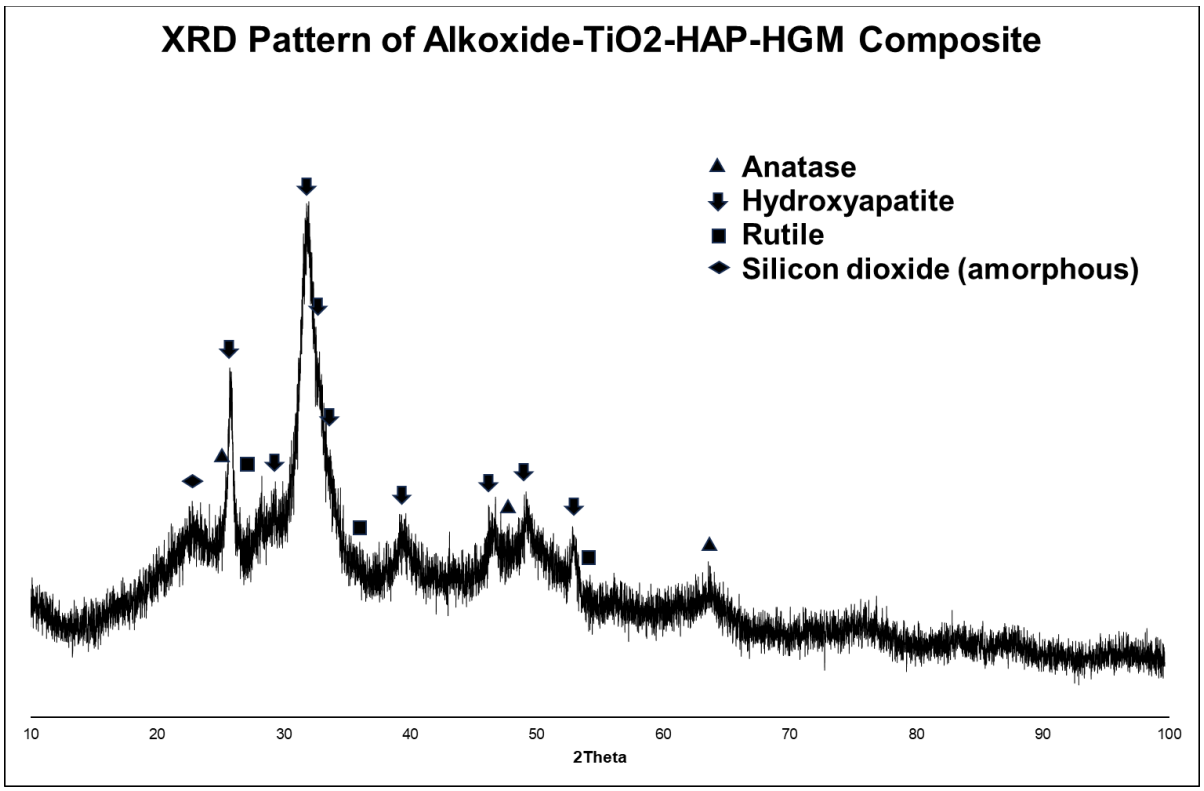

Table 84. The components of the alk-TiO_2-HAP-HGMs given as % composition by mass.

Component of Alkox-TiO_2-HAP-HGM	% Composition by mass
HGMs	38.5%
Hydroxyapatite	19.5%
TiO_2	42.0%

Table 85. Table of hkl planes with associated 2Theta.

Anatase	
2Theta	***hkl***
25.2	(101)
37.7	(004)
47.9	(200)
53.8	(105)
54.9	(211)
62.5	(204)
74.8	(215)

Table 86. Table of hkl planes with assigned 2theta.

Hydroxyapatite (HAP)	
2Theta	***hkl***
25.9	(002)
31.3	(211)
39.7	(130)
46.7	(222)
49.5	(213)
53.2	(004)

Material made from chemically precipitated HAP from the calcium carbonate in scallop shells in a solution doped with anatase were prepared and are samples 10, 11, 12 and 13 and are shown in Chart 46. XRD patterns of the products of co-precipitating anatase with HAP formed from using scallop shells as the sources of calcium carbonate. Samples 10 and 12 which used the more concentrated 1.0 mol dm^{-3} dipotassium phosphate solution produced HAP peaks that were more clearly resolved, although were less crystalline than anatase, as shown by the anatase peaks dominating the sample. The assigned hkl peaks for all samples are listed in Table 85. Table of hkl planes with associated 2ThetaTable 85 for anatase, and Table 86 for HAP.

Chart 46. XRD patterns of the products of co-precipitating anatase with HAP formed from using scallop shells as the sources of calcium carbonate.

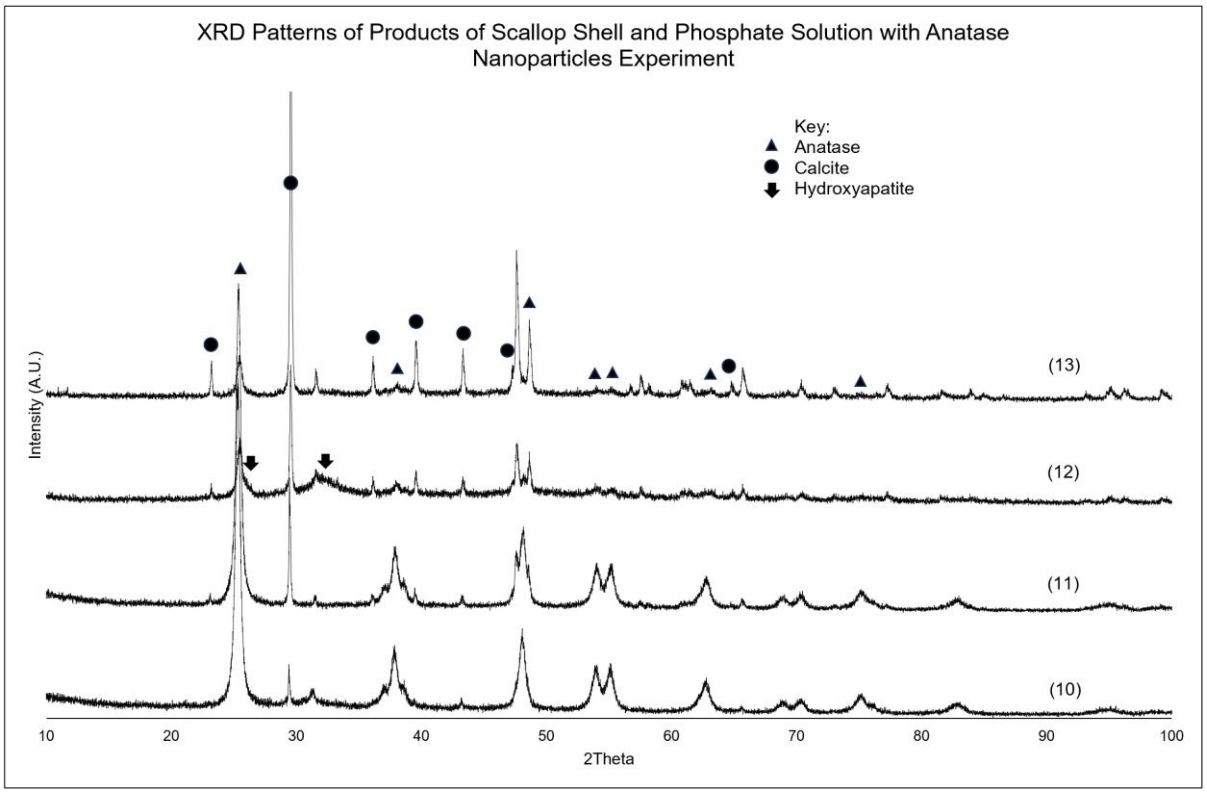

Chart 47. XRD patterns of the TiO_2-HGM samples formed from co-precipitation of CaHGMs with phosphate solution.

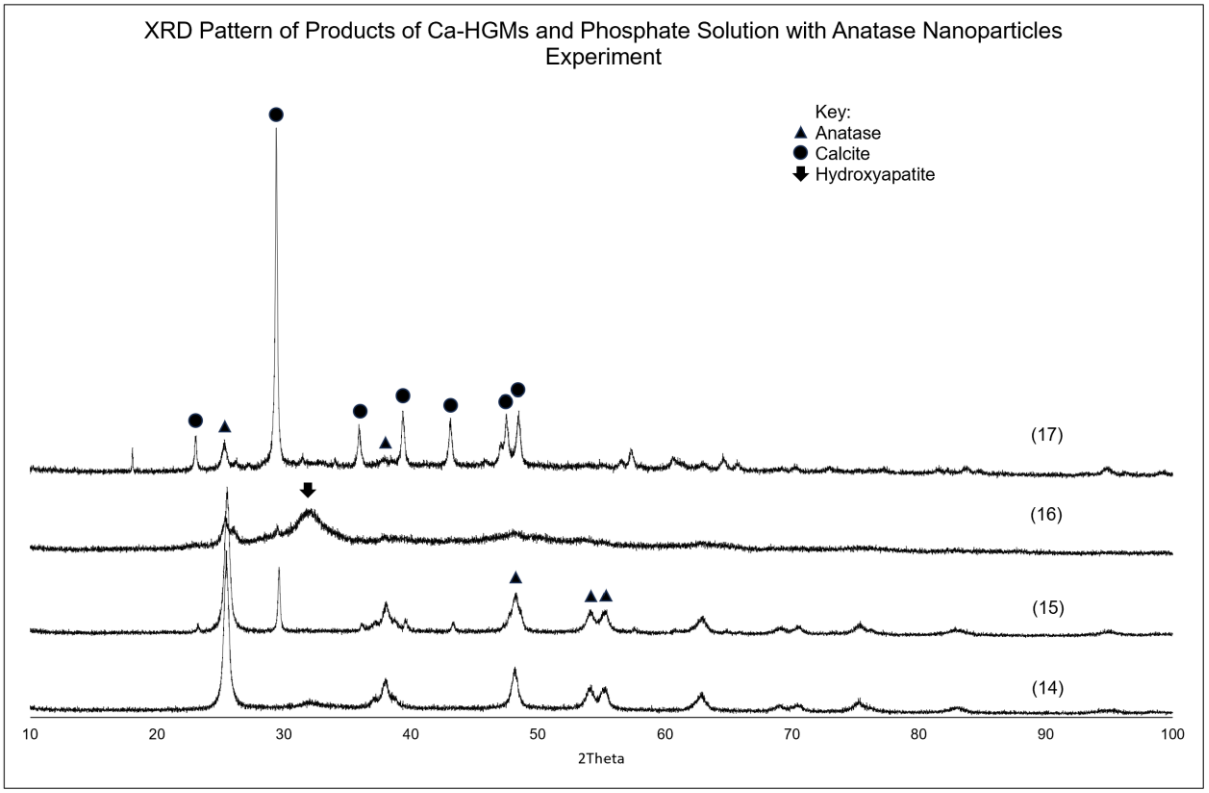

Overall, the conclusion that can be gained from the XRD patterns of the various TiO_2-HAP materials is that the more concentrated 1.0 mol dm^{-3} solution of dipotassium phosphate was more successful at converting the calcium carbonate in hydroxyapatite.

10.5 FT-IR spectroscopic analysis of the composite materials

FT-IR spectra of the samples were obtained in order to characterise the materials, shown in Chart 48. FT-IR Spectra of all TiO2-HAP samples prepared – intensities have been adjusted to allow overlay and Chart 49. FT-IR spectra of the anatase-HAP-HGMs- intensities have been adjusted to allow overlay by identifying peaks associated with specific functional groups, shown in Table 87. Assignment of band present in the IR spectra. In particular, the presence of peaks associated with carbonate indicate that the calcium carbonate was not fully converted into hydroxyapatite, and peaks associated with phosphate groups were indicative of hydroxyapatite forming successfully.

The bands associated with carbonate vibrational modes between 1500-1300 cm^{-1}, and it can be seen that these are particularly strong for samples 11, 13, 15, and 17 these peaks are wide and broad, indicating the presence of significant amounts of carbonate within the samples, and hence incomplete conversion of calcium carbonate to the calcium phosphate of HAP. This is assumed to be due to the 0.1 mol dm^{-3} dipotassium phosphate solution being too dilute to cause the full conversion of calcium carbonate to HAP.

In contrast, in samples 10, 12, 14, and 16 show barely perceptible bands in the 1500-1300 cm^{-1} region associated with carbonate, indicating a much greater conversion of calcium carbonate to HAP. These samples were made using the more concentrated 1.0 mol dm^{-3} dipotassium phosphate solution, and FT-IR can be used to confirm that the more concentrated 1.0 mol dm^{-3} dipotassium phosphate solution presents the better method for achieving conversion of calcium carbonate into HAP.

There are no strong peaks associates with water in the region 3400-3200 cm^{-1}, and the bands associated with Ti-O bonds in the region around 690 cm^{-1} indicate where anatase has been incorporated into the material, however other bands occur in this region, and hence FT-IR is not appropriate for characterising the Ti-O bonds.

Table 87. Assignment of band present in the IR spectra.

Freq cm-1	Functional Group
3400 - 3200	O-H Stretching
1800 - 1600	C=O stretching vibration
1490-1400	CO_3^- asymmetric stretch
1440-1310	O-H bending vibration
1300 -750	Si-O-Ca broad stretching vibration
1200 - 1100	Phosphate stretching vibration
1130 - 1000	Si-O-Si stretching, band becomes broader as silicon chain gets longer
804	Si-O symmetric stretch
710	Si-O symmetric stretch
690	Ti-O
609	Ca-O bond

Chart 48. FT-IR Spectra of all TiO_2-HAP samples prepared – intensities have been adjusted to allow overlay.

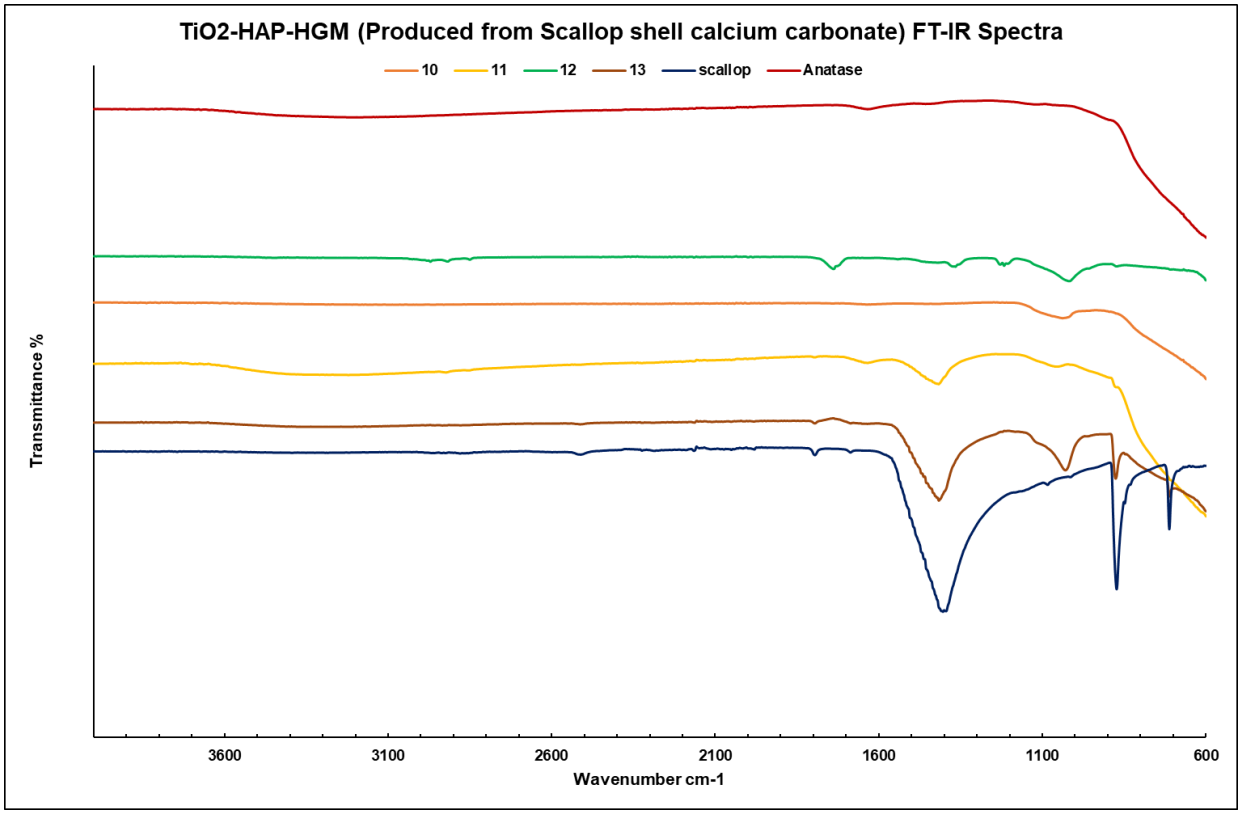

Chart 49. FT-IR spectra of the anatase-HAP-HGMs- intensities have been adjusted to allow overlay.

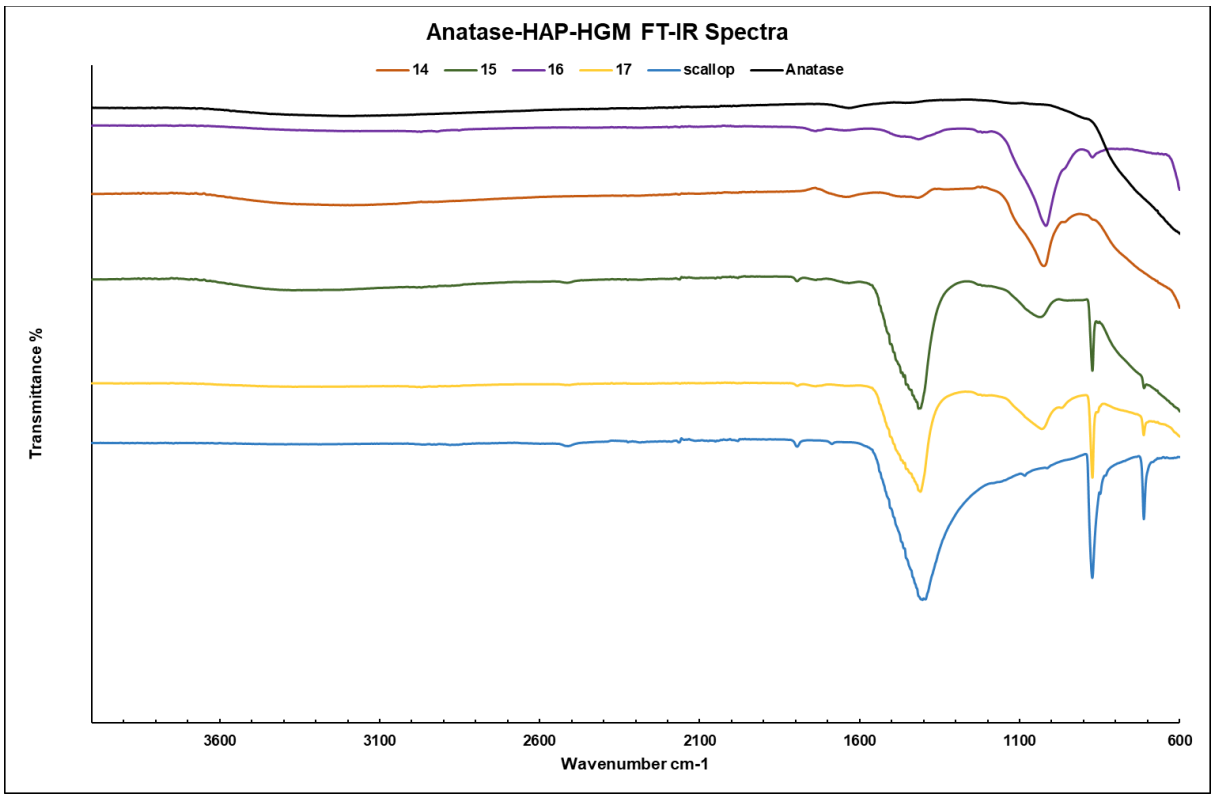

The main conclusion that can be drawn from the FT-IR data is that the 1.0 mol dm^{-3} solution of dipotassium phosphate was more successful at achieving the conversion of calcium carbonate into hydroxyapatite.

10.6 BET – Surface Area Analysis of two composite materials

The following BET, BJH and adsorption/desorption isotherm data is for the HAP-HGMs that produce with the calcium carbonate component being derived from scallop shells (scsh-HAP-anatase. The surface area of this sample is relatively low, at only 13.23 m^2/g. In contrast, the HAP-HGMs had a surface area of 54.7 m^2/g, which is very high, especially because the microsphere is completely hollow, which can be seen from the cross section in Chapter 10 Figure 5. The reason that the surface area decreased upon addition of anatase to the HAP-HGM lattice could be due to anatase occupying the pores present in the HAP of the HAP-HGMs. The surface area and mean pore diameters are shown in Table 88, while the BET plots are shown in Figure 90. BET plot of schsh-HAP-anatase and Figure 91. BET plot of anatase-HAP-HGMs.

Table 88. Surface area and mean pore diameters of scsh-HAP-anatase and anatase-HAP-HGMs.

Sample	S_{BET} (m^2/g)	Mean Pore Diameter (nm)
Scsh-HAP-anatase	13.23	25
Anatase-HAP-HGMs	16.99	46

Figure 90. BET plot of schsh-HAP-anatase.

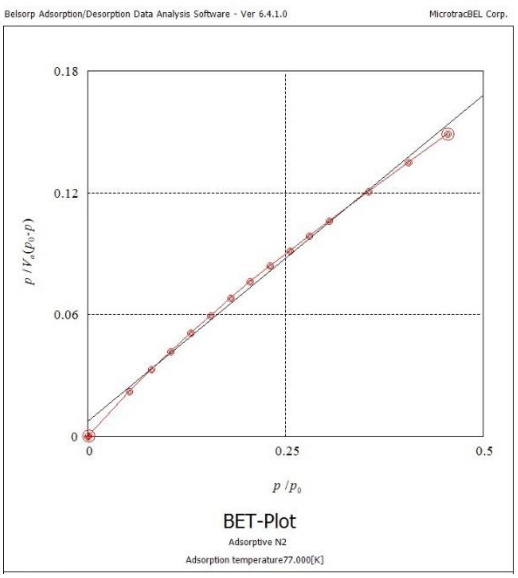

Figure 91. BET plot of anatase-HAP-HGMs.

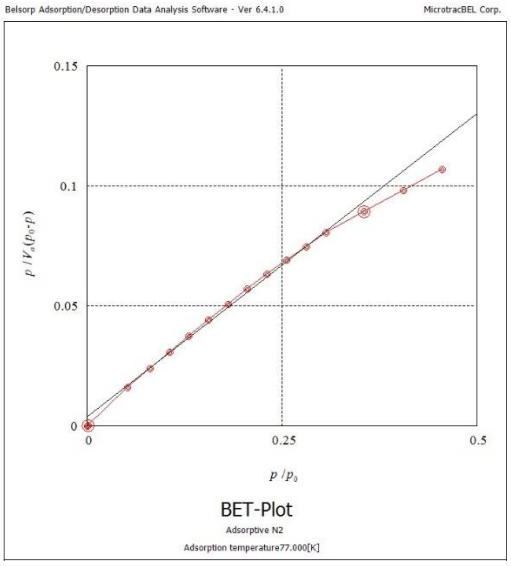

10.7 N_2 Adsorption/Desorption Isotherm

The N_2 adsorption desorption isotherm of the scsh-HAP-anatase sample displayed in Chart 50. Adsorption/desorption isotherm of scsh-HAP-anatase is classified as a type III isotherm due to the gradual increase in adsorption and the lack of any plateau. A type III isotherm is consistent with non-porous materials, which may be because the hydroxyapatite layer on the HAP-HGMs is a relatively thin layer, with a thickness ranging from 1 – 2 µm, while the radius of the HGMs averages 20 µm. The isotherm resembles the isotherms obtained for the HAP-HGMs in Chapter 8. The adsorption desorption N_2 isotherm for the anatase-HAP-HGM sample is displayed in Chart 51. Adsorption/desorption isotherm of anatase-HAP-HGM.

The adsorption desorption isotherm of the anatase-HAP-HGM sample is similar to that of the anatase-HAP-HGMs, although the desorption curve drops below zero for the volume of N_2 adsorbed, indicating an instrumental issue.

Chart 50. Adsorption/desorption isotherm of scsh-HAP-anatase.

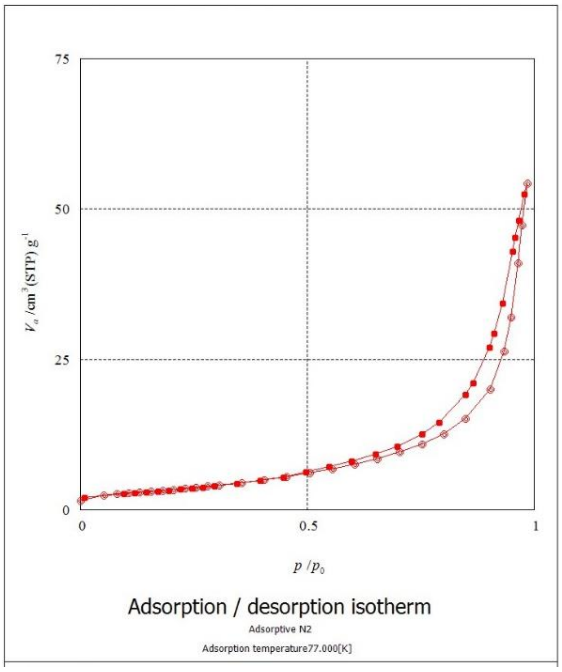

Chart 51. Adsorption/desorption isotherm of anatase-HAP-HGM.

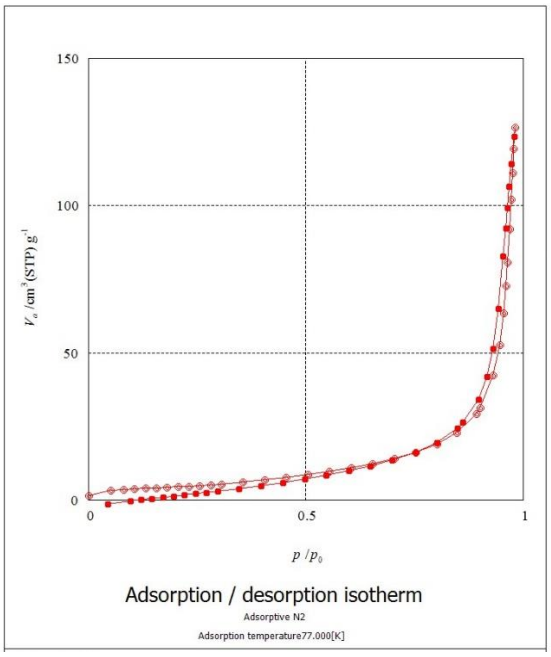

10.8 BJH Plot for Pore Size Distribution

The BJH plot for the scsh-HAP-anatase composite shows a much narrower mean pore radius and a smaller distribution of pore sizes than the anatase-HAP-HGM composites, which show a larger distribution of pore sizes, with two distinct maxima in the plot representing two particularly common pore radii. Given that both plots contain biomimetic HAP and have a maxima at 2 – 3 nm, which is also shared by the BJH plot of the HAP-HGMSs, it could be concluded that the pores in this region are attributable to the biomimetic HAP component of these materials. These BJH plots are shown in Figure 92. BJH plot of scsh-HAP-anatase Figure 93. BJH plot of anatase-HAP-HGMs

Figure 92. BJH plot of scsh-HAP-anatase.

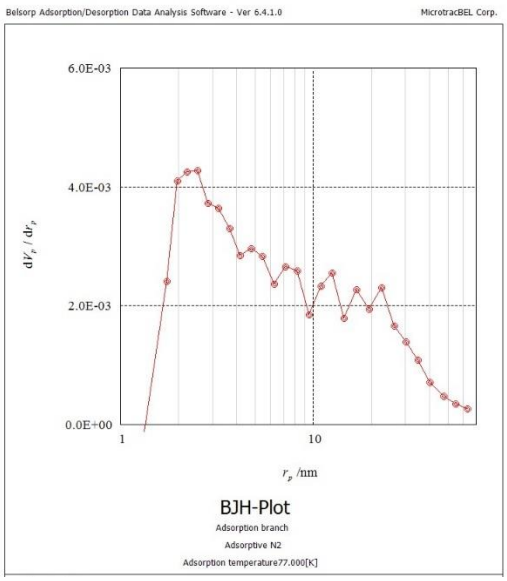

Figure 93. BJH plot of anatase-HAP-HGMs.

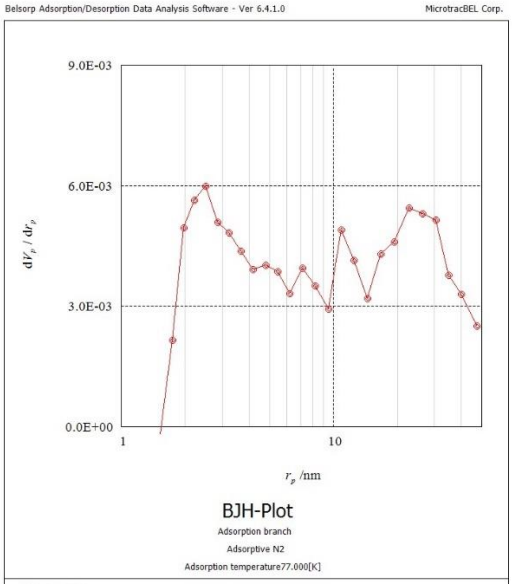

10.9 Thermo-gravimetric Analysis

TGA curves of the three TiO_2-HAP composites were obtained after the three materials had been used to remove EE2 from solution. Step changes in the range 25 – 200 °C are attributed to the loss of water across Figure 94. TGA curve of alk-TiO2-HAP-HGMs, Figure 95. TGA curve of Scsh-HAP-anatase and Figure 96. TGA curve of Anatase-HAP-HGMs. The step in Figure 14 that begins at approximately 650 °C and ends at approximately 750 °C is attributed to the thermal decomposition of calcium carbonate within the scsh-HAP-anatase.

The jagged natures of the TGA curves in Figure 94 and Figure 96 is likely due to fluctuations in weight loss which may be due to volatile release of compounds from the sample. The noticeable although poorly defined step between 500 – 600 °C in Figure 94 could potentially be due to the HGMs melting in the alk-TiO_2-HAP-HGMs, as a similar (but much smaller step) is present in the Figure 96, the TGA curve for the anatase-HAP-HGMs.

Figure 94. TGA curve of alk-TiO_2-HAP-HGMs.

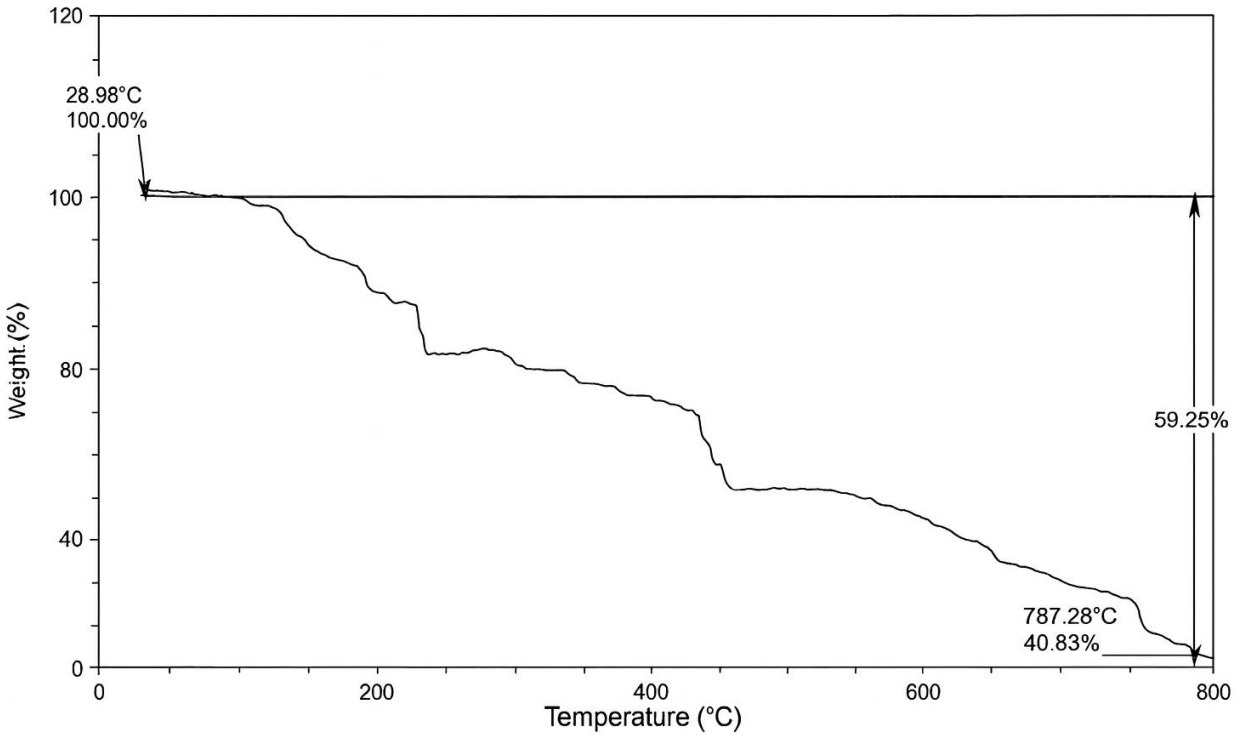

Figure 95. TGA curve of Scsh-HAP-anatase.

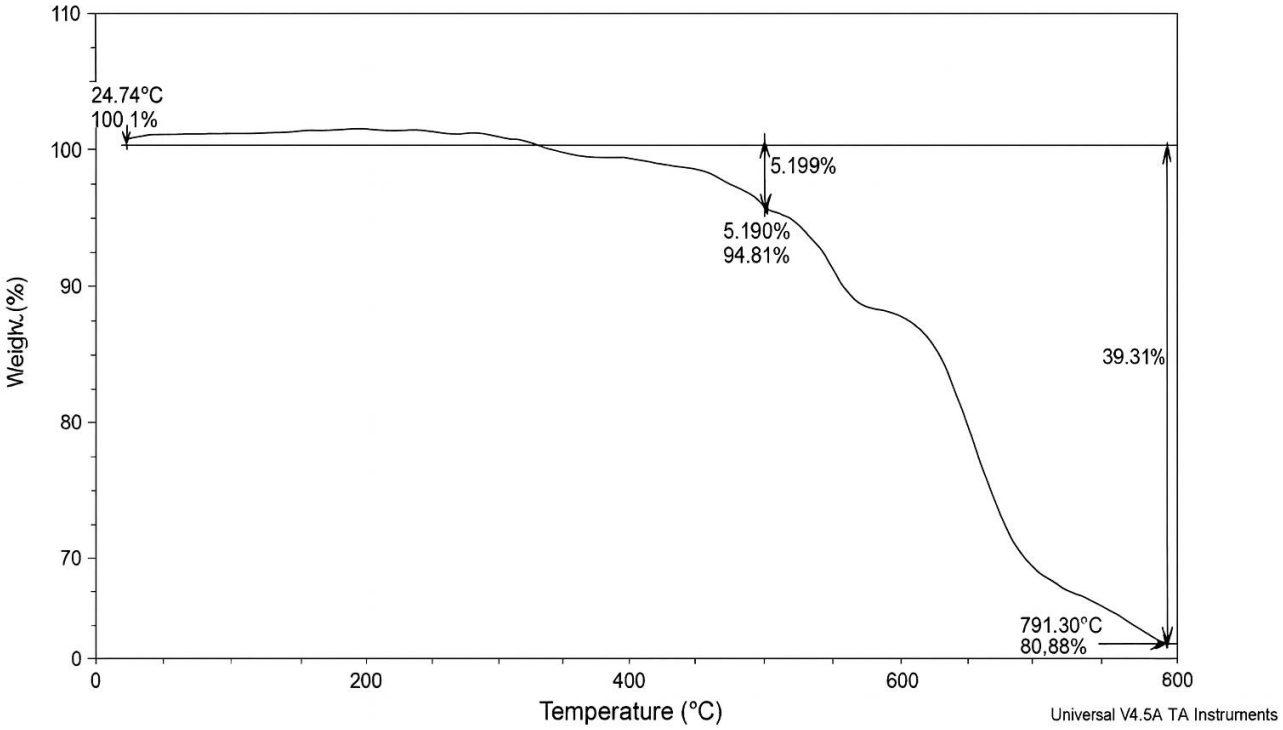

Figure 96. TGA curve of Anatase-HAP-HGMs.

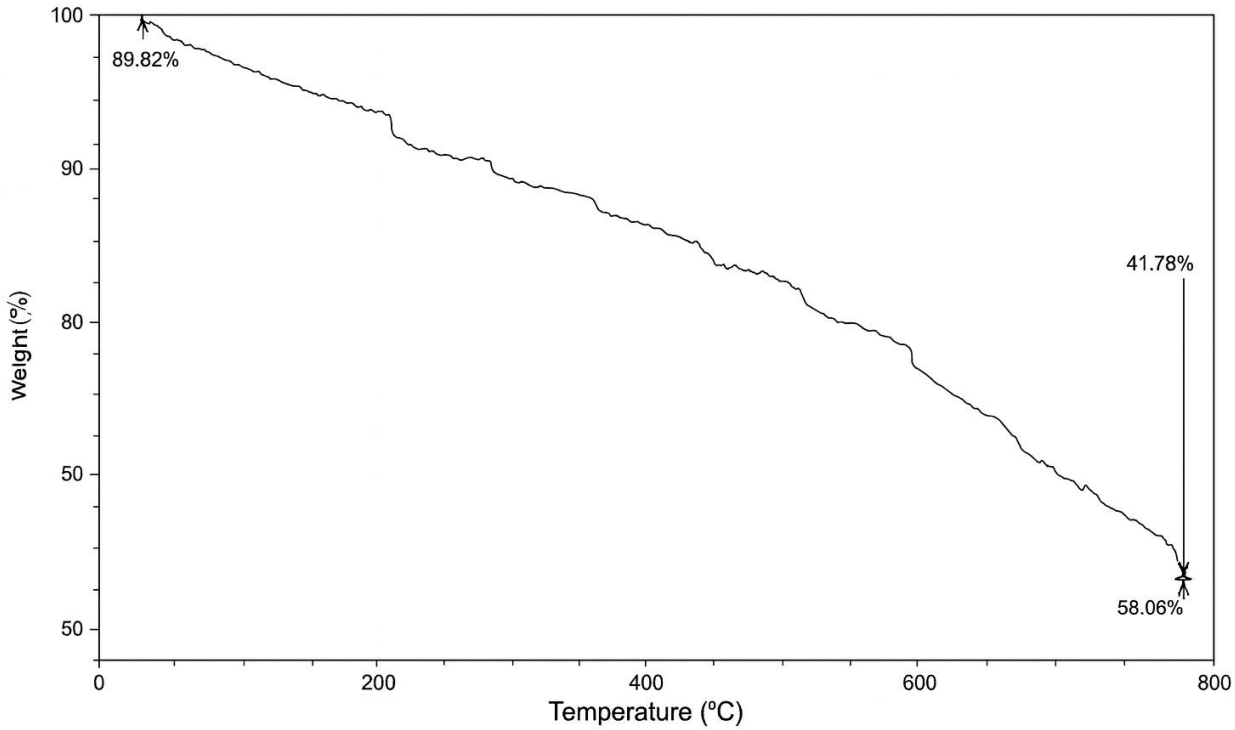

10.10 Chapter Summary

Composites of TiO_2 and hydroxyapatite were successfully synthesised using chemical precipitation in the presence of anatase nanoparticles to incorporate anatase into the HAP-HGMs to produce anatase-HAP-HGMs, although anatase tended to aggregate and was found in very high concentrations on a small number of the regions on the outside of the anatase-HAP-HGMs. Drying pre-made TiO_2 synthesised using the TNW1 method was limited in its success, as SEM images showed the TiO_2 coating peeling off. In contrast, adding the HAP-HGMs into the TNW2 reflux reaction, and filtering off the solid material after heating at 90 °C produced an evenly distributed coating of TiO_2 micro-rods that were pervasive across the surfaces of the alk-TiO_2-HAP-HGMs. EDX was instrumental in analysing the distribution of TiO_2 across the microspheres, and the linescans in particular were useful for showing the showing of TiO_2.

Due to the overlapping peaks of the XRD pattern of the alk-TiO_2-HAP-HGMs it was not possible to calculate the average crystallite size using the Scherrer equation. Instead, the % composition by mass was calculated by considering mass increases at each stage of the reaction, while also considering the extent of particle loss from the washing process, and the amount of HAP formed from a stoichiometric reaction based on the mass of calcium carbonate. The conclusion that can be gained from analysing the XRD patterns and FT-IR spectra is that the 1.0 mol dm^{-3} solution of dipotassium phosphate was able to convert the calcium carbonate into hydroxyapatite, whereas the 0.1 mol dm^{-3} solution of dipotassium phosphate left significant amounts of calcium carbonate within the samples, indicating the full conversion of calcium carbonate to hydroxyapatite was not achieved.

The SSA was calculated using a BET plot, and was found to have decreased relative to the HAP-HGMs, being just 13.23 m^2/g for the anatase-HAP-HGMs, and 16.99 m_2/g for the scsh-HAP-anatase. The mean pore diameter for the scsh-HAP-anatase was found to 25 nm, which

is far larger than the anatase-HAP-HGMs, which had a mean pore diameter of 46 nm.

The adsorption desorption isotherm of the anatase-HAP-HGMs closely resembles the isotherm produced for the HAP-HGMs in Chapter 8. The isotherm is characterised by the absence of a sharp initial increase in N_2, instead following a slow rate of N_2 adsorption that only increases at higher pressures. The presence of a small hysteresis loop in the higher pressure is characteristic of a mesoporous material.

11. Chapter 11 – Removal of EE2 from Aqueous Solution

11.1 Introduction

This chapter contains the results of EE2 removal by the composite materials and materials produced in intermediate stages of the syntheses. Known concentration of EE2 were run on HPLC to obtain an integrated area associated with a given concentration. A trendline through these points was produced, which was then assessed for its R^2 values, where $R^2 > 0.99$ was considered acceptable. A range of filters used in the literature to filter EE2 solutions were investigated for their tendency to retain EE2, which could invalidate the results for EE2 removal if EE2 removal was misattributed to the adsorbent/photocatalytic materials. Finally, the results of the experiments aimed at quantifying the removal of EE2 from solution using the composite material, named alk-TiO_2-HAP-HGM are included, where a series of materials were also tested for their ability to remove EE2 from solution in order to provide a comparison for the composite material. The use of HPLC-UV has a relatively high limit of detection and limit of quantification relative to other techniques such as HPLC-FLD, GC-MS, HPLC-MS and UPLC-RMS. The implications of this are discussed in Chapter 12.

11.2 Selection of Filter

A range of filters were tested to determine the extent to which EE2 became adsorbed to the filters. PTFE filters in size of 0.22 µm and 0.45 µm were tested, in addition to 0.45 µm cellulose filters, 0.45 µm PVDF filters, and 0.7 µm glass fibre filters. A 1.0 mL aliquot of a solution of EE2 of concentration 10 ppm was passed through a filter, and HPLC used to determine the concentration of the EE2 solution that had passed through the filter. This process was repeated a further four times, totalling 5 samples of 10 ppm solution through the same filter. This process was repeated a further two times with an average taken of the concentration of EE2. The results are included in Table 89. EE2 removed from solution by filters, expressed as percent of 10

ppm.

A high percentage of EE2 removal indicates that EE2 became stuck to the filter, meaning the filter would not be appropriate for use in filtering the solutions prior to HPLC, as low concentrations of EE2 could be misattributed to the composite material, whereas a low percentage of EE2 removal by the filters is favoured. The results contained in Table 89 were incorporated into Chart 52 to show the extent of EE2 removal by the filters.

The first run of PTFE 0.45 μm filters retained the least EE2, allowing 98.3% of EE2 in solution to pass though. In contrast, PTFE 0.22 μm filters retained over 90% of the EE2 in solution. PVDF filters retained high amounts of EE2 in the initial use, however repeated uses of the same filters retained less and less EE2. This effect was also seen with the cellulose filters, where the initial use of the filter retained a large proportion of the EE2 in solution, however repeated uses of the same filter retained less EE2.

Given the results in Chart 52, the PTFE 0.45 μm was chosen for all subsequent analyses as this removed the lowest percentage of EE2 from the 10 ppm solution, where just 1% of the EE2 was lost to the filter. Each filter was used once and then discarded. Secondly, it would have been good to have a rationale for differences seen from SEM and u-ftir images of the filters before and after use could have indicated if the EE2 was precipitating out of solution and adsorbing on the surface of the filters, or become absorbed into the material of the filter itself.

Table 89. EE2 removed from solution by filters, expressed as percent of 10 ppm

Filter	Run	% of EE2 retained on filter
PVDF 0.45 µm	1	100%
	2	89%
	3	62%
	4	38%
	5	27%
Glass Fibre 0.7 µm	1	18%
	2	7%
	3	6%
	4	5%
	5	6%
Cellulose 0.45 µm	1	56%
	2	23%
	3	17%
	4	11%
	5	10%
PTFE 0.45 µm	1	1%
	2	2%
	3	10%
	4	11%
	5	11%
PTFE 0.22 µm	1	91%
	2	92%
	3	92%
	4	94%
	5	95%

Chart 52. Bar chart showing percent of EE2 retained on filters. Lower values for EE2 retention are preferred

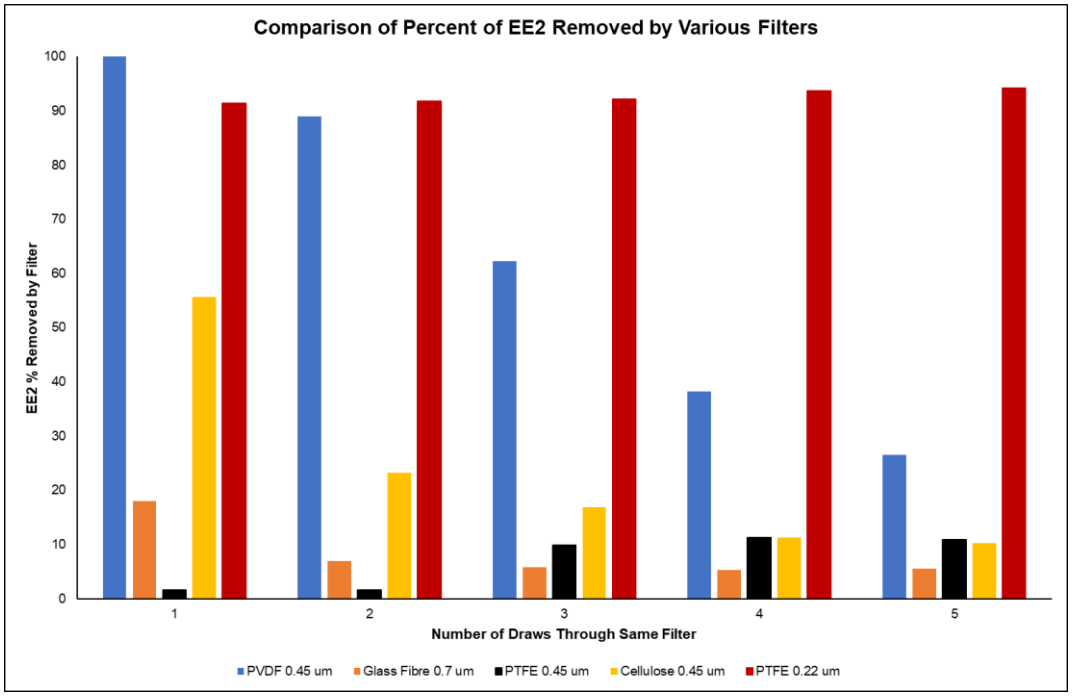

11.3 Initial Test of EE2 Removal

An initial test of EE2 removal was carried out using the raw and intermediate materials to explore the potential for EE2 removal. The alkoxide-TiO_2-HAP-HGM was a prototype of the alk-TiO_2-HAP-HGM used in later EE2 removal experiments, formed by drying the calcined TiO_2 gel on to the HAP-HGMs, whereas the alk-TiO_2-HAP-HGM was formed by adding the HAP-HGMs to the TiO_2 sol, workign up the reaction, the filtering off the products. The alkoxide-TiO_2-HAP-HGMs included a black carbonaceous component (likely formed by the solvents polymerising), and in the alk-TiO_2-HAP-HGMs this carbon component was avoided, producing a composite of TiO_2 and HAP-HGMs.

The control experiemnt showed a loss of approximetaly 10% EE2, likely due to to the combined of the PTFE filters, photolysis, and adsorption of EE2 to the cracks, scratches or defects of the glass vessels. This experiment was performed by adding the same mass of material to the EE2 solutions, which explains the high removal ability of the HGMs – an equivalent mass of HGMs would consist of a far greater number of particles – mean a greater number of opportunities for an adsorbing interaction to occur between the silanol group on the surface of an HGM and an EE2 molecule.

Both the HAP-HGMs and CaHGMs performed well, with the HAP-HGMs removing approximately 60% of the EE2 present in solution in the initial 20 min. the rate of EE2 removal slowed noticeably from time = 40 min onwards, but contineud to remove a further 15%, totaling 75% EE2 removal in 3 hr. The CaHGMs removed the greatest amount of EE2 overall, but the initial rate of EE2 removal was slower than the HAP-HGMs, although after 3 hr the EE2 removal by the CaHGMs reached 80%.

The alkoxide-TiO_2-HAP-HGMs performed similarly to the anatase nanoparticles, which is interesting as the characterisation data indicates that the TiO_2 component is concealed by the polymerised carbon, and that further work is need to ensure the TiO_2 component is exposed and available for photocatalysis. It is likely that the anatase nanoaprticles are aggregating which would prevent efficient photocatalysis, given that the in the literature EE2 removal efficiencies by TiO_2 can reach up to 100%. This finding further supports the hypothesis that anatase nanoparticles should be supported on a scaffold to ensure a larger surface area of anatase sites are available for photocatalysis, in order to minimise the effect of the tendency of anatase nanoparticles to form aggregates. These results are shown in Chart 53.

Chart 53. Change in EE2 concentration measured with HPLC.

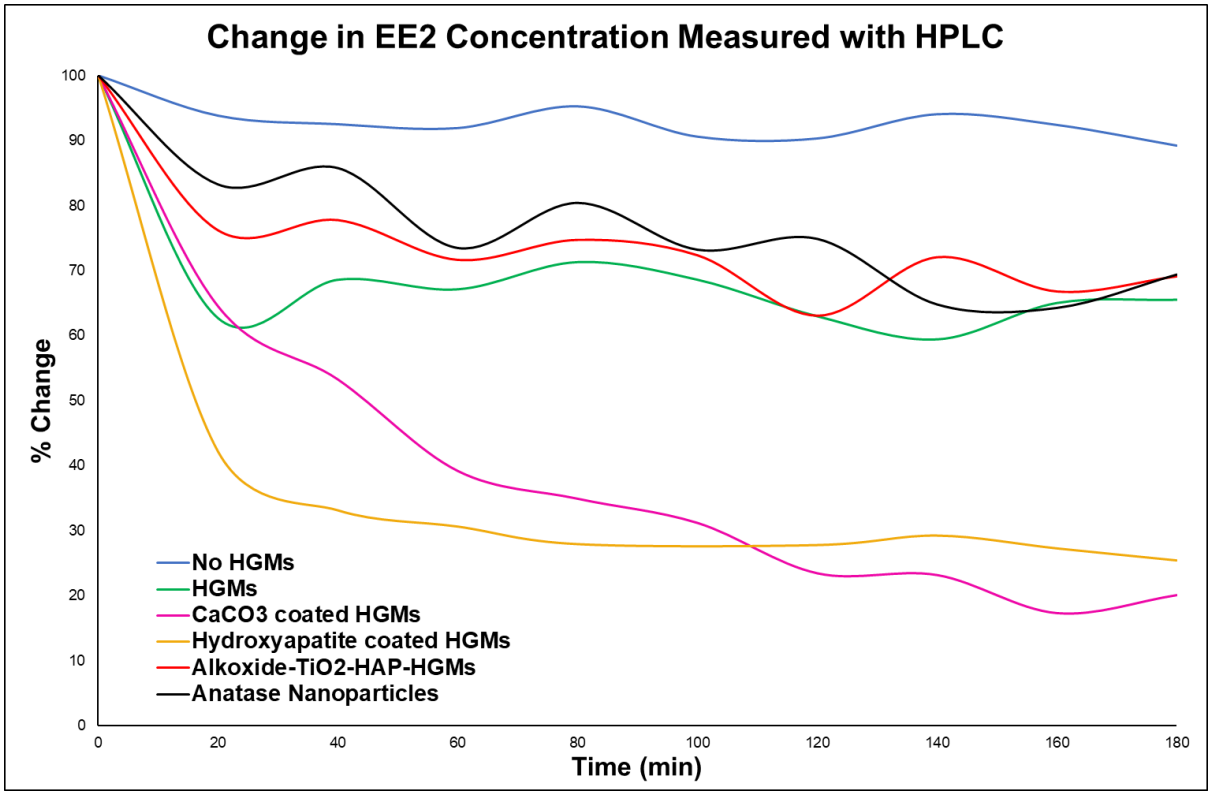

11.4 Batch Settling Technique

The batch settling technique aimed to replicate realistic conditions where the composite material would be used to removed EE2 from water. This method assumes the operator has sufficient electricity to operate a UV lamp but not enough to operate an electrical stirring mechanism. This method aims to replicate conditions where electricity supply is unreliable, but may be available from a single solar panel. The setting is assumed to be extremely rural. The method used to perform this experiment is contained in Chapter 6 – Methods. From time = -0.5 h the EE2 solutions were added to the materials listed in Table 2 and at time = 0 h the UV lamp was switched on, initiating the process of photocatalysis in materials that contained TiO_2.

Overall, the materials that contained both adsorbing components and photocatalytic components outperformed materials that were either adsorbing or photocatalytic. The control sample contained no adsorbing or catalytic material but was subjected to 0.5 h in the dark followed by 12 h of exposure to UV light.

The results of EE2 removal from solution using this technique are depicted in Chart 2, where the highest EE2 removal was achieved by the scsh-HAP-anatase, which removed 65.68%, the anatase-HAP-HGMs, which removed 55.74%, and the alk-TiO_2-HAP-HGMs, which removed 43.03%. GAC was the next highest performer, at 31.55%, followed by anatase, at 29.47%. The HAP-HGMs and CaHGMs performed similarly, removing 27.67% and 27.12% of the EE2 respectively. The HGMs were capable of removing a small amount EE2, removing <16% of the EE2 in solution, likely from the hydrophobic nature of EE2 resulting in its interaction with the HGMs resulting in an interaction between the HGMs and EE2, especially if there was any organic contaminants on the HGMs from the manufacturing process that were also hydrophobic. In the control experiment, <10% of the EE2 was removed after 12 hr.

Granular activated carbon (GAC) outperformed all the materials with solely adsorbent

properties and also anatase, however all of the materials with both photocatalytic and adsorbent materials outperformed GAC. These data are displayed in Chart 55, which shows the results of EE2 removal using the batch settling method.

All of the materials displayed some oscillation in the concentration of EE2 in solution in the initial hour, which is consistent with EE2 removal in the literature (Feng, 2010). The small difference in oscillation is attributed to the errors inherent in the HPLC-UV method used to quantify the EE2 in solution. This data is shown in Chart 54, Chart 55, Batch settling method EE2 removed mg/g material in 12 h Table 90 and Table 91.

Chart 54. EE2 removal achieved by batch settling process.

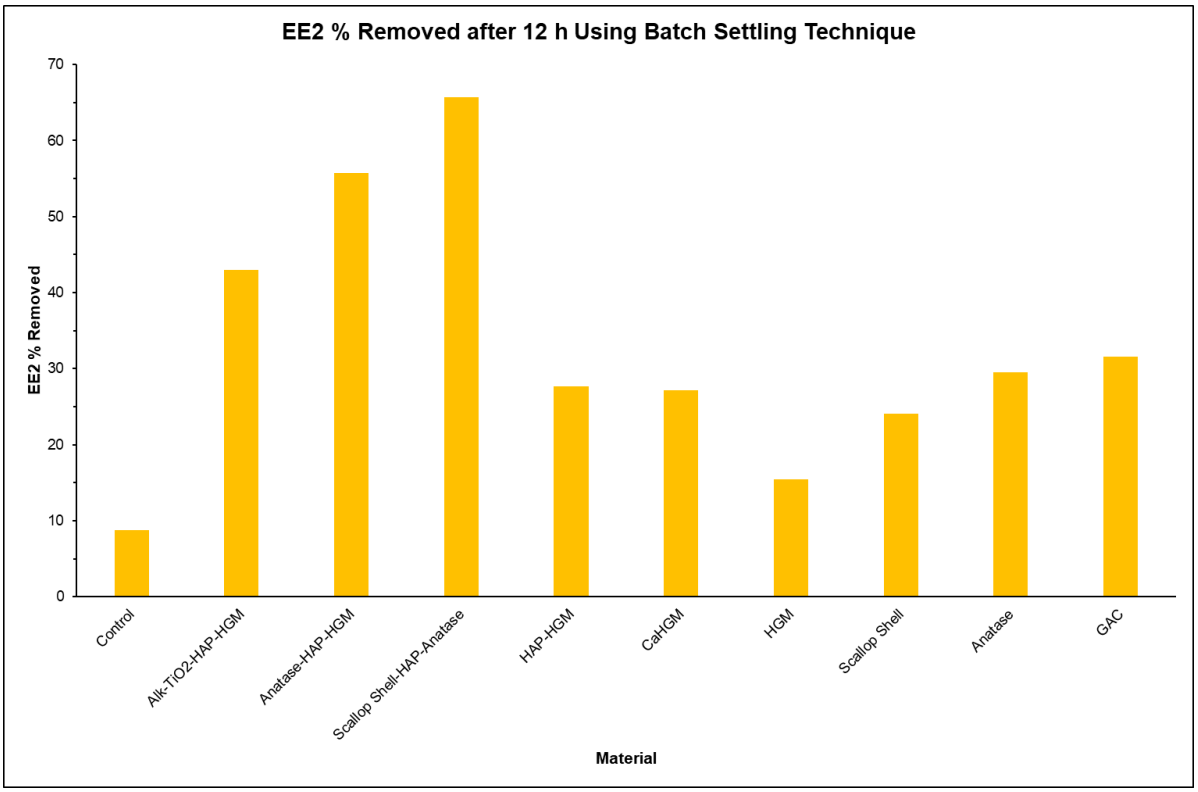

Table 90. EE2 removed in mg/g material using batch settling technique.

EE2 removed in mg /g material using batch settling technique										
Time (h)	**Alk-TiO_2-HAP-HGM**	**HGM**	**CaHGM**	**Anatase-HAP-HGM**	**Control***	**HAP-HGM**	**Scallop Shell-HAP-Anatase**	**Scallop Shell**	**Anatase**	**GAC**
-0.50	0.00	0.00	0.00	0.00	0.00	0.00	0.00	0.00	0.00	0.00
0.00	0.30	0.26	0.30	0.34	0.23	0.33	0.34	0.27	0.28	0.52
0.17	0.38	0.27	0.32	0.47	0.22	0.39	0.38	0.19	0.35	0.46
0.33	0.46	0.28	0.37	0.46	0.21	0.40	0.41	0.27	0.38	0.46
0.50	0.45	0.31	0.36	0.54	0.20	0.41	0.50	0.30	0.36	0.51
1.00	0.49	0.28	0.46	0.63	0.20	0.58	0.57	0.33	0.41	0.50
2.00	0.47	0.35	0.57	0.81	0.22	0.68	0.68	0.44	0.50	0.55
3.00	0.68	0.37	0.57	0.87	0.22	0.68	0.95	0.48	0.55	0.65
6.00	0.92	0.39	0.65	1.18	0.27	0.83	1.52	0.58	0.77	0.82
12.00	1.40	0.50	0.88	1.82	0.26	0.90	2.14	0.79	0.96	1.03
*as no material was added to the control experiment, this value is mg of EE2 removed from solution										

Table 91. EE2 % removed using batch settling technique.

EE2 % removed using batch settling technique										
Time h	**Control**	**Alk-TiO_2-HAP-HGM**	**Anatase-HAP-HGM**	**Scallop Shell-HAP-Anatase**	**HAP-HGM**	**CaHGM**	**HGM**	**Scallop Shell**	**Anatase**	**GAC**
-0.50	0	0	0	0	0	0	0	0	0	0
0.00	7.44	9.19	10.33	10.42	10.12	9.08	8.10	8.44	8.50	15.94
0.17	7.39	11.68	14.38	11.60	11.99	9.74	8.35	5.69	10.70	14.06
0.33	6.91	14.26	14.22	12.69	12.23	11.34	8.45	8.19	11.52	14.26
0.50	6.69	13.84	16.45	15.38	12.57	10.99	9.42	9.08	10.96	15.71
1.00	6.65	15.19	19.39	17.42	17.69	13.99	8.71	10.27	12.70	15.29
2.00	7.18	14.45	24.79	20.83	20.90	17.55	10.68	13.39	15.36	17.03
3.00	7.35	20.74	26.77	29.13	20.85	17.46	11.45	14.59	16.85	20.00
6.00	9.03	28.32	36.22	46.77	25.40	20.09	11.84	17.78	23.60	25.13
12.00	8.81	43.03	55.74	65.68	27.67	27.12	15.42	24.11	29.47	31.55

Chart 55, Batch settling method EE2 removed mg/g material in 12 h.

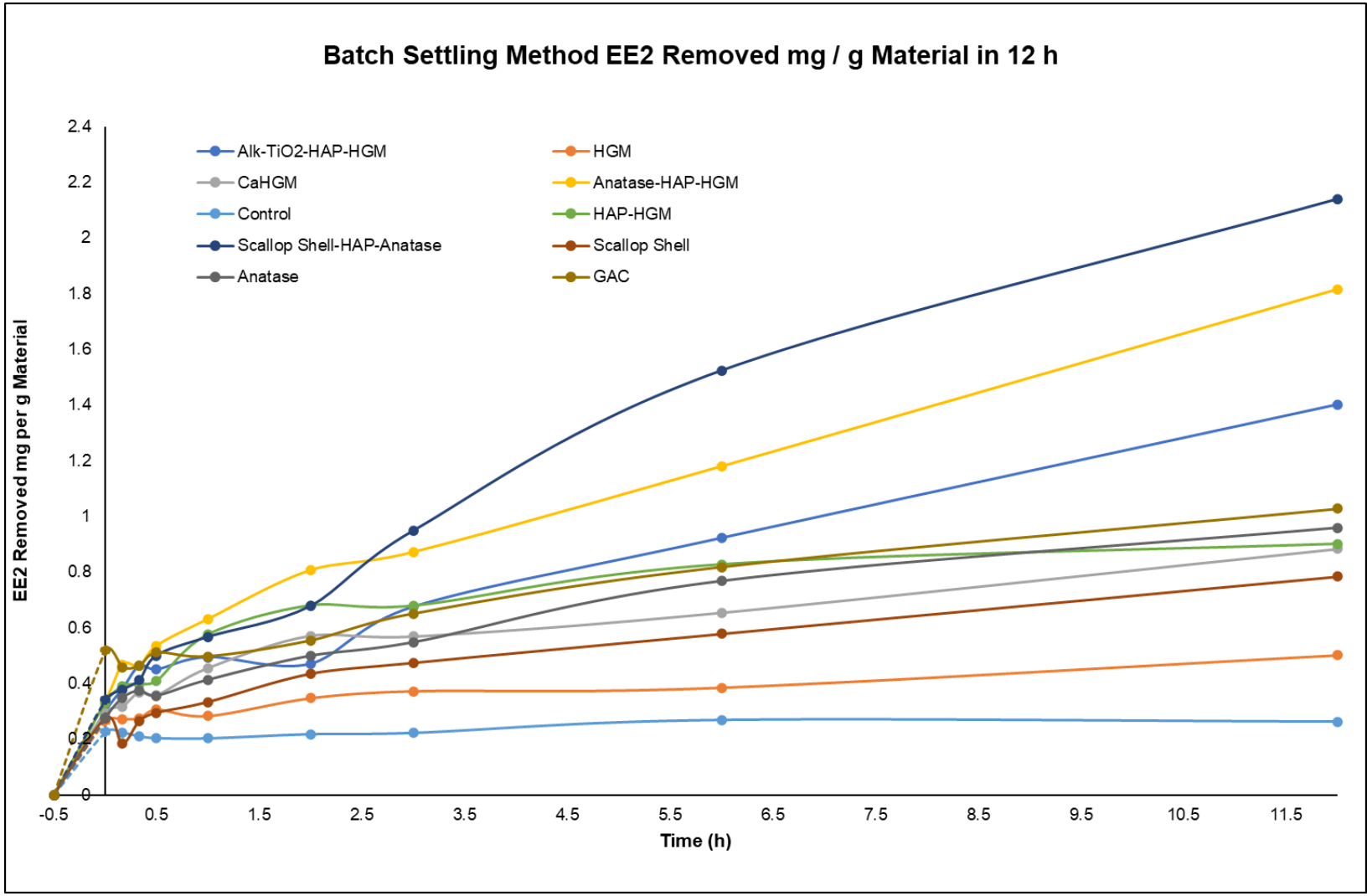

11.5 Synergistic Effect of Photocatalytic – Adsorbent Systems

A significant synergistic effect is evident in the materials that combine photocatalytic components and adsorbing materials, where the amount of EE2 removed from solution is nearly double the EE2 removed by either the photocatalyst or the adsorbent for systems containing anatase, as can be seen in Chart 56 Chart 57 and Chart 58. The effect is less pronounced but still significant for the material containing TiO_2 produced using the hydrolysis of titanium tetraisopropoxide, which is expected as the materials containing anatase contained a greater proportion of TiO_2 than the alk-TiO_2-HAP-HGM material, which can be seen in Chart 56.

Chart 56. EE2 removal by alk-TiO_2-HAP-HGMs, HAP-HGMs and Anatase.

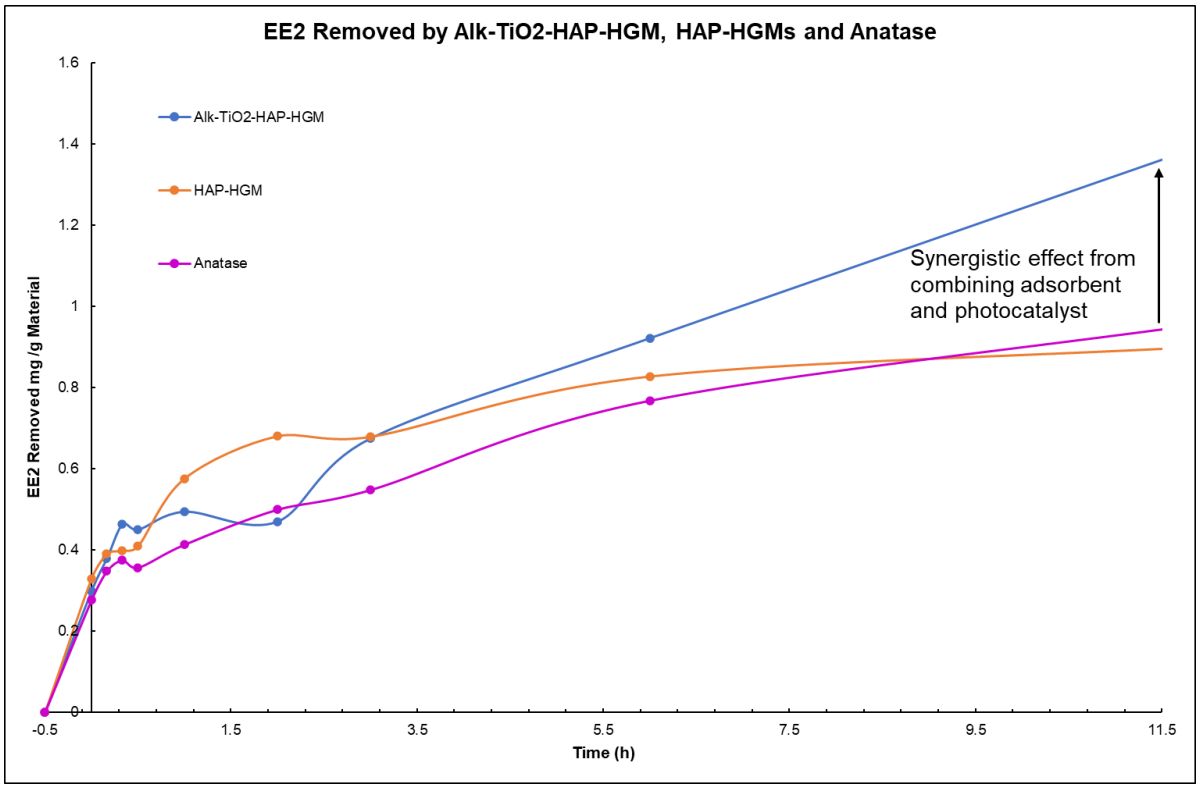

Chart 57. EE2 Removed by Anatase-HAP-HGMs, Anatase, and HAP-HGMs.

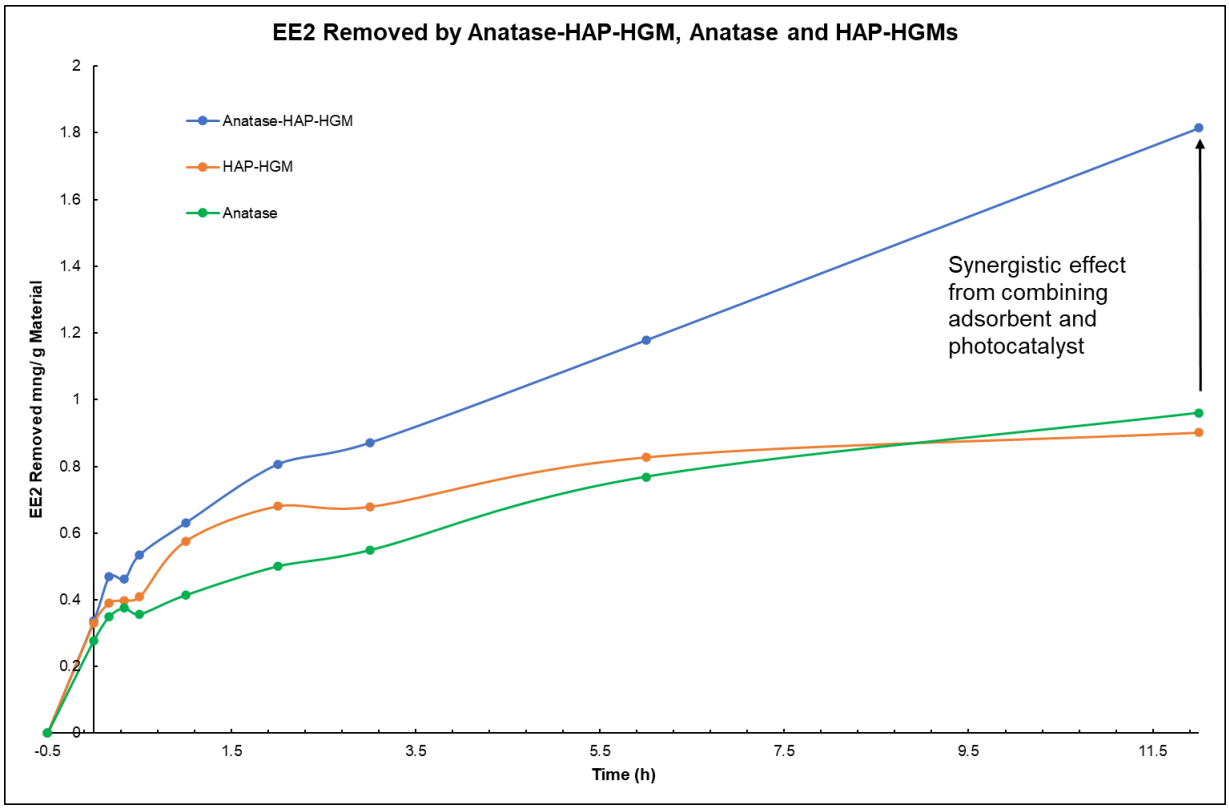

Chart 58. EE2 removed by scallop shell-HAP-anatase, scallop shell and anatase.

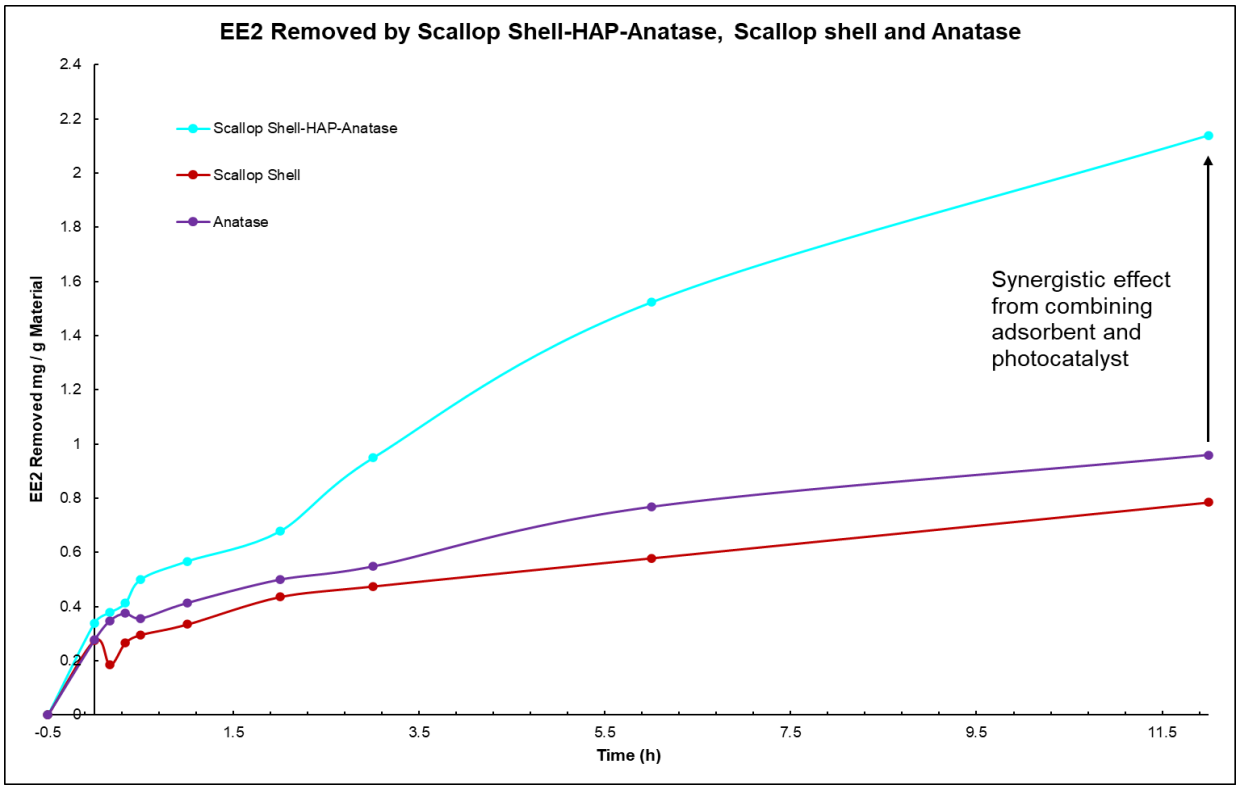

11.6 EE2 Removal Using Batch Stirring Technique

The batch stirring method used agitation on a shorter timescale to effect EE2 removal. This method is consistent with bench scale laboratory techniques, where a solution containing the target molecule for removal is stirred with the adsorbent or photocatalytic material with stirring or an equivalent form of agitation, and in the case of a photocatalytic reaction, with exposure to light capable of initiating the photocatalytic reaction.

Under these conditions GAC outperformed all samples. Although the initial values of EE2 removal up to time = 40 min showed GAC performing the worst, the upward trend of EE2 for GAC indicates that under idealized laboratory conditions GAC had the highest removal rate.

Comparing the removal rates of the other materials shows that the scsh-HAP-anatase material again outperformed all other TiO_2/HAP composites. It is assumed that the recovery and washing procedure aimed at removing the EE2 adsorbed from the batch settling experiment was insufficient, and either more washes with an increased desorption time are necessary, or calcination at a temperature range of 175 – 375 °C in order the ensure the full thermal decomposition of EE2 and degassing of the materials to prepare them for repeated use. This result is disappointing, but it is further evidence of the difficulty of working with EE2, and the difficulty of recovering EE2 from when the EE2 has adsorbed to organic matter or is being retained in the environment after release into the aquasphere. The figures for EE2 removal are contained in Table 92. EE2 removed in mg EE2 per g material using batch stirring method and are displayed in Chart 59. EE2 removal using the batch stirring technique.

Table 92. EE2 removed in mg EE2 per g material using batch stirring method.

EE2 Removed in mg/g Material Using Batch Stirring Method					
Time (h)	**GAC**	**Alk-TiO_2-HAP-HGM**	**Anatase HAP-HGM**	**Scallop Shell-HAP-Anatase**	**CaHGM**
-0.50	0.00	0.00	0.00	0.00	0.00
0.00	0.44	0.88	1.19	1.05	1.07
0.17	0.58	1.05	0.98	1.33	1.00
0.33	0.90	1.05	0.96	1.17	1.01
0.50	1.27	1.01	0.83	1.37	0.93
1.00	1.44	1.05	1.13	1.72	0.96
2.00	1.94	1.16	1.21	2.00	1.09
3.00	2.73	1.33	1.34	2.40	1.25

Chart 59. EE2 removal using the batch stirring technique.

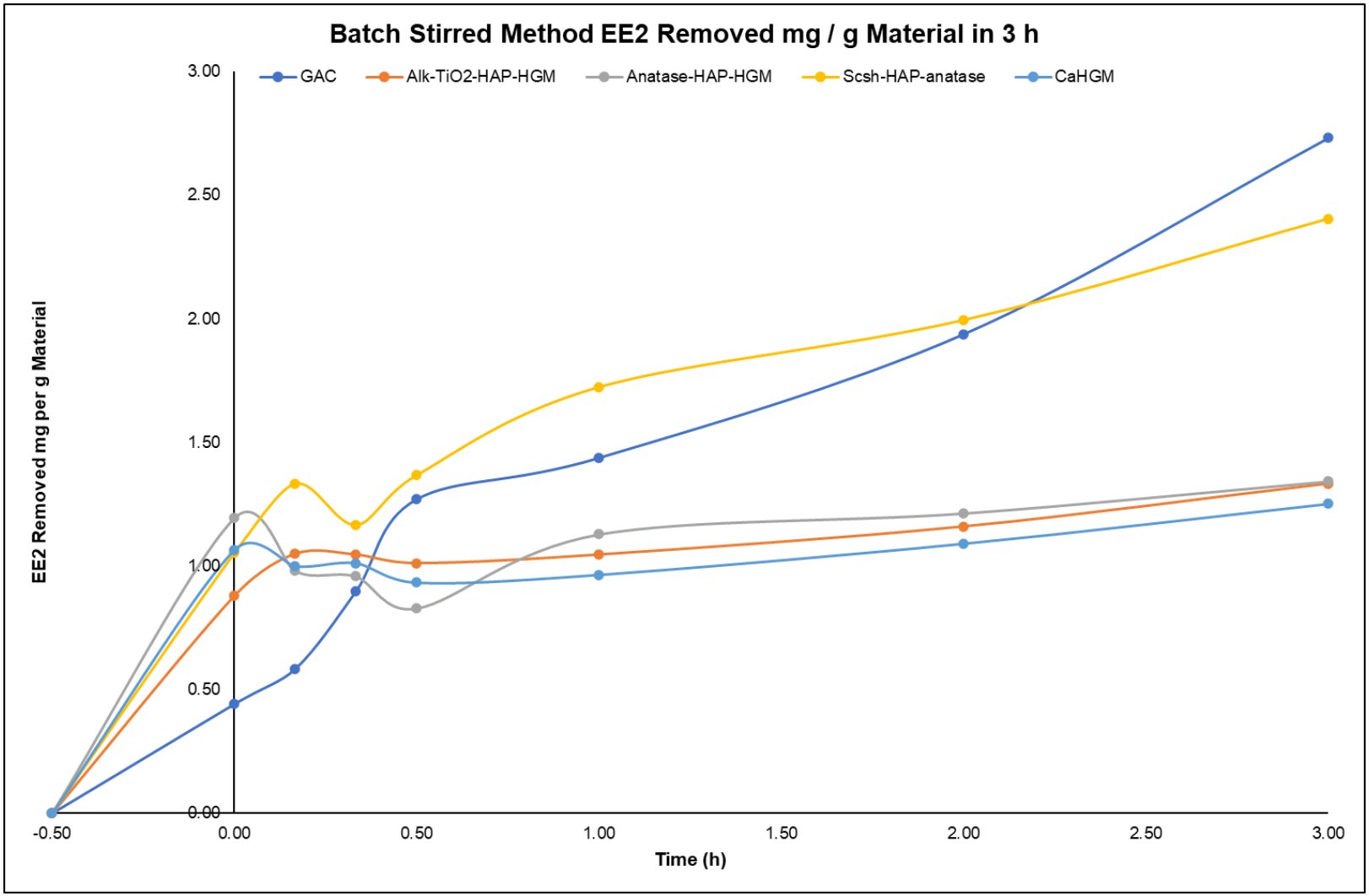

11.7 Adsorption Kinetics

The first 30 minutes of the batch settling experiments were conducted in the dark with no UV to initiate photocatalysis, hence the initial 30 minutes were used to determine the rate of adsorption for all materials. As time progresses adsorptions sites on the material become occupied, and the rate of adsorption slows. The limitations of determining the rate of adsorption in this way are that any materials where adsorption is governed by the rate of diffusion may not have reached equilibrium. As the control experiment does not show significant EE2 removal by UV in the absence of photocatalysts, it is assumed that adsorption proceeds as usual in the presence of UV light for the non-photocatalytic samples. It should be noted that due to the low concentration of EE2 of the solution, the values contained in the table are not representative of the maximum rates of EE2 adsorption which could be derived from more concentrated EE2 solutions. The rates of adsorption for the batch settling method and the batch stirring method are shown in Table 93 and Table 94.

Table 93. Rates of adsorption for materials in first 30 min of experiment with no UV irradiation for batch settling method.

Rate of Adsorption for Batch Settling Method – Initial 30 min with no UV *Control solution contained no material; hence this value is mg of EE2 removed		
Material	**mg EE2 adsorbed /g material**	**Rate of adsorption mg/g material per hour**
Alk-TiO_2-HAP-HGM	1.00	2.00
HGM	0.88	1.76
CaHGM	0.99	1.97
Anatase-HAP-HGM	1.12	2.24
Control*	0.75	1.50
HAP-HGM	1.10	2.20
Scallop Shell-HAP-Anatase	1.13	2.26
Scallop Shell	0.92	1.83
Anatase	0.92	1.85
GAC	1.73	3.46

Table 94. Rates of adsorption for materials in first 30 min of experiment with no UV irradiation for batch stirring method.

Rate of Adsorption for Batch Stirring Method – Initial 30 min with no UV		
Material	**mg EE2 adsorbed / g material**	**Rate of adsorption mg/g per hour**
GAC	0.44	0.88
Alk-TiO_2-HAP-HGM	0.88	1.76
Anatase-HAP-HGM	1.19	2.39
Scallop shell-hap-anatase	1.05	2.11
CaHGM	1.07	2.13

11.8 Comparison with Kinetic Models

Four kinetic models of adsorption were compared to the experimental data for EE2 for the adsorbent materials tested using the batch settling method. The equations used to compare the data are described in the methods chapter, and the models used were:

i) Pseudo-first order model

ii) Pseudo-second order model

iii) Intraparticle diffusion (Weber Morris) model

iv) Elovich model

Comparing the R^2 values obtained for the various adsorbents indicates that the Elovich adsorption model is the closest fit for the materials with the exception of the HAP-HGMs, where the pseudo-second order model and the Elovich model are both 0.99.

A close fit with the Elovich adsorption model indicates that it is likely a chemical reaction is the driving force behind the mechanism of adsorption. In this work it is assumed that chemisorption plays a role in the adsorption mechanism of EE2 to the materials tested. Furthermore, the Elovich model is particularly suitable for adsorbents with heterogeneous adsorption sites with a range of adsorption energies, which represents well the TiO_2-HAP composites and also the HAP-HGMs and CaHGMs, where the HAP-HGMs have exposed Ca sites on the a-plane, and PO_4 sites on the c-plane. Likewise, the CaHGMs consist of Ca and CO_3, moieties on the surface which could acts as sites for adsorption.

It must be said that this work and reliability of this work would have been strengthened by increasing the number of measurements at different time intervals, and comparing the adsorption data to a greater variety of models. The intraparticle diffusion model was a poor fit for all cases tested and has not been included in Table 95.

Table 95. Comparison of goodness of fit of kinetic models for materials.

Alk-TiO_2-HAP-HGM				
	PFO	PSO	Elovich	
q_e	13.96 ± 1.91	16.53 ± 2.40	α	19.9 ± 3.76
k_1	0.317 ± 0.097	0.022 ±0.011	β	0.517 ± 0.039
r^2	0.79	0.87	r^2	0.98
Anatase-HAP-HGM				
	PFO	PSO	Elovich	
q_e	18.18 ± 1.96	22.33 ± 2.50	α	9.95 ± 1.85
k_1	0.305 ± 0.072	0.014 ± 0.005	β	0.170 ± 0.022
r^2	0.90	0.93	r^2	0.96
HAP-HGM				
	PFO	PSO	Elovich	
q_e	9.29 ± 0.40	10.69 ± 0.33	α	27.16 ± 5.00
k_1	0.886 ± 0.107	0.099 ± 0.012	β	0.482 ± 0.034
r^2	0.96	0.99	r^2	0.99
Scsh-HAP-HGM				
	PFO	PSO	Elovich	
q_e	25.33 ± 2.60	34.77 ± 4.22	α	6.21 ± 0.86
k_1	0.182 ± 0.036	0.004 ± 0.002	β	0.092 ± 0.014
r^2	0.96	0.97	r^2	0.98
CaHGM				
	PFO	PSO	Elovich	
q_e	8.22 ± 0.57	9.61 ± 0.57	α	19.91 ± 3.76
k_1	0.840 ± 0.161	0.100 ±0.023	β	0.513 ± 0.039
r^2	0.90	0.96	r^2	0.98

11.9 UV/Vis spectroscopy – EE2 Degradation

UV/Vis spectroscopy was used to measure the changes in absorbance for EE2 during treatment with UV and alk-TiO_2-HAP-HGMs. UV/Vis spectroscopy alone is not the preferred method used to quantify the amount of EE2 in solution, as HPLC-UV, HPLC-MS and LC-MS are the standard techniques used in the literature. A preliminary experiment using UV/vis spectroscopy was employed in order to assess if this spectroscopic technique could be applied to quantify EE2 in solution during UV irradiation in the presence of the alk-TiO_2-HAP-HGM composite material. This is shown in Chart 60. UV/Vis spectra overlaid for time = 0, 2 min, 4 min, 6 min, 8 min and 10 min

If the spectra had been consistent with the absorbance max decreasing over time, this method could have been applied. However, the absorbance max shifted towards the right in the graph, indicating the absorbance max was occurring at shorter wavelengths, which is indicative of more conjugated chemical species. This finding indicates that a photocatalytic process is very likely to be taking place, however from this data the concentration of EE2 in solution cannot be determined due to the presence of other species. For this reason, using UV/Vis spectroscopy alone was not pursued as a method to determine EE2 concentration, confirming the reason the chromatographic methods are favoured by researchers for determining EE2 concentration.

Chart 60. UV/Vis spectra overlaid for time = 0, 2 min, 4 min, 6 min, 8 min and 10 min.

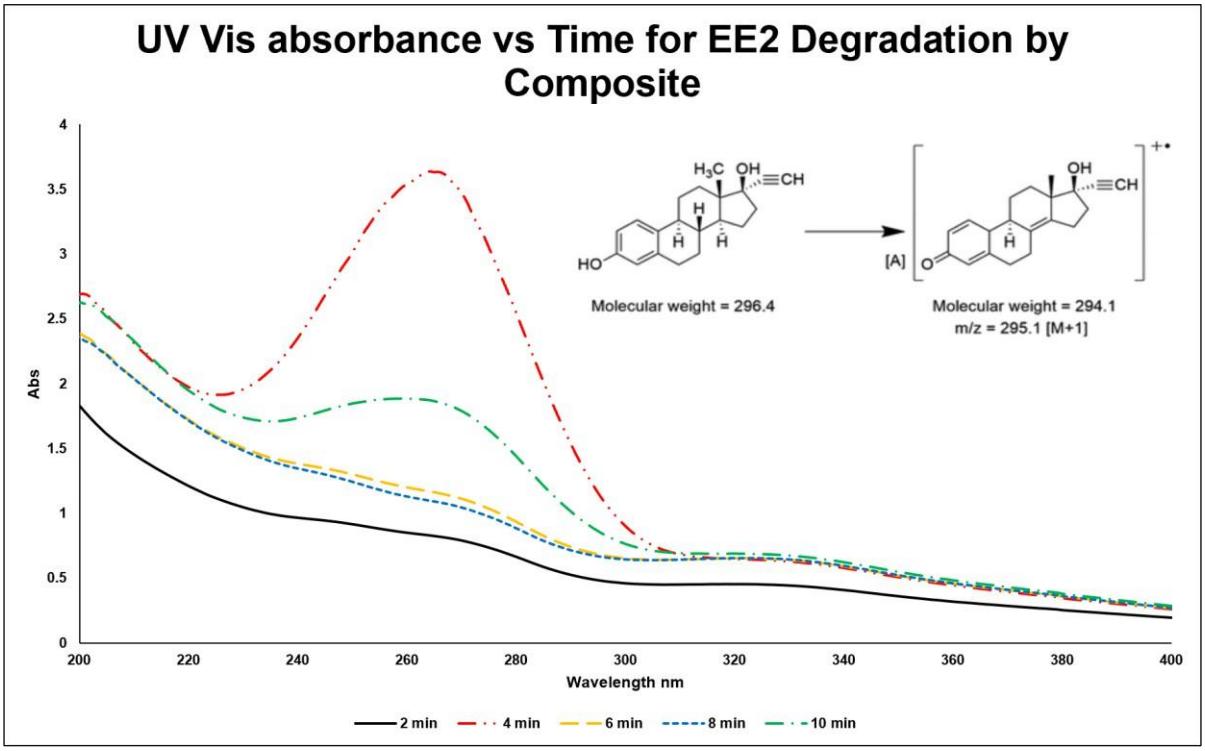

11.10 LC-MS – Transformation Product Analysis

LC-MS was used to investigate the transformation products of EE2 degradation after treatment with the alk-TiO_2-HAP-HGM material. Mass spectrometry used in this manner could be useful in identifying the products of EE2 degradation by comparing the mass/charge ratio of the dominant peaks in the mass spectrum with possible molecular ion fragments of the same mass, which provides evidence for the possible degradation pathways undergone by EE2 upon treatment with the alk-TiO_2-HAP-HGM material while under UV irradiation.

However, LC-MS only gives the mass/charge ratio of the molecule detected, and while the chemical structure of the molecular ion can be inferred from its mass-charge ratio, there is no guarantee that it is a given ion as ions with the same mass/charge ratio cannot be distinguished from each other. Furthermore, there is also the risk that fragments generated by ionisation are misattributed to photocatalytic degradation.

Molecules with a greater molecular mass than the original target molecule can be the product of polymerization or coupling reactions, and in the case of EE2 can signal the transformation of the molecule into a less estrogenic molecule.

Figure 97. EE2 molecule with numbered carbons.

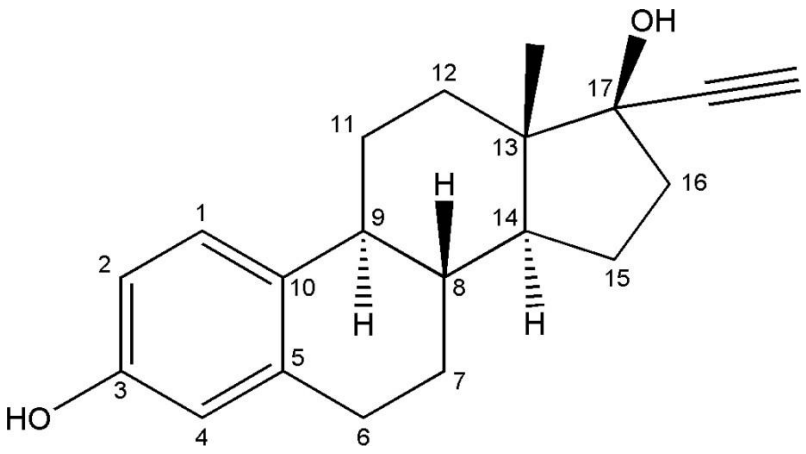

EE2 has a molecular mass of 296 g/mol, and the mass spectrum of EE2 is shown in chart, and was taken from the NIST chemistry webbook. The most abundant peak in a mass spectrum is named the base peak, and the base peak in the mass spectrum of EE2 is at 213 m/z, while the molecular ion peak is found at 296 m/z. There are also major peaks found at 160 m/z, 133 m/z and 228 m/z.

Figure 98. EE2 mass spectrum source: NIST chemistry webbook.

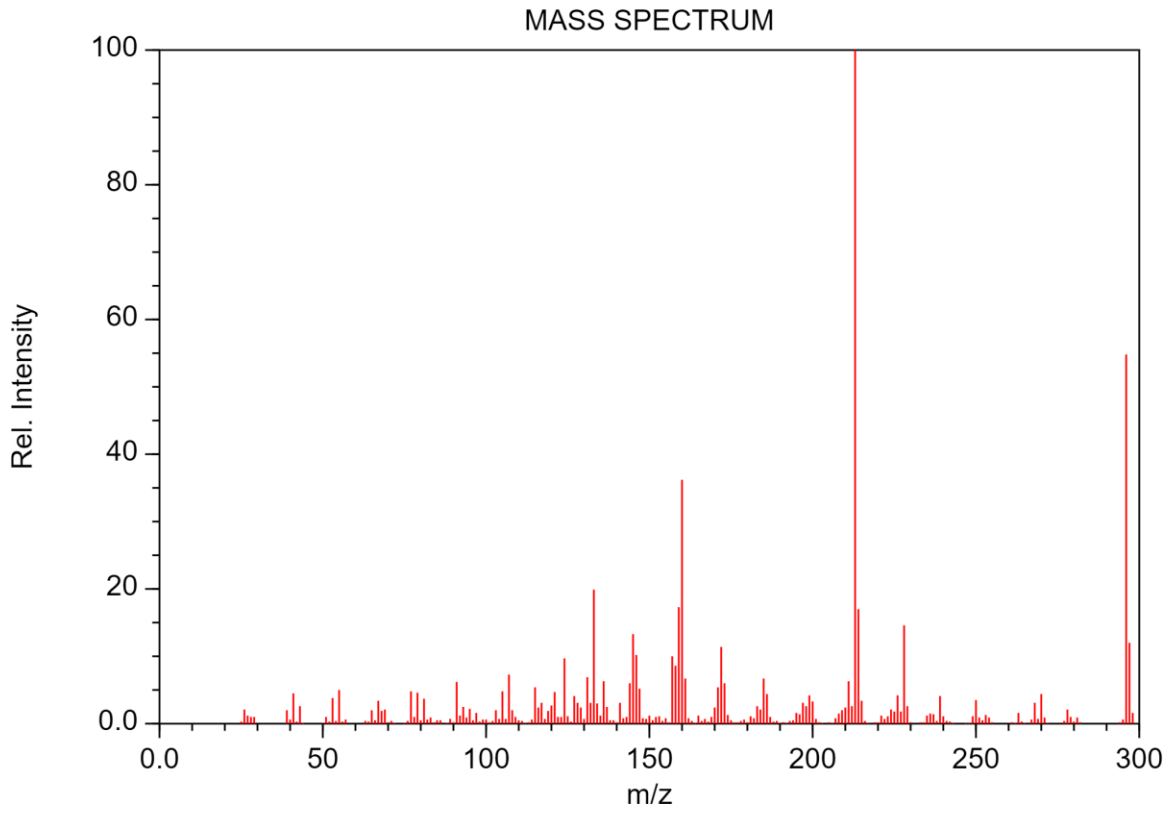

The mass spectrum in Chart 61 is the EE2 standard prior to treatment with UV light and the alk-TiO_2-HAP-HGM particles. The base peak is at 319.1 m/z, which corresponds to the sodium adduct of EE2. The other peaks have a low relative abundance when compared to the base peak, which indicates that few EE2 molecules have undergone significant fragmentation, and most EE2 molecules have survived the ionisation process as relatively intact sodium adducts. The relative abundances of the major peaks are shown in Table 96.

Table 96. Relative abundance of fragments produced by LC-MS of EE2 solution before photocatalytic treatment.

M/Z	Abundance
182.9	5000
279	1550
319.1	62000
320.1	7000
464.4	3000
612.3	1000
949	500
389.7	500

Chart 61. Mass spectrum of EE2 from LC-MS prior to photocatalytic treatment.

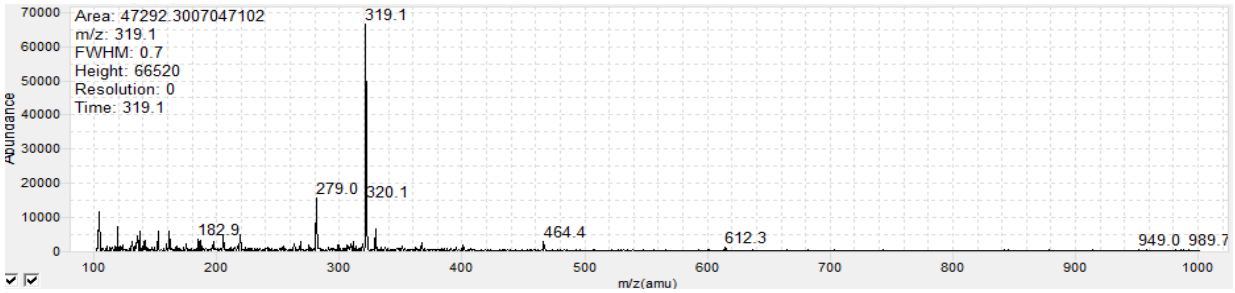

The mass spectrum of the EE2 after treatment with alk-TiO_2-HAP-HGMs and UV light is shown in Chart 62 and shows there are no significant peaks at 296 m/z, which would indicate intact EE2 molecules, and the base peak is now at 307 m/z, having decreased from 319 m/z before treatment with UV and the alk-TiO_2-HAP-HGM. The possible structures of the transformation products of EE2 degradation using UV and the alk-TiO_2-HAP-HGM are contained the table below. These suggestions are based on the mass of the transformation product, comparisons with products identified in the literature, and for the peak corresponding to a species with a mass of 307 m/z the fact that the maxima of the UV spectra tend towards longer wavelengths, which is indicative of more conjugated species. The relative abundances of the main peaks are shown in Table 97. Finally, two possible structures of the transformation products are included in Table 98.

Table 97. Relative abundance of fragments after photocatalysis of EE2 with alk-TiO_2-HAP-HGMs.

M/Z	Abundance
150	19500
202.9	9500
307.1	38500
365	10000
471.2	3500
541.1	2000
585.5	1000

Chart 62. Mass spectrum of EE2 from LC-MS after photocatalytic treatment.

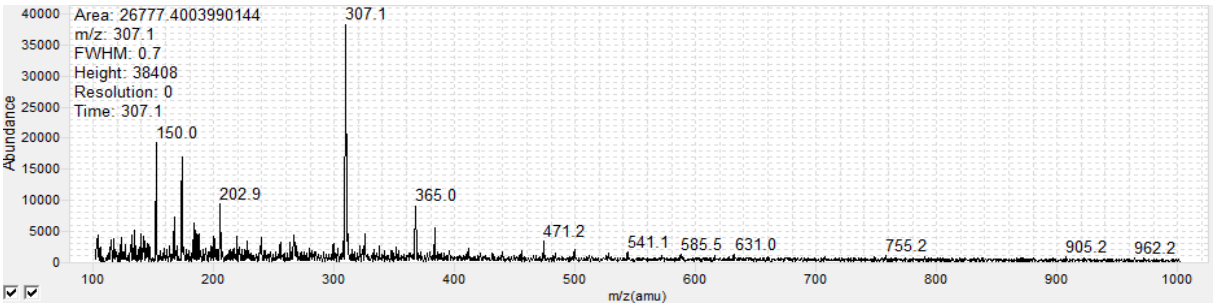

Table 98. Proposed chemical structures of products of photocatalysis.

Mass/charge ratio	Possible fragment(s)	Ref
202.9	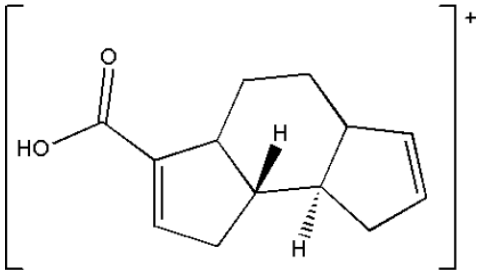	(Wei, 2018)
307.1	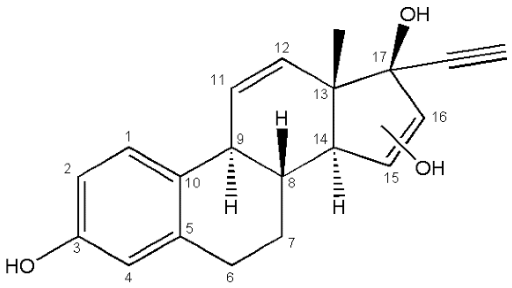	

11.12 Summary of Chapter 11

In this chapter the efficacy of a variety of materials with adsorbent properties, photocatalytic properties, and a combination of adsorbent and photocatalytic properties were tested for their ability to remove EE2 from aqueous solution at a concentration of 10 ppm. HPLC-UV was used as the method to quantify the quantify the amount of EE2 in solution, and an analysis of five types of filters was conducted on a stock solution of EE2 in order to select a filter that did remove significant quantities of EE2 from the solution. UV/Vis spectroscopy was assessed as a potential method to quantify the EE2 in solution using $A = \varepsilon cl$, however, a rapidly oscillating absorbance max made this method unsuitable, due to the possible transformation products from photocatalysis and the shift of the absorbance max to longer wavelengths, in addition to the limits of the instrument. It was decided that HPLC-UV was the best method for separating any possible transformation products and quantifying solely the amount of EE2 in solution. Finally, LC-MS analysis was performed on a solution of EE2 and also on a solution of EE2 treated with alk-TiO_2-HAP-HGMs, some potential structures of the transformation products were proposed.

GAC removed slightly more EE2 than the HAP-HGMs, removing 31.55% versus the 27.67% of EE2 by the HAP- HGMs, however, the benefit of using the HAP-HGMs is that they were produced using ambient temperatures, which in the context of green materials makes them more favourable than activated carbon, which requires treatment at elevated temperatures.

A comparison of four kinetic models, pseudo first order, pseudo second order, intraparticle diffusion and Elovich were performed for the removal of EE2 using the alk-TiO_2-HAP-HGMs, anatase-HAP-HGMs, scsh-HAP-anatase, HAP-HGMs, and CaHGMs. It was found that the Elovich model best described the adsorption kinetics of all materials tested

with the r^2 value for the HAP-HGMs being 0.99 and the Ca-HGMs being 0.98. Of note, the HAP-HGMs adsorbent kinetics were also equally well described by the pseudo-second order model, which also had an r^2 value of 0.99. However, due to the limited number of data points used, this statement would have more validity if more measurements were taken at intervening times

The effect of combining adsorbent and photocatalytic materials was such that the removal of EE2 exceeded by the combined materials exceeded the removal of EE2 achieved by GAC. This provides evidence that the combination of adsorbents and photocatalysts present a new and effective method for the removal of EE2 form water solutions.

12. Chapter 12 – Discussion

12.1 Introduction

This chapter contains a discussion of the characterisation and analytical methods used in this work, before discussing the results obtained in chapters 7, 8, 9, 10, and 11. This chapter covers the results of selecting and preparing the hollow glass microsphere substrate, the process used to grow the hydroxyapatite layer on the HGMs, the processes used to produce titanium dioxide on the surfaces of the HAP-HGMs, the characterisation data of the titanium dioxide component, the characterisation data for the full alkoxide-titanium dioxide – hydroxyapatite – hollow glass microsphere (alk-TiO_2-HAP-HGM), the results of using this material to remove EE2 from aqueous solution, and the kinetic data for the removal of EE2 using this alk-TiO_2-HAP-HGM. This chapter then goes on to discuss the relevance of this work to EE2 removal from water, and the impact of this work on future research, and the implications of this work to the wider field of remediating contaminated water using green materials.

SEM was used extensively in this work to assess the various chemical treatments applied to substrates, including alkali washing of the HGMs, the results of treatment of the CaHGMs with dipotassium phosphate solution, The various morphologies obtained with the TNW series of reactions, and to compare the products of the methods used to add a TiO_2 component to the HAP-HGMs, which include drying pre-made TNW1 micro-rods on to the HAP-HGMs, incorporating anatase into the HAP-HGMs to form anatase-HAP-HGMs, and to form the alk- TiO_2-HAP-HGMs. In the absence of SEM imaging, it would have been much more difficult to confirm that the coatings applied to the microspheres had adhered well to the microspheres, or if the coatings were present in the bulk material.

EDX was used in this work to confirm the distribution of elements across the surfaces of the microspheres were well dispersed or poorly dispersed, and was also used to confirm that the halide salts had not entered into the TiO_2 lattice, but played a role as a nucleation point around which the TiO_2 rods had coalesced. EDX was useful in revealing that in the anatase- HAP-HGMs, the anatase had aggregated in some regions on the surface of the HAP-HGMs, and were not well and evenly dispersed across the surface of the HAP-HGMs. In contrast, EDX was able to demonstrate that the TiO_2component of the HAP-HGMs was evenly distributed across the surfaces of the microspheres. The limitations of EDX are that the elemental quantification is only valid at the surface of the analysed material, and is not representative of the true elemental composition of the entire sample. Nevertheless, EDX was a useful characterisation method for understanding the distribution of the coatings applied to the materials. In particular, the linescan was useful for confirming the changing proportion of elements found at different regions of the microspheres.

XRD patterns were widely and extensively used in this work to characterise the materials in Chapters 7 – 10. In the samples containing mixtures of highly crystalline species, such as calcium carbonate and calcium hydroxide, XRD pattern analysis was extremely useful for quantifying the various phases present. In the HAP-HGMs and Bio-Oss comparison, although the major peaks actually consisted of many overlapping peaks, the comparison between the known pattern (Bio-Oss) and the unknown pattern (HAP-HGMs) allowed the confirmation that the HAP-HGMs did contain HAP. However, the overlapping peaks around the (211) peak made phase quantification difficult, and it was necessary to manually check the HAP-HGM pattern against different types of HAP in the database to confirm its lattice parameters. XRD pattern analysis of the TNW series was problematic, as the TNW samples were not calcined in an effort to produce a low temperature synthetic route towards TiO_2. However, an XRD pattern analysis of the calcined TNW sample did confirm

that TiO_2 was present in the sample.

AFM was used to try an assess the roughness and texture and the HGMs and CaHGMs, however this method was not found to be appropriate for topology mapping of the microspheres because the small size of the microspheres resulted in the AFM probe slipping and generating noise. Working at the smallest scale possible for the AFM negated some of these issues, however other factors, such as the microspheres becoming stuck to the probe, and in some causes the probe launching the microspheres out of the analysis area, meant this characterisation technique was not employed for further studies of the surfaces of the materials, and instead SEM was preferred.

TGA was useful as this method permitted the calculation of the mass of the calcium carbonate component on the CaHGMs, based on the assumption that calcium carbonate decomposes at a given temperature range, and that calcium carbonate decomposes into calcium oxide and carbon dioxide, and that the mass loss in this range was due to the loss of carbon dioxide.

UV/Vis spectroscopy alone was not found to be a suitable method for EE2 quantification. This is likely due to the presence of transformation products from the photocatalysis of EE2 interfering with the UV/Vis spectrum of EE2, resulting in overlapping spectra and obscuring the spectrum associated with EE2. Instead, HPLC equipped with a UV detector was chosen as the method to quantify the amounts of EE2 remaining in solution. The HPLC method developed had a low sensitivity relative to other techniques reported in the literature, such as HPLC-MS, and accordingly, a higher concentration of EE2 had to be used in the experiments than is truly representative of a typical environmental sample.

12.2 Hollow Glass Microsphere Selection and Characterisation

The aim of this section was to select he most appropriate HGMs to use as the substrate, and to prepare the surfaces of the HGMs to facilitate the growth of a layer of hydroxyapatite followed by the addition of TiO_2. The rationale for using the HGMs was to give the final composite material a spherical shape resulting in compressive strength and predictable packing arrangements, and also with the intention of producing a material that has buoyancy and therefore floats, in order to ensure an adequate percentage of the beads were able to be recovered. The ultimate aim was to grow hydroxyapatite around the HGMs, and then add titanium dioxide to the bead in order to add photocatalytic activity, to produce a material with combined adsorbent and photocatalytic functionality. The following paragraphs outline the process of preparing these beads and the results of applying these beads to the removal of EE2 from water.

Initially, the selection process involved investigating four different types of untreated HGMs, where the uncoated HGMs based on size uniformity and also shell thickness uniformity, and the diameters of the beads were also investigated and compared. Images of the four types of HGMs were obtained using SEM, and the software ImageJ was then used to estimate the diameters of the HGMs, and calculate the mean HGM diameter and standard deviation of HGM diameter. The software was instructed to assume that the HGMs were spherical particles, and also to ignore any particles larger than 100 μm in diameter. Visual inspection shows that the assumption that the HGMs are spherical is valid, although it could be expected that a very small number of HGMs were not spherical. This would mostly be due to the presence of fragments of HGMs, as there is little variation in the shapes of the HGMs.

The upper limit of the HGM diameter was set at 100 μm, in order to prevent the software

from counting clumps or aggregates of HGMs as a single large particle. According to the manufacturers information the HGMs have a mean diameter of 30/40/50 μm, although significantly larger or significantly smaller HGMs were present, there were no HGMs found that exceeded 100 μm in diameter, although HGMs as large as 80 μm were found in the sample, this was a rare find and an exception to the generally consistent size of the HGMs.

The HGMs were characterised using XRD, SEM, EDX, FTIR, and AFM. The HGMs produced a broad and shallow peak with a maximum at 2theta = 23 °, which is characteristic of amorphous silica. There were no other peaks present in the XRD pattern of the untreated microspheres. SEM images produced of the HGMs exhibited surfaces that were extremely smooth and free from any distinct topological features. AFM imaging was also used to gather information on the topology of the microspheres, however this method was not appropriate for imaging spherical particles, as the HGMs would either become stuck to the AFM probe, necessitating careful removal, or the spheres rolled away when the tip of the probe moved over the surfaces of the HGMs. Nevertheless, AFM images were produced, which also showed the surfaces of the HGMs to be smooth, although the value of the AFM images is to confirm the findings from the SEM images.

The FTIR spectrum of the unwashed HGMs shows a small peak in the 1200 – 800 cm^{-1} range which is associated with Si-O-Si and Si-OH bonds. If present, physisorbed water would result in peaks in the range of 1630 – 1620 cm^{-1}, however there are no peaks in the region. In addition, the present of water could be inferred from a wide shallow band around 3200 cm^{-1}.

The concept of growing hydroxyapatite on the HGMs was inspired by bioglass, where 4S5S glass is converted into hydroxyapatite by soaking the glass in synthetic body fluid.

The 4S5S glass consists of Na_2–CaO–SiO_2–P_2O_5 which grows a layer of apatite using the ions contained in the SBF. The hydroxyapatite formed has been used to enhance bone growth as the hydroxyapatite is a biocompatible material that permits and promotes osseointegration of the bioglass.

The growth of hydroxyapatite directly on silica glass was not anticipated to be possible, or if possible, was not expected to be extensive or attached securely to the surface of the silica glass. It was assumed that the presence of CaO and Na in bioglass provide nucleation points that anchor the developing hydroxyapatite crystals to the surface of the bioglass. Devising a method of incorporating calcium ions into the bioglass using minimal reagents and under ambient conditions was therefore deemed necessary.

Soaking the HGMs in calcium hydroxide was explored as a possible method to incorporate calcium into the silica lattice, as it is possible to grow sodium silicate on the surfaces of HGMs by washing the HGMs with sodium hydroxide. Sodium hydroxide is commonly used to wash the surfaces of HGMs prior to engaging in reactions, as NaOH is effective for cleaning organic residues off the HGMs surfaces. However, washing the HGMs in NaOH resulted in widespread damage to the HGMs, with the majority of HGMs exhibiting fractures and cracking, which resulted in the HGMs no longer being fit for purpose. This result was unexpected, as steps were taken to ensure the HGMs were treated gently – for example, using a wooden spatula in place of a metal spatula to prevent HGM breakage.

The widespread destruction of the HGMs was also caused by washing the HGMs in a solution of potassium hydroxide, of the same concentration, although in the case of the potassium hydroxide wash, the damage to the HGMs was more devastating, with an estimate of over 90% of the HGMs being lost due to catastrophic damage to the integrity of the HGMs.

It was therefore a surprise to find that the HGMs washed in calcium hydroxide were not only intact, but also coated in an even layer of crystals. XRD analysis of the HGMs with these crystals showed that the crystals largely consisted of calcium carbonate (93%), with small amounts of calcium silicate (1%). A small amount of calcium hydroxide (6%) was present in these crystals. It was assumed that the calcium silicate was located at the interface of the calcium carbonate crystals and the silica HGM substrate, and that the calcium silicate formed a bridge that joined the calcium carbonate crystals to the silica HGM surface.

In order to determine if the calcium carbonate crystals were firmly adhered to the surfaces of the HGMs or if the calcium carbonate crystals had only precipitated on the surfaces of the HGMs, one sample of the $CaCO_3$-HGMs were ultrasonicated in water and a separate sample of $CaCO_3$-HGMs were ultrasonicated in ethanol. The aim of this procedure was to attempt to dislodge the $CaCO_3$ crystals.

It was found that washing the HGMs in sodium hydroxide cause significant and severe particle breakage. This was unexpected as multiple researchers have previously sodium hydroxide to wash microspheres with no significant amounts of HGM destruction being reported. This effect of widespread HGM destruction was replicated and consistent with potassium hydroxide washes, and due to the extent of particle damage neither sodium hydroxide nor potassium hydroxide washes were pursued as methods for HGM washing. However, washing the HGMs with calcium hydroxide resulted in the growth of calcium carbonate crystals on the surfaces of the HGMs with uniform thickness and morphologies.

In order to determine if the crystal that formed on the HGMs were from undissolved calcium hydroxide that had settled on the surfaces of the CaHGMs, or the products of a precipitation reaction, the I/I_0 intensities of the calcium hydroxide found in the XRD

pattern of the CaHGMs was compared to the I/I_0 intensities of the calcium hydroxide reagent in Chapter 7 Table 12. The most intense peak of calcium hydroxide portion of the CaHGMs corresponds to the (100) plane, while the reagent calcium hydroxide has its most intense peak corresponding to the (101) plane. The different I/I_0 intensities found between the calcium hydroxide reagent and calcium hydroxide on the surfaces of the CaHGMs indicate that the calcium hydroxide on the surfaces of the CaHGMs was formed *in situ*. Furthermore, there was no significant mass of calcium carbonate in the calcium hydroxide reactant, which was concluded from an XRD pattern of the calcium hydroxide reagent.

12.3 Growing Hydroxyapatite on the Hollow Glass Microspheres

This section discusses the results of the attempts to grow hydroxyapatite on the surfaces of the HGMs. Chemical precipitation was the chosen method to achieve this, as the chemical precipitation methods are low temperature, do not use specialist equipment or require technical training, and do not require the use of large amounts of energy, meaning chemical precipitation is a cost-effective method of synthesising hydroxyapatite.

It is known that calcium carbonate can be converted into hydroxyapatite through treatment with phosphate ions in a chemical precipitation process. These phosphate ions can come from phosphoric acid – which risks the release of hydrogen gas, and is not found to be overly successful in the literature, or from phosphate salts, which does not produce hydrogen gas but risks the absorption of the metallic component of the phosphate salts into the hydroxyapatite lattice, substituting calcium ions.

There is precedent for the growth of hydroxyapatite on glass in the literature: the growth of hydroxyapatite on glass has been achieved with the use of bioglass as the substrate, and bioglass contains 24.4% calcium oxide, CaO. Given that silicon dioxide reacts with calcium hydroxide to form calcium silicate (Armelao, 2000), it was hypothesised that

treating the HGMs with calcium hydroxide solution would also produce calcium silicate, therefore incorporating calcium into the silicon dioxide network of the HGMs. The calcium in the HGMs would then act as a nucleation point for the growth of hydroxyapatite on the HGMs.

Hydroxyapatite has previously been grown on bioglass, containing 24% calcium, via immersion in simulated body fluid. Simulated body fluid contains a number of ions including Na^+, Ca^{2+}, Mg^{2+}, K^+, Cl^-, HCO_3^-, HPO_4^{2-}, SO^{2-} (Jones, n.d.) which have complex interactions in the mixture. In this work the process of hydroxyapatite growth on silica glass has been simplified significantly, using just three reagents: calcium hydroxide and dipotassium hydrogen phosphate, and a hollow glass microsphere substrate.

After having treated the CaHGMs with dipotassium phosphate solution, the most obvious change in the particles were the extensive growth of a crystalline material over the microspheres forming a crust that encompassed the microspheres entirely. All the microspheres were well coated with this crystalline material, and the spherical shape of the microspheres had been preserved. Unlike many attempts in the literature to coat microspheres, the coated microspheres did not form large aggregates of solid material into which the microspheres were embedded, but the single microspheres were all evenly coated and remained as free individual microspheres. This means that this process is promising for the production of discrete microspheres for water purification, as this method of growing hydroxyapatite grows a layer of hydroxyapatite around the microspheres without aggregating the microspheres into one solid mass, which would not be suitable for use in water purification due to the lowered surface area as a result of aggregation.

The XRD pattern of the HAP-HGMs produced using chemical precipitation from chemical reagents was characteristic of HAP reported in the literature, with a particularly strong similarity drawn between the HAP-HGMs and Bio-Oss. The peaks were all in the correct

2Theta locations, with the dominant peaks being the same in both the HAP-HGMs and Bio- Oss, and was the peak associated with the (211) plane. Chapter 8, Table 9 contains the lattice parameters for the HAP-HGMs and Bio-Oss, where the lattice parameters a = b = 9.42 for the HAP-HGMs, but for Bio-Oss a = b = 9.39, which indicates a slightly larger unit cell. In addition, the unit cell volume for HAP-HGMs is larger than Bio-Oss, standing at 529.1 $Å^3$, in contrast to the unit cell of Bio-Oss, which is 525.6 $Å^3$. This is assumed to be due to the fact that Bio-Oss is a naturally derived form of hydroxyapatite, and may contain substitutions in the lattice, particularly from contaminants such as Na or carbon. In addition, the Bio-Oss is deproteinised, which may not have totally removed all contaminants (Xu, 2023). Overall, the close agreement of the lattice parameters of the HAP-HGMs and Bio-Oss indicate that this is a successful, low energy method of producing a coating of hydroxyapatite on the CaHGMs.

The surface area of the hydroxyapatite-HGMs was 54 m^2/g. Given that the highest surface area hydroxyapatite achieved in the literature is in the region of 250 – 300 m^2/g, the fact that the HGMs are completely hollow, and the hydroxyapatite forms as a thin crust around the outside of the HGMs, this is an excellent result comparable to the highest surface areas achieved in the literature. In addition, the surface area of Bio-Oss is 79.7 m^2/g, meaning that a hollow HAP-HGM has a surface area that is comparable to commercially available HAP derived from bovine bone.

In contrast, the method that used scallop shell to produce hydroxyapatite was much less successful. The reason for this was assumed to be because the no acidic treatment of the calcined to dissolve the calcium carbonate ions, which resulted in the formation of HAP only on the surfaces of the calcium carbonate particles. Acidic treatment was avoided in order to prevent the formation of dicalcium phosphate, which occurs at low pH, whereas at higher pH, hydroxyapatite forms. Finally, dipotassium phosphate solution with

concentration of 1.0 mol dm^{-3} was adequate for forming hydroxyapatite. 0.1 mol dm^{-3} was too dilute to effect the complete transformation of the calcium carbonate into hap. This means that chemical precipitation is a low cost, low energy, low impact and low effort method of producing hydroxyapatite suitable for non-medical applications.

12.4 Incorporating Anatase into the HAP reaction Mixture

Anatase was loosely incorporated into the hap matrix, in a method adapted from the procedure used to generate self-cleaning HAP on the surface of marble (Sassoni, 2018), where the role of TiO_2 was to degrade contaminants. This method was fairly successful, in that anatase was incorporated into the HAP-matrix, however the anatase was not evenly distributed across the coated microsphere, with EDX evidence indicating that the anatase had aggregated, which is a common occurrence for anatase nanoparticles in water. This may be due to the fact that TiO_2 is insoluble in water, and so the TiO_2 powder was not evenly distributed throughout the reaction mixture, combined with the tendency of nanoparticles of titanium dioxide to aggregate in aqueous solution.

This method may be suitable for immobile structures for the purpose of preventative conservation, however for the purpose of actively removing and destroying EE2 in the application of water purification, the resulting product of HGMs coated with TiO_2 doped hap were too fragile in that the coating was easily dislodged by mechanical action. Moreover, there is also the issue that anatase aggregates may be too deeply embedded in the hydroxyapatite structure to be available to effect photocatalytic degradation of the EE2 molecules

However, the method of using chemical precipitation with the reagents DAP and limewater was very effective at producing hydroxyapatite. This method of hap production is low cost, low energy, and uncomplicated in comparison to the more elaborate methods of

hydroxyapatite synthesis. A particular benefit of this method is the avoidance of the high calcination temperatures typically used in hydroxyapatite synthesis, which makes this reaction favourable in the context of reducing the energy demand required for the production of adsorbing materials.

Although this method is suitable for the production of hydroxyapatite, the addition of anatase through co-precipitation resulted in aggregates of anatase. Therefore, a different approach to titanium dioxide application resulting in a more even distribution of TiO_2 to the hydroxyapatite substrate was developed.

12.5 Optimising the Sol-Gel Method for Titanium Dioxide Micro-Rods

The sol gel method was chosen to produce the TiO_2 portion of the combined adsorbent/photocatalytic material because this method can be utilized at ambient temperature to produce a coating of titanium dioxide, meaning it is therefore highly appropriate for producing a coating of TiO_2 on a substrate of HAP-HGMs. As TiO_2 is insoluble in ethylene glycol, the hydrolysis of titanium tetraisopropoxide results in the formation of $Ti(OH)_4$ forming, four condensation steps between the $Ti(OH)_4$ species results in a lattice network of TiO_2 forming. This reaction was selected due to the low number of steps and reagents required for this reaction, and the absence of a high temperature calcination step, which in the context of synthesis of green materials was thought to be favourable.

The disadvantages of using this reaction are that ethylene diamine is a hazardous reagent, and the lack of a high temperature calcination step to increase the crystallinity of the TiO_2 phases present within the sample meant characterisation of the TiO_2 micro-rods using XRD pattern analysis presented some difficulties. The role of calcination is to add enough heat

energy to cause to the lattice to vibrate enough to result in the reorientation of the atoms in the TiO_2 lattice into a more crystalline structure, which can then be characterised using XRD patterns. Without calcination, the phase of TiO_2 most likely to form is amorphous (Hanaor, 2011). This means that the photocatalytic activity of the TiO_2 produced via this method may not be as high as pure anatase. In the context of producing a green material using low energy methods, this was considered an acceptable compromise, however other researchers may prefer enhanced photocatalytic ability over energy use and costs to produce this material.

In the XRD pattens of the TNW series, TNW2, TNW5, TNW9 and TNW10 contained peaks at 2Theta = 27.45 °, which corresponds to the (110) plane of rutile. The XRD does not show sharp well-defined peaks for anatase and rutile at 2theta = 25 ° and 27 °, which is typical for anatase and rutile respectively, however this could be because the anatase and rutile phases have not formed perfectly spherical crystals, instead they have formed along a one- dimensional axis. Anatase in particular does show a peak at 2theta = 47 °, which is characteristic of the (200) plane.

In order to overcome this a sample of TNW4 was calcined at 1200 °C, and the XRD pattern of the residue (Chart 36. XRD patterns showing reagent, TNW4, and TNW4 after heating showing sharp peaks associated with anatase and rutile) displayed peaks characteristic of anatase and rutile, confirming that TiO_2 was present in the sample. These reactions confirm that ambient temperatures can be used to produce titanium dioxide, and that the calcination step at 400- 500 °C is not essential to the formation of titanium dioxide, but is helpful for characterisation of the final product using XRD. This also ruled out other possibilities that had been considered, such as the possibility of side reactions occurring that did produce TiO_2, such as the formation of sodium titanate, which would have produced a crystalline

peak if present.

This also raises another issue with the XRD pattern analysis. Crystallite sizes were calculated using a Scherrer constant of 0.9, which is appropriate for spherical crystallites. Nevertheless, using a constant of 0.9 was thought adequate to produce an estimate of crystallite size, although it must be highlighted that this is indeed only an estimate, but is relevant for comparing the crystallite sizes produced by the different TNW reactions.

The identity of the TiO_2 phase was also confirmed using Raman spectroscopy. The spectra presented in Chart 40. Raman shifts of all the TNW samples and Table 70. Assigned Raman bands found in TNW series Raman Spectra indicate close agreement of the measured Raman bands in the TNW series and the literature values associated with rutile. This was particularly evident for the B_{1g} band and the multi-photon scattering process band, where all TNW samples produced a peak at a higher wavenumber. In contrast, the TNW series showed good agreement with the wavenumbers associated with the E_g and A_1g bands, which indicates that rutile is present in the samples, although some distortion in the TiO_2 lattice may be due to a reaction of the surface of the TiO_2 with the carbonaceous coating, or some small amounts of unhydrolysed titanium tetraisopropoxide.

Within the sol-gel reaction used, ethylene diamine acts as a templating agent encouraging growth along one axis. This is evident in the comparison of the morphologies produced by the TNW reaction omitting ethylene diamine, which resulted in large cuboidal structures, in contract to the TNW reactions that used ethylene diamine, which resulted in much longer and narrower structures.

The halide salts used in this reaction appear to act as a nucleation point, around which the TiO_2 rods project outwards. This was demonstrated in the EDX elemental maps contained Table 77. Elemental maps of constituent elements of TNW4 embedded in epoxy resin,

where a cross section of TNW4 revealed a cubic mass at the centre of the TiO_2 spherulite, that was extremely high sodium and chloride, and very low in other elements. This conclusion is supported by the high crystallinity of the peaks associate with halite and sylvite in the XRD patterns of the TNW series, which indicates that the salts were not dissolved and incorporated as ions into the TiO_2 lattice.

In the literature the heating step was accomplished in an autoclave, where it is assumed that the high pressure prevented the formation of micro-rods, instead forming flats sheets of TiO_2. In contrast, performing this reaction under ambient pressure conditions allows the growth of micro rods. When the heating method used is reflux, as in TNW2, it is thought that the lack of flat surfaces, and motion of the solvents

The presence of the carbonaceous material in the TNW series was assumed Heating to 180 – 200 °C causes the TiO_2 to catalyse a polymerisation reaction of the ethylene glycol solvent, resulting in layers of crystalline carbon. In order to produce a synthesis route that avoids this, it was decided to avoid the step at 200 °C.

The mixed phases present in the TNW samples however according to the literature, a mixture of anatase and rutile is more effective for photocatalysis because the rutile-anatase interface acts as a p-n junction, which assists in promoting excited electrons into the conduction band from the valence band and maintaining charge separation once the electrons have become excited. Preventing electron-hole recombination is a strategy used to enhance photocatalytic properties with success in the literature

The benefit of having both anatase and rutile polymorphs is that a p-n junction exists at the interface between the anatase and rutile, which has been shown in the literature to enhance the rate of photocatalysis by facilitating charge separation and hence preventing charge recombination, which allows the radical species generated by the process of photocatalysis

time in which they may attack the target molecules.

The overall conclusion is that amorphous titanium dioxide is forming, and when calcined at 200 °C mixed phases of TiO_2 form. In TNW2 the dominant phase was rutile, whereas in TNW10 the dominant phase was anatase. Given that TNW10 was also covered in the carbonaceous coating, it is thought that the refluxing process of TNW2 is most suitable for the aim of producing a TiO_2 coating on the HAP-HGMs.

12.6 Synthesising the Hierarchical Titanium Dioxide-Hydroxyapatite-Hollow Glass Microsphere

The coating of the HAP-HGMs with the TiO_2 micro-rods was achieved by inserting the previously synthesised HAP-HGMs into the reaction mixture, with the aim of producing HAP-HGMs coated in titanium dioxide microrods. This synthesis method was successful, and the results of this process were termed the alk-TiO_2-HAP-HGMs.

The XRD pattern of TiO_2 layered on hydroxyapatite is most consistent with panguite, a rare polymorph of TiO_2. It was thought that the TiO_2 micro-rods that formed the surface of the alk-TiO_2-HAP-HGMs were unlikely to be panguite, instead indicated that there are substitutions in the TiO_2 lattice. These substitutions should be due to the TiO_2 stoichiometry being disrupted due to bonding between TiO_2 and hydroxyapatite, or terminal Ti-O bonds being joined to moieties from the hydroxyapatite component of the HAP-HGMs.

This finding advances the field of titanium dioxide-hydroxyapatite composites because it proves that titanium dioxide can be grown on hydroxyapatite, which has not been the focus of prior research, whereas growth of hydroxyapatite on titanium dioxide has previously been demonstrated. The TiO_2-HAP interface is associated with increased production of

free radicals under photo-exposure, so this material has the added benefit of improved ability to engage in photocatalysis due to increased density of free radicals.

12.7 Measuring the Concentration of EE2 in Solution

This section discusses the results of the methods used to measure the concentration of EE2 in solution. Two methods were used to measure the concentration of EE2 in solution. The first method was an attempt to UV/Vis to determine the concentration of EE2 in solution. The second method was more traditional, using HPLC-UV to determine the concentration of EE2 in solution.

Initially, UV/Vis spectroscopy thought to be able to measure the concentration of EE2 in solution, however, when EE2 was subjected to UV/Vis spectroscopy, the absorbance maxima of the curves at varying times did not show a decrease as time progressed. Moreover, the location of the absorbance maximum for different times also shifted to higher wavelengths, which may indicate the formation of more conjugated species, and hence provide evidence of photocatalysis due to more conjugated species forming as part of the degradation pathway (Wei, 2018). A further consideration is that EE2 could potentially be photolyzed in the presence of UV radiation, resulting in the molecule undergoing degradation. If photolytic degradation of EE2 were to occur the results would be invalidated as the concentration of EE2 would decrease, but this decrease would be attributed to removal via the adsorbing materials.

Before HPLC could be used to quantify the amount of EE2 in solution, the solutions had to be filtered to remove the adsorbing materials. This was for two reasons: to prevent any solids from being introduced to the column, which would impact column flow and nullify the results, and also to ensure the process of adsorbance had been halted at time = t, in order to ensure the results are accurate. If adsorbing materials were still present in the

aliquot that had been removed for HPLC analysis, then the process of adsorption would continue, resulting in a much lower concentration of EE2 at time = *t* than is accurate. For this reason, the filtering process must be performed quickly, to limit the ongoing process of adsorption.

For this reason, it was decided that filtering the aliquot as the sample was being withdrawn from the reaction mixture would be the fastest way to remove the adsorbents from the sample. Other methods have been used to filter out solids and suspended particles from solutions of EE2, such as filtering through a glass microfiber filter with vacuum pump (Fonseca, 2013), however it should be noted that these methods may prolong contact time between the EE2 solution and the suspended solids. When the solids that are being filtered out are sand or grit, or solids without strongly adsorbing properties, increased contact times do not present a strong risk of affecting the extent of EE2 adsorption on to the solids. When the solids are adsorbing materials, prolonging the contact time of EE2 with the solids risks producing invalid results for the concentration of EE2 at time = *t*.

The filters tested were PTFE 0.22 µm, hydrophobic PTFE 0.45 µm, cellulose 0.45 µm, and glass filters. PTFE filters 0.22 µm removed over 90% of the EE2 and were hence discarded. PVDF 0.45 µm also removed significant amounts of EE2, but removed decreasing amounts of EE2 as each filter was re-used. The cellulose 0.45 µm removed 56% of the EE2 initially, but removed less EE2 as each filter was re-used. The glass fibre filter 0.7 µm performed better, removing 5-7% of the EE2, likely due to the larger pore size of the filter. The PTFE 0.45 µm performed the best, removing the least EE2 at just 1% EE2 removed on the first use. Therefore, the PTFE 0.45 µm filters were chosen to filter out the materials from the EE2 solutions, and were each used just once.

12.8 Removal of EE2 from Aqueous Solution

This section of the discussion chapter is dedicated to comparing and explaining the EE2 removal rates achieved by the various substances tested. The materials tested for EE2 removal rates are listed here, with the names used in the tables in Chapter 11 given in brackets. The materials were:

i. hollow glass microspheres (HGMs),
ii. calcium carbonate coated hollow glass microspheres (CaHGMs),
iii. hydroxyapatite coated hollow glass microspheres (HAP-HGMs),
iv. Titanium dioxide from the alkoxide reaction in Chapter 9 and hydroxyapatite coated hollow glass microspheres (alk-TiO_2-HAP-HGMs),
v. anatase nanoparticles (anatase),
vi. a composite of anatase and hydroxyapatite HGMs (anatase-HAP-HGMs),
vii. crushed and calcined scallop shell as a source of free calcium carbonate, (scallop)
viii. hydroxyapatite produced from scallop shells, doped with anatase (scsh-HAP-anatase)
ix. granular activated carbon (GAC)
x. a control experiment, that included no adsorbent or photocatalytic materials

The concentration of EE2 was measured at timed intervals using the materials as adsorbents. The adsorption data was compared with kinetic models predicted by the literature, in order to elucidate the adsorption mechanisms governing the removal of EE2.

The method used to quantify the concentration of EE2 was an HPLC procedure adapted from Lopez-Velazquez et Al. (Lopez-Velasquez, 2021). The flat baseline present in all chromatograms indicated that this method had a low sensitivity, and the peaks corresponding to EE2 were separate and distinct from solvent peaks, and were very symmetrical with little tailing. Although this method had a low sensitivity, relative to other

methods of EE2 quantification, it was thought to be adequate for the removal of EE2 from solution starting with a 10 ppm EE2 solution. The major issue with this experiment lies with the accuracy and error inherent in the measurement of the concentration of EE2. The limit of detection was high at 0.06 ppm, calculated using the method of 3.3 x (σ/S) and the limit of quantification higher, at 0.17 ppm, calculated using the method of 10 x (σ/S).

In this work, a compromise was struck between environmentally relevant values of EE2, the solubility of the EE2 powder used to prepare the standards, and the aim of avoiding concentrations of EE2 so high that the EE2 aggregates and precipitates out of water, thus invalidating any adsorption data. The EE2 was dissolved in methanol prior to dilution into a solution containing 10% methanol 90% water, as the solubility of EE2 in water is low at approximately 4.8 mg/L (de França, 2020) in water, and solubility decreases as ionic strength of the solution increases. In contrast, the EE2 present in water sources has been excreted by organisms and has been found to be present in water at concentrations higher than this – up to 48 mg/L in the Pirajibu and Sorocaba rivers in Brazil.

Prior to HPLC analysis, the aliquots were filtered using a hydrophilic cellulose membrane filter 0.45 μm. Previously a PTFE membrane filter of 0.22 μm and PTFE membrane filter of 0.45 μm were tested, however both of the PTFE membranes filters were hydrophobic. When the PTFE membrane filters were tested using 10 ppm EE2 solution, the concentrations of the EE2 solutions that had been filtered through these PTFE membrane filters were in the range of 1 – 2 ppm, indicating that approximately 80 – 90 % of the EE2 in solution had been retained on these filters. Accordingly, these filters were discarded and cellulose membrane filters were tested to determine if EE2 was retained on these filters. Cellulose membrane filters were selected for two reasons. The first reason is that regenerated cellulose membrane filters (<0.22 μm) had been used successfully (Reis, 2023), and the second reason is that cellulose is a hydrophilic material. A key assumption

here is that EE2 would not stick to the membrane filters if they were hydrophilic, due to the hydrophobic nature of EE2, as demonstrated by the high percentage of EE2 retained on the hydrophobic PTFE filters, and the relatively high $LogK_{ow}$ value of EE2. However, the cellulose membranes also proved to be a poor choice as the concentration of EE2 adsorbed in to these filters was unpredictable with a huge range in EE2 concentration after filtering. PVDF membranes were also assessed for their ability to filter a solution without removing EE2, and were found to remove over 90% of the EE2, again, making these filters a poor choice for this experiment.

12.9 Batch Settling Technique

The batch settling technique was intended to reflect realistic use of materials to remove EE2 from water, where the material would be added to the water containing EE2, left in the dark for 30 minutes, then exposed to UV light and left for a given timeframe. The role of the light is to initiate the photocatalytic reaction, and for TiO_2 the light required is UV. The future of this research is to doped the TiO_2 with species that reduce the size of the TiO_2 bandgap, allowing the photocatalytic reactions to be initiated by visible light.

After 12 hours of treatment with UV light, the control experiment experienced an 8.81% loss of EE2 from solution, most likely from a combination of interaction with any surface defects in the vessel, a small loss to the PTFE filter, and also the mechanism of photolysis.

The first material tested for EE2 removal were untreated HGMs. The HGMs were tested in order to determine whether the adsorption of EE2 was due entirely to the adsorbents or if the scaffold of the material had a significant effect. It was not anticipated that the HGMs would have a significant removal ability for EE2, although a limited amount of EE2 was expected to be retained on the HGMs due to the terminal silanol groups of the HGMs, which have the ability to hydrogen bond and could therefore form strong electrostatic

bonding interactions with the EE2 hydroxyl moieties. Furthermore, the high $\log K_{ow}$ of EE2 indicates that EE2 is more hydrophobic, meaning it is not likely to fully solvated by water molecules. This is why methanol was used in the stock solution to assist in the dissolution of EE2. Overall, the HGMs were poor at removing the EE2 from solution, removing only slightly more EE2 than was also lost in the control experiment. It can be concluded from this results that the HGM component of the materials was not responsible for the removal of EE2 from solution, instead illustrating the tendency of EE2 to aggregate due to its hydrophobicity.

Of the adsorbent materials, GAC achieved the highest removal percentage of EE2, removing 31.55%, which exceeds the removal obtained by the HAP-HGMs (27.67%) and the CaHGMs (27.12%). However, the difference in % removal between the HAP-HGM, CaHGMs and GAC is not very large, indicating that HAP-HGMs and CaHGMs present a possible alternative to GAC, especially in the context of green materials, as the HAP-HGMs and CaHGMs were produced using ambient temperatures. In addition, the CaHGMs outperformed the scallop shell, which achieved an EE2 removal of 24.11%, which suggests that immobilising the adsorbent material on HGMs allows an increased rate of EE2 removal. This could have been further explored by comparing the surface area of the scallop shell and the CaHGMs, which would have allowed a comparison of EE2 removed per m^2 of material. Overall, the HAP-HGMs were capable of adsorbing more EE2 than is present in water sources in all but the worst two locations listed in Chapter 1 Table 1.

Both calcium carbonate and hydroxyapatite contain calcium ions Ca^{2+}, and both also contain anions which are overall non-polar, in the form of carbonate and phosphate ions. Carbonate and phosphate are both non polar species due to their symmetry, which negates

the effects of the C-O and P-O bonds which are themselves polar. This mixture of positive cations and non- polar anions may be the ideal solution to the removal of endocrine disrupting compounds, because the EDCs have properties such as lipophilicity - that allow them to cross the cell membrane - which arise from non-polar parts of the molecule and hence would interact with the non-polar carbonate and/or phosphate component, but EDCs also contain OH bearing groups such as phenol which would be attracted to the calcium ions by the electrostatic force of attraction between opposing charges. This effect can be seen in where polyamide with a surface area of just 20 m^2/g adsorbed EE2 very strongly in comparison to high surface area activated carbon, with surface area ranging from 600 – 1000 m^2/g.

A significant synergistic effect was evident from all the materials that combined photocatalytic materials with adsorbent materials, which were the samples: Alk-TiO_2HAP-HGM, Anatase-HAP-HGM, and scallop shell-HAP-Anatase. This effect was most pronounced in the scallop shell-HAP-Anatase material, where this material removed 65.68% of the EE2. This finding demonstrates that materials containing anatase were capable of removing a greater amount of EE2 than the material containing an amorphous TiO_2 sol-gel process. Nevertheless, the alk-TiO_2-HAP-HGMs were capable of removing approximately 30% more EE2 over a 12-hour time period than GAC.

An intermediate reactant in the form of CaHGMs was also tested for its ability to remove EE2 from solution. The rationale of testing calcium carbonate coated HGMs was to determine whether the active part of hydroxyapatite with respect to EE2 removal was the calcium component, the phosphate component, or the hydroxyapatite material overall. Furthermore, it was thought worthwhile to test calcium carbonate as waterways rich in calcium carbonate in the stream bed are known as chalk streams and are widely regarded

for the clarity of their waters (Berrie, 1992).

In the literature much attention has been paid to optimising activated carbon for the purpose of removing contaminants from water. Activated carbon is effective at removing contaminants such as oils, greases and other organic liquids from water via the process of adsorption. The hydrophobic nature of activated carbon indicates that AC would be an effective adsorbent for the similarly strongly hydrophobic EE2. Indeed it was found that activated carbon adsorbed bisphenol A primarily through hydrophobic interactions, although the existence of a hydrophilic microdomain also contributed to the overall bonding interaction, to the extent that BPA molecules first occupied high energy hydrogen bonding sites, before spreading to lower energy hydrophobic interaction sites (Zhou, 2014). This finding implies that although most molecules are interacting with the activated carbon through hydrophobic interactions, hydrophilic interactions in the form of hydrogen bonding form first, and using hydrogen bonding as a tool to speed up the rate of adsorption is a useful and effective method to enhance water purification.

12.10 Mechanism of Adsorption by HAP-HGMs

Adsorbents such as AC are often optimised to increase their surface area, and hence increase the number of possible adsorption sites. However, the effect of a high surface area can be exceeded if other interactions are possible. For example, polyamide 612 (20 m^2/g) is a more effective adsorbent than Darco or Norit (600 – 1000 m^2/g) (Han, 2012), although the polyamide referred to here is able to interact with EE2 through π-π interactions, as well as hydrogen bonding. From this example, it seems clear that when there are additional mechanisms for the interaction of EE2 with the adsorbent, a higher surface area does not provide improved adsorption of EE2. However, when the materials contain similar chemical species and thus provide similar routes for adsorption of EE2, it is likely that a

higher surface area improves adsorption. This is evident from Table 90. EE2 removed in mg/g material using batch settling technique, where in the initial 30 min of the experiment – before the initiation of photocatalysis, the anatase-HAP-HGMs adsorbed 1.12 mg/g of EE2, in contrast to the alk-TiO_2-HAP-HGMs which only adsorbed 1.00 mg/g EE2.

The exact mechanism of adsorption of EE2 to the HAP-HGMs has not yet been fully determined, although the comparison of the removal of EE2 by the HAP-HGMs to the kinetic models suggests the mechanism may be chemisorption. This is consistent with the literature (Feng, 2010) (Sahoo, 2020) (Han, 2012) (Yasir, 2022) (Yasir, 2022) (Lu, 2021) (Leite Vieira, 2022), where the kinetic model that best fits EE2 removal is found to be the Elovich model. The Elovich model represents adsorption to sites with heterogeneous surfaces, which is applicable to TiO_2-HAP composites, where Ti, O, Ca, P, and H are exposed.

Kovalova et al. also found that hydrogen bonding contributed to the overall mechanism of EE2 adsorption, The mechanisms of EE2 adsorption include hydrophobic interactions, hydrogen bonding, π-π interactions (Pan, 2014), host-guest interactions, pore filling effect (Sun, 2011), dipole-dipole interactions, electrostatic interactions, and molecularly-imprinted polymer adsorption (Leite Vieira, 2022). The mechanism for the adsorption of EE2 is most likely to be hydrogen bonding between the OH groups of EE2 and sites on the adsorbent. Furthermore, the hydrophobic nature of EE2 is likely to play a role in the driving force behind its adsorption with secondary interactions then occurring as a result of electrostatic interactions occurring between the adsorbent and EE2.

In the wider context of water remediation from water contamination, the combined TiO_2-HAP materials present a novel method for decontaminating water, due to the ion-exchange capacity of HAP allowing the removal of metal ion contaminants, in addition to the

demonstrated ability of TiO_2 to photocatalytically degrade organic contaminants.

12.11 Limitations of this work

The limitations of using HPLC were that is cannot be guaranteed that no EE2 was retained on the stationary phase of the column, meaning it could be possible that the results are not truly accurate. Performing this experiment in triplicate was the method used to offset this potential issue, as was inspecting the chromatogram and comparing the chromatogram against chromatograms of calibration samples used to confirm that peaks were appearing in the correct places and there were no additional peaks, and that the peaks associated with EE2 were symmetrical with no tails, which would indicate that EE2 was being retained on the column instead of being moved through and out of the column.

The limitations of using a UV detector were that there is disagreement in the literature between whether using a wavelength of 220 nm or 280 nm is more appropriate for EE2 concentration measurements. In this work both wavelengths were examined and the HPLC peaks at 220 nm were more clearly defined than the peaks at 280 nm in all cases. In many cases the peaks were not at all visible at 280 nm.

The EE2 removal experiments would have benefitted from multiple rounds of testing the ability to regenerate the materials. This would have resulted in a more definitive response for the ability to recycle and reuse the adsorbent/photocatalysts over multiple uses. Furthermore, a comparison of the photocatalytic degradation kinetics using the Langmuir-Hinshelwood model would have provided valuable insight into the rate constant achieved by the alk-TiO_2- HAP-HGMs.

The kinetic models tested were the non-linear forms of the models fitted with origin pro, and were chosen based on the models presented in the literature. This means the

information they provide is limited, and comparing a greater range of models, including diffusion models, would have permitted a more definitive statement regarding the mechanism of adsorption. As it stands, the only firm conclusion that can be drawn from the comparison of kinetic data to the models is that the pseudo second order and Elovich models describe EE2 adsorption to the HAP-HGMs more effectively than the pseudo-first order model or the intraparticle diffusion model.

Other limitations also include that a water matrix containing natural organic matter (NOM) was not investigated, so there is no information on how or if NOM competes with EE2 for adsorption sites. However, EE2 is known to adsorb to solid material, so the presence of NOM could increase the removal of EE2 from the water matrix by providing an additional surface to adsorb to. NOM was therefore not included in the water matrix in order to ensure that adsorption was solely due to the adsorbent. In addition, this work was intended to mimic real world scenarios and uses of adsorbent/photocatalytic systems. This work would have benefited enormously from repeating the EE2 removal experiments using optimized conditions to determine the maximum possible amount of EE2 that could be removed to provide a realistic comparison to removal rates achieved in the literature. As it stands, 43 – 65% is removal is adequate, especially as the combined photocatalytic materials outperform commercially available GAC, while also providing the added dimension of destruction of EE2, negating the need for dealing with a secondary waste stream generated when adsorbents are used to remove contaminants from water.

In addition, changing the pH of water matrix was not tested, which could have offered information about the mechanism of adsorption in due to protonation at low pH. However, maintaining neutral pH was a more realistic model of wastewater treatment processes than testing EE2 adsorbence under high or low pH conditions. Nevertheless, this work would have befitted from testing EE2 adsorption at low pH for the information that could be

extracted regarding the actual mechanism of EE2 adsorption.

The avoidance of calcination of the materials also presented some difficulties in the characterisation of the materials used in this work. The HAP component of the HGMs could have been easier to analyse if calcination have been performed, and the ensuing increase in crystallinity resulted in more define and distinct peaks, reducing the extent of peak overlap that made characterisation so difficult. However, the XRD pattern of a calcined sample of a TNW reaction contained peaks corresponding the 2theta values of TiO_2, confirming that TiO_2 was present in the pre-calcined sample in an amorphous form.

Overall, this work has advanced the field of water purification by offering a new insight into the requirements of a suitable adsorbent for removal of EE2 from water. This work has demonstrated that HAP-HGM could present an alternative to AC adsorbents for the purpose of water remediation from EE2 contamination. Furthermore, the HAP component of the HAP-HGMs has been demonstrated to be an effective adsorbent for metal ion contaminants, which AC is not used for, indicating the applicability of HAP to the removal of a wider range of contaminants than AC.

12.12 Outcomes of this work

In this work five key characteristics were used to define a method as green: minimal use of hazardous substances during material synthesis and method deployment; energy efficiency and renewable inputs; reusability and facile regeneration of materials; use of abundant, non-toxic and materials with benign products of degradation if released into the environment; and low environmental/carbon footprint and end-of-life impact.

The raw materials required to produce the TiO_2/HAP materials vary in the renewability of their synthesis methods. TiO_2 requires high temperature, which may be associated with a higher carbon footprint for the production of anatase from its feedstocks, as outlined in

Chapter 3, while the sol-gel synthesis route can produce TiO_2 at less extreme temperatures, this route may require the use reagents that are harmful or toxic, such as ethylene diamine. The non-renewable feedstocks required to produce TiO_2, however, may be offset by the recyclability of TiO_2, as the TiO_2 containing materials can be used for multiple cycles of water purification, then reprocessed (often through washing in the TiO_2 in ethanol) to ready the TiO_2 material for further use cycles. If accidentally released into the environment, there are no known hazardous products of degradation associated with TiO_2, and hence a minimal end-of-life impact. While the synthesis methods of anatase may not be considered fully green due to the high temperatures and chemical reagents required for its synthesis, it may be considered a green material in other respects, due to its minimal impact on the environment in the case of inadvertent release, its reusability and recyclability, and its minimal end of life impact.

The HGMs also require high temperatures for their manufacture which indicates a larger carbon footprint, but have wide ranging applications in the construction, oil & gas, automotive and aerospace industries, meaning they are a readily available material. While it was initially thought necessary to use the HGMs as a template to direct HAP growth from chemical reagents, this was later found to not be totally necessary, and efforts to improve the "green" rating of the TiO_2/HAP could include excluding the HGMs from the materials, hence decreasing the number of materials required to produce the TiO_2/HAP materials. Consisting largely of silicon dioxide, there are no known chemical hazards associated with their accidental release into the environment, although consuming the microspheres may be associated with adverse outcomes if the HGMs shatter *in vivo*, resulting in mechanical damage to soft tissues. Excluding the HGMs from the TiO_2/HAP materials could therefore be argued to increase the green rating of these materials.

The use of food waste to obtain scallop shells to produce the HAP component meets all

the requirements set out to define a green material. Being derived from living organisms means HAP derived from scallops can be considered renewable, their use diverts material away from landfill, there are no credible adverse consequences to the inadvertent release of scallop shell derived HAP to the environment, there is a low carbon footprint due to this feedstock's status as a waste material, and there is minimal end of life impact.

Overall, the alk-TiO_2-HAP-HGMs were successful at removing EE2 from solution, although comparable materials containing anatase (the anatase-HAP-HGMs and scsh-HAP-anatase materials) were capable of removing a greater proportion of EE2 from solution. The combined TiO_2-HAP materials were capable of removing more EE2 than is found globally in all but the two regions most contaminated with EE2. Hence this material is widely applicable to for the resolution of the issue of water contamination with EE2. The materials also demonstrated reusability after a trivial cleaning step via an ethanol wash, a solvent that can also be obtained from renewable feedstocks.

These findings show that combining adsorption and photocatalysis produces a synergistic effect that outperforms either photocatalysis or adsorption working alone. The most effective material contained anatase, hydroxyapatite and calcium carbonate, which outperformed GAC on a mass for mass basis. This presents an advancement to the field of water remediation, as combining adsorbent and photocatalytic systems is still novel work: adsorbents remove contaminants but do not destroy them, and photocatalysis may incompletely degrade contaminants, whereas combined adsorbent/photocatalytic systems provide complementary features the take advantage of the useful aspects of adsorbents and photocatalysts, while compensating for the limitations of adsorbents and photocatalysts.

The hydroxyapatite portion of the most successful combined photocatalytic material was

generated using food waste, while the titanium dioxide used presents a small hazard in the form of free nanoparticles. Capturing the titanium dioxide nanoparticles in a composite material significantly reduces the risk of inhalation, ingestion or intradermal exposure. Concerted efforts were also made to avoid calcination at high temperatures at every stage of synthesis, with the highest temperature used not exceeding 200 °C. The photocatalytic/adsorbent system can be powered with UV/light generated via renewable energy, fulfilling the second condition. Regeneration of the materials was achieved with an ethanol wash; however, the material performance would be improved with calcination to remove organic contaminants. As the composite material is made of hydroxyapatite (the same mineral as bone), it assumed to be benign. TiO_2 has until recently has been widely consumed in food products the material has not been assessed to be at risk of causing harm if accidentally dispersed into the environment, but based on their known chemical properties, there are limited credible mechanisms to cause harm as a result of inadvertent release to the environment, particularly when it is bonded to a larger structure and is not in free nanoparticle form. However, separation of the composite into the original HAP and TiO_2 components for true end-of-life processing and recycling has not been attempted and it would likely to prove challenging to fully cleave any calcium-oxygen-titanium chemical bonds. Nevertheless, repeated cleaning, regeneration and recycling steps are possible – the TiO_2-HAP composites would be resilient to high temperature calcination which would remove traces of organic contaminants causing a decrease in material activity, allowing the TiO_2/HAP to be fully regenerated, with trivial washes in ethanol repeated between cycles of use.

In conclusion, the TiO_2/HAP materials offer a pathway towards a sustainable alternative to activated carbon, that is capable of removing more EE2 than GAC. While the TiO_2 feedstock materials and HGMs may not have the most green origins or manufacturing

specification, the potential indefinite reusability of the TiO_2/HAP materials can arguably offset this, particularly if the feedstocks are obtained from ready-made sources which would otherwise be discarded into landfill, e.g. the TiO_2 intended for use in food no longer permitted in the EU.

Finally, evidence is provided in this work that a combined adsorbent-photocatalytic system for water purification is as effective as the industry standards for both adsorbents and photocatalysts. Furthermore, the addition of TiO_2 to HAP provides evidence that the presence of the photocatalyst does not significantly hinder adsorption, meaning that combined adsorption-photocatalysis systems are a viable way forward for the field of water purification.

12.13 Steps Towards Full-Scale Deployment

The basic function of a photocatalytic reactor is providing contact between the illuminated catalyst and the contaminants (Alalm, 2021). There are consequently many different designs for photocatalytic reactors, generally divided between batch-mode and continuous-mode. The factors that must be considered to achieve full-scale deployment of the water purification material are outlined in Section 3.9 Photocatalysis: Scale-up Operation Introduction & Key Challenges. Full scale deployment would require:

- Catalyst recovery: ensuring stable immobilization to avoid nanoparticle release.
- Light distribution: maximizing oxidative photon flux across the reactor volume.
- Mass transfer limitations: achieving adequate contact between pollutants, light and active sites in turbid water.
- Durability under real-world conditions: chemical fouling, catalyst deactivation, and harsh water matrices (Plakas, 2017).

Designing a green photocatalytic reactor would furthermore necessitate the use of a green

energy source to provide power for the UV source. With recent developments in solar power, it is assumed that an appropriately scaled solar power supply would be sufficient. In addition, using the TiO_2-HAP composite for water purification would be performed after the coagulation, flocculation, sedimentation and filtration stages, as part of the disinfection stage, after the large solids and debris have been removed in previous stages.

Scale up methods with high degradation efficiencies are reported in Table 99. Photocatalytic reactors used for scaling up water purification . It should be noted that in this table 100% degradation efficiency indicates that the concentration of the pollutant was below the LoD of the instruments or methods used to quantify the contaminant and does not necessarily indicate 100% degradation of the contaminant.

Table 99. Photocatalytic reactors used for scaling up water purification (Alalm, 2021).

Reactor Type	**Photo-catalyst**	**Pollutant**	**Irradiation Source**	**Max Degradation %**	**Reaction Time (min)**	**No of Reuse Cycles**	**Degradation % at Last Cycle**
Moving bed reactor	TiO_2 nanotubes/ graphene	Bisphenol A	350 W Xe lamp	100%*	30	5	92%
Fluidized bed reactor	MnO_2/ GAC	Aniline, benzo-thiazole	25 W poly-chromatic UV lamp	84.7%	60	-	-
Photo-catalytic PVDF membrane	$ZnIn_2S_4$	Fluvastatin	500 W Xe lamp	99.75%	180	6	91.53%
Photo-catalytic graphene oxide membrane	g-C_3N_4	Rhodamine B	300 W Xe lamp with 420 nm cut-off filter	98.7%	90	-	-
Solar membrane reactor	TiO_2	Tartrazine	Natural solar light	78%	300	2	67%
Photo-catalytic polymer membrane	TiO_2	Methylene blue	Solar lamp	100%*	40	9	100%*
Coated plate reactor	W-TiO_2	Sulfa-methazine	400 W metal-halide lamp	100%*	120	5	90.3%
Tubular continuous-flow with attached catalyst	TiO_2	Acid Red 27	30 W UV-C lamps	100%*	-	-	-
Falling film reactor	TiO_2	Chlor-toluron	24 W UV lamp	100%*	250	-	-

Submerged coated plate	Ru-WO_3/ZrO_2	Multiple bacteria	400 W metal-halide lamp	100%*	240	4	100%*
Submerged coated plate	S-TiO_2	2,4-dichloro-phenol	400 W metal-halide lamp	98%	480	5	80%
Coated plate reactor	ZrV_2O_7/ graphene nano-platelets	Chlor-pyrifos	400 W metal-halide lamp	96.8%	90	5	91%
Magnetic aggregation bed reactor	$CoFe_2O_4$-Ag_2O	Methyl orange	600 W LED lamp	92%	60	3	80%
Submerged coated plate	Fe-Cr-N-TiO_2	Direct blue 15	20 W LED lamp	100%*	60	-	-
Submerged membrane reactor	Fe-ZnS/g-C_3N_4	p-nitro-phenol	500 W Xe lamp	93.5%	300	-	-
Micro–meso-reactor	TiO_2	Cr(VI)	1700 W Xe lamp	100%*	60	10	70%

There are many methods available to scale-up photocatalytic materials from bench scale to pilot scale. This may mean that there has not yet been a fully optimised method developed that can be applied to various photocatalysts, suggesting difficulties with scale up, as the contaminated water must be in close proximity to the photocatalyst while also permitting penetration of UV light – indicating limitations to the dimensions of photocatalytic reactors, which may in turn, hinder scale up efforts beyond pilot scale. Nevertheless, the numerous methods reported in Table 99 indicate that there are multiple successful methods possible for scale-up. The methods reported in Table 99 that are most applicable to the TiO_2-HAP composites examined in this work are:

i. Moving bed reactor used for degradation of bisphenol A.
ii. Fluidised bed reactor using MnO_2/GAC
iii. Photocatalytic PVDF membrane used for degradation for fluvastatin

The moving bed reactor was demonstrated using an immobilised TiO_2/graphene nanotubes photocatalyst and achieved a maximum degradation efficiency of 100%, with 92% degradation achieved after 5 cycles (Surenjan, 2019). The target contaminant was

bisphenol A, which is an EDC and shares some structural similarities to EE2. It can reasonably be concluded that this pilot-level photoreactor could be successfully implemented using the TiO_2/HAP composites as the photocatalytic material. The disadvantage of using this method is as the volume of the reactor is increased there is the risk of increasing the distance the photons travel before reaching the photocatalyst, which could reduce the rate of electron excitation. Mitigating this requires the size of the UV lamp to increase in scale with the volume of the reactor, which increases energy demand. This means the moving bed reactor may not be appropriate for water treatment at the largest scale for municipal water treatment, but may still be useful for treatment of industrial effluent. This is shown in Figure 99 where the UV light is arrayed along the walls of the container with the light directed inwards.

Figure 99. Fluidised bed reactor using TiO_2/graphene nanotube photocatalyst.

A fluidised bed reactor which used MnO_2/GAC as a photocatalyst/adsorbent material was deployed at pilot scale and achieved >84% TOC mineralisation of aniline and benzothiazole (Ferreiro, 2021) may provide a more viable example to model to achieve scale-up of the process of using UV and TiO_2/HAP composites to perform water decontamination. This setup differs from that reported in (Surenjan, 2019), as the MnO_2/GAC was not immobilised, and the UV lamp arranged axially in the centre of the

photoreactor. Although the 84% contaminant removal appears lower than other options described in Table 99, this work was achieved in the presence of competing ions such as nitrates, phosphates and chlorides. This means that the matrix used was more representative of the typical water matrix present in "real-life" conditions, in contrast to the ideal conditions (i.e. water plus one single contaminant of interest) often reported in scientific papers. The disadvantage of this method is that it is operated in batch mode, which necessitates plant "down-time" as the photocatalyst/adsorbent is recovered between treatments. The pilot plant is shown in Figure 100. Fluidised bed reactor using MnO2/GAC for water treatment.

Figure 100. Fluidised bed reactor using MnO_2/GAC for water treatment.

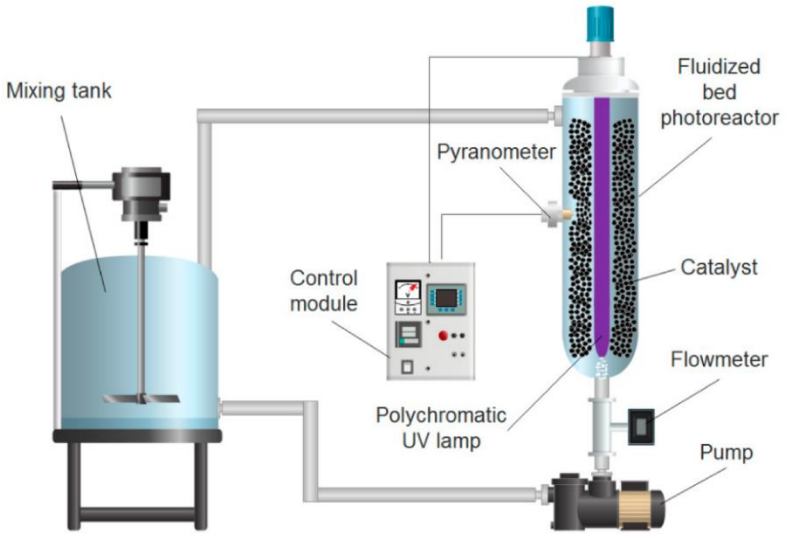

Immobilising the photocatalyst on a membrane has multiple advantages – immobilising the photocatalyst on a membrane solves the issue of suspended photocatalyst separation and the presence of the photocatalyst on the membrane provides anti-fouling properties that improve membrane performance. In particular, $ZnIn_2S_4$ was immobilised on a PVDF membrane for removal of fluvastatin from water, with a removal efficiency of 97.19% and a TOC removal efficiency of 53.29% (Liu, 2020). PVDF filters were demonstrated in

Chapter 11 to be effective at removing EE2, initially removing 100% of this EDC, meaning combining PVDF filters with the TiO_2/HAP composites in a photocatalytic/polymer membrane reactor could be the most appropriate way to scale-up the materials for use in a pilot plant. The disadvantage of this method is that it is batch flow, whereas continuous flow would be preferred for increased throughput and possibility for greater volume of water purified. To combat this, using multiple membrane reactors acting in parallel with staggered start times to ensure constant operation of the water purification system would allow a system that is almost as effective as a continuous flow reactor. The photocatalyst/membrane cell reactor that inspired this proposal is shown in Figure 101. Reactor using a photocatalyst immobilised on a PVDF membrane

Figure 101. Reactor using a photocatalyst immobilised on a PVDF membrane.

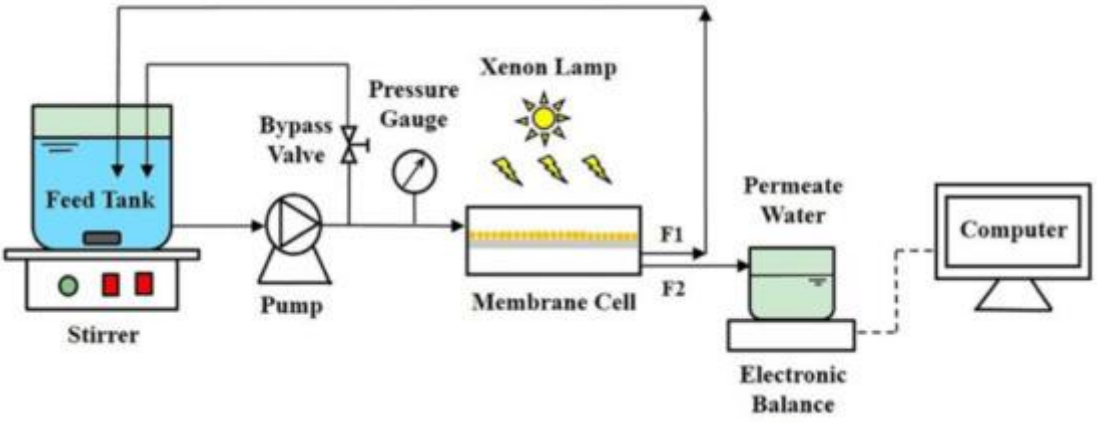

Of the three possible methods presented here to scale-up the TiO_2/HAP composites to pilot-scale water treatment applications and beyond, it must be stated that the variety of photocatalytic reactor designs design, reported and implemented in the literature demonstrate that there not yet one final “one-size-fits-all” possibility that can be applied to every photocatalyst. The general problems pervade: ensuring adequate exposure of the contaminant to the photocatalyst to permit photocatalytic degradation; ensuring sufficient

exposure of the photocatalyst to UV light without inhibiting mixing of the photocatalyst with the water/contaminant matrix; and recovering a satisfactory amount of the photocatalyst after use such that the recovered photocatalyst can be used multiple times to guarantee the economic viability of the photocatalyst. At present, every photocatalytic reactor system reported in the literature has a unique disadvantage – no perfect system has been reported yet. Therefore, all photocatalytic reactors present a compromise in some form – whether in efficiency of degradation, efficiency of photocatalyst recovery, the time taken, or the energy required to achieve full contaminant degradation. Nevertheless, because of the possibility of full contaminant degradation and the critical importance of clean potable water, pursuing multiple avenues of water decontamination and continuing to explore multiple methods of purifying water is an essential avenue of research for human health, quality of life and longevity.

12.14 Future Research Aims

This work indicates that that continued research on adsorbent/photocatalytic systems is a necessary and integral part of the field of water remediation. In the context of this work, TiO_2 should be doped to bring the band gap energy down to wavelengths of visible light, resulting in a process that can be conducted using natural sunlight. This would be the next step towards developing a truly green and effective water treatment method, as a combined adsorbent- photocatalytic material that is able to achieve photocatalysis under visible light would remove the need for UV light.

The TiO_2-HAP material should also be tested against a range of contaminants found in the water supply, including metal ions, other endocrine disrupting compounds and persistent organic contaminants, in order to demonstrate the effectiveness of HAP at removing metal ion contaminants due to its ion-exchange ability, and the synergistic effect of combining TiO_2 and HAP into a composite material.

13. Chapter 13 – Conclusions and Future Work

The aim of this work was to provide a method of water purification that is capable of completely removing all contaminants from water. This thesis aimed to achieve that goal by producing a hybrid material with adsorptive and photocatalytic properties, in order to simultaneously remove contaminants from solution and (if they are organic contaminants) destroy them photocatalytically. This work also aimed to produce this material using the fewest number of steps and chemical reagents possible, and to avoid the use of high temperatures whenever possible. This thesis achieved that goal by providing the synthesis route and characterisation data for a novel composite hierarchical material that has the ability to remove organic contaminants from water by adsorption, then photocatalytically

degrade them. The novel composite material is comprised of titanium dioxide coated on to hydroxyapatite, which in turn has been grown from the surfaces of hollow glass microspheres, resulting in a material that has the adsorbent properties associated with hydroxyapatite, with the photocatalytic properties of titanium dioxide.

The novel composite was produced using ambient temperatures, avoiding the high temperatures often used in hydroxyapatite synthesis. The fact that hydroxyapatite was successfully synthesised using so few reagents is an important advancement, as hydroxyapatite has previously been synthesised under mild conditions using SBF, which contains a range of ions in order to mimic blood plasma, which complicates and obscures the process by which hydroxyapatite is formed. Furthermore, the high surface area of the hydroxyapatite product obtained using this chemical precipitation route is very promising for future applications that require a high surface area such as adsorption. It should be noted that the presence of calcium silicate did seem to promote the growth of hydroxyapatite, and the absence of calcium silicate limited the extent of hydroxyapatite formation.

The efficacy of the novel hierarchical composite material was demonstrated through the removal of EE2 from water. EE2 was selected as the target molecule for removal because this form of estrogen has the highest estrogenic potential and the slowest degradation rate relative to the other estrogens, and has been slowly but surely accumulating in aquatic systems around the globe. According to the results the bulk of EE2 was removed within the first 20 minutes of treatment, before plateauing. This indicates that the mass of material used to purify the water was insufficient, and that a greater mass of the composite would be capable of removing the EE2 from solution entirely within 20 minutes.

The removal experiments completed using CaHGMs and HAP-HGMs indicated that calcium carbonate (CaHGMs) and calcium phosphate (i.e., hydroxyapatite in the HAP-

HGMs) were particularly well-suited to achieving the removal of EE2, and it thought that this is due to the positively charged calcium ions interacting with the negatively charged regions of the EE2 molecule, for example the oxygens from the OH groups through the electrostatic force of attraction between opposing charges, while the non-polar carbonate and phosphate groups interact with the non-polar carbon backbone of the EE2 molecule. This finding has implications for the future of water purification, because it implies that water purification can be obtained easily and reliably through the use of adsorbents with properties similar to calcium carbonate and calcium phosphate – a solid containing positively charged species to interact with OH groups and a non-polar species to interact with the non-polar carbon component of organic pollutants.

The future of this work is to continue the process of optimising the properties of the hierarchical composite material and optimising the conditions in which the composite is expected to work. These tasks include:

i. Optimise the hydroxyapatite component of the composite by continuing to increase its surface area in order to maximise adsorption.

ii. Investigate the desorption of the EE2 from the hydroxyapatite component in order to confirm the uptake of EE2 by hydroxyapatite.

iii. Optimise the titanium dioxide component by doping it with other metals to decrease the band gap into the visible light range – removing the need for ultraviolet treatment to initiate photocatalysis.

iv. Optimise the conditions used for contaminant removal by using a greater mass of the novel composite for water purification, in a set up resembling an activated carbon cartridge in order to ensure the solution containing EE2 makes physical contact with the novel composite, which leads to (v):

v. Separating the adsorption and photocatalysis stages to determine if separating the stages improves EE2 removal rates, or if EE2 removal is highest during simultaneous adsorption and photocatalysis.

vi. Use artificial intelligence to construct a model to predict EE2 removal rates when various parameters within the hybrid system are altered in order to streamline the process of optimising the rate of contaminant removal.

vii. Apply the novel composite to water contaminated with a range of species in order to determine the extent of contaminant removal in more complex systems that contain natural organic matter, heavy metal ions, microbes and other species that may compete with EE2 for adsorption sites.

In conclusion, this thesis demonstrated that a hybrid material that combined adsorption and photocatalysis for the purpose of water purification by removing EE2 was highly effective. This composite material was produced using low energy processes, which is critical for the future of water purification due to factors such as the high cost of fossil fuel, both environmentally and financially, and means that this composite can be produced worldwide without restrictions such as access to expensive and sophisticated laboratory equipment. This thesis paves the way for new solutions to water purification by providing new options and materials capable of fully purifying water.

14. References

Aarthy, S, Thenmuil, D and Manohar, P (2019) 'Exploring the effect of sintering temperature on naturally derived hydroxyapatite for bio-medical application', J. Mater. Sci. Mater. Med., 30, article 21.

Adam, D, Ongsuwan, N and Chotisuwan, S (2023) 'Photo-reforming of glycerol catalyzed by CuO/TiO_2 supported on hydroxyapatite', Sains. Malays., 52, pp. 2713-2723.

Adeogun, A, Ofudje, A and Idowu, M (2018) 'Facile development of nano size calcium hydroxyapatite based ceramic from eggshells: synthesis and characterization', Waste Biomass Valori., 9, pp. 1469-1473.

Al-Hajji, L, Ismail, A, Bumajdad, A, Alsaidi, M, Ahmed, S, Al-Hazza, A and Ahmed (2021) 'Photodegradation of powerful five estrogens collected from wastewater treatment plant over visible light driven Au/TiO_2 photocatalyst', Environ. Technol. Innov., 24, article 101958.

Alalm, M, Djellabi, R, Meroni, D, Pirola, C, Bianchi, C and Boffito, D (2021) 'Toward scaling-up photocatalytic process for multiphase environmental applications', Catalysts, 11, article 562.

Alosfur, F, Ouda, A, Ridha, N and Abud, S (2019) 'High photocatalytic activity of TiO_2 nanorods prepared by simple method', Mater. Res. Ex., 6, article 065028.

An, Y, Zheng, P and Ma, X (2019) 'Preparation and visible-light photocatalytic properties of the floating hollow glass microspheres - TiO_2/Ag_3PO_4 Composites', RSC Adv., 9, pp. 721-729.

An, Y, Zheng, P and Ma, X (2020) 'Preparation of the floating HGMs-Ag_3PO_4 composites and the visible light photocatalytic properties', Mater. Res. Express, 7, article 015049.

Anwar, N, Kassim, A, Lim, H, Zakarya, S and Huang, N (2010) 'Synthesis of titanium dioxide nanoparticles via sucrose ester micelle-mediated hydrothermal processing route', Sains. Malays., 39, pp. 261-265.

Aris, A, Shamsuddin, A and Praveena, S (2014) 'Occurrence of 17-alpha-ethinylestradiol (EE2) in the environment and effect on exposed biotas: a review', Environ. Int., 69, pp. 104-119.

Armelao, L, Bassan, A, Bertoncello, R, Biscontin, G, Daoli, S and Glisenti, A (2000) 'Silica glass interaction with calcium hydroxide: a surface chemistry approach', J. Cult. Herit., pp. 375-384.

Asahi, R, Morikawa, T, Ohwaki, T, Aoki, K and & Taga, Y (2001) 'Visible-light photocatalysis in nitrogen-doped titanium oxides', Science, 293, pp. 269-271.

Athanasiou, D, Romanos, G and Falaras, P (2016) 'Design and optimization of a photocatalytic reactor for water purification combining optical fiber and membrane technologies', Chem. Eng. J., 305, pp. 92-103.

Bachina, A, Almjasheva, O, Popkov, V, Nevedomskiy, V and Gusarov, V (2021) 'Heat- stimulated crystallization and phase transformation of titania nanoparticles,', J. Crys. Growth., 576, article 126371.

Balasooriya, I, Chen, J, Gedara, S, Han, Y and Wickramanatne, M (2022) 'Applications of nanohydroxyapatite as adsorbents: a review', Nanomat., 12, article 2324.

Bao, R, Liu, B, Zhang, T, Wu, B, Dong, E, and Yuwen, C. 'Rutile TiO_2 production: optimization of microwave calcination of metatitanic acid using response surface methodology', Chem. Eng. Technol., 45, pp. 1826 - 1834.

Baranowska-Wojcik, E, Szwajgier, D, Oleszczuk, P and Winiarska-Mieczan, A (2020) 'Effects of titanium dioxide nanoparticles exposure on human health - a review', Biol. Trace Elem. Res., 193, pp. 118-139.

Barron, M, Young, T, Johnston, K and Williams, R (2003) 'Investigation of processing parameters of spray freezing into liquid to prepare polyethylene glycol polymeric particles for drug delivery', AAPS Pharm. Sci. Tech., 4, article 12.

Bayer AG (2023) Femodene. Electronic Medicines Compendium. Available at: https://www.medicines.org.uk/emc/files/pil.1123.pdf (Accessed: 16 February 2026).

Benotti, M, Stanford, B, Wert, E and Snyder, S (2009) 'Evaluation of a photocatalytic reactor membrane

pilot system for the removal of pharmaceuticals and endocrine disrupting compounds from water,', Water Res., 43, pp. 1513-1522.

Berrie, A (1992) 'The chalk stream environment', Hydrologia, 248, pp. 3-9.

Bhandari, R, Wang, X, vom Saal, F and Tillitt, D (2020) 'Transcriptome analysis of testis reveals the effects of developmental exposure to bisphenol A or 17-alpha ethinylestradiol in medaka (Oryzias latipes)', Aquat. Toxicol., article 105553.

Cai, Y, Liu, Y and Yan, W (2007) 'Role of hydroxyapatite nanoparticle size in bone cell proliferation', J. Mater. Chem., 17, pp. 3780-3787.

Cargouet, M, Perdiz, D, Mouatassim-Souali, A, Tamisier-Karolak, S and & Levi, Y (2004) 'Assessment of river contamination by estrogenic compounds in Paris area (France)', Sci. Total Environ., 324, pp. 55-66.

Carvalho, R, Isecke, B, Carvalho, E and Teran, F (2017) 'Photocatalytic oxidation of a 17a-Ethinylestradiol by UV-activated TiO_2 in batch and continuous-flow reactor', J. Chem. Eng. Mater. Sci., 8, pp. 10-16.

Challagulla, S, Tarafdar, K, Ganesan, R and Roy, S (2017) 'Structure sensitive photocatalytic reduction of nitroarenes over TiO_2', Sci. Rep., 7 article 8783.

Cheikh, S, Imessaoudene, A, Bollinger, J, Hadadi, A, Manseri, A, Bouzaza, A, Assadi, A, Amrane, A, Zamouche, M, El-Jery, A and Mouni, L (2023) 'Complete elimination of the ciprofloxacin antibiotic from water by the combination of adsorption–photocatalysis process using natural hydroxyapatite and TiO_2', Catalysts, 13, article 336.

Chen, X and Burda, C (2008) 'The Electronic Origin of the Visible-Light Absorption Properties of C-, N- and S-Doped TiO_2 Nanomaterials', J. Am. Chem. Soc., 130, pp. 5018-5019.

Chen, Y, Zhang, Y, Shi, X, Yang, X, Luo, L and Jiang (2022) 'Controllable synthesis of Bi_2SiO_5/$Bi_4Si_3O_{12}$ heterostructure and its specific adsorption and photocatalytic performance', Solid State Sci., 132, article 106986.

Chun, S, An, S, Lee, S, Kim, J and Chang, S (2014) 'Optimization of sulfamethoxazole degradation by TiO_2/hydroxyapatite composite', Korean J. Chem. Eng., 31, pp. 994-1001.

Clouzot, L, Marrot, B, Doumenq, P and Roche, N (2008) '17α-Ethinylestradiol: An endocrine disrupter of great concern. Analytical methods and removal processes applied to water purification, a review', Environ. Prog., 27, pp. 383-396.

Coleman, H, Routledge, E, Sumpter, J, Eggins, B and Byrne, J (2004) 'Rapid loss of estrogenicity of steroid estrogens by UVA photolysis and photocatalysis over an immobilised titanium dioxide catalyst', Wat. Res., 38, pp. 3233-3240.

Colina-Márquez, J, Machucha-Martínez, F and Li Puma, G (2015) 'Modelling the photocatalytic mineralization in water of commercial formulation of estrogens 17-beta-estradiol and nomegestrol acetate in contraceptive pills in a solar powered compound parabolic collectors', Molecules, 20, article 13354.

Combalbert, S and & Hernandez-Raquet, G (2010) 'Occurrence, fate and biodegradation of estrogens in sewage and manure', Appl. Microbiol. Biotechnol., 86, pp. 1671-1692.

Corominas, L, Foley, J, Guest, J, Hospido, A, Larsen, H, Morera, S and Shaw, S (2013) 'Life cycle assessment applied to wastewater treatment: state of the art', Water Res., 47, pp. 5480-5492.

Crini, G and Lichtfouse, E (2019) 'Advantages and disadvantages of techniques used for wastewater treatment', Environ. Chem. Lett., 17, pp. 145-155.

Czerwonka, G and Kaca, W (2012) 'Comparing methods of 17α-ethinylestradiol (EE2) determination in surface water', Pol. J. Environ. Stud., 21, pp. 1089-1093.

da Silva Procópio, A, Vieira de Andrade, F, Soares Silva, F and José de Andrade, S (2023) 'Removal of 17α-ethinylestradiol (EE2) from aqueous solutions by peanut shells (Arachis hypogaea): adsorption

kinetic, isothermal, and thermodynamic studies', Wat. Prac. Technol., 18, pp. 2543-2560.

de França, J.F, Pickler, T.B and Jozala, A.F (2020) 'Determination of 17-alpha-ethinylestradiol and toxic metals in surface waters and estimation for daily intake', Environ. Monit. Assess., 192, article 21.

de Liz, M, de Lima, R, do Amaral, B, Marinho, B, Schneider, J, Nagata, N and Peralta-Zamora, P (2018) 'Suspended and immobilized TiO_2 photocatalytic degradation of estrogens: potential for application in wastewater treatment processes', J. Braz. Chem. Soc., 29, pp 380-389.

Della Bella, E, Parrilli, A and Bigi, A (2018) 'Osteoinductivity of nanostructured hydroxyapatite-functionalized gelatin modulated by human and endogenous mesenchymal stromal cells', J. Biomed. Mater. Res. Part A, 106, pp. 914-923.

Di Valentin, C, Pacchioni, G and Selloni, A (2007) 'Electronic structure of defect states in hydroxylated and reduced rutile TiO_2(110) surfaces', Phys. Rev. Lett., 97, article 166803.

Dias, R, Daam, M, Diniz, M, Mauricio, R, Drinking water treatment residuals, a low cost and environmentally friendly adsorbent for the removal of hormones - a review (2023) Water. Process. Eng., 56, article 104322.

Eddy, N, Ukpe, R, Garg, R, Garg, R, Odoiongenyi, A, Ameh, P and Akpet, I (2023) 'Enhancing water purification efficiency through adsorption and photocatalysis: models, applications, and challenges', International Journal of Environmental and Analytical Chemistry, 105, pp. 1577-1594.

Zhang, Z., Hu, J., 'Effect of environmental factors on estrogenic compounds adsorption by MIP', Water Air Soil Poll., 210, pp. 255 - 264.

Fadeev, I, Shvorneva, L, Barinov, S and Orlovskii, V (2003) 'Synthesis and structure of magnesium-substituted hydroxyapatite', Inorg. Mater., 39, pp. 947-950.

Farrugia, C, Di Mauro, A, Lia, F, Zammit, E, Rizzo, A, Privitera, V, Impellizzeri, G, Buccheri, M, Rappazzo, G and Grech, M (2021) 'Suitability of Different Titanium Dioxide Nanotube Morphologies for Photocatalytic Water Treatment', Nanomaterials, 11, article 708.

Feng, J, Ran, X, Wang, L, Xiao, B, Lei, L, Zhu, J, Liu, Z, Xi, X, Feng, G, Dai, Z and Li, R (2022) 'The Synergistic Effect of Adsorption-Photocatalysis for Removal of Organic Pollutants on Mesoporous $Cu_2V_2O_7/Cu_3V_2O_8$/g-C_3N_4 Heterojunction', Int. J. Mol. Sci., 23, article. 14264.

Feng, Y, Zhang, Z, Gao, P, Su, H, Yu, Y, Ren, N and 1-3 (2010) 'Adsorption behaviour of EE2 (17α-ethinyl estradiol) onto the inactivated sewage sludge: Kinetics thermodynamics and influence factors', J. Haz. Mat., 175.

Ferreira, L, Castro-Alferez, M, Nahim-Granados, S, Polo-Lopez, M, Lucas, M, Puma, G and Fernandez-Ibanez, P (2020) 'Inactivation of water pathogens with solar photo-activated persulfate oxidation', Chem. Eng. J., 381, article 122275.

Ferreiro, C, Villota, N, Lombrana, J, Rivero, M, Zuniga, V and Rituerto, J (2021) 'Removal of Aniline and Benzothiazole Wastewaters Using an Efficient MnO_2/GAC Catalyst in a Photocatalytic Fluidised Bed Reactor', Materials, 14, article 5207.

Fleet, M, Liu, X and King, P (2004) 'Accommodation of the carbonate ion in apatite: An FTIR and X-ray structure study of crystals synthesized at 2-4 GPa', Am. Min., 89, pp. 1422-1432.

Fonseca, A, Cardoso, M and Esteves, V (2013) 'Determination of estrogens in raw and treated wastewater by high-performance liquid chromatography-ultraviolet detection', J. Environ. Anal. Toxicol., 4, article 1000203.

Fujishima, A, Zhang, X and Tryk, D (2008) 'TiO_2 photocatalysis and related surface phenomena', Surf. Sci. Rep., 63, pp. 512-582.

Luis, P (2018) 'Fundamental Modelling of Membrane Systems, Membrane and Process Performance' 1st Ed., Oxford, England.

Gallouze, H, Akretche, D, Daniel, C, Coelhoso, I and Crespo (2021) 'Removal of synthetic estrogen from

water by adsorption on modified bentonites', J. Environ. Eng. Sci., 38, pp. 4-14.

Gao, P, Fan, X, Wang, W and Yang, C (2023) 'Sustainable technologies for adsorptive removal of estrogens from water: a comprehensive review for current advances', J. Environ. Chem. Eng., 11, article 110780.

Gennari, F and Pasquevich (1998) 'Kinetics of the anatase–rutile transformation in TiO_2 in the presence of Fe_2O_3', D. J. Mater. Sci., 33, pp. 1571-1578.

Goh, K, Wong, Y, Singh, R, Chandran, H, Wong, S and Sara Lee, K (2022) 'Irradiation time- dependent study of eggshell-derived hydroxyapatite powder synthesized by microwave- assisted wet chemical precipitation method', J. Ceram. Proc. Res., 23, pp. 158-164.

Gomez-Vazquez, O, Correa-Piña, B, Zubieta-Otero, L, Castillo-Paz, A, Londoño-Restrepo, S and Rodriguez-García, M (2021) 'Synthesis and characterization of bioinspired nano- hydroxyapatite by wet chemical precipitation', Ceram. Int., 47, pp. 32775-32785.

Guo, X, Yan, H, Zhao, S, Zhang, L, Li, Y and Liang, X (2013) 'Effect of calcining temperature on particle size of hydroxyapatite synthesised by solid state reaction at room temperature', Adv. Powder Technol., 24, pp. 1034-1038.

Han, J, Qiu, W, Cao, Z, Hu, J and Gao, W (2013) 'Adsorption of ethinylestradiol (EE2) on polyamide 612: molecular modelling and effects of water chemistry', Wat. Res., 47, pp. 2273-2284.

Han, J, Qiu, W, Meng, S and Gao, W (2012) 'Removal of ethinylestradiol (EE2) from water via adsorption on aliphatic polyamides', Water Research, 46, pp. 5715-5724.

Hanaor, D and Sorrell, C (2011) 'Review of the anatase to rutile phase transformation', J. Mater. Sci., 46, pp. 855-874.

Harja, M and Ciobanu, G (2018) 'Studies on adsorption of oxytetracycline from aqueous solutions onto hydroxyapatite,', Sci. Total Environ., 628, pp. 36-43.

Heo, J, Flora, J, Her, N, Park, Y, Cho, J, Son, A and Yoon, Y (2012) 'Removal of bisphenol A and 17β-estradiol in single walled carbon nanotubes–ultrafiltration (SWNTs–UF) membrane systems', Sep. Purif. Technol., 90, pp. 39-52.

Horn, M, Scwerdtfeger, C, Meagher, E, 'Refinement of the structure of anatase at several temperatures', Z. Kristallogr., 136, pp. 273 - 281.

Hoyle, C, Dai, S, Tanner, R and Jabbarzadeh, A (2020) 'Effect of particle roughness on the rheology of suspensions of hollow glass microsphere particle', J. Non-Newton. Fluid Mech., 276, article 104235.

Hu, M, Yao, Z, Liu, X, Ma, L, He, Z and Wang, Z (2018) 'Enhancement mechanism of hydroxyapatite for photocatalytic degradation of gaseous formaldehyde over TiO_2/hydroxyapatite', J. Taiwan Inst. Chem. Eng., 85, pp. 91-97.

Huang, B, Sun, W, Li, X, Liu, J, Li, Q, Wang, R and Pan, X (2015) 'Effects and bioaccumulation of 17β-estradiol and 17α- ethynylestradiol following long-term exposure in crucian carp', Ecotoxicol. Environ. Saf., 112, pp. 169-176.

Hussain, H, Hassan, M and Agool, I (2016) 'Synthesis of titanium dioxide (TiO_2) nanofiber and nanotube using different chemical method', Optik, 127, pp. 2996-2999.

In, Y, Amornkitbamrung, U, Ho, M and Shin, H (2020) 'On the crystallization of hydroxyapatite under hydrothermal conditions: role of sebacic acid as an additive', ACS Omega, 5, pp. 27204-27210.

Ivanets, A, Shashkova, I, Kitikova, N, Maslova, M, Mudruk, N and Taiwan, J (2019) 'New heterogeneous synthesis of mixed Ti-Ca-Mg phosphates as efficient sorbents of 137Cs, 90Sr and 60Co radionuclides', Inst. Chem. Eng., 104, pp. 151-159.

Jarošová, B, Filip, J, Hilscherová, K, Tuček, J, Šimek, Z, Giesy, J, and Zbořil, R, (2015) 'Can zero-valent nanoparticles remove waterborne estrogens', Luděk Bláha. J. Environ. Manage., 150, pp. 387-392.

Javadinejad, H and Ebrahimi-Kahrizsangi, R (2021) 'Thermal and kinetic study of hydroxyapatite formation by solid-state reaction', Int. J. Chem. Kinet., 53, pp. 583-595.

Jayaweera, H, Siriwardane, I and de Silva, K (2018) 'Synthesis of multifunctional activated carbon nanocomposite comprising biocompatible flake nano hydroxyapatite and natural turmeric extract for the removal of bacteria and lead ions from aqueous solution', Chem. Cent. J., 12, article 18.

Jiang, C, Luo, Y, Yang, S, Li, J, Wang, J, Lund, P and Zhang, Z (2020) 'A review of the compound parabolic concentrator (CPC) with a tubular absorber', Energies, 13, article 695.

Jiang, L, Gu, Y, Guo, H, Liu, L and Chen, J (2017) 'Efficient removal of 17 alpha- ethinylestradiol (EE2) from water using freshly formed Fe-Mn binary oxide', RSC Adv., 7, pp 23802-23811.

Johnson, A, Belfroid, A and Di Corcia (2000) 'Estimating steroid oestrogen inputs to activated sludge treatment works and observation on their removal from the effluent', A. Science Total Environ., 256, pp. 163-173.

Johnson, A, Belfroid, A and di Corcia, A (2000) 'Estimating steroid oestrogen inputs to activated sludge treatment works and observations on their removal from the effluent', Sci. Total. Environ., 256, pp. 163-173.

Jones, J, 'Review of bioactive glass: from Hench to hybrids' Acta Biomater., 2103, pp. 4457 - 4486.

Jung, C, Park, J, Lim, K, Park, S, Heo, J, Her, N, Oh, J, Yun, S and Yoon, Y (2013) 'Adsorption of selected endocrine disrupting compounds and pharmaceuticals on activated biochars', J. Hazard. Mater., 263, pp. 702-710.

Kato, S, Iwata, M and Nonami, T (2002) 'Preparation and Characterization of TiO_2 and Apatite Coated Photocatalyst', J. Soc. Mater. Sci. Jpn., 51, pp. 599-603.

Khamova, T. V, Frank-Kamenetskaya, O. V, Shilova, O.A, Chelibanov, V. P, Marugin, A. M, Yasenko, E. A, Kuz'mina, M, A, Baranchikov, A. E and Ivanov, V. K (2018) 'Hydroxyapatite/anatase photocatalytic core-shell prepared by sol-gel processing', Crystallogr. Rep., 63, pp. 254-260.

Khan, S, Al-Shahry, M and Ingler, W (2002) 'Efficient photochemical water splitting by a chemically modified n-TiO_2', Science, 297, pp. 2243-2245.

Khiri, M, Matori, K and Zainuddin, N (2016) 'The usability of ark clam shell (Anadara granosa) as calcium precursor to produce hydroxyapatite nanoparticle via wet chemical precipitate method in various sintering temperature', SpringerPlus, 51, article 1206.

Kiat Ng, C, Domilondo Bope, C, Nalaparaju, A, Cheng, Y, Lu, L, Wang, R and Cao, B (2017) 'Concentrating synthetic Estrogen 17-alpha-ethinylestradiol using microporous polyethersulfone hollow fiber membranes: experimental exploration and molecular simulation', Chem. Eng. J., 314, pp. 80-87.

Klaic, M and Jirsa, F (2022) '17-alpha-ethinylestradiol (EE2): concentrations in the environment and methods fro wastewater treatment and methods for wastewater treatment - an update', RSC adv., 12, pp. 12794-12805.

Komazaki, Y, Shimizu, H and Tanaka, S (1999) 'A new measurement method for nitrogen oxides in the air using an annular diffusion scrubber coated with titanium dioxide', Atmos. Environ., 33, pp. 4363-4371.

Kovalova, K, Knappe, D, Lehnberg, K, Kazner, C and Hollander, J (2013) 'Removal of highly polar micropollutants from wastewater by powdered activated carbon,', Environ. Sci. Poll. Res., 20, pp. 3607-3615.

Krishnan, T, Nie, N, Abdullah, W, Awang, M, Mansor, S (2022) 'Titanium dioxide sol-gel/ zinc oxide powder-coated clay beads in photocatalytic reactor', J. Teknol., 85, pp. 71 - 79.

Kumar, V, Avisar, D, Prasanna, L, Betzalel, Y and Mamane (2020) 'Rapid visible light degradation of EE2 and its estrogenicity in hospital wastewater by crystalline promoted g-C_3N_4', H. J. Hazard. Mater., 398, article 122880.

Lak, A, Mazloumi, M and Mohajerani, M (2008) 'Rapid formation of mono-dispersed hydroxyapatite nanorods with narrow-size distribution via microwave irradiation', J. Am. Ceram. Soc., 91, pp. 3580-3584.

Larcher, S, Delbes, G, Robaire, B and Yargeau, V (2012) 'Degradation of 17alpha- ethinylestradiol by ozonation – identification of the by-products and assessment of their estrogenicity and toxicity,', Environ. Int., 39, pp. 66-72.

Leal, C, Mesquita, D, A, aral, A and Ferreira, E (2020) 'Environmental impact and biological removal processes of pharmaceutically active compounds: The particular case of sulfonamides, anticonvulsants and steroid estrogens,', Crit. Rev. Env. Sci. Tec., 50, pp. 698-742.

Leite Vieira, R, Borim Pickler, T, Mena Segato, T. C, Faustino Jozala, A and Grotto, D (2022) 'Biochar from fungiculture waste for adsorption of endocrine disruptors in water', Scientific Reports, 12, article 6507.

Li, J, Kuang, D, Feng, Y, Zhang, F and Liu, M (2013) 'A novel electrochemical sensor based on nanocomposite film electrode for sensitive determination of environmental hormone bisphenol A', Asian J. Chem., 25, pp. 3147-3153.

Li, J, Sun, J, Ren, L, Lei, T, Li, J, Jin, J, Luo, S, Qin, S, Gao, C and Lei, T (2023) 'Properties and preparation of TiO_2-HAP@PVDF composite ultrafiltration membranes', Polym. Compos., 44, pp. 7499-7509.

Li, L, Iqbal, J, Zhu, Y, Wang, F, Zhang, F, Chen, W, Wu, T and Du, Y (2020) 'Chitosan/Al_2O_3-HA nanocomposite beads for efficient removal of estradiol and chrysoidim from aqueous solution', Int. J. Bio. Macromol., 145, pp. 686-693.

Li, X, Xie, J, Jiang, C, Yu, J, Zhang, P, 'Review on design and evaluation of environmental photocatalysts', 14, Front. Environ. Eng., 12, article 14.

Li, Y, Zhou, H, Zhu, G, Shao, C, Pan, H, Xu, X and Tang, R (2015) 'High efficient multifunctional Ag_3PO_4 loaded hydroxyapatite nanowires for water treatment', J. Hazard. Mater., 299, pp. 379-387.

Lima, D, Baeta, B, Aquino, S, Libiano, M and Afonso (2014) 'Removal of Pharmaceuticals and Endocrine Disruptor Compounds from Natural Waters by Clarification Associated with Powdered Activated Carbon', R. Water. Air. Soil. Pollut., 225, pp. 1-12.

Linley, S and Reisner, E (2023) 'Floating carbon nitride composites for practical solar reforming of pre-treated wastes to hydrogen gas', Adv. Sci., 10, article 2207314.

Linsebigler, A, Lu, G and Yates, J (1995) 'Photocatalysis of TiO_2 surfaces - principles, mechanism and selected results', Chem. Rev., 95, pp. 735-758.

Liu, G, Yang, H, Pan, J, Yang, Y, Lu, G and Cheng, H (2013) 'Titanium dioxide crystals with tailored facets. Chemical Reviews', Chem. Rev., 114, pp. 9559-9612.

Liu, T, Wang, L, Liu, X, Sun, C, Lu, Y, Miao, R and Wang, X (2020) 'Dynamic photocatalytic membrane coated with $ZnIn_2S_4$ for enhanced photocatalytic performance and antifouling property', Chem. Eng. J., 379, article 122379.

Liu, Y and Gao (2014) 'Photodegradation of endocrine disrupting chemicals by ZnO nanorod arrays', W. Mol. Cryst. Liq. Cryst., 603, pp. 194-201.

Lopez-Velasquez, K, Villaneuva-Rodriguez, M, Meija-Gonzalez, G and Herrera-Lopez, D (2021) 'Removal of 17-alpha ethinylestradiol and caffeine from wastewater by UASB-Fenton Coupled System', Environ. Technol., 42, pp. 3771-3782.

Lu, J, Wu, J and Wu, J (2021) 'Adsorption and desorption of steroid hormones by microplastics in seawater', Bull. Environ. Contam. Toxicol., 107, pp. 730-735.

Luo, L, Xia, L, Tan, W, Li, J, Barrow, C, Wang, W and Shu, L (2019) 'The TiO_2 (B) nano-belts with excellent performance prepared via alkaline stirring hydrothermal method and its application to remove

17a-ethynylestradiol', Environ. Sci. Pollut. Res., 26, pp. 34018-34026.

Machado, K. S, Cardoso, F. D, Azevedo, J. C. R and & Braga (2014) 'Occurance of female sexual hormones in the Iguazu river basin, Curitiba, Paraná State, Brazil', C. B. Acta Sci. Technol., 36, pp. 421-427.

Madhumathi, K, Shalumon, K and Rani, V (2009) 'Wet chemical synthesis of chitosan hydrogel–hydroxyapatite composite membranes for tissue engineering applications', Int. J. Biol. Macromol., 45, pp. 12-15.

Mamaghani, A, Haghighat, F and Lee (2019) 'Hydrothermal/solvothermal synthesis and treatment of TiO_2 for photocatalytic degradation of air pollutants: Preparation,', C. Chemosphere, 219, pp. 804-925.

Manikandan, V, Packialakshmi, J, Bharti, B, Jayanthi, P, Dhandapani, R, Velmurugan, P, Elango, D, Paramasivam, R, Mohanavel, V, Syed, A, Elgorban, A, Bahkali, A and Muthupandian, S (2022) 'Efficient one-pot synthesis of $TiO_2/ZrO_2/SiO_2$ ternary nanocomposites using Prunus × Yedoensis leaf extract for enhanced photocatalytic dye degradation', Oxid. Med. Cell. Longev., 2022, article 3088827.

Margot, J, Kienle, C, Magnet, A, Weil, M, Rossi, L, de Alencastro, L, Abegglen, C, Thonney, D, Chèvre, N, Schärer, M and Barry, D (2013) 'Treatment of micropollutants in municipal wastewater: ozone or powdered activated carbon', Sci. Total Environ., 461, pp. 480-498.

Mironyuk, I, Soltys, L, Tatarchuk, T and Savka, Kh (2020) 'Methods of titanium dioxide synthesis (review)', J. Phys. Chem. Solids, 21, pp. 462-477.

Mohan, D, Sarswat, A, Ok, Y and Pittman, C (2014) 'Organic and inorganic contaminants removal from water with biochar', Biores. Technol., 160, pp. 191-202.

Moreira, N, Sousa, J, Macedo, G, Bibeiro, A, Barreiros, L, Pedrosa, M, Faria, J, Pereira, M, Castro-Silva, S, Segundo, M, Manaia, C, Nunes, O and Silva, A (2016) 'Photocatalytic ozonation of urban wastewater and surface water using immobilized TiO_2 with LEDS: micropollutants, antibiotic resistance genes and estrogenic activity', Water Res., 94, pp. 10-22.

Moreno-Santos, Rios-Hurtado, A, J, Flores-Villaseñor, S, Esmeralda-Gomez, A, Guevara-Chavez, J, Lara-Castillo, F and Escalante-Ibarra, G (2023) 'Hydroxyapatite growth on activated carbon surface for methylene blue adsorption: effect of oxidation time and $CaSiO_3$ addition on hydrothermal incubation', Appl. Sci., 13, article 77.

Morin-Crini, N. et al. (2022) 'Removal of Emerging Contaminants from Wastewater Using Advanced Treatments. A Review', Environ. Chem. Lett., 20, pp. 1333-1375.

Muhlfeld C, Geiser M, Kapp N, Gehr P, Rothen-Rutishauser B (2007) 'Evaluation of pulmonary titanium dioxide nanoparticle distribution using the "relative deposition index": Evidence for clearance through microvasculature', Part Fibre Toxicol., 4, pp. 24-35.

Munir, M, Salman, S, Ihsan, A and Elsaman, T (2022) 'Synthesis, characterization, functionalization and bio-applications of hydroxyapatite nanomaterials: an overview', Int. J. Nanomedicine, 17, pp. 1903-1925.

Muralithran, G and Ramesh, S (2000) 'The Effects of sintering temperature on the properties of hydroxyapatite', Ceram. Int., 26, pp. 221-230.

Murugiah, K, Zakaria, M, Suhaimi, H and Caesarendra W, Sambudi, N (2021) 'Synthesis and characterisation of hydroxyapatite (HAp) from Asiatic Hard Clam (Meretrix meretrix) and Blood Cockle Clam (Anadara granosa) using wet precipitation process', IEEE NBEC, 2021, pp. 1-6.

Nayak, A and Bushan, B (2021) 'Hydroxyapatite as an advanced adsorbent for removal of heavy metal ions from water: focus on its applications and limitations' Mater. Today Proc., 46, pp. 11029-11034.

Nijpanich, S, Hagio, T, Murase, K, Park, J, Kamimoto, Y, Sakdapipanich, J, Terashima, C, Chanlek, N and Ichino, R (2022) 'A tri-layer floating photocatalyst/adsorbent for the removal of organic compounds from wastewater: Layer-by-layer deposition of silicalite-1 and titania on hollow glass microspheres', Environ. Tech. Innov., 26, article 102242.

Nonami, T, Hase, H and Funakoshi, K (2004) 'Apatite coated titanium dioxide photocatalyst for air purification', Catal. Today, 96, pp. 113-118.

Nonami, T, Hase, H and Funakoshi, K (2004) 'Apatite-coated titanium dioxide photocatalyst for air purification', Catal. Today, pp. 113-118.

Noor, S, Othman, M, Khongnakorn, W, Sinsamphanh, O, Abdullah, H, Puteh, M, Tak, T, Zakria, H, El-Badawy, T, Ismail, A, Rahman, M and Jaafar, J (2022) 'Bisphenol A removal using visible light driven Cu_2O/PVDF photocatalytic dual layer hollow fibre membrane', Membranes, 12, article 208.

Noviyanti, A, Asiyiah, E, Permana, M, Swiyanti, D, Suryana, S and Eddy, D (2022) 'Preparation of hydroxyapatite-titanium dioxide composite from eggshell by hydrothermal method: characterization and antibacterial activity', Crystals, 12, article 1599.

Nyankson, E and Kumar, R (2019) 'Removal of water-soluble dyes and pharmaceutical wastes by combining the photocatalytic properties of Ag_3PO_4 with the adsorption properties of halloysite nanotubes', Mater. Today Adv., 4, p. 100025.

Oana, K, Kobayashi, M, Yamaki, D, Sakurada, T, Nagano, N and Kawakami, Y (2015) 'Applicability assessment of ceramic microbeads coated with hydroxyapatite-binding silver /titanium dioxide ceramic composite earthplus (TM) to the eradication of Legionella in rainwater storage tanks for household use', Int. J. Nanomed., 10, pp. 4971-4979.

Oana, K, Kobayashi, M, Yamaki, D, Sakurada, T, Nagano, N and Kawakami, Y (2015) 'Applicability assessment of ceramic microbeads coated with hydroxyapatite-binding silver /titanium dioxide ceramic composite earthplus (TM) to the eradication of Legionella in rainwater storage tanks for household use', Int. J. Nanomed., 4, pp. 4971-4979.

Oliveira, A, Visoli, L and Enzweiler, H (2022) 'Photocatalytic reactors and their scale up: literature review', Conjecturas, 22, pp. 509-530.

Oliveira, H, Ferreira, L, Bertazzoli, R and Longo, C (2015) 'Remediation of 17-alpha- ethinylestradiol aqueous solution by photocatalysis and electrochemically-assisted photocatalysis using TiO_2 and TiO_2/WO_3 electrodes irradiated by a solar simulator', Water Res., 72, pp. 305-314.

Oliveira, M, Barroso, B, Almedia, J, Moraes, M and Rodrigues, C (2020) 'Photoelectrocatalytic degradation of 17-alpha-ethinylestradiol and estrone under UV and visible light using nanotubular oxide arrays grown on Ti-0.5wt% W', Environ. Res., 191, article 110044.

Ong, W, Tan, L, Ng, Y, Yong, S and Chai, S (2016) 'Graphitic carbon nitride (g-C_3N_4)-based photocatalysts for artificial photosynthesis and environmental remediation: are we a step closer to achieving sustainability', Chem. Rev., 116, pp. 7159-7329.

Orozco-Hernández, L, Gomez-Olivan, L, Elizalde-Velazquez, A, Natividad, R, Fabian-Castono, L and SanJuan-Reyes, N (2019) '17-beta-estradiol: significant reduction of its toxicity in water treated by photocatalysis', Sci. Total Environ., 669, pp. 955-963.

Pailler, J, Krein, A, Pfister, L, Hoffmann, L and Guignard, C (2009) 'Solid phase extraction coupled to liquid chromatography-tandem mass spectrometry analysis of sulfonamides, tetracyclines, analgesics and hormones in surface water and wastewater in Luxembourg', Sci. Total Environ., 407, pp. 4736-4743.

Pan, B, Lin, D, Mashayekhi, H and Zing, B (2008) 'Adsorption and hysteresis of bisphenol A and 17-alpha ethinylestradiol on carbon nanomaterials', Environ. Sci. Technol., 42, pp. 5480-5485.

Pan, B, Sun, K and Xing (2010) 'Adsorption Kinetics of 17-alpha-ethinylestradiol and bisphenol A on carbon materials II Concentration dependence', B. J. Soil. Sediment., 10, pp. 845-854.

Pan, Z, Stemmler, E, Cho, H, Fan, W, LeBlanc, L, Patterson, H and Amirbahman, A (2014) 'Photocatalytic degradation of 17alpha-ethinylestradiol (EE2) in the presence of TiO_2-doped zeolite', Vol. 279, 279, pp. 17-25.

Pastre, M, Coutinho, R, Renno, M, Hosima, H, Pagliari, B, Marques, B, da, A. Silva, Bila, D, Kuznetsov, A and Marques, M (2024) 'Simultaneous removal of E1, E2, EE2 and levonorgestrel from water using

TiO_2 catalyst anchored on activated carbon: Processes optimization, materials characterization, and assessment of the estrogenicity reduction', Environ. Res., 263, article 120173.

Phromma, S, Wutikhun, T, Kasamechonchung, P, Eksansri, T and Sapcharoenkun, C (2020) 'Effect of calcination temperature on photocatalytic activity of synthesized TiO_2 nanoparticles via wet ball milling sol-gel method', Appl. Sci., 10, article 993.

Pilot-scale LED photocatalytic system utilizing 3D bioinspired sponge photocatalyst for the removal of amoxicillin, tetracycline, and ciprofloxacin from hospital wastewater. Kubiak, A., Jaruga, M., Chem. Eng. J., 510, article 161758.

Pio, L and Yeo, W (2018) 'The microstructure and mechanical properties of titanium dioxide nanotubes synthesized in the fluoride-based electrolyte', Metal. Mater. Eng., 24, pp. 83-92.

Plakas, K, Sarasidis, V, Patsios, S, Lambropoulou, D and Karabelas, A (2017) 'Novel pilot scale continuous photocatalytic membrane reactor for removal of organic micropollutants from water', Chem. Eng. J., 304, pp. 335-343.

Preparation and characterization of TiO_2 and apatite coated photocatalyst. Kato, S., Iwata, M., Nonami, T. 6, J. Soc. Mater. Sci. Jpn., 51, pp. 599 - 603.

Prokić, D, Vukčević, M and Kalijadis, A, (2020) 'Removal of Estrone, 17β-Estradiol, and 17α-Ethinylestradiol from Water by Adsorption onto Chemically Modified Activated Carbon Cloths', Fiber Polym., 21, pp. 2263-2274.

Qasim, A, Jamil, L and Chen, Q (2017) 'Synthesis and characterization of photocatalytic performance of rutile TiO_2 nanorod arrays for solar hydrogen generation', SJUOZ, 5, pp. 79-87.

Rabahi, A, Assadi, A, Nasrallah, N, Bouzaza, A, Maachi, R, Wolbert, D (2019) 'Photocatalytic treatment of petroleum industry wastewater using recirculating annular reactor: comparison of experimental and modeling', Environ. Sci. Pollut. Res., 26, pp. 19035 - 19046.

Rajesh, R, Hariharasubramanian, Dominic, Y and 8, Phosphorus, Sulfur (2012) 'Chicken bone as a bioresource for the bioceramic (hydroxyapatite)', and Silicon Relat. Elem., 187, pp. 914-925.

Ramesh, S, Loo, Z, Tan, C, Kelvin Chew, W, Ching, Y, Tarlochan, F, Chandran, H, Krishnasamy, S, Bang, L and Sarhan, A (2018) 'Characterization of biogenic hydroxyapatite derived from animal bones for biomedical applications', Ceram. Int., 44, pp. 10525-10530.

Rehman, F, Zhao, C, Jiang, H, Selke, M and Wang, X (2016) 'Photoactivated TiO_2 nanowhiskers and tetra sulphonatophenyl porphyrin normoglycemic effect on diabetes mellitus during photodynamic therapy', J. Nanosci. Nanotechnol., 16, pp. 12691-12694.

Rehman, F, Zhao, C, Wu, C, Li, X, Jiang, H, Selke, M and Wang, X (2016) 'Synergy and translation of allogenic bone marrow stem cells after photodynamic treatment of rheumatoid arthritis with tetra sulfonatophenyl porphyrin and TiO_2 nanowhiskers', Nano Res., 9, pp. 3305-3321.

Reis, R, Dhawle, R, Du Pasquier, D, Tindall, A, Frontistis, Z, Mantzavinos, D, de Witte, P and Cabooter, D (2023) 'Electrochemical degradation of 17α-ethinylestradiol: transformation products, degradation pathways and in vivo assessment of estrogenic activity', Environ. Int., 176, article 107992.

Rocha, R, Honorio, L, Bezerra, R, Trigueiro, P, Duarte, T, Fonseca, M, Silva-Filho, E and Osajima, J (2022) 'Light-activated hydroxyapatite photocatalysts: new environmentally- friendly materials to mitigate pollutants', Minerals, 12, article 523.

Rocha, R, Morais, A, Araujo, F, Honorio, L, Silva, M, Furtini, M, Vieira, E, da Silva-Finho, E and Osajima, J (2025) 'Enhanced photocatalytic performance of TiO_2@Er-Hydroxyapatite composite for cationic dye and drug removal', Am. Chem. Soc., 10, pp. 5351-5361.

Rovani, S, Censi, M, Pedrotti Jr, S, Lima, É, Cataluña, R and Fernandes, A (2014) 'Development of a new adsorbent from agro-industrial waste and its potential use in endocrine disruptor compound removal', J. Hazard. Mater., 271, pp. 311-320.

Sadrieh, N, Wokovich, A, Gopee, N, Zheng, J, Haines, D, Parmiter, D, Siitonen, P, Cozart, C, Patri, A, McNeil, S, Howard, P, Doub, W and Buhse, L (2010) 'Lack of significant dermal penetration of titanium dioxide from sunscreen formulations containing nano- and submicron-size TiO_2 particles', Toxicol. Sci., 115, pp. 156-166.

Sahoo, T and Prelot, B (2020) 'Chapter 7 - Adsorption processes for the removal of contaminants from wastewater: the perspective role of nanomaterials and nanotechnology. Nanomaterials for the detection and removal of wastewater pollutants', 7th Ed., Elsevier, pp. 161-222.

Salma-Ancane, K, Stipniece, L and Irbe, Z (2016) 'Effect of biogenic and synthetic starting materials on the structure of hydroxyapatite bioceramics,', Ceram. Int., 42, pp. 9504-9510.

Sanseverino, J, Gupta, R, Layton, A, Patterson, S, Ripp, S and Saidak, L (2005) 'Use of Saccharomyces cerevisiae BLYES Expressing Bacterial Bioluminescence for Rapid, Sensitive Detection of Estrogenic Compounds', Appl. Environ. Microbiol., 71, pp. 4455-4460.

Sassoni, E, D'Amen, E, Roveri, N, Scherer, G and Franzoni, E (2018) 'Photocatalytic hydroxyapatite-titania nanocomposites for preventive conservation of marble', Conf. Ser.: Mater. Sci. Eng., 364, article 012073.

Scala-Benuzzi, M, Takara, E, Alderete, M, Soler-Illia, Schneider, R, Raba, J and Messina, G (2018) 'Ethinylestradiol quantification in drinking water sources using a fluorescent paper based immunosensor', Microchem. J., 141, pp. 287-293.

Scanlon, D, Dunnill, C, Buckeridge, J, Shevlin, S, Logsdail, A, Woodley, S, Catlow, R, Powell, M, Palgrave, R, Parking, I, Watson, G, Keal, T, Sherwood, P, Walsh, A and Sokol, A (2013) 'Band alignment of rutile and anatase TiO_2', Nature Mater., 12, pp. 798-801.

Shakeel, M, Jabeen, F, Shabbir, S, Asgar, M, Khan, M and Chaudhry, A (2015) 'Toxicity of nano-titanium dioxide (TiO_2-NP) through various routes of exposure: a review', Biol. Trace Elem. Res., 172, pp. 1-36.

Shaltout, A, Allam, M and Moharram, M (2011) 'FTIR spectroscopic, thermal and XRD characterization of hydroxyapatite from new natural sources', Spectrochim. Acta - Part A Mol. Biomol. Spectrosc., 83, pp. 56-60.

Shanika-Fernando, M, Wimalasiri, A, Dziemidowicz, K, Williams, G, Koswattage, K, Dissanayake, D, Nalin de Silva, K and de Silva, R (2021) 'Biopolymer based nanohydroxyapatite composites for the removal of fluoride, lead, cadmium and arsenic from water', ACS. Omega., 6, pp. 8517-8530.

Sheng, G, Qiao, L and Mou, Y (2011) 'Preparation of TiO_2/Hydroxyapatite composite and its photocatalytic degradation of methyl orange', J. Environ. Eng., 137, pp. 611-616.

Shi, H, Magaye, R, Castranova, V and Zhao, J (2013) 'Titanium dioxide nanoparticles: a review of current toxicological data', Part. Fibre Toxicol., 10, article 15.

Shi, X, Wu, S, Yang, C, Li, L, Li, H, Jiang, F and Luo, L (2023) 'Understanding the synergistic adsorption-photocatalytic degradation of EE2 using ZnO/Bi_2MoO_6 {0 1 0}', J. Alloys and Compd., 968, article 172118.

Singh, A., Ramachandran, S., Gumpu, M., Zsuzsanna, L., Vereb, G., Kertesz, S., Gangasalam, A (2021) 'Titanium dioxide doped hydroxyapatite incorporated photocatalytic membranes for the degradation of chloramphenicol antibiotic in water', J. Chem. Technol. Biotechnol., Vol. 96, pp. 1057 - 1066.

Soares Filho, A, Cruz Filho, J, Lima, M, Carvalho, L, Silva, L, Costa, J, Dantas, T and Luz, G (2018) 'Photodegradation of 17α- ethynylestradiol (EE2) on nanostructured material of type WO_3-SBA-15', Water. Air. Soil. Pollut., 229, article 268.

Song, J, Shi, M, Xia, L, Dai, J, Luo, L, Wang, H, Shu, L and Jiang, F (2023) 'The comparative study on inhibitory effect of natural organic matters on the TiO_2 and activated carbon/TiO_2 composites for the removal of 17α-ethinylestradiol', Chemosphere, 333, article 138930.

Sugita, T, Mori, M, Nakane, H, Mase, A and Itabashi, H (2013) 'Preparation of hydroxyapatite-coated

anatase by photoinduced superhydrophilic reaction of TiO_2 for water purification', Chem. Lett., 42, pp. 209-211.

Sun, K, Ro, K, Guo, M, Novak, J, Mashayekhi, H and Xing, B (2011) 'Sorption of bisphenol A, 17 alpha-ethinyl estradiol and phenanthrene on thermally and hydrothermally produced biochars,', Bioresour. Technol., 102, pp. 5757-5763.

Sun, Q, Zhu, G and Wang, C (2019) 'Removal characteristics of steroid estrogen in the mixed system through an ozone-based advanced oxidation process', Water Air Soil Poll., 230, article 218.

Surenjan, A, Pradeep, T and Philip, L (2019) 'Application and performance evaluation of a cost-effective vis-LED based fluidized bed reactor for the treatment of emerging contaminants', Chemosphere, 228, pp. 629-639.

Svenson, A, Allard, A and Ek, M (2003) 'Removal of estrogenicity in Swedish municipal sewage treatment plants', Wat. Res., 37, pp. 4433-4443.

Swope, R, Smyth, J and Larson, A (1995) 'H in rutile-type compounds: I. Single-crystal neutron and X-ray diffraction study of H in rutile', Am. Mineral., 80, pp. 448-453.

Tang, H, Prasad, K, Sanjinés, R, Schmid, P and Lévy, F (1994) 'Electrical and optical properties of TiO_2 anatase thin films', J. Appl. Phys., 75, pp. 2042-2047.

Tang, Y, Zhang, M, Nawaz, S, Tian, X, Wang, H and Wang, J (2021) 'TiO_2 hierarchical nano blooming-flower decorated by Pt for formaldehyde detection,', Nanotechnology, 32, article 365601.

Tang, Z, Liu, Z, Wang, H, Dang, Z and Liu, Y (2021) 'Occurrence and removal of 17α-ethynylestradiol (EE2) in municipal wastewater treatment plants: Current status and challenges', Chemosphere, 271, article 129551.

Teoh, M, Ng, C, Lee, K, Singh, R, Chuah, Y, Lim, Y, Tan, C and Yeo, W (2023) 'Synthesis and characterization of chicken bone derived hydroxyapatite incorporating pectin,', Chem. Eng. Technol., 46, pp. 2504-2512.

Theodorakopoulos, G, Arfanis, M, Sanchez-Perez, J, Aguera, A, Aponte, F, Markellou, E, Romanos, G and Falaras, P (2023) 'Novel pilot-scale photocatalytic nanofiltration reactor for agricultural wastewater treatment', Membranes, 13, article 202.

Torres, N. H, Aguiar, M. M, Ferreira, L. F, Américo, J. H, Machado, A. M and Cavalcanti, E. B (2015) 'Detection of hormones in surface and drinking water in Brazil by LC-ESI-MS/MS and ecotoxicological assessment with Daphnia magna', Environ. Monit. Assess., 187, article 379.

Trelleborg (2024) Eccospheres Data Sheet SID-350z Microspheres.

Ulfyana, D, Anugroho, F, Sumarlan, D and Wibisono, Y (2018) 'Bioceramics synthesis of hydroxyapatite from red snapper fish scales biowaste using wet chemical precipitation', IOP Conf. Ser. Earth Environ. Sci., 131, article 012038.

Vella, K (2018) Commission Implementing Decision (EU) 2018/840. Official Journal of the European Union.

Vigneshwaran, S, Sirajhudeen, P, Nabeena, C and Meenakshi, S (2021) 'In situ fabrication of ternary TiO_2 doped grafted chitosan/hydroxyapatite nanocomposite with improved catalytic performance for the removal of organic dyes: experimental and systemic studies', Colloids Surf. A, 611, article 125789.

Wahab, G, Gouda, M and Ibrahim, G (2019) 'Study of physical and mechanical properties for some of Easter Desert dimension marble and granite utilized in building decoration', Ains. Shams. Eng. J., 10, pp. 907-915.

Wan, L, Han, J, Tian, W, Li, N, Chen, D and Lu, J (2023) 'Barium titanate - covalent organic framework core-shell nanoparticles for adsorption-enhanced piezo-photocatalysis', Chem. Eng. J., 462, article 142324.

Wang, J, He, B and Kong, X (2015) 'A study on the preparation of floating photocatalyst supported by

hollow TiO_2 and its performance', Appl. Surf. Sci., 327, pp. 406-412.

Wang, J, Li, C, Luan, X, Li, J, Wang, B, Zhang, L, Xu, R and Zhang, X (2010) 'Investigation on solar photocatalytic activity of TiO_2 loaded composite: TiO_2/Skeleton, TiO_2/Dens and TiO_2/HAP', J. Mol. Catal. A Chem., 320, pp. 62-67.

Wang, R, Ren, D, Xia, S, Zhang, Y and Zhao, J (2009) 'Photocatalytic degradation of bisphenol A (BPA) using immobilized TiO_2 and UV illumination in a horizontal circulating bed photocatalytic reactor (HCBPR)', J. Hazard. Mater., 169, pp. 926-932.

Wei, W, Li, J, Liu, Z, Yang, X, Naraginti, S, Xu, X and Wang, X (2018) 'Visible light photocatalytic mineralization of 17α-ethinyl estradiol (EE2) and hydrogen evolution over silver and strontium modified TiO_2 nanoparticles: mechanisms and phytotoxicity assessment,', RSC. Adv., 8, pp. 4329-4339.

Wu, V, Tang, S and Uskoković, V (2018) 'Calcium phosphate nanoparticles as intrinsic inorganic antimicrobials: the antibacterial effect', ACS Appl. Mater. Interfaces, 10, pp. 34013-34028.

Xiao, Q, Zhang, Y, Bi, S, Wu, Y and Yang, S (2024) 'Optimized synthesis of cysteine functionalized nanocrystallione hydroxyapatite for synchronous decontamination of Cd(II) and Pb(II)', J. Environ. Chem. Eng., 12, article 111734.

Xu, G, Wang, T, Shen, C, Zhou, J, Wan, B, Forouzanfar, T, Lin, H and Wu, G (2023) 'In-vitro physicochemical characterisation of a novel type of bone defect-filling granules=BpNcCaP in comparison to deproteinized bovine bone (Bio-Oss)', Nano. Transmed., 2, article 9130016.

Xu, M, Huang, C, Lu, J, Wu, Z, Zhu, X, Li, H, Xiao, L and Luo, Z (2021) 'Optimizing Adsorption of 17-alpha-Ethinylestradiol from Water by Magnetic MXene Using Response Surface Methodology and Adsorption Kinetics, Isotherm and Thermodynamics Studies', Molecules, 26, article 3150.

Xu, W, Yan, W, Huang, W, Miao, L and Zhong, L (2014) 'Endocrine-disrupting chemical in the Pearl River Delta and coastal environment', Environ. Geochem. Health., 36, pp. 1095-1104.

Yamamoto, H and Liljestrand, H.M (2004) 'Partitioning of selected estrogenic compounds between synthetic membrane vesicles and water: effects of lipid components', Environ. Sci. Tech., 38, pp. 1139-1147.

Yang, L, Zhu, Y, He, G and Tao, J (2022) 'Multifunctional photocatalytic filter paper based on ultralong nanowires of the calcium-alendronate complex for high performance water purification', ACS Appl. Mater. Interfaces, 14, pp. 9464-9479.

Yao, J, Zhang, Y, Wang, Y, Chen, M, Huang, Y, Cao, J, Ho, W and Lee, S (2017) 'Enhanced photocatalytic removal of NO over titania/hydroxyapatite (TiO_2/HAp) composites with improved adsorption and charge mobility ability', RSC Adv., 7, article 24683.

Yasir, M, Sopik, T, Lovecka, L, Kimmer, D and Sedlarik, V (2022) 'The adsorption kinetics, and interaction of various types of estrogen on electrospun polymeric nanofiber membranes', Nanotechnology, 33, article 075702.

Yasir, M, Šopík, T, Patwa, R, Kimmel, D and & Sedlaříš, V (2022) 'Adsorption of estrogenic hormones in aqueous solution using electrospun nanofibers from waste cigarette butts: Kinetics, mechanism, and reusability', EXPRESS Polym. Lett., 16, pp. 624-648.

Yoon, Y, Westerhoff, P, Snyder, A and Esparza, M (2003) 'HPLC-fluorescence and adsorption of bisphenol A, 17 beta-estradiol and 17-alpha estradiol on powdered activated carbon', Wat. Res., 37, pp. 3530-3537.

Yu, Y, Zhu, Y, Qi, C and Wu, J (2017) 'Hydroxyapatite nanorod-assembled hierarchical microflowers: rapid synthesis via microwave hydrothermal transformation of $CaHPO_4$ and their application in protein/drug delivery,', Ceram. Int., 43, pp. 6511-6518.

Zhang, B, Cao, S, Du, M, Ye, X, Wang, Y and Ye, J (2019) 'Titanium dioxide (TiO_2) mesocrystals: synthesis, growth mechanisms and photocatalytic properties,', Catalysts, 9, article 91.

Zhang, H, Cui, D, Wang, B, Han, Y, Balimane, P, Yang, Z, Sinz, M and Rodrigues, A (2007) 'Pharmacokinetic drug interactions involving 17alpha-ethinylestradiol: a new look at an old drug', Clin. Pharmacokinet., 46, pp. 133-157.

Zhang, J, Liu, J, Peng, Q, Wang, X and Li, Y (2021) 'Co-doped TiO_2 nanostructures for visible-light photocatalytic hydrogen production', Adv. Energy Mater., 11, article 2002643.

Zhang, Q and Li, C (2020) 'Effect of water to methanol ratio on the structural, optical and photocatalytic properties of titanium dioxide thin films prepared by mist chemical vapour deposition', Catal. Today, 358, pp. 172-176.

Zhang, Q and Li, C (2020) 'High Temperature Stable Anatase Phase Titanium Dioxide Films Synthesized by Mist Chemical Vapor Deposition', Nanomaterials, 10, article 911.

Zhang, Q, Wu, M and Zhao, W (2005) 'Electroless nickel plating on hollow glass microspheres', Surf. Coat. Tech., 192, pp. 213-219.

Zhang, X and Yates, M (2018) 'Enhanced Photocatalytic Activity of TiO_2 Nanoparticles Supported on Electrically Polarized Hydroxyapatite', ACS Appl. Mater. Interfaces, 10, pp. 17232-17239.

Zhang, X, Yin, Y, Sun, Z, Du, Y, Ma, S and Wu, Y (2016) 'Cr/S/TiO_2-Loaded hollow glass microspheres as an efficient and recyclable catalyst for the photocatalytic degradation of indigo carmine under visible light', Quim. Nova, 39, pp. 956-961.

Zhang, Y, Venugopal, J, El-Turki, A, Ramakrishna, S, Su, B and Lim, C (2008) 'Electrospun biomimetic nanocomposite nanofibers of hydroxyapatite/chitosan for bone tissue engineering', Biomaterials, 29, pp. 4314-4322.

Zhang, Z, Feng, Y, Liu, Y, Sun, Q, Gao, P and Ren, N (2010) 'Kinetic degradation model and estrogenicity changes of EE2 (17a-ethinylestradiol) in aqueous solution by UV and UV/H_2O_2 technology', J. Hazard Mater., 181, pp. 1127-1133.

Zheng, J, Hu, M and Zhu, L (2021) 'Removal behaviours of aerobic granular sludge on estrogens: adsorption kinetics and removal mechanism', J. Wat. Pro. Eng., 44, article 102410.

Zhou, H, Yang, M, Hou, S, Ni, X, Bi, Y, Wang, W, Kutty, M and Yang, L (2017) 'Tailoring the morphological features of hydrothermally synthesized mesoporous hydroxyapatite using polyphenols and phosphate sources,', Ceram. Int., 43, pp. 12851-12856.

Zhou, H, Zhou, Y, Li, H and Wang, F (2012) 'Fate and removal of endocrine-disrupting compounds', Water Environ. J., 26, pp. 435-444.

Zhou, X, Wei, J, Liu, K, Liu, N and Zhou, B (2014) 'Adsorption of Bisphenol A Based on Synergy between Hydrogen Bonding and Hydrophobic Interaction', Langmuir, 30, article 13861.

Zogheib, L, Della Bona, A, Tomomitsu Kimpara, E and Mccabe, J (2011) 'Effect of hydrofluoric acid etching duration on the roughness and flexural strength of a lithium disilicate-based glass ceramic', Braz. Dent. J., 22, pp. 45-50.